



Method Development of New Chemically Sensitive Detectors for Size Exclusion Chromatography

Zur Erlangung des akademischen Grades eines
DOKTORS DER NATURWISSENSCHAFTEN
(Dr. rer. nat.)

von der KIT-Fakultät für Chemie und Biowissenschaften
des Karlsruher Instituts für Technologie (KIT)

genehmigte
DISSERTATION

von
M.Sc. Carlo Bennet Botha
aus Paarl, Südafrika

Dekan\Referent:	Prof. Dr. Manfred Wilhelm
Korreferent:	Prof. Dr. Wolf-Gerald Hiller (TU Dortmund)
Tag der mündlichen Prüfung:	18. Februar 2021

Die vorliegende Arbeit wurde von Juni 2017 bis November 2020 unter der Betreuung von Herrn Prof. Dr. Manfred Wilhelm am Institut für Technische Chemie und Polymerchemie (ITCP) des Karlsruher Institut für Technologie (KIT) - Universitätsbereich angefertigt.

Ich versichere hiermit wahrheitsgemäß, die Arbeit selbstständig verfasst, alle benutzten Hilfsmittel vollständig und genau angegeben, und alles kenntlich gemacht zu haben, was aus Arbeiten Anderer unverändert oder mit Abänderungen entnommen wurde, sowie die Satzung des KIT zur Sicherung guter wissenschaftlicher Praxis in der jeweils gültigen Fassung beachtet zu haben. Darüber hinaus versichere ich, dass die in der Arbeit verwendeten Ergebnisse in dem vom Prüfungsausschuss festgelegten Zeitraum der Arbeit entstanden sind.

Carlo Bennet Botha

Karlsruhe, den 08. März 2021.

...Vir my liefste vrou, Marilize Botha.

"He who loves practise without theory is like a sailor who boards ship without a rudder and compass and never knows where he may cast."

- Leonardo da Vinci

Abstract

Polymers are becoming more complex, as their end-use is increasingly more sophisticated. Knowledge on the structure-property relationships is crucial in understanding their micro- and macroscopic behaviour. This facilitates the need for more advanced characterization techniques, where molecular spectroscopy hyphenated to size exclusion chromatography (SEC) is one approach to meet the demand.

In this thesis, the development of new on-line chemically sensitive characterization techniques for polymer analysis, in combination with SEC, was realized. These hyphenations to SEC consisted of benchtop NMR ($F = 60$ MHz, $B_0 = 1.45$ T, ^1H Larmor frequency) and EC-QCL (in the mid-IR range) spectrometers. These spectrometers present new possibilities of overcoming the limitation of chemically sensitive detection in liquid polymer chromatography through its high level of polymer detail with respect to molar mass and chemical composition. The combined set-ups allow for the simultaneous two-dimensional measurement and correlation of the molar mass distribution as a function of the chemical composition. In addition, a proof of principle related to a novel sinusoidal injection approach for SEC to enhance the sensitivity without pre-concentration steps is demonstrated.

Hyphenating spectroscopy to SEC introduces certain intrinsic problems such as: (1) relatively low sample concentration after chromatographic separation ($c < 0.5$ g/L), thus low signal-to-noise (S/N) ratios; (2) strong solvent signal overlapping in regions of interest for the analyte (factor of ≥ 1000), especially with the use of non-deuterated solvents; and (3) complex infrastructure for high field NMR. Therefore, the full optimization of the hyphenated benchtop NMR and selective optimization of the EC-QCL spectrometer to SEC with reference to sensitivity, selectivity and solvent signal suppression is of importance and presented. For the SEC-NMR hyphenation, solvent (CHCl_3 and THF) signal suppression of a factor of up to 500 is achieved by means of T_1 -selective pulse sequences and post data acquisition numerical subtraction methods. Substantial improvements with respect to sensitivity (S/N up to 260 for PMMA, $-\text{OCH}_3$) and selectivity (FWHM < 5 Hz on-line) was achieved compared to previous work. Typical homopolymers, blends and copolymers are investigated, characterizing their composition related to molar mass and chemical composition. The SEC-EC-QCL hyphenation has a unique sensitivity, allowing for the on-line detection limit of an injected mass of 0.5 μg (considering the carbonyl stretch of PMMA), which is in the range of a factor of ca. 30 lower than that reported for SEC-FTIR hyphenation. These results validate the potential of the new hyphenated chromatography methods, which can greatly facilitate qualitative and quantitative polymer

analyses. Furthermore, sinusoidal SEC injection, compared to that of conventional SEC injection (normalized to the acquisition time), had an overall improvement in S/N of a factor of 70. This enhancement illustrates the potential to be exploited with for example benchtop NMR hyphenation to SEC, where sensitivity is always a challenge.

Zusammenfassung

Polymere werden durch anspruchsvollere Endanwendungen zunehmend komplexer. Kenntnisse über die Struktur-Eigenschafts-Beziehungen sind entscheidend für das Verstehen ihres mikro- und makroskopischen Verhaltens. Dies fördert den Bedarf an fortschrittlicheren Charakterisierungstechniken. Ein Ansatz hierzu ist die Molekülspektroskopie gekoppelt mit der Größenausschlusschromatographie (engl. size exclusion chromatography, SEC).

In dieser Dissertation wurden neue chemisch sensitive on-line Charakterisierungstechniken für die Polymeranalyse mit der SEC entwickelt. Dabei wurde ein benchtop Kernmagnetresonanzspektrometer (engl. nuclear magnetic resonance, NMR) ($F = 60$ MHz, $B_0 = 1.45$ T, ^1H Larmor Frequenz) sowie ein external cavity quantum cascade laser (EC-QCL), mit mittlerem IR Bereich, mit der SEC gekoppelt. Dieser Aufbau ermöglicht die simultane zwei dimensionale Messung und korrelation der molaren Masse als Funktion der chemischen Zusammensetzung. Durch diese detaillierten Informationen über das Polymer werden neue Möglichkeiten in der chemisch sensitiven Detektion in der flüssigen Polymerchromatographie eröffnet. Zusätzlich dazu wurde der Machbarkeitsbeweis des Ansatzes einer neuartigen sinusförmigen Injektionsmethode in der SEC gezeigt, um die Sensitivität ohne Aufkonzentrierung der Probe zu erhöhen.

Die Kopplung mit der SEC bringt intrinsische Probleme mit sich, wie: (1) eine relativ geringe Probenkonzentration nach der chromatographischen Trennung ($c < 0.5$ g/L), und ein geringes Signal zu Rausch Verhältnis (engl. signal-to-noise ratio, S/N), (2) starke Lösungsmittelsignale, welche mit den Analytsignalen überlappen, sowie (3) eine komplizierte Infrastruktur für hochfeld NMR. Aufgrund dessen wurde eine vollständige Optimierung der SEC-NMR Kopplung und eine selektive Optimierung der SEC-EC QCL Kopplung in Bezug auf die Sensitivität, Selektivität und der Lösungsmittelsignalunterdrückung durchgeführt. Bei der SEC-NMR Kopplung wurde eine Lösungsmittelsignalunterdrückung, für die Lösungsmittel CHCl_3 und THF, um den Faktor von bis zu 500 durch T_1 -selektive Pulssequenzen und numerische Subtraktionsmethoden nach der Datenerfassung erreicht. Substantielle Verbesserungen der Sensitivität (S/N von bis zu 260 für PMMA, $-\text{OCH}_3$) und der Selektivität (full width at half maximum < 5 Hz on-line) wurden, verglichen mit zuvor geleisteten Arbeiten, erzielt. Typische Homopolymere, Polymermischungen und Copolymere wurden untersucht und deren Zusammensetzung in Bezug auf die molare Masse und chemische Zusammensetzung charakterisiert. Die SEC-EC-QCL Kombination besitzt mit einem on-line Detektionslimit von $0.5 \mu\text{g}$ injizierte Masse (unter Berücksichtigung der Carbonyl-Bande von PMMA), welches um den Faktor von etwa 30 tiefer liegt als bei

den bisherigen SEC-Fourier-Transform-Infrarotspektrometer Kopplungen, eine einzigartige Sensitivität. Diese Ergebnisse bestätigen das Potential zur erleichterten Polymeranalyse von kombinierten chromatographischen Methoden. Daneben führt die Methode der sinusförmigen Injektion, verglichen mit der herkömmlichen SEC-Injektionsmethode, zu einer Gesamtverbesserung des S/N, normiert zur Messzeit, um den Faktor von 70. Aufgrund dieser Verbesserung eignet sich diese Methode auch zur Anwendung bei der SEC-NMR Kopplung, bei welcher die Empfindlichkeit üblicherweise eine Herausforderung darstellt.

Contents

Abstract	vi
Zusammenfassung	viii
1 Introduction	1
1.1 Introduction and Motivation	1
1.2 Research Objectives	5
2 Theoretical Perspectives	6
2.1 Liquid Chromatography (LC) of Polymers	6
2.1.1 Introduction	6
2.1.2 Theoretical Considerations of Polymer Chromatography	8
2.1.3 Size Exclusion Chromatography (SEC)	9
2.1.4 Separation Mechanism	9
2.1.5 Molar Mass Distribution of Polymers	13
2.1.6 Band broadening and Separation Efficiency	14
2.1.7 Detectors in Liquid Chromatography	18
2.2 Nuclear Magnetic Resonance (NMR) Spectroscopy	20
2.2.1 Introduction	20
2.2.2 Quantum Mechanical Considerations of the NMR Phenomenon	21
2.2.3 Interactions in NMR Spectroscopy	26
2.2.4 Magnetization, Pulsed NMR, and Relaxation	28
2.2.5 Medium-Resolution (MR) NMR spectroscopy	32
2.2.6 NMR Spectroscopy in a Flowing Liquid	38
2.2.7 Design Considerations of NMR Flow Cells	41
2.3 Quantum Cascade Lasers (QCL)	43
2.3.1 Introduction	43
2.3.2 Fundamentals and Operating Principle	46
2.4 Advanced Digital Data Evaluation	49
2.4.1 Introduction	49
2.4.2 Signal, Noise and Sensitivity	50
2.4.3 Digital Signal Processing	53

3	Hyphenation of Chromatography and Spectroscopy: Information-Rich Detectors	56
3.1	Introduction	56
3.2	Fourier Transform Infra-Red (FT-IR) Spectroscopy	57
3.3	Mass Spectrometry (MS)	58
3.4	High-Field and Benchtop NMR Spectroscopy	59
3.5	Quantum Cascade Lasers (QCLs)	60
4	SEC-NMR Method Development: Optimization of Selectivity and Sensitivity	62
4.1	Introduction	62
4.2	Flow Cell Development for SEC-MR-NMR Hyphenation	64
4.2.1	Introduction	64
4.2.2	Design	65
4.2.3	Benchmark Experiment	67
4.2.4	Application to SEC-NMR	72
4.3	Optimization of SEC Conditions	75
4.3.1	Introduction	75
4.3.2	Column Selection	75
4.3.3	Overloading	79
4.3.4	Flow Rate and Flow Cell Optimization	82
4.4	Optimization of NMR parameters	88
4.4.1	Introduction	88
4.4.2	Pulse Calibration	89
4.4.3	Acquisition Length and Repetition Time (Recycle Delay)	93
4.4.4	Receiver Gain	97
4.4.5	Pulse Sequences for Solvent Suppression	99
4.5	Numerical Solvent Suppression	109
4.5.1	Introduction	109
4.5.2	TMDE Stand-Alone Application	109
4.5.3	Apodization and Zero-filling	112
4.5.4	Phase correction	117
4.5.5	Smoothing: SEC Dimension	119
4.5.6	Reference/Solvent Subtraction	121
4.5.7	Baseline Correction: SEC Dimension	125
4.6	Application Examples of SEC-NMR Hyphenation	127
4.6.1	Introduction	127
4.6.2	Physical Blend Identification	129
4.6.3	Block Copolymer Analysis	132
4.6.4	Sensitivity Limits	146
4.6.5	Industrial Polymer Application	149
4.7	Standard Operating Procedure (SOP): SEC-MR-NMR	156

5	EC-QCL Instrument Evaluation	158
5.1	Introduction	158
5.2	EC-QCL Instrumental Set-up	160
5.2.1	Introduction	160
5.2.2	Pulse-mode Operation, Tuning Range, and Specifications	161
5.3	Selective Optimization of Measurement Parameters	164
5.3.1	Introduction	164
5.3.2	Column Selection	165
5.3.3	Pulse Averaging	166
5.3.4	Timing Irregularities	168
5.4	Numerical Data Treatment	171
5.4.1	Introduction	171
5.4.2	Baseline Correction and De-noising	174
5.5	Sensitivity Limits	177
5.5.1	Introduction	177
5.5.2	LOD and LOQ Determination	177
5.6	EC-QCL as Potential SEC detector	179
5.6.1	Introduction	179
5.6.2	Homopolymers and Blends	179
5.6.3	Functionalized Homopolymer	181
6	Novel SEC method for S/N Enhancements	185
6.1	Introduction	185
6.2	Interlaced SEC Injections	187
6.3	Proof of Principle: Novel Sinusoidal SEC Injections	191
7	Conclusion and Outlook	200
	Acknowledgement	205
	Nomenclature	208
	Trigonometric Identities	211
	List of Figures	211
	List of Tables	215
	Bibliography	217
	Appendices	231
A.1	TMDE GUI Documentation	231
A.2	QCL GUI Documentation	252
A.3	Technical Drawing	267
A.4	Pulse Sequences	268

A.4.1	1HMonitor_1Pulse-spoil_V3_CB	268
A.4.2	1HMonitor_IvR-spoil_V3_CB	270
A.5	Hardware Photos	273
A.6	Hardware Description	277
A.6.1	SEC System	277
A.6.2	Benchtop NMR Spectroscopy System	278
A.7	Materials Description	280
Publications & Conference Contributions		282

Chapter 1

Introduction

The continuous advancement of synthetic polymers, and their commercial relevance, facilitates the ever-evolving structure-property relationships, and the growing interest to understand their macroscopic behaviour in terms of the properties of individual molecules. This requires the development of more advanced analytical approaches as characterization techniques. The following section provides a brief overview of the origin of synthetic polymers, the idea behind the research, its relevance, including the outline of the thesis layout.

1.1 Introduction and Motivation

Throughout the history of humankind, there has always been a dependence on certain resources to advance as a species. According to archaeological studies, certain materials rise to the top, of which the major historical material stages can loosely be classified into the Stone-, Bronze-, and Iron-ages. This allowed for systematic advancements of the species, for example, the stone age enabled humans to control fire and make sharp objects, whereas the Bronze age resulted in trading networks, for material exchange such as metals and other goods. The iron age saw the development of cheaper tools, enabling the establishment of more permanent settlements. However, one important material that has always been around in the natural world and played a significant role, are polymers, which include: wood, starch, cotton, silk and rubber. These have been used for many years without truly understanding what they really are. The accidental discovery of natural rubber vulcanization by Charles Goodyear in 1839^[1] catapulted synthetic polymers into the success story they are today and can be marked as the beginning of the next material stage - the plastic age. It has become an indispensable part of everyday life. This year, 2020, marks an important anniversary, as 100 years ago Hermann Staudinger, a professor at the University of Karlsruhe between 1907–1912 in the field of organic chemistry, postulated the theory that polymers are long-chained covalently bonded macromolecules comprising monomers, in his 1920 publication 'Über Polymerisation'.^[2,3] It is the work and ideas of Staudinger that gave life to the field of polymer and macromolecular chemistry. The first fully synthetic polymers

commercially produced were polyvinyl chloride (PVC) and Bakelite, a phenol-formaldehyde resin. The development of the Ziegler-Natta catalysts enabled the large scale production of α -olefins in the mid-20th century, such as polyethylene (PE), specifically high density PE, and tactic polypropylene (PP), mainly isotactic-PP. It is only after this that fully synthetic polymers truly started and became readily available. As of 2018,^[4] the worldwide production of plastics was roughly 360 Mt/a, with the European demand contributing to 51.2 Mt/a, and Germany having the highest demand in the European Union of 24.6%. This amounted to a turnover of 360 billion euros for the European plastics industry in 2018. This is a testament to the great economic importance of polymer chemistry, further explaining the need for research in this field.

The most important bulk polymers are PE, PP, PVC, polyurethanes (PU), polyethylene terephthalate (PET), and polystyrene (PS).^[4] These are mostly homopolymers, and their structure-property relationships are determined by the chemical composition (CC) of the repeating monomer units, physical interactions between specific chains, the chain length, and topology. The interest in polymers as materials is ascribed to their ease in moldability and variety in material properties. To improve these aspects or develop speciality plastics, a deeper understanding of the molecular structure of the polymer, and its relation to macroscopic behaviour, is required. The enhancement of a polymer's properties is typically achieved by either blending it with various other homopolymers, co-polymerizing different monomers to form block copolymers, or functionalizing it with specific functional groups. Performing property enhancements typically increase the complexity of the material, generating multicomponent materials, and facilitating the need to understand how the macroscopic behaviour is influenced in terms of the properties of individual molecules. To correlate and describe these molecular structure-property relationships, powerful analytical tools and the development thereof, are essential. "Complex" polymers are defined as heterogeneous in more than one distributed property, e.g. even linear copolymers are distributed in both molar mass and chemical composition. The material properties considered to be important for a polymer can vary significantly, however, they can be characterized into three main molecular parameters: (1) chemical composition (CC), (2) molar mass (MM), and (3) functionality and topology distributions. Consequently, the applications of polymers are not only determined based on their chemical composition, but frequently their distribution of the physico-chemical parameters.^[5, p. 1] Adequately understanding and monitoring these distributions aid in the improvement of polymer performance, and the ability to predict long-term behaviour. Separation science in conjunction with powerful spectroscopic techniques are important tools for the determination of polymer distributions. A brief summary of different characterization techniques commonly used for polymer analysis is given in **Table 1.1**.

The molecular information obtainable by the various techniques in Table 1.1, can truly be exploited when combining some of them. This will not only provide information on an individual parameter, but rather on multiple parameters and their interrelation. Information on the polymer chain length, i.e. molar mass distribution, is always of importance as it dictates a major part of the processing application and performance,

Table 1.1: Summary of polymer parameters, application properties, and characterization techniques.^[5, p. 2]

Polymer parameter	Application properties	Characterization technique ^a
Molar mass distribution	Elongation, tensile strength, adhesion, viscosity, processing	Liquid chromatography, SEC
Chemical composition	Solubility, biodegradability, chemical resistance	Spectroscopy, e.g. NMR, IR, MS
Topology	Viscosity, flow, diffusion	SEC-MALLS-VISC
Copolymer sequence	Miscibility, rigidity	SEC-spectroscopy, gradient-LAC, 2D-LC

^a SEC: size exclusion chromatography, NMR: nuclear magnetic resonance spectroscopy, IR: infrared spectroscopy, MS: mass spectrometry, MALLS: multi-angle laser light scattering, VISC: viscometry, LAC: liquid adsorption chromatography, 2D-LC: two dimensional liquid chromatography, i.e. LAC-SEC

and is commonly characterized via liquid chromatographic techniques, with size exclusion chromatography (SEC) being the most popular technique. The fundamental principle of liquid chromatography and various spectroscopic detectors used with it, are detailed in **Chapter 2** (p. 6). In SEC, species are separated based on their hydrodynamic volume in solution followed by analytical detection. The standard detectors used in SEC, i.e. refractive index-, UV-, light scattering-, or viscometry detectors, are generally only sensitive to changes in the bulk properties, and are thus limited in providing information on the chemical composition of a homopolymer, blend or copolymer. To circumvent this problem, hyphenating liquid chromatography with chemically sensitive spectroscopic detectors, such as Fourier transform infrared (FTIR)- or nuclear magnetic resonance (NMR) spectroscopy, is an attractive approach. These hyphenated methods provide the molar mass distribution as a function of the chemical composition. The off-line hyphenation of SEC and FTIR has been reported in literature.^[6] It is however, more convenient to perform hyphenation measurements on-line. Consequently, a variety of on-line approaches capable of providing all the relevant information in a 'one-shot' experiment, such as SEC-FTIR,^[7] SEC hyphenated to IR quantum cascade lasers (QCL),^[8] and SEC-NMR at high fields ($F > 300$ MHz, $B_0 > 7.05$ T),^[9] have been reported, and **Chapter 3** (p. 56) provides a literature review on these. Due to the high investment cost, required expertise, designated laboratory space required for high field NMR equipment, and size as detector for liquid chromatography, it is unfavourable in a standard set-up. This led to the approach of replacing high field with low field ($F < 100$ MHz, $B_0 < 2.35$ T) NMR spectrometers, with the first proof of concept reported by Cudaj et al.^[10] on a 20 MHz benchtop NMR spectrometer. Due to the low field strength and lack of sensitivity, it was at the time not possible to perform on-line SEC-NMR measurements without severely compromising the integrity of the SEC separation. The technological advancements in permanent magnet design, especially the Halbach array set-up,^[11,12] within the last decade has allowed for a major improvement in field homogeneity,

enabling improved spectral resolution for medium resolution (MR, $F = 40\text{--}100$ MHz) class NMR instruments. The benefits of these spectrometers are its ease in maintenance (no N_2 and He liquid cooled gasses required), small size, and relatively low investment cost.^[13] With these advances, the question of possibly hyphenating NMR to SEC and using this as detector for SEC was revisited in the working group of Prof. M. Wilhelm, using a new generation medium resolution benchtop NMR spectrometer. The successful hyphenation of a MR-NMR spectrometer at 62 MHz to SEC was achieved, without compromising the integrity of the liquid chromatographic separation.^[14,15] Hyphenating spectroscopy to SEC induces certain intrinsic problems, such as: (1) low sample concentration (c) after chromatographic separation ($c \ll 1$ g/L), resulting in low signal-to-noise (S/N) ratios and, (2) strong solvent signal overlap in regions of interest for the analyte, especially with the use of non-deuterated solvents.

The aim of this work is to fully optimize the hyphenated benchtop SEC-MR-NMR with reference to sensitivity, selectivity, flow cell development, and solvent signal suppression, and will be presented in **Chapter 4** (p. 62). In addition to SEC-MR-NMR hyphenation, the evaluation of an external cavity quantum cascade laser (EC-QCL) comprising different mid-IR light sources was performed, and is presented in **Chapter 5** (p. 158). As EC-QCL has a major improvement in sensitivity compared to a standard FTIR spectrometer, as shown by Morlock et al.^[8] The first results on this prototype EC-QCL hyphenated to SEC have recently been reported by Kübel et al.^[16] The major advantage of this QCL is that it typically has a factor of 10^4 more photons per wavenumber, but with a limited bandwidth ($\tilde{\nu} = \sim 200$ cm^{-1}). The increased sensitivity provides the potential for detection of rare (trace) groups or end-group analyses in conjunction with SEC.

With SEC's poor efficiency (i.e. throughput),^[17] new developments in the field of liquid chromatography for sensitivity enhancement without pre-concentration steps are subject to modern research.^[18] One such an example is an approach called interlaced SEC injections, which instead of the conventional one injection per measurement route, performs multiple timed sequential injections before the total elution of the first injection. This can enhance separation throughput by as much as a factor of 2, and was first illustrated by Farnan et al.^[19] The idea behind this approach was used to develop a new injection technique, sinusoidal SEC, which is based on a periodic oscillating input signal to increase the sensitivity per time unit. This input signal is achieved by using techniques from HPLC, where a solvent and analyte gradient table is constructed and fed into the SEC, creating a sinusoidal concentration gradient of the sample. As a result of the sinusoidal nature of the response signal of the sinusoidal chromatogram, a discrete Fourier transformation (DFT) can be applied. This transformed signal is then used to determine the respective phase-angles of species with different molar masses, and to determine the S/N . The proof of principle is presented in **Chapter 6** (p. 185), with its potential use with the benchtop NMR spectrometer, to enhance S/N .

1.2 Research Objectives

The main objectives of this study were the following:

SEC-MR-NMR method development

- The development of custom flow cells for the hyphenation of NMR to SEC, and allowing for the optimum performance with respect to S/N and peak-shape retention.
- The optimization of SEC to allow for the maximum amount of analyte transferred to the NMR for detection, whilst retaining the separation integrity. The main optimization parameters include: (1) the SEC column selection, (2) control of column overloading, and (3) flow rate.
- The optimization of the NMR parameters to obtain the highest possible S/N , due to the inherent restriction in field strength of the benchtop NMR spectrometer. The optimization parameters include the following: (1) pulse length calibrations, (2) acquisition length, (3) receiver gain, and (4) pulse sequences for solvent suppression.
- The development of post data acquisition processing software, to focus on the following: (1) apodization and zero-filling, (2) phase-correction, (3) filtering in the SEC dimension, (4) references and solvent subtraction, and (5) baseline correction in the SEC dimension.
- The evaluation of the developed method when applied to polymer application, including a look at the system limits.

SEC-EC-QCL Evaluation

- The optimization of selected measurement parameters that would enable the first test as potential detector for SEC, which includes: (1) column and flow cell selection, (2) pulse averaging, and (3) timing irregularities.
- The development of post-processing of acquired data, considering baseline correction and de-noising for S/N enhancement.
- Exploring the technique as potential chemically sensitive detector for SEC by applying it to application examples, including a look at the system limits.

Proof of principle: Novel Sinusoidal-SEC injections

- The development of a new liquid chromatographic approach to enhance the sensitivity.

Chapter 2

Theoretical Perspectives

2.1 Liquid Chromatography (LC) of Polymers

The forthcoming section will provide an overview of the theoretical aspects related to the use of liquid chromatography as analytical technique for the characterization of polymers. It will then go into more detail on one of the separation mechanisms found in liquid chromatography, i.e. size exclusion chromatography (SEC), and elaborate on the more technical aspects related to this separation mechanism, and ending with the type of detectors typically employed in liquid chromatography.

2.1.1 Introduction

High performance liquid chromatography¹ (HPLC) is one of the most powerful fractionation tools available to the modern day polymer analyst. This can be ascribed to its high sample throughput, accuracy, and versatility. Different operational modes allow the characterization of a variety of polymer properties, such as molar mass (MM), chemical composition (CC), functionality or molecular architecture. High performance liquid chromatography is mainly employed as a separation tool, where the fundamental principles for separation in any liquid chromatographic (LC) technique are based on the selective distribution of analytes between the stationary and mobile phases. Separation results in different retention times for the components in a given sample. An analytes' retention time is governed by its adsorption or partition equilibria between the mobile and stationary phases. This distribution is defined by the distribution (or partition) coefficient, K_d :^{[22, p. 25][23, p. 19]}

$$K_d = \frac{C_{SP}}{C_{MP}}, \quad (2.1.1)$$

where C_{SP} and C_{MP} are the concentrations of the analyte in the stationary- and mobile-phase, respectively. In liquid chromatography the separation process can be described by

¹Chromatography is also one of the oldest separation techniques, although officially found in 1900 by Mikhail Tsvet,^[20] earlier reports in the book of Exodus in the Bible describes how Moses turned bitter water into drinkable water by casting a certain tree into a fountain, which is the basis of ion-exchange chromatography.^[21, Ex. 15:23–25]

the following equation:

$$V_e = V_i + V_p K_d, \quad (2.1.2)$$

where V_e is the retention volume of the solute, V_i is the interstitial column volume, and V_p is the pore volume of the packing, better defined as the stationary phase volume. The distribution coefficient (K_d) of the analyte, in both the mobile- and stationary phases, is thermodynamically related to the difference in the Gibbs free energy (ΔG).^{[23, p. 19][24, p. 33][5, p. 7]} The change in the Gibbs free energy can arise from both the change in the enthalpic (ΔH) and entropic (ΔS) contributions. This is due to interaction of the analyte with the stationary phase and limited pore dimension that restricts the analyte to occupy all possible conformations, respectively. The dependence of the distribution coefficient on these contributions can be expressed as follows:

$$\Delta G = \Delta H - T\Delta S = -RT \ln K_d, \quad (2.1.3)$$

where

$$\Delta G = G_{stationary} - G_{mobile}.$$

After rearrangement, $\ln K_d$ can be expressed as

$$\ln K_d = \frac{\Delta G}{-RT} = \frac{\Delta S}{R} - \frac{\Delta H}{RT}, \quad (2.1.4)$$

where ΔG is the difference in Gibbs free energy, ΔH and ΔS are the changes in enthalpy and entropy, respectively, T is the absolute temperature, and R is the universal gas constant ($R \approx 8.314 \text{ J/mol.K}$). The change in the Gibbs free energy may be a result of the following: (1) the pores of the stationary phase, having limited dimensions, restricts the possible conformations of the macromolecule, and as a result will decrease the conformational entropy (ΔS); and (2) when the analytes enter the pores of the stationary phase, they may have an affinity for the pore walls, and result in a change in the enthalpy (ΔH).^[25,26] Depending on the choice of the chromatographic system and chemistry of the analyte, either entropic or enthalpic interactions or even both may occur. The general case for the distribution coefficient can be expressed as follows:

$$K_d = K_{SEC} K_{LAC}, \quad (2.1.5)$$

where K_{SEC} and K_{LAC} is the distribution coefficients for size exclusion chromatography (SEC) and liquid adsorption chromatography (LAC) referring to the entropic and enthalpic interactions, respectively. If the contribution of either the entropic or enthalpic interactions overrides the other, the overriding interaction will determine the overall operational mode. For example, if entropic contributions are the dominating factor, the size exclusion mode will dominate the separation mechanism. It is also possible to express the retention volume (or elution volume, V_e) in a time- instead of a volume-scale, since the retention time, t_R , is

related to the elution volume, V_e , by the flow rate value of the mobile phase, \dot{v} , as shown in **Equation 2.1.6**

$$t_R = \frac{V_e}{\dot{v}}. \quad (2.1.6)$$

Although both the retention-time and -volume can be used in analyte retention determination, it is more convenient to use the retention volume (V_e). The retention volume enables the direct comparison of results obtained on the same chromatographic system but at different flow rates. This becomes particularly useful when comparing results obtained from a one-dimensional chromatographic system with a two-dimensional chromatographic system. The different operational modes in HPLC consist of *Size Exclusion Chromatography (SEC)*, *Liquid Adsorption Chromatography (LAC)* and *Liquid Chromatography at Critical Conditions (LC-CC)*, which all depend on the choice of the mobile and stationary phases as well as the temperature. The modes differ with regard to their dependence of the elution volume on molar mass (see **Figure 2.1**).

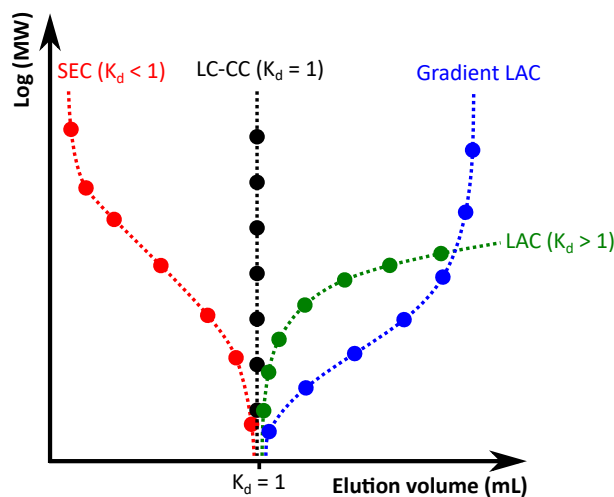


Figure 2.1: Depiction of the chromatographic behaviour related to the elution volume dependence on the molar mass of the different operational modes in HPLC, i.e. SEC, LC-CC, LAC and gradient LAC (using a solvent gradient ramp).^[5, p. 10]

In the forthcoming sections the SEC operational mode will be discussed with regard to its basic principles and potential as polymer analysis tool.

2.1.2 Theoretical Considerations of Polymer Chromatography

The retention/retardation of species in liquid chromatography can mainly be described in terms of the distribution coefficient related to the partition function of a given polymeric species. The latter occurs between that of the mobile and stationary phase within the column, corresponding to the interstitial column volume, V_i , i.e. the volume occupied by the solvent outside the porous particles of the stationary phase, and the pore volume, V_p , defined by

$$K = \frac{V_e - V_i}{V_p}. \quad (2.1.7)$$

The various different regimes in liquid chromatography, in which the distribution coefficient may assume different values, is classified in terms of the adsorption interaction parameter, c_{int} , introduced by de Gennes.^{[27][5, p. 17]} It is measured in inverse length ($c_{int} = \text{nm}^{-1}$) and strongly depends on the composition of the chromatographic system, i.e. mobile and stationary phase composition, including the temperature.^[5, p. 17]

2.1.3 Size Exclusion Chromatography (SEC)

Chromatography techniques can be subdivided into a variety of different methods depending on the composition of the solute, mobile, and stationary phase, as these would dictate the dominating separation mechanism. The focus within this work was on one of the most widely used techniques, size exclusion chromatography, due to its simplicity in combination with various detectors and the information provided with respect to polymers, namely the molar mass distribution. This is of great importance in understanding the structure-properties relationships. The technique was developed in the late 1950s by G. H. Lathe and C. R. Ruthven.^[28,29] However, it was not possible to fractionate synthetic high molar mass polymers until 1964, as explained in the work published by J. C. Moore.^[30] The stationary phase comprised a cross-linked polystyrene network with a well defined pore size distribution, which inevitably led to an increase in research activity in the field.^[30] Following this development, the technique evolved into one of the most widespread techniques for the characterization of the molar mass and molar mass distribution of synthetic polymers.^[31–35]

2.1.4 Separation Mechanism

In SEC the separation of the species are based on their size in solution (hydrodynamic volume, V_H).^[36] The hydrodynamic volume ($V_H \propto [\eta] \cdot M$) of a given molecule is related to its radius of gyration (R_g), which can differ with respect to the shape of hydration, and is directly proportional to the molar mass and molar mass distribution. The stationary phase consists of a rigid structure containing porous particles with a defined pore size distribution. The space among the particles and pores is saturated with a mobile phase.^[37] The sample/analyte is introduced into the system via an injection in the form of a dilute solution (concentration $\ll 1\text{g/L}$) in the same solvent used for the mobile phase, into chromatographic columns that are continuously being flushed with the mobile phase. This should preferably be a thermodynamically good solvent for the polymer under investigation, in order to limit any non-exclusion effects, e.g. minimizing any form of enthalpic interaction between the analyte and stationary phase. Finally, the concentration of analyte eluting from the column is detected on-line by a concentration sensitive detector, most commonly a differential refractive index (DRI) detector, see **Section 2.1.7**. The separation of a given molecular size range is governed by the pore size and pore size distribution of the packed stationary phase particles. The analyte permeates into the respective pores; smaller molecules can occupy more space and permeate deeper into more pores, as opposed to larger molecules which are excluded from the pores with an effective size smaller than that of the molecule. As a result, larger molecules exit the chromatographic column first followed by molecules of decreasing hydrodynamic volume in solution (see **Figure 2.2**).

Consequently, two limits exist in SEC: (1) the total exclusion limit and (2) total permeation limit, which correspond to the largest and smallest molecules, respectively. These limits are dictated by the particle size, pore size and pore size distribution of the stationary phase. This separation principle is generally accepted and referred to as *steric exclusion*, and is also the major separation mechanism in SEC. The main separation mechanisms present in SEC are; (1) steric exclusion, (2) restricted diffusion and (3) separation by flow.

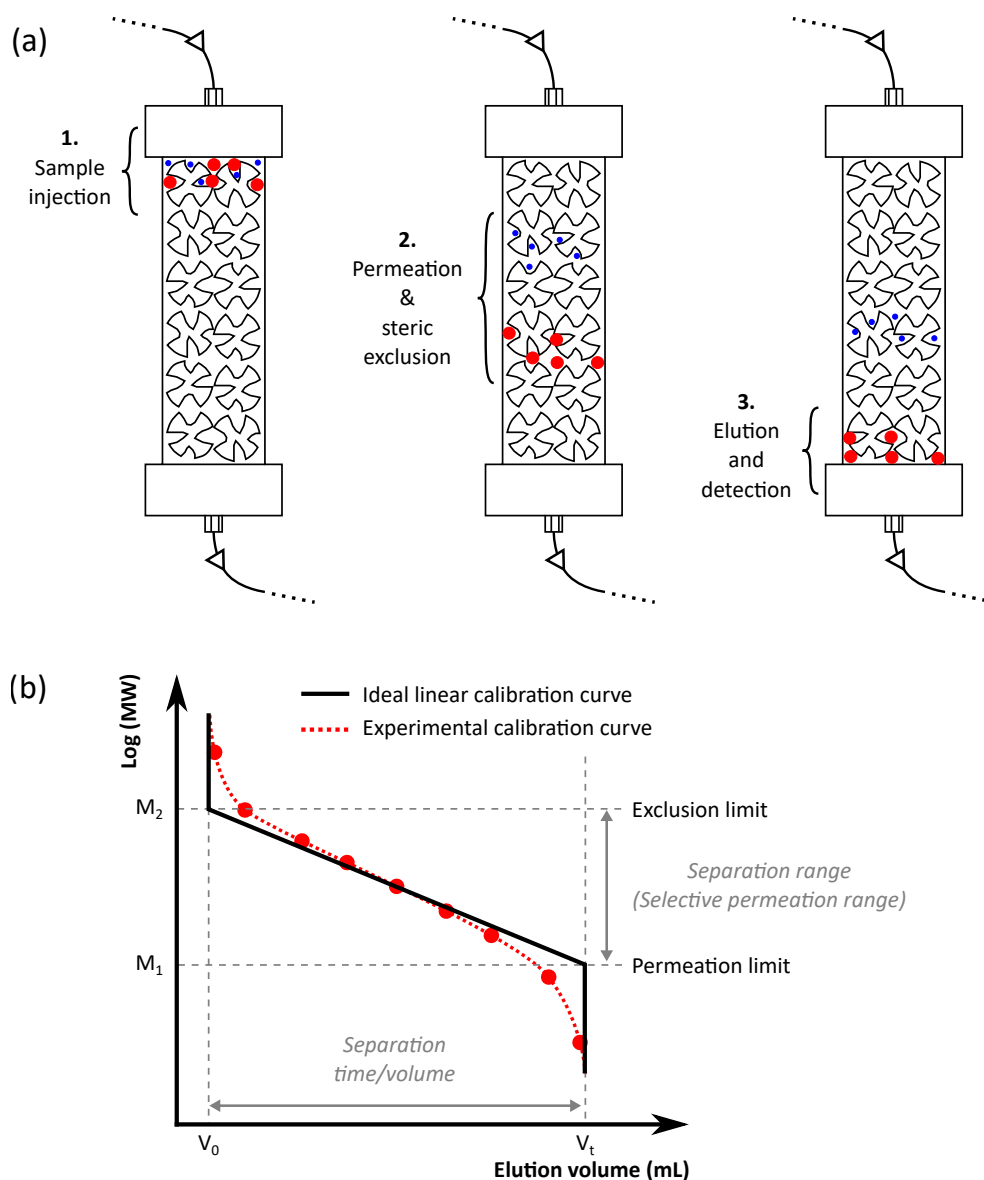


Figure 2.2: Schematic depiction of the (a) separation/fractionation of molecules with different hydrodynamic volumes in solution by the porous stationary phase. There are three main steps involved: (1) sample introduction via injection, (2) the permeation and steric exclusion of the different molecules, and (3) the elution and detection of fractionated molecules. (b) Depiction of the separation ranges, ideal and experimental calibration curves of SEC.^[38] Molecules consisting of a hydrodynamic volume above that of the total exclusion limit will only access the total outer volume, V_0 , of the column. Below the permeation limit, molecules penetrate all available volume, i.e. the outer column volume including the pore volume, V_t , as a result no fractionation occurs. Molecules consisting of a hydrodynamic volume between V_0 and V_t will be eligible for effective separation.^[39]

Size exclusion chromatography is governed predominantly by entropic contributions. Considering an ideal SEC separation mechanism, the only contributing factor would be that of the entropic contribution, as it can be assumed that there are no enthalpic contributions present. This would result in a separation which will be solely governed by the hydrodynamic volume of the molecules, excluding any additional interactions between the analyte and stationary phase (i.e. $\Delta H = 0$). Therefore, the distribution coefficient in ideal SEC can be described by

$$K_{SEC(ideal)} = \exp\left(\frac{\Delta S}{R}\right),$$

where (2.1.8)

$$\Delta S = S_{stationary} - S_{mobile}.$$

The entropy, S , is a measure of the total degree of disorder of the given system, defined by

$$S = k_B \ln \Omega,$$
(2.1.9)

where k_B is the Boltzmann constant and Ω is defined as the number of equally probable micro-molecular states.^[40, p. 5] The relative probability of both small and larger molecules to access an individual pore size, larger than that of the molecule size, is depicted in **Figure 2.3**.

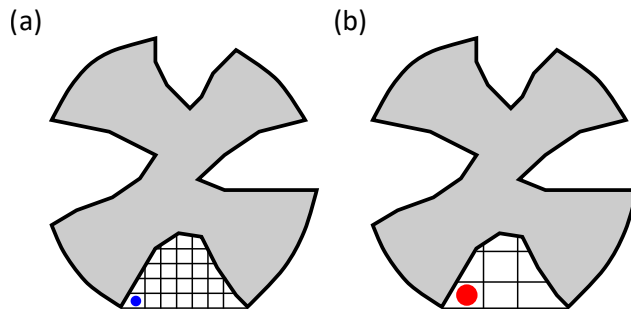


Figure 2.3: Depiction of the entropy related to molecule retention in a porous particle in SEC. In (a) smaller molecules have a larger probability to occupy equally probable states than that of (b) larger molecules.^[40, p. 5]

Taking **Figure 2.3** into consideration, the total number of possibilities in which the individual molecule can occupy space within the given pore volume is defined by the number of grid positions allowed, which represents the individual conformational states. As can be seen the smaller molecule has a larger possibility of equally probable states (in turn possessing a larger entropy) than that of the larger molecule, therefore, spending more time within the pore volume and as a result being retained longer. Since the total number of equally probable states within the pore volume is still much smaller than that of the interstitial column volume for a given molecule, the process of permeation in SEC causes a decrease in entropy.^[40, p. 5] In SEC, the interaction parameter is strongly negative, $\Delta S < 0$, resulting in the distribution coefficient ranging from $0 < K_{SEC} < 1$. The separation in 'ideal' SEC is also temperature independent, considering **Equation 2.1.8**. The smaller the

molecular size, the more pore volume they can penetrate and the longer they are retained in the porous stationary phase. This is due to a less severe change/loss in the conformational entropy and easier re-establishment of the thermodynamic equilibrium. It is, therefore, clear from the distribution coefficient that larger molecules will not be retained as much as their smaller counterparts, and will in some cases be completely excluded from the porous particles, due to a too severe change/loss in conformational entropy and unfavourable thermodynamic equilibria. As a result these molecules will be eluted first followed by decreasing molecular size (see **Equation 2.1.2**). Typically, the experimental conditions in SEC allow for the establishment of a diffusion equilibrium and, consequently, steric exclusion is usually the dominant separation mechanism. In contrast to other variations of liquid chromatography, where the elution volumes can reach very high values in SEC is limited by the interval $V_0 - V_t$, where

$$V_t = V_0 + V_i \quad (2.1.10)$$

is the total volume occupiable by the mobile phase in the column, and V_0 is the total volume of the mobile phase outside the pores, also known as the total exclusion limit. The effective volume of an SEC column in which molecules can elute is typically in the range $0.4V_c - 0.8V_c$, where V_c , is the volume of the column and is defined by

$$V_c = V_0 + V_i + V_g, \quad (2.1.11)$$

where V_g is the total volume occupied by the solid stationary phase. Consequently, due to the limited elution volume range in SEC, the selectivity of SEC is lower than that of other types of liquid chromatography. The distribution coefficient is independent of the length and internal diameter of the chromatographic column, but depends on the pore size and pore size distribution of the stationary phase material. Considering that this property of the distribution coefficient allows for a good comparison between the results obtained by employing different stationary phases under different experimental conditions, it is rarely used and the retention volume itself is typically used to construct SEC chromatograms. The remaining two types of separation mechanisms in SEC, restricted diffusion and separation by flow, are not used as frequently as steric exclusion but still should be taken into consideration. In restricted diffusion, the separation mechanism is based on the idea that the time required for macromolecules to permeate/diffuse in and out of the available pore volume is comparable to the total time spent within a given column zone/volume. This means that the permeation depth is governed by the diffusion coefficient of the polymer in solution, which scales with the molecular size. In other words the large molecules will only penetrate slowly into the available pores and as a result will not penetrate into the entire available volume, therefore, not fully occupying the given chromatographic zone. The principle of restricted diffusion therefore implies that the retention volume is dependent on the applied flow rate, which is generally not true. However, this principle is partially dominating the separation of high molar mass ($MM > 1\,000$ kg/mol) polymers at high flow rates ($\dot{v} > 0.5$ mL/min). Separation by

flow, also referred to as hydrodynamic chromatography, is based on the premise of the flow of the mobile phase through narrow capillaries with a parabolic flow profile. This occurs when the chromatographic column is packed not with porous particles but rather with solid non-porous particles, creating a capillary system as a result of void formation between these particles. There exists an exclusion volume (defined above) for a given molecule at/close to the channel walls, dictated by its geometrical dimensions. Looking back at Figure 2.3 (p. 11) and considering that larger molecules are statistically more frequently outside the pore volume of the particle than its smaller counterpart, it is fair to conclude that with non-porous particles they will be closer to the capillary centre. This will allow for a faster flow through the system and, therefore, elute earlier than that of smaller molecules which can be situated closer to the capillary walls where the flow velocity is slower. This phenomenon of separation by flow is more prone to take place at regions of high molar masses ($MM > 1\,000\text{ kg/mol}$). The latter is the reason why the determination of a chromatographic systems' total exclusion limit is not always as straightforward to conduct.^{[33, p. 43][37][35, p. 104]}

It is important to note that ideal SEC separates polymers with respect to their molecular dimensions, inadvertent of the functionality present.^[5, p. 18]

2.1.5 Molar Mass Distribution of Polymers

In general, polymers are mixtures of macromolecules (of the same chemistry) comprising different chain lengths, i.e. hydrodynamic volumes in solution. Typical synthetic polymers do not comprise a single molecular mass present but rather a collective molecular mass distribution (MMD), which in turn can be characterized by means of the different statistical moments of the distribution.^[33, p. 77] In order to measure the molar mass (MM) in SEC, it is typically calibrated with well defined, narrowly distributed polymer standards (calibration standards).^[38] While this is the simplest and most widely used technique for system calibration, it is generally restricted by the availability of calibration standards.^{[40, p. 13][41,42]} From the resulting chromatograms, there are typically two widely used unique types of average molar masses calculated; the number-average molar mass (\overline{M}_n) and weight-average molar mass (\overline{M}_w). Additionally, these values can be determined by light scattering (M_w) or colligative methods such as osmometry (M_n). The number-average molar mass is the ordinary arithmetic MM of the polymeric chains and the weight-average molar mass is the average MM of the polymeric chains, and are defined in the following equations:

$$\overline{M}_n = \frac{\sum n_i \cdot M_i}{\sum n_i} \quad (2.1.12)$$

and

$$\overline{M}_w = \frac{\sum n_i \cdot M_i^2}{\sum n_i \cdot M_i}, \quad (2.1.13)$$

where n_i is the number of molecules of a certain chain length and M_i is its molar mass. Apart from these two average molar masses, there exist two more that are used less frequently, but are equally important, the Z-average molar mass (\overline{M}_z) and viscosity-average

molar mass, (\overline{M}_η). The Z-average molar mass, which is classically determined by means of sedimentation equilibrium methods, provides insight into the longer chains present in a mixture of macromolecules and described by

$$\overline{M}_z = \frac{\sum n_i \cdot M_i^3}{\sum n_i \cdot M_i^2}. \quad (2.1.14)$$

The Z-average, of the radius of gyration can also be determined by more advanced methods such as static light scattering or X-ray scattering.^[43,44] Finally, the viscosity average molar mass, as the name suggests, is determined by dilute solution viscometry, and described by

$$\overline{M}_\eta = \left(\frac{\sum n_i \cdot M_i^{1+\alpha}}{\sum n_i \cdot M_i} \right)^{1/\alpha}, \quad (2.1.15)$$

where α is the Mark-Houwink exponent and at first approximation is close to \overline{M}_w . The molar mass distribution (MMD) refers to a functional relationship which describes the number of moles of each polymeric chain (n_i), having a given molar mass (M_i), but the MMD is typically simplified to the dispersity index, \mathcal{D} (formerly poly dispersity index, PDI, but now deprecated by IUPAC).^[45] It is calculated from the number-average and weight-average molar masses obtained by SEC, and is fundamentally a measure for the width of the distribution. A dispersity index equal to one, indicating a uniform species (e.g. proteins), would refer all polymer chains being of the same length and molar mass, i.e. sample uniformity. Therefore, the dispersity is a measure of the heterogeneity of chain lengths (hydrodynamic volume) of molecules in a mixture. The dispersity index is defined by

$$\mathcal{D} = \frac{\overline{M}_w}{\overline{M}_n}. \quad (2.1.16)$$

It is also not possible to obtain a dispersity index value of less than one, since $M_w \geq M_n$, resulting in $\mathcal{D} \geq 1$. Consequently, the higher the dispersity index value, the broader the molar mass distribution. Taking the various molar masses obtainable by SEC into consideration, **Figure 2.4** depicts an idealized probability of these molar masses as a function of the retention/elution volume. It should be noted that the molar mass at peak maxima, M_p , is frequently used as specification for calibration standards. However, $M_n \approx M_p$ and is only valid in cases for symmetrical distributions.

In order to bypass the use of calibration standards to obtain absolute molar mass information, a molar mass sensitive detector, e.g. a multi-angle laser light scattering (MALLS) detector, can be utilized to determine the absolute molar masses and molar mass distributions of polymeric species.

2.1.6 Band broadening and Separation Efficiency

In liquid chromatography, a very dilute sample concentration ($c \ll 1$ g/L) is introduced into the chromatographic system ideally as a narrow rectangular analyte band. As the analyte band migrates through the column, it experiences fractionation of the different molecular sizes and additional analyte dilution resulting in (1) an increase in band width,

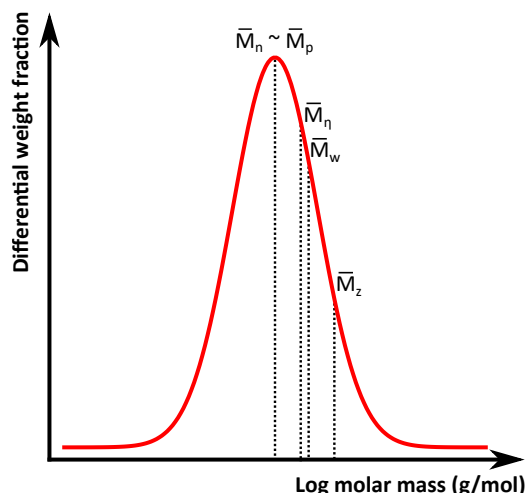


Figure 2.4: Illustration of an idealized symmetrical SEC distribution indicating where the typical molar mass averages would fall in the molar mass distribution of a polymeric species, including: $\bar{M}_n \approx \bar{M}_p < \bar{M}_w < \bar{M}_z$.^{[33, pp. 10, 53–55][35, pp. 105–112]}

and (2) a reduction in signal intensity at the point of elution. These effects are visually represented in **Figure 2.5**.^[40, pp. 12–14]

The effect of band broadening on pure, low D compounds can be utilized to determine the *separation efficiency* of the chromatographic system. Band broadening is a crucial parameter in liquid chromatography as it has a negative effect on the chromatographic *resolution*. Liquid chromatography is fundamentally a deconvolution process, in relation to the separative transport relative to the dispersive transport.^{[33, pp. 65–74][35, pp. 105–112]} It systematically fractionates the different molecular sizes within a polymeric species as it elutes from the column into separated peaks. However, band broadening has the inverse effect: it re-convolutes the different molecular size fractions resulting in overlap and finally spreading out the eluting peaks. The latter makes the analysis of both the peak identification and peak-size challenging.^{[33, pp. 64–74][35, pp.105–112]} The effect of band broadening is especially critical in the determination of accurate relative molar mass distribution information

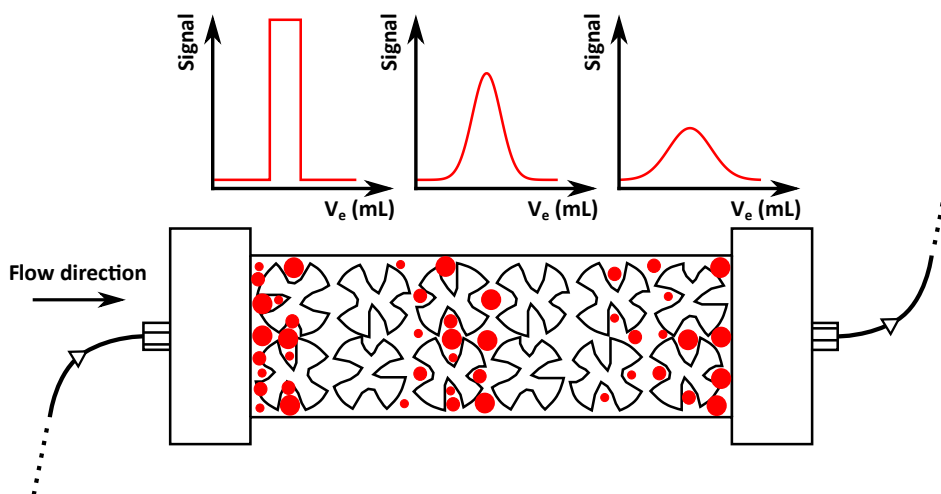


Figure 2.5: Depiction of band broadening within the chromatographic column, showcasing how fractionation and sample dilution affects the peak width and signal intensity. The initial injection represents an ideal delta-like analyte band profile.

(i.e. using a calibration curve). A small deviation in the SEC peak shape, as a result of band broadening, has large molar mass errors, especially for narrowly distributed systems. Therefore, it is important to minimize system band broadening (i.e. excessive extra-column volume, which is controllable by the chromatographer) as much as possible in order to ensure improved separation efficiency and high MMD accuracy.^{[33, pp. 64–74][35, p. 108]}

The major contributing phenomenon of band broadening can be divided into three major sources: (1) diffusion along the column, *eddy diffusion*; (2) the resistance of solute to *mobile and stationary phase mass transfer*; and (3) the void volume (also known as the dead volume) of the chromatographic system. For a detailed review on these phenomena refer to the following references.^{[46][33, pp. 81, 86, 359][35, p. 107]} As the chromatographic band broadening phenomenon is defined as a random statistical process of solute mixing, it is subject to statistical analyses. Conventional band broadening parameters are derived from a Gaussian peak-shape function, as it is the best model to approximate the peak shapes obtained in SEC,

$$G_d = \frac{A_{\text{int}}}{\sigma\sqrt{2\pi}} \cdot e^{-\frac{(V - V_e)^2}{2\sigma^2}}, \quad (2.1.17)$$

where G_d is the detector response, A_{int} is the peak integral area, σ the standard deviation of the Gaussian peak and V and V_e is the elution volume and elution volume at the peak apex. The standard deviation describes the peak width/broadness of the chromatographic peak. Typically, the width at the baseline, W_b , or full width at half maximum, $W_{1/2}$, is also used to characterize peak width and is related to the standard deviation as $W_b = 4\sigma$ and $W_{1/2} = 2.325\sigma$. The band broadening parameters related to the Gaussian peak-shape function are depicted in **Figure 2.6**.

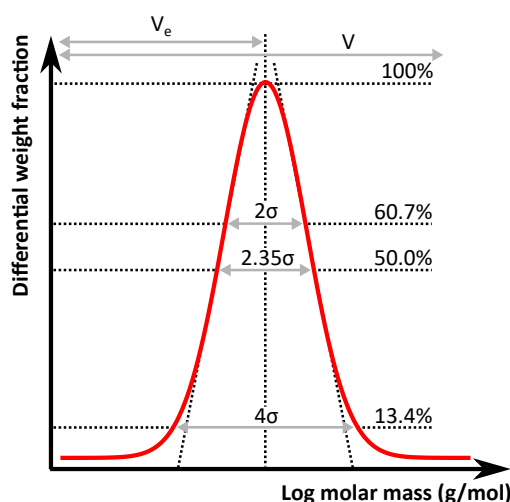


Figure 2.6: The band broadening parameters related to the Gaussian peak-shape function, illustrating the full width at half maximum, $W_{1/2} = 2.35\sigma$, and the base width, $W_b = 4\sigma$, of a chromatographic peak with an ideal Gaussian distribution.^{[46–48][33, p. 53][35, p. 105]}

The degree of both band broadening and separation efficiency of a given chromatographic system can be characterized by means of *plate theory*.^{[33, p. 55][35, p. 107]} It is a phenomenon used to explain band broadening by random fluctuation around the average retention/elution

volume by means of a simulated partition model within a chromatographic column first applied by Martin and Synge.^{[33, p. 55][35, p. 107]} In plate theory the *number of theoretical plates*, N , and the *height equivalent to a theoretical plate (HETP)*, H , are used to quantify these effects. The number of theoretical plates can be determined from a chromatogram using a narrowly dispersed, and preferably low molar mass, compound by employing **Equation 2.1.18**:

$$N = 16 \left(\frac{V_e}{W_b} \right)^2 = 5.54 \left(\frac{V_e}{W_{1/2}} \right)^2, \quad (2.1.18)$$

with the plate height described by

$$H = \frac{L}{N}, \quad (2.1.19)$$

where L is the column length. Both the theoretical number of plates and plate height only applies to isocratic and isothermally generated chromatograms.^[49,50] These two equations can also be used to compare different chromatography columns and packing materials related to band broadening and separation efficiency. The relationship between separation efficiency and parameters defining the separation process was developed by van Deemter et al.^[50] and is expressed as follows:

$$H = A + \frac{B}{\nu} + C \cdot \nu, \quad (2.1.20)$$

where ν is the linear velocity of the mobile phase ($\nu = \text{cm/s}$), A is related to the diffusion along the column (eddy diffusion), B the longitudinal diffusion coefficient and C the mass transfer between the mobile and stationary phases. The higher the value of H the broader the peak and reduced separation efficiency for a given column length. The van Deemter equation defines three fundamental principles which contribute to the chromatographic performance: (1) the solute flow paths through the packing material, or eddy diffusion; (2) longitudinal diffusion as a result of concentration differences in the mobile phase, also referred to as axial diffusion; and (3) resistance to mass transfer due to restricted diffusion speeds in and out of the porous stationary phase that causes band broadening of the analyte band. Therefore, according to the van Deemter equation, there is an optimum linear velocity where the terms add up to provide an optimal (i.e. minimum) plate height (column performance, resolution) as depicted in **Figure 2.7**.

In practice, linear flow velocities slightly higher than ν_{opt} are often used, to have a better compromise between required chromatographic resolution and measurement time. In conclusion the linear flow velocity plays a vital role in band broadening and separation efficiency. It greatly affects the concentration per unit time and in turn the signal response of the detected eluate. The importance of the linear flow velocity will become more apparent in (see **Section 4.2**, p. 64) where the residence time distribution of the eluate will be described in detail.

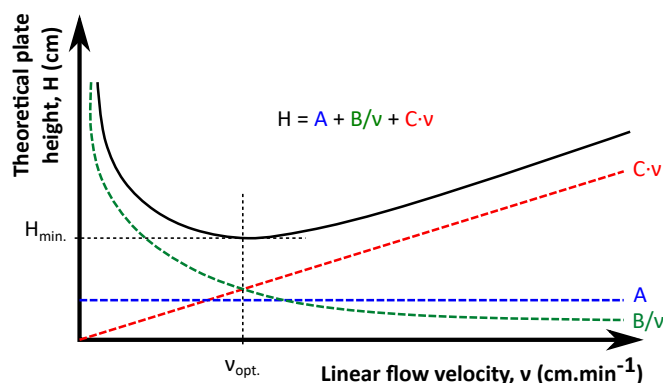


Figure 2.7: Illustration of the van Deemter curve and the effects of the various terms on the theoretical plate height. As seen from the curve, there exists an optimum linear velocity, $\nu_{\text{opt.}}$, where the terms add up to give the lowest point, $H_{\text{min.}}$, of the van Deemter curve. Here the diffusion behaviour of the solutes through the column is at an optimum/minimum and the band broadening is minimized and separation efficiency improved.^[50–52]

2.1.7 Detectors in Liquid Chromatography

The detection techniques used for a sample subjected to liquid chromatography (LC) are one of the most important parts in the separation set-up, since without any means of detection, separation is of little to no use. Detectors are used to monitor the fractions of the molecules of a given solute eluting after chromatographic separation. The main qualities of a good detector should include (but are not limited to) the following: (1) adequate sensitivity, (2) responds to all the solutes or have a predictable preference (selectivity), (3) reliability and robustness, (4) linear response to the solute concentration, and (5) non-destructivity towards the solutes.^[53] In essence, a detector monitors the change in the mobile phase composition as a function of time and converts it into an electrical signal,^{[33, p. 230–289][35, pp. 127–143]} after which it is then further acquired and processed. The response factors of all detectors depend on the chemical composition of an eluate, and so in most cases also on the molecular weight.^[54] In high performance liquid chromatography (HPLC), there are a broad variety of instruments available for the detection of analytes after chromatographic separation. However, only a few are applicable to SEC. The detectors employed for the characterization and identification of polymers can be categorized into two main classes: (1) concentration and (2) molar mass (physical) sensitive detectors, as listed in **Table 2.1**. The most relevant concentration and molar mass sensitive detectors for SEC include: (1) differential refractive index (DRI), (2) ultra-violet (UV), (3) infrared (IR), (4) viscometer, and (5) light scattering detectors.^[33,35,55–60]

Evaluating the two types of detectors in LC, concentration sensitive detectors function on the basis of producing a signal (response) as a function of time, which is determined by the concentration of a given analyte at each time slice eluting from the chromatographic system. One of the most important parameters for concentration sensitive detectors is the *limit of detection*, LOD (LOD), which represents the lowest injected amount detectable under certain chromatographic conditions. These types of detectors are exemplified by DRI-, UV/visible (UV/Vis)-, IR- and evaporative-detectors.^{[33, pp. 231, 240, 281, 437][35, pp. 130–135]} In general, concentration sensitive detectors are the most commonly used detectors in SEC, as

Table 2.1: Categorization of LC detectors according to their applicability.^[5, p. 44]

Concentration Sensitive Detectors ^a		Molar Mass Sensitive Detectors ^b
<i>Selective Detectors:</i>	<i>Universal Detectors:</i>	<i>Viscometers:</i>
UV/Vis	DRI	Single capillary
IR	Conductivity	Differential
QCL ^d	Density	<i>Light Scattering Detectors:</i> LALLS ^d , MALLS, RALLS ^d
Fluorescence ^c	ELSD ^d	
Electrochemical ^c		
¹ H-NMR		

^a The information obtained typically combines in an *additive* fashion.^{[33, p. 230][35]}

^b The information obtained typically combines in an *synergistic* fashion.^{[33, p. 230][35]}

^c These detectors cannot be applied to most polymers.^[5, p. 44]

^d QCL: quantum cascade laser, ELSD: evaporative light scattering detector, LALLS: low-angle laser light scattering, RALLS: right-angle laser light scattering.^[5, p. 44]

they are sensitive enough to meet the minimum detection requirements for the determination of the molar mass-averages and -distribution using Mark-Houwink calibration curves and peak position.^{[33, p. 220][35, pp. 140–143]} Additionally, they are required in multi-detection set-ups where molar mass sensitive detectors, such as viscometer or light scattering (see **Table 2.1**), are employed to determine molar mass relevant information. In general, these types of detectors consist of spectroscopic detectors, which enable the detection of specific functional groups present in a polymeric substance. There are two main subdivisions of concentration sensitive detectors: (1) selective and (2) universal detectors (see **Table 2.1**). Selective detectors are selective towards a specific property of the analyte, such as photometric detectors. The UV/Vis detector is the most frequently used, which is selective towards analytes possessing a *chromophore* absorbing UV or visible light, e.g. due to de-localized π -electrons. Universal detectors, in general, only detect a bulk property of a given mobile phase. Consequently, these detectors provide a concentration specific signal, but are limited in providing information on chemical composition,^[43] with the exception of ¹H-NMR spectroscopy. Therefore, it is imperative to choose a detector or multi-detector set-up (typical for copolymers),^[5, p. 55] which is appropriate for the detection of a given polymeric species. There are two fundamental requirements for using concentration selective detectors: (1) the molecule must contain a functionality towards which the detectors are selective and (2) the molecules' functionality should not absorb in the same wavelength range as the mobile phase.^[5, pp. 44–47]

Molar mass sensitive detectors provide information on the molar mass, as well as the concentration of the analyte as a function of time slice of the polymer peak. Since the signal response is dependent on both the molar mass and concentration, it has to be combined with a concentration sensitive detector in order to determine the MM.^[5, pp. 47–52] These detectors are also less frequently applied to interaction chromatography, i.e. LAC, LC-CC or gradient LAC, since the separation generally occurs via chemical composition and in order to have improved separation- and measurement-efficiency, solvent gradients are frequently applied, making the use of these detectors less feasible. Light scattering

detection allows for the direct determination of the absolute molar mass distribution of a polymer with similar chemical composition.^[5, pp. 47–52] Consequently, these detectors are more frequently applied to SEC instruments, since (1) the need for calibration of concentration sensitive detectors with (limited) calibration standards to obtain molar mass information is not required, and (2) SEC, in general, is conducted with an isocratic mobile phase. In addition, using light scattering detectors with more than one angle, e.g. a multi-angle laser light scattering (MALLS) detector, it is possible to obtain information on the radius of gyration, R_g , of a polymer. The use of a viscosity detector yields the *intrinsic viscosity distribution* of the polymer, however, this is prone to retention errors, yielding incorrect MMD. Thus, the combination of light scattering- and viscosity-detection with a concentration sensitive detector provides the highest accuracy of results, and is also referred to as *triple-SEC detection*,^{[40, p. 20][5, p. 58][34]} which also provides insight on the branching of a polymeric species.^[5, pp. 47–52]

2.2 Nuclear Magnetic Resonance (NMR) Spectroscopy

"I can't explain that attraction in terms of anything else that's familiar to you. For example, if we said the magnets attract like as if they were connected by rubber bands, I would be cheating you. Because they're not connected by rubber bands, I should be in trouble, you soon ask me about the nature of the bands and secondly if we were curious enough, you'd ask me why rubber bands tend to pull back together again, and I would end up explaining that in terms of electrical forces, which are the very things that I'm trying to use the rubber bands to explain, so I have cheated very badly, you see. So I'm not going to be able to give you an answer to why magnets attract each other except to tell you that they do."

– Richard Feynman, 1983 BBC interview - Fun to Imagine

This section is dedicated to nuclear magnetic resonance (NMR) spectroscopy, providing a theoretical overview of the technique, and then focussing on NMR spectroscopy in a flowing liquid with the corresponding technical considerations.

2.2.1 Introduction

Nuclear magnetic resonance (NMR) spectroscopy is the study of the interaction of electromagnetic radiation, in the radio frequency¹ (RF) range of ca. 4 MHz–1.2 GHz,^[61, p. 453] with the magnetic spin moment of atomic nuclei (see **Figure 2.8**).

It is perhaps one of the most important and versatile analytical techniques for structure elucidation of compounds and applied to a variety of research fields. The fascination with NMR spectroscopy, from a purely intellectual point of view, is the complexity of the subject.

¹The radio frequency range relevant for ¹H-NMR spectroscopy is between that of the earth's magnetic field $F \approx 2$ kHz ($B_0 \approx 50$ μ T) and $F = 1.2$ GHz ($B_0 = 28.2$ T).

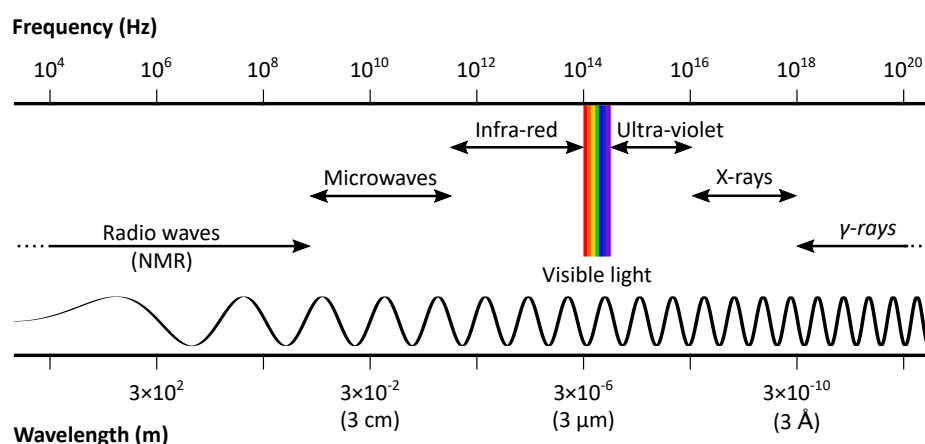


Figure 2.8: Electromagnetic spectrum, illustrating the major categories of electromagnetic waves.

It is this complexity of NMR spectroscopy which is the subject of much frustration to those trying to understand and apply NMR spectroscopy. The reason for many researchers enduring the frustration is the gained 'reward'. Nuclear magnetic resonance spectroscopy provides a plethora of chemical information (depending on the sample composition), such as local environments, i.e. electron density, connectivity and stereochemistry of individual atoms,^[62] including internuclear distances and evidence of molecular interaction.^[63–65] It is also a useful technique for the quantitative determination of absorbing species, and is one of the few analytical techniques which can be applied to species in the gas-, liquid- and solid-phase(s).^[61, p. 453] This section is devoted to provide a basic introduction into the principles of the NMR phenomenon and related terms, representing the minimum knowledge required for a comprehensive read regarding ^1H -NMR and SEC hyphenation. A more in-depth coverage on the principles can be found in the mathematically dominated texts of both Abragam^[66] and Ernst et al.^[67] A good overview of the introduction, background and application can be found in the texts of Derome^[68] and Cavanagh et al.^[69] Within this section, the focus will not only be on conventional solution state NMR spectroscopy, but also on NMR spectroscopy in a flowing liquid.

2.2.2 Quantum Mechanical Considerations of the NMR Phenomenon

In contrast to other spectroscopic techniques, such as UV/Vis and IR spectroscopy, where the outer electrons are involved in the absorption process, in NMR spectroscopy the nuclei of atoms are involved in the absorption process.^[61, p. 453] The most straightforward model to describe the processes in NMR spectroscopy, is the classical vector model of magnetism.^[70, p. 22] It is important to note that the vector model only describes chemical shifts but not spin-spin couplings. The most important information gained from the vector model is that nuclei with a spin $I \neq 0$ have the ability to induce a free induction decay (FID) in a coil, i.e. a magnetic field, by precession in the x/y-plane, i.e. perpendicular to the B_0 field along the z-axis.^[70, p. 131] Nuclear magnetic resonance spectroscopy is based on measuring the magnetic properties (local and global magnetic fields) of atomic nuclei, using those nuclei to further probe the surrounding electron density/structure and other neighbouring nuclei.^[71] In order for this process to occur, the nuclei possess the quantum

mechanical property of *nuclear spin angular momentum*, P , inherited from quarks.^[71,72] The angular momentum of the nuclear spins are described by the *spin quantum number*, I , where the total spin angular momentum is $I\hbar$, with \hbar being Planck's constant. The value of I is an intrinsic property ascribed to a given nucleus. All atomic isotopes with an odd number of protons or neutrons have a non-zero spin quantum number, i.e. $I \neq 0$, making them eligible for NMR spectroscopy. To quantize the maximum angular momentum, the spin quantum number must have an integer or half-integer multiples of $h/2\pi$.^[61, p. 454] The postulation that the angular momentum of a system is quantized, was introduced by Bohr based on the studies on the hydrogen atom.^[70, p. 6] The magnitude of the nuclear spin angular momentum is described by^[72]

$$|P| = \hbar\sqrt{I(I+1)}, \quad (2.2.1)$$

where $\hbar (= h/2\pi)$ is the reduced Planck's constant. Since P is a vector, the orientation must be considered. In an applied external magnetic field, along the z-axis, the possible values related to the z-component of the nuclear spin angular momentum is described by

$$P_z = \hbar m_I, \quad (2.2.2)$$

where the observable magnetic quantum states, m_I , is defined by

$$m_I = I, (I-1), (I-2), \dots, -I. \quad (2.2.3)$$

The four most important nuclei to chemists, ^1H , ^{13}C , ^{19}F and ^{31}P all possess a spin quantum number of $I = \frac{1}{2}$. There are a few simple rules which can be deduced for the possible spin configurations: (1) nuclei with an even mass number have integer spin values, (2) odd mass number nuclei have half-integer spin values, and (3) nuclei with an even number of protons and neutrons have a zero spin value.^[71] Therefore, considering **Equations 2.2.1–2.2.3**, there are two possible values for P_z , which are $+\frac{1}{2}\hbar$ and $-\frac{1}{2}\hbar$. If a single spin configuration is considered, a quantum mechanical formalism is required, since the atomic phenomena do not behave classically.^[70, p. 39] The quantum mechanical formalism is defined by the operator corresponding to its total energy, the Hamiltonian, $\hat{\mathcal{H}}$. The resulting eigenvalues of the operator, including their corresponding superpositions, are the allowed configuration states of the system. Since the subsystems of states, important to NMR spectroscopy, are generally isolated from other molecular states, it is often sufficient to consider isolated spins. Depending on the spin quantum number, the maximum number of discrete spin states possessed by a nucleus is $N_{states} = 2I + 1$.^[61,71–73, p. 454] The eigenfunction describing the different spin states of a nucleus with $I = \frac{1}{2}$, can be defined as $|+\frac{1}{2}\rangle$ or $|-\frac{1}{2}\rangle$.² Since every physical observable has an associated operator, the eigenfunction can be redefined to describe the observed spin state, in this case along the z-axis, as

²In quantum mechanics the ket notation (or Bra-ket notation) is frequently used for quantum states.

$$I_z|m_I\rangle = m_I|m_I\rangle; \quad (2.2.4)$$

$$I_z|+\frac{1}{2}\rangle = +\frac{1}{2}|+\frac{1}{2}\rangle, \quad I_z|-\frac{1}{2}\rangle = -\frac{1}{2}|-\frac{1}{2}\rangle,$$

where I_z is the operator describing the observed nuclear spin angular momentum along the z-axis. This results in an eigenfunction series describing the operators for the nuclear spin angular momentum observed in the x-, y-, and z-axes. In order to determine the energy of the spin system a Hamilton operator is therefore required. The construction of the Hamilton operator can be derived from classical electromagnetism, for the energy of a magnetic moment placed in an applied magnetic field. The magnetic moment of the nuclei, μ , is proportional to the nuclear spin angular momentum and defined by

$$\mu = \gamma P, \quad (2.2.5)$$

where the proportionality constant, γ , is the gyromagnetic ratio, unique to each nucleus. The gyromagnetic ratios for the aforementioned atoms are listed in **Table 2.2**.

Table 2.2: Magnetic properties of the four selected nuclei consisting of a spin quantum number $I = \frac{1}{2}$.^[61, p. 455]

Nucleus	Isotopic abundance (%)	Gyromagnetic ratio (Radians·T ⁻¹ ·s ⁻¹)	Relative sensitivity to ¹ H ^a
¹ H	99.9	2.68×10^8	1.00
¹³ C	1.07	6.73×10^7	0.0159
¹⁹ F	100	2.52×10^8	0.832
³¹ P	100	1.08×10^8	0.0665

^a At a constant magnetic field with equivalent nuclei.^[61, p. 455]

In an applied external magnetic field, B_0 , the magnetic moment of a spin $\frac{1}{2}$ nucleus becomes oriented in one of two directions with respect to the magnetic field, referred to as parallel ($m = +\frac{1}{2}$, lower energy state) and anti-parallel ($m = -\frac{1}{2}$, higher energy state) to the applied magnetic field, depending on its magnetic quantum state. The component of the angular momentum for these states, in any direction, will consist of the positive integer (1, 2, 3, ...) or half-integer multiples ($\frac{1}{2}, \frac{3}{2}, \dots$) of I . The value of I is determined by the lowest energy state (ground state) spin configuration of the protons and neutrons in the nuclei.^[71] The energy associated with the spin states is proportional to the magnetic moment, μ , and the applied external magnetic field, B_0 , and defined as

$$E = -\mu B_0, \quad (2.2.6)$$

after mathematical rearrangement of **Equations 2.2.5** and **2.2.6**. The applied magnetic field, per definition, is parallel to the z-axis. A Hamilton operator, which is the basis for calculating the time evolution of a system, can be defined, according to first order perturbation theory,^[74] for $I = \frac{1}{2}$ with a gyromagnetic ratio, γ , parallel to the applied magnetic field, as

$$\hat{\mathcal{H}} = -\gamma\hbar I_z B_0, \quad (2.2.7)$$

where γ is the gyromagnetic ratio of the given atomic isotope. Consequently, the energy difference is dependent on the applied magnetic field, known as the *Zeeman effect*, describing the relation between nuclear spin orientation and energy states in a static homogeneous magnetic field.^[74] **Equation 2.2.7** is known as the Zeeman Hamilton operator, of which the respective energy of the eigenstates can be obtained by applying the Schrödinger equation described as follows:

$$\begin{aligned} \hat{\mathcal{H}}|m_I\rangle &= E|m_I\rangle \\ &= -\gamma\hbar I_z B_0|m_I\rangle \\ &= -\gamma\hbar m_I B_0|m_I\rangle \\ \therefore E &= -\gamma\hbar m_I B_0. \end{aligned} \quad (2.2.8)$$

The selection rule for the NMR transitions is that m_I is only allowed to change by one unit, therefore, with $m_I = \pm\frac{1}{2}$, a transition between the two states results in a change in energy. This transitional energy is defined by

$$\Delta E = \gamma\hbar B_0. \quad (2.2.9)$$

The transition between the respective spin states are known as *Zeeman splitting*, depicted by the energy level diagram in **Figure 2.9**.

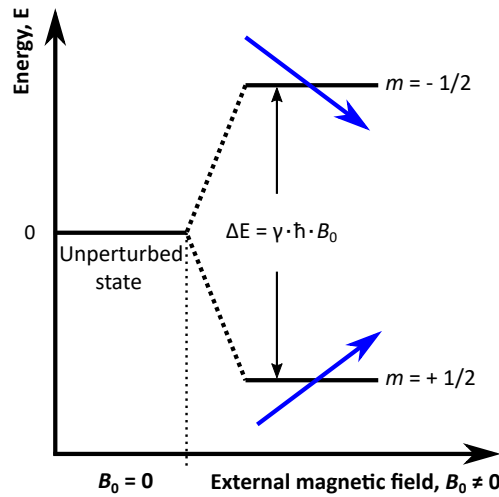


Figure 2.9: The energy, E , as a function of the static homogeneous magnetic field, B_0 for nuclei with a spin quantum number of $I = \frac{1}{2}$. The two orientations of the spin angular momentum, P , in the applied external magnetic field, B_0 , lead to an energy splitting ΔE .^[61,74, p. 455]

Transitions between the two states can be induced by irradiating the nuclei with electromagnetic waves of a certain frequency, ν_0 , allowing for

$$\Delta E = \gamma\hbar B_0 = h\nu_0 = \frac{h\gamma B_0}{2\pi}. \quad (2.2.10)$$

Considering the expression of the frequency in angular terms, an equivalent expression is

given by substitution of the frequency, ν_0 , with the angular frequency, $\omega_L (= 2\pi\nu)$. This gives the expression for the *Larmor frequency* or *resonance frequency*,

$$\omega_L = \gamma B_0, \quad (2.2.11)$$

where ω_L is the characteristic Larmor or resonance frequency. In order to visualize the process of nuclear spin in an external applied magnetic field, the nuclei can be imagined as simple bar magnets. As these bar magnets are subjected to a magnetic field, they start to align within the magnetic field, to occupy the most energetically favoured position, i.e. lowest energy, spinning rapidly around the north-south axis. Due to gyration of the rotating axis of the spinning bar magnets, the force applied by the field to the rotational axis causes an out-of-plane movement perpendicular to this plane. Thus, resulting in the precession of the bar magnets, i.e. the axes of the rotating bar magnets move in a circular fashion, around the field vector of the externally applied magnetic field, B_0 . The resulting macroscopic magnetization in the applied magnetic field, B_0 , is described by the Bloch equations,^[70,75, p. 21] and is derived from the totality of all specific magnetic moments. The frequency at which these spins precess is the Larmor or resonance frequency. A deflection of the nuclear spins can be generated from their precessional movement/orbit, by applying a second field, the radio frequency field, B_1 , perpendicular to the static B_0 field. This process is illustrated in **Figure 2.10**, which is the classical depiction of the nuclear spins or macroscopic magnetization in NMR spectroscopy. A more in-depth description of magnetization, pulsed NMR, and relaxation will be given in **Section 2.2.4**.

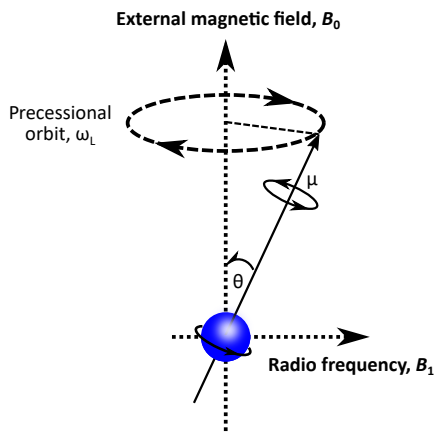


Figure 2.10: Simplified illustration of the precession of nuclei in the presence of an applied external magnetic field, B_0 , and a perpendicular radio frequency, B_1 . The magnetic moment of the particle is represented by μ , and θ is the angle between the magnetic field vector and spin axis.^[61, p. 457]

The quantum mechanical description of the behaviour of the atomic nucleus is the fundamental principle in which NMR spectroscopy is performed. The transition between the given energy states (see **Figure 2.9**) as a result of the electromagnetic irradiation at a certain frequency is defined by the Larmor equation (see **Equation 2.2.11**). The absorption frequency of a given nucleus is proportional to the applied external magnetic field, and it is this that enables structural elucidation in NMR spectroscopic experiments. There is not only one isolated nucleus in a given sample, but rather an ensemble of nuclei

that could occupy a given spin/energy state. As a result an ensemble of spins needs to be considered and applied to the theory in order to compensate for this. Furthermore, the magnetization (spins) tend to align with the applied magnetic field in thermodynamic equilibrium, resulting in the population of the energy levels (i.e. the ground and excited eigenstates for an ensemble of n nuclei) according to the *Boltzmann distribution*.^[73]

$$\frac{N_\beta}{N_\alpha} = \exp\left(\frac{-\Delta E}{k_b T}\right) = \exp\left(\frac{\gamma \hbar B_0}{k_b T}\right) \approx 1 - \frac{\gamma \hbar B_0}{k_b T} \quad (2.2.12)$$

$$\text{for } k_b T \gg \gamma \hbar B_0,$$

where N_α and N_β are defined as the populations of the lower and higher energy states, respectively, k_b is the Boltzmann constant and T the thermodynamic temperature.³ At room temperature, $k_b T$ is relatively large compared to that of ΔE for NMR spectroscopy experiments. It is therefore desired that B_0 is as large as possible to allow for the highest possible difference between the population of lower and higher energy states (see **Figure 2.9**), as the relative difference directly increases the signal. Consequently, the macroscopic net magnetization, M_0 , for an ensemble of n nuclei can be defined as the sum of all the individual magnetic moments, μ_i ,^[76, p. 14] given as

$$M_0 = \sum_{i=1}^n \mu_i. \quad (2.2.13)$$

In order to treat the overall behaviour of the spins in terms of the macroscopic magnetization, allow for a transfer from a quantum mechanical- to classical-formalism of NMR spectroscopy. This has the advantage that the classical formalism provides a simplified view of the NMR experiment.

2.2.3 Interactions in NMR Spectroscopy

Aside from the Zeeman effect, there are a variety of additional interactions of the nuclear spins through chemical bonds and space due to the close proximity of these nuclei and with their electronic environment. These NMR interactions include *quadrupolar interactions*, *chemical shift*, *homo- and hetero-nuclear dipolar coupling*, *J-coupling*, and *RF irradiation*.^[76, pp. 24–28] All of these interactions are based on the quantum mechanical perturbations of the spin system in its unperturbed state defined by the Zeeman interaction. The perturbations are time-dependent and -independent Schrödinger equations, and a Hamilton operator can be defined for each as follows:

$$\mathcal{H}\psi = E\psi, \quad (2.2.14)$$

and

³The success of an NMR experiment depends on a very small excess of lower energy protons. Based on the relative number of protons in the higher and lower eigenstates for a sample subjected to a $B_0 = 1.45$ T field at $T = 25$ °C, calculated from Equation 2.2.12, the excess of lower energy protons is a mere ~10 ppm.

$$i\hbar \frac{\partial \psi(t)}{\partial t} = \hat{\mathcal{H}} \psi(t), \quad (2.2.15)$$

where ψ is the wave function and t the time component. **Equation 2.2.14** provides the time-independent energy eigenstates for a given spin system. **Equation 2.2.15** describes all time-dependent processes in a spin system, such as the excitation and relaxation to and from different energy states. The integration of Equation 2.2.15 leads to the time evolution of a given spin system. The interactions of nuclear spins can collectively be described for nuclei with a spin quantum number $I \neq 0$. The differentiation between external and internal fields of the nuclear spin interactions can be described by the corresponding Hamilton operator,

$$\begin{aligned} \hat{\mathcal{H}} &= \hat{\mathcal{H}}_{ext.} + \hat{\mathcal{H}}_{int.}, \\ &\text{with} \\ \hat{\mathcal{H}}_{ext.} &= \hat{\mathcal{H}}_Z + \hat{\mathcal{H}}_{RF} \\ &\text{and} \\ \hat{\mathcal{H}}_{int.} &= \hat{\mathcal{H}}_Q + \hat{\mathcal{H}}_{CS} + \hat{\mathcal{H}}_D + \hat{\mathcal{H}}_J, \end{aligned} \quad (2.2.16)$$

where the Hamilton operators denoted by Z , RF , Q , CS , D and J refer to the Zeeman, radio-frequency irradiation, quadrupolar, chemical shift, dipolar coupling and J -coupling NMR interactions, respectively. The aforementioned interactions and their respective Hamilton operators are summarized in **Table 2.3**.

Table 2.3: Description of the various Hamilton operators with respect to different NMR interactions including their resulting effects.^{[76, pp. 24–28][77]}

Hamilton operator/NMR interaction ^a	Resulting effect
$\hat{\mathcal{H}}_Z = -\gamma \hat{I}_z \vec{B}_0$	Resonance at ω_L
$\hat{\mathcal{H}}_Q = \frac{eQV_{field}}{2I(2I-1)\hbar} \frac{1}{2} (3\hat{I}_{1z}\hat{I}_{2z} - \hat{I}_1 \cdot \hat{I}_2)$	Line-broadening/-splitting
$\hat{\mathcal{H}}_{RF} = -\vec{B}_1 \gamma \{ \hat{I}_x \cos(\varphi) + \hat{I}_y \sin(\varphi) \}$	Rabi oscillation
$\hat{\mathcal{H}}_{CS} = \left\{ -\omega_L \sigma_{iso} + \frac{1}{2} \sigma_{cs} (3 \cos^2 \theta - 1 - \eta_{cs} \sin^2 \theta \cos 2\varphi) \right\} \hat{I}_z$	Shift relative to ω_L
$\hat{\mathcal{H}}_D = -\frac{\mu_0 \hbar \gamma_1 \gamma_2}{4\pi r^3} \frac{1}{2} (3\hat{I}_{1z}\hat{I}_{2z} - \hat{I}_1 \cdot \hat{I}_2)$	Line-broadening/-splitting
$\hat{\mathcal{H}}_J = -2\pi J (\hat{I}_1 \cdot \hat{I}_2)$	Line-splitting

^a A more in-depth quantum mechanical description related to these NMR interactions can be found in the textbook by Schmidt-Rohr and Spiess (1994).^[76, pp. 16–24]

\vec{B}_0 : static homogeneous magnetic field, $-\vec{B}_1$: induced magnetic field, γ : gyromagnetic ratio, σ : chemical shift tensor, r : distance, μ_0 : vacuum permeability, θ : orientational angle between the spin pair vector and \vec{B}_0 , Q : quadrupolar moment, e : elemental charge, V_{field} : field gradient.^{[76, pp. 24–28][77]}

Not all interactions are relevant to liquid state proton NMR spectroscopy (listed in Table 2.3). The quadrupolar interaction, i.e. $I \geq 1$, does not play a role in proton NMR spectroscopy and will not be discussed in further detail. Furthermore, the homo- and hetero-nuclear dipolar coupling is based on interaction of different spins through space.

However, since the focus is on proton NMR spectroscopy in liquids, the molecular motion is considered as a statistical and relatively fast process with respect to the time scale in NMR spectroscopy, and as a result the dipolar coupling is typically on average zero for measurements in solution. It is however important not to discard these couplings completely as they are responsible for the relaxation processes when magnetization is transferred in a process called *Nuclear Overhauser Effect (NOE)*. Consequently, this affects the line widths for given resonant signals.^[66] In the case of J-coupling, the molecular motion is an indirect interaction of two nuclear spins, which is mediated through chemical bonds. This interaction results in the splitting of resonant signals related to the bonding status of the given atom.^[78] The chemical shift is related to de-shielding of nuclear spins by electrons of the surrounding bonds. This occurs due to the magnetic susceptibility of electrons. They shield nuclei from the externally applied magnetic field, B_0 , resulting in the nuclei experiencing a smaller effective local magnetic field, $B_{0, \text{eff}}$. This results in an anisotropic and inhomogeneous effect, which is dependent on the total number of electrons present, inductive, and mesomeric effects, including the hybridization of the given atom. Taking this into consideration, nuclei which are chemically identical, can be chemically unequal due to their geometric positions in the molecule, and therefore, result in slightly different energy splittings and observed Larmor frequencies (Equation 2.2.11). This change in the frequency is referred to as the chemical shift, as the electrons surrounding the nuclei give a direct indication of the chemical structure of a molecule. This principle allows NMR spectroscopy to differentiate between the same type of nuclei and provides a direct correlation to chemical structure elucidation. Since the electrons are magnetically susceptible, the interaction is proportional to the magnetic field, therefore, the chemical shift is relative to the applied magnetic field. Moreover, the chemical shift is generally not reported in absolute difference of resonance frequency in *Hertz*, Hz, instead it is expressed related to the resonance frequency of a reference compound. Consequently, to allow for a more convenient way to compare results obtained on different field strengths and remove the dependency on the applied magnetic field strength, the ppm scale is introduced,^[71]

$$\delta(\text{ppm}) = \frac{v_s - v_{ref}(\text{Hz})}{v_{ref}(\text{MHz})}, \quad (2.2.17)$$

where v_s and v_{ref} is the sample- and reference-frequency, respectively. This provides a unitless value expressed in *parts per million*, ppm, since the chemical shifts are small compared to that of the resonant frequencies.

2.2.4 Magnetization, Pulsed NMR, and Relaxation

As discussed at the end of **Section 2.2.2**, being able to treat the behaviour of an ensemble of spins in the system in terms of magnetization allows for the transfer from a quantum mechanical to a classical description of NMR spectroscopy. A classical description of the magnetization in a magnetic field can be used, which contains all relevant parameters to characterize most magnetic-resonant properties of nuclei with a spin quantum number of $I = \frac{1}{2}$ without couplings to other spins. If the magnetization vector, \vec{M} , is subjected to a

homogeneous magnetic field, \vec{B} , it responds as if it is subject to a torque. This yields the description of the motion for magnetization as^[76, p. 14]

$$\frac{d}{dt}\vec{M} = \gamma\vec{M} \times \vec{B}. \quad (2.2.18)$$

If \vec{B} is static, i.e. time-independent, along the z-axis so that $\vec{B} = (0, 0, B_0)$, it yields the characteristic Bloch equations, which do not take relaxation processes into consideration,

$$\begin{aligned} \frac{dM_x(t)}{dt} &= M_y(t)\gamma B_0 \\ \frac{dM_y(t)}{dt} &= -M_x(t)\gamma B_0 \\ \frac{dM_z(t)}{dt} &= 0, \end{aligned} \quad (2.2.19)$$

which are solved by the magnetization and have the solution,

$$\vec{M}(t) = \begin{bmatrix} M_x(t) \\ M_y(t) \\ M_z(t) \end{bmatrix} := \begin{bmatrix} M_x(0) \cos(\omega_0 t) - M_y(0) \sin(\omega_0 t) \\ M_y(0) \cos(\omega_0 t) + M_x(0) \sin(\omega_0 t) \\ M_z(0) \end{bmatrix}, \quad (2.2.20)$$

where ω_0 is the resulting Larmor frequency (see Equation 2.2.11, p. 25). The resulting equations describe the precession of the magnetization vector about the applied magnetic field vector depicted in **Figure 2.11**.

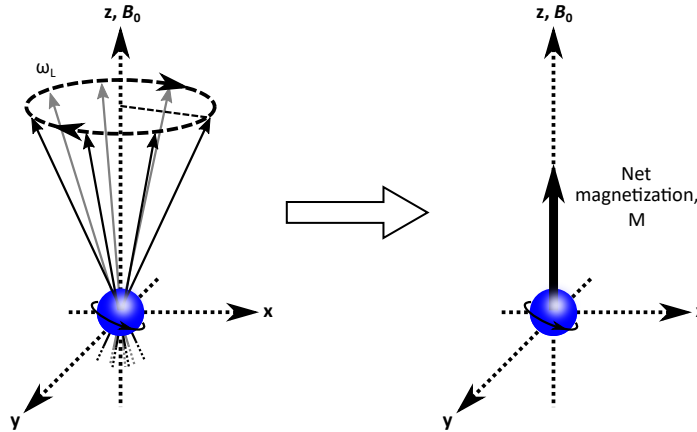


Figure 2.11: Depiction of the magnetization, M , in the vector model, illustrating the precession of the magnetic moments of the nuclei subjected to an external magnetic field, B_0 , with a corresponding z-axis alignment. The precessional orbit, i.e. Larmor frequency is represented by ω_L . The ensemble of spins aligned with the magnetic field vector leads to a net magnetization, M , parallel to B_0 .^[79]

The transition to the rotating frame of reference, with the magnetization precession about \vec{B}_0 , is identical to the Larmor frequency derived in the quantum mechanical description in Section 2.2.2 (p. 21). This illustrates how the classical and quantum mechanical formalism coincide. Considering Figures 2.10 and 2.11, applying a transverse time-dependent varying field/pulse \vec{B}_1 to \vec{B}_0 , with frequency of ω_0 , referred to as radio frequency (RF) irradiation, yields a flip of the magnetization, which is affected by the precession of the magnetization along the field axis of \vec{B}_1 , with a frequency $|\omega_1| = \gamma|\vec{B}_1|$, in the rotating

frame reference.^[76,80, p. 15] If the precessing polarized component of B_1 , with the same direction of the precessing magnetization vector is considered, B_1 can be described by

$$B_1(t) = B_1 \cos(\omega_0 t) - B_1 \sin(\omega_0 t), \quad (2.2.21)$$

where the $B_1 \cos(\omega_0 t)$ and $-B_1 \sin(\omega_0 t)$ terms represent the x- and y-component, respectively. Substituting into **Equation 2.2.18**, leads to the solution for the magnetization with a second oscillating magnetic field, \vec{B}_1 , of

$$\vec{M}(t) = \begin{bmatrix} M_x(t) \\ M_y(t) \\ M_z(t) \end{bmatrix} := \begin{bmatrix} M_0 \sin(\omega_1 t) \sin(\omega_0 t) \\ M_0 \sin(\omega_1 t) \cos(\omega_0 t) \\ M_0 \cos(\omega_1 t) \end{bmatrix}, \quad (2.2.22)$$

with the addition of \vec{B}_1 into the rotating frame of reference, it is appropriate to introduce a new frame of reference for describing the evolution of the magnetization vector precessing around the z-axis with a given Larmor frequency. The x- and y-axes become x' and y', respectively, whereas $z = z'$. Upon RF irradiation with the \vec{B}_1 field at ω_1 for a given time interval, t_p , the magnetization will tilt with an angle,^[76, p. 15]

$$\theta = \gamma B_1 t_p. \quad (2.2.23)$$

Considering a commonly used flip angle of $\theta = 90^\circ$, the RF irradiation must be applied for a duration that fulfils **Equation 2.2.23**. These *RF pulses* are typically applied for a short time burst of $t_p = 1\text{--}100 \mu\text{s}$, resulting in a square wave with a spectral bandwidth in the range of several hundred kHz. A simple single pulse experiment is illustrated in **Figure 2.12**.

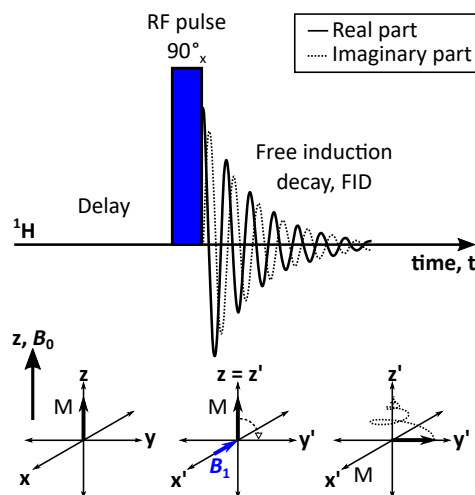


Figure 2.12: Depiction of the pulse sequence of a single pulse NMR experiment and the associated magnetization behaviour. In this illustration a 90° x-pulse flips the net magnetization into the x'/y'-plane (obeying the right hand rule), after which the net magnetization returns back to the z-axis as the thermal equilibrium is re-established via relaxation processes. This process, including the resulting data are known as *Free Induction Decay* (FID).

During these 90° RF pulses the magnetization is completely transferred to the x'y'-plane of the rotating frame. The response of the spin system by manipulation of magnetization by

RF pulses, i.e. an NMR signal which can be regarded as an oscillating magnetic flux density inducing a voltage in the NMR probe, is the fundamental basis of NMR spectroscopy. Pulsed NMR experiments have become the dominant paradigm since the 1970s over the classical continuous-wave (CW) NMR experiments. In pulsed NMR all the frequencies are excited simultaneously (think of hitting all the keys of a piano at once instead of one at a time) by applying an RF pulse (Figure 2.12) to a given system. As data are collected and stored in the time-domain and NMR spectroscopists are more interested in the frequency-domain response of a given spin system, a conversion from the time-domain, $f(t)$, to frequency-domain, $F(\omega)$, is required. Fortunately, with this conversion is accomplished by means of the Fourier transformation, \mathcal{F} , using the following equation:

$$f(t) \xleftrightarrow{\mathcal{F}} F(\omega) = \int_{-\infty}^{\infty} f(t)e^{i\omega t} dt. \quad (2.2.24)$$

The transformation is performed on discrete data, in practice, by the Cooley-Tukey algorithm that typically requires 2^n time data points.^[81] The vector model is useful for explaining simple NMR phenomena. However, it is limited for more complex experiments, where additional tools such as the *density matrix* or *product operator formalism* are required.^[79,80,82,83] Immediately after RF irradiation, the magnetization starts to return to thermal equilibrium by *relaxation* of the magnetization. The relaxation process occurs via two mechanisms: (1) *transversal relaxation* in the xy-plane; and (2) *longitudinal relaxation* along the \vec{B}_0 field direction, the z-axis. The relaxation process of the magnetization towards equilibrium can be described by Bloch's semi-empirical set of differential rate equations, considering **Equation 2.2.19** (p. 29), with the resulting solutions for the magnetization as^[76, p. 14]

$$\vec{M}(t) = \begin{bmatrix} M_x(t) \\ M_y(t) \\ M_z(t) \end{bmatrix} := \begin{bmatrix} \{M_x(0) \cos(\omega_0 t) + M_y(0) \sin(\omega_0 t)\} \exp\frac{-t}{T_2} \\ \{M_y(0) \cos(\omega_0 t) + M_x(0) \sin(\omega_0 t)\} \exp\frac{-t}{T_2} \\ M_z(0) + (1 - \exp\frac{-t}{T_1}) \{M_z(\infty) - M_z(0)\} \end{bmatrix}, \quad (2.2.25)$$

where T_1 and T_2 define the longitudinal- and transversal-relaxation, respectively. Since the RF pulse disturbs the spin system, it involves the exchange of energy between the spin system and surrounding environment, after which the polarization gets dissipated to its original level, also referred to as *spin-lattice* relaxation, T_1 . In general, the magnitude of the T_1 time is determined by the type of nucleus, magnetic surroundings (especially local B_0 -field fluctuations), the strength of B_0 and molecular size. Each spin of the atoms within a molecule can have different T_1 times, which is also influenced by the exact state of the surrounding spins.^[84] Some of the influences originate from dipolar and scalar coupling to the surrounding nuclei or paramagnetic impurities, such a molecular oxygen (O_2) with a triplet ground state in the sample. The spins exchange energy not only with the surrounding environment but also amongst themselves. This energy exchange involves the de-phasing of spins with different Larmor frequencies, due to local fluctuations in the magnetic field over time in the x'/y'-plane, and is called *spin-spin* relaxation, T_2 . This is generally a faster

process than T_1 relaxation, especially in the solid state. Consequently, the relaxation times T_1 and T_2 provide important information related to the interactions between different nuclei. There are a variety of phenomena leading to the decaying behaviour of spin systems as a function of time or the resulting line broadening of resonant signals in NMR spectroscopy, which can be classified as coherent and incoherent interactions. The reader is referred to Schmidt-Rohr et al.^[76, p. 129] for a detailed description. In order to determine the T_1 and T_2 relaxation times, there are three well-known pulse sequences to obtain the desired information, which are the inversion recovery pulse sequence^[70, pp. 160–162] for T_1 estimation, and the Hahn-Echo^[78,85] and Carr-Purcell-Meiboom-Gill (CPMG)^[86,87] pulse sequences for T_2 estimation.

2.2.5 Medium-Resolution (MR) NMR spectroscopy

Starting with the fundamental question why medium-resolution NMR spectrometers should be used instead of its highly sought after counterpart – the high field (HF) NMR spectrometer? The argument is perhaps not so straightforward, and potentially more related to intellectual fascination associated to obtaining chemically resolved spectra on field strengths (including related technological advancements), which was not possible four decades ago. Although HF-NMR spectrometers offer a plethora of advantages and play a central part in analytical chemistry, they have their disadvantages. Some of them include: (1) initial investment costs, (2) the size and safety requirements of the magnets, (3) the need for cryogenic liquids, and (4) designated expertise. With reference to this thesis, employing HF-NMR spectroscopy as chemically sensitive detector for chromatography complicates method development, due to the aforementioned imposed restrictions, making smaller benchtop type spectrometers more feasible. With the recent advancements in cryogen-free permanent magnets, they meet the demand for using them as on-line chemically sensitive detectors. These instruments employ permanent magnets with proton resonances of $F = 40\text{--}100$ MHz (i.e. magnetic field strength, $B_0 = 0.5\text{--}2.3$ T, ^1H Larmor frequency); have relatively small dimensions ($60 \times 45 \times 40$ cm); have reduced investment cost (5–20 times lower than high field instruments);^[62] do not require cryogenic liquids, e.g. liquid N_2 or He, thus reducing consumables, need minimal maintenance; and are easy to operate. More recently, the new generation of low/medium field NMR spectrometers has emerged, which like all low field NMR spectrometers, are based on rare earth permanent magnets (e.g. SmCo, NdFeB and AlNiCo alloys), with improved field homogeneity, due to the Hallbach magnet arrangement.^[88] This has enabled the new generation spectrometers to record conventional NMR spectra with sufficient resolution.^[88] The technological advancements in low field NMR spectrometers, have allowed these instruments to pave the way forward for NMR to become a highly accessible commodity in a variety of fields such as process control, reaction monitoring, and most importantly the exposure at academic level.^[88] Due to their compact size, they are ideal to use for on-line set-ups (see the dimensions column in **Table 2.4**). Furthermore, since most of the benchtop spectrometers have an open cavity style probe head, it not only allows for conventional static NMR measurements, but also for flow cells to be utilized for continuous-flow experiments. The need for deuterated

solvents is also not a major limitation anymore, as these spectrometers are equipped with an integrated external field frequency lock system (e.g. ^{19}F), further facilitating its cost efficiency. Nonetheless, lower magnetic field strengths are synonymous with a compromise: reduction in sensitivity (reduced magnetic field, B_0) and resolution (reduced frequency range). As a result, benchtop NMR spectrometers are limited with respect to their detection limits and require high sample concentrations, typically in the range of several tens of millimoles (mM). A major limitation related to permanent magnets is their sensitivity to temperature fluctuations outside the magnet. Generally, rare earth magnets are optimally stable at ambient temperatures between $T = 20\text{--}30\text{ }^\circ\text{C}$. Variations outside of this range severely affects the magnet stability.^[88] An overview of five commercially available benchtop type NMR spectrometers are provided in Table 2.4. The specification provided on these instruments are all based on the available product specification sheets.^[89–96] Additionally, a comparison between the Bruker, Magritek, and Nanalysis instruments was performed in order to establish the validity of the technical specification related to sensitivity provided on the product specification sheets. The measurements were performed on a 1% ethylbenzene in $\text{CDCl}_3 + 2\%$ TMS standard, see **Figure 2.13**.

Table 2.4: Summary of commercially available benchtop NMR spectrometers in 2020.^[62;89–97]

Company	Trade name	Nuclei	Number of Nuclei	MHz (¹ H)	Linewidth FWHM (Hz)	Sensitivity ^a (S/N)	Weight (kg)	Lock	Sample ^b	Dimensions (cm)	Auto-sampler				
Bruker	Fourier 80	¹ H ¹³ C	2	80	< 0.5	> 1500	94	External	Tube	50×70×60	No				
				Magritek	Spinsolve 43	¹ H ¹³ C ¹⁹ F ^c	2 or 3	43	< 0.5	> 100	55	External	Tube	58×43×40	Yes
								Spinsolve 60	¹ H ¹³ C ¹⁹ F ^c	2 or 3	60	< 0.5	120	60	External
Spinsolve 80	¹ H ¹³ C ¹⁹ F ^c	2 or 3	80								0.5	> 200	72	External	Tube
			Spinsolve Ultra	¹ H ¹³ C ¹⁹ F ^c	2 or 3	43 or 60	< 0.2	> 70	72	External	Tube	58×43×40	Yes		
Nanalysis	NMReady-60Pro	¹ H ¹³ C ¹⁹ F ⁷ L _i ¹¹ B ¹⁵ N ²⁹ Si ³¹ P ¹²⁹ Xe				2	60	≤ 1.0	100	25	Internal	Tube	30×28×49	Yes	
							100Pro	¹ H ¹³ C ¹⁹ F ¹¹ B ²⁹ Si ³¹ P ⁷ L _i ¹¹ B ¹⁵ N	2	100	< 1.0	220	97	Internal	Tube
			Oxford Instruments	X-pulse	¹ H ¹³ C ¹⁹ F ²³ Na ²⁹ Si ³¹ P ⁷ L _i ¹¹ B					2, 3 or 8	60	< 0.35	> 120	172	Internal
Thermo Fischer	PicoSpin 45 II	¹ H(¹⁹ F)				1	45	< 1.8	> 1000		5	Internal	Capillary	18×15×29	No
							PicoSpin 82 II	¹ H(¹⁹ F)	1		82	< 1.6	> 4000	19	Internal

^a Sensitivity: signal-to-noise (S/N) ratios given are dependent on test conditions; Magritek, Nanalysis and Oxford use 1% ethylbenzene, Bruker 10% ethylbenzene and ThermoFischer 100% water. The noise, N, is defined as the standard deviation of a peak free region.

^b Sample: all spectrometers use standard 5 mm (outer diameter) tubes with the exception of ThermoFischer, which use a 0.4 mm capillary with 40 μL sample volume. The sample temperatures range between T = 20–70 °C.

^c Other nuclei are possible on request.

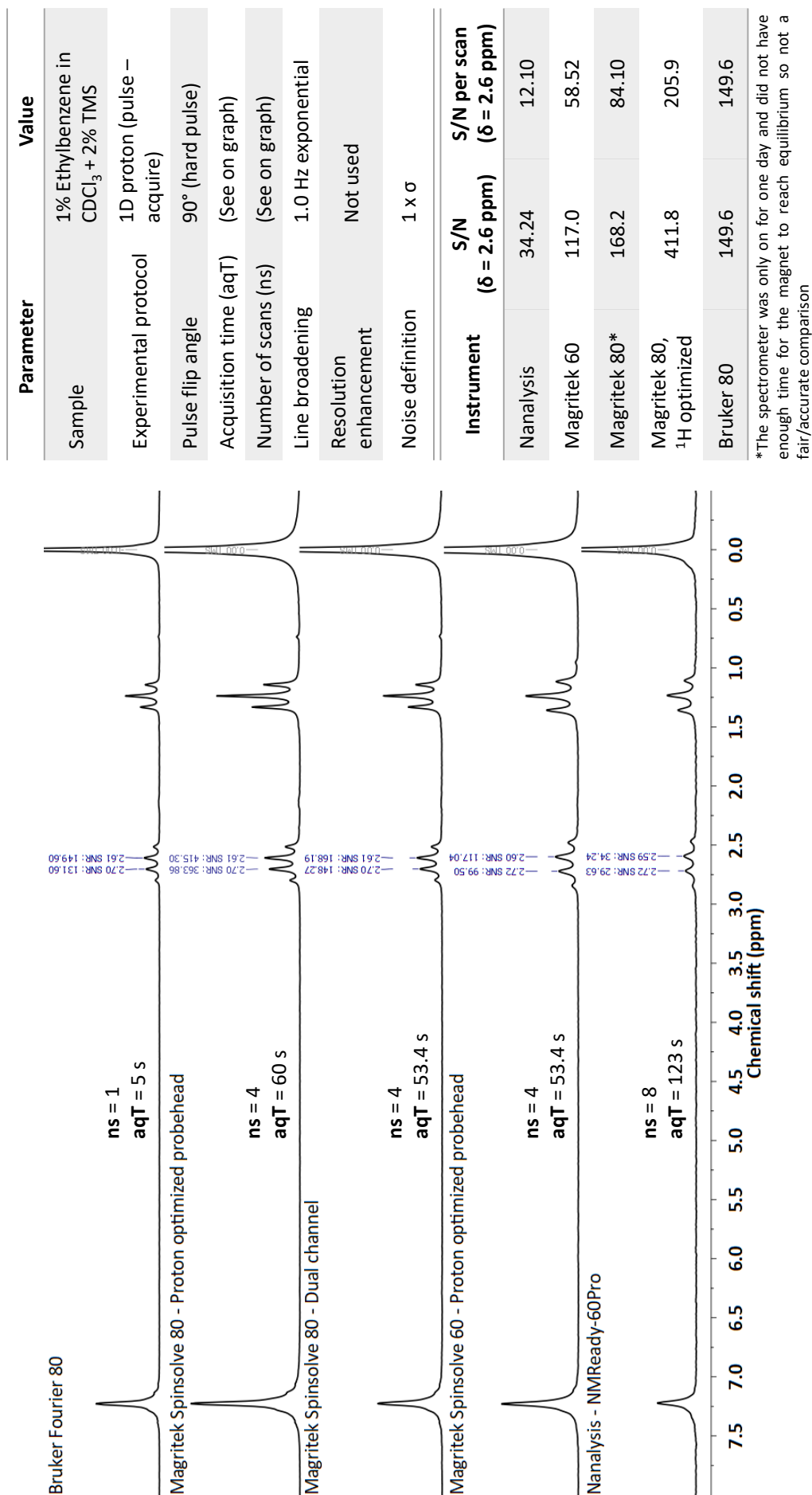


Figure 2.13: Instrument comparison between Bruker, Magritek, and Nanalysis performed on 1% ethylbenzene in CDCl₃ + 2% TMS. The tabular insets provide an overview of the experimental and processing parameters used, including the signal-to-noise (S/N) ratios back-calculated to a single scan, based on the resonance peaks located at $\delta = 2.4$ – 3.0 ppm. High field NMR S/N values are defined as $S/2\sigma$, whereas in low field it is S/σ , where σ is the standard deviation of the noise. In MestreNova software, S/N value are determined based on the HF NMR definition. Consequently, to normalize data to a single scan for benchtop NMR, the obtained S/N value has to be multiplied by two, and then divided by the \sqrt{n} , where n is the number of scans.

In order to generate a magnetic field strength adequate for NMR experiments for permanent magnets, a variety of magnet arrangements exist. Since the focus of this work is on spectroscopically resolved NMR experiments and not time-domain NMR, only the cylindrical Halbach arrangement will be illustrated, as the instrument used within the scope of this thesis are based on it. The reader is referred to Blümich^[98, pp. 929–930] for an overview related to the different available arrangements. The Halbach arrangement has become more popular in the field of benchtop NMR spectroscopy because of its improved field homogeneity and compact size.^[99,100] The individual magnets in the Halbach array are placed in such a way that magnetic field is augmented inside the cylindrical cavity and attenuated externally. As a result there are practically no stray fields present with this arrangement (2 Gauss line⁴ within spectrometer).^[11,101] Low stray fields are another benefit of the Halbach arrangement, which makes it attractive for applications such as instrument hyphenation and benchtop use. A schematic depiction of the Halbach array is illustrated in **Figure 2.14**.

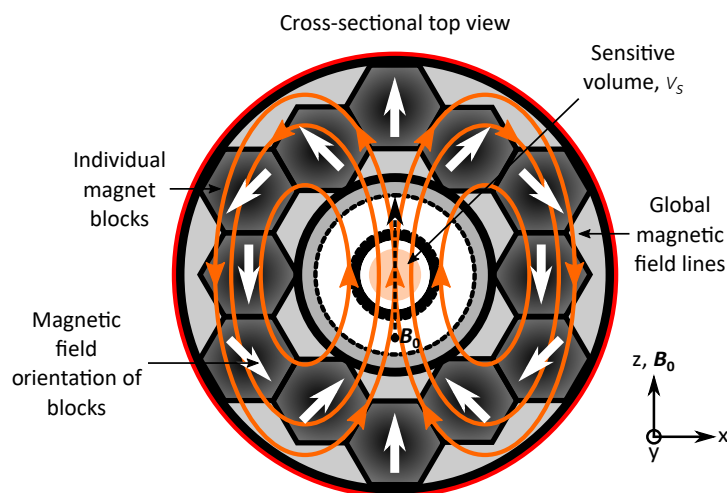


Figure 2.14: Depiction of a cylindrical Halbach magnet array, showing the polarization of individual magnet blocks required to establish a homogeneous magnetic field, B_0 . The sensitive volume is displayed with an orange circle in the centre of the arrangement.

An important consideration is that the sensitive volume, V_s , is proportional to the physical size of the magnet, i.e. a reduction in magnet size consequently reduces the size of the sensitive volume.^[68, pp. 36–37, p. 43] Furthermore, for each magnet geometry the ratio between the magnet size and corresponding sensitive volume size is a constant.^[12] Permanent magnets designated for benchtop type NMR spectrometers are made of mostly samarium-cobalt (SmCo) or neodymium-iron-boron (NdFeB) alloys, whose magnetic characteristics vary with different stoichiometric ratios.^[12,102–105] **Table 2.5** summarizes some of the most important material characteristics for permanent magnets. The coercivity, H_{ci} , describes the maximum external field strength a given magnet can be exposed to before it completely loses its magnetic flux density. The possibility to use specific magnetic

⁴The 5 Gauss line is a safety precaution typically employed for high field spectrometers and magnetic resonance imaging, serving as a reminder that the magnetic field strength increases rapidly towards the magnet. Typically marked at a certain distance from the magnet core, signifying the limit beyond which ferromagnetic objects are prohibited.

materials in a Halbach arrangement is limited by this parameter. For example, iron, Fe, and aluminium-nickel-cobalt, AlNiCo, undergo self de-magnetization when employed in a Halbach arrangement. As previously mentioned, permanent magnets are sensitive to temperature fluctuations. The Curie temperature, T_c , of a given magnetic material is the factor that limits the thermal stability of the magnetic field, i.e. limits the temperature application. Additionally, above the Curie temperature ferromagnetic properties are lost, rendering only paramagnetic behaviour. Correspondingly, the change in the magnetic field strength, B_0 , as a function of temperature, is a direct correlation to the robustness with respect to temperature fluctuations. The SmCo and NdFeB alloys typically have temperature coefficients of the residual magnetization in the range of $-(0.03\text{--}0.05\%) \text{ }^\circ\text{C}$ and $-(0.08\text{--}0.11\%) \text{ }^\circ\text{C}$, respectively.^[12,102–105]

Table 2.5: An overview of magnetic properties for a selection of permanent magnet materials.^[12,102–105]

Material	Coercivity, H_{ci} (kA/m)	Max. magnet energy density, BH_{max} (kJ/m ³)	Curie Temperature, T_c (°C)	Max. field strength, B_0 (T) ^a
Fe	0.01–0.2	12.8	770	0.5–1.5
AlNiCo	30–150	45	700–860	1.25
SmCo	3200	240	700–850	1.5
NdFeB	800–950	223–414	310	2.0
Ceramic	260	30	750	0.4
Flexible	110	5	100	0.16

^a For the alloys SmCo and NdFeB the values are based on a Halbach array geometry. In the case of Fe and AlNiCo the values correspond to pole- and horseshoe-magnets, respectively. This magnet arrangement is due to self-demagnetization of Fe and AlNiCo when used in the Halbach array geometry. The maximum field strength value of the ceramic magnet is based on an arc segment geometry.^[12,102–105]

In **Figure 2.15**, permanent and superconductive magnets are compared with respect to their signal-to-noise, based on an NMR water standard in conventional 5 mm NMR tubes using solenoidal or birdcage radio frequency (RF) coils. With the latest advancements in magnetic material, permanent magnets have a physical limitation of $B_0 = 2$ T, a strong contrast to the $B_0 = 24$ T achieved by its high field counterparts. As illustrated by Danieli et al.,^[12,99] a solenoidal RF coil is the preferred choice for permanent magnets due to the factor ~ 3 improvement in S/N over conventional birdcage RF coils.

For the solenoidal RF coil geometry (see **Figure 2.16**) used in benchtop spectrometers, the theoretical relationship between the coil dimensions and sensitivity, as assessed by the RF field, B_1 , per unit current i , is described by^[106, p. 224]

$$\frac{B_1}{i} = \frac{\mu n}{d\sqrt{1 + (\frac{l}{d})^2}}, \quad (2.2.26)$$

where n is the number of turns, μ is the permeability of free space, d is the coil diameter, and l its length. As indicated by **Equation 2.2.26**, the coil sensitivity is inversely dependent on the coil diameter for a fixed length-to-diameter ratio. Employing coils with diameters of $d \leq 3$ mm, the internal alternating current (AC) resistance of the coil is responsible for the

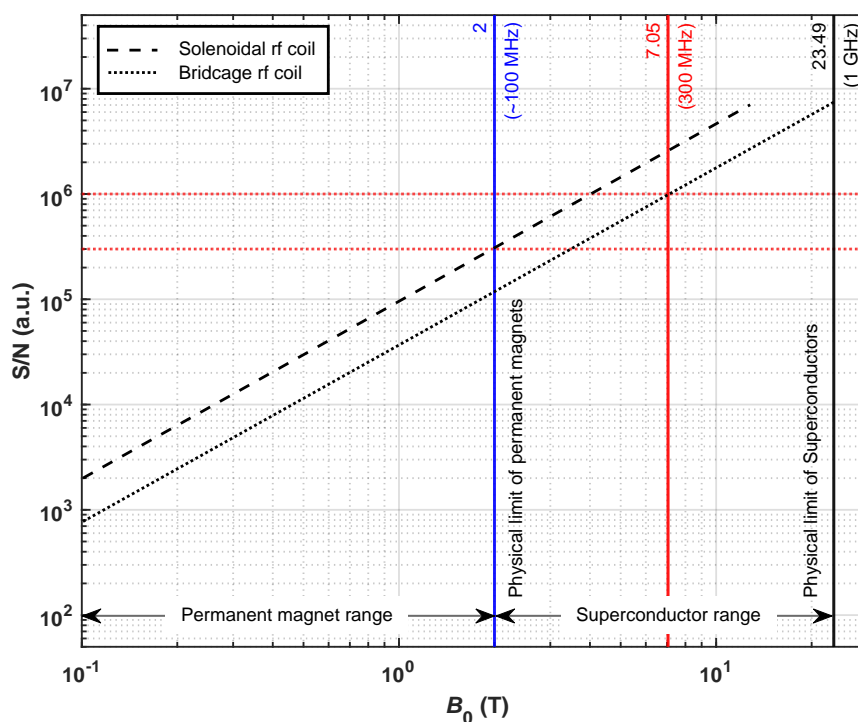


Figure 2.15: Depiction of the signal-to-noise (S/N) ratios for an NMR water standard in conventional 5 mm NMR tubes as a function of the magnetic field strength, B_0 , for permanent and superconductive magnets. The black dashed and dotted lines represents solenoidal and birdcage RF coils used with the aforementioned magnets, respectively. Additionally, the vertical blue and black lines corresponds to the maximum possible magnetic field strength of permanent and superconductive magnets, respectively. Danieli, J. Perlo, B. Blümich, F. Casanova: Small Magnets for Portable NMR Spectrometers. *Angew. Chem. Int.* 2010, 49, 4133–4135. Copyright Wiley-VCH Verlag GmbH & Co. KGaA. Reproduced with permission.^[12]

major noise contribution. The internal resistance is dependent on the winding geometry, i.e. wire diameter, number of turns, and gap between consecutive turns, including the resistivity of the conductor.^{[106, pp. 223–224][107]}

2.2.6 NMR Spectroscopy in a Flowing Liquid

In this work, the major focus was on performing NMR spectroscopy on a flowing liquid, i.e. the on-line detection of species in solution after chromatographic separation. Special problems occur when applying NMR spectroscopy to continuous-flow systems, which significantly affect the sensitivity and resolution, as will be discussed in the forthcoming section. Performing NMR spectroscopy on continuous-flow systems was reported as early as the 1950s.^[108] In the initial investigation, it was reported that the intensity of the NMR signals were proportional to the flow rate. In addition, the effect of the flow rate on the T_1 and T_2 times was also investigated.^[109] Following this, numerous investigations were performed, in order to obtain a comprehensive understanding of the effects occurring in continuous-flow experiments through the sensitive volume of an NMR flow cell.^[13,110] These initial investigations, which contributed to understanding continuous-flow NMR spectroscopy, led to method development that strongly focussed on the improvement of

S/N , enabling quantitative analysis by means of shorter repetition times and performing detailed NMR measurements of the flow itself.^[111,112] In contrast to conventional (static) NMR spectroscopy, where the sample is introduced into the applied magnetic field and has an infinite time period for NMR spectra acquisition, continuous-flow NMR spectroscopy only allows for a distinct *residence time*, τ , within the sensitive volume of the spectrometer, typically in the range of a few seconds. The residence time is dependent on two factors: (1) the sensitive volume of the flow cell within the sensitive volume of the spectrometer, and (2) the flow rate.^{[106, p. 1][107]} A generalized depiction of a continuous-flow NMR cell illustrating these regions of importance is shown in Figure 2.16.

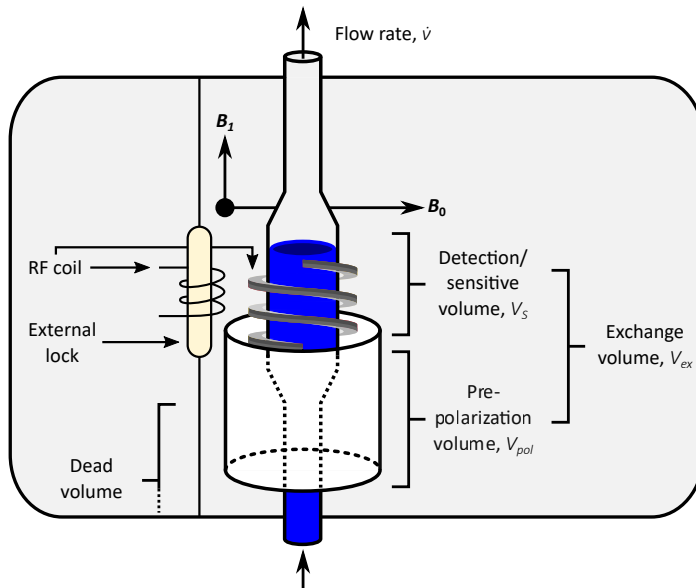


Figure 2.16: Illustration of the detection principle in continuous-flow NMR spectroscopy, where V_s is the detection or sensitive volume, V_{pol} is the pre-polarization volume, V_{ex} is the total exchange volume, and \dot{v} is the volumetric flow rate. All components are situated within the NMR spectrometer.^[106, p. 2]

The average residence time within the sensitive volume of the NMR spectrometer, is defined by

$$\tau = \frac{V_s}{\dot{v}}, \quad (2.2.27)$$

where V_s is the sensitive volume and \dot{v} is the flow rate. This leads to an effect commonly referred to as the *in-flow effect*.^[110] During a pulsed NMR experiment, excited spins are flowing out of the sensitive volume and are replaced by unexcited spins flowing into it (see Figure 2.16). During a simple pulse experiment (see Figure 2.12, p. 30), the repetition time is much longer than the RF pulse- and acquisition-times. This leads to an effect where the saturated spins are replaced by freshly unsaturated spins during the repetition time or recycle delay of the NMR experiment. This leads to a potential enhancement in the S/N per time unit, based on the assumption that the replacement took place under thermal equilibrium. This effect, also referred to as the effective longitudinal relaxation rate under flow, is approximated as:^[99]

$$\frac{1}{T_1^{flow}} = \frac{1}{T_1^{static}} + \frac{1}{\tau}. \quad (2.2.28)$$

Additionally, the in-flow effect leads to the shortening of the effective T_1^{flow} relaxation time by decreasing the residence time, τ , in comparison to the conventional static conditions, T_1^{static} . This leads to the potential advantage of decreasing the repetition time, leading to S/N enhancement while retaining quantitative conditions.^[111] It should be noted that the reduction of the repetition time should be performed with caution, as the aforementioned advantage is only valid when or if the excited spins are replaced by completely polarized spins. Therefore, in an ideal case, spins flowing into the sensitive volume would have undergone pre-polarization by means of polarization build-up (Figure 2.16) and are already in thermal equilibrium, i.e. the Boltzmann distribution is established in the static magnetic field, B_0 . For this to occur, the polarization build-up requires a sufficient amount of time, typically $3-5 \times T_1^{static}$ measured under static conditions, in the pre-polarization volume. This is especially difficult to implement for benchtop type NMR spectrometers due to their reduced magnet size. Consequently, achieving this condition is rarely met, even by employing moderate to low flow rates.^[110] One solution is to increase the polarization region within the set-up by employing intricate flow cell designs containing a spiral region. This will enable a longer path length within the sensitive volume of the NMR spectrometer.^[100,113,114] Unfortunately, this approach leads to an increase in excess volume (band broadening) and back-mixing, reducing the time/volume resolution, which is unfavourable in chromatography. The continuous-flow of the analyte and mobile phase causes a certain probability that some of the spins excited by the RF pulse and consequently polarized, exhibiting transverse magnetization, will flow out of the sensitive volume prior to being fully relaxed (i.e. before acquisition is completed). Consequently, these spins exhibit a higher effective transverse relaxation time, T_2^{flow} , than under static conditions, T_2^{static} . This effect is referred to as the *out-flow effect* in literature^[107, pp. 2-3] and, analogous to **Equation 2.2.28**, is defined by

$$\frac{1}{T_2^{flow}} = \frac{1}{T_2^{static}} + \frac{1}{\tau}. \quad (2.2.29)$$

The pulse repetition times can be reduced according to the decrease in the effective longitudinal relaxation rate, T_1^{flow} , whereas an increase in flow rate at a specific detection volume result in line-broadening, observed by measuring the peak full width half maximum (FWHM), due to a reduction in the effective transverse relaxation rate, T_2^{flow} , given by

$$FWHM_{static} = \frac{1}{\pi T_2} \quad (2.2.30)$$

$$FWHM_{flow} = FWHM_{static} + \frac{1}{\tau}.$$

Therefore, the out-flow effect is responsible for negatively affecting the resolution of NMR spectra, i.e. line-broadening is highly dependent on the flow rate/flow cell volume ratio (see **Figure 2.17**).^[106, p. 3] Consequently, the theoretical maximum sensitivity obtainable

by continuous-flow NMR experiments is achieved when the pulse repetition time exactly matches the residence time, τ , in the NMR flow cell.^[106, p. 4]

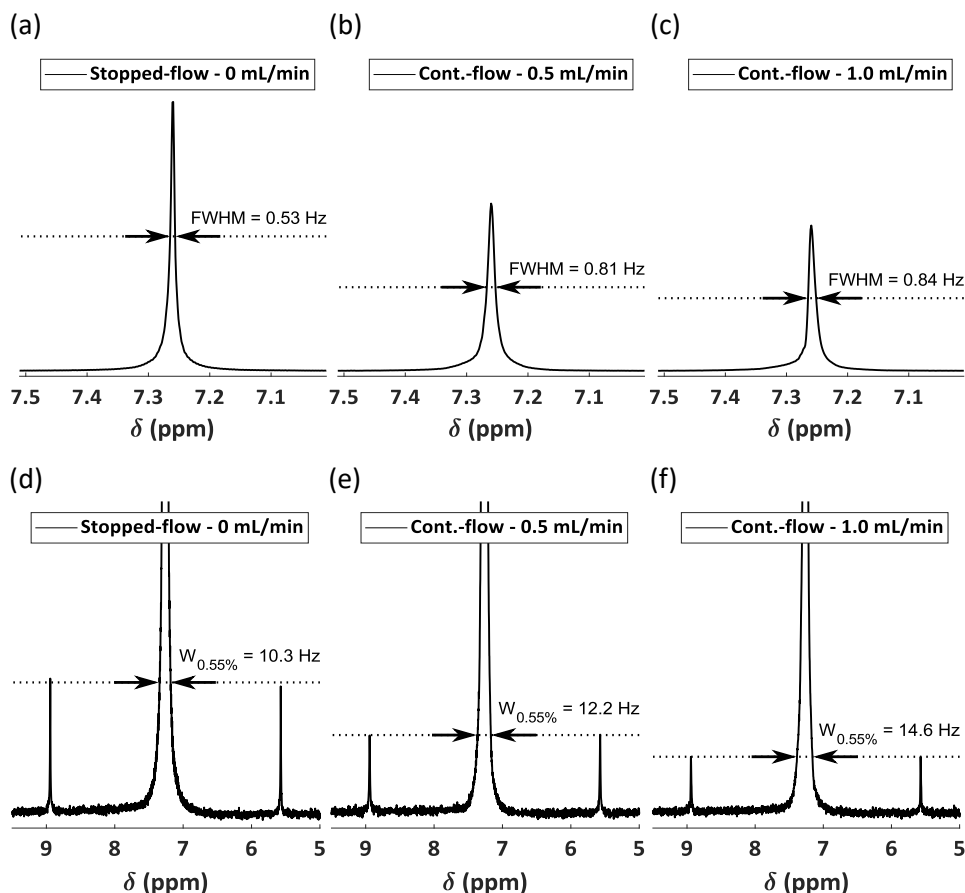


Figure 2.17: Effect of flow conditions on resolution of chloroform ^1H -NMR spectra (62 MHz, 1.45 T, Spinsolve 60, see Table 2.4, p. 34) at flow rates of 0 mL/min (stopped-flow), 0.5 mL/min, and 1.0 mL/min. The broadening at the full width at half maximum (FWHM) is illustrated in figures (a)–(c), and at the 0.55% of the peak height (i.e. peak height of the ^{13}C -satellites) in figures (d)–(f).

2.2.7 Design Considerations of NMR Flow Cells

The main requirement in the design of a continuous-flow NMR flow cell is that the mobile phase has to be completely transferred, i.e. a positive displacement of the mobile phase, in order to avoid back mixing, which is of particular importance to SEC-NMR hyphenation to retain resolution. In the first approach, in the context of high field NMR spectroscopy, for designing suitable NMR flow cells for the continuous recording of NMR spectra, conventional probes were employed.^[106,115, p. 5] Typically, the high field NMR spectra were recorded under rotation of the NMR tube with a rotational frequency of ca. $F = 20$ Hz to compensate for B_0 magnetic field inhomogeneities. The first pioneers, Watanabe and Niki,^[106,115, p. 5] adapted the NMR probe to gain sensitivity by introducing two thin-wall Teflon capillaries within the rotating NMR tube, one capillary to introduce the mobile phase and analyte and the second for removing it, transforming it into a continuous-flow set-up. The problem with this design was two-fold, firstly a complete transfer of the mobile phase by using the second capillary was not guaranteed resulting in unwanted back mixing, and secondly

memory effects were introduced into the capillaries at the bottom of the NMR tube due to rotation.^[106, p. 5] This led to the redesign of the NMR tube with a more robust and simple approach, in which a 'bubble' was introduced into a glass capillary by widening it at a designated region. This new 'bubble cell' flow cell design, introduced in the 1980s, was highly successful compared to the first approach and was used for the acquisition of the first continuous-flow NMR experiments on permanent iron magnets^[116–120] and superconducting cryomagnets,^[118,121–128] and is still the design of choice currently. The most common geometry of flow cell employed in high field NMR spectroscopy consists of the U-type geometry depicted in **Figure 2.18**, whereas for low to medium field NMR spectroscopy the vertically straight geometry is preferred and is depicted in Figure 2.16. In order to avoid the formation or trapping of air bubbles, the mobile phase is typically introduced into the flow cell against gravity, from the bottom to the top.

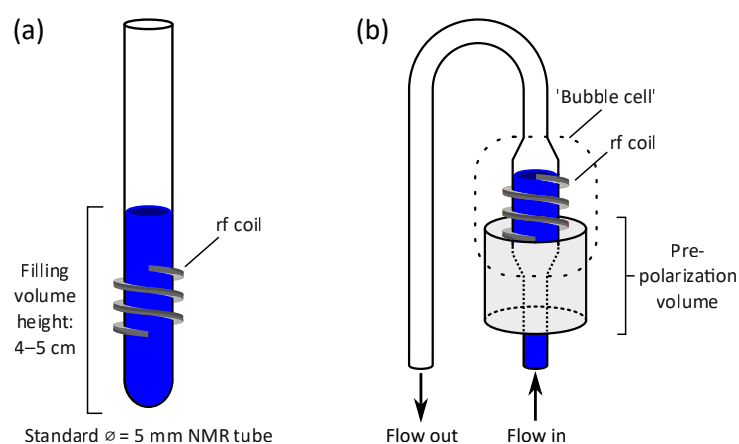


Figure 2.18: The (a) standard and (b) U-type flow cell design (completely within the magnet) for high field NMR spectroscopy. See Figure 2.16 for a depiction of the flow cell geometry typically employed for permanent magnet NMR spectrometers.^[106, p. 2]

In the case of on-line LC-NMR hyphenation, the vertical geometry (see Figure 2.16) is mostly used.^[107,129–133] The U-type flow cell geometry has some limitations such as distortion of the central symmetry of the external magnetic field in the z-direction, and rotation is not possible. In contrast to the conventional NMR tube, the continuous-flow cell design has a much higher *filling factor*, i.e. the ratio of the sample volume to that of the NMR detection volume. Additionally, the flow cell volume is an important parameter to take into consideration, as by increasing the volume the sensitivity of the NMR experiment can be increased. However, this leads to a reduction in the time/volume resolution of a continuous-flow experiment. For liquid chromatography, the flow cell volume is generally in the range of $V = 60\text{--}120\ \mu\text{L}$. Therefore, the flow cell volume for continuous-flow NMR experiments is a trade-off between NMR sensitivity and chromatographic resolution.^[106, pp. 5–9] From a purely NMR perspective, there is typically no problem to differentiate between signals obtained from major or minor components, consequently allowing some tolerance for a reduction in chromatographic resolution, i.e. peak broadening, for the gain in NMR sensitivity. The latter is especially valid when working at low to medium field strengths, and NMR sensitivity enhancements is generally the focus point for method development. A more in-depth description related to the flow cell design developed and optimized in this

thesis will be provided in **Chapter 4, Section 4.2** (p. 64).

2.3 Quantum Cascade Lasers (QCL)

This section will provide an overview on the quantum cascade laser (QCL), including a brief description of its origin and operating principles.

2.3.1 Introduction

Quantum cascade lasers are semi-conductor lasers, and have a fundamental difference from classical semi-conductor lasers, in the sense that they only employ a single type of carrier charge, i.e. electrons, in which light transmission takes place due to inter-subband transitions (ISB) within a two-dimensional structure of quantum wells and barriers of heterostructure (also known as unipolar lasers). Quantum cascade lasers emit in the infrared region of the electromagnetic spectrum (see Figure 2.8, p. 21) and compared to conventional black body radiation sources (globars, typically silicon carbide, SiC) have a 10^4 times higher radiation power per wavenumber.^[134,135] The first reported work on QCLs began in the early 1970s, when the possibility of amplifying electromagnetic waves in a semi-conductor super lattice was suggested by Kazarnikov and Suris,^[136] following the work of Esaki and Tsu,^[137] who fabricated the first one-dimensional periodic potential multi-layer by systematically varying the composition during epitaxial growth resulting in a mono-crystalline super-lattice. These developments led to the first QCL realized in 1994 at Bell Laboratories by Faist et al.^[138,139] and are often regarded as the principal example of "bandgap engineering". The reason for this is that the energy-spacing between the subbands, and consequently the frequency at which light is emitted, can be engineered artificially by simply varying the size of the quantum wells. A time line related to some of the most significant milestones of QCL development over the last five decades is depicted in **Figure 2.19**. The reader is directed to a comprehensive review article on MID-IR developments (up to 2001) by Gmachl et al.^[140] A fundamental characteristic of QCL technology, is the use of periodic multiple quantum-well (MQW) segments or modules, such that a single charged carrier leads to the generation of numerous photons as it is being transported through the various recurrent segments or modules. Modern QCLs cover a relatively large wavelength range of $\lambda = 3\text{--}190\ \mu\text{m}$ ($\tilde{\nu} = 3333\text{--}53\ \text{cm}^{-1}$),^[141–145] and additionally up to $\lambda = 215\ \mu\text{m}$ ($\tilde{\nu} = 47\ \text{cm}^{-1}$) when magnetic field operations are used, surpassing any laser source based on semi-conductors in this vast range of the electromagnetic spectrum. The spectral width of the tunable range is an important parameter for external cavity quantum cascade lasers (EC-QCLs). The first EC-QCL have been commercially available since 2006^[146] and generally have spectral widths of up to a wavenumber of $\tilde{\nu} = 200\ \text{cm}^{-1}$. Moreover, QCLs, as illustrated by Faist et al.,^[138,139,147] have primarily been achieved in the conduction band of n-doped InGaAs/InAlAs, GaAs/AlGaAs, and InGaAs/AlAsSb heterostructures. All of the aforementioned super-conducting materials have been used at a wavelength of

$\lambda \sim 10 \text{ }\mu\text{m}$ ($\tilde{\nu} \approx 1000 \text{ cm}^{-1}$), which corroborates the versatility of the QCL concept: it can be tailored to material specifics and incorporate advances in material-growth technology. The reader is referred to the text of Faist.^[139] for a detailed description of the subject.

2.3.2 Fundamentals and Operating Principle

In order to understand the operating principle of QCLs, a brief description of the key differences between inter-band and inter-subband lasers will be provided. As aforementioned, the characteristic property of light emission in QCLs is through their occurrence of inter-subband transitions, which is fundamentally different than inter-band operations used in, for example, diode lasers. The latter rely on the recombination of ‘injected’ electrons to emit photons, where the radiative transition takes place between the conduction and valence bands, and the emission wavelength is determined by the physical width of the bandgap, which is a material property, see **Figure 2.20**. Consequently, different materials are required in order to change the wavelength. In Figure 2.20 the different cases for inter-band and inter-subband transitions are depicted. Figure 2.20 (a) illustrates a crude sketch of the radiative inter-band transitions for a quantum well (potential well or hole) in both the conduction and valence bands. In the aforementioned case, the main purpose of the quantum well is to act as spatial barrier in which the ‘injected’ electrons and holes are concentrated into a very small volume. This allows for a higher statistical probability of radiative recombination to occur. Inter-band radiative transitions involves the recombination of an electron from the conduction band into a quantum well (hole) from the valence band. As a result, inter-band lasers are intrinsically bipolar and also common for most classes of semi-conductor lasers. In contrast to inter-band transitions, inter-subband transitions occur within the subband states of either the conduction band or valence band with the same in-plane dispersion. Figure 2.20 (b) depicts the quantum well of only the conduction band, containing the energy levels of two subbands, including the corresponding radiative transition within.^[150] Contrary to inter-band lasers, the states are not separated by an energy gap. Therefore, any transition that allows for the required momentum exchange, permits the scattering of an electron from the upper to lower energy states, where the transition energy is merely the difference between the confinement energies of the individual electronic states.^[139, p. 3] Having the transitions within the respective subbands has two advantages: (1) the frequency of radiation can be designed by varying the bandgap (width) of the quantum wells based on the same heterostructure materials; (2) the radiative recombination leads to an energy dispersion of the subbands, in the two-dimensional density of states $k(||)$, which yields a delta-function-like joint density of these states at the transitional energy, resulting in an improved gain. The latter is limited by the non-radiative relaxation life-time of intersub-sub transitions, which are generally much faster ($t \approx 1$ ps) than non-radiative inter-band transitions ($t \approx 1$ ns), which is attributed to a rapid polar longitudinal optical (LO) phonon¹ inter-subband scattering mechanism inherent to semiconductor heterostructure. Consequently, the amount of population inversions achievable between the subbands are limited by the low life-time limits. In order to circumvent this problem, inter-subband lasers generally contain a multitude of cascade modules that enable sufficient gain achievement for effective lasing. Cascading is possible with inter-subband transitions due to its inherent unipolar nature.

¹A phonon (a quasiparticle) is a collective excitation in a periodic, elastic rearrangement of atoms or molecules in condensed matter, specific to solids with the exception of some liquids.^[151]

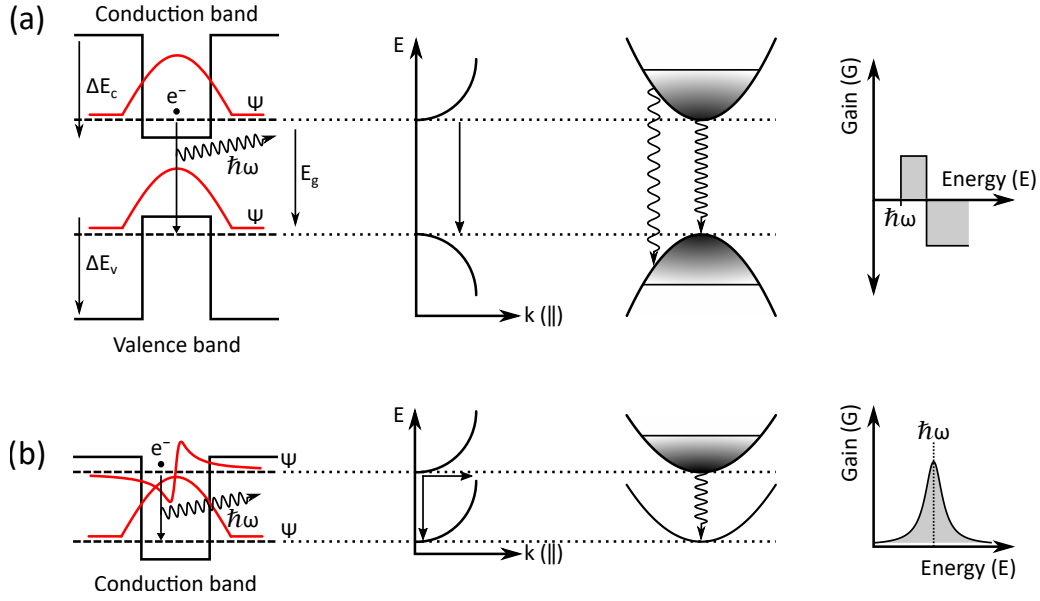


Figure 2.20: Depiction of (a) a radiative inter-band, and (b) radiative inter-subband transition between states (electrons and two-dimensional quantum wells). The wavefunctions, Ψ , of the electrons within the potential wells are also illustrated. The abbreviations and symbols used within the figure are as follows: e^- : electron, ΔE_c : conduction band energy, ΔE_v : valence band energy, E_g : physical energy gap, $\hbar\omega$: Planck-Einstein relation, E : energy, $k(\parallel)$: k-vector for a two-dimensional density of states for a parabolic in-plane dispersion.^[139, pp. 3–4]

The photons generated by means of recombination, Figure 2.20 (a), will have an energy, described by

$$E_{ph} = E_g + \Delta E_c + \Delta E_v, \quad (2.3.1)$$

where E_g is the physical bandgap of the quantum well material (typically on the order of $E = 1$ eV or $\lambda \sim 1.24 \mu\text{m}$) and essentially determines the frequency of radiation, ΔE_c and ΔE_v are the conduction and valence band confinement energies, respectively (see Figure 2.20). It should be noted that the E_g term is the most prominent in the given expression, which intrinsically is indicative that the potential lasing wavelength is directly proportional to the chosen material system (e.g. InGaAs/InAlAs or GaAs/AlGaAs) rather than on the epitaxial design. Inter-subband systems, Figure 2.20 (b), are becoming more favourable, due to the increasing demand of higher gain and longer wavelengths.

The distinguishing factor between the optical transition of inter-bands and inter-subbands is the gain spectrum (see gain spectrum of Figure 2.20), where it is broad and delta-like, respectively. For inter-band systems, the gain spectrum is broad due to thermal distribution, resulting from electron and quantum well distribution within the bands, of the energy carriers, generally depicting an absorption for the energies on the higher energy side of the spectrum. In the case of inter-subband systems (e.g. QCLs), the joint density of states is delta-function like, behaving optically much like atomic systems.^[139, p. 3] Despite this, the resulting gain spectrum has a finite width due to scattering as a result of collisional (homogeneous) broadening and material dependent (inhomogeneous) broadening of the subbands.^[142,148] As depicted in Figure 2.20, inter-subband gain spectra will have a

Lorentzian distribution, dictated by the Kramers-Kronig transformations.

One of the key benefits of QCLs is the ability to re-use electrons, unlike its counterpart inter-band lasers, which can only emit one photon per injected electron-hole pair. Quantum cascade lasers can emit many more photons per electron transit through the super lattice structure, which is why QCLs produce high levels of differential gain compared to inter-band lasers. In order for the aforementioned to occur, electrons must undergo a repetitive radiative transition in an efficient process, where the higher energy subband is populated after depopulation of the lower energy subband, which is achieved through *resonant tunnelling*. A simplified depiction of this process is shown in **Figure 2.21**. Efficient resonant tunnelling through the potential barriers is achieved when the energy confined states in adjacent quantum wells are well matched.

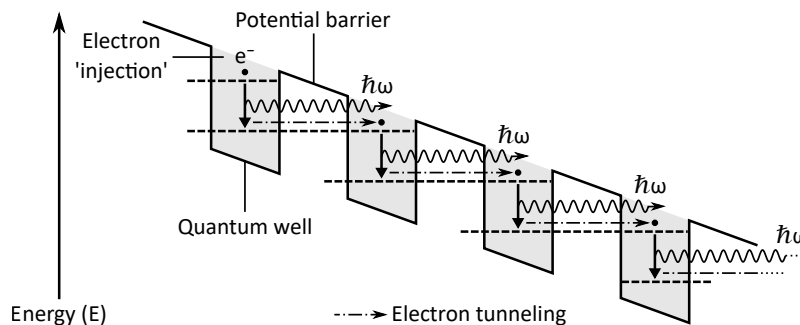


Figure 2.21: A simplified depiction of the basic principle behind the operation of a QCL. Following the introduction/injection of an electron into an excited subband, it emits a photon due to relaxation from a higher to lower energy state within the subband. The emitted photon has an energy corresponding to the spacing of the respective subbands. The lower energy electron undergoes the process of electron tunneling into the excited state of the adjacent quantum well. This process continues, creating a cascaded process (think of it as a domino effect) allowing for increased photon emission resulting in high levels of differential gain.^[152, pp. 8, 315]^[138]

The entire potential curve is shifted by applying an external voltage to the heterostructure, as illustrated in Figure 2.21. The energetic distance between the respective subband states are dependent on the width of the quantum well, including the thickness of the corresponding semi-conductor layer. It should be noted that the quantum well and potential barriers consist of several layers of different thickness, of which some are only a few atomic layers thick, e.g. according to Faist et al. up to ca. 9 Å.^[147] The photons produced within the cascading process get reflected from the surfaces of the super lattice material, in that the laser chip itself acts as a Fabry-Pérot resonator.² Within this thesis an external cavity quantum cascade laser (EC-QCL) has been utilized. The external cavity configuration refers to the use of a tunable wavelength filter outside the physical laser cavity.^[139, p. 186] The EC-QCL has the benefit that it provides access to the entire gain spectrum of the laser, consequently providing the largest achievable tuning range for a single semi-conductor laser chip (typically $\tilde{\nu} > 200 \text{ cm}^{-1}$). The latter makes it desirable for the application of multiple gas components or liquids, which intrinsically have broad absorption lines.^[139, p. 186] In general, EC-QCL devices are used in the Littrow or Littman-Metcalf configuration.^[154] A

²Fabry-Pérot lasers have the simplest quantum cascade laser design. Other designs include the distributed feedback-, external cavity- and extended tuning-lasers.^[139, pp. 168, 186]^[153]

simple depiction of the Littrow configuration is presented in **Figure 2.22**.

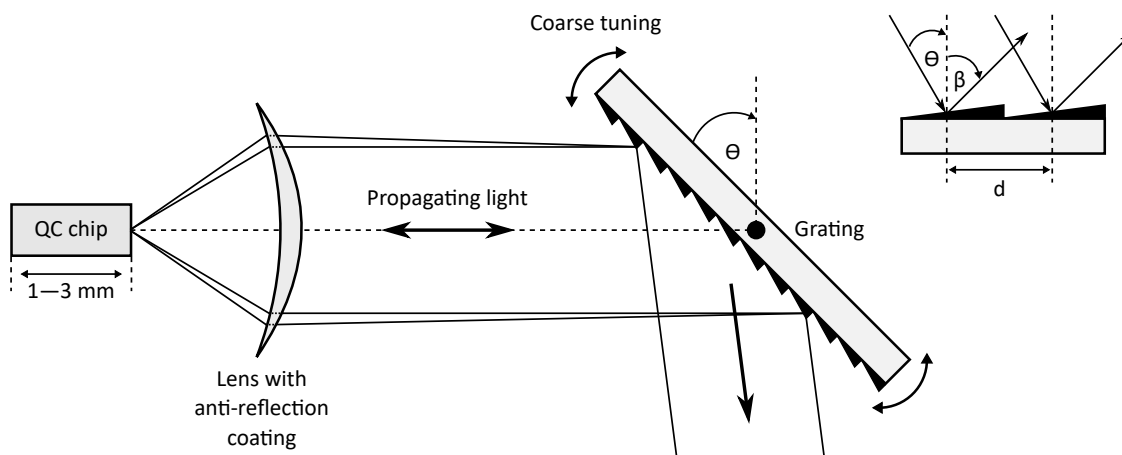


Figure 2.22: Schematic depiction of the Littrow configuration used in EC-QCLs. The incident light is focused through a lens containing an anti-reflection coating and diffracted by a grating at an angle, β , depending on the wavelength, λ . The black arrows used in the middle of the light beam indicates the direction of propagation, therefore the need for an anti-reflection coating to avoid QC chip damage. The smaller arrows on the top and bottom of the grating depict coarse tuning. The coarse tuning of the EC-QCL is achieved by varying the diffraction grating angle, θ described by $\lambda = 2d\sin\theta$, where d is the distance between the grating grooves.^{[154][139, p. 186]}

The application of QCLs as a chemically sensitive detector will be discussed in more detail in **Chapter 4, Section 5.6** (p. 179). The EC-QCL spectrometer used within the scope of this work was applied as a chemically sensitive detector for size exclusion chromatography.

2.4 Advanced Digital Data Evaluation

The following section provides an introduction to signal processing, with an overview on various approaches to improve the signal-to-noise (S/N) ratio of a given signal, and ends with a brief summary of digital signal processing.

2.4.1 Introduction

The interfacing of measurement instrumentation and computer-based data acquisition has become standard practice in modern laboratories, due to the advantages of having digitally recorded data. The latter enables easy signal processing,¹ data analysis and storage, by employing the vast number of digital computer-based numerical methods available. The ability to manipulate digital data allows for the transformation of complex signals into more usable forms, enabling the detection and measurement of desired peak information, reduction of noise to enhance sensitivity, improvement in resolution, compensation of system artefacts, and decomposition of complex signals into their individual components, to name

¹Signal processing in this context is defined as the continuous x,y numerical data recorded by scientific instruments as a time-series, where the x-component corresponds to the time or another quantity like energy or wavelength such as in the case of various forms of spectroscopy.

but a few advantages.^[155, p. 10] Digital processing hardware also allows for programmable operations, which enables signal processing functions to be performed via software with more ease by the hardware. The latter facilitates a greater degree of flexibility in system design, especially in the case of method development.^[156, p. 2] Furthermore, the precision achieved by digital systems is higher than its counterpart – analogue systems, which has led to rapid development in digital signal processing theory and applications.^[156, p. 2] In this thesis, digital signal processing has been extensively used to develop post data acquisition treatment for the processing, manipulation and enhancement of signals obtained from chromatographic and spectroscopic instrumentation (see **Appendices A.1**, p. 231, and **A.2**, p. 252). The forthcoming section deals with the origins of signal and noise, and the interplay between these parameters, including some available strategies that enable the improvement in sensitivity of SEC-NMR experiments. The relatively low sensitivity of NMR spectroscopy as a technique makes these aspects especially important when hyphenating NMR to SEC. Since the quantum cascade laser used within this work is much more sensitive than the NMR spectrometer, more attention is devoted to NMR signal processing. Some of the principles and strategies are used for QCL signal processing as well, and will become apparent in **Section 5.4** (p. 171).

2.4.2 Signal, Noise and Sensitivity

The sensitivity of an instrument is defined as the minimum level of input, which produces a signal (a change in the voltage) with specified power/intensity or *Signal-to-Noise* (S/N) ratio. In the spectroscopy context, sensitivity can be understood as the amount of material required to produce a spectrum with an adequate S/N within a given time frame. For exact definitions and limits, sample properties, the nuclei involved, and the experiment must be described. In practice, greater sensitivity means that the same experiment can be performed with either less sample material or time.

One of the key parameters in signal processing is experimental measurement error, which, regardless of the expertise or instrument sophistication involved, is inevitable. Experimental measurement error is (generally) subdivided into two major groups: (1) *systematic*- and (2) *random-errors*. Systematic errors are typically defined as consistent varying data with either less- or greater-than, within a certain percentage, the true/correct value, and as the name suggests is systematic, typically with an observable trend between measurements. In contrast, random errors have unpredictable variations in their response, which may either occur from time-to-time within a single measurement, between measurements or both. This type of error is commonly referred to as *noise* or *stochastic noise*. There is a plethora of noise sources, which may further be subdivided into two categories: (1) chemical noise, which arises from the sample being analyzed (e.g. chemical equilibria); and (2) instrumental noise, which is associated with instrumental components (e.g. thermal/Johnson noise, shot noise, flicker/ f^{-1} noise or environmental noise).² The reduction of noise in any measurement is a crucial parameter as noise contains unwanted information that degrades the accuracy

²There is also digitization noise as a result of rounding numbers to a preset fixed value of digits, also known as *quantization noise*

and precision of an analysis. In general the main strategy of improving the sensitivity is by minimizing the amount of noise at each step in the system as much as possible. In signal processing, sensitivity can be improved and noise reduced by filtering, and/or smoothing, e.g. using low-pass digital filters, algorithms such as a moving average or matrix transformation, called convolution such as convolution kernel.

The *limit of detection* (LOD) in spectroscopy depends greatly on the desired information, molecular size, and instrumentation. In the field of analytical chemistry the LOD is defined as the lowest concentration that allows for reliable signal detection, and is generally regarded to be $S/N \geq 3$.^[157, pp. 112–114] In order for reliable quantification of a given signal, the minimum concentration of an analyte should correspond to the *limit of quantification* (LOQ), which is defined as having an $S/N \geq 10$.^[158] The characterization and quantification of small molecules ($MM < 900$ g/mol)^[159] with the use of modern high-field magnets ($F > 300$ MHz) and cryoprobes is possible up to microgram and micromolar level using various $^1\text{H-NMR}$ techniques.^[160–163] For benchtop NMR spectrometers ($F = 40\text{--}100$ MHz), this is limited due to the intrinsic drawback of the lower field strength, however, with the recent advancement in this field it is possible to reach milligram and millimolar levels (see Figure 2.15, p. 38) within a standard 5 mm outer diameter test tube.^[164]

Signal-to-Noise (S/N) ratio

The S/N and sensitivity are proportional, i.e. the same gain in sensitivity can be achieved either by halving the noise or by doubling the signal. Both of these parameters have been subject to investigation and improvement during the method development stages of most techniques involving spectroscopy. Furthermore, the S/N is a way to describe the sensitivity of a measurement. In electronics, the signal-to-noise ratio, where the available power is proportional to the square of the *Root Mean Square* (RMS) values of the voltage ratio between a signal (V_{sig}) and background noise (V_n), is described by^[165, p. 1026]

$$S/N = \frac{V_{sig}^2}{V_n^2}. \quad (2.4.1)$$

Due to the very broad range of values given by this ratio it is often defined in decibels (dB), and **Equation 2.4.1** can be expressed as,

$$S/N_{dB} = 10 \text{Log}_{10} \left(\frac{V_{sig}^2}{V_n^2} \right). \quad (2.4.2)$$

This simplistic definition of the S/N is less practical due to the rapidly changing amplitudes of the electrical signals as a function of time, for example in NMR spectroscopy or QCLs. Alternatively, a more comprehensible and practical definition is employed, in which the signal intensity is related to the standard deviation of the detected system noise in the spectra, described by^[79,166]

$$S/N = \frac{S}{2\sigma}, \quad (2.4.3)$$

where S is the amplitude of the given signal in a processed spectrum and σ the *standard*

deviation of the noise. This is a rather intuitive definition, as the standard deviation in principle describes how severe the background noise affects the signal. The noise is generally considered to have a normal (Gaussian) distribution, i.e. the noise most often affects the signal in either a positive or negative change of σ or less, or with a total range of 2σ , and this, related to the signal intensity, results in the S/N . It also matches the visual comparison of the noise floor and the signal height, as the signal from the noise floor similarly varies typically from $-\sigma$ to $+\sigma$, or within a range of 2σ . The standard deviation can be estimated from the peak-to-peak noise in the baseline, N_{ptp} , where N_{ptp} is estimated as 5σ ,^[67] as described by^[79,166]

$$S/N = \frac{S}{2\sigma} \cong \frac{S}{2N_{ptp}/5} = 2.5 \left(\frac{S}{N_{ptp}} \right). \quad (2.4.4)$$

Similar S/N definitions, as described in **Equation 2.4.4**, are employed in a variety of other fields, such as image analysis, where electrical signals are indirectly considered for quantification purposes.

Signal Averaging and Acquisition Time

One of the major advantages of Fourier transform NMR-spectroscopy is the possibility of signal averaging recorded data.^[70, pp. 268–269] The most convenient way of increasing the signal, is to simply numerically add the results of two or more identical spectroscopy experiments. Considering an NMR experiment, where a single pulse-and-collect experiment results in a signal intensity of I , adding for example two FIDs from subsequent experiments, result in an FID with a signal intensity of $2I$. This works on the premise that the signal in both cases are identical, excluding random noise errors, and will match precisely, therefore, yielding a perfect constructive interference. The addition of FIDs, therefore, results in a coherent addition of the 'wanted' signals. Important to note is that the added FID will now exhibit $\sqrt{2}$ the noise of a single pulse-and-collect experiment. Since the noise (still considering an NMR experiment), which is derived mainly from thermal electromagnetic fields generated in the sample and probe, is random (stochastic) and not phase coherent, it will only add up partially, leading to an increased S/N . Each individual repetition of the experiment which is co-added or averaged together is more commonly referred to as a *transient*. This is a well-known way of signal enhancement, and is performed routinely by (NMR) spectroscopists and method developers.

The improvement in S/N can be quantified by calculating/determining how the noise adds up. The noise is generally considered to have a normal (Gaussian) distribution and is random, resulting in the sum of the noise being treated as a sum of two, independently and normally distributed random variables with identical standard deviations and means. As a result, the sum is also normally distributed for such variables, and the properties of the new normal distribution can easily be calculated. The standard deviation of the noise is σ , and consequently the *variance* is σ^2 , with the new variance simply being the sum of variances, from which the standard deviation is obtained by taking the square root, as shown in **Equation 2.4.5**,

$$\begin{aligned}\sigma_{new}^2 &= \sigma_1^2 + \sigma_2^2, \\ \sigma_{new} &= \sqrt{\sigma_{new}^2} = \sqrt{2\sigma^2} = \sqrt{2}\sigma.\end{aligned}\tag{2.4.5}$$

Taking this equation and combining it with the S/N equation (**Equation 2.4.3**), the new S/N resulting from the co-addition of two identical experiments can be described by

$$S/N_{new} = \frac{S_{new}}{2\sigma_{new}} = \frac{2S}{2\sqrt{2}\sigma} = \sqrt{2}\frac{S}{2\sigma} = \sqrt{2}S/N.\tag{2.4.6}$$

Doubling the amount of transients will yield $\sqrt{2} \approx 1.414$ times the S/N compared to that of the original signal.³ Thus, in order to double the S/N , four times as many transients are required,

$$S/N_{new} = \sqrt{4}\frac{S}{2\sigma} = 2S/N.\tag{2.4.7}$$

The total measurement time is quadrupled for every doubling of the S/N . The measurement time, therefore, increases quadratically compared to S/N , and the signal-to-noise ratio is proportional to the square root of the total acquisition time, t , described by

$$S/N \propto \sqrt{t}.\tag{2.4.8}$$

This is of paramount practical use, as from the equation above it might be considered that an arbitrarily low sample concentration might produce a spectrum with adequate S/N if a suitable number of transients are acquired. This is true to some extent, but ineffective, as the square root function is equivalent to the law of diminishing returns.⁴ Thus, to increase the S/N by a factor of ten, it would require a hundredfold increase in number of transients. With this fundamental relationship between S/N and measurement time, the sensitivity in spectroscopy can be expressed as S/N normalized to time, described by

$$\text{Sensitivity} = \frac{S}{2\sigma\sqrt{t}}.\tag{2.4.9}$$

2.4.3 Digital Signal Processing

All spectroscopic instrumentation works on the concept of converting a response, whether chemical or physical, into a continuous signal, i.e. a time-dependent physical change is mapped to a time-dependent function (time or space). The latter is referred to as an *analogue signal*. In order to perform *digital signal processing* (DSP), the continuous analogue signal must be converted into a discrete-time signal by means of an interface, known as an *analogue-to-digital converter* (ADC) in order to perform computer-based

³Fun fact: the square root of two is known as Pythagoras' constant, and is the first irrational number ever discovered.^[167, pp. 37–41]

⁴In economics, the law of diminishing returns refers to the incremental reduction of output in a production process with an incremental increase of a single variable, whilst all other variables are held at a fixed value. In other words, a certain point will be reached, where the additions of the input result in progressively smaller (diminishing) increases in output.

processing, e.g. discrete Fourier transformation (DFT).^{[156, p. 5][168]} The basic principle behind the signal conversion is depicted in **Figure 2.23**.

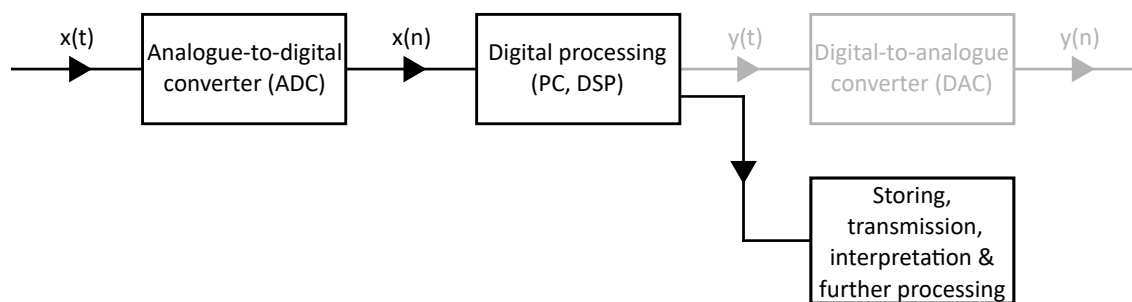


Figure 2.23: Illustration of a digital signal processing system where the input signal, $x(t)$, is a continuous function of a real-valued variable, time (t), which is defined over the interval $(-\infty, \infty)$, $\Delta t \rightarrow \infty$, and gets converted into a time-discrete signal, $x(n)$. The abbreviations PC and DSP refers to personal computer and digital signal processing, respectively. The greyed out digital-to-analogue (DAC) procedure is also a possible signal processing route, however, not used within the context of this work.

One of the major advantages of processing a digital (programmable) signal is the reconfiguration flexibility, allowing for a DSP operation to be reconfigured by simply changing the respective program. Accuracy is another advantage of DSP, as DSP allows for a much more sophisticated and accurate control over signal manipulation. Large amounts of digital signals are also more easily stored than their counterpart analogue signals. After the continuous analogue signal (typically a voltage) enters the ADC, it is sampled into a discrete-time signal (which contains a sequence of real numbers) for a given acquisition time. The sampled signal then undergoes digitization/quantization, which involves the replacement of the real numbers with an approximation from a finite set of discrete values. The higher the amount of levels, also referred to as bits,⁵ within the digitizer, the more accurately the signal is represented. This has another major importance in that the amount of digitization/quantization noise is reduced with a higher bit digitizer (most NMR spectrometers use 12–16 bit digitizers).^[169, p. 16] If a signal exactly matches the size of an n -bit ADC the signal gets digitized to 2^n-1 numbers, thus for a 16-bit ADC one bit would be used for designating the sign value and the remaining 15 bits determine the magnitude, therefore, the maximum dynamic range is 32 767:1, which is the limiting factor with respect to sensitivity of a measurement. It should be noted that at some point using higher bit digitizers is not cost-efficient and can be circumvented by increasing the dynamic range of a digitizer by performing oversampling, depending on the maximum sampling rate required.^[168,170] The process is illustrated in **Figure 2.24**.

Digital signal processing is a vast research field on its own and benefits many different disciplines. The reader is referred to the text of Proakis et al.^[156] for a more in-depth step-by-step explanation of the fundamentals of digital signal processing.

⁵A bit is short for a binary digit, which can have a value of either 0 or 1.

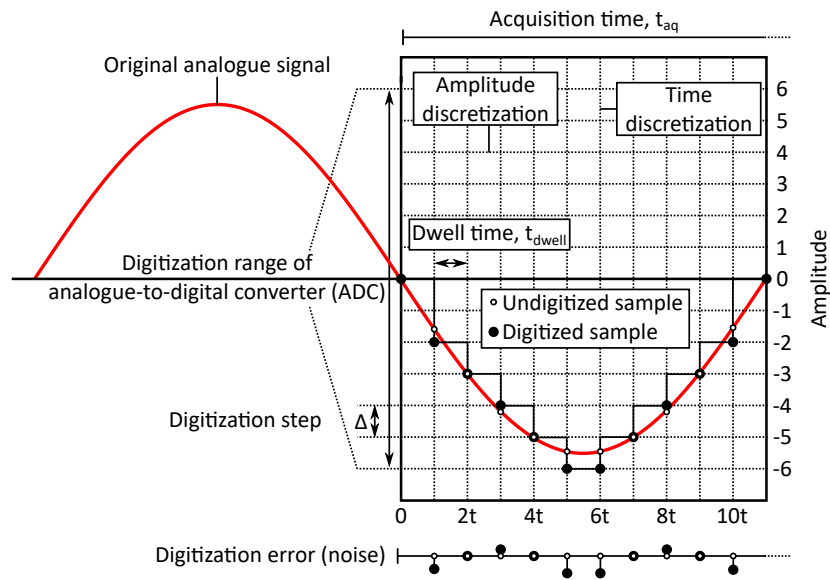


Figure 2.24: Depiction of how a continuous-time signal is digitized to a discrete-time signal, illustrating the digitization/quantization errors, which gets translated into noise. The sampling rate, not defined on the graph, is $1/t_{dwell}$ with its dimensional unit in Hertz (Hz).

Chapter 3

Hyphenation of Chromatography and Spectroscopy: Information-Rich Detectors

Chapter 3 is dedicated to the various spectroscopic techniques hyphenated to chromatography allowing for uniquely correlated information to be obtained. The focus is a descriptive literature overview, highlighting the breakthroughs achieved in hyphenating the various spectroscopic techniques to liquid chromatography. The spectroscopic techniques investigated comprised of; Fourier-transform infra-red (FT-IR) spectroscopy, mass spectrometry (MS), high field (HF) and benchtop NMR spectroscopy, and ending with QCLs.

3.1 Introduction

The on-line coupling of chromatography to spectroscopy is also referred to as hyphenation.^[171,172] The correlation of compositional changes to the molar mass distribution (MMD), or specific component characterization of polymeric species, especially complex systems, is highly sought after due to the rapid information gained in a single experiment. This typically also provides direct insight into the structure-properties relationship of a given species. There are a variety of information-rich detectors available for the purpose of obtaining information on the chemical composition (CC) of compounds, such as FT-IR, mass spectrometry (MS), NMR and QCLs.^[7,8,171,173,174] Using the aforementioned detectors as stand-alone 1D techniques provides information on the bulk chemical properties of polymers. However, these detectors are generally not able to provide additional information such as differentiating between a block copolymer, physical blend, or mixture of both. This is where the power and versatility of hyphenating liquid chromatography to information-rich detectors come into play, as it provides the necessary separation step in order to accurately characterize polymers. When polymeric species are separated into various different polymer components, and characterized by means of an information-rich detector, the true strength of a 2D correlated technique can be exploited. In liquid chromatography (LC), there are

various modes of operation used for the separation of polymers (see **Chapter 2.1**, p. 6). However, the focus in the forthcoming section will be the hyphenation of information-rich detectors to size exclusion chromatography (SEC), as this was the LC operational mode of choice in this work. Size exclusion chromatography is the most widely used chromatographic technique for the characterization of molar mass distribution (MMD) of polymers, and is of particular importance as molar mass information generally has a direct correlation to the final mechanical properties. A very thorough description of the LC hyphenations that are of particular importance to polymer characterization was summarized by Pasch et al.,^[5, pp. 183–242] and topics related to biomedical, pharmaceutical and food by Albert et al.^[106, pp. 45–138] In the case of molecular analysis of polymers there are three fundamental material characteristics to consider: (1) molar mass distribution (MMD), (2) chemical composition (CC), and (3) topology, facilitating the need for more sophisticated 2D (or even 3D) characterization of the molecules in solution, see **Figure 3.1**.

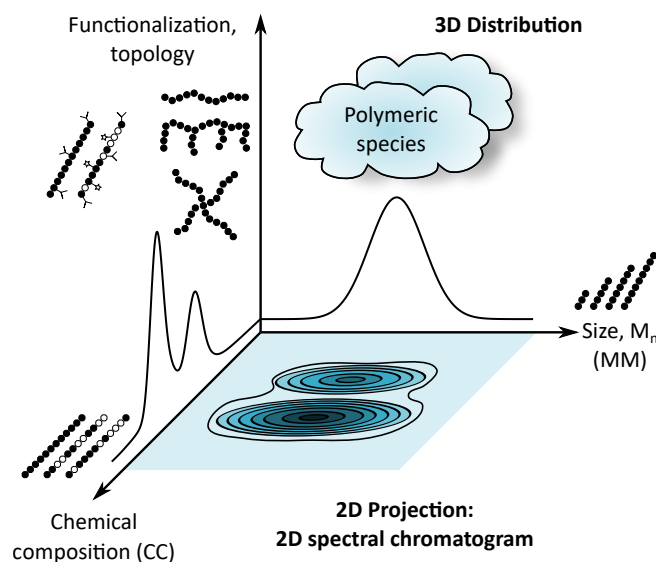


Figure 3.1: Distribution of the three important molecular characteristics of polymeric species portrayed as a 3D cloud, projected as a 2D spectral chromatogram. The depiction describes the fundamental idea behind the power of hyphenated techniques. Adapted from Beskers et al.^[7] with permission from the Royal Society of Chemistry.

3.2 Fourier Transform Infra-Red (FT-IR) Spectroscopy

Analysing complex polymeric species after chromatographic separation (CC or MM) often involves prior knowledge on their bulk chemical properties. Once the bulk chemical composition with respect to the polymer components, i.e. monomers, is known, the chromatographic separation technique can be optimized for the desired analysis. A reliable and time-efficient approach to determine these bulk properties, is to use infra-red spectroscopy. It has the advantage that it is a chemical sensitive (i.e. atomic structure – see Table 2.1, p. 19) detector with respect to organic functional groups (mid-IR, $\lambda = 3\text{--}15\ \mu\text{m}$, Figure 2.8, p. 21), which enables the analysis of a wide variety of molecules. This is also due to chemical compounds having their fundamental vibrational modes in the mid-IR region

of the electromagnetic spectrum. Additionally, it is a quantized process, involving the infra-red radiation interaction between molecules, resulting in the respective characteristic bending and stretching vibrational transitions, thus, providing information on the molecular structure and for example monomer composition.^[175, pp. 16–25] The corresponding IR intensity depends on the sample concentration and the absolute electrical dipole moments of a specific vibration and resulting population. As a result, IR detectors typically require a calibration of the extinction coefficient in order to perform quantitative analysis. Hyphenating an IR spectrometer to LC is also a means of method validation of an established separation technique (this is of more relevance to other modes of LC such as LAC or LC-CC). The hyphenation of IR to LC can be performed either off- or on-line. In general, the off-line mode is the preferred choice for two reasons: (1) no solvent interference and (2) improved sensitivity.^{[40, pp. 157–158][5, pp. 183–188]} However, this is a more time-consuming procedure, since it involves two steps: (1) solvent removal after chromatographic separation by means of an LC-Transform interface, and (2) the independent IR analysis of the fractionated species. An upgrade related to solvent evaporation-and-detection on-line has been developed by the company Spectra Analysis (DiscovIR, Marlborough, MA, USA), where the need for a two-step process of solvent evaporation and independent IR analysis, as in the case of the LC-Transform, is bypassed. A more detailed description can be found in the work of Dwyer et al.^[176] In the work of Besker et al.,^[7,177] meticulous optimization of the S/N ratio and numerical solvent signal subtraction allowed for the successful realization of on-line SEC-FT-IR characterization of common polymers such as polystyrene (PS), polymethylmethacrylate (PMMA) and polyisoprene at typical chromatographic conditions. The latter, unlike the aforementioned techniques, do not require the removal of the solvent/mobile phase. A particular successful hyphenation of SEC-FT-IR, is in high-temperature SEC characterization of polyolefins, using the high boiling-point solvent 1,3,5-trichlorobenzene, which fortunately has the correct spectroscopic transparency (due to not having a dipole) for olefin characterization.^[178]

3.3 Mass Spectrometry (MS)

The principle of solvent evaporation is synonymous with mass spectrometry (MS), especially the hyphenation of MS to gas chromatography (GC), as both are vapour phase techniques. The hyphenation of LC to MS, which is more complex than GC-MS due to the liquid-to gas-phase conversion-step requirement, is achieved using the following methods: (1) electro-spray ionization (ESI), (2) atmospheric pressure chemical ionization (APCI), (3) thermospray ionization (TSP), and (4) particle beam chemical ionization (PBCI).^[5, p. 204] The hyphenation of liquid adsorption chromatography (LAC) to MS is extensively used to obtain detailed information on the structural properties of polymers. However, it is limited to the lower molar mass end of the spectrum ($MM < 5000$ g/mol).^{[179–181][5, p. 205]} Additionally, the hyphenation of LC to MS also enables a more in-depth insight into polymer architecture (see Figure 3.1).^[182] Apart from using 1D liquid chromatography, more advanced 2D-LC techniques, such as LAC \times SEC, is used to separate polymers by their intrinsic chemical and physical properties prior to MS detection. Two dimensional

LC is also possible due to the one critical advantage of MS, its sensitivity, which typically has a detection limit in the picogram range ($m = 10^{-12}$ g).^[183] The hyphenation of MS to SEC is slightly more challenging than its interactive mode counterparts (i.e. LAC or LC-CC), mainly due to the higher molecular sizes being characterized by SEC. The latter makes the conversion process difficult, since larger molecules are not prone to be readily vaporized or ionized, and SEC-MS is therefore mainly used with oligomeric species. Mass spectra are generally complex to interpret, especially to the untrained user, due to the vast amount of fragmentation products associated with it. Fortunately, soft ionization techniques such as ESI, are particularly useful, since it allows for intact oligomer or polymer ions, reducing the amount of fragmentation products. The use of ESI-MS still results in complex mass spectra, as larger molecules require more than a single charge, typically producing a mixture of differently charged fragmentation products (ions). In addition to ESI, matrix-assisted laser desorption/ionization time-of-flight (MALDI-ToF) mass spectrometry allows for the extension of the accessible mass range to species with molar mass averages of up to $MM \approx 500$ kg/mol.^[5, p. 206] It has the drawback that it is not an on-line technique, as in the case of ESI-MS, since it is based on a desorption process of molecules from a solid surface, i.e. the matrix. Apart from mass spectroscopy being a very powerful tool for providing polymer architectural information, it also serves as a more precise method of molar mass determination. Furthermore, a direct quantitative comparison of polymers with different chain lengths is not possible, due to the probability of ionization occurrence of molecular particles. The characterization of polymers, including polyethyleneoxide (PEO), polyesters, resins, and polymethyl methacrylate (PMMA) has been successfully realized by SEC-ESI-MS.^[5, p. 205] An extensive review related to mass spectrometry and hyphenated techniques can be found in the work of Crotty et al.^[173] and Gruending et al.^[174]

3.4 High-Field and Benchtop NMR Spectroscopy

In the field of spectroscopy, nuclear magnetic resonance (NMR) spectroscopy is the most powerful analytical tool for obtaining structural information on organic species in solution (see Section 2.2, p. 20). This is ascribed to the possibility of differentiating between structural, conformational and optical isomers. Nuclear magnetic resonance spectroscopy is also a quantitative technique, as the signal is directly proportional to the amount of contributing nuclei, eliminating the need for prior calibration.^[5, p. 219] Pertaining to the high selectivity of NMR spectroscopy, it has some disadvantages, with the first major one being its low sensitivity compared to that of FT-IR, MS and QCLs. Secondly, the structure elucidation of a completely unknown species containing overlapping or overcrowded resonance frequencies, might be highly complex to near impossible. The hyphenation of liquid chromatography with NMR, especially high field NMR ($F > 300$ MHz, $B_0 > 7$ T, ^1H), is a well-established technique. Furthermore, LC-(HF)-NMR has been successfully applied to various homopolymers^[184,185] and copolymers.^[9,10,186,187] High field NMR spectroscopy is the method of choice when hyphenating LC to NMR, due to the inherent sample concentration considerations in LC and NMR. In general, NMR requires relatively

large sample concentrations for adequate sensitivity due to the unfavourable Boltzmann distribution.^[188, p. 30] The signal-to-noise (S/N) ratio is directly related to the magnetic field strength and scales approximately with $B_0^{7/4}$.^[67, p. 151] As a result, high field strengths (up to $B_0 = 28$ T) have been the hallmark of LC-NMR hyphenation,^[9,186,189–191] with the sensitivity being the major obstacle to overcome when using low- to medium-field strength magnets ($F = 20\text{--}80$ MHz, $B_0 = 0.5\text{--}2$ T). The disadvantage of HF-NMR spectrometers compared to its lower field benchtop counterparts, is that they are costly in both acquisition and operation, and typically require a vast amount of operational experience, making it a less feasible option for non-dedicated NMR research groups and industry. Apart from being sensitive to the chemical composition of molecules (independent of molar mass), it can also reliably provide molar mass estimates up to $MM \approx 20$ kg/mol via end-group analysis.^[192–194] In contrast, SEC has a limitation on injected analyte concentration: SEC columns can only separate dilute solutions without losing chromatographic separation integrity (typically 1 g/L and 3 g/L for analytical and semi-preparative columns, respectively). Additionally, hyphenation to SEC leads to a further reduction in sample concentration after chromatographic separation. The solvent-to-analyte ratio after chromatographic separation is typically in the range of 1000:1, resulting in a substantial amount of unwanted solvent signals when protonated solvents are used. The latter facilitates the need for dedicated pulse sequences for adequate solvent suppression or even the use of deuterated solvents (i.e. spectroscopic-transparent solvents) in SEC. However, the use of deuterated solvents is typically avoided, as they are generally expensive and, therefore, not suitable for routine analysis. The hyphenation of LC to both high fields^[9,185,186] and low fields (based on permanent magnet designs)^[10,187] has been successfully realized. The first stopped-flow LC-NMR experiment has been reported in 1978 by Watanabe and Niki^[115] on the investigation of isomeric dimethylphenols using a 60 MHz NMR spectrometer. Shortly following their work, the first continuous-flow experiment was reported by Bayer et al.^[116] in 1979. In SEC-NMR the main field of interest lies in the investigation of copolymer compositional analysis. The work by Hiller et al.^[195] on the investigation of PS-*b*-PMMA ($F = 500$ MHz, $B_0 = 11.7$ T, ^1H) is an example of this, as well as the solvent suppression techniques involved when using protonated solvent, including the associated limitations. Furthermore, the work of Cudaj et al.^[187] illustrates the approach of SEC-NMR hyphenation at low fields ($F = 20$ MHz, $B_0 = 0.5$ T, ^1H) and highlights the necessity of using slightly higher field strengths. Improved permanent magnet designs, allowing higher field strengths, has opened new possibilities for hyphenating low- to medium-field benchtop NMR spectrometers to LC (see **Section 2.2.5**, p. 32). In this thesis exploitation of these technological advances is made and the optimization of SEC-NMR at medium field strength ($F = 62$ MHz, $B_0 = 1.45$ T, ^1H) hyphenated to SEC for improved S/N using protonated solvents is presented.

3.5 Quantum Cascade Lasers (QCLs)

As mentioned in **Section 3.2** (p. 57), FT-IR spectroscopy is of great interest in the field of analytical chemistry due to its sensitivity and robustness. It is, however, somewhat

restricted when hyphenated to LC due to the necessity of spectroscopically transparent mobile phases when performed on-line, due to the absorption of mid-IR (see Figure 2.8, p. 21) radiation by matrix components. A particularly important aspect is the optical path length, which should be sufficiently low (generally between $\lambda = 10\text{--}50\ \mu\text{m}$) to ensure high S/N values in the water window region ($\tilde{\nu} = 950\text{--}1650\ \text{cm}^{-1}$, mid-IR) of the fingerprint range. Consequently, reducing the optical path length typically limits the overall sensitivity. One way to overcome this limitation is by increasing the intensity of the light source. This is where QCLs show great promise (see **Section 2.3**, p. 43), since they can also be employed with longer optical path lengths. The latter is especially valid when the demand for sensitivity and not selectivity, based on multi-wavelength measurements, is required. Considering liquid-based analysis, where the matrix is a solution, broad absorption bands occur, making selectivity rather challenging using this approach. Therefore, separation of the components prior to detection is required to achieve the desired selectivity. The first reported on-line hyphenation with a QCL was by Lendl et al.^[196] in 2000, using flow injection analysis (FIA), where they investigated phosphate concentrations in Diet Coke™. Shortly after this publication in 2001, Edelmann et al.^[197] published the first successful LAC-DFB-QCL hyphenation (DFB: distributed feedback laser), where they investigated glucose and sucrose in red wine. Additionally, QCLs have successfully been used in gas absorption measurements,^[198–200] due to the very narrow absorption bands (retaining selectivity) which is ideally suited for the narrow spectral widths ($\tilde{\nu} \approx 200\ \text{cm}^{-1}$) of QCLs, and photo-acoustic spectroscopy.^[201] There have only been few reported applications of LC-QCL hyphenation to date, which can possibly be ascribed to the following: (1) QCL technology is still relatively new, (2) high investment-costs, and (3) the sensitivity achieved by mass spectrometry is not likely to be matched by QCLs based on absorption measurements. The first SEC-EC-QCL hyphenation was demonstrated by Morlock et al.^[8] on a PS/PMMA blend sample with a detection limit achieved for the PMMA fraction of $m = 3.5\ \mu\text{g}$ injected mass (0.15 mol% on PMMA in PS/PMMA blend). Following this Kübel et al.^[16] published an improved limit of detection of $m = 0.45\ \mu\text{g}$ injected mass for the PMMA fraction measured on-line for a PS/PMMA blend. This illustrated the potential of (EC)-QCLs as detectors in chromatography, especially for the detection of rare functionalities such as end-groups or branching points in polymer characterization. The latter will be especially powerful when used in combination with mass spectrometry, resulting in unprecedented detection limit availability in conjunction with information extraction. The use of EC-QCLs would also be the recommended LC detector opposed to DFB-QCLs, since the wavelength in EC-QCLs can be selected or set making it more versatile, which is not possible for DFB-QCLs requiring multiple individual lasers for a certain wavelength range.

Chapter 4

SEC-NMR Method Development: Optimization of Selectivity and Sensitivity

This chapter is divided into five sections, all having a method development theme in order to improve existing or novel methods to obtain the highest yielding performance. The method development sections consist of the following; flow cell development, optimization of SEC, and NMR parameters, numerical solvent suppression, and concluding Chapter 4 with application examples of SEC-NMR hyphenation.

4.1 Introduction

The development of advanced synthetic routes for polymeric materials and more complex formulations used in modern-day products, requires ever-evolving sophisticated analytical techniques. The reason is that standard one-dimensional experiments (i.e. SEC or NMR) do not fulfil the necessary requirements to provide an adequate amount of information in a one-off experiment. This can be circumvented by employing two-dimensional techniques, where multiple material properties can be analysed simultaneously, providing correlated information in a single experiment. The development of hyphenated techniques, especially liquid chromatography (LC) in combination with molecular spectroscopy, is a promising approach to fulfil the necessary requirements. Considering the existing liquid chromatographic hyphenations mentioned in **Chapter 3** (p. 56) and their applicability to routine SEC analysis, it becomes apparent that NMR spectroscopy (especially high-field NMR spectroscopy) is one of the most powerful analytical tools available. However, high field NMR as an on-line detector is limited due to high investment cost and complexity. The development of lower cost- and expertise-intensive NMR spectrometers based on permanent low-field magnets has allowed for NMR spectroscopy to become more accessible. The hyphenation of a low-field NMR spectrometer was already undertaken in this working group.^[187] Unfortunately, the NMR spectrometer was previously less effective as a routine chemically sensitive detector

for SEC due to its low field strength ($F = 20$ MHz, $B_0 = 0.47$ T). Apart from the highly sensitive mass spectrometer, which unfortunately is restricted in detectable molar mass ($MM < 5000$ g/mol) and high in cost, a good alternative detector is an IR spectrometer, as it is low in cost and maintenance, and provides adequate sensitivity. The realization of a standard FT-IR spectrometer hyphenated to SEC has also been achieved within this working group and is now a standard technique employed by companies, e.g. Polymer Standards Services (PSS GmbH, Mainz). Due to the technological advancements made in recent years related to benchtop NMR spectrometers (see Section 2.2.5, p. 32), the possibilities of MR-NMR spectroscopy as a chemically selective detector for SEC became more apparent. As Cudaj et al.^[10] performed remarkable work on the technology available at the time, further method development was required where the benefit of both dimensions can be fully exploited. Additionally, a fundamental pre-requisite of the hyphenation is that the technical complexity be low enough for chromatographers to operate the detector without NMR expertise. In the forthcoming sections, detailed focus will be on method development with respect to the optimization of selectivity and sensitivity of a medium resolution benchtop ^1H -NMR spectrometer hyphenated to an SEC instrument. The NMR spectrometer acts as an on-line chemically sensitive detector (see Section 2.2, Table 2.1, p. 19). A key parameter in the development is to retain typical SEC selectivity, i.e. not to overload the columns to obtain a sufficient amount of signal, while acquiring on-line NMR data with the highest possible sensitivity through thorough system optimization using protonated solvents. Additional parameters are flow cell design (see **Section 4.2**), pulse sequences (see **Section 4.4.5**) and numerical data evaluation (see **Section 4.5**). **Figure 4.1** provides a schematic depiction of how the benchtop NMR spectrometer can be integrated into an SEC set-up in conjunction with standard detectors such as UV and DRI. Refer to the photograph in **Appendix A.5 (Figure A.1, p. 273)** to have an impression of the developed set-up.

The main idea behind the work is to obtain chemical composition information on the polymer eluent from SEC. In the first dimension, SEC separates the molecules according to their hydrodynamic volume in solution, providing molar mass and molar mass distribution information. The second dimension provides the corresponding chemical composition of the analyte, producing on-line chemical composition information as a function of the molar mass distribution. Numerical solvent subtraction and post acquisition data processing of SEC-MR-NMR measurement are performed on an in-house written MATLAB^{TM1} software referred to as *Time-resolved nuclear Magnetic Detection of Eluates, TMDE* (see **Appendix A.1, p. 231**). In addition to SEC-MR-NMR method development, the investigation of novel chromatographic techniques as potential for signal enhancement will be explored, which will comprise interlaced/multiple injection chromatography and Fourier-transform SEC using sinusoidal injections. Furthermore, an investigation using higher intensity light sources, such as an external-cavity quantum cascade laser (EC-QCL), allowing for improved sensitivity when hyphenated to SEC, will be demonstrated. The SEC-EC-QCL will utilize some of the ideas developed in the SEC-MR-NMR method development for data analysis,

¹version: 9.8.0.1359463, R2020a

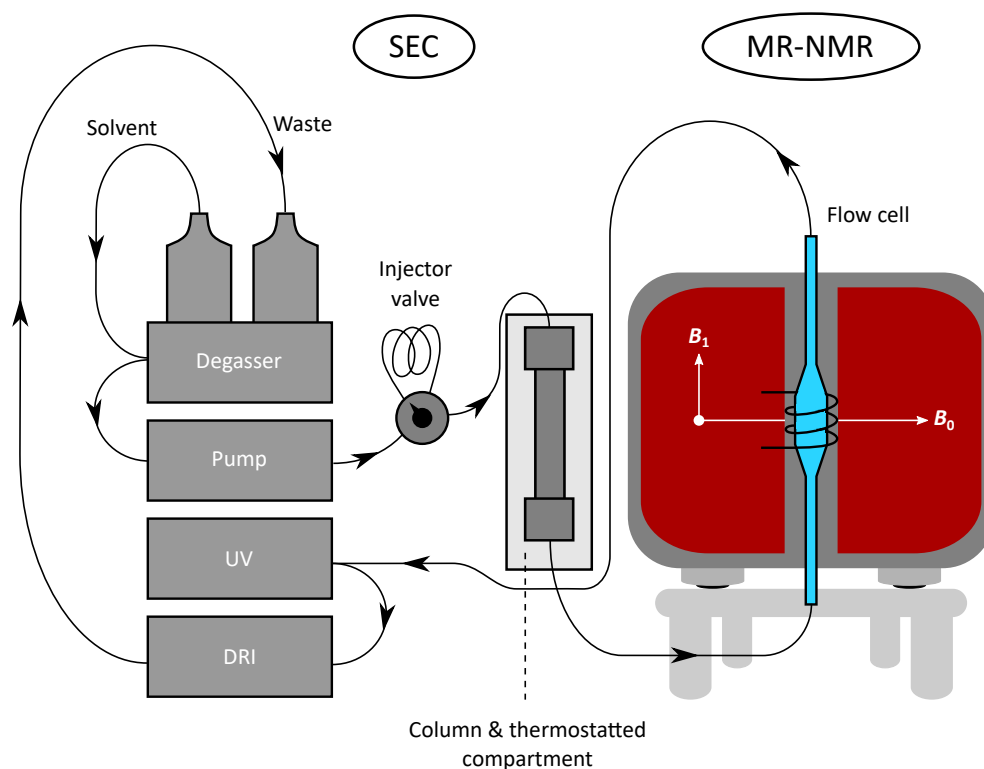


Figure 4.1: A diagram of the SEC-MR-NMR set-up, comprising a 62 MHz, ^1H -NMR spectrometer. The set-up resembles a general SEC set-up, with the NMR spectrometer just as an 'add-on' detector. All parts are connected with 0.25 mm i.d. polytetrafluoroethylene (PTFE) tubing – see Appendix A.5 (Figure A.1, p. 273) for a photograph of the set-up and Figure 2.16 (p. 39) for the detection principle in continuous flow NMR spectroscopy experiments. Additionally, the column is thermostatted to $T = 26.5\text{ }^\circ\text{C}$ to match the NMR magnet temperature, avoiding shim degradation. Adapted from Botha et al.^[15] with permission from the Royal Society of Chemistry.

also employing an in-house written MATLABTM software (see **Appendix A.2**, p. 252).

4.2 Flow Cell Development for SEC-MR-NMR Hyphenation

The forthcoming section is divided into four subsections and provides a short introduction followed by the design aspects of flow cells, a benchmark experiment used within the study to quantify the performance of the developed flow cells, and finally evaluating it in SEC-NMR applications.

4.2.1 Introduction

The design and construction of custom flow cells for hyphenating spectroscopy to chromatography is perhaps one of the most important starting points in the method development process. It is also the proverbial Achilles heel of the system, as a poorly designed flow cell will unavoidably make the optimization process of sensitivity and selectivity a hard and frustrating endeavour. In order to have a successful flow cell design, the flow cell used within this work had to fulfil the spectroscopic requirements, i.e. allowing for the

highest possible signal response, as well as adhering to chromatographic needs, with a major emphasis being on retaining peak resolution, i.e. not amount to severe peak broadening (see **Section 2.1.6**, p. 14). Taking this into consideration, the interplay between sufficient signal response and retaining resolution had to be optimized to obtain the best results. This would require that the flow cell volume is as low as possible, to reduce back-mixing and peak broadening, but still large enough to fulfil sufficient resident times of the analyte for NMR spectroscopy. Furthermore, the inner geometry of the flow cell should be optimized to reduce unwanted flow effects, such as turbulent flow and dead volume that contribute to back-mixing and band broadening.² Therefore, it has to adhere to certain requirements, from an NMR perspective, which include: (1) it should be large enough for sufficient analyte detection, where an increase in the volume lowers the time-resolution of an on-line measurement; (2) the analyte residence time should be similar to (or slightly longer than) the repetition time of the pulse sequence to reduce in- and out-flow artefacts;^[202] (3) it should have maximum sample volume (V) in the coil/active region (see **Figure 4.2**) for the highest S/N ($S/N \sim V$),^[203] however, this can be compensated for, to a certain degree, by optimizing the ADC (see **Section 2.4.3** p. 53) receiver gain prior to acquisition; and (4) should comprise a material which can easily be manufactured, yet rigid enough for routine usage and not have residual protons or ferromagnetic components affecting the quality of the NMR spectra. Additionally, from a chromatography perspective, the flow cell should not increase band-broadening, and should be stable against common SEC solvents. Since there were no flow cells meeting these requirements commercially available, they had to be redesigned. A technical drawing, allowing for the reproduction of the most promising flow cell can be found in **Appendix A.3** (p. 267). It should be noted that many of the ideas on the construction style is merely an extension on the ideas from literature – see Section 2.2.7, (p. 41). The optimization parameters will be presented in the next section, including some of which has already been published.^[15]

4.2.2 Design

The design of the flow cell, has to allow for a compromise between the in- and out-flow effects (see **Section 2.2.6**, p. 38). This is ascribed to the geometry of the flow cell which affects the flow regime within its active region. In order to optimize the sensitivity (S/N) and residence time distribution (RTD), the flow cells were custom built and compared with each other using a benchmark experiment. The flow cells' total internal volume varied between $V = 320\text{--}1010\ \mu\text{L}$, and they were built from borosilicate glass capillaries. The following geometric factors were varied: (1) the length of the active region (coil region of NMR spectrometer), (2) internal diameter (i.d.) of both the capillary and active regions, and (3) the entrance/exit geometry (or shape), as seen in Figure 4.2.

The total length of all the flow cells was $l = 500\ \text{mm}$, with a $\varnothing = 5\ \text{mm}$ outer diameter (o.d.), and internal diameters (i.d.) of the capillaries of either $d_{\text{cap.}} = 0.4$ or $0.8\ \text{mm}$. Furthermore, the capillaries were widened, having internal diameters of either $d_{\text{act.}} = 2.6$,

²Turbulent flow and back-mixing is not necessarily always bad, as it could also assist in homogenizing a sample. However, when it comes to chromatography it has adverse effects, as it completely destroys the integrity of the chromatographic separation.

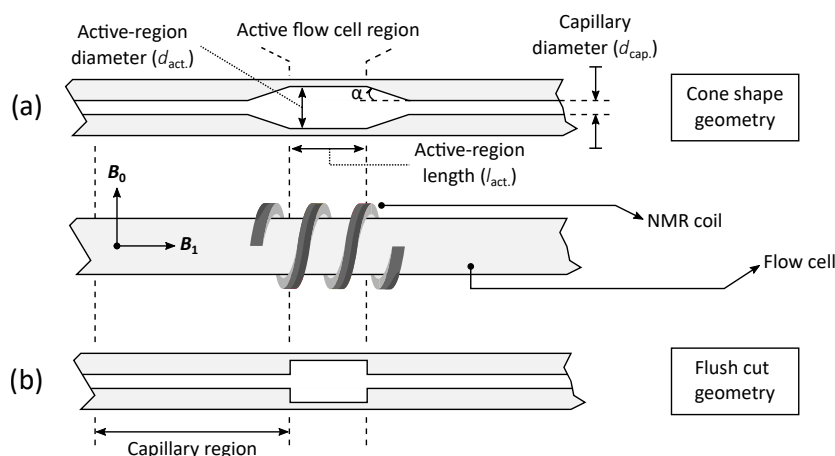


Figure 4.2: Depiction of the flow cell geometries with differing diameter transitions that were designed and tested: (a) conical shaped- (cone), and (b) flush cut-geometries (no cone). The most relevant parameters are listed in the figure, including the cone shape angle, α – see **Figure 4.1** (p. 64) and **Table 4.1**. Adapted from Botha et al.^[15] with permission from the Royal Society of Chemistry.

3.4 or 4 mm at the active region (coil region) of the NMR spectrometer, with active region lengths of $l_{\text{act.}} = 9, 12, 15, 18$ or 45 mm. The connection of the narrow capillaries to the cylindrical active region comprised a transition section with two types of geometries: (1) conical shaped (cones), and (2) flush cut (no cones). The cones have $\alpha \approx 30^\circ$ angles, which can mostly be ascribed to the flanging tool used by the glass blower (see Figure 4.2). Eleven different flow cells were constructed and compared to the flow cell provided by Magritek GmbH (Aachen, Germany) for reaction monitoring (FC1 in Table 4.1). It should be noted that the disadvantage of this flow cell is its large volume ($V_{\text{tot}} = 1013 \mu\text{L}$), compared to the ca. $V = 60 \mu\text{L}$ typical dead volume of DRI detectors.^[7]

Apart from the flanged section of the conical shaped geometry, the flow cells are mostly cylindrical glass capillaries, and under certain conditions, the flow within these capillaries is typically laminar (also referred to as streamlined), as seen in **Figure 4.3**. As a thin layer is in contact with the glass wall, the glass wall exerts a restriction force on the liquid, reducing its linear velocity; yet, it still has a finite velocity. In contrast, the liquid layer adjacent to the more central layer travels faster due to lower friction, resulting in the longitudinal velocity profile representing a paraboloid. In laminar flow, the liquid elements remain within one lamina (neglecting diffusion), as the liquid moves longitudinally along the capillary. In contrast to laminar flow, turbulent flow³ causes an irregular motion of the liquid elements along the capillary. Under turbulent conditions the liquid elements are not confined to definite laminae, but rather move in a fast, radial mixing pattern, which includes Eddy currents – see Figure 4.3. Additionally, higher pressures are required to achieve the same (positive) liquid displacement under turbulent conditions, as opposed to laminar flow (at the same capillary dimensions). In the case of turbulent flow, the pressure reduction is approximately $\Delta P \propto \sqrt{\text{flow rate}}$, whereas in laminar flow it is $\Delta P \propto \text{flow rate}$ (Hagen-Poiseuille's law). In an ideal case a plug flow would be the preferred choice,

³In haemodynamics, turbulence is typically accompanied with audible vibrations, and upon the existence of turbulence within a human's cardiovascular system, it is detected as a murmur.

from a design perspective, as the highest S/N would be obtained. Since that is practically unrealistic, a laminar flow profile was preferred over that of a turbulent flow profile (see Figure 4.3), since a laminar flow would preserve the chromatographic integrity to a better degree than turbulent flow, as the liquid elements remain within the lamina.

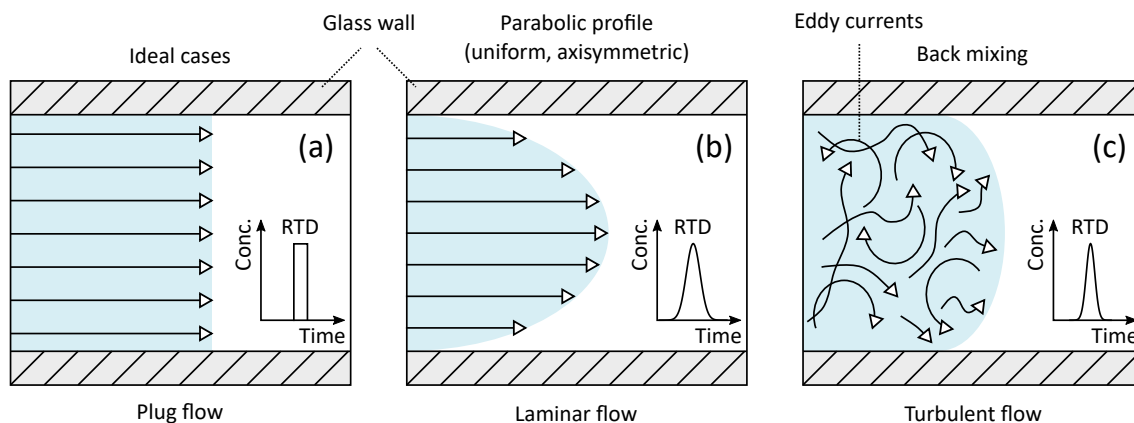


Figure 4.3: Depiction of flow profiles encountered in capillaries: (a) plug flow, representing the ideal case for on-line detection; (b) laminar flow having a uniform (axisymmetric) distribution (also referred to as parabolic Poiseuille flow); and (c) turbulent flow. The insets in each figure illustrate the expected residence time distribution (RTD) under identical capillary conditions.

4.2.3 Benchmark Experiment

The flow profile within a capillary, whether laminar or turbulent, can be predicted on the basis of the dimensionless Reynolds number, Re . It represents the ratio of internal to viscous forces, and can be expressed for liquids flowing through a capillary as

$$Re = \frac{\rho D \bar{v}}{\eta}, \quad (4.2.1)$$

where ρ is the density, D is the internal diameter (i.d.) of the capillary, \bar{v} is the average linear velocity, and η is the viscosity. This provides a simple first approximation of the dominant flow profile within the flow cell. In general, laminar flow is typically observed for $Re < 2300$ and turbulent flow occurs for $Re > 2900$.^[204] **Equation 4.2.1** suggests that larger capillary diameters, increased linear velocities, and low liquid viscosities result in turbulent flow. The Reynolds number prediction was applied to the given flow cells and presented in **Figure 4.4**.

It is evident from Figure 4.4 that the predicted Reynolds numbers are far below an $Re = 2300$ for the different solvents employed, indicating that for the flow cell dimensions used within this study the predominant flow profile is expected to be laminar. It should be noted that these predictions do not compensate for a diameter transition from a narrow to wider back to narrow capillary (see Figure 4.2, p. 66), and different transition geometries. However, it still provides a first estimation of the predominant flow regime that could be expected.

In laminar and turbulent flow there is an unavoidable velocity profile across the flow cell

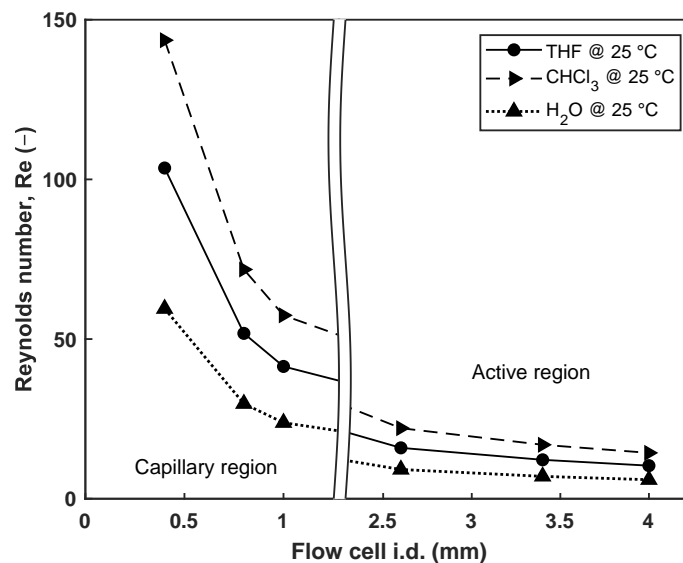


Figure 4.4: Prediction of the flow profile for the different capillaries used for flow cell design and construction (see Table 4.1) using three solvents: (1) tetrahydrofuran (THF), (2) chloroform (CHCl_3), and (3) water (H_2O) at 20 and 25 °C, respectively, with a volumetric flow rate of 1 mL/min. The graph is divided into two parts, the capillary region (left) and the active region (right). See Figure 4.2 (p. 66) for a classification of the different regions of the flow cell.

(or tube), consequently, making certain parts of the fluid move faster than that of the average velocity, and other parts slower (also as a result of friction with the neighbouring glass wall). This results in a residence time distribution (RTD). The RTD is an important parameter to optimize as this will severely affect the minimum detectable molar mass distribution (\bar{M}) and obtainable signal in NMR spectroscopy. There are various techniques available to measure the RTD, however, within the context of this work only a single benchmark experiment was utilized to determine this. In the benchmark experiment the flow rate was adjusted to a volumetric flow rate of 1 mL/min, after which a $V = 20 \mu\text{L}$ solution of cyclohexane in chloroform (5/95 v/v%) was injected into the SEC-NMR set-up without a chromatographic column, using chloroform as mobile phase. The NMR and DRI data were recorded for five minutes, including a three minute pre-recording of the NMR data to ensure timely data recording and reproducible results. The NMR parameters used for data acquisition were as follows: a 90° hard pulse with a dwell time of $t_{\text{dwell}} = 100 \mu\text{s}$ and repetition time of $t_{\text{rep.}} = 270 \text{ ms}$, consisting of 2048 (2k) data points with one scan per spectrum and a total of 1650 spectra, performed at a temperature of $T = 26.5 \text{ }^\circ\text{C}$. As shown in Figure 4.3 (p. 67), in plug flow all the analyte exits the capillary at a time given by the average residence time, volume/volumetric flow rate (V/\dot{v}). Consequently, plug flow should result in no distribution of residence times, making it the ideal case, but rarely found in practice. Laminar flow produces a parabolic velocity distribution, leading to a wide range of available residence times. In this case, the maximum velocity, ν_{max} within a capillary is twofold the average velocity, ν_{ave} , resulting in analytes travelling at the maximum velocity having a minimum time, t_{min} , within the capillaries. This can be expressed as^[205]

$$t_{min} = \frac{t_{ave}}{2}. \quad (4.2.2)$$

This relation also indicates that there will be a relatively broad RTD with laminar flow. The velocity profile for turbulent flow is not as steep as with laminar flow, and the maximum velocity and minimum residence time, according to literature, can be expressed by^[205]

$$\begin{aligned} \nu_{max} &= 1.20\nu_{ave} \\ t_{min} &= 0.83t_{ave}. \end{aligned} \quad (4.2.3)$$

This indicates that the residence times are narrower for turbulent than laminar flow and the processing would be more uniform. However, since the back-mixing (and Eddy currents) as well as higher back pressure are too severe to retain chromatographic integrity, turbulent flow is not preferred. In both cases, the aforementioned equations can be utilized to calculate the residence time distribution, correspondingly, providing the time required for 50% of the injected analyte to exit the capillary. In general, the residence time distribution corresponds similarly to the time of the maximum analyte concentration in the residence time distribution curve (see insets in Figure 4.3, p. 67).^[205]

The optimal specifications of the flow cell for SEC hyphenation should: (1) prevent artificial band broadening, (2) allow delivery of maximum sample volume to the NMR detector, with low B_0 interaction, and (3) provide the ability to withstand a back pressure of at least three bars. All the flow cells were designed, built, and tested to obtain the best compromise between the first two requirements. In order to quantify the RTD of the flow cell and the dwell time of the analyte at the point of detection in the active region, the aforementioned benchmark experiment can be carried out. The experiment provides a simple way of extracting information on band broadening. Furthermore, the convenience of the experiment is also attributed to cyclohexane (C_6H_{12} , $\delta = 1.43$ ppm) and chloroform ($CHCl_3$, $\delta = 7.26$ ppm) having well resolved chemical shifts and single (Lorentzian) lines in the NMR spectrum with sufficient intensity and uncomplicated data to interpret.⁴ The results are reported in Table 4.1, with the illustration of these effects on five selected flow cells signifying the major differences in the design in **Figure 4.5**.

It is evident from Table 4.1 and Figure 4.5, a general trend of more pronounced tailing for larger flow cells exists (see T_f in Table 4.1). There is also a relation between the flow cell geometry and the internal diameter of the capillary region. The full width at half maximum (FWHM) of the NMR peaks had the same order of magnitude for all the flow cells. This is expected due to strong apodization applied. In a well-designed flow cell, the NMR signal trace should have a similar shape, and not have excessive tailing. Considering the FWHM of the DRI traces, four distinct groups were observed: (a) FC1 and FC5, (b) FC2–FC4, (c) FC7 and FC8, and (d) FC6, FC9, and FC10.

For group (a), the broad FWHM is mainly caused by the larger volume of the flow cells in comparison to the injection band. Considering the profiles of FC1 and FC5 in Figure 4.5,

⁴Important: the power supply in Europe has a frequency of ~ 50 Hz, and can be visible in the NMR spectrum at $\delta = 0.80$ ppm on the Spinsolve 60 spectrometer, which should not be confused for an artefact or satellite peak of the cyclohexane.

Table 4.1: An overview of the performance of custom built flow cells compared to the commercially available flow cell from Magritek GmbH (Aachen, Germany), FC1, based on a benchmark experiment. Flow cell (FC) FC9 was the optimum in terms of band broadening in both the spectroscopic and chromatographic dimension and was used as standard FC in all subsequent work, unless stated otherwise.^[15]

Flow cell	Capillary i.d. (mm)	Linear velocity (ν), capillary (mm/min) ^a	Entrance/exit shape	NMR-active region length (mm)	NMR-active region i.d. (mm)	Linear velocity (ν), active (mm/min) ^a	V_{active} (μL)	V_{total} (μL)	FWHM _{DRI} (min.)	T_{r}^{b} , DRI (–)	FWHM _{NMR} (Hz)
No FC	–	–	–	–	–	–	–	–	–	–	–
FC1 ^c	1.0	1273	Cone	60	4.0	79.6	628	1013	0.05	1.06	–
FC2	0.8	1989	No cone	15	2.6	188	80	323	0.20	4.11	7.33
FC3	0.8	1989	No cone	15	3.4	110	136	380	0.23	4.59	7.08
FC4	0.8	1989	No cone	15	4.0	79.6	188	432	0.22	3.92	6.89
FC5	0.8	1989	No cone	45	4.0	79.6	565	794	0.35	3.39	7.21
FC6	0.8	1989	Cone	15	4.0	79.6	188	450	0.16	3.73	7.24
FC7	0.4	7958	No cone	15	4.0	79.6	188	250	0.086	5.12	7.16
FC8	0.4	7958	No cone	15	3.4	110	136	197	0.086	7.70	7.67
FC9^d	0.8	1989	Cone	15	4.23	71.2	211	496	0.097	1.94	8.03
FC10	0.8	1989	Cone	18	4.24	71.2	226	516	0.15	3.46	8.87
FC11	0.8	1989	Cone	9	4.23	71.2	127	404	0.24	3.23	6.96
FC12	0.8	1989	Cone	12	4.23	71.2	169	444	–	–	6.85

^a The linear velocity was calculated using the default flow rate of 1 mL/min.

^b Tailing factor $T_{\text{r}} = (a + b)/2a$, where a and b are the distances in min. (or mL) of the peak edge relative to the midpoint of the peak at $1/20^{\text{th}}$ of the peak height.

^c The commercially available flow cell from Magritek GmbH (Aachen, Germany).

^d The best performing flow cell for the intended use in SEC-NMR hyphenation.

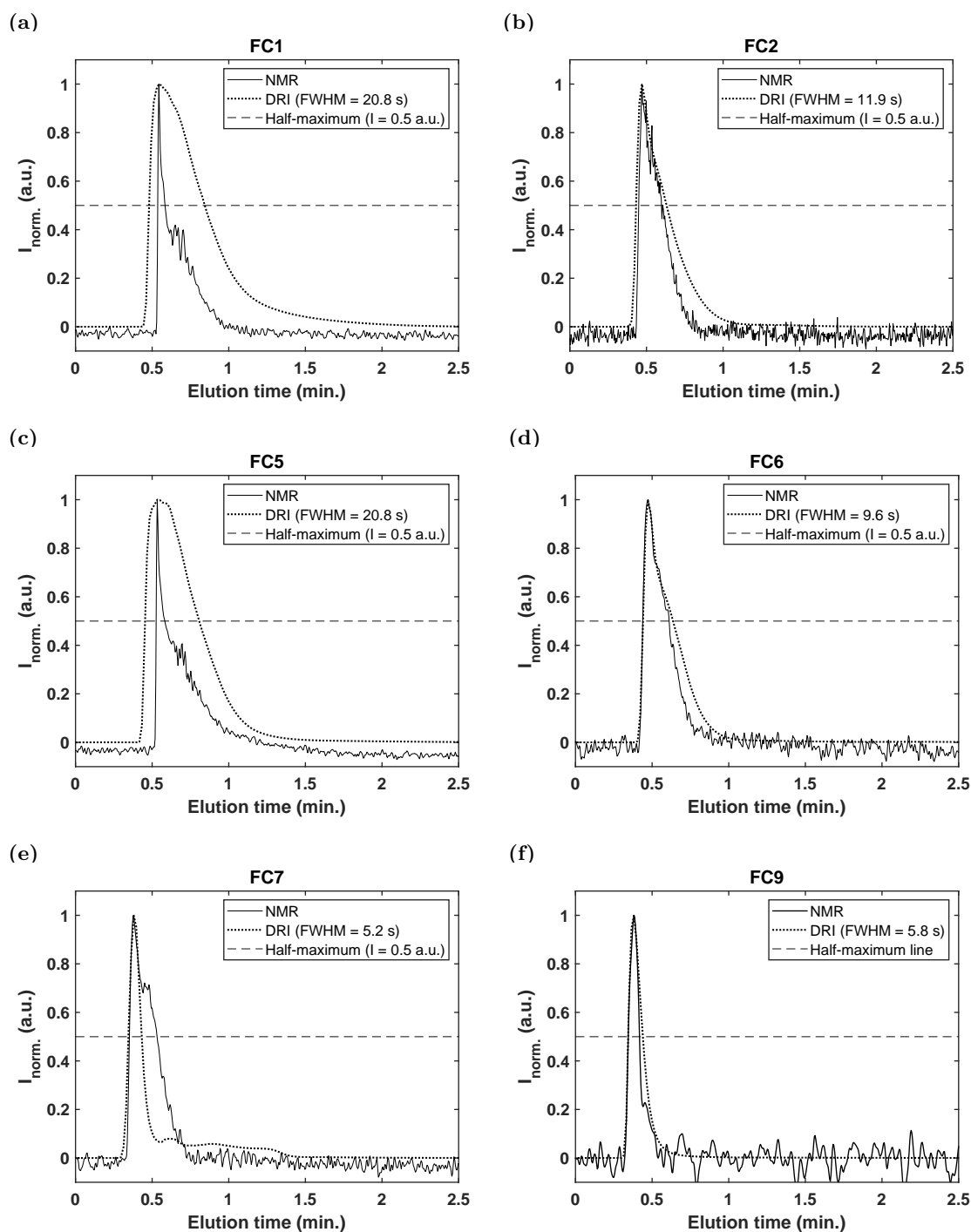


Figure 4.5: The residence time distribution (RTD) mapping of the ^1H -NMR signal using five selected flow cells; FC1, 2, 5, 6, 7, and 9 (see Table 4.1) by means of a cyclohexane in CHCl_3 (5/95 v/v%, benchmark experiment) solution. The corresponding DRI traces have also been overlaid to provide a full overview of how the flow cells affect the flow profile of the analyte. The RTD mapping provides further insight into the mixing behaviour, mass transfer and dilution of the analyte occurring in each flow cell.

it is clear that severe band broadening occurs due to excessive dilution. In addition, it seems that analyte-jetting occurs at the point of entering the flow cells, due to the volume mismatch of the analyte band (see **Section 2.1.6**, p. 14) to the active region in both cases, and potentially due to the geometry of FC5.

In group (b), all the flow cells had the same transition geometries, which comprised the flush cut geometries (no cones), with only the volume changing slightly. The band broadening occurs because stagnant zones within the flow cells, prevent the analyte from completely exiting the flow cell quickly.

In group (c) the reduction in the capillary region from $d_{\text{cap.}} = 0.80$ to 0.40 mm (i.d.) to more closely match the 0.25 mm i.d. PTFE SEC tubing, had an adverse effect, since the smaller capillaries did not match well with the active region volume of the flow cell, resulting in the formation of 'analyte-jets', in conjunction with stagnant zones due to the geometry, causing significant peak tailing, as can be seen for profile FC7 in Figure 4.5.

In group (d), FC 6, 9, and 10, the best overall performance in both the SEC and NMR dimensions was observed, consisting of cone shaped geometries and $d_{\text{cap.}} = 0.80$ mm i.d. capillaries. Looking at the profile of FC9 in Figure 4.5, it is clear that the SEC- and NMR-traces match relatively well, indicating no severe flow instabilities or stagnant zones being present. Consequently, flow cells with $d_{\text{cap.}} \leq 0.80$ mm i.d. for the capillary regions are preferred to minimize in- and out-flow effects. It is assumed that the sequential step increase (with respect to i.d.) from the SEC tubing (0.25 mm i.d.) to the capillary region of the flow cell ($d_{\text{cap.}} \leq 0.80$ mm i.d.) in combination with the cone geometries, assisted in reducing flow instabilities as the analyte flowed through the larger active region of the flow cell. Furthermore, the slight increase in the FWHM in the NMR dimension can be attributed to less effective shimming as a result of magnetic susceptibility originating from the flow cells, as they have fluctuations in wall thickness.⁵ A crucial parameter in the hyphenation of NMR to SEC is the S/N , as there already exists a limitation with respect to the available sensitivity. Nevertheless, this was not used to approximate the flow cell performance as the results may be misleading due to the nature of the benchmark experiment. It is important to note that optimizing S/N is as important as studying the in- and out-flow effects to guarantee an all-round well performing flow cell. From the results presented in Table 4.1 and Figure 4.5, FC9 provided the best compromise between both chromatographic- and spectroscopic-band broadening. It was also a close match to the case where no flow cell was used. Based on these findings, FC9 was selected as the flow cell of choice for the current application.

4.2.4 Application to SEC-NMR

The SEC-NMR experiments were performed using a polystyrene (PS, $M_n = 30\,300$ g/mol, $D = 1.03$) standard, and chloroform as mobile phase, to validate the results obtained from the benchmark experiments. Employing a well-known narrowly distributed calibration standard such as PS, makes the developmental process more reliable. The sample does not have intrinsic anomalies which could complicate experimental data and since it has a well-defined structure comparison with data from, e.g. literature, it is more reliable. The effect of the different flow cells on the corresponding SEC traces compared to that of the absence of an NMR flow cell, which is regarded as the best possible case for the given SEC-NMR set-up, is illustrated in **Figure 4.6**.

⁵Obtaining a homogeneous glass wall thickness is highly dependent on the skill-set of the glass-blower.

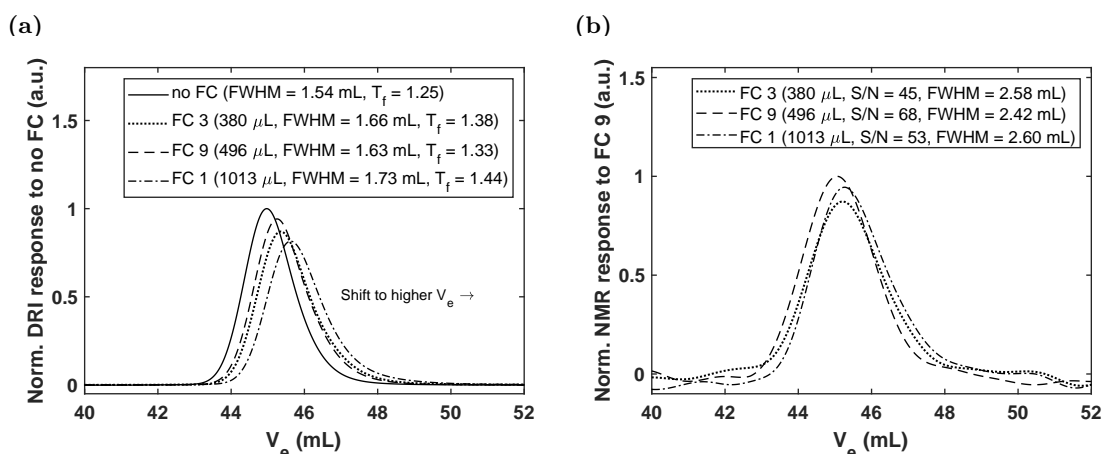


Figure 4.6: Performance of the custom-built flow cells, based on the chromatographic separation of a polystyrene calibration standard ($M_n = 30\,300$ g/mol, $D = 1.03$, injected mass = 1 mg, $\dot{v} = 1$ mL/min). Figure (a) illustrates the effect of three different flow cells, FC1, FC3, and FC9 on the DRI trace compared to no flow cell. Figure (b) illustrates the corresponding NMR elugram traces of the flow cell only looking at the *ortho*-aromatic (C–H, $\delta = 6.6$ ppm) protons of the polystyrene. A semi-preparative linear M column (300 x 20 mm i.d), with styrene-divinylbenzene (SDV) packing material was utilized. Adapted from Botha et al.^[15] with permission from the Royal Society of Chemistry.

Flow profiles reflect the actual peak broadening resulting from excess dead volume and corresponding flow instabilities due to the flow cell geometries. A clear trend is observed from the DRI traces in Figure 4.6 (a), where the FWHM and tailing factor increase with an increase in the total flow cell volume, corresponding with observations from the benchmark experiment. Flow cells with a flush cut geometry have more stagnant zones, where the analyte (1) never reaches these zones (low S/N), and/or (2) slowly diffuse in and out causing peak tailing to occur. These unwanted flow effects are not found in the conical shaped geometry, which has no stagnant zones (see Figure 4.2, p. 66). To quantify the peak broadening, the chromatograms (DRI traces) were fitted via a Gaussian function, and the FWHMs are reported in **Table 4.2**.

Table 4.2: Quantification of flow cell effects on the chromatographic and spectroscopic dimensions for an SEC-NMR experiment. A polystyrene calibration standard ($M_n = 30\,300$ g/mol, $D = 1.03$, injected mass = 1 mg, $\dot{v} = 1$ mL/min in CHCl_3) was used, with a semi-preparative Linear M column (styrene-divinylbenzene (SDV) packing material 300 x 20 mm i.d.).

Flow cell	Relative S/N , DRI (–)	FWHM, DRI ^a (mL)	T_f ^b , DRI (–)	FWHM, NMR (mL)	S/N , NMR (–)
No FC	1.0	1.54	1.25	–	–
FC1	0.82	1.73	1.44	2.60	53
FC3	0.87	1.66	1.38	2.58	45
FC9	0.94	1.63	1.33	2.42	68

^a The FWHM and injection volume can be utilized to estimate the dilution factor, $D_f = \text{FWHM}/\text{injection volume}$, for a given column and flow cell combination.

^b Tailing factor, see footnote of Table 4.1 (p. 70).

Considering the effect on signal intensity of the respective flow cells relative to where no flow cell was used, the signal intensity for FC1, FC3, and FC9 decreased by 20%, 14%, and

6%, respectively. The FWHM relative to no flow cell increased by 11.4%, 7.5%, and 5.6% for FC1, FC3, and FC9, respectively. Finally, the tailing factor also increased by 14.9%, 10.1%, and 7.2% for FC1, FC3, and FC9, respectively, relative to no NMR flow cell being employed.

To illustrate the relationship between the S/N more clearly, a lower sample concentration was used, which amounted to a total injected mass of 1 mg polystyrene per measurement, illustrated in Figure 4.6 (b). There is a reduction in S/N relative to FC9 of 22.1% and 33.8% for FC1 and FC3, respectively (same integral area but lower peak maximum). Furthermore, there is a 7.4% and 6.6% increase in FWHM for FC1 and FC3, respectively, in the NMR dimension relative to FC9. These trends, for both the SEC and NMR dimensions, are expected as any additional detector leads to an increase in peak broadening due to the unavoidable addition of system dead volume. Initially, the hypothesis was that a smaller flow cell volume would lead to a better compromise between NMR sensitivity and chromatographic resolution (i.e. band broadening). The illustrated results indicated a different trend and emphasized the importance of the flow cell geometry, corresponding to what is observed in the benchmark experiment. The differences between the flow cells, using a narrowly distributed calibration standard, was significant, and the increased peak width (5.6% increase in FWHM) for the best flow cell, FC9, was acceptable considering the accuracy of SEC as a technique. The effect should be less pronounced in the case of broader calibration standards, i.e. $D > 1.5$, due to the inevitable decrease in localized analyte concentration. In the case of static NMR measurements (no flow), the cell size will not influence the NMR results as severely as in constant flow rate measurements, since the phenomena of in- and out-flow are not present. In addition, much longer measurement time windows are possible. In the case of constant flow rate measurements, an increase in peak broadening was accompanied by a reduction in signal intensity, and ultimately resulted in decreased S/N values. The observed deviations for the NMR signals are more pronounced than that of the SEC signals due to peak broadening resulting in a localized reduction in analyte concentration. The latter should, therefore, be considered when hyphenating SEC with NMR spectroscopy. The relative (expected) signal loss would be less severe in the case of a sample with a broad dispersity ($D > 1.5$), than for the illustrated sample, as the localized concentration of a broadly distributed sample is considerably less.

In summary, the recommended flow cell for the hyphenation of NMR to SEC is listed in Table 4.1 as FC9, which is the most relevant to the work performed within this thesis. A flow cell could also be selected that would fulfil the need required for a desired experiment, for example, in the case of performing reaction monitoring. The standard Magritek flow cell (listed as FC1 in Table 4.1) could be a better fit, as the solution viscosity might increase during such an experiment or the chemical rate is rather slow compared to the RTD and the need for a larger flow cell becomes more apparent.

4.3 Optimization of SEC Conditions

The following section is dedicated to the optimization of the SEC conditions to obtain the best performance when hyphenating NMR to SEC. An introductory overview is provided as to why optimization is required, followed by column selection and overloading considerations, and finally, flow-rate optimization and flow cell selection.

4.3.1 Introduction

In the development of SEC-MR-NMR hyphenation, the fundamental idea was to develop the technique in such a way that it is a universally applicable chemically selective detector for SEC. It was, therefore, imperative that potential application not be limited to specific chromatographic questions. Consequently, adjustments or modifications to the SEC system should be restricted. To fulfil this need, no restrictions were placed on: (1) molar mass ranges, (2) solvents/mobile phases, and (3) polymer chemical composition/type (i.e. synthetic, water soluble, proteins, polysaccharides etc.). After elimination of these restrictions, the remaining parameters are universal and will not influence the separation mechanism in SEC but would ensure improved quality of the developed method and reproducibility. These parameters will be presented in the forthcoming section, including some of which has been published.^[15]

Once a desired stationary and mobile phase of an SEC method has been established (with the sample chemistry being the dominating factor), method optimization with respect to the sample specific molar mass and molar mass distribution, i.e. dispersity, is advantageous to system performance. The latter becomes especially important when analyzing polymers with $MM > 1\ 000\ \text{kg/mol}$. An intrinsic contrast exists in the hyphenation of NMR to SEC, as SEC performs at its optimum (mostly regarding resolution) with dilute sample concentrations, whereas spectroscopic sensitivity is best at higher sample concentrations. This is important in the optimization of the respective dimensions, consequently, resulting in a compromise between the techniques to obtain the best performance when hyphenated as a single instrument. See **Appendix A.6** (p. 277) for a description of the instrument specification of the SEC system.

4.3.2 Column Selection

The columns utilized within this study can be differentiated according to the following parameters: column dimensions, chemistry of the stationary phase, particle size-, and pore size-distribution. These parameters are summarized in **Table 4.3**.

A major part of the method development utilized styrene-divinylbenzene (SDV)-type columns, as they are more robust towards a variety of applicable organic solvents. The modified acrylate copolymer (SUPREMA) and Polyester copolymer networks (GRAM) columns are speciality columns for specific polymers and molar mass distributions to allow for the appropriate mobile phase being employed with them and to minimize any form of

Table 4.3: The SEC columns and parameters used within this study. All the columns originate from PSS GmbH (Mainz, Germany).

Column dimensions ^a (mm)	Stationary phase ^b	Particle size distribution (μm)	Pore size distribution (\AA)	Separation range (kg/mol)	Mobile phase
300×8^c	SDV - Linear M	5	mixed bed ^d	0.1–1 000	organic ^e
300×20^c	SDV - Linear M	10	mixed bed	0.1–1 000	organic
300×20	SDV - High	10	10 000 000	4000–30 000	organic
300×20	SUPREMA 100	10	100	0.1–100	aqueous
300×20	GRAM - Preparative Linear	10	mixed bed	0.6–1 000	polar organic ^f

^a length x internal diameter.

^b SDV - Styrene-divinylbenzene-copolymer network, SUPREMA - modified acrylate copolymer network, GRAM - Polyester copolymer network.

^c 8 mm corresponds to analytical and 20 mm to semi-preparative (or preparative) columns.

^d Mixed beds are blends of pore sizes designed for specific molar mass ranges. It does not give the conventional S-type calibration curve (see **Figure 2.2**, p. 10) but rather an entirely linear calibration curve.

^e For non- to medium-polar solvents, e.g. THF, Toluene, TCM, DCM.

^f For polar organic solvents, e.g. DMAc, DMF, NMP, DMSO.

interaction that would otherwise not be possible with the SDV-type columns. The linear M columns, which have a mixed pore size distribution that were mostly employed within this work, are columns with linear calibration curves as opposed to the S-type calibration curve (see **Figure 2.2**, p. 10). Although the latter has a better separation efficiency, the linear M columns are more robust towards a larger molar mass range and the perfect candidates for method development.

As previously mentioned, SEC performs at its best with dilute polymer solutions. Therefore, the limit between column overloading (see **Section 4.3.3**) and acceptable separation strongly depends on the sample. Column overloading is proportional to the concentration and the molar mass distribution (MMD). In addition the type of column, i.e. the particle size and pore size distribution also plays a major role. Consequently, the best compromise needs to be established for each hyphenated combination. However, approximation for samples of similar chemistry are possible. An easy method for determining the correct combination of sample, mobile and stationary phase, with respect to polarity, the "magic triangle" can be utilized, see **Figure 4.7**. The determining factor is generally the sample polarity, as this dictates the choice of mobile phase to be used, and in turn the stationary phase to obtain interaction-free chromatography.

In selecting the appropriate column dimensions, the two variables that can be changed are the column length and/or the diameter, which fundamentally change the total volume of the column, including the separation efficiency. In general, the longer a column, the better

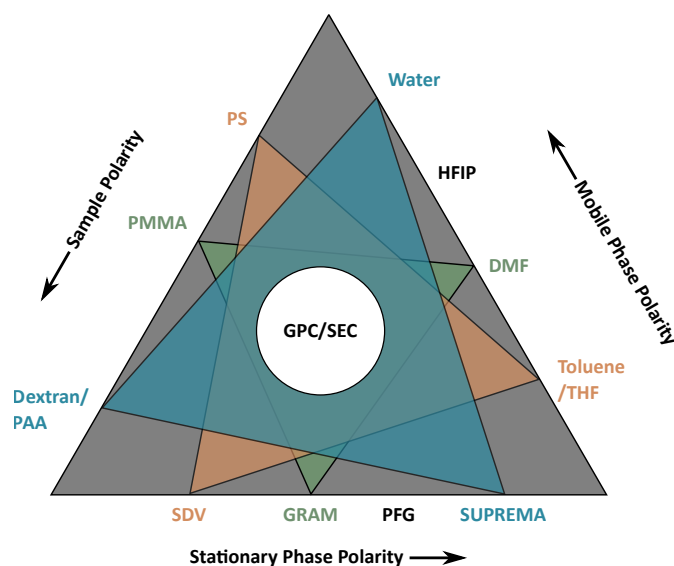


Figure 4.7: The "magic triangle" for the correct SEC column selection, taking the polarities of the sample, mobile-, and stationary-phase into consideration. The abbreviations used: PS: polystyrene, PMMA: polymethyl methacrylate, PAA: polyacrylic acid, SDV: styrene-divinylbenzene copolymer network, GRAM: Polyester copolymer network, PFG: polar modified silica, SUPREMA: modified acrylate copolymer network, THF: tetrahydrofuran, DMF: dimethylformamide, HFIP: hexafluoroisopropanol. Adapted from reference.^[206]

its separation efficiency. This unavoidably increases the measurement times (if we assume a fixed diameter); therefore, it is a trade-off between separation efficiency and measurement time. As the separation efficiency of SEC is inferior to that of interactive chromatography, a fixed length of 300 mm was chosen for all columns, leaving only the diameter as variable. Having fixed column lengths and only changing the diameter therefore, increases the volume of the column. This is an important parameter, as the column diameter should in principle be chosen on the amount of material that has to be separated. Since a benchtop NMR spectrometer is being hyphenated to SEC, it is clear that a larger sample amount is required to provide adequate sensitivity therefore, it is logical to assume that bigger is better (as a first approximation). In the field of SEC, two standard column diameters prevail, 8 mm analytical and 20 mm semi-preparative columns (depending on the supplier), which depend on their stationary phase specification, and are suitable for sample quantities of up to 0.1 mg and 1 mg injected masses, according to the manufacturer. **Table 4.4** provides a more detailed description on the recommended sample concentrations to use with the corresponding molar mass and molar mass distribution for a single analytical column.

The factor of 2.5 increase in diameter size from the 8 mm i.d. analytical to 20 mm i.d. semi-preparative column increases the cross-sectional area of the semi-preparative column to a factor of 6.25, allowing a factor of 6.25 more mass to be injected. As with the sample concentration recommendation listed for the analytical column in Table 4.4, these are also valid for the semi-preparative column, but adjusted by the corresponding cross-sectional area increase. The column dimensions also play a crucial role with respect to the experimental conditions of the specific SEC experiment. In the case of analytical

Table 4.4: Recommended sample concentration related to molar mass and molar mass distribution, including injection volume based on a single analytical column (300 × 8 mm i.d.) using a 20 μL injection volume.^[207]

Sample (kg/mol)	Concentration guidelines (g/L)	Recommended injected mass (mg)
0.1–10 ($\mathcal{D} < 1.1$)	2 (0.2%) ^a	0.04
10–1000 ($\mathcal{D} < 1.1$)	2–1 (0.2–0.1%)	0.04–0.02
> 1000 ($\mathcal{D} < 1.1$)	0.5 (0.05%)	0.01
0.1–1000 ($\mathcal{D} > 2.0$)	4–5 (0.4–0.5%)	0.08–0.1

^a Refers to the w/v% relative to the sample molar mass.

columns, the generally accepted optimum flow rate is 1 mL/min, as it provides a good compromise between measurement time, mobile phase consumption, and chromatographic resolution. However, for a semi-preparative column this would be 6.25 mL/min (with both flow rates amounting to a linear velocity of $\nu \approx 20$ mm/min within the column). Semi-preparative columns, while allowing a larger injected mass, deliver the same analyte concentration to the detector as the analytical column. If both columns are operated at a flow rate that differ by a factor of 6.25, similar S/N in SEC-NMR experiments should be obtained. In order to exemplify this, separation was conducted on both the analytical (8 mm i.d.) and semi-preparative (20 mm i.d.) columns as comparison using a PS-*b*-PMMA sample (64/36 mol%, $M_n = 230\,000$ g/mol, $\mathcal{D} = 1.07$) with a sample concentration of $c = 2$ g/L, and flow cell, FC9 (see Table 4.1). As these columns vary by a factor of 6.25, the injection volume should, therefore, be adjusted accordingly. The injection volumes were $V = 100$ and 500 μL for the analytical and semi-preparative column, respectively. It should be noted that it was only possible to have a factor of 5 difference with respect to the injected volume, as the limit was imposed by the available injection loops. Nevertheless, the effect of the volume size difference will still be signified considerably. The results are illustrated in **Figure 4.8**.

The flow cells affect the width of the analyte band and, as evident from Figure 4.8, the NMR flow cell affects both the peak height and width, resulting in a slightly better outcome for the semi-preparative column (see Figure 4.8). The main advantage of the semi-preparative column is the use of larger injection volumes. It is beneficial with respect to the flow cell, since the NMR flow cell volume is much smaller than the analyte peak width. Considering that all the flow cells in Table 4.1 have total flow cell volumes of $V_{\text{tot.}} \approx 320$ – 1020 μL, they correspond to a detection cell for an analytical column of $V \approx 50$ – 161 μL, which is in the volume range of the standard SEC detectors (e.g. $V_{\text{UV}} = 40$ μL and $V_{\text{DRI}} = 60$ μL). While the NMR flow cell volume size matches well with the size of the semi-preparative column, it will be at its limit for an analytical column. The flow rate was selected to ensure the same linear flow velocity, ν , of 0.32 cm/min (ν , inside the respective columns) for both columns ($\dot{\nu} = 0.16$ and 1 mL/min for the analytical and semi-preparative column, respectively). The linear velocity within the active region of the flow cell would be slower for the analytical column ($\nu \approx 11.4$ mm/min) as opposed to the semi-preparative column ($\nu \approx 71.2$ mm/min). The column-to-flow-cell mismatch is clearly visible for both the DRI

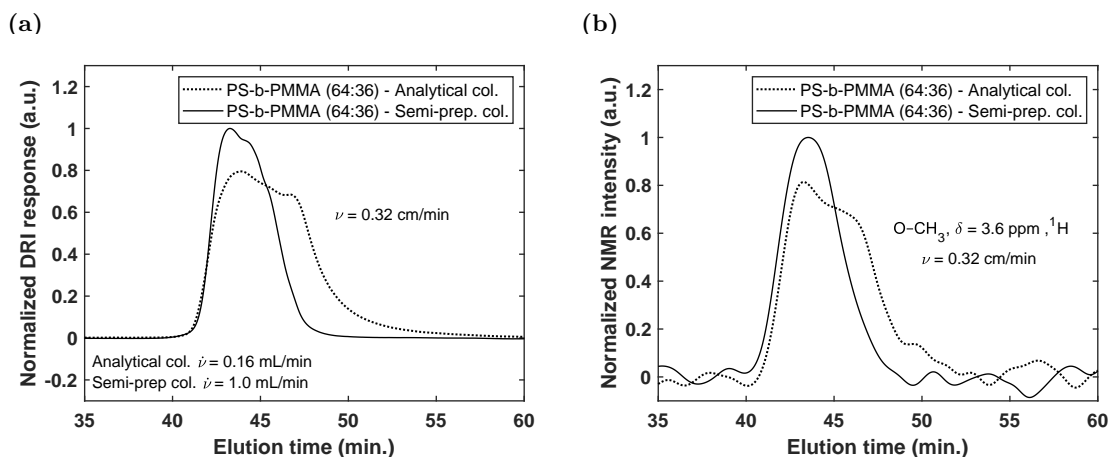


Figure 4.8: Column-to-flow cell mismatch and its effects on the (a) DRI and (b) NMR signal. The sample was a PS-*b*-PMMA (64:36 *mol%*, $M_n = 230\,000$ g/mol, $D = 1.07$) copolymer, with a sample concentration of 2 g/L and injected volumes of 100 and 500 μL for the analytical and semi-preparative column, respectively. This equated to 0.2 and 1.0 mg injected mass for the analytical and semi-preparative column, respectively. The flow cell had a total volume of 496 μL and is listed as FC9 in Table 4.1. In (a) the FWHM for the DRI traces were as follows; analytical column FWHM = 6.02 min and semi-preparative FWHM = 3.85 min. For the NMR elugrams in (b) the S/N values were as follows; analytical column $S/N = 21.3$ and semi-preparative column $S/N = 25.8$, and the corresponding FWHM were 5.5 Hz and 3.6 Hz. Adapted from Botha et al.^[15] with permission from the Royal Society of Chemistry.

and NMR traces in Figure 4.8. The latter is evident when looking at the peak-heights and -widths (FWHM) of the two columns, with the semi-preparative column resulting in an improved performance (see Figure 4.8). This can be ascribed to the analytical column having an analyte band with lower volume ($V = 100\ \mu\text{L}$) than the semi-preparative column ($V = 500\ \mu\text{L}$). Consequently, when this small analyte band from the analytical column passes through the NMR flow cell, which has a factor of ~ 5 larger volume, band broadening occurs. This occurs on a volume- and not time-scale, resulting in peaks with the same elution time (see Equation 2.1.6, p. 8) but more severe band broadening. To quantify the SEC statistics, such as the number of theoretical plates (N), asymmetric factor (A_s) and tailing factor (T_f), these values were calculated from the DRI traces (see Section 2.1.6, p. 14). The number of theoretical plates for the semi-preparative column increased by 67%, with a corresponding reduction of 14% and 28% in the asymmetric- and tailing-factor, respectively, relative to the analytical column. These values are only valid for the column-flow-cell combination under these specific conditions.

In summary, the better size match of the semi-preparative column to the NMR flow cell led to a 27% increase in the signal intensity and a factor of 1.5 improvement in S/N relative to the analytical column. Considering these improvements, the semi-preparative column was chosen as the column of choice when using flow cells with total volumes larger than that of the standard SEC detectors, and to avoid column-to-flow-cell mismatch.

4.3.3 Overloading

In the hyphenation of NMR to SEC, an essential part of the experimental success is the sample concentration, as stronger signal intensities and improved S/N values can

be achieved by simply increasing the sample concentration or injected volume. Ideally the largest possible sample concentration should be used for spectroscopic techniques, as this would increase the S/N values, nearly linearly as a function of the sample concentration.^{[188, p. 43][203]} As described before, this will have an adverse effect for SEC, since larger sample concentrations prohibit accurate molar mass determinations, due to an increased band broadening (see Section 2.1.6, p. 14). Consequently, it is imperative that for the hyphenation of chromatography to spectroscopy, an optimized compromise with respect to sample concentration is established. There is no universal optimum sample concentration and/or injected volume, as these parameters are highly sample dependent (MM and MMD) and needs to be established for each sample under investigation (see Table 4.4 for sample concentration recommendations). The molar mass of the sample under investigation needs to be considered especially, as a too high concentration of a high molar mass species will lead to a highly viscous analyte band. This will in turn hinder the diffusion process within the column due to a phenomenon referred to as column (stationary phase) overloading. This typically yields a shift to higher elution volumes, resulting in a reduction in the measured molar masses and increased dispersities, when employing a conventional calibration curve for molar mass estimations.^[33, p. 84] Additionally, the optimum sample concentration also varies for broadly distributed samples (e.g. industrial samples), and narrowly distributed samples (e.g. calibration standards), as the localized concentration within the column is generally lower for broadly distributed samples, and column overloading or viscous fingering^{[5, p. 86][33, p. 171][208]} happens at much higher concentrations. The injected mass can be higher for lower molar mass species with a broader dispersity index. The total injected mass affects both the peak position, i.e. elution volume, and peak shape. In order to establish the optimum concentration for a given sample at a specific injected volume, the sample concentration should systematically be lowered until the peak-shape and -position remain constant. Only the integral of the peak should change as a function of the injected mass or concentration. In the case where the detector signal becomes too low due to a severe reduction in sample concentration, the injected volume should be increased.^{[5, p. 86][33, pp. 118, 170][37]}

There is no universal limit before column overloading occurs. When employing semi-preparative columns, the focus is also less on obtaining the best separation efficiency but more on the amount of substance, compared to analytical columns where the focus is more on obtaining good separation efficiency. It is still important to try and retain the separation efficiency as much as possible, no matter which columns are utilized. The most reliable method for determining the column overloading limit is to perform a concentration series, to obtain the best S/N values with optimal separation efficiency for a specific sample on a hyphenated technique. To illustrate these effects, two PS standards, broad ($D = 1.65$, $M_n = 87\ 100$ g/mol) and narrow ($D = 1.02$, $M_n = 30\ 300$ g/mol), with variable injected volumes and consequently variable injected masses were measured on a semi-preparative (Linear M) SEC column in chloroform (CHCl_3) at a flow rate of 1 mL/min. The results are illustrated in **Figure 4.9**.

The chromatograms of the samples were evaluated with a PS calibration curve using the

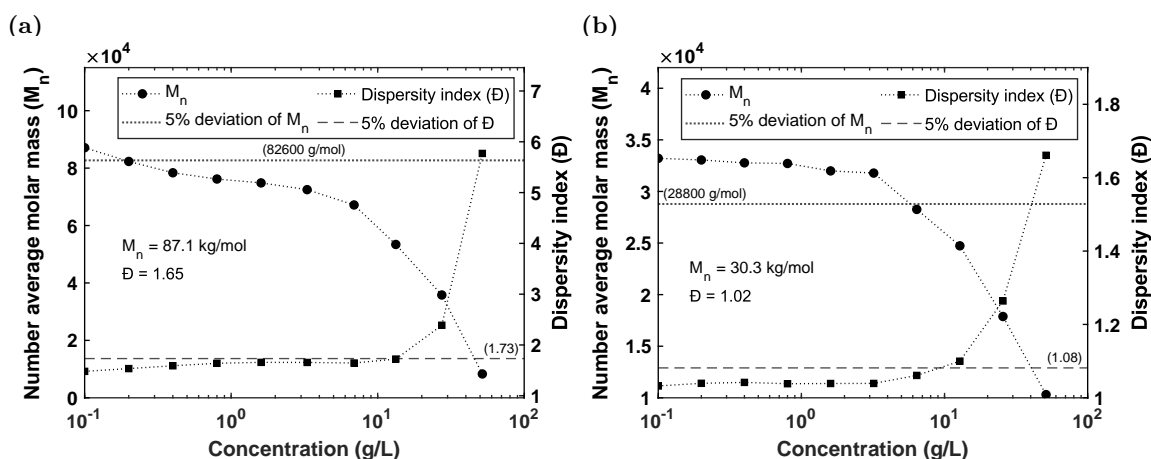


Figure 4.9: Column overloading based on molar mass and D estimations on two PS samples. In (a) the PS sample had a molar mass of $M_n = 87\ 100$ g/mol and a dispersity index of $D = 1.65$, and in (b) an $M_n = 30\ 300$ g/mol and $D = 1.02$. Both concentration series were conducted in CHCl_3 at a $\dot{v} = 1$ mL/min, using an injection loop of $V = 500$ μL on a semi-preparative Linear M SEC column.

WinGPC software (see Appendix A.6, p. 277). The corresponding dispersity indexes, D , and number average molar masses, M_n , were back-calculated relative to the PS calibration curve. For illustration purposes the molar masses and corresponding dispersity values were plotted against the injected mass for both the broadly distributed (see Figure 4.9 (a)) and narrowly distributed (see Figure 4.9 (b)) samples. The dispersity index axis starts at one, as this is the lowest limit. Within each plot, a 5% deviation line was inserted to show how the values differ with higher injected masses compared to the certified values for each sample. It is clear from the dispersity index that the narrowly distributed sample shows an earlier deviation above the 5% limit than the broader (and higher molar mass) sample. This is ascribed to the higher localized concentration within the column, resulting in more pronounced column overloading effects. The evaluated dispersity index, D , can be used as a measure of the band broadening occurring, as this also gives an indication at which concentration column overloading starts to occur.

It is good practise to consider the average molar masses, e.g. M_n and M_w , in conjunction with the dispersity indexes, as small peak distortions change the average molar mass values. The dispersity index may appear not to be affected too severely, depending on the calibration curve, even with a shift in the peak position due to incorrect molar masses. Slight column overloading can usually be recognized by looking at the quality of the chromatogram, i.e. it should have a normal distribution profile. In addition to using the dispersity index and molar mass averages, it is always good practise to perform qualitative chromatogram comparisons relative to a chromatogram of a highly diluted sample. Upon column overloading, the presence of small shoulders or slight distortions of peak shapes become apparent. To illustrate the peak shape distortion and reduction in separation efficiency as a function of sample concentration (injected mass), the resulting chromatographic elugrams from the narrowly distributed sample described above are plotted in **Figure 4.10**.

In Figure 4.10 (b), shifts to higher elution volumes can already be seen at a low sample

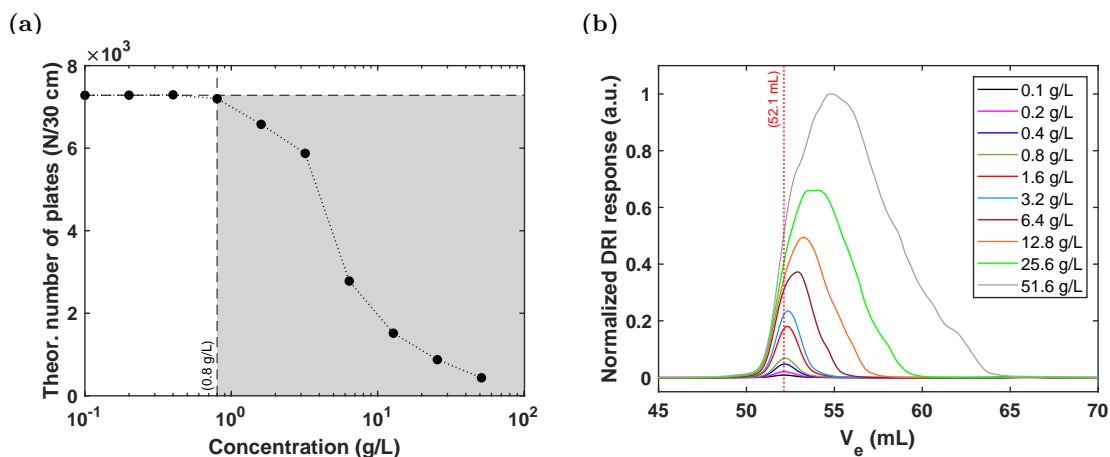


Figure 4.10: The effect of column overloading on (a) the calculated number of theoretical plates and (b) peak shape of a PS sample ($M_n = 30\,300$ g/mol, $\bar{D} = 1.03$), obtained on a semi-preparative column at a flow rate of 1 mL/min in chloroform and an injection loop of 500 μ L. The presence of viscous fingering also starts to become apparent at higher sample concentrations.

concentration of 0.8 g/L (0.4 mg injected mass), although the \bar{D} in Figure 4.9 (b), a relative measure, does not deviate yet. Severe peak shape distortions are visible starting at a sample concentration of 3.2 g/L (1.6 mg injected mass). These effects would be more pronounced on an analytical column. In Figure 4.10 (a), a severe reduction in separation efficiency per column length is clearly visible beyond a sample concentration of 0.8 g/L (0.4 mg injected mass).

For the hyphenation of spectroscopy to SEC, the major focus is often not to have the most accurate molar mass or molar mass distribution determinations, but rather to obtain a comprehensive idea on the chemical composition as a function of different molar mass fractions. Obtaining highly accurate molar mass and molar mass distribution information, can typically be achieved by means of a light scattering detector in combination with a concentration sensitive detector (see **Section 2.1.7**, p. 18) such as a standard DRI detector. In the current development, typical deviation in the range of 5–10% for the dispersity and molar mass averages was accepted, as this was within the experimental error of the method, since calibration standards were employed for back-calculations of these values. It was therefore found that the upper limits for the two samples were 4 mg ($\bar{D} = 1.03$) and 10 mg ($\bar{D} = 1.65$) injected mass for the narrowly and broadly distributed samples, respectively. As mentioned, there are no universal injected masses and the values provided here should only serve as a guideline, since the upper limit values are highly sample dependent. An average improvement in S/N of a factor of 2 was obtained within this work, by performing measurements at or slightly above the provided overloading limits.

4.3.4 Flow Rate and Flow Cell Optimization

An important parameter to quantify peak quality and separation efficiency in chromatography is the flow rate (or linear velocity) of the mobile phase. According to the well-known Van Deemter equation (see Figure 2.7, p. 18)^[37,50] an optimal flow rate exists for chromatography, that allows for the highest possible separation efficiency. The resolution of

SEC is less affected by using low linear flow velocities of the mobile phase as opposed to liquid adsorption chromatography (LAC).^{[5, p. 17][33, p. 97]} Consequently, it is imperative that the possibility of lower linear flow velocities in SEC should be exploited for NMR spectroscopy. This would enable longer residence time distributions (RTDs) within the NMR flow cell, resulting in higher S/N values (according to Equations 2.4.8 and 2.4.9, p. 53), reduced in- and out-flow effects, improved resolution (see Figure 2.17, p. 41), and solvent suppression/subtraction (see Section 2.2.6, p. 38).

The detection coil of the NMR spectrometer covers an active volume of $V < 140 \mu\text{L}$ (assuming a coil length of $l = 7 \text{ mm}$ and a maximum cavity diameter of $\varnothing = 5 \text{ mm}$). Depending on the linear flow velocity utilized (see Table 4.1 for a summary of the different velocities for each flow cell), the analyte has typically $t < 20 \text{ s}$ (at a flow rate of $\dot{v} = 1 \text{ mL/min}$) for the given flow cells, in which it remains within the active region of the flow cell. For on-line SEC-NMR measurements, the peak broadening in the NMR dimension depends severely on flow rate and, in turn, the S/N (see Figure 2.17, p. 41, looking at CHCl_3). Therefore, it is imperative to find the optimum linear flow velocity for a given NMR flow cell that provides either the best S/N value or the best compromise between S/N and measurement time. To illustrate this, benchmark experiments (see **Section 4.2.3**) were performed using FC4 and FC9 (see Table 4.1, p. 70) and the corresponding results are summarized in **Table 4.5** and **Figure 4.11**.

Table 4.5: Effect of flow rate on the ^1H -NMR signal of cyclohexane in CHCl_3 (5/95%, benchmark experiment) employing FC4 (188 μL) and FC9 (211 μL – see Table 4.1 (p. 70)), without an SEC column.

Flow rate (mL/min)	$\text{RT}_{\text{Theo}}^{\text{a}}$ (s)		$\text{RT}_{\text{Exp}}^{\text{b}}$ (s)		FWHM ^c (Hz)		$S/N_{\text{Norm}}^{\text{d}}$ ($\delta = 1.43 \text{ ppm}$)	
	FC4	FC9	FC4	FC9	FC4	FC9	FC4	FC9
0	∞	∞	∞	∞	3.10	1.86	1.0	1.0
0.1	52.8	59.0	86.8	63.4	7.16	6.97	0.43	0.48
0.2	26.4	29.5	72.7	39.5	6.89	6.52	0.51	0.47
0.5	10.6	11.8	44.1	25.2	6.75	6.40	0.53	0.53
1.0	5.28	5.90	24.8	17.9	7.11	6.50	0.48	0.71
2.0	2.64	2.95	17.6	10.5	8.91	8.54	0.18	0.30

^a Residence time (theoretical) [= detection volume/flow rate]. The detection volume is calculated using the internal diameter of the flow cell and a coil length of 7 mm, with $V = \pi r^2 l$.

^b Residence time (experimental), calculated by the time difference between the peak start and end.

^c Full width at half maximum (FWHM) in the NMR dimension.

^d Normalized signal-to-noise ratio with respect to the S/N at $\dot{v} = 0 \text{ mL/min}$ in the NMR dimension. At $\dot{v} = 0 \text{ mL/min}$ only a single NMR scan was performed to obtain the values.

As evident from Table 4.5 and Figure 4.11 the resolution (FWHM) of the spectra decreased by a factor of 2.3 and 3.7 for FC4 and FC9, respectively, after the onset of constant flow rate measurements and then decreased slightly as the flow rate was increased to $\dot{v} = 0.5 \text{ mL/min}$. This was followed by an increased broadening of the peaks at flow rates exceeding $\dot{v} = 1 \text{ mL/min}$. The signal-to-noise (S/N) ratios for both of the flow cells decreased by more than a factor of 2 after the onset of the constant flow rate, followed by

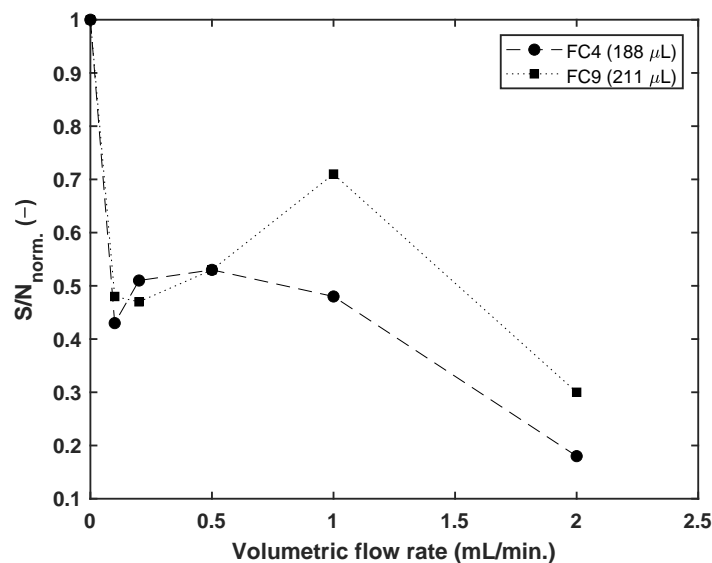


Figure 4.11: The S/N (normalized to the S/N at $\dot{v} = 0$ mL/min – see Table 4.5) for FC4 (flush cut geometry) and FC9 (cone geometry – see Figure 4.2, p. 66) as a function of the flow rate using benchmark experiments (see Section 4.2.3, p. 67). The S/N increases as the analyte (spins) spends enough time within the pre-polarization volume to reach a polarization equilibrium.

an increase for FC4 up to $\dot{v} = 0.5$ mL/min and $\dot{v} = 1$ mL/min for FC9, after which the S/N ratio drastically decreased at increasing flow rates. This trend can be described in terms of the residence time distribution and the pre-polarization volume (see Section 2.2.6, p. 38). These parameters (including the in and out-flow effects) lead to an overall effect resulting in a special trade-off regarding the choice of the flow rate. In Figure 4.11 the effect of the flow rate on the S/N ratios for both flow cells is illustrated. Apart from the evident maximum at static flow conditions, a second maximum is observed when a constant flow rate is applied. Initially, the in-flow effect improves the sensitivity by continuously replacing 'fresh' spins into the active region of the flow cell, followed by a certain flow rate range, where the replenishment is conducted by partially polarized spins. This results in the existence of an optimal flow rate range, where a compromise between sensitivity per time unit and resolution exists. In MR-NMR spectrometers where this pre-polarization volume is restricted (short), this optimum compromise leads to a relatively low flow rate range, as in the case of the current NMR spectrometer. The latter is of importance, especially in the case where the NMR spectrometer is hyphenated to a chromatography unit, where a fast sample transfer from the chromatographic column to the NMR flow cell is required to allow for improved time resolution of the on-line data acquisition.

As illustrated before, the flow cell geometry plays a vital role in the obtainable S/N values, as it severely affects the in- and out-flow behaviour of the analyte. As described in Section 4.2 (see Figure 4.3, p. 67), a plug flow would be the ideal case scenario with no stagnant zones within the NMR flow cell. This would enable analyte bands to pass the NMR coil (detection region) more homogeneously, resulting in improved resolution. Of course, obtaining a plug flow profile is highly improbable and a laminar flow profile is achieved in reality due to the low Reynolds number and Newtonian viscosities. Subsequently, a

hypothesis is made that a stable flow profile only develops after a certain point within the NMR flow cell, due to solvent and analyte moving through the flow cell as a step function resulting from different capillary diameters being employed. This would result in the analyte (and solvent) moving from smaller i.d. tubing in the capillary region (see Figure 4.2, p. 66) to the widened active region, and should have a slightly different profile at various positions in the active region of the flow cell. In order to test this hypothesis, the effect of the position of the active region relative to the NMR coil was investigated to obtain the optimum flow cell position. This would also ensure more reproducible results, as the flow profile should be more stable at the optimum position relative to the detection coil. The flow cell of choice, FC9 (see Table 4.1, p. 70) was used to investigate the optimum flow cell position. The mid-point of the flow cell was taken as the reference point of the measurements. The flow cell was moved in 1 mm increments, relative to the mid-point. At each position, an NMR magnet shimming protocol was executed at a constant flow rate of 1 mL/min with a stock solution of a polymethyl methacrylate (PMMA) calibration standard ($M_n = 38\,100$ g/mol, $D = 1.06$, $c = 2$ g/L in CHCl_3) continuously pumped through the NMR spectrometer, looking at the changes in the methoxy ($-\text{OCH}_3$) peak intensities. The results are depicted in **Figure 4.12**.

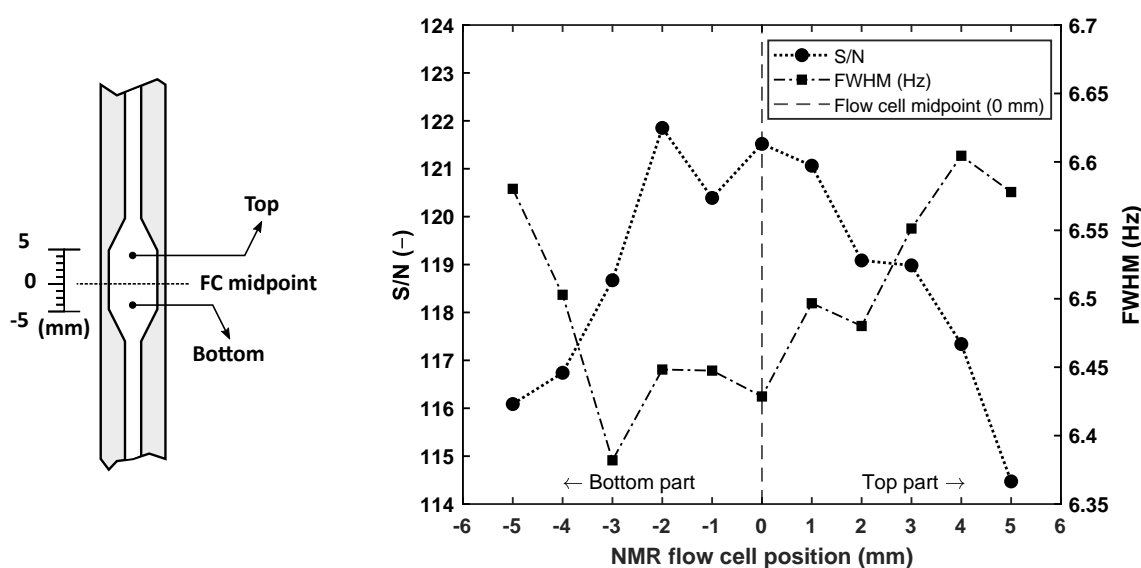


Figure 4.12: Effect of the flow cell position relative to the NMR coil for FC9 (see Table 4.1). The schematic inset to the left depicts the different regions within the active region of the NMR flow cell, which corresponds to the experimental data illustrated on the right. A polymethyl methacrylate (PMMA) calibration standard ($M_n = 38\,100$ g/mol, $D = 1.06$) with a concentration of 2 g/L in CHCl_3 were continuously pumped through the NMR spectrometer, without an SEC column. The methoxy group ($-\text{OCH}_3$) was utilized to illustrate the effect of the flow cell position relative to the NMR coil on the S/N and line-width values of the NMR signal. The NMR acquisition parameters consisted of 200 FIDs, consisting of 4 transients per spectrum, with a 90° hard pulse (0 dB, 12 μs) and a repetition time of 500 ms.

The S/N and FWHM values of the methoxy ($-\text{OCH}_3$) group from the PMMA were used to quantify the effect of the flow cell position and establish whether or not the proposed hypothesis was correct. As seen from Figure 4.12, a clear trend is visible, where the S/N

values deteriorates the closer the NMR flow cells' entry and exit geometries get to the NMR detection coil. This S/N reduction can be ascribed to two factors: (1) as the glass thickness closer to the entry and exit geometry of the flow cell is slightly thicker and more inhomogeneous, the detection volume decreases and the shimming protocol is less effective due to the magnetic susceptibility of the glass; and (2) the flow profile is not stable at these positions, reducing the effective concentration per time slice in addition to magnetic field distortions, which smears out the NMR lines, consequently reducing the S/N values and potentially also changing the line shape. At the flow cell midpoint and ± 2 mm around it, the best results with respect to S/N and FWHM values are obtained, where the midpoint (0 mm) has an S/N value of 121.5. In addition, the best S/N value is obtained at an FC position of -2 mm. The aforementioned trend can be explained as follows: (1) close to and at the flow cell midpoint, the largest detection volume is obtained ($S/N \sim V$)^[203] with the highest collective concentration per time slice; (2) at positions larger than the midpoint (top part – see Figure 4.12), dilution effects come into play and the S/N values progressively start to deteriorate again. In order to determine if the optimum position, i.e. highest S/N value at -2 mm (see Figure 4.12), outperforms the midpoint position and validate the trend observed in Figure 4.12, the same PMMA standard described above was analyzed in a full SEC-NMR experiment using a semi-preparative column (see Appendix A.6, p. 277 for details) with an injected mass of 2 mg. **Figure 4.13** illustrates the outcome of the investigation.

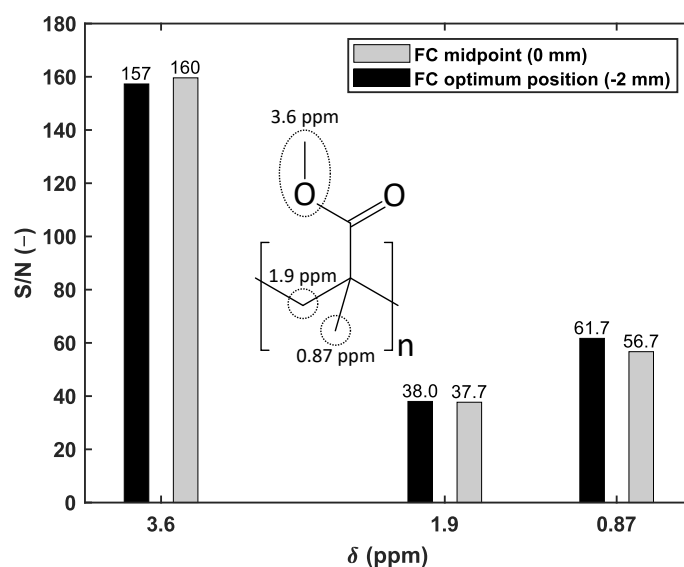


Figure 4.13: Effect of the flow cell position relative to the NMR coil in an SEC-NMR measurement. The S/N value at the midpoint (0 mm) and optimum position (-2 mm), as seen in Figure 4.12, are compared using a PMMA calibration standard ($M_n = 38\,100$ g/mol, $D = 1.06$), with an injected mass of 2 mg at a flow rate of 1 mL/min using chloroform as mobile phase. The NMR acquisition parameters consisted of 200 FIDs, 4 transients per spectrum, a 90° hard pulse (0 dB, 12 μ s), and a repetition time of 500 ms.

It is evident from Figure 4.13, that the results coincide with that observed in Figure 4.12, in that the established optimum position is at -2 mm (see Figure 4.12). However, the overall improvement of the S/N at the optimum position versus the midpoint is not significant for

an SEC-NMR measurement. The methoxy ($-\text{OCH}_3$) peak had a slightly higher S/N ($= 160$) at the midpoint compared to an S/N value of 157 at the optimum position. For the aliphatic peaks ($-\text{CH}_2-$, $\delta = 1.9$ ppm), $S/N_{\text{optimum position}} = 38.0$ and $S/N_{\text{midpoint}} = 37.7$, and methyl groups ($\alpha\text{-CH}_3$, $\delta = 0.87$ ppm), $S/N_{\text{optimum position}} = 61.7$ and $S/N_{\text{midpoint}} = 56.7$, the S/N values at the optimum position improved slightly over that of the midpoint of the flow cell. In the context of this work, it was decided that the midpoint position of the NMR flow cell is an acceptable compromise between achieving the best S/N and reproducibility, as the gain in sensitivity is negligibly low as a function of invested time. The flow cell's inner geometry would vary from manufacturer to manufacturer and, consequently, also the optimum point for the flow cell position. This would result in a new investigation for every new flow cell employed with minimal benefit. Thus, for the remainder of the presented work, the flow cell midpoint was chosen as the position of choice.

A flow rate comparison was performed for a full SEC-NMR experiment to finalize the illustration of the effect of the flow rate on the S/N values of both the NMR- and DRI-detectors. As established before (see Figure 4.11, p. 84), the optimum flow rate for FC9 (see Table 4.1) is at a flow rate of 1 mL/min. The flow rate comparison was performed at flow rates of 1–4 mL/min (0.32–1.3 cm/min) for the SEC-NMR measurement to clearly signify the change (see **Figure 4.14**). A PS/PMMA blend ($M_n = 18\,100/48\,000$ g/mol, $D = 1.05/1.03$) with an injected mass of 0.5 mg using tetrahydrofuran (THF) as mobile phase was used to exemplify the effect in a full SEC-NMR measurement.

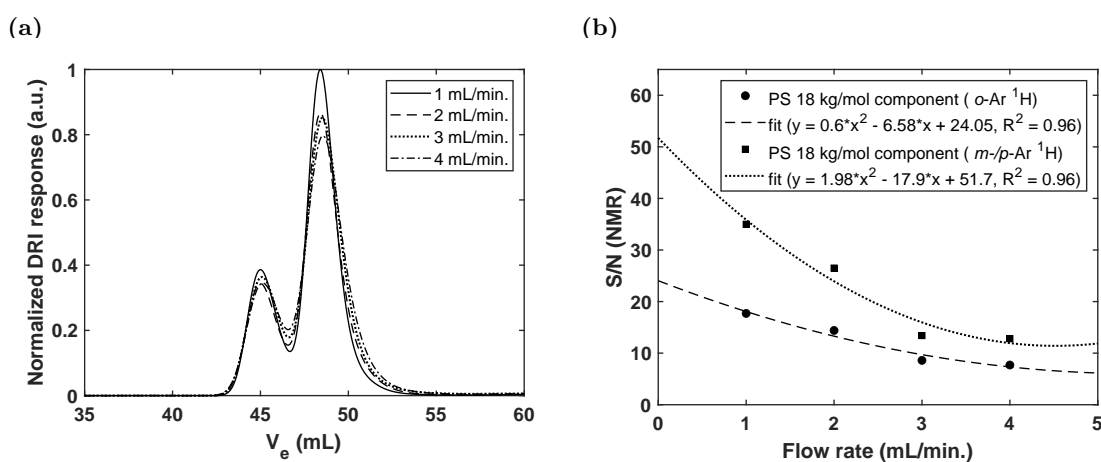


Figure 4.14: Effect of the flow rate on both the (a) DRI- and (b) NMR-detectors in an SEC-NMR experiment. The sample consisted of a PS/PMMA blend ($M_n = 18\,100/48\,000$ g/mol, $D = 1.05/1.03$) with a sample concentration of 1 g/L and an injected volume of 500 μL using tetrahydrofuran (THF) as mobile phase on a semi-preparative column (300 \times 20 mm i.d.). The NMR analysis (Figure (b)) was only performed on the PS component, where the DRI traces (Figure (a)) illustrate the entire blend. Flow cell, FC9 (see Table 4.1, p. 70), was utilized for the SEC-NMR measurements. The flow rate was limited to 1 mL/min as minimum – see text for details. Adapted from Botha et al.^[15] with permission from the Royal Society of Chemistry.

As seen in Figure 4.14, both the NMR- and DRI-responses decreased as a function of increased flow rate. The reduction in signal intensity is predominantly due to shorter residence times within the active region of the NMR flow cell, which in turn reduces the acquisition time of the analyte, as presented in Table 4.5 and Figure 4.11. In Figure 4.14 (a), the reduction of the DRI signal intensity, is due to broadening of the analyte band, as a

result of in- and out-flow effects which are more severe at elevated flow rates for FC9. In the case of Figure 4.14 (b), the NMR results were fitted with an empirical exponential function, to illustrate the reduction in S/N as a function of the flow rate. The idea of the relation between the flow rate and the S/N is presented in **Equation 4.3.1**:

$$\left. \begin{array}{l} S \propto t \propto \frac{1}{\dot{\nu}}; \\ N \propto \sqrt{t} \propto \sqrt{\frac{1}{\dot{\nu}}} \end{array} \right\} \Rightarrow \frac{S}{N} \propto \frac{1}{\sqrt{\dot{\nu}}} = \dot{\nu}^{-0.5}, \quad (4.3.1)$$

where S is the signal, N the noise, t the analyte residence time and $\dot{\nu}$ the flow rate (see Section 2.4, p. 49 for detailed definitions of the signal and noise). The influence of the recycle delay on the solvent suppression/subtraction and amount of total noise should be taken into account for a more in-depth view on the prediction of Equation 4.3.1, which in the context of the work presented was not further investigated. In Figure 4.14 (b), scattering of the data points around the empirical exponential function is visible, which can be ascribed to the variations in the flow profile with the NMR flow cell. As discussed before, the flow profile is an important variable for obtaining good S/N values, as it dictates how much of the sample passes by the NMR detection coil per time unit. In addition, if the formation of analyte 'jets' were present within the active region of the flow cell, this would also significantly reduce the obtainable S/N values. A reduced flow rate results in an improved quality of the NMR spectra. In addition, it does not affect the performance in terms of SEC resolution. A flow rate of 1 mL/min was chosen as the flow rate of choice for SEC-NMR measurements as it is still within an acceptable measurement time frame. The S/N at $\dot{\nu} = 1$ mL/min was a factor of 2.3 higher compared to $\dot{\nu} = 4$ mL/min.

4.4 Optimization of NMR parameters

The forthcoming section provides a description of the NMR spectrometer to enhance performance when hyphenated to an SEC instrument and performing measurements under continuous-flow. The section is divided into five subsections, providing a brief introduction, followed by pulse calibration considerations, the acquisition length and repetition time dependence when sensitivity is a challenge, optimal receiver gain settings and the pulse sequences utilized mostly within this study.

4.4.1 Introduction

The emerging class of medium resolution ($F = 40$ – 100 MHz, i.e. magnetic field strength, $B_0 = 1.0$ – 2.3 T, ^1H) benchtop NMR instruments (see Section 2.2.5, p. 32), with improved spectral resolution (FWHM < 0.5 Hz, under static conditions), despite their lower field strength, has major advantages as chemically sensitive detectors for SEC, as discussed in **Section 3.4** (p. 59). These instruments are designed in such a way as to utilize the powerful methods which are the driving force behind modern NMR spectroscopy, such as programmable pulse sequences, and tailor shaped pulses, including designated pulse

field gradients (PFG). As most of these benchtop-style NMR spectrometers (see Table 2.4, p. 34), including the Spinsolve 60 used within this work, are designed to be used 'as is', hardware alteration, unlike the SEC instrumentation described before, is not the route of choice for optimization. Instead, the adaptation of the experimental parameters of a given pulse sequence employed for data-acquisition and -processing is the focal point. The Spinsolve 60 NMR spectrometer used within this work was not equipped with a designated PFG coil, imposing restrictions on the development of tailor shaped pulse sequences such as the *water* suppression by *gradient tailor excitation* (*WATERGATE*) pulse sequence.^[202,209] As non-deuterated solvents are employed, a gradient coil would be highly beneficial for the purpose of solvent suppression. As mentioned, there exists a compromise between certain parameter when performing method development, which should be optimized to best suit the scientific question at hand. **Figure 4.15** represents the idea behind this compromise.

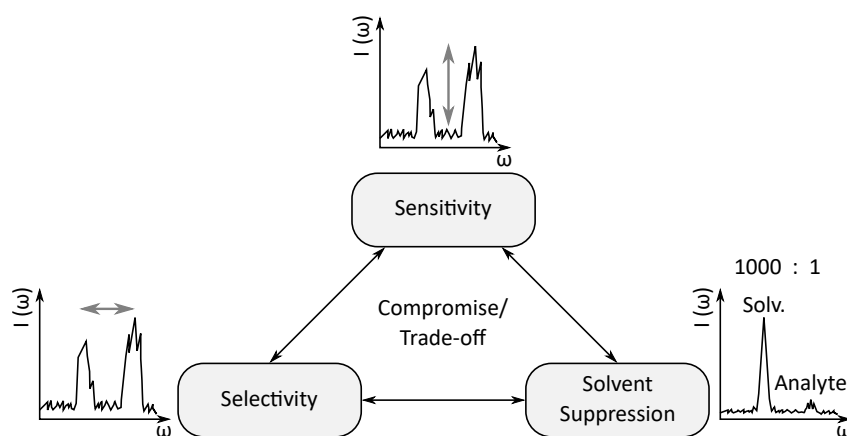


Figure 4.15: The compromise between parameters when performing method development using a benchtop NMR spectrometer. It is the proverbial Vitruvian Man (by Leonardo da Vinci, circa 1490) of SEC-NMR method development, where finding the right 'proportions' are essential for experimental success.

The forthcoming sections will describe the developmental procedure in obtaining the best performance on the Spinsolve 60 NMR spectrometer (see Appendix A.6, p. 277) for SEC-NMR hyphenation.

4.4.2 Pulse Calibration

It is essential that the radio frequency (RF) pulses employed are as precise as possible to perform successful NMR experiments. It is, therefore, required for the instrument user to either know at which pulse length the 90° pulse angle is, and if not, to calibrate it accordingly. The 90° pulse length (within the rotating frame of reference – see Figure 2.12, p. 30), per definition, is defined as the time required for the given NMR spectrometer, to rotate the magnetization from their equilibrium position, along the z-axis, into the xy-plane. The RF power dictates the strength of the RF magnetic field component and, as a result, how fast the net magnetization is rotated by the RF radiation. In the case of a 90° pulse length, the tipping angle (also referred to as a nutation), is defined as a 90° rotation around the (+)x-axis, resulting in the net magnetization of the nuclear spins to be rotated

from the (+)z-axis onto the (-)y-axis. The remaining three axes include: (-)x-, (+)y-, and (-)z-axes, which form the basis of phase cycling.^[210] As the pulse lengths are arguably one of the most important user-controllable parameters. with respect to length and phase, on an NMR spectrometer and, in addition, most (modern) pulse sequences contain either 90° pulse angles or composites thereof, it is advantageous, not only in method development but in general to perform pulse calibration experiments. There are a variety of ways to calibrate the 90° pulse length on an NMR spectrometer,^[211] however, the nutation experiment (derived from magnetic resonance imaging, MRI),^[212] was used. The nutation experiment uses a single array with a sequential increase of the pulse lengths, e.g. from $\theta = 0^\circ$ –720° (or larger tipping angles), and is possibly the most beneficial experiment.⁶ Therefore, such a nutation experiment was conducted on the Spinsolve 60 NMR spectrometer with 1 μs progressive pulse length increments up to 160 μs using an NMR (shimming) standard, that is a 90:10 weight/weight% (w/w%) deuterium oxide (D₂O)/water (H₂O) mixture, provided by Magritek GmbH (Aachen, Germany). The respective intensities and phases of the observed signals are illustrated in **Figure 4.16** (presented in 2 μs steps to avoid figure crowding).

In general the nuclear rotation is achievable by either changing the power of the RF pulse or by changing the pulse length. Changing the pulse length is often preferred as it is easier to adjust the timing of a given experiment, whilst keeping the RF power constant (as is the case in Figure 4.16). As illustrated in Figure 4.16, by increasing the pulse length the net magnetization is rotated, determined by the phase of the signal, resulting in a sinusoidal-type oscillation of the signal intensities. From this simple experiment, the 90° pulse angle can be back-calculated from the 360° cross-over point (pulse width, pw, at $90^\circ = 360^\circ/4$), since the 180° cross-over point is too dependent on the repetition time,^[213] which was established to be $\sim 11.5 \mu\text{s}$. Additional information can also be obtained, of which the RF homogeneity is arguably one of the most important parameters. A great deal of time is invested in magnet shimming in NMR spectroscopy to ensure a homogeneous nature of the static magnetic field, B_0 , since transverse magnetization precession is about B_0 . Considering the Larmor equation (see Equation 2.2.11, p. 25) it suggests that with a distribution of B_0 across a given sample volume, there will be a subsequent distribution in the resonant frequencies, i.e. line broadening. Therefore, the more homogeneous the B_0 field across the detection volume, the better the NMR resolution (i.e. smaller line widths) and signal intensities. With the latter in mind, the B_1 field, must also be considered during NMR experiments. During an RF pulse (taking the rotating frame of reference into account), the NMR resonance (on-resonant) will experience an effective field (B_{eff}), which is equivalent to the magnetic field strength as a result of the RF pulse (B_1 field). Since there is a limited number of dimensions of the NMR coil within the probe head relative to the sample, and the sample is not being spun, the B_1 field, as in the case of B_0 field, will not be homogeneous across the entire detection volume. As with the transverse precession about the z-axis in the xy-plane during an (x) RF pulse, it will precess about the x' axis in

⁶From this experiment, NMR experts, by simple inspection, can obtain information on a multitude of aspects; such as the 90° pulse length, radio frequency homogeneity, radiation dampening, probe arcing, incorrect relaxation delays (T_1) and radiation damping to name just a few.^[211]

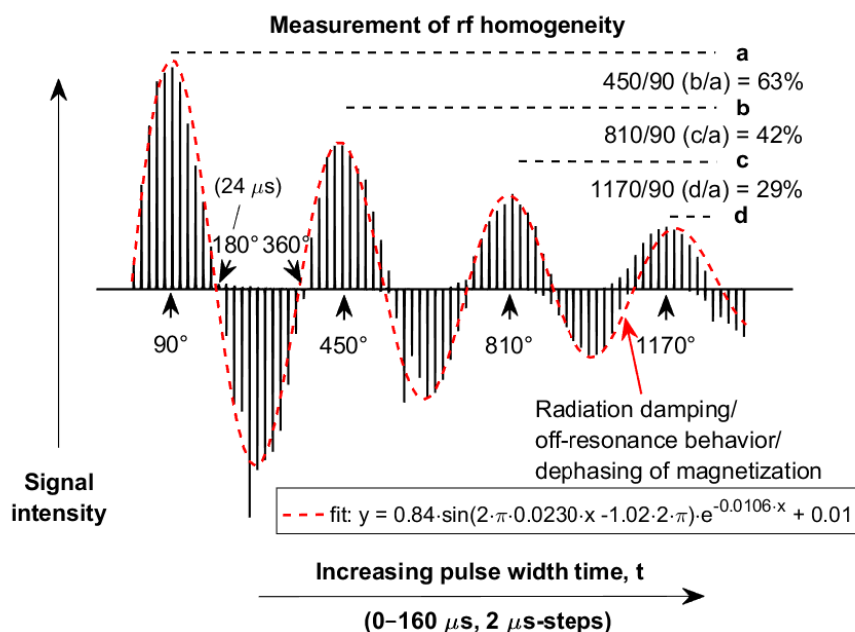


Figure 4.16: A conventional nutation experiment for calibration of the pulse width using a D₂O:H₂O (90:10) NMR standard. Each spectrum is obtained by linearly increasing the pulse length (see Equation 2.2.23, p. 30), resulting in a sinusoidal signal intensity oscillation, from which the correct pulse length for a given pulse angle can be determined. The respective maxima (90°, 450°, 810° and 1170°) and cross-over flip angles at 180° and 360° are indicated on the graph. The point of severe de-phasing of the magnetization is also indicated on the graph with a red arrow. Additional information like the RF homogeneity can also be obtained from the nutation experiment by taking the ratio of the indicated signal maxima to the 90° maximum (label 'a'). As can be seen by increasing the pulse flipping angle the RF homogeneity decreases. The NMR experimental conditions were the following: one-pulse NMR experiment, 1 scan per transient, 16 384 (16k) data points per FID with 1 Hz exponential line broadening, repetition time of 47.95 s ($> 5 \times T_1$), a dwell time of 200 μ s with a 5 kHz bandwidth, a receiver gain of 31 dB and zero-filling factor of 1. The 90° pulse angle was back-calculated from the cross-over point at 360° to be $\sim 11.5 \mu$ s.

the z-y'-plane (in the rotating frame of reference), with the precession being affected by the inhomogeneity of the B_1 field. Consequently, the magnitude of the net magnetization for a 90° pulse (450°, 810°, ...) will greatly depend on the B_1 field homogeneity.^[214] In general, the RF homogeneity, using a nutation experiment is expressed as the ratio of the signal intensity at a flipping angle of 810° relative to the 90° angle (according to classical NMR conventions). As depicted in Figure 4.16, the RF homogeneity for the Spinsolve 60 NMR spectrometer is $I_{810^\circ}/I_{90^\circ} = 42\%$ (0.42). Good RF homogeneity is especially required when using (physically) shorter sample probes, which to some degree is true for the NMR flow cells being employed within the study as they comprise reduced active region lengths compared to conventional 5 mm NMR tubes.^[215]

As the aim is to obtain sufficient signal intensities, especially for SEC-NMR hyphenation, and since a lower field strength NMR spectrometer is utilized within this study, the 90° pulse angle, as seen from Figure 4.16, provides the highest signal intensity. However, it is important to take the length of the NMR sample into account, as this could have a substantial effect on the 90° pulse length. The latter is due to the RF (B_1 field)

inhomogeneity (see description above). When decreasing the NMR sample tube length, and centred accordingly, it is assumed to be in a more homogeneous region of the RF field opposed to longer samples. Consequently, it is expected that the 90° pulse length would be shorter for shorter samples. In the case of standard 5 mm NMR sample tubes, it typically has a sample length of 4–5 cm, where FC9 (see Table 4.1, p. 70) has an active region length of 18 mm (1.8 cm). As measurements for SEC-NMR hyphenation are conducted on-flow as opposed to conventional (static) NMR experiments, and FC9 has a shorter (active region) sample length, appropriate pulse calibration is required. A nutation experiment (similar to Figure 4.16) was performed using FC9 and since the focus is to analyze polymeric species, a PS-*b*-PEMA (50_{PS}:50_{PEMA}), in-house synthesized (courtesy of Dr. M. Heck) block-copolymer sample with an $M_w = 168\,000$ g/mol ($D = 1.65$) at both static (0 mL/min) and on-flow (1 mL/min) conditions were investigated. The results are illustrated in **Figure 4.17**.

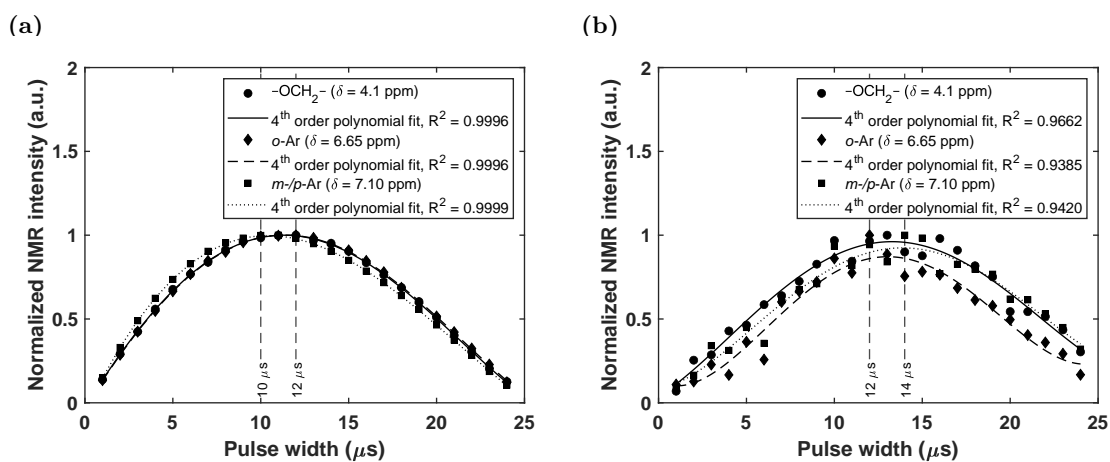


Figure 4.17: Effect of flow rate on the 90° pulse length at reduced sample lengths by employing FC9 (see Table 4.1) using a PS-*b*-PEMA (50_{PS}:50_{PMMA}, $M_w = 168\,000$ g/mol, $D = 1.65$) block-copolymer sample at (a) static- (0 mL/min) and (b) continuous-flow conditions (1 mL/min), using chloroform as solvent. The NMR experimental conditions were: 1Pulse-spoil (see Appendix A.4, p. 268), 2048 data points per FID, receiver gain setting of 37 dB, with a dwell time of 200 μ s corresponding to a 5 kHz bandwidth, and no zero-filling. The 90° pulse lengths were found to be at (a) 11 μ s and (b) 12.5 μ s.

As shown from Figure 4.17, there is a slight change in the respective signal maxima intensity range when at (a) static- (0 mL/min) and (b) continuous-flow conditions (1 mL/min), from 10–12 μ s to 12–14 μ s for static- and continuous-flow conditions, respectively. The reduction of the pulse length under static conditions (pulse length at $90^\circ = 11$ μ s) can be explained due to the shorter sample length (18 mm) of FC9, as described above, due to slightly more homogeneous B_1 field experienced by the sample. In the case of Figure 4.17 (b), two major differences can be observed, (1) the pulse length corresponding to a 90° pulse angle (signal maxima) is at 12.5 μ s, and (2) there is more scattering due to phasing artefacts, which originate from the in- and out-flow effects in conjunction with the pre-polarization experienced by the sample. Consequently, it is advised to mostly check/calibrate the 90° pulse length for a given sample under investigation to obtain the optimum conditions with respect to signal intensity. It has been found that for the majority of the samples

investigated within this study, the 90° pulse lengths were between 12–13 μs . In order to minimize the variables for the method developmental procedure and to enable a better comparison between different samples, 12 μs pulse lengths were used for the majority of the samples presented within this study, unless stated otherwise.

4.4.3 Acquisition Length and Repetition Time (Recycle Delay)

An important feature of on-flow NMR measurements is that when continuously pumping the sample and solvent through the NMR detection volume during acquisition, nuclear spins which have received an RF pulse are constantly being replaced by pre-polarized (assuming under thermal equilibrium) nuclear spins that have not yet received an RF pulse. Consequently, as described in Section 2.2.6 (p. 38), the apparent relaxation delay of the experiment is affected, resulting in both the effective T_1^{flow} and T_2^{flow} relaxation times decreasing as the residence time within the NMR flow cell is reduced, compared to static conditions.^[126,216–218] The T_1 value at static conditions are representative of the time constant the nuclear spins require to return to thermal equilibrium after RF irradiation. The latter has an intrinsic limitation on the repetition time of an NMR experiment. In the case of on-flow (continuous-flow) experiments, when the sample is continuously passing by the detection volume (of the NMR coil) during sample acquisition, the nuclear spins are continuously being replaced by new spins, and subsequently at a faster rate than the static T_1 value. This has a major benefit in that the recycle delay between consecutive scans can be faster, i.e. shorter recycle delays. The net effect is that the total measurement time of a pulse sequence can be reduced when performing continuous-flow experiments amounting in more rapid pulse sequences, more importantly, for samples with longer T_1 times. To improve the sensitivity of an NMR measurement, the most common way is to increase the number of transients (or scans) per spectra (see Section 2.4.2, p. 52) as the $S/N \sim \sqrt{n}$, with n being the number of averaged transients (or scans). Faster pulse sequence repetition times (time between the start of two consecutive scans) implies acquiring shorter free induction decays (FIDs) and intrinsically reduces the NMR resolution (i.e. selectivity), as a result of line broadening. The residence time within the NMR detection volume decreases, resulting in a decrease in the T_2^{flow} times (see Section 2.2.6, p. 38 and Figure 2.17, p. 41). As illustrated in Figure 4.15 (p. 89), it is imperative that sensitivity and selectivity are considered together.^{[14,15,107][106, pp. 1–5]}

An inversion recovery experiment was performed on a PS-*b*-PEMA block-copolymer sample (50_{PS}:50_{PEMA}, $M_w = 168\,000$ g/mol and $D = 1.65$) to determine the effect of flow rate on the longitudinal relaxation times (T_1) of the different resonance groups present. The resonant groups on which were focused included the *ortho* (*o*)- and *meta* (*m*)-/*para* (*p*)-aromatic (Ar) protons ($\delta_{o\text{-Ar}} = 6.65$ ppm and $\delta_{m\text{-}/p\text{-Ar}} = 7.10$ ppm) of the PS component and the alkoxy ($-\text{OCH}_2-$) group ($\delta = 4.1$ ppm) of the PEMA component. The apparent T_1 times at a flow rate range of 0–2 mL/min are presented in **Figure 4.18**.

The effect of reduced residence time on the apparent T_1 times are clearly seen for the PS-*b*-PEMA sample. When using this information to adjust the acquisition time of a pulse sequence, care should be taken in not setting the acquisition time too short as this will

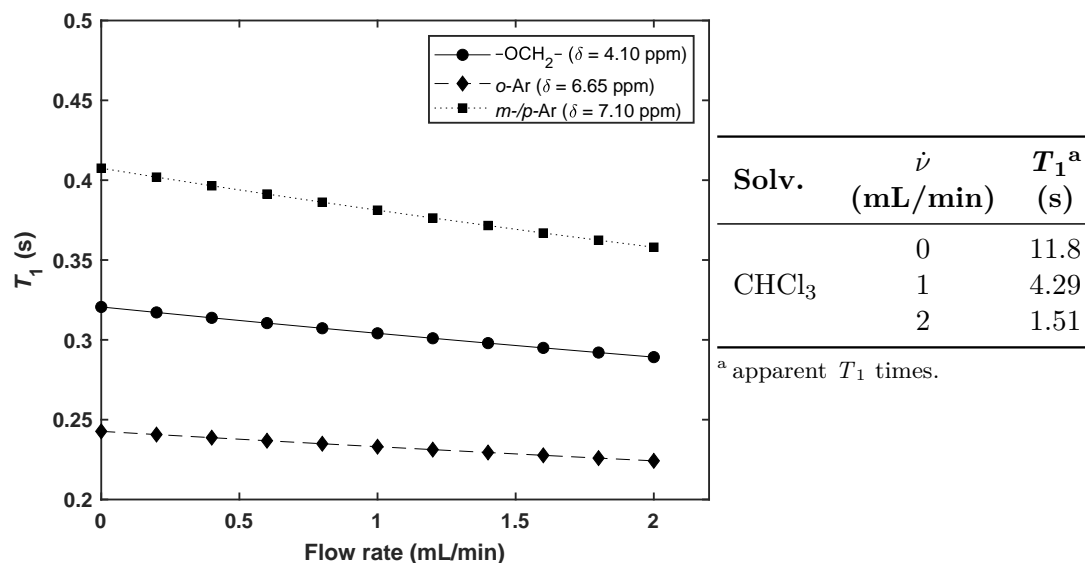


Figure 4.18: The reduction of the apparent longitudinal (T_1) relaxation times as a function of flow rate on a PS-*b*-PEMA (50_{PS}:50_{PMMA}, $M_w = 168\,000$ g/mol, $D = 1.65$) block-copolymer sample (degassed and Ar purged). The T_1 times considered are the alkoxy ($-\text{OCH}_2-$, $\delta = 4.10$ ppm) group of the PEMA component and the *ortho* (*o*)- and *meta* (*m*)-/*para* (*p*)-aromatic (Ar) protons ($\delta_{o\text{-Ar}} = 6.65$ ppm and $\delta_{m\text{-}/p\text{-Ar}} = 7.10$ ppm) of the PS component, measured in chloroform using an inversion recovery pulse sequence and FC9 (see Table 4.1, p. 70). The corresponding numerical values are listed in Table A.1 (p. 280).

result in sinc (unnormalized sinc function = $\sin x/x$, normalized sinc function = $\sin(\pi x)/\pi x$) artefacts, also more intuitively referred to as wiggles, as seen in **Figure 4.19**, which has a similar effect to FID clipping (see **Section 4.4.4**).

This occurs if the acquisition time is shorter than the effective T_2 time (more commonly referred to as T_2^* , T_2 -star)⁷ of the given resonance species, such that the signals have an incomplete decay period (FID) by the end of the acquisition. The shortening of the FID acquisition length which reduces the resolution, can be circumvented by the extension of the acquisition time, however, this is not a practical solution for SEC-NMR hyphenation because of the time limitation imposed by the residence time distribution within the detection volume of the NMR spectrometer. Longer acquisition times result in a decrease in accumulated transients, which reduces the S/N . A simple technique to overcome this problem is to perform zero filling (see Section 4.5.3), which in addition requires apodization, instead of increasing the acquisition time. In this approach, zero amplitude data points are added to the end of the FID, increasing the overall number of data points. Performing zero-filling, e.g. by a factor of 2, improves the resolution, however, this is a limited process. Apart from zero-filling, applying an appropriate decaying function, referred to as apodization (see Section 4.5.3), prior to performing Fourier transformation (see Equation 2.2.24, p. 31) also improves S/N . This is achieved by 'smoothing' the FID

⁷The star is typically used to differentiate between the "true relaxation time" and apparent relaxation time.

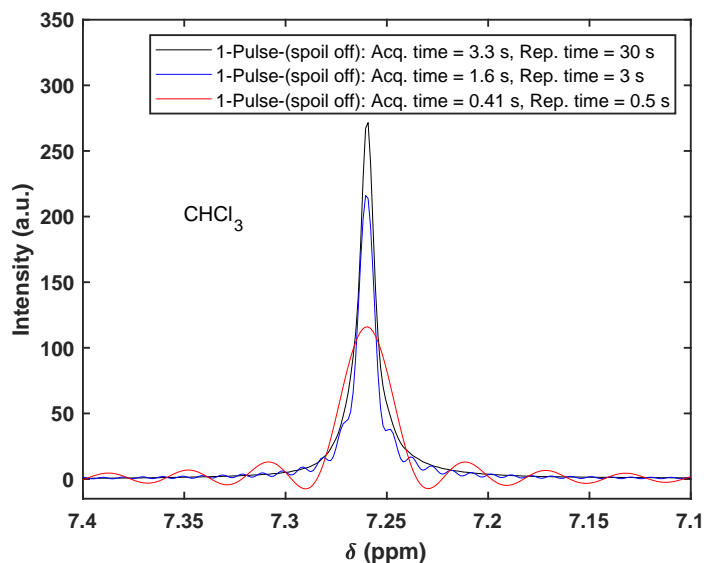


Figure 4.19: Sinc (wiggles) artefacts as a result of FID clipping due to short acquisition lengths of CHCl_3 . The 'wiggles' are clearly visible at the baseline of the NMR spectra as the acquisition time is decreased. In this case, the 1-Pulse-spoil sequence is used without the spoil pulse (i.e. crusher gradient), further indicating the need for a crusher gradient when using this pulse sequence (see Section 4.4.5).

and removing any truncation and allowing for a smooth decay to baseline level, reducing sinc artefacts in the spectrum. Apart from decreasing the resolution by having a short FID, a short recycle delay has a secondary effect resulting in a large residual magnetization (left over typically from the solvent) in the xy -plane after the end of the acquisition time. This typically necessitates the employment of a crusher gradient at the end of a short FID to de-phase any remaining coherences and allow for efficient RF pulsing, which is especially required for SEC-NMR hyphenation. A simple pulse sequence combining a 90° read pulse followed by a crusher gradient after acquisition, was implemented by Dr. K.-F. Ratzsch, followed by first optimization by Dr. J. Höpfner^[14] and then adapted to this work (see Appendix A.4, p. 268). The amplitude and duration of the crusher gradient was adapted from a pulse sequence called '1Pulse-H' provided with the Spinsolve Expert software from Magritek GmbH (Aachen, Germany). The adapted pulse sequence is referred to as *1-Pulse-spoil*, and produces a T_1 filter for solvent suppression (see **Section 4.4.5**, p. 99). The crusher gradient (where the linear shim coils, x , y and z are employed) is not significantly visible within a single scan; however, the second pulse will already give a signal of its FID and the echo of the previous FID. Generally, the spoil pulse gives a stable solvent signal suppression, and T_2^* of the polymer is short enough. In the case of employing a crusher gradient, a 'final' (potentially unreproducible, i.e. time changing) waiting period is required for the data transfer and storage, which is highly hardware dependent, i.e. depends on the quality of the electronics. The pulse sequence had the requirement that the waiting period should be as efficient (i.e. short) as possible to enable faster recycle delay periods and improve solvent suppression (see Section 4.4.5). However, the latter should be handled with care as this could distort the analyte signal intensities due to incomplete

relaxation for the respective resonance frequencies present in the sample, due to different T_1 times. The longitudinal relaxation times typically has a difference of a factor of 5 between solvent and analyte, depending on the solvent-analyte combination.^[194] To investigate what the effect of decreasing the repetition time has, a series of SEC-NMR experiments were performed on a PMMA calibration standard ($M_n = 31\,000$ g/mol, $D = 1.08$) using CHCl_3 as mobile phase, employing constant SEC parameters. **Figure 4.20** represents the acquired S/N and FWHM values of the PMMA standard looking at the methoxy group ($-\text{OCH}_3$, $\delta = 3.58$ ppm) and aliphatic alpha methyl group ($\alpha\text{-CH}_3$, $\delta = 0.85$ ppm).

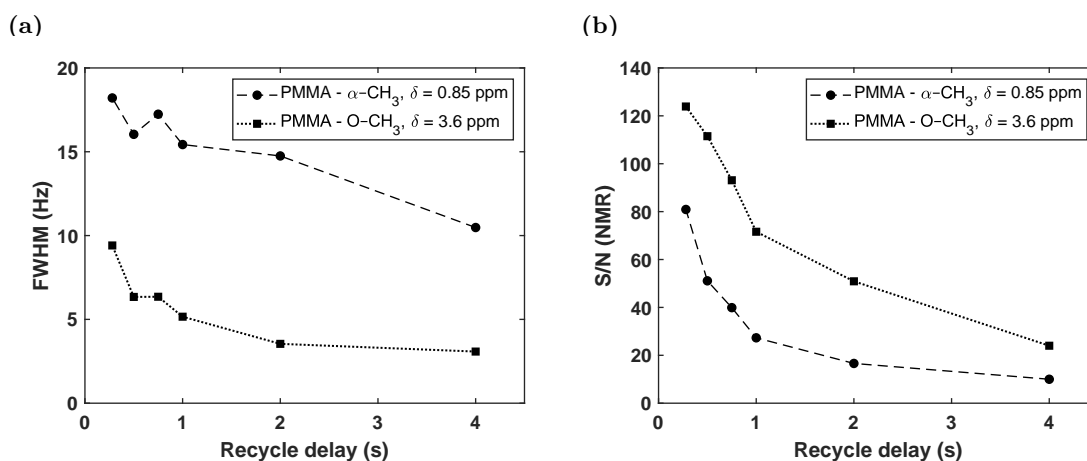


Figure 4.20: The effect of the recycle delay on the FWHM and S/N of a PMMA calibration standard ($M_n = 31\,000$ g/mol, $D = 1.08$) using a sample concentration of 2 g/L (with a 500 μL injection loop) and CHCl_3 as mobile phase (with in-line degassing) at a flow rate of 1 mL/min in combination with FC9 (see Table 4.1). The data represents the resonances of the methoxy group ($-\text{OCH}_3$, $\delta = 3.58$ ppm) and aliphatic alpha methyl group ($\alpha\text{-CH}_3$, $\delta = 0.85$ ppm). Adapted from Botha et al.^[15] with permission from the Royal Society of Chemistry. Measurement courtesy of Dr. J. Höpfner.

It is clear from Figure 4.20 (a) and (b) that the observed trend, i.e. with a reduction in the recycle delay time there is an increase in FWHM- and S/N -values, is expected. The increase in the S/N is much more pronounced than that of the FWHM of the given peaks. This effect, although not presented here, are much more severe for the solvent peak than the analyte peaks, as the analyte peaks are already broadened by isotropic dispersion of the chemical shifts. As the major focus of the SEC-NMR hyphenation is on the application to polymers, the use of a shorter recycle delay is acceptable, as NMR peak broadening is less of a concern, due to the short T_1 and T_2 times of polymers. Furthermore, using shorter recycle delay times assists in a faster overall pulse sequence, which is highly advantageous, since there is only a limited amount of time ($t < 20$ s for FC9 at 1 mL/min) available to acquire the desired data during continuous-flow measurements. For the pulse sequence to be applicable to a wider range of polymers, a recycle delay of 0.5 s was chosen as this is sufficient for polymer FID acquisition (with respect to T_1 decay) and allows for sufficient solvent suppression of the chloroform signal (see Section 4.4.5) under SEC conditions, using a flow rate of 1 mL/min including a degasser (removal of oxygen), without significant loss of analyte intensity.

4.4.4 Receiver Gain

The interplay between the obtainable signal-to-noise (S/N) ratio in an NMR spectrum and the effect the receiver gain setting has on it, can be drastic in NMR experiments. In the case of SEC-NMR hyphenation, having a high enough receiver gain setting assists in boosting S/N values, but caution should be taken due to the use of protonated solvents. Employing protonated solvents will more readily lead to ADC (see Section 2.4.3, p. 53) overloading as opposed to deuterated solvents used in conventional NMR measurements, as the ADC is mostly affected by the strongest (highest intensity) peak. Using a too low receiver gain setting affects both the signal and noise, as only a fraction of the available digitization steps of the ADC is utilized. This will, unavoidably, lead to an NMR spectrum containing a higher degree of digitization noise (see Figure 2.24, p. 55), consequently lowering the S/N ratio. On the contrary, by systematically increasing the receiver gain value, the acquired FID will be digitized using more of the available digitization steps of the ADC (this is dominated by the bit-size of the ADC). An additional advantage of increasing the receiver gain setting, is that the thermal noise in an acquired FID is lower or similar to the size of the digitization steps of the ADC. As a result the noise, unlike the signal, will not be amplified significantly up to the point of the digitization step of the ADC. After reaching receiver gain settings which allows for the noise to be in the same dimension as the ADC digitization step, it will be amplified in the same way as the signal by further increasing the receiver gain. Consequently, the S/N ratio of the spectrum will increase steadily as the receiver gain setting is increased, however, the relationship between signal and noise increase as a function of receiver gain setting is not linear. The receiver gain setting has a critical point at which the signal will exceed the available limit of the digitization range of the ADC, the FID will undergo a process referred to as 'clipping', which occurs at the onset of the FID, resulting in NMR spectrum distortions. The distortions are present in the form of sinc artefacts, which result in the formation of NMR spectrum 'wiggles'. **Figure 4.21** illustrates a series of (protonated) chloroform spectra as a function of the receiver gain settings in order to exemplify the effect. The receiver gain was adjusted to match the FID intensity to the ADC window (16 bit) to obtain the optimum S/N , by using the full dynamic range on the ADC.

It is evident from Figure 4.21 (c) that by increasing the receiver gain setting the S/N ratio has an initial increase of up to about 35 dB, after which it plateaus to a critical receiver gain setting of 52 dB, at which the ADC digitization range is reached and overloading occurs. This results in the 'clipping' of the initial part (most intense part) of the FID, consequently, the Fourier transformation of the clipped (distorted) signal will result in sinc artefacts, with baseline distortions in the NMR spectrum (typically present as 'wiggles' – see Figure 4.19, p. 95). These distortions are observable in the FWHM and phase angle off-set of the NMR spectrum and are correlated, as seen in Figure 4.21 (c) and (d). These experiments were extensively conducted on chloroform (CHCl_3) and tetrahydrofuran (THF) as these solvents were used for the majority of the experiments within this work. The consensus when working with protonated solvent in the SEC-NMR hyphenation, using a Spinsolve 60 NMR spectrometer (or any other NMR spectrometer), is to first establish the

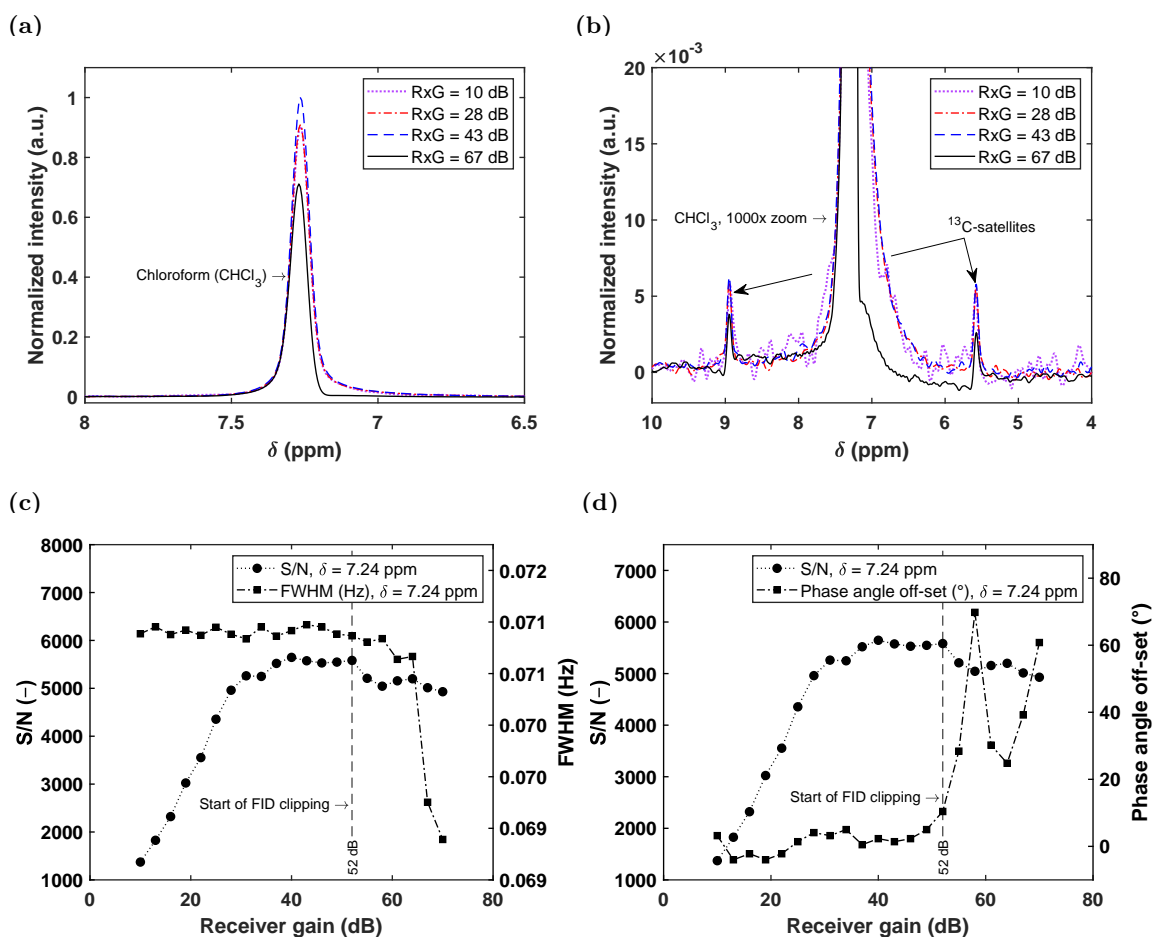


Figure 4.21: Effect of the receiver gain settings on S/N and FWHM on CHCl_3 . The measurements were performed under static conditions (0 mL/min). Figure (a) illustrates the NMR spectra normalized to a receiver gain setting of 43 dB (highest S/N) and (b) depicts a magnified region close to the baseline to show the peak distortion occurring when overloading the ADC (see Section 4.5.7). In both Figure (a) and (b) the abbreviation RxG in the legend entries refer to receiver gain. The relationship between receiver gain and FWHM, as well as receiver gain and phase angle off-set are illustrated in Figure (c) and (d), respectively. The pulse sequence employed was the 1-Pulse-spoil (see Appendix (A.4, p. 268)). Adapted from Botha et al.^[15] with permission from the Royal Society of Chemistry.

maximum receiver gain setting based on the protonated solvent employed and adjust the setting accordingly for SEC-NMR measurements of polymeric species. The receiver gain increments on the Spinsolve 60 NMR spectrometer is designed to be changed in increments of 3 dB starting at -17 dB up to 70 dB (where 0 dB corresponds to 1 mW). To have the best possible S/N ratio for a given polymeric species under investigation, it is recommended to use a receiver gain setting of 2–3 (e.g. 6–9 dB) values lower than the solvent maximum, e.g. receiver gain max prior to FID clipping for $\text{CHCl}_3 = 52$ dB, therefore, use a receiver gain = 43 or 46 dB, and not 49 dB as this is too close to the upper limit. The latter would ensure good S/N while avoiding the risk of running into ADC overloading. The receiver gain maximum for protonated THF has been established to be at 58 dB, compared to 52 dB for CHCl_3 . As mentioned before, the S/N increases strongly up to a value of 35 dB for CHCl_3 under static (0 mL/min) conditions. To establish if this is true under continuous-flow conditions, a PMMA calibration standard ($M_n = 38\,100$ g/mol, $\bar{D} = 1.06$)

at a flow of 1 mL/min with an injected mass of 1 mg, was investigated. The corresponding results are represented in **Figure 4.22**.

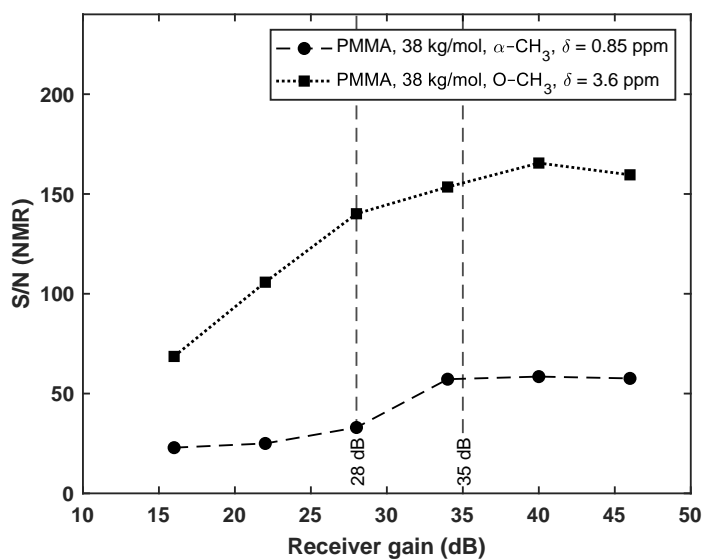


Figure 4.22: Effect of receiver gain settings on the S/N ratio of a PMMA calibration standard ($M_n = 38\,100$ g/mol, $D = 1.06$) at 1 mL/min using CHCl_3 as mobile phase with an injected mass of 1 mg on a semi-preparative linear M SDV column (see Table 4.3) as stationary phase. The 1-Pulse-spoil pulse sequence was utilized, with a total of 2600 acquired FIDs, averaging 4 scans per NMR spectrum. The total measurement time amounted to ~ 90 min. Adapted from Botha et al.^[15] with permission from the Royal Society of Chemistry.

Similar to Figure 4.21, under continuous-flow condition, using a PMMA calibration standard, the S/N value increased significantly up to a value of 35 dB, after which no pronounced effect is observed. The receiver gain setting was investigated from 15–46 dB, since the measurement was conducted in chloroform. It is recommended that when analyzing polymeric species in either chloroform or THF with the current set-up, measurements should be conducted above a receiver gain value of 35 dB. For the illustrated example in Figure 4.22, operating at receiver gain settings above 35 dB results in an increased S/N by a factor of 1.2 compared to the standard recommended receiver gain setting of 28 dB. These recommendations are instrument specific and these settings depend heavily on NMR spectrometer electronics. Additionally, phase cycling was investigated to determine whether the removal of unwanted coherent signals in NMR experiments would assist in noise reduction and avoid artefacts due to the ADC zero point off-set, consequently improving the S/N ratio. However, it was found that phase cycling for long continuous SEC-NMR measurements only improves the S/N by a factor of 1.03. This was not significant enough to explore in more detail.

4.4.5 Pulse Sequences for Solvent Suppression

The pulse sequences employed within this work consisted of T_1 -selective sequences, where differences in the T_1 -times between the protonated solvent and analyte were exploited. The two pulse sequences employed are the 1-Pulse-spoil and inversion recovery (IvR)-spoils

sequences as presented in **Figure 4.23** and will be discussed in the forthcoming section.

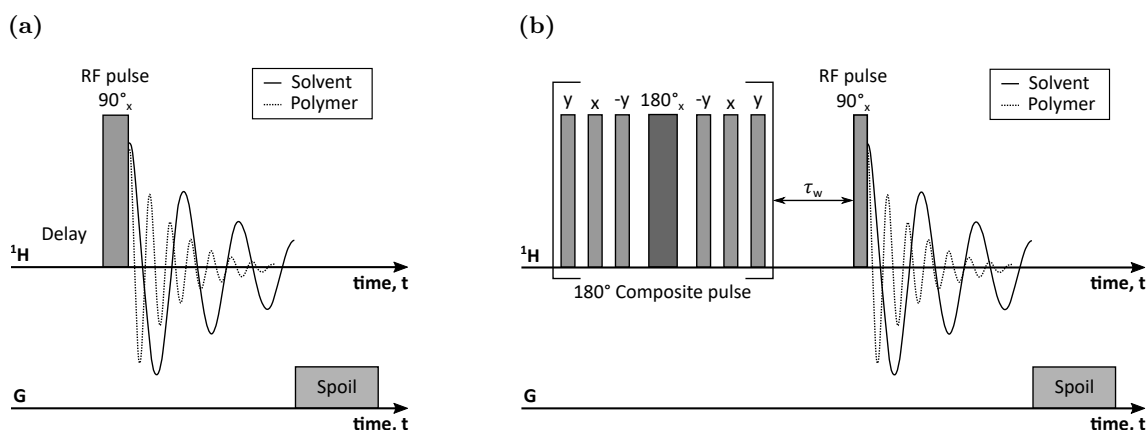


Figure 4.23: The (a) 1-Pulse-spoil and (b) IvR-spoil pulse sequences typically employed for SEC-NMR measurements. The 1-Pulse-spoil pulse sequence has the following acquisition parameters: acquisition time: ~ 410 ms, spoil gradient: 20 ms, repetition time: 500 ms and typically accompanied by 4 transients per spectrum. The spoil amplitude was set at 5000 a.u. for all measurements, which corresponds to 0.5 mT/m by employing the linear (x, y, and z) shim coils. The inversion recovery, IvR-spoil, pulse sequence consisted of a 180° composite pulse containing six 90° pulses and one 180° pulse (with different phases). This was followed by a waiting time, τ_w , which is adjusted to the T_1 of the solvent employed to ensure effective solvent suppression, including the spoil block at the end of the sequences as implemented by Dr. J. Höpfner. The waiting period was typically around 500 ms for CHCl_3 and THF. The acquisition parameters consisted of the following: acquisition time: 410 ms, spoil gradient: 20 ms (amplitude = 5000 a.u.) and a repetition time: 1 s (see Appendix A.4, p. 268). The IvR-spoil is a factor of 2 slower than the 1-Pulse-spoil pulse sequence. The length should be taken into account (with respect to residence time) when performing SEC-NMR measurements.^[14,15]

As illustrated in Figure 4.15 (p. 89), solvent suppression plays a pivotal role in experimental success. For SEC-NMR hyphenation using protonated solvents, the solvent-to-analyte ratio is in favour of the solvent, typically in excess of a factor of 1000, resulting in substantially intense (unwanted) solvent signals measured. It is, therefore, necessary to suppress the strong (residual) solvent resonances to ensure that the dynamic range of the receiver gain and/or the ADC is not overloaded. This is particularly useful due to the potential of performing measurements at higher receiver gain settings, ensuring the highest possible sensitivity, making optimum use of the ADC (see Section 4.4.4, p. 97).^[219] One simple way to overcome this problem is by performing a two-step analytical measurement (see Chapter 3, p. 56), where SEC fractionation is performed, followed by solvent evaporation, and then re-dissolving the collected fraction in deuterated (so-called 'spectroscopically-transparent') solvents prior to NMR measurement. A second approach is to use these 'spectroscopic-transparent' solvents as mobile-phase in SEC-NMR hyphenation, eliminating the solvent evaporation step required with protonated solvents. However, the use of deuterated solvents is not an economically viable option, as these solvents are generally expensive, which is not suitable for routine SEC-NMR analysis. Furthermore, deuterated solvents still contain small amounts of protonated solvents, which in some cases may need to be removed if they overlap with polymer signals. Another simple technique to suppress strong solvent signals, e.g. H_2O , is by means of incorporating a saturation block into the pulse sequence, i.e. the use of a low RF field at the Larmor frequency of the

solvent. Unfortunately, this technique has three drawbacks: (1) it makes the pulse sequence slow and in SEC-NMR hyphenation speed is required; and (2) protons from the analyte which are in chemical exchange with the solvent, will also be suppressed due to saturation transfer,^[70, p. 273] and (3) any analyte signal with neighbouring peaks will be weakened. This is where techniques which exploits T_1 relaxation times become valuable. One of these pulse sequences is the inversion recovery sequence.^[70, p. 273] Consequently, this highly facilitates the need for solvent-suppression to circumvent the aforementioned problems. Fortunately, in the case of SEC-NMR hyphenation, most of the species being analyzed are of a polymeric nature, which typically means they have a very large molar mass (hydrodynamic radius in solution), compared to the solvent. This intrinsically affects the respective relaxation times of the analyte due to their larger nature, resulting in restricted mobility causing shorter relaxation times (T_1 and T_2).^[187] To illustrate this effect, a PMMA calibration standard series, with a molar mass range of 730–1 010 000 g/mol were analyzed and the corresponding T_1 -values plotted against the numbered-average molar mass (M_n), as illustrated in **Figure 4.24**.

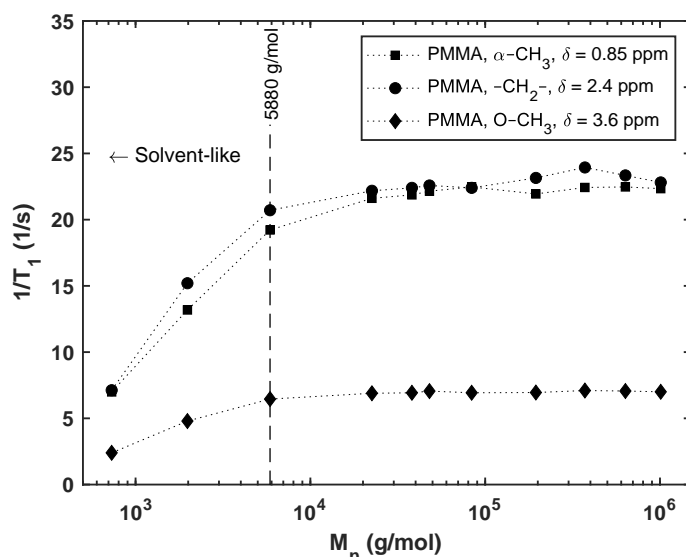


Figure 4.24: The effect of molar mass on the T_1 -values of a PMMA calibration standard series, with a molar mass range of 730–1 010 000 g/mol and narrow dispersity indexes of $D = < 1.1$, recorded under static conditions (0 mL/min) in CDCl_3 (99.9%) with a sample concentration of 34 g/L (not degassed). The T_1 values were determined using the standard inversion recovery pulse sequence built into the Spinsolve software, however, the parameters were set as follows; number of scans per spectrum: 4, acquisition time: 6.4 s, repetition time: 30 s, maximum inversion time: 10 s.

As the molar masses are increased, the T_1 -values start to plateau, which corresponds to lower T_1 -values due to restricted movement. It is this principle difference that will be exploited by means of the T_1 -selective pulse sequences. It is important to note that care should be taken when a polymeric species approaches its oligomeric form, as it starts to behave more like solvent (small) molecules and solvent suppression by means of T_1 -selective pulses becomes more challenging. For the solvent-analyte combination used within this study, the small solvent molecules had T_1 -values in the second range (ca. 2–4 s

depending on the solvent and oxygen content), whereas the analytes have T_1 -values in the millisecond range (ca. 100–300 ms depending on the molar mass). This is highly advantageous, as there are no designated pulsed field gradient coils, which is typically required for more sophisticated frequency selective tailored pulse sequences for solvent suppression, like the WATERGATE and *water suppression enhanced through T_1 effects* (WET) sequences.^[202,209] The T_1 -selective pulse sequences have the additional advantage of (partially) suppressing more than a single resonance, as long as they have a longer T_1 than the analyte.

As defined in the Master thesis of Ms. B. Mayerhöfer, and to stay consistent for comparison within this work to allow for a more reliable comparison, the same definition is utilized. That is, the suppression factor, $F_{suppr.}$, is given by the ratio of the S/N of the unsuppressed spectra (acquisition time $> 5 \times T_1$ of the solvent), S/N_0 , to the S/N of the spectra, where solvent suppression is applied, $S/N_{suppr.}$, given by

$$F_{suppr.} = \frac{S/N_0}{S/N_{suppr.}}. \quad (4.4.1)$$

Equation 4.4.1 provides a straightforward measure for solvent suppression efficiency, and provides insight to the extent of analyte signal suppression. An ideal pulse sequence will enable the highest possible suppression factor for the solvent resonance, but has little to no effect on the sensitivity and selectivity of the analyte resonances. In addition, it is also advantageous to take the baseline distortions due to solvent suppression into consideration, as this provides insight into the given range where analyte signals can be measured reproducibly and quantitatively, and is also important for data processing such as numerical baseline subtraction (see **Section 4.5**). It is also important to consider the width of the solvent resonance, especially when there are analyte peaks in close proximity, e.g. CHCl_3 and the (*m*-/*p*-) aromatic protons of PS. The pulse sequences employed for solvent suppression could naturally be investigated for a plethora of solvent-analyte combinations. The forthcoming section presents data on the two solvents mostly employed during this study, which includes CHCl_3 (single resonance at $\delta = 7.24$ ppm) and THF (two multiplet resonances with peak maxima at $\delta = 3.58$ ppm and 1.88 ppm). These solvents are employed in chromatography due to their large applicability to a variety of polymeric materials. Furthermore, two well-known and -documented polymers, PS and PMMA, were also used as benchmark polymers, for the following reason; both PS and PMMA have resonant frequencies at or close to the resonant frequencies of the selected solvents. This makes it suitable for solvent suppression efficiency evaluation. In addition, PMMA has a specific resonant frequency of interest, the methoxy group ($-\text{OCH}_3$, $\delta = 3.58$ ppm), which is very narrow, well separated and a symmetric singlet, which enables reliable quantification.

To illustrate the suppression efficiency of the 1-Pulse-spoil pulse sequence, and evaluate the corresponding results without numerical solvent subtraction, two calibration standards PS ($M_n = 30\,300$ g/mol, $D = 1.03$, $c = 2$ g/L) and PMMA ($M_n = 31\,000$ g/mol, $D = 1.08$, $c = 3$ g/L) were measured and the suppression factors of the solvent (CHCl_3) and analyte resonances were investigated. The acquisition time of the FID and the total repetition time of the pulse sequence were varied. The results are depicted in **Figure 4.25**.

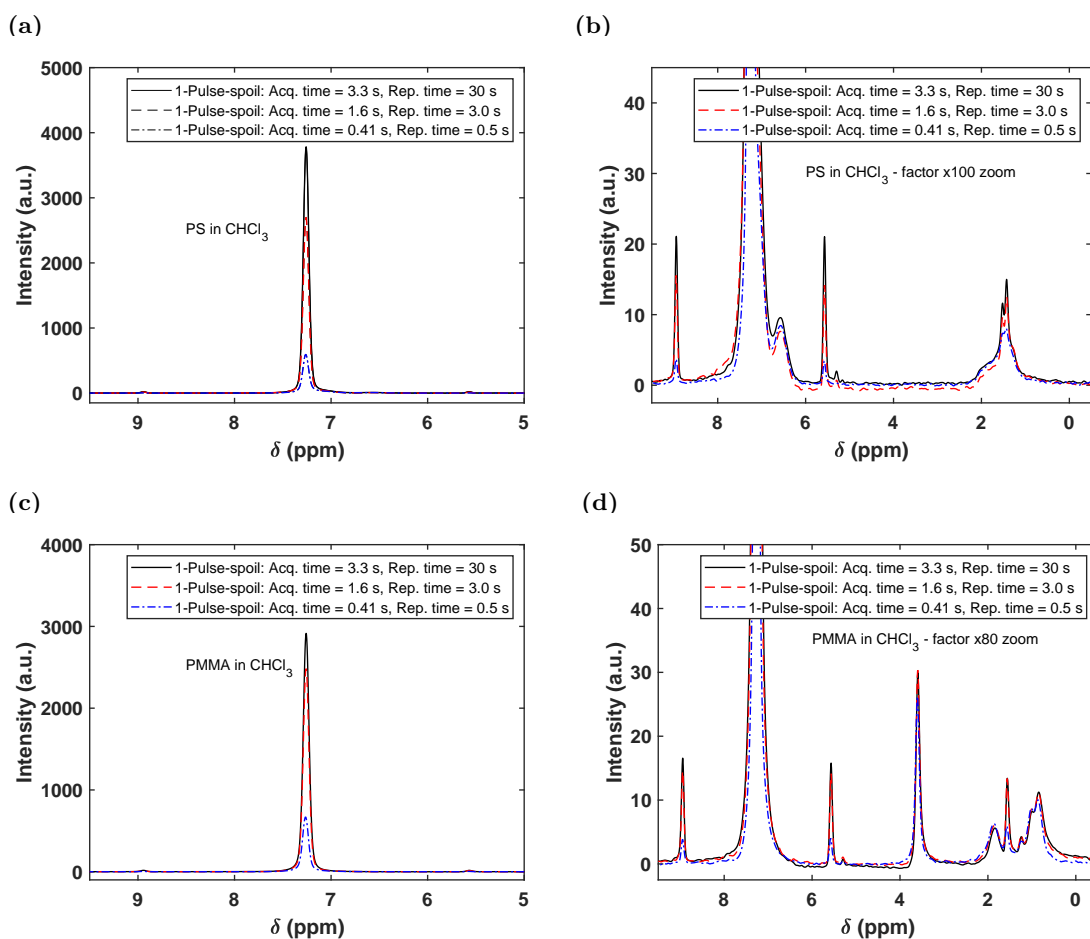


Figure 4.25: The measure of suppression efficiency of the 1-Pulse-spoil pulse sequence on the solvent and analyte resonances of PS ($M_n = 30\,300$ g/mol, $D = 1.03$, $c = 2$ g/L) in (a) and (b) and PMMA ($M_n = 31\,000$ g/mol, $D = 1.08$, $c = 3$ g/L) in (c) and (d). In figure (a) and (c) the entire solvent peak, CHCl₃, is depicted and in figure (b) and (d) the zoomed-in regions of the PS and PMMA resonances, respectively. The measurements were performed under static conditions using FC9 (see Table 4.1, p. 70), by only varying the FID acquisition time and the total repetition time.

From Figure 4.25, it is evident that when reducing the repetition time (recycle delay, RD), the solvent signal (depicted in Figure 4.25 (a) and (c)) decrease significantly. However, in the case of the analyte resonance of the PS (Figure 4.25 (b)) and PMMA (Figure 4.25 (d)), the change is not as severe as in the case of the solvent. The T_1 -filter is based on the fast repetition of the scans that leaves the solvent in a high degree of saturation, whereas the polymeric resonances can relax to a large degree. The suppression factors are listed in Table 4.6.

The suppression of the 1-Pulse-spoil pulse sequence is quantified in terms of the suppression factors relative to the experiment with an acquisition time of 3.3 s and repetition time of 30 s. As presented in Table 4.6, by shortening the recycle delay, the suppression factors for the solvent ($\delta = 7.24$ ppm) and the resonance frequencies of PS ($\delta = 6.58$ ppm and 1.52 ppm) remained relatively unchanged with a slight improvement in solvent suppression, and not too severe analyte suppression for the aromatic PS protons ($\delta = 6.58$ ppm) and the aliphatic protons ($\delta = 1.52$ ppm). However, by further decreasing the acquisition time and repetition time to 0.41 s and 0.5 s,^[14] respectively, an improvement for solvent suppression

Table 4.6: Evaluation of the 1-Pulse-spoil pulse sequence suppression efficiency in terms of the suppression factor, F . The measurements are relative to Run 1 with a recycle delay of 30 s for both a PS (2 g/L) and PMMA (3 g/L) using FC9 under static conditions in chloroform and a low receiver gain setting of 28 dB.

PS								
Run	RD (s)	Noise (a.u.)	S/N (-)			$F_{suppr.}$ (-)		
			7.24 ppm	6.58 ppm	1.52 ppm	7.24 ppm	6.58 ppm	1.52 ppm
1 ^a	30	0.0870	43 162	109	133	–	–	–
2 ^b	3	0.0882	30 799	86.9	110	1.40	1.26	1.21
3 ^c	0.5	0.0876	6 761.4	96.4	83.9	6.38	1.13	1.58
PMMA								
Run	RD (s)	Noise (a.u.)	S/N (-)			$F_{suppr.}$ (-)		
			7.24 ppm	3.58 ppm	0.85 ppm	7.24 ppm	3.58 ppm	0.85 ppm
1	30	0.0983	29 867	311	115	–	–	–
2	3	0.0972	25 441	307	114	1.17	1.01	1.01
3	0.5	0.0976	6 872.0	269	103	4.35	1.16	1.12

^a 1-Pulse-spoil: Acquisition time = 3.3 s, recycle delay (RD) = 30 s, number of scans per spectrum (ns) = 4.

^b 1-Pulse-spoil: Acquisition time = 1.6 s, recycle delay (RD) = 3 s, ns = 4.

^c 1-Pulse-spoil: Acquisition time = 0.41 s, recycle delay (RD) = 0.5 s, ns = 4.

of a factor of 6.38 is achieved with analyte suppression factors of 1.13 and 1.58 for the aromatic and aliphatic protons, respectively.

Considering the PMMA sample listed in Table 4.6, it is clear that the solvent suppression is supported by a reduction in the acquisition times and repetition times of the pulse sequence, with suppression factors of 1.17 and 4.35 for run 2 (acquisition time = 1.6 s and repetition time = 3 s) and run 3 (acquisition time = 0.41 s and repetition time = 0.5 s), respectively. Similarly to the PS, the analyte suppression of the PMMA resonances, methoxy group ($\delta = 3.58$ ppm) and aliphatic group ($\delta = 0.85$ ppm), remained relatively unchanged with suppression factors of 1.01 ($\delta = 3.58$ ppm) and 1.01 ($\delta = 0.85$ ppm) for run 2 and 1.16 ($\delta = 3.58$ ppm) and 1.12 ($\delta = 0.85$ ppm) for run 3. This clearly indicates the advantage of reducing the acquisition parameters in conjunction with the crusher gradient. As the T_1 is much shorter for the polymers than in the case of the solvent (CHCl_3), the short repetition time of 0.5 s is sufficient to suppress the solvent resonance by a factor of 4–7, without a significant loss in analyte intensity.

The use of the crusher gradient after acquisition is a key parameter to minimize phase distortions (due to echoes in subsequent transients), and to reduce artefacts (sinc) due to an insufficient decay time of the FID.^[14] In addition, for SEC-NMR measurements, similar suppression factors are expected, as the solvent is degassed through the SEC system, minimizing molecular oxygen (a paramagnetic material), which significantly contributes to the reduction in relaxation times of solvent protons. Consequently, by solvent degassing, it further increases the difference between the T_1 of the solvent and analyte, allowing for more efficient solvent suppression. The use of the T_1 -filter is limited to cases with large

T_1 differences, with respect to spectral density,⁸ between the solvent and analyte of high molar mass polymeric species in low molar mass solvent, as is the case for SEC-NMR and not HPLC-NMR. Furthermore, fast repetition times are directly correlated to the accessible resolution via acquisition time, which cannot be varied independently, as a result of spectral distortions arising due to T_1 -weighing.^[15]

The second approach to solvent suppression based on T_1 -filtering, was the inversion recovery pulse sequence, IvR-spoil (see Figure 4.23 (b)). The IvR-spoil pulse sequence is based on the standard inversion recovery experiment for T_1 determination built into the SpinsolveExpert software by Magritek GmbH (Aachen, Germany). The pulse sequence works on the premise of inverting the net magnetization from the z - to $-z$ -axis, by means of a 180° composite pulse, followed by a delay, τ_w , which typically corresponds to the T_1 relaxation time of the solvent. After this delay, a 90° read pulse is applied, which rotates the magnetization of the relaxed polymer resonances into the xy -plane, and any residual solvent magnetization gets rotated again along the $-z$ -axis, resulting in no solvent resonances being detected. In principle, this pulse sequence should yield the best suppression efficiency for the solvent resonances with minimal analyte suppression. This technique is well-known for solvent suppression within the NMR spectroscopy field, and originally applied to protein analysis for the suppression of water resonances by Patt et al.^[220] Additionally, this approach was reported by Cudaj et al.^[10,187] in the first attempts of SEC hyphenation to a low field (20 MHz, 0.5 T) benchtop NMR spectrometer using THF as mobile phase. A challenge faced by Cudaj et al.^[10,187] was that the suppression efficiency decreased when performing measurements under continuous-flow conditions opposed to static conditions. This could potentially be ascribed to the degassing procedure used, resulting in longer T_1 -times for the solvent. As previously mentioned, the τ_w time is dependent on the T_1 -time of the solvent, therefore, in order to obtain the best solvent suppression the T_1 -value should be determined and incorporated for each solvent employed. The solvent longitudinal relaxation times for THF and CHCl_3 typically varies between 1–3 s, however, the optimum waiting times for solvent suppression for the custom developed on-line monitoring pulse sequence were all in the range of 400–600 ms when employing the fastest repetition time available. By employing shorter waiting times, the apparent T_1 shortens, which is also described in literature by Benz et al.^[221] Applying shorter repetition times to the inversion recovery pulse sequence is referred to as *super water elimination Fourier transform* (WEFT) NMR spectroscopy. The reader is referred to Inubushi et al.^[222] (Figure 1) for a more detailed description of the WEFT pulse sequence principle. As described in Section 4.2, there is a limited time period in which the analyte can be measured during an SEC-NMR measurement. Subsequently, the shortening of the delay, τ_w , of the inversion recovery pulse sequence is highly advantageous, especially in the case of THF, which has two multiplet resonances. The latter allows for an improved time resolution, and an increased sensitivity due to the acquisition of more transients (see Section 2.4.2, p. 50). Major efforts in pulse sequence optimization with respect to the inversion recovery pulse sequence were performed by Ms. B. Mayerhöfer, and thoroughly

⁸The spectral density, or more commonly power spectral density (PSD), describes the spectral energy distribution (intensity) present in a signal as function of the frequency, per unit frequency (or per time unit).^[70, p. 275, 247]

explained in the corresponding M.Sc. thesis.^[223] To illustrate the suppression efficiency of the inversion recovery pulse sequence, a pulse sequence comparison series was conducted, where the 1-Pulse-spoil pulse sequence is compared to the inversion recovery pulse sequence looking at chloroform and THF. In the case of the chloroform suppression comparison, it depicts results under both static (0 mL/min) and on-line (1 mL/min) conditions including a PS calibration standard ($M_n = 30\,300$ g/mol, $D = 1.03$, 40 g/L static, 5 g/L on-line). The on-line measurements were performed by preparing a 5 g/L stock solution of PS in chloroform and continuously cycling it through the NMR spectrometer, i.e. analyte acquisition is not restricted to a certain acquisition window as is the case for SEC-NMR measurements. For THF suppression, only on-line results are depicted. The collective summary of the results are presented in **Figure 4.26**.

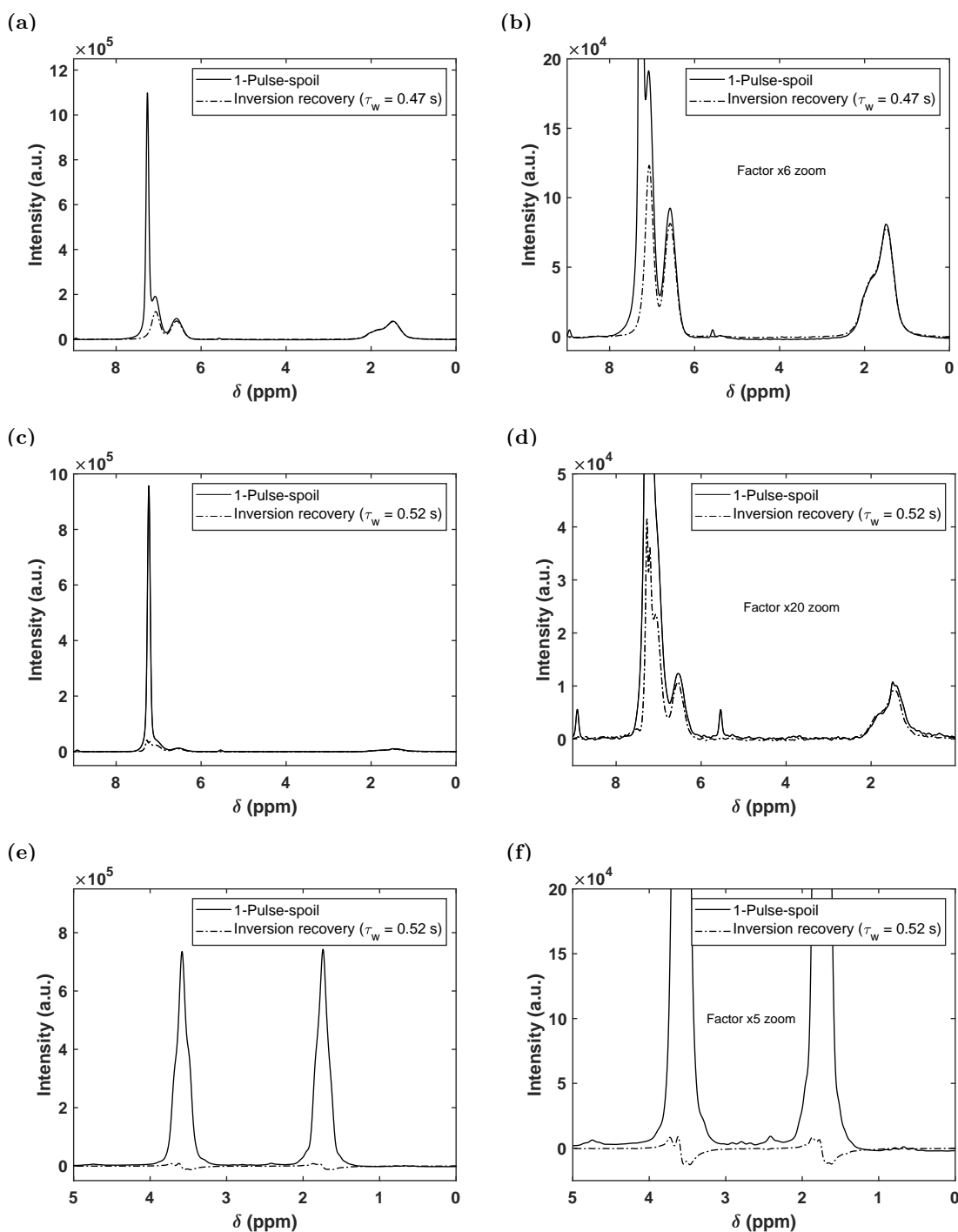


Figure 4.26: The 1-Pulse-spoil and inversion recovery pulse sequence applied to CHCl_3 and THF. In figure (a) and (b) the pulse sequences are applied to PS ($M_n = 30\,300$ g/mol, $D = 1.03$, $c = 40$ g/L) under static conditions in CHCl_3 with a waiting time of 0.47 s and repetition time of 1 s for the inversion recovery pulse sequence compared to the 1-Pulse-spoil sequence (0.5 s repetition time). Figure (c) and (d) illustrates the same PS sample (5 g/L) under continuous-flow conditions in chloroform using a flow rate of 1 mL/min, with a $\tau_w = 0.52$ s and repetition time of 1 s compared to the 1-Pulse-spoil sequence (0.5 s). Figure (e) and (f) show the inversion recovery pulse sequence (repetition time = 1 s) in comparison to the 1-Pulse-spoil pulse sequence and is applied in continuous-flow on pure THF in an SEC-NMR measurement. The pulse sequences consisted of the following experimental parameters: number of scans = 4 and acquisition time = 0.41 s, the optimum delay time, τ_w , was determined manually prior to measurement. Measurements courtesy of Ms. B. Mayerhöfer.

It is clear from Figure 4.26 (a) and (b) that under static conditions and when employing the optimum waiting time, τ_w , for the inversion recovery pulse sequence, the solvent resonance was barely visible (only as a small shoulder) next to the (*m-/p-*) aromatic protons of PS. With additional fine-tuning of the pulse sequence, it is in principle possible to fully suppress the residual chloroform resonance using the inversion recovery pulse sequence. As seen in Figure 4.26 (c) and (d), when performing the solvent suppression under continuous-flow conditions, the suppression efficiency decreases, which was also established by Cudaj et al.^[10] This can be ascribed to the in-flow effect, as there are continuously new 'fresh' spins entering the detection region. Furthermore, it is clear from Figure 4.26 (e) and (f) that the solvent suppression of the THF on-line is effective when comparing the inversion recovery pulse sequence to that of the 1-Pulse-spoil sequence. In addition, it is evident that the inversion recovery pulse sequence gives a negative solvent signal for a too short delay time, τ_w , however, this can partly be circumvented by manual phasing. The corresponding suppression efficiency results are listed in **Table 4.7** for the results depicted in Figure 4.26 (c) and (d).

Table 4.7: Comparison of the solvent suppression efficiency of the 1-Pulse-spoil and inversion recovery pulse sequences applied to PS ($M_n = 30\ 300$ g/mol, $D = 1.03$, $c = 5$ g/L) in CHCl_3 at $\dot{v} = 1$ mL/min relative to an unsuppressed spectrum (1-Pulse) under static conditions. All measurements were performed with a total of 4 scans per spectrum.

PS								
Pulse sequence	RD (s)	Noise (a.u.)	S/N (-)			$F_{suppr.}$ (-)		
			7.24 ppm	6.58 ppm	1.52 ppm	7.24 ppm	6.58 ppm	1.52 ppm
1 ^a	60	110.4	18 028	106	88.3	–	–	–
2 ^b	0.5	125.7	7 611.5	98.2	85.5	2.40	1.08	1.03
3 ^c	1.0	109.0	380.78	98.1	84.0	47.3	1.08	1.05

^a 1-Pulse: Acquisition time = 3.3 s, recycle delay (RD) = 60 s, number of scans per spectrum (ns) = 4.

^b 1-Pulse-spoil: Acquisition time = 0.41 s, recycle delay (RD) = 0.5 s, ns = 4.

^c Inversion recovery: $\tau_w = 0.52$ s, Acquisition time = 0.41 s, recycle delay (RD) = 1.0 s, ns = 4.

As seen in Table 4.7 with respect to the suppression factors, for both the aliphatic ($\delta = 1.52$ ppm) and (*o-*) aromatic ($\delta = 6.58$ ppm) protons of PS, they are nearly 1, indicating very low analyte suppression which is highly favourable. Taking the chloroform resonance ($\delta = 7.24$ ppm) into account, it is clear that the inversion recovery pulse sequence is highly effective with a suppression factor of 47 compared to the suppression factor of 2 for the 1-Pulse-spoil pulse sequence under continuous-flow conditions (1 mL/min). The pre-defined requirements of an effective pulse sequence have been met for both these pulse sequences. It should be taken into account that the 1-Pulse-spoil, compared to the IvR-spoil, pulse sequence is twice as fast due to its shorter repetition time, which is especially of importance when the acquisition window is restricted to $t = < 10$ s, which is typically the case for SEC-NMR measurements. Additional application examples of the respective pulse sequences will be exemplified in **Section 4.6**, where the fundamental importance of these pulse sequences will become apparent within the larger context that is SEC-NMR hyphenation.

4.5 Numerical Solvent Suppression

The following section is dedicated to the development of an in-house written data processing software, referred to as Time-resolved nuclear Magnetic Detection of Eluates (TMDE), that enables the post data acquisition processing of the SEC-NMR data. The section provides the highlights of what the software package can do, alongside the various data processing procedures followed throughout the developmental procedure.

4.5.1 Introduction

The experimental parameters related to method development typically have physical limits as to what can be altered or adapted to obtain the best possible performance from a given system. This does not, however, refer to the proverbial 'end-of-the-road' in the optimization procedure. Where the physical limit of system hardware, related to possible adaptations, are reached, post data acquisition processing takes over in the form of signal processing (see Section 2.4, p. 49). In contrast to data acquisition on a designated instrument, post acquisition processing involves computation, with the fundamental advantage that it can be automated and customized to a specific end-use and generally with a high yielding outcome. In the case of the design of an experiment, the experimental parameters can be rather diverse, depending on the scientific question at hand with respect to acquisition parameters and steps involved on a given instrument, e.g. an NMR spectrometer. In contrast, post data acquisition processing involves a more systematic approach, i.e. computational thinking,⁹ that requires a certain processing pattern to achieve the desired end-goal, which in principle is relatively simple to design in advance. In addition, it allows for more information to be extracted or derived from the acquisition parameters. As multiple software packages had to be developed within the framework of project Q1 of the SFB 1176, with the guidance of Dr. J. Höpfner, a plan was devised as to what the best possible route would be for designing an interlinked platform that could be applied to various other problems. The conceptual idea is schematically depicted in **Figure 4.27**. It should be noted that due to the size and complexity of the software packages (for SEC-NMR and SEC-EC-QCL) an entire team was involved in the development, which included two post-doctoral employees, Dr. J. Höpfner (SEC-NMR) and Dr. J. Kübel (SEC-EC-QCL), the author and an assistant, Ms. A. Bucka.

4.5.2 TMDE Stand-Alone Application

Emphasis was placed on developing appropriate signal processing to obtain the optimum system performance for SEC-NMR hyphenation, as the S/N of the analytes' NMR signal is a major challenge due to the low sensitivity of the medium-resolution NMR spectrometers.

⁹Computational thinking (CT)^[224] is related to a problem-solving approach that involves the expression of problems and their corresponding solutions in such a fashion that a computer could execute it. It is to a certain degree very similar to playing the combinatorial-number placement puzzle Sudoku, which requires a logic-based approach to solve.

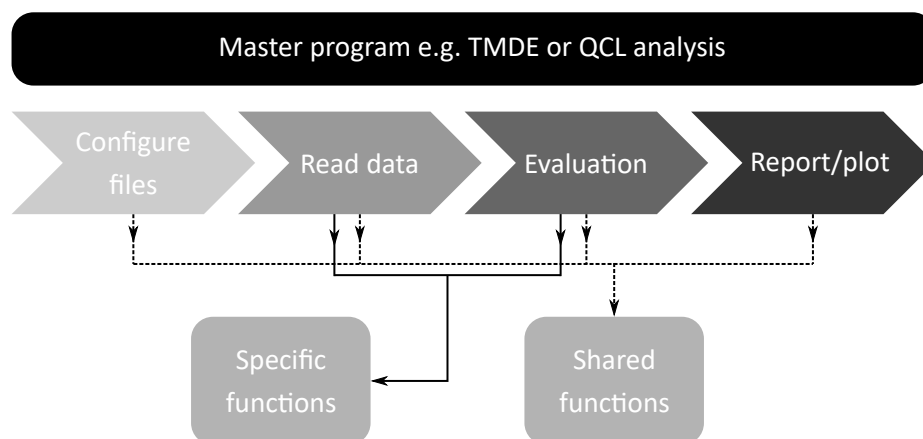
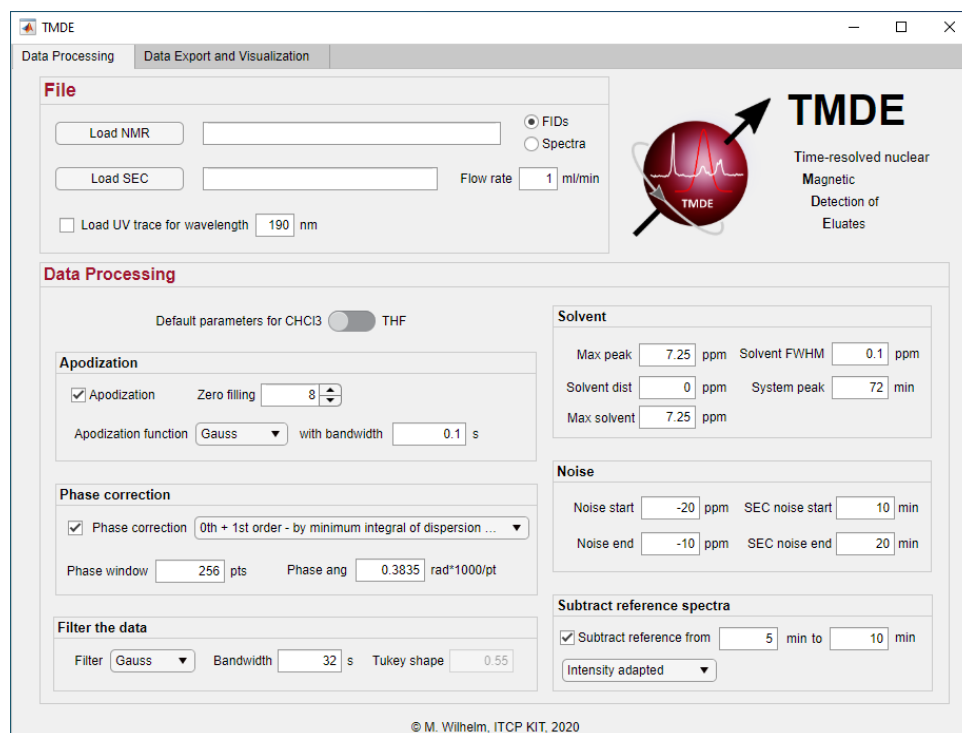


Figure 4.27: An interlinked software platform for post data acquisition processing. The general work-flow includes the correct configuration of files, reading it into the software, followed by data evaluation/processing and finally the reporting and visual representation of results. Within the work-flow, specific functions related to certain applications can be utilized, e.g. NMR vs QCL, and shared functions, which are interchangeably used between different platforms.

The data processing software, named *Time-resolved Nuclear Magnetic Detection of Eluates* (TMDE), is an in-house written MATLAB[®] script. A part of the raw script was initially started by Dr. K.-F. Ratzsch, followed by major advances and contributions being made by Dr. J. Höpfner^[14] into a useable version and further optimized during the course of this work. Furthermore, the TMDE MATLAB[®] script was originally in the raw programming language form, as this allowed more advance and freely changeable alterations to be made to the script during data processing. However, this has the disadvantage that the user has to be proficient in programming using MATLAB[®] to understand and decipher script which has been written by multiple authors with different styles, making troubleshooting (or debugging) complex. The raw script comprised ~ 7800 lines of code, which includes 48 external functions, designed to be for a specific use or shared between software platforms (see Figure 4.27). In order to avoid the aforementioned problems, and to ensure that results are comparable between users, the raw script was transformed, within this study, with the assistance of Ms. A. Bucka into a stand-alone software application, depicted in **Figure 4.28**. Thus, eliminating the need to have a MATLAB[®] license, and providing a more user-friendly interface, with a step-by-step user documentation (see Appendix A.1, p. 231), ensuring effective use and knowledge transfer (a black box to some degree).

The NMR data are stored as FIDs during an SEC-NMR measurement due to timing interferences with the pulse sequences (see Section 4.4.5), which prevents real-time data evaluation. Subsequently, the TMDE software allows for the evaluation of the stored data in both the NMR and SEC dimensions. The evaluation steps are: (1) Fourier transformation of the raw FIDs into the frequency domain (see Equation 2.2.24, p. 31), (2) apodization and zero filling, (3) phase correction, (4) smoothing/filtering in the SEC dimension, (5) solvent spectrum subtraction, (6) automatic peak finding, and (7) baseline correction in the SEC dimension (typically by means of a 2nd order polynomial fit).^[14,15] Finally, the software reports, stores, and visually presents the data statistics for each peak. The corresponding signal-to-noise (S/N) ratios are determined from the maximum peak height of interest

(a)



(b)

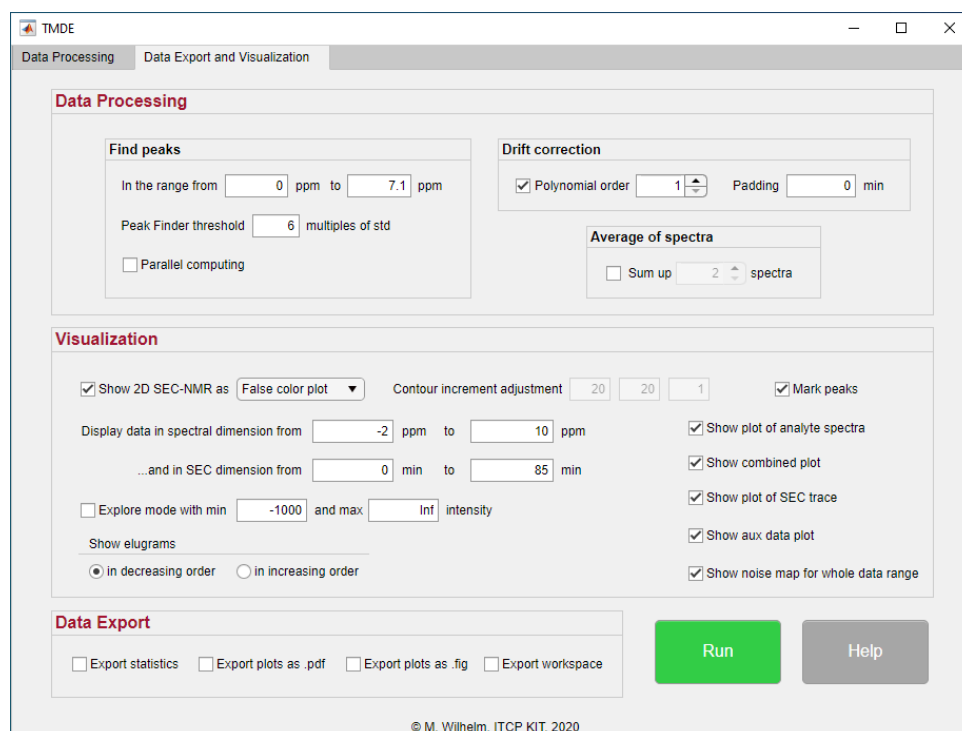


Figure 4.28: The TMDE graphical user interface (GUI) for the signal processing of SEC and NMR data. Figure (a) is the 'Data Processing' panel, which involves most of the signal processing capabilities. Figure (b) represents the 'Data Export and Visualization' panel, which still involves a small section on 'Data Processing', but is mostly dedicated to the various possibilities of exporting/saving data as well as figure/result representation. See Appendix A.1 (p. 231) for a detailed description of each processing panel, including its various functions in the TMDE GUI documentation.

(S) to the standard deviation (σ) of the noise ($\sigma = N$) in a signal-free region of the NMR spectrum (typically -15 to -30 ppm), after the sequential corrections were performed in steps (1)–(7).

Numerical solvent suppression is performed in a two-step procedure, one in the NMR- and the other in the SEC-dimension. Firstly, a reference spectrum containing the solvent signal, including trace components like stabilizers, water contamination etc., is determined by averaging the spectra between 5–10 min elution time (on the current SEC-NMR set-up), prior to sample elution, which on the semi-preparative columns employed will not occur before 30 min at 1 mL/min. This averaged reference is then subtracted from each spectrum, after appropriate scaling to allow for the highest peaks (most intense) in both spectra to match in order to account for minute intensity fluctuation due to, for example, ADC drifts. Secondly, an individual 2nd order polynomial (usually) is fitted to the baseline, typically starting at 10 min up to the onset of the SEC system peak at ~ 72 min, excluding the peak region. The corresponding baseline is then subtracted from the data to remove drifts in the solvent, trace components and background noise. This two-step approach reduces the solvent signal intensity tremendously, which will become apparent in the forthcoming sections. Prior to the execution of the second step, the analyte peak regions must be identified, which is completed by using the peakfinder function in the TMDE software. The total number of peaks found are limited by the pre-set threshold (chosen to be 6 times the standard deviation of the noise in a peak free region). The resulting area for each peak is calculated by searching for the point where the peak intensity has decayed to within the respective noise level in both dimensions. The S/N ratio of each resulting peak is determined by taking the peak maximum and dividing it by the standard deviation of the data in the signal-free region of the spectrum (e.g. -15 to -30 ppm). Finally, the peak shape is quantified by the full-width at half-maximum (FWHM), and tailing-maximum (FWTM), with the latter corresponding to 1/10th of the peak height. The filtering is performed independently in both dimensions (see Figure 3.1, p. 57) at different stages of the workflow. This enables the subsequent improvement of the S/N in a multitude of steps, which will be discussed and demonstrated in the forthcoming sections.

4.5.3 Apodization and Zero-filling

After data import, prior to transforming the acquired FIDs from their time to frequency domain via the Fourier transformation (achieved with the Cooley and Tukey algorithm which is a fast Fourier transform, FFT, requiring 2ⁿ time data points as presented in Equation 2.2.24, p. 31), the FIDs can be optimized with a couple of techniques allowing for the improved performance of the FFT algorithm. The most significant techniques are possibly apodization (also referred to as convolution) and zero-filling. Apodization is a special transformation which involves the multiplication of the FID data points with a *window function* that emphasizes different portions of the data set. The most significant attribute of apodization is filtration, where the signal is stripped of some of its noise components. Considering an FID, it comprises decaying sine and cosine waves, where the end-part of the FID (most likely) contains more noise than the onset of the FID, and

the end-part also has low or no signal intensity. By apodizing the FID data, the onset is emphasized and the end or tail of the FID is de-emphasized. Apodization can be seen as the broadening of one function by another, and by doing so enhances the S/N ratio, but at the cost of resolution. In general, these window functions can be selected for an intended objective, such as S/N improvement, or resolution enhancement (with a reduction in S/N), or artefact reduction, i.e. using a sine-bell function. It should, however, be noted that the use of window functions to enhance one parameter typically comes at the expense of another (it always comes down to a balance – see Figure 4.15, p. 89). Arguably, one of the most widely used window functions in NMR spectroscopy is the exponential function (also referred to as the Line Broadening function, applied typically with 1 Hz broadening) due to its shape compared to the FID, or more powerful Gaussian functions.

Apodization is also useful to remove boundary-effects; as in cases where the signal has not fully decayed to baseline level during FID acquisition, resulting in an abrupt ending of the signal, which will result in truncation artefacts (similar to FID clipping as seen in Section 4.4.3, p. 93) after Fourier transformation. Apodization, in conjunction with zero-filling, will ensure a smooth transition of the signal to baseline level, significantly reducing sinc artefacts. It is especially useful in cases where the acquisition of the FIDs are short, which is of particular relevance in this work. The TMDE software has five designated window functions for apodization, listed in **Table 4.8** and illustrated in **Figure 4.29**.

Table 4.8: Summary of the five window functions used for apodization in the TMDE software.

Function name	Function
Exponential	$I(t) = \exp(-\frac{t}{\sigma})$
Lorentz	$I(t) = \frac{1}{t^2 + (\sqrt{2} \ln 2\sigma)^2}$
Gaussian	$I(t) = \exp\left(-\frac{t^2}{2\sigma^2}\right)$
Lorentz-Gaussian	$I(t) = \exp\left(\frac{t}{T_{2,Sol.}^*} - \frac{t^2}{2\sigma^2}\right)$
Traficante	$I(t) = \frac{\exp\left(-\frac{t}{T_{2,Anal.}^*}\right)}{\exp\left(\frac{t}{T_{2,Anal.}^*}\right) + \exp\left(\frac{t-t_{AQ}}{T_{2,Sol.}^*}\right)}$

σ = standard deviation of peak width.

t = measurement time, e.g. FID.

t_{AQ} = FID acquisition time.

T_2^* = effective T_2 of the solvent (Sol.) and analyte (Anal.).

Note: T_2 is the true T_2 caused by atomic/molecular interactions, where T_2^* is the 'observed' T_2 , representing the true T_2 , including magnetic field inhomogeneities. $T_2^* \leq T_2$.

The Fourier transformation of the FID will produce the exact same amount of data points as is originally in the FID signal. This can lead to more coarse looking signals if a lower number of data points were collected. One way to overcome this is by sampling the time-domain (FID) data for a longer period of time. This is not always possible or time-efficient. Alternatively, the block size of the acquisition memory can artificially be increased by supplementing the time-domain data by a string of samples with zero amplitude prior

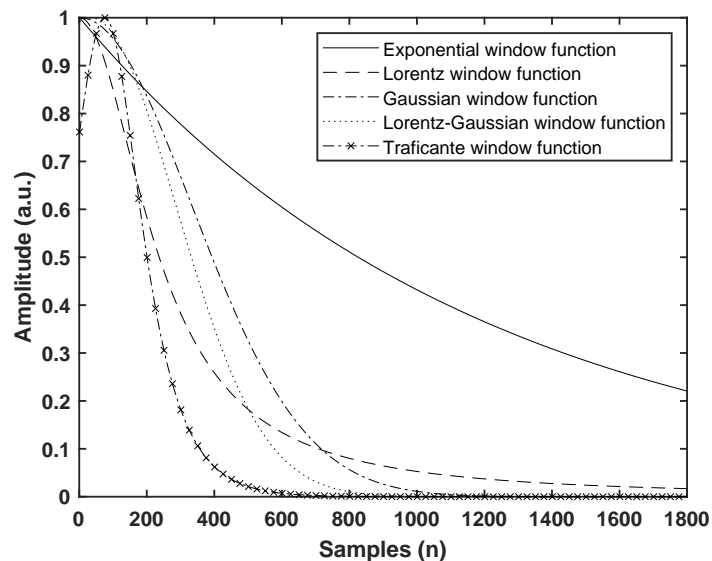


Figure 4.29: The five window functions used for apodization in the NMR dimension (with fixed parameter), built into the TMDE software to illustrate the shape of the window functions. The following standard deviation parameters, σ , were used for the illustration purpose: Exponential: $\sigma = 0.03$ s, Lorentz: $\sigma = 0.02$ s, Gaussian: $\sigma = 0.01$ s, Lorentz-Gaussian: $\sigma = 0.008$ s and $T_2^* = 0.40$ s, and Trafficante: $T_2^* = 0.40$ s. The analytical form of the functions are shown in Table 4.8 (p. 113).

to Fourier transformation. This will result in an FID with more data points, while not adding any noise or signal. This process is referred to as zero-filling. In general, this produces smoother signals and can enhance the S/N by a factor of $\sqrt{2}$,^[225] and also assists in enhancing FFT speed by zero-filling to 2^n number of data points. Furthermore, it is also considered that zero-filling to double the amount of acquired data points in an FID is the optimal zero-filling factor, as it improves the resolution and reduces the noise, by introducing information contained within the real part to the imaginary part and vice versa. It should be noted that, typically, zero-filling to more than double the amount of acquired data points in the FID, is performed for aesthetic reasons, i.e. smoother peaks, but has no additional benefit. The extrapolation of a time series by a string of zeros, is inefficient in the sense that it is not the most authentic representation of the signal.^[70, p. 336] More advanced techniques like the maximum entropy method or linear prediction can be used to improve the appearance of a signal in a more authentic manner. These techniques are typically extensive in computational time (less for linear prediction), and more complex to apply.^[70, p. 336] Therefore, the simplicity accompanied by the benefits is why zero-filling is such a popular technique.

It has been found that for SEC-NMR hyphenation, a zero-filling factor between 2–8 is sufficient for improving S/N , smoothing and enhancing resolution. Apodization and zero-filling is performed together prior to Fourier transformation. To illustrate the effect of apodization and zero-filling (although zero-filling was kept constant to a zero-filling factor of 8) a PMMA calibration standard ($M_n = 31\,000$ g/mol, $D = 1.08$, $c = 2$ g/L) was analyzed via SEC-NMR in chloroform at a flow rate of 1 mL/min by applying a Gaussian window

function and varying the bandwidth (twiddle factor, σ – see Table 4.8) from 0.08–16 Hz, with the result illustrated in **Figure 4.30**.

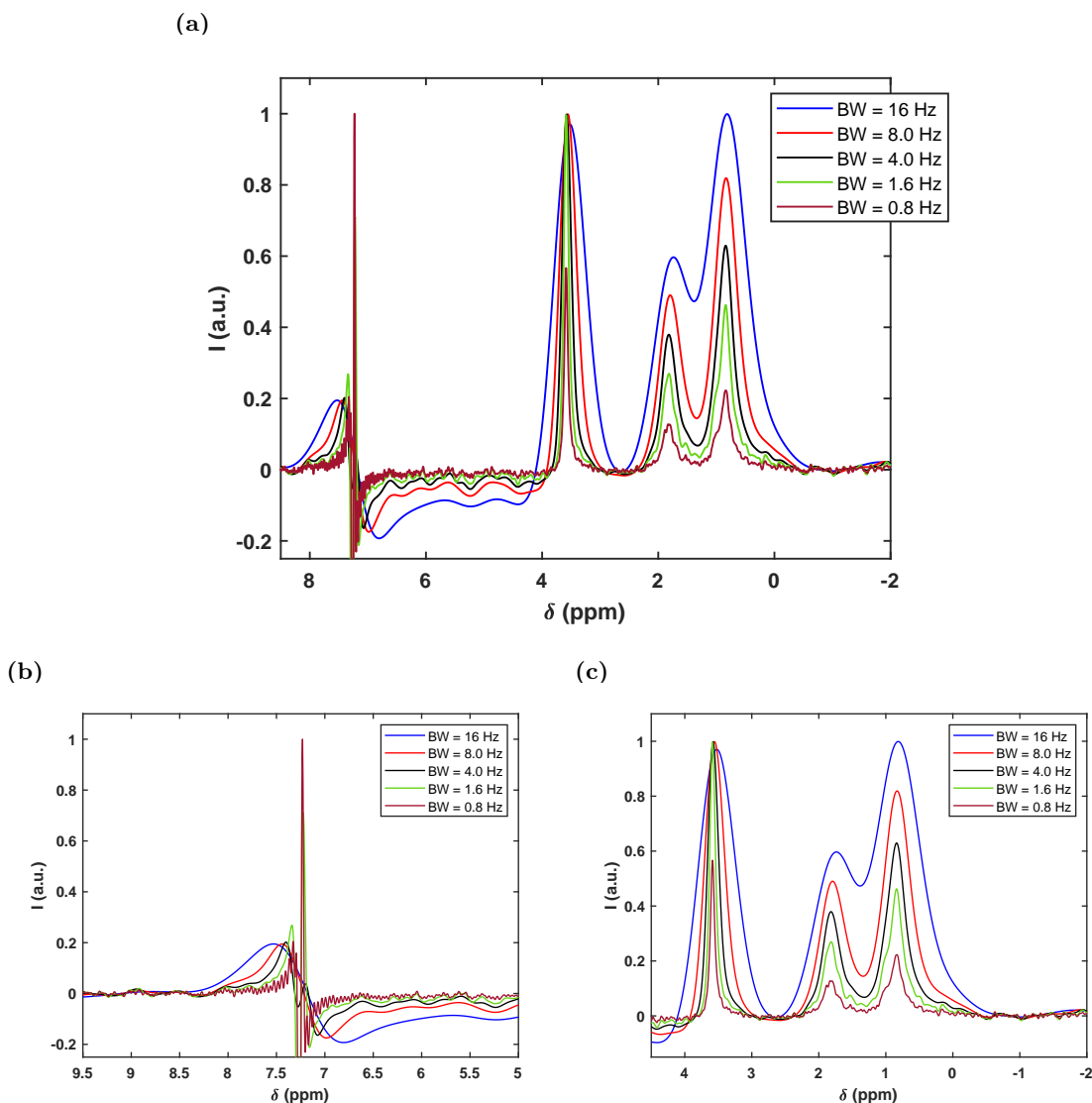


Figure 4.30: Effect of apodization using a Gaussian window function on a PMMA calibration standard ($M_n = 31\,000$ g/mol, $D = 1.08$, $c = 2$ g/L) signal depicting the full ^1H -NMR spectrum in Figure (a). The SEC-NMR measurement was performed at $\dot{v} = 1$ mL/min, with 1 mg injected mass in CHCl_3 . The apodization strength was varied by changing the standard deviation parameter, σ , from 0.8–16 Hz, with a constant zero-filling factor of 8. Figure (b) and (c) represent the zoomed-in regions of the solvent (CHCl_3) and the PMMA resonances of interest, respectively.

It is clear from Figure 4.30, that by changing the bandwidth, i.e. line broadening, of the Gaussian window function from 0.8–16 Hz, there is a clear change in the peak shape of the respective resonances, including a broadening of the peaks, as expected. There exists an optimum, after which the S/N would not be increased further, but that in fact, would result in a decrease in the S/N due to severe peak broadening. This effect is illustrated in **Figure 4.31**. The apodization and zero-filling in this example is performed in conjunction with smoothing/filtration in the SEC dimension and will become more apparent in **Section 4.5.5**. The results depict the corresponding S/N and FWHM values of the PMMA standard by only looking at the methoxy group ($-\text{OCH}_3$, $\delta = 3.6$ ppm), as

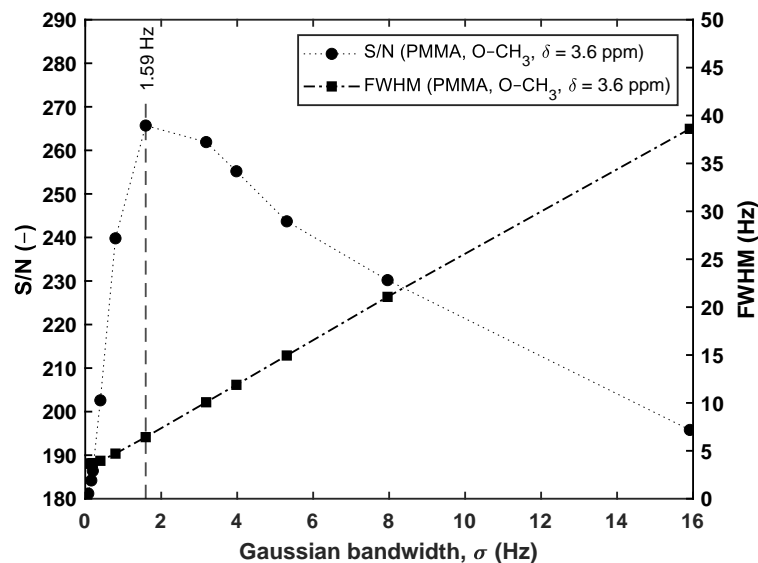


Figure 4.31: Optimum bandwidth on S/N and FWHM of a PMMA calibration standard only taking the methoxy group ($-\text{OCH}_3$, $\delta = 3.6$ ppm) into consideration, using a Gaussian window function and a constant zero-filling factor of 8. The function is listed in Table 4.8. The optimum bandwidth was established at 1.59 Hz (in the TMDE software the value is given in seconds, which corresponds to $\sigma = 0.1$ s, conversion from seconds to Hertz: $((1/\text{s})/(2\pi))$). In conjunction with apodization and zero-filling, the data was processed using an SEC filter (20 s Gaussian – see Section 4.5.5).

small effects would easily be seen on this peak due to its peak shape. There is a sharp increase in S/N , with the maximum being at a bandwidth of 1.59 Hz (listed as 1.6 in Figure 4.30 due to the rounding), after which the S/N then systematically decrease again as the bandwidth is increased. Subsequently, the FWHM also seem to increase linearly with an increase in the bandwidth of the Gaussian window function. It has been found that by using a Gaussian bandwidth with a standard deviation of $\sigma = 0.1$ s (i.e. 1.59 Hz in the spectral dimension) to force FIDs to zero, works for a variety of polymers when performing SEC-NMR measurements, with the Gaussian window functions being typically the best approach. Furthermore, a comparison of all the window functions (see Table 4.8) incorporated into the TMDE software was performed on the PMMA calibration standard ($M_n = 31\,000$ g/mol, $D = 1.08$, $c = 2$ g/L) to illustrate the effect of the various filters on the S/N ratio as a function of the FWHM, without filtration in the SEC dimension to more clearly illustrate the effect of apodization on the raw signal, depicted in **Figure 4.32**. As evident in Figure 4.32, there exists an optimum S/N ratio in the FWHM range of 8–12 Hz, corresponding to a bandwidth of $\sigma = 0.80$ – 3.98 Hz, when comparing the different window functions. The general recommendation when performing apodization and evaluating the results, is to ensure the highest S/N with the lowest amount of peak broadening. However, there is no universal optimum, thus it is subject to the discretion of the analyst and sample being analyzed. It does, however, provide a good estimation as starting point in data processing. For this reason, a Gaussian window function for apodization with a bandwidth of $\sigma = 0.1$ s and zero-filling factor of 8 has been set as default parameters in the TMDE software, as this provides a good starting point and is

typically applicable to a multitude of polymeric species.

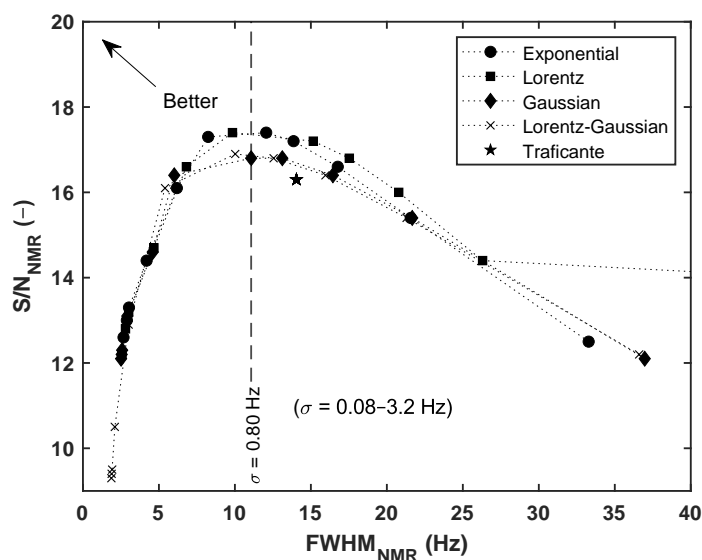


Figure 4.32: Evaluation of the five apodization functions based on S/N ratio and FWHM of the methoxy group ($-\text{OCH}_3$, $\delta = 3.6$ ppm) of a PMMA calibration standard ($M_n = 31\,000$ g/mol, $D = 1.08$, $c = 2$ g/L). By changing the filter bandwidth from $\sigma = 0.08$ –16 Hz, the S/N could be improved at the expense of peak broadening. See Table 4.8 and Figure 4.29 for an overview of the window functions and their respective shapes.

4.5.4 Phase correction

The NMR spectrum obtained after performing apodization and zero-filling, followed by Fourier transformation, does not typically consist of a pure absorption signal. As the data is collected from NMR spectrometers that typically use quadrature detection, both the sine and cosine components of the FID are recorded. These signals from the FID then gets digitized and used as complex numbers, i.e. real and imaginary parts, prior to being Fourier transformed. Ideally, the real and imaginary parts should coincide with the cosine and sine components of the acquired signal, producing the pure absorption signal (real part) and dispersion signal (imaginary part). The latter is impossible to obtain due to several reasons, but most likely due to the small time delay between the application of the RF pulse and acquisition of the FID. This typically yields spectra with phase distortions around the (suppressed) solvent resonance frequencies. Furthermore, the situation is worsened when performing continuous-flow measurements, as illustrated in Figure 4.17 (p. 92). Fortunately, the pure absorption signals are not lost and can be restored, using algorithms which perform phase correction, typically consisting of a constant phase correction in conjunction with a frequency dependent phase correction. Phase correction is performed by one of seven different techniques built into the TMDE software, and listed in **Table 4.9**

The simplest way of correcting the phase is by a 0th-order phase correction, the first technique listed in Table 4.9, as this is a global adjustment made to the first point of the FID, which affects every signal identically. The 0th order phase correction can be regarded as changing the receiver phase, which is applied for every 360° of rotation. The

Table 4.9: Summary of the seven phase correction techniques implemented into the TMDE software.

Phase correction technique	0 th order	1 st order
Phase angle of the 1 st point in FID	✓	×
Min. integral of dispersion spectrum	✓	×
Min. integral of dispersion spectrum	✓	✓ (fixed correction value)
Min. after solvent spectrum subtrac.	✓	×
Max. entropy method	✓	✓
Adjusting ¹³ C peaks to same height	✓	×
Interactive phase correction tool	✓	✓

phase correction requires both the real and imaginary part of the signal, and the corrected data points can be calculated relatively simply, where the phase correction, ϕ , are given by^{[70, pp. 220, 221][226]}

$$\begin{aligned} R_{L, new} &= -I_M \sin \phi + R_L \cos \phi \\ I_{M, new} &= R_L \sin \phi + I_M \cos \phi, \end{aligned} \quad (4.5.1)$$

where ϕ is the phase correction angle, and R_L and I_M the real and imaginary parts of the signal, respectively. Another possibility for phase correction is by minimizing the integral of the dispersion spectrum by performing 0th order phase correction, listed as the second technique in Table 4.9. In most cases it is recommended to extend the correction to account for frequency dependent phase errors, which is conducted by means of a 1st order (or linear) phase correction given by

$$R_{L, new} = -I_M \sin\left(\phi_0 + \phi_1 \frac{i}{n_{pts}}\right) + R_L \cos\left(\phi_0 + \phi_1 \frac{i}{n_{pts}}\right), \quad (4.5.2)$$

where ϕ_0 and ϕ_1 are the 0th and 1st order phase correction angles, respectively. The index (or change) of the data point is given by, i , and the total number of data points by n_{pts} . In general, the 0th and 1st order phase corrections are sufficient to correct most NMR spectra, which is why the phase correction listed third in Table 4.9 has been set as default setting in the TMDE software, with an adjustable fixed angle (0.384 radians \times 1000/point for CHCl_3 and 0.471 radians \times 1000/point) for phase correction when performing SEC-NMR measurements. However, this is not always sufficient for the correction of more complex phase errors, such as off-resonance effects due to the RF pulses or the used filters resulting in a non-linear phase response. Techniques such as the maximum entropy technique^[227] are powerful, but typically require more extensive computational time compared to the other techniques. Furthermore, the option exists to perform 0th order phase correction in chloroform by just adjusting the heights of the ¹³C-satellites, which assists the correction of phase distortions. Finally, an interactive PZ-Phasetool, designed and developed by

Prof. P. Blümler^[228] has also been incorporated into the TMDE software, as it has a multitude of adaptations that can be made, in an interactive way, to perform the best possible phase correction. This is particularly useful for solvents that have multiple resonant frequencies such as THF.

4.5.5 Smoothing: SEC Dimension

As already seen in Section 4.5.3 (p. 112), filtering is advantageous, as it improves the S/N but frequently (not always) increases the peak width. Therefore, a similar approach was applied to the data acquired in the SEC dimension. The objective was to obtain the maximum S/N , while increasing the peak width within a certain threshold. In the case of SEC, an arbitrarily chosen threshold of 10% increase in FWHM of the peak due to filtering was deemed acceptable, as this is within the measurement error of the technique to allow for a comparison of the effect of different SEC filters. Only three filters were chosen for filtration in the SEC dimension, as opposed to the five filters used in the NMR dimension, consisting of a (1) boxcar averaging, (2) Gaussian, and (3) Tukey window function, represented in **Figure 4.33**.

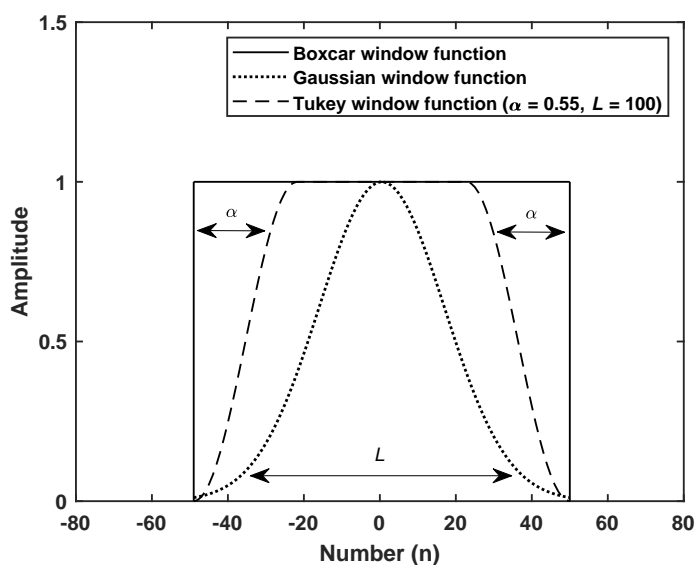


Figure 4.33: The three window functions; (1) boxcar, (2) Gaussian, and (3) Tukey, which can be used for smoothing in the SEC dimension. Adapted from Botha et al.^[15] with permission from the Royal Society of Chemistry.^[229,230]

For the boxcar average, the smoothing of irregularities, i.e. noise, and S/N enhancement in waveform is performed at a certain width (or weighting), W . The data points are filtered at n data points ($n - \frac{W}{2}$; $n + \frac{W}{2}$) around the current data points, and are averaged with the same weighting to obtain the average, smoothed, data point. The box of averaging is then moved to the following data point and the process is repeated. Increasing the width of the function, leads to stronger smoothing and, as with apodization, will yield a higher S/N value at the expense of resolution, since at first approximation the $S/N \propto \sqrt{W}$. Apart from the boxcar, the data is either folded with a Gaussian window function (see Table 4.8)

or with a tapered cosine (Tukey) window function (with modifications by Dr. J. Höpfner), defined by^[15,229,230]

$$f(x) = \begin{cases} 0, & 0 \leq x < u; \\ \frac{1}{2} \{1 + \cos [2\frac{\pi}{r} (x - \frac{r}{2})]\}, & u \leq x < u + \alpha \\ 1, & u + \alpha \leq x < n - u - \alpha \\ \frac{1}{2} \{1 + \cos [2\frac{\pi}{r} (x - 1 + \frac{r}{2})]\}, & n - u - \alpha \leq x < u - \alpha \\ 0, & n - u \leq x \leq n, \end{cases} \quad (4.5.3)$$

with r being a real number between 0 and 1 and $u = \frac{n-L}{2}$. The Tukey function is a numerically more complex approach, however, it is based on the simple idea of replacing the borders of a rectangular window function in a smoother way by half-sides of a cosine function. It has two free variable parameters, L and α , where L controls the width at the base of the function, and α the degree of tapering, i.e. the cosine contribution to the borders, and n is the total number of points in the smoothed data set. The strength of the function increases with an increase in the L and α , however, the α parameter also introduces artefacts in the form of wiggles into the results and has to be optimized for each application.

In order to demonstrate the effect of the addressed window functions, it was applied to SEC-NMR data of a PMMA calibration standard ($M_n = 30\,000$ g/mol, $D = 1.06$, $c = 4$ g/L) using chloroform as mobile phase. The peak under investigation is the methoxy group ($-\text{OCH}_3$, $\delta = 3.6$ ppm), and was chosen due to peak shape and position in the spectrum, i.e. among the narrowest polymer peaks found, and the influence of smoothing is easier detected, similar to the window functions used for apodization in Section 4.5.3. Furthermore, the peak is also well resolved and separated, thus enabling S/N and FWHM determination more simply and reliably. The corresponding results are illustrated in **Figure 4.34**.

The unique characteristics of a smoothing algorithm is obtained by varying the available free parameter(s) for each of the window functions (L and α in the case of the Tukey window function) and recording the respective S/N and FWHM values. As seen from Figure 4.34, the increase in S/N ratio is accompanied with the undesired increase in the FWHM, as expected for smoothing functions. The three fixed values used for the α parameter used for the Tukey window function is shown in the graph. Applying the boxcar filter results in an almost linear response of the FWHM as a function of S/N , while a more non-linear, i.e. curved, response is obtained for the Gaussian and Tukey filters. Furthermore, a lower α value leads to stronger curvature. Related to the pre-defined criteria of a 10% increase in width for the SEC dimension, depicted as the wide (top) dashed line in Figure 4.34, the boxcar average, although one of the most well-known filters, show the least amount of improvement in S/N . The Gaussian filter is a naturally stronger filter which is confirmed by the data set. The best results found for the Tukey filter, depended on the chosen α -value, where an $\alpha = 0.55$ has been found to be the best performing for the current application

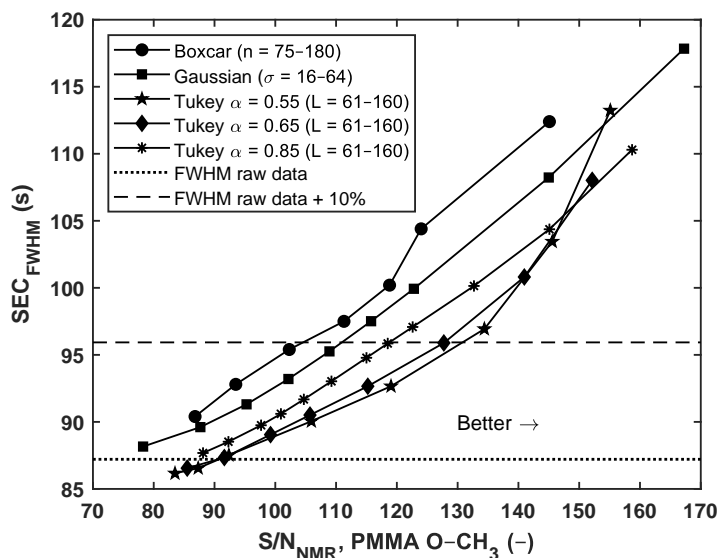


Figure 4.34: Effect of the different SEC window functions used for smoothing on the S/N and FWHM, determined on the methoxy group ($-\text{OCH}_3$, $\delta = 3.6$ ppm) of a PMMA calibration standard ($M_n = 30\,000$ g/mol, $D = 1.06$, $c = 4$ g/L). The dotted and dashed lines represent the raw FWHM data and raw FWHM data plus a 10% increase, respectively. The 1-Pulse-spoil pulse sequence (see Figure 4.23, p.100) had a total of 2600 recorded FIDs, 4 scans per spectrum, a receiver gain setting of 28 dB, flow rate of 1 mL/min, and injected mass of 2 mg. Adapted from Botha et al.^[15] with permission from the Royal Society of Chemistry.

with an SEC measurement time of 85 min and typical FWHMs = 5 mL. A lower α -value yields a higher S/N at the given FWHM. However, care should be taken with using a lower α -value as wiggles, i.e. sinc artefacts, become more pronounced in the NMR spectrum. It was found that the wiggles became pronounced at $\alpha < 0.55$. Subsequently, lower α -values were not further explored within this context. The results depicted in Figure 4.34 show an improvement in S/N of a factor of 1.2 when using a Tukey window function with an $\alpha = 0.55$ over the boxcar filter, without loss in selectivity.

One crucial parameter that should be taken into account is the chosen threshold, as the results are dependent on that, and the best S/N was established based on the crossing of the characteristic function at the 10% increase mark. If higher FWHM_{SEC} is tolerated, e.g. above 30%, it is clear that the Gaussian filter shows the best performance. As discussed in Section 4.5.3, the Gaussian filter is typically employed for filtering in the NMR dimension. It is recommended that a Gaussian-Tukey ($\alpha = 0.55$) combination set is used for the 2D-filtration of SEC-NMR data. Figure 4.32 and Figure 4.34 should be viewed simultaneously to establish the optimum filtering combination for a given sample when performing SEC-NMR measurements.

4.5.6 Reference/Solvent Subtraction

The dual-step approach related to solvent subtraction, is one of the most important procedures in post data acquisition processing, following the smoothing in the SEC dimension. A dual-step approach was chosen due to the two available (time-related)

dimensions, i.e. the spectroscopic and chromatographic dimensions. As the first dimension is the spectroscopic dimension, the first step is to take a reference spectrum in a region containing no analyte peaks and then apply it globally to all the data, i.e. subtracting the reference spectrum from every single acquired spectrum. This is provided via two approaches: (1) the solvent peak height of the subtracted spectrum is adjusted to the corresponding height of the solvent peak in the spectrum where the reference is being subtracted from, i.e. intensity adapted subtraction; and (2) keeping the peak height of the subtracted reference fixed when applied to all the spectra, i.e. fixed intensity subtraction. The two options are provided to give user flexibility, which depend on the stability of the system. Where the stability fluctuates due to poor shimming, severe shim degradation or solvent anomalies occurring during the course of an SEC run (typically 90 min when using a semi-preparative column – see Table 4.3, and flow rate of 1 mL/min), the intensity adapted approach becomes more useful. The fixed intensity subtraction is better suited where measurement stability was not compromised and proved to be more effective in cases where the resonances of the solvent has been suppressed, to a large extent, by the use of the T_1 selective pulse sequences (see Section 4.4.5, p. 99).

For the optimized SEC-NMR system and the corresponding pulse sequences, the reference spectrum is generated by averaging spectra between the first 5–10 min of the experiment. Here only pure solvent is eluting and injection fluctuations as a result of an initial pressure spike followed by a drop, is normally equalized again after 5 min. Using the semi-preparative column at $\dot{v} = 1$ mL/min allows the user to select a region from 0–30 min as no analyte peaks are expected within the time frame, unless there are problems like analyte carry-over¹⁰ or very high molecular mass polymer eluting at the exclusion limit of the column. However, there might be some cases where it is more efficient to take a reference spectrum just before the analyte peaks elute from the column, or by extending the measurement time and taking the reference after the SEC system peak whereafter nothing but solvent should elute, as illustrated in **Figure 4.35**. Furthermore, to ensure solvent subtraction is as efficient as possible, it is also necessary that the solvent peak shape is well-defined (see **Figure 4.36**) to avoid unwanted artefacts.

This is improved by increasing the zero-filling factor up to 8, however, zero-filling is generally inefficient, since it has a 'poor' representation of the authentic signal, but has the benefit of simplicity. A technique such as the maximum entropy method (MEM), used for phase correction, is a beneficial approach as it can be used for simultaneous S/N and resolution enhancement.^[70, pp. 184–185] This would be beneficial as the peak width and shape will not be affected as much, compared to using an exponential window function (S/N enhancement) or sine-bell window function (resolution enhancement). The benefit of using the MEM is that the authenticity of the peaks is retained, and provides solutions in an unbiased form, compared to other window functions. The reader is referred to Homans^[70, pp. 184–185] and the literature therein for a more in-depth description of the MEM. Furthermore, if the

¹⁰Analyte carry-over in SEC typically occurs (1) when a measurement has ended abruptly and the analyte has not exited the column prior to starting a new measurement, or (2) when the analyte is not in ideal SEC mode, resulting in interaction with the stationary phase, causing it to elute after the system peak.

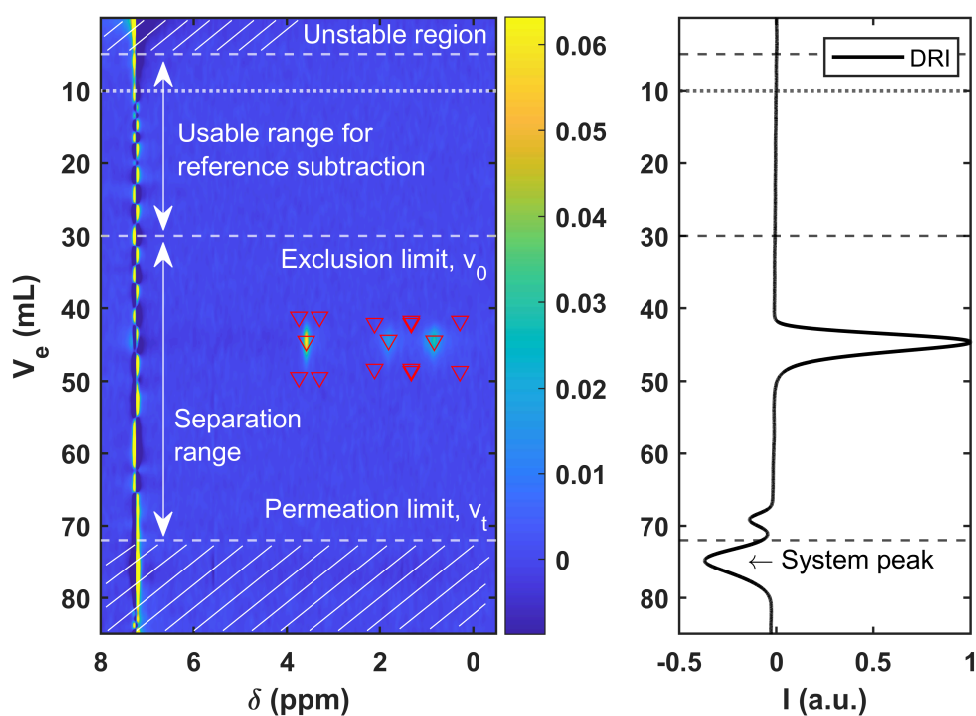


Figure 4.35: The region associated with reference subtraction. Regions of relevance include: (1) the unstable region between 0–5 min which is not used; (2) the default reference subtraction range between 5–10 min marked with a dotted line; (3) the available range for reference subtraction between 5–30 min marked with dashed lines; (4) the separation range between 30–72 min where the analyte peaks are expected to elute; and finally (5) the region which includes the system peak between 72–85 min. The sample used for illustration is a PMMA calibration standard ($M_n = 31\,000$ g/mol, $D = 1.08$, $c = 2$ g/L) in CHCl_3 at 1 mL/min. See Figure 2.2 (p. 10) for an explanation on the limits associated to chromatography. In addition, see Figure 4.38.

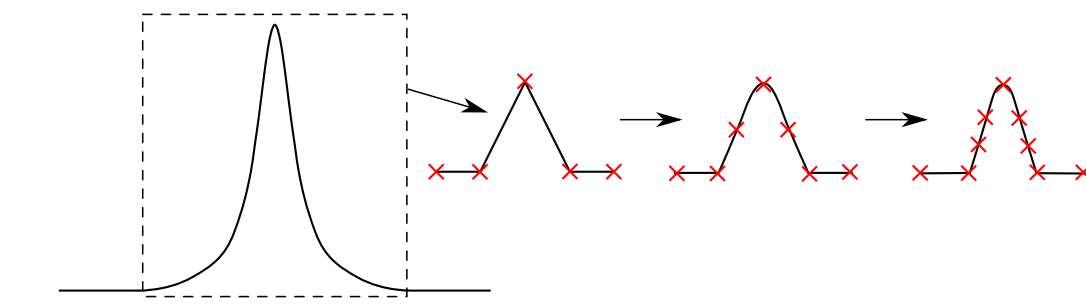


Figure 4.36: Improved definition of the NMR peak shape for solvent subtraction.

solvent subtraction is performed correctly, it can reduce the residual solvent intensity by a factor of > 100 whilst having little to no effect on the respective analyte resonances.^[14] To illustrate the effect, a PMMA calibration standard ($M_n = 31\,000$ g/mol, $D = 1.08$, $c = 2$ g/L) in CHCl_3 was investigated, with the corresponding results presented in **Figure 4.37**.

Furthermore, by better defining the peak via the maximum entropy method, an additional improvement in solvent subtraction can be achieved. The corresponding numerical results are listed in **Table 4.10**. It is clear that as soon as solvent subtraction is applied, looking at the entry referred to as zero-filling, $\text{ZF} = 8$, the solvent intensity has reduced by a

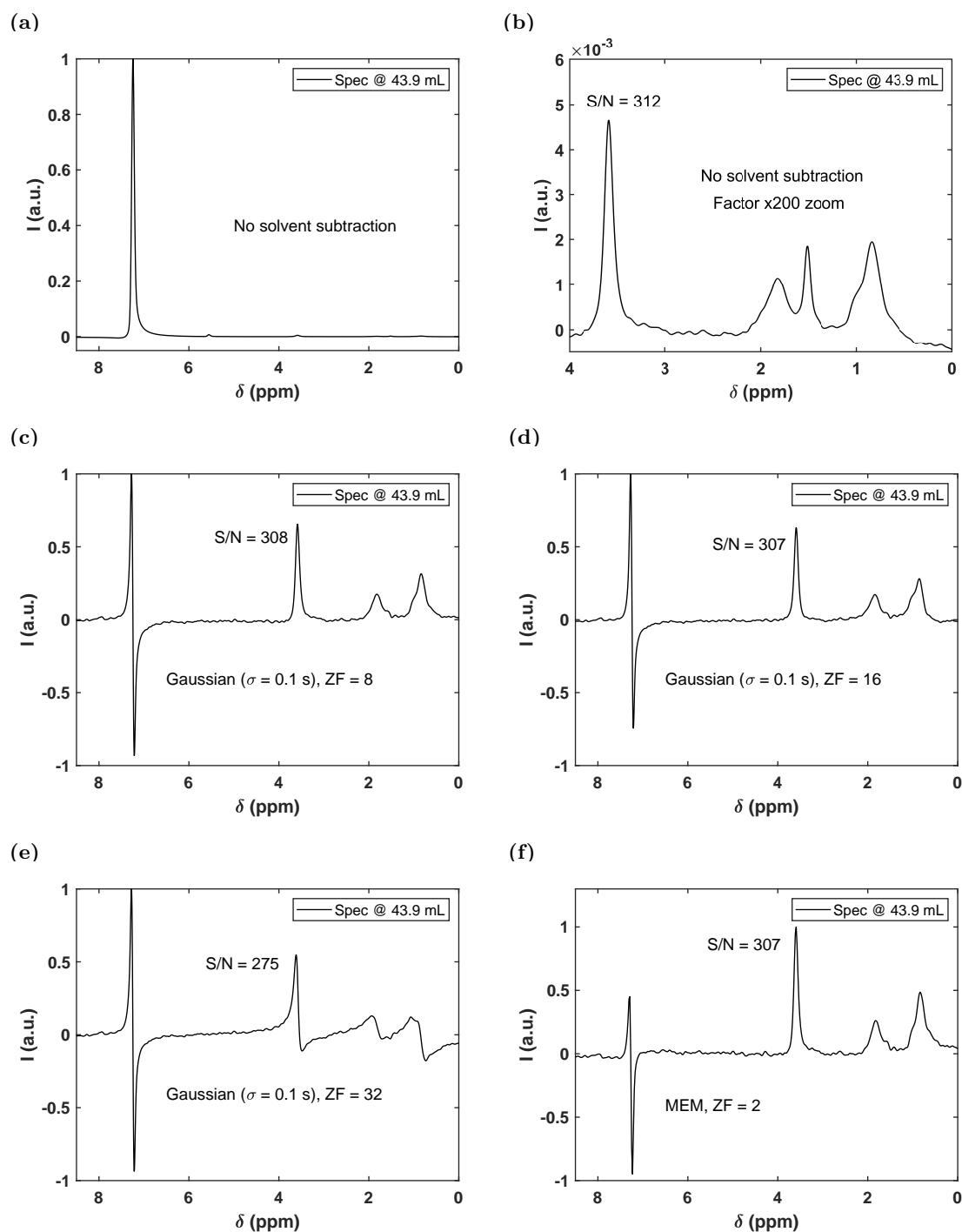


Figure 4.37: The effect of solvent subtraction on solvent peak reduction using a PMMA calibration standard ($M_n = 31\,000$ g/mol, $D = 1.08$, $c = 2$ g/L) at $\dot{v} = 1$ mL/min in CHCl_3 , using FC9 as flow cell (see Table 4.1, p. 70), and the 1-Pulse-spoil pulse sequence. Figure (a) and (b) represent the NMR spectrum without solvent subtraction and zoomed in spectrum, respectively. Figures (c)–(e) represent the NMR spectrum after solvent subtraction using a Gaussian window function for apodization with a band width of $\sigma = 0.1$ s (1.59 Hz) and zero-filling factor (ZF) from ZF = 8 to ZF = 32. Figure (f) represent the data after solvent subtraction but incorporating the maximum entropy method in conjunction with a ZF = 2. The shoulder peak present in figure (b) at $\delta = 1.5$ ppm is not present in figure (c)–(f) as it is a contaminant that was removed by solvent subtraction.

factor of 94 relative to no subtraction, with the analyte resonances remaining similar. When increasing the zero-filling factor, it is clear that the peaks are broadened too much

Table 4.10: The effect of solvent subtraction on solvent peak reduction on a PMMA calibration standard ($M_n = 31\,000$ g/mol, $D = 1.08$, $c = 2$ g/L) at $\dot{v} = 1$ mL/min in CHCl_3 , using FC9 as flow cell (see Table 4.1, p. 70), and the 1-Pulse-spoil pulse sequence.

Method	S/N (-)			
	7.24 ppm	3.59 ppm	1.83 ppm	0.85 ppm
No subtraction	67 460	312.3	125.2	130.7
ZF = 8	716.7	307.7	81.80	148.1
ZF = 16	767.1	307.2	83.80	137.0
ZF = 32	726.3	274.6	65.00	60.90
MEM ^a	389.0	307.2	79.50	148.3

^a Maximum entropy method.

and upon subtraction, although the reduction in solvent subtraction factor remain in the range of 90, the analyte peaks are more affected, as is clearly visible for a zero-filling factor of 32. Applying the MEM technique, the solvent is reduced by a factor of 173, which clearly shows the advantage to a well-defined peak prior to subtraction. Furthermore, the analyte peaks remain relatively unchanged, which is the desired effect. It would be nearly impossible (automatically via TMDE) to completely remove baseline distortions due to solvent subtraction, as the solvent amount and quality, with respect to its longitudinal relaxation (T_1 , as it is not degassed), is different at the point of analyte elution compared to 'bulk' solvent in the rest of the experiment, and since the reference subtraction is applied globally. This could, to some degree, be achieved better by performing individual data processing, but would defeat the purpose of having designated automated software.

4.5.7 Baseline Correction: SEC Dimension

Baseline correction is typically viewed together with solvent (or baseline) subtraction. In a 'good' spectrum, where there is no information other than stochastic noise, the data points should be as close as possible to zero. These data points are what is generally referred to as the *baseline*. Experimental errors (e.g. noise and drifts) and limitations are the main cause of baseline distortions, which can inevitably lead to complicating data interpretation and is especially important in obtaining the accurate quantification of the signal, i.e. correct S/N values. Baseline correction is a technique typically employed to remedy these distortions, and is mostly performed by fitting the bias in the baseline prior to subtractions from a given spectrum. The idea to perform baseline correction in this way originates from the work conducted by Beskers et al.^[7,177] on SEC-FTIR hyphenation, and by applying the baseline correction in the SEC dimension with promising results. This idea was incorporated into the TMDE software. The idea of baseline correction (considering it as drift correction) involves the following: (1) the baseline error is assumed to follow a certain trend due to instabilities such as solvent quality, (2) pump pulsation, and (3) pressure fluxes due to analyte viscosity, to name a few, consequently, the baseline is fitted with a polynomial. The severity and quality of the baseline will dictate the polynomial order to be employed, to every data point in the spectral dimension along the time axis.

The fitted baseline then gets subtracted from the corresponding data set to account for 'long-term' drifts. The simplest correction is a linear (first order polynomial) correction, in which is assumed the baseline follows the linear equation; $y = mx_i + c$, where x_i is the index of the data points and m and c are coefficients. Within the TMDE software, only three options have been provided for baseline correction; 1st, 2nd, and 3rd order polynomial fits. No higher order polynomials have been included as the results would be of little to no use with baseline distortions requiring higher fit orders and would be more favourable to repeat the measurement. Furthermore, a peak padding option have also been introduced, which allows for a certain range before and after an analyte peak to be excluded from the polynomial fit, ensuring no distortions to the analyte peak due to baseline corrections. In general, padding around the analyte- and system-peaks is performed, and the first 10 min of the measurement is also excluded from the baseline correction due the aforementioned instabilities associated to this time period of an SEC-NMR measurement.^[14] **Figure 4.38** illustrates the principles of drift correction and peak padding.

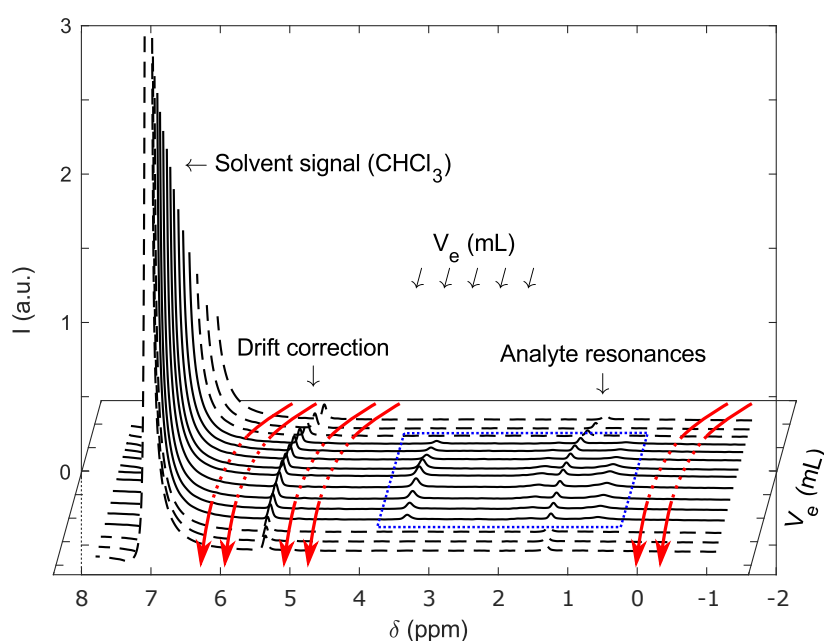


Figure 4.38: Drift correction along the SEC dimension for the NMR spectrum. The drift correction is a polynomial fit and indicated as red lines on the figure (the dotted parts indicates padding around the peak). It is fitted before and after analyte elution (solid black lines), to the remainder of the peak free data (dashed black lines) at each resonance frequency, and subtracted from the data set. The blue dotted rectangle indicates the analyte resonances of interest. This enables efficient drift correction, solvent subtraction and allows for the calculation of accurate statistics such as S/N values. This process is perhaps better understood when viewed in conjunction with Figure 4.35.

A summary of the obtainable S/N -values and FWHM of a PMMA calibration standard ($M_n = 28\,700$ g/mol, $D = 1.08$, $c = 2$ g/L) when applying the different order baseline corrections are provided in **Table 4.11**. By changing the drift correction to higher order polynomials, the S/N -values for the analyte resonances of the PMMA sample remain relatively constant, as expected. However, it is clear that S/N for the solvent (CHCl_3 , $\delta = 7.26$ ppm) is reduced by a factor of 1.15, i.e. $S/N_{\text{no correction}} = 705$ to $S/N_{2^{\text{nd order}}} = 612$, when using a second order polynomial fit for drift correction, after

which the S/N increases when using the third order fit.

Table 4.11: Application of different order baseline corrections to an SEC-NMR measurement of a PMMA calibration standard ($M_n = 28\,700$ g/mol, $D = 1.08$, $c = 2$ g/L).

Analyte peak	S/N (-)			
	No correction	1 st order	2 nd order	3 rd order ^a
CHCl ₃	705	841	612	1050
O-CH ₃ (PMMA)	266	264	263	263
-CH ₂ - (PMMA)	70.4	71.1	72.2	72.7
α-CH ₃ (PMMA)	121	123	121	121

^a The values for the analyte resonances did not show an improvement.

A PMMA calibration standard ($M_n = 28\,700$ g/mol, $D = 1.08$, $c = 2$ g/L) was analyzed in CHCl₃ to illustrate the combined achieved optimization of applying the TMDE software to an SEC-NMR measurement, presented in **Figure 4.39**. The raw data after FFT without any data treatment, is depicted in Figure 4.39 (a) compared to the data after applying the full data treatment of the TMDE software, presented in Figure 4.39 (b).

As seen in Figure 4.39 (a), without any data treatment being applied to the acquired data set, the NMR spectra is severely dominated by the large residual solvent resonance at $\delta = 7.24$ ppm, with the ¹³C-satellites ($\delta = 8.7$ and 5.8 ppm) and residual water contamination ($\delta = 1.5$ ppm) being clearly visible. However, with appropriate magnification, the polymer signals can still be observed. The S/N for the methoxy group (-OCH₃, $\delta = 3.6$ ppm) is $S/N = 15$ and $S/N = 3000$ for the chloroform resonant peak. After applying the full data treatment, with the procedures involved being explained during the course of this section, the S/N for the -OCH₃ has been increased to $S/N = 263$ and $S/N = 444$ for the CHCl₃ peak. An additional benefit of the data treatment, is that the residual undesired contamination can be removed from the final result, which facilitate the interpretation of the corresponding data. Furthermore, the 2D data treatment results in a factor of 16 optimization in S/N .

4.6 Application Examples of SEC-NMR Hyphenation

The following section is dedicated to the exemplification of using SEC-NMR as an advanced characterization technique for the investigation of polymers. It will provide an overview on the potential of the developed technique with a focus on the characterization of a physical blend of two homopolymers, block copolymer analysis, the sensitivity limits of the technique and its application to industrial related samples.

4.6.1 Introduction

Developing a hyphenated technique such as SEC-NMR, with the NMR acting as a chemically sensitive detector that is universal and applicable on-line, enables the identifica-

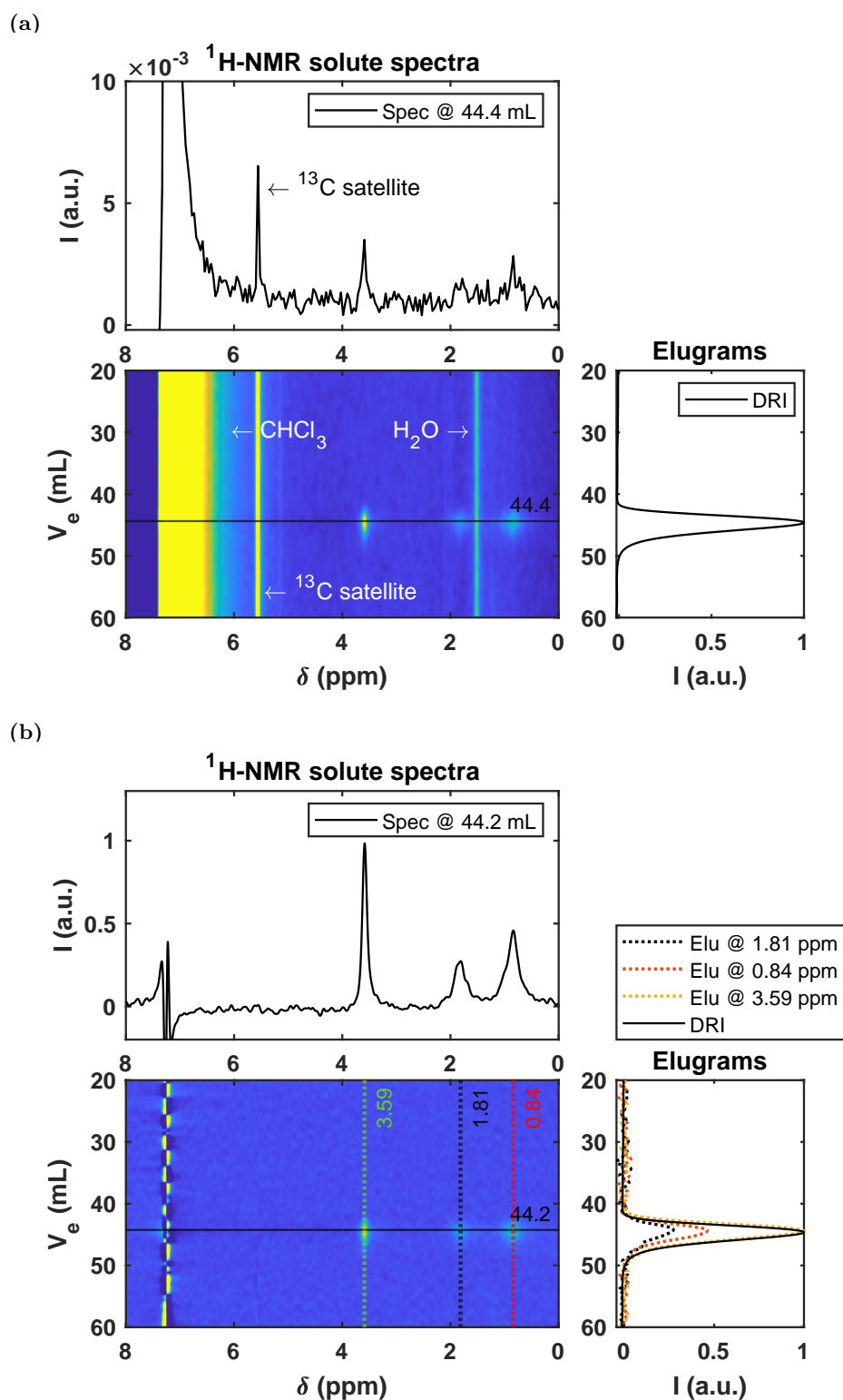


Figure 4.39: SEC-NMR data set of a PMMA calibration standard ($M_n = 28\,700$ g/mol, $D = 1.08$, $c = 2$ g/L in CHCl_3 at 1 mL/min using FC9). Figure (a) represents unprocessed data consisting only of the raw FFT data with the corresponding NMR (with a factor of 100 zoom) and differential refractive index (DRI) traces, and (b) represents the full data treatment of the optimized set-up. For solvent suppression the 1-Pulse-spoil pulse sequence was used, with 2600 recorded FIDs, and 4 scans per spectrum. See Figure 4.23 (p. 100) for more details. Adapted from Botha et al.^[15] with permission from the Royal Society of Chemistry.

tion/structure elucidation of compounds as a function of the different eluting species and/or molar mass (see Figure 3.1, p. 57). The idea is that any polymeric species can be used in combination with any solvent after chromatographic separation, that enables the determination of standard SEC parameters, M_w , M_n and D with the simultaneous detection of the chemical composition of the eluting species. The latter will be discussed in the forthcoming section. The technique can be used for the determination of the molar mass distribution (MMD) and chemical composition of homo- and co-polymers. The main advantage of hyphenating SEC with NMR for the analysis of co-polymers is the possibility for the simultaneous detection of each monomer unit with the NMR acting as a true quantitative concentration sensitive detector. This allows for the determination of the chemical composition of copolymers at any given elution volume without the need for detector calibration. Furthermore, the limits will also be explored for the given set-up, ultimately illustrating the possibilities of the hyphenated technique when using a medium resolution (62 MHz) NMR spectrometer. In addition, the application of SEC-NMR to more complex industrial-based samples will be presented.

4.6.2 Physical Blend Identification

The standard detectors employed for SEC include a differential refractive index detector (DRI) and/or a UV detector, which are mainly sensitive to the change of the physical properties of the eluates. These detectors provide some information on the chemical composition, but is limited to the presence of e.g., chromophores (delocalized π -electrons) in the case of a UV detector. In essence these detectors provide a concentration specific signal (if the same polymeric species elutes), while providing little to no information on chemical composition of the species, further limiting the identification of eluates. As polymeric species become more specialized, the level of complexity also increases, thus facilitating the need for analytical techniques that provide more information on the chemical composition of species. The most important aspect of the SEC-NMR technique, is that it has the ability to correlate chemical composition information as a function of the molar mass distribution in a ‘one-shot’ experiment. To illustrate the differentiation between a polymer blend, where the blend consists of two homopolymers with different hydrodynamic volumes, it was subjected to SEC-NMR characterization. The technique cannot differentiate between a blend and a copolymer in cases where the blend has two homopolymers of similar hydrodynamic volumes in solution, as the result would be the same as for a copolymer, which co-elutes. Therefore, in order to characterize a binary blend and copolymer more accurately, additional in-depth NMR experiments are required, e.g. end-group analysis. To illustrate how SEC-NMR can differentiate between overlapping peaks, a physical blend of 1:1 wt% PS/PMMA ($M_n = 50\,000/22\,500$ g/mol, $D = 1.03/1.03$) were investigated. **Figure 4.40** depicts the ^1H -NMR spectra of the respective PS and PMMA homopolymers. The SEC-NMR measurement was performed using a sample concentration of 2 g/L, with an injection loop of 500 μL , a semi-preparative column and a flow rate of 1 mL/min. The sample concentration was chosen to minimize the risk of column overloading. The corresponding results are displayed in **Figure 4.41** depicting the resulting 2D spectral

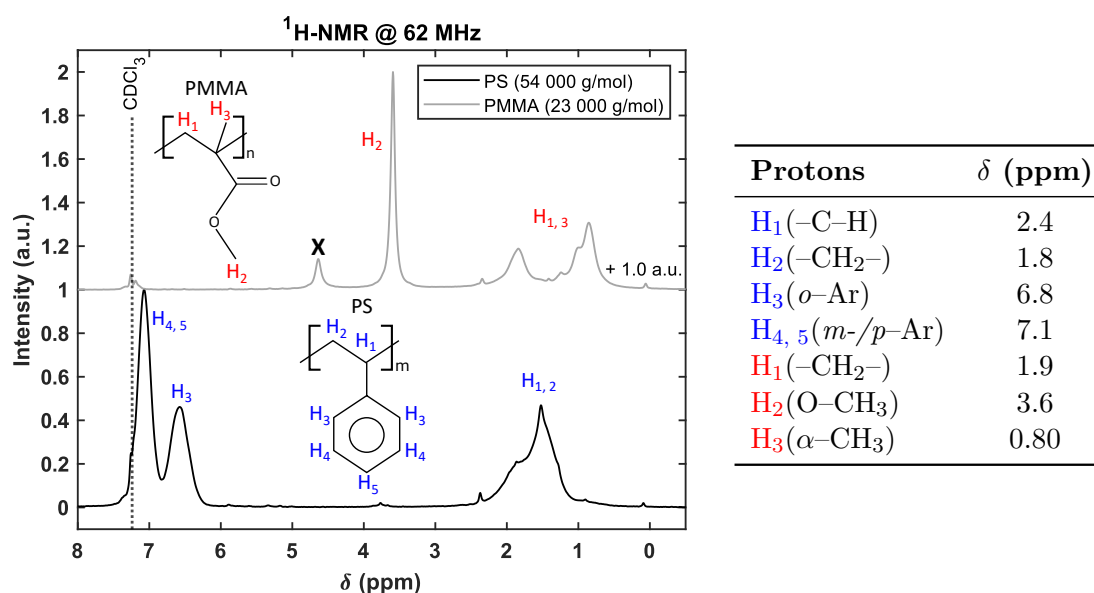


Figure 4.40: Static $^1\text{H-NMR}$ spectra of the PS ($M_n = 50\,000$ g/mol, $D = 1.03$) and PMMA ($M_n = 22\,500$ g/mol, $D = 1.03$) homopolymers at 62 MHz in CDCl_3 used as reference for the SEC-NMR measurements. Sample concentrations were approximately 30 g/L for each sample and was analyzed in standard 5 mm (outer diameter) NMR tubes. The NMR parameters were as follows: FID acquisition time: 6.5 s, total repetition time: 15 s, and number of scan per spectrum: 40. The 'X' is an H_2O contaminant from the CDCl_3 .

chromatogram of the PS/PMMA blend as a contour plot for the SEC-NMR measurement. As seen from Figure 4.41, there is an incomplete SEC baseline separation between the two species, i.e. a shoulder (53.1 mL) on the main DRI peak (49.3 mL) due to the PS and PMMA components having a similar hydrodynamic volume in solution. However, the identification of the blend was possible due to the polymeric species having at least one unique proton resonance group. The region between a chemical shift of $\delta = 6.3\text{--}7.2$ ppm displays the aromatic protons of PS and the resonance at $\delta = 3.6$ ppm corresponds to the methoxy group ($-\text{OCH}_3$) of the PMMA component. By extracting the 1D NMR slices at the two respective elution volumes, i.e. 49.3 and 53.1 mL, each spectrum was considered to be representative of the respective homo-polymer with no detectable traces (i.e. 'contamination') of the other compound. In addition, it is also clear from Figure 4.41, that all the respective polymer peaks are directly visible. The corresponding peak locations, S/N -values, and peak widths are provided in **Table 4.12**. As evident in Table 4.12, the narrow analyte peaks are considerably broader on-flow compared to the static measurements, for example the CHCl_3 increases by a factor of 9 on-flow ($\text{FWHM}_{\text{static}} = 0.5$ Hz to $\text{FWHM}_{\text{on-flow}} = 4.5$ Hz), which is due to a variety of effects such shorter FID acquisition times and in- and out-flow effects.^[231] The results presented in Table 4.12 are the extracted data from the TMDE software after data processing, with the S/N values ranging from $S/N = 23$ for the aliphatic protons ($\delta = 1.44$ ppm) to $S/N = 114$ for the methoxy group ($\delta = 3.59$ ppm), and the CHCl_3 peak still being a factor of 5 more intense than the methoxy group (highest analyte S/N).

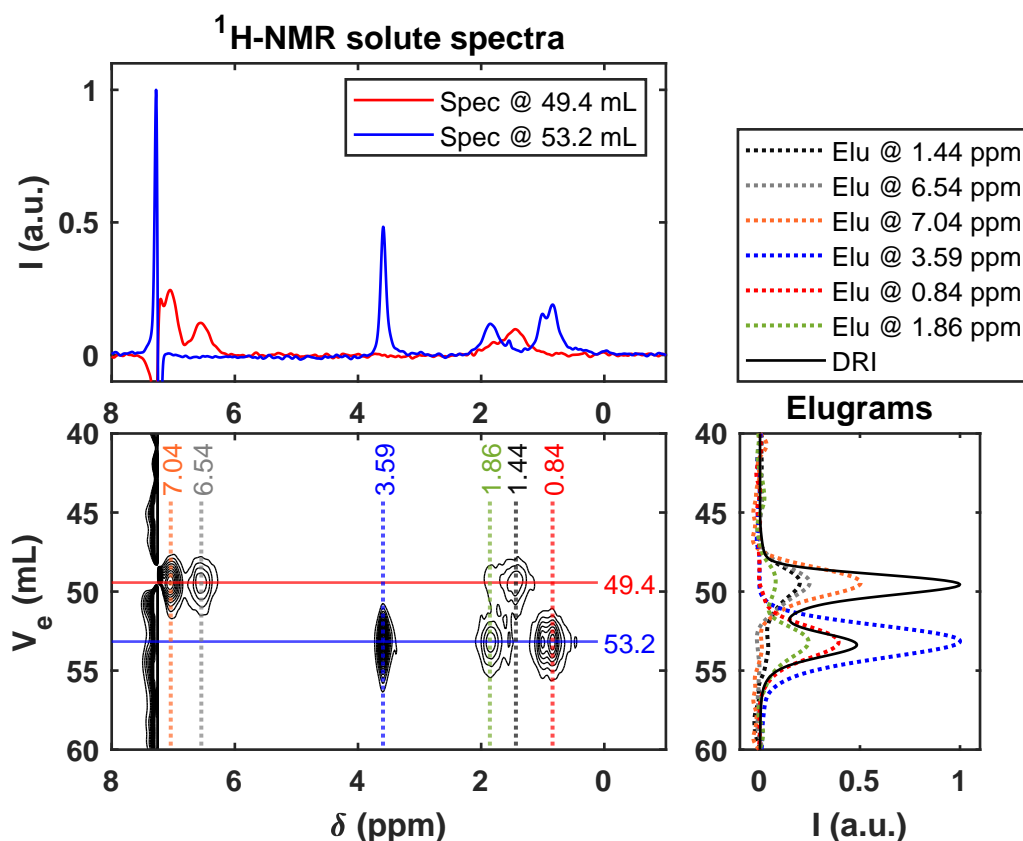


Figure 4.41: Characterization of a 1:1 wt% PS/PMMA ($M_n = 50\,000/22\,500$ g/mol, $D = 1.03/1.03$) physical blend using the SEC-NMR developed technique using chloroform as mobile phase at a flow rate of 1 mL/min with FC9 (see Table 4.1) and the 1-Pulse-spoil sequence. The top graph represents the 1D NMR data extracted from the 2D data set (contour map) at the peak maxima for each component. The contour map (bottom left), with 1–10 steps at 0.05 intensity increments, of the SEC-NMR data in the region of interest. Two distinct resonance groups are observable and identified at 49.4 and 53.2 mL for the PS and PMMA components, respectively. The bottom right figure are the corresponding projections of the elugram cuts for the various resonant frequencies detected in the NMR dimension, overlaid with the DRI trace. Adapted from Botha et al.^[15] with permission from the Royal Society of Chemistry.

Table 4.12: The analyte statistics reported by the TMDE software for a physical blend of 1:1 wt% PS/PMMA ($M_n = 50\,000/22\,500$ g/mol, $D = 1.03/1.03$) measured with SEC-NMR in CHCl_3 .

Analyte peak	V_e (mL)	δ (ppm)	S/N (processed)	FWHM on-flow (Hz)
CHCl_3	continuous	7.26	544	4.50
<i>m</i> -/ <i>p</i> -Ar C-H (PS)	49.3	7.05	59.1	CHCl_3 overlap
<i>o</i> -Ar C-H (PS)	49.3	6.54	28.6	14.6
O- CH_3 (PMMA)	53.1	3.59	114	6.47
- CH_2 - (PMMA)	53.1	1.86	27.1	18.1
C-H/ - CH_2 - (PS)	49.3	1.44	23.0	31.8
α - CH_3 (PMMA)	53.1	0.84	44.6	20.7

4.6.3 Block Copolymer Analysis

As described before, hyphenating NMR to SEC is desirable as it simplifies the $^1\text{H-NMR}$ spectrum by separating the different components in the chromatographic column prior to acquisition. This allows for the direct monitoring of composition changes during the separation process, i.e. on-line, as the eluate is sampled directly ('real time'). The unique advantage of hyphenating NMR to SEC is the ability to quantify these composition changes as a function of the molar mass in a fast and reliable way. The optimized 2D developed technique will be used to demonstrate the respective shift in the bulk polymer composition to be monitored directly by continuous-flow measurement, by applying it to a single, non-blended block copolymer of PS-*b*-PMMA (64:36 mol%, as determined by HF-NMR, presented in **Figure 4.42** and **Table 4.13**, $M_n = 230\,000$ g/mol, $D = 1.07$, $c = 28$ g/L), which elutes from the chromatographic system as a single peak. It should be noted that the measurement of the PS-*b*-PMMA block copolymer is semi-quantitative as the repetition time of the pulse sequence is only $2.2 \times T_1$ of the longest analyte T_1 . The block copolymer was dissolved in CHCl_3 , with a 1 mg injected mass, and measured at a flow rate of 1 mL/min. The corresponding results are depicted in **Figure 4.43**.

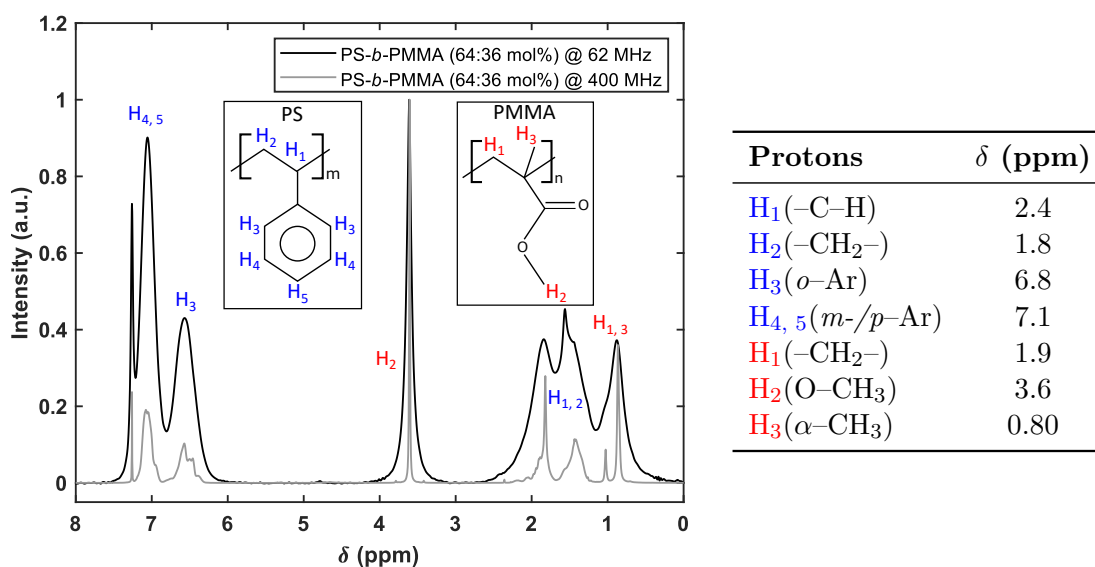


Figure 4.42: High field and Low field NMR spectra comparison of the PS-*b*-PMMA (64:36 mol%, $M_n = 230\,000$ g/mol, $D = 1.07$) block copolymer in CDCl_3 . The sample concentration was ca. 30 g/L, and 256 scans per spectrum was applied in conjunction with a line broadening of 1 Hz for both the high field and low field measurements. Furthermore, for the high field analysis a 30° pulse angle (10 μs pulse length) was used with an FID acquisition time of 4.1 s at 25°C . For the benchtop analysis a 90° pulse angle (7 μs pulse length) was applied with an FID acquisition time of 6.6 s and repetition time of 15 s, at $T = 26.5^\circ\text{C}$.

Figure 4.43 (a) illustrates the 2D contour plot with the corresponding extracted eluograms (right) at the respective resonance frequencies and $^1\text{H-NMR}$ spectrum (top) at the peak maxima of elution, $V_e = 43.4$ mL. In Figure 4.43 (b), the chemical compositional changes as a function of the elution volume is depicted. The extracted $^1\text{H-NMR}$ spectrum is a composite spectrum and comprise both the aromatic protons from the PS

Table 4.13: Ratios of the respective blocks for the PS-*b*-PMMA sample as determined from high- and low-field NMR spectroscopy. In addition, the longest T_1 was also determined for the block copolymer at 62 MHz.

Spectrometer	Normalized integral ratios (PS _{Ar} :PMMA _{Meth})	<i>mol%</i> PS	<i>mol%</i> PMMA	Longest T_1 (ms)
400 MHz	2.91 : 1.0	63.6	36.4	–
62 MHz	3.32 : 1.0	66.6	33.4	224 ^a

^a The longest T_1 in the molecule is the methoxy group ($-\text{OCH}_3$, $\delta = 3.57$ ppm) of the PMMA component. Determined by the standard inversion recovery pulse sequence built into the Spinsolve software.

component at $\delta = 6.51$ – 7.1 ppm and the methoxy resonance of the PMMA component at $\delta = 3.57$ ppm. The corresponding aliphatic region is depicted in the chemical shift range of $\delta = 0.80$ – 2.0 ppm. Subsequently, the elugrams were taken only at the *o*-aromatic ($\delta = 6.51$ ppm) and methoxy ($\delta = 3.57$ ppm) peaks for the PS and PMMA components, respectively, and overlaid with the DRI trace. The molar mass of the PS block of the copolymer can be determined by using the SEC-NMR on-flow data of the PS calibration curve. The S/N and FWHM values for the PS-*b*-PMMA sample is reported in **Table 4.14**.

Table 4.14: The analyte statistics reported by the TMDE software for the PS-*b*-PMMA (64:36 *mol%*, $M_n = 230\,000$ g/mol, $D = 1.07$) block copolymer in CHCl_3 at 1 mL/min with a total injected mass of 1 mg measured with SEC-NMR in CHCl_3 .

Analyte peak	V_e (mL)	δ (ppm)	S/N (processed)	FWHM on-flow (Hz)
CHCl_3	continuous	7.26	222	4.48
<i>m</i> -/ <i>p</i> -Ar C-H (PS)	43.4	7.05	28.8	CHCl_3 overlap
<i>o</i> -Ar C-H (PS)	43.4	6.54	15.4	8.72
$\text{O}-\text{CH}_3$ (PMMA)	43.4	3.59	25.8	7.49
$-\text{CH}_2-$ (PMMA)	43.4	1.86	11.7	PS overlap
C-H/ $-\text{CH}_2-$ (PS)	43.4	1.44	12.1	PMMA overlap
α - CH_3 (PMMA)	43.4	0.84	13.7	11.8

The major advantage of the SEC-NMR technique is that it can provide the individual concentrations of both monomer units. Therefore, it is possible to determine the chemical composition (CC) of the copolymer without using calibration standards. Based on the data presented in Figure 4.43 (b), the average CC can be determined at different elution volumes. The individual NMR elugrams are presented as a solid line for the PS and as a dashed line for the PMMA components. The simultaneous detection of the PS and PMMA allows for the determination of the average CC of the block copolymers dependent on the elution volume. The SEC-NMR elugrams and CCs were obtained by normalizing the two ortho aromatic protons ($\delta = 6.51$ ppm) and the three methoxy protons ($\delta = 3.57$ ppm) to one proton and then applying a correction factor to extrapolate the CC information, and indicate the change of the relative amounts of the two species during the elution. The approach used is similar to what has been described in literature by Hiller et al.^[195] It is, theoretically, possible to quantify the relative amounts of the polymer at any time during

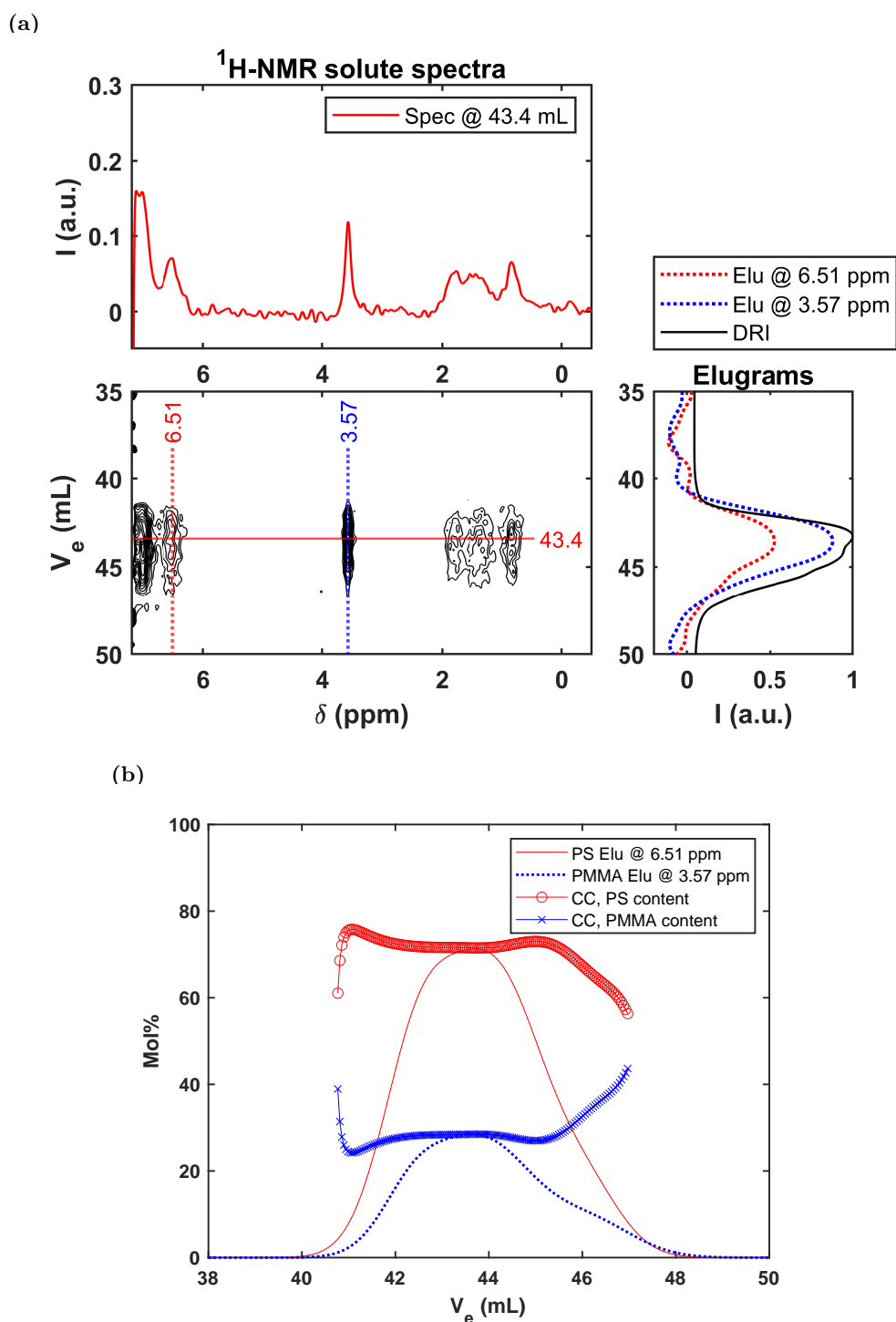


Figure 4.43: SEC-NMR analysis of a PS-*b*-PMMA (64:36 mol%, $M_n = 230\,000$ g/mol, $D = 1.07$) block copolymer in CHCl_3 at 1 mL/min with a total injected mass of 1 mg. In figure (a) the corresponding 1D extracted data, i.e. elugrams (right) and $^1\text{H-NMR}$ spectrum (top), from the 2D contour map (1–20 steps, 0.01 intensity increments) of the SEC-NMR data in the region of interest are presented. The top part of figure (a) represents the $^1\text{H-NMR}$ spectrum for the group of signals that can be identified at 43.3 mL. The right part of figure (a) represents the corresponding elugram cuts for the PS ortho-aromatic ($\delta = 6.51$ ppm) peak and the PMMA methoxy group ($-\text{OCH}_3$, $\delta = 3.57$ ppm), overlaid with the DRI trace. Figure (b) represents the chemical composition of the block copolymer as a function of elution volume, with the representative NMR elugrams of the *o*-aromatic protons ($\delta = 6.51$ ppm) of the PS component and the methoxy group ($-\text{OCH}_3$, $\delta = 3.57$ ppm). Adapted from Botha et al.^[15] with permission from the Royal Society of Chemistry.

the elution of the block copolymer by integrating the PMMA and PS resonances in the spectrum. This information was used to construct Figure 4.43 (b). As described before, the PS component, only looking at the *o*-aromatic peak since it is not affected by the solvent suppression as in the case of the *m*-/*p*-aromatic ($\delta = 7.1$ ppm) resonance, amounts to two protons, and the PMMA methoxy resonance to three protons. The percentages of the two monomers can be determined using the following equations:

$$mol_{o\text{-Ar}}(t_i)\% = \frac{\left(\frac{\int o\text{-Ar}(t_i)}{2}\right)}{\left(\frac{\int o\text{-Ar}(t_i)}{2}\right) + \left(\frac{\int \text{PMMA}(t_i)}{3}\right)} \times 100 \quad (4.6.1)$$

$$mol_{\text{PMMA}}(t_i)\% = 100 - mol_{o\text{-Ar}}(t_i),$$

and weight%

$$wt_{o\text{-Ar}}(t_i)\% = \frac{\left(\frac{\int o\text{-Ar}(t_i)}{2} \times MM_{(o\text{-Ar})}\right)}{\left(\frac{\int o\text{-Ar}(t_i)}{2} \times MM_{(o\text{-Ar})}\right) + \left(\frac{\int \text{PMMA}(t_i)}{3} \times MM_{(\text{MMA})}\right)} \times 100 \quad (4.6.2)$$

$$wt_{\text{PMMA}}(t_i)\% = 100 - wt_{o\text{-Ar}}(t_i)\%,$$

where $mol_{o\text{-Ar}}(t_i)\%$ and $mol_{\text{PMMA}}(t_i)\%$ are the relative mole percentages of the styrene and methyl methacrylate monomers at a specific time increment, t_i . The respective integral values for the PS and PMMA components are presented by $\int o\text{-Ar}$ and $\int \text{PMMA}$ at a given elution time (or volume), and $MM_{(o\text{-Ar})}$ and $MM_{(\text{MMA})}$ are the molar masses of the styrene and methyl methacrylate monomers, respectively. As presented in Figure 4.43 (b), the compositional changes in $mol\%$ of the two respective blocks differ slightly for the HF-NMR data of 64:34 $mol\%$ with a PS and PMMA $mol\%$ of 69% and 31%, respectively. The latter is within the margin of error of the experiment and can be ascribed to the lower magnetic field strength being employed, including the differences in T_1 of the respective copolymers, i.e. $T_{1, \text{PS (Arom.)}} = 213$ ms and $T_{1, \text{PMMA (Methoxy)}} = 224$ ms. Furthermore, the increase in the $mol\%$ of the PMMA component can be explained in terms of the following assumptions: (1) in living polymerization, the PS anions have a Poisson distribution;^{[232][233, pp. 284–294]} and (2) every PS anion has an equal probability to 'consume' the MMA monomers present in the reaction.^[234, pp. 1–20] Based on the aforementioned premise, the PS-*b*-PMMA block copolymer, has a macro chain length distribution for the PS component, and a micro chain length distribution for the PMMA components on every chain (length) of the PS. This results in a distribution on a distribution, with the main assumption that the smaller chains of PS is rich in PMMA content, i.e. longer chain lengths of PMMA, and the inverse case for larger chains of PS. The conceptual idea is represented in **Figure 4.44**.

The separation and identification were achieved by considering the individual resonances, which, as presented in Figure 4.43, appear over the different chemical shift ranges. Furthermore, the results were plotted against the DRI trace to illustrate the extracted elugrams

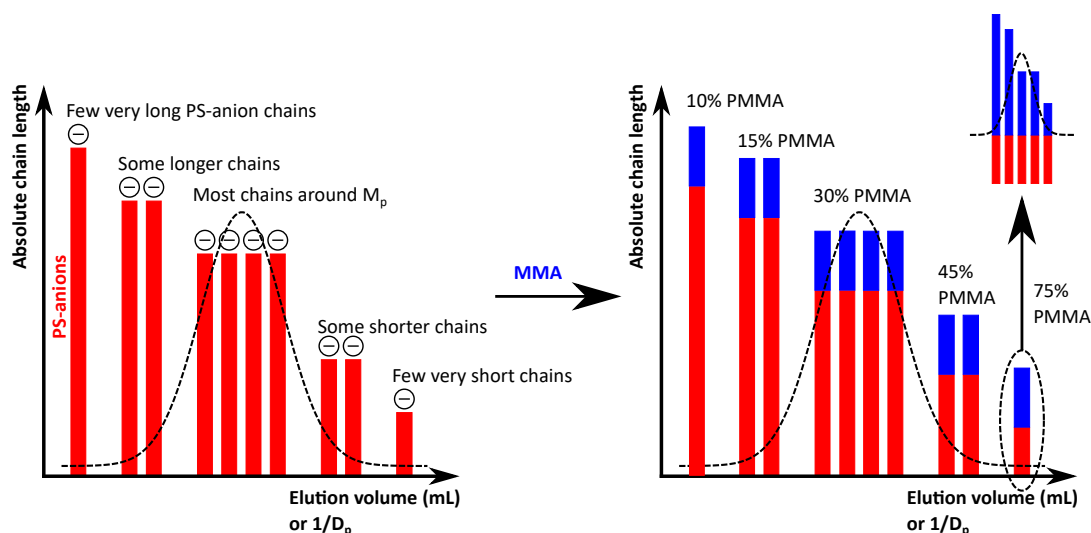


Figure 4.44: The multiple distributions obtainable within a block copolymer. The figure on the left illustrates the macro chain length distribution of the PS component of the first synthesized block and the figure on the right depicts that shorter chains of PS is rich in PMMA and, in addition, has a distribution on a distribution. The PS-block was synthesized first. Synthesis courtesy of Mr. L. Faust.

of each resonance peak. In Figure 4.43 (a) the $^1\text{H-NMR}$ spectrum of the compound was extracted at 43.4 mL, which exhibits all the resonance peaks for both PS and PMMA, indicating that the sample is either a copolymer or two homopolymers with similar hydrodynamic volumes in solution. This illustrates that the technique can successfully be applied for characterizing homo- and copolymers. In particular, the chemical composition of copolymers (or overlapping homopolymers in a blend) can be determined with the advantage of detecting each monomeric species simultaneously without prior calibration. In addition, information on the polymer microstructure can be obtained. To further illustrate the capability and limitation of the SEC-NMR technique a series of three polystyrene (PS)/polyethyl methacrylate (PEMA) block copolymers (PS-*b*-PEMA) with varying block ratios were analyzed. See **Table 4.15** and **Figure 4.45** for details.

Table 4.15: Ratios of the respective blocks for the PS-*b*-PEMA sample series as determined from high field (400 MHz) NMR spectroscopy. In addition, the weight average molar mass and the longest T_1 values are provided.

Sample	M_w (g/mol)	\bar{D}	Relative integral ratios (S/EMA) ^a	mol% PS	mol% PEMA	Longest T_1 (ms)
PEMA5	144 400	1.08	1.0/0.05	95.2	4.80	212 ^b
PEMA30	112 700	1.36	1.0/0.41	70.9	29.1	223 ^b
PEMA50	146 100	1.34	1.0/0.90	52.6	47.4	240 ^d

^a S: styrene and EMA: ethyl methacrylate monomers.

^{b-d} Associated to the *o*-Aromatic PS protons ($\delta = 6.54$ ppm).

To evaluate the chemical compositional changes of the PS-*b*-PEMA series as a function of molar mass under continuous-flow conditions, the longest T_1 value had to be determined in

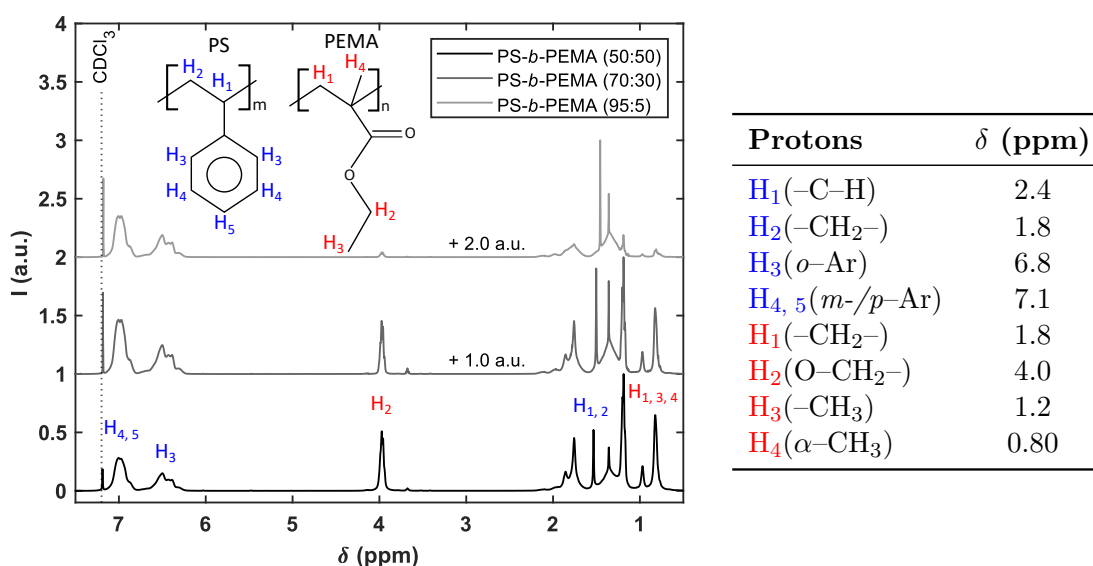


Figure 4.45: High field (400 MHz) ^1H -NMR spectra comparison of the PS-*b*-PEMA block copolymer series. See Table 4.15 for details related to the various block compositions and molar masses. The sample concentration was ca. 30 g/L, and 256 scans per spectrum were applied in conjunction with a line broadening of 1 Hz for both the high field and low field measurements. Furthermore, for the high field analysis a 30° pulse angle (10 μs pulse length) was incorporated with an FID acquisition time of 4.1 s and receiver gain of 113 dB at 25 $^\circ\text{C}$.

order to adjust the pulse sequence acquisition time to allow for $5\text{--}8 \times T_1$ to ensure (semi) quantitative measurements. The T_1 values were measured on-flow, by employing a 40 mg stock solution of the respective samples dissolved in 200 mL CHCl_3 , and continuously pumped through the SEC-NMR setup (without an SEC column). These values were determined using an inversion recovery pulse sequence with the same setting as described in the caption of Figure 4.24 (p. 101), with the respective T_1 values being listed in Table 4.15. Similar to what is depicted in Figure 4.24, the T_1 values decrease with increasing flow rates. As previously mentioned, it is important to use short recycle delays for optimal chromatographic resolution without losing much sensitivity. As the longest T_1 values (see Table 4.15) are in the range of ca. 200 ms, the use of the 1-Pulse-spoil pulse sequence had to be adapted slightly to allow for the repetition time to be in the semi quantitative regime of $> 3 \times T_1$. Furthermore, as illustrated in Figure 4.17 (p. 92) the use of a 90° pulse angle (pulse length of 12 μs) provides good NMR sensitivities at a recycle delay time (repetition time) of 500 ms. The effect of the recycle delay on the respective samples was also investigated. The results for the PS-*b*-PEMA (50:50 *mol%* – see Table 4.15) are presented in **Figure 4.46** to illustrate the effect under both static- and continuous-flow conditions.

As seen from Figure 4.46 (a), under static conditions (no flow), the highest NMR intensities are obtained around a repetition time of 1 s, after which the S/N results remain relatively unchanged. However, in Figure 4.46 (b), a different scenario is seen, as the optimal recycle delay under flow at 1 mL/min indicates to be 0.75 s, after which, for the various resonance frequencies, the NMR intensities seem to vary significantly, all indicating a

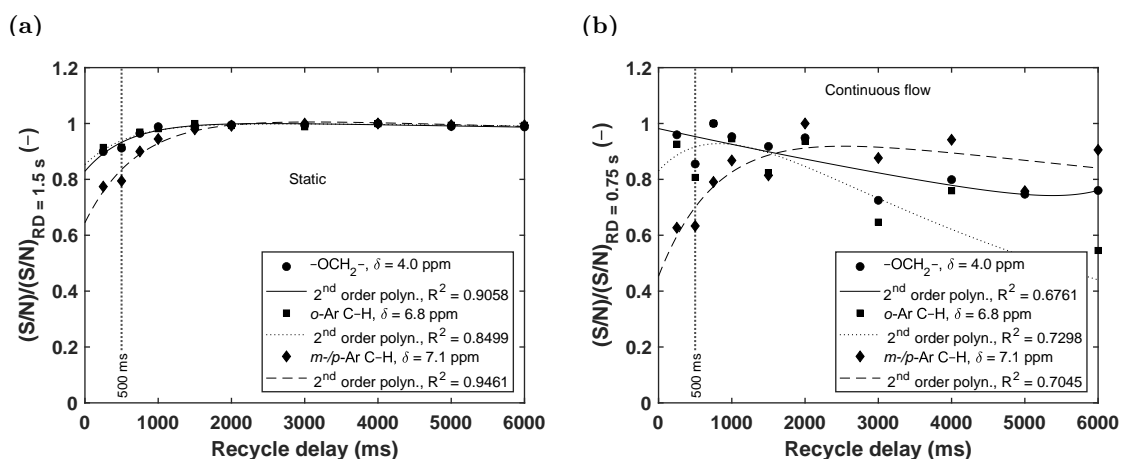


Figure 4.46: The effect of the recycle delay (acquisition length) on the S/N of a PS-*b*-PEMA (50:50 *mol%* – see Table 4.15) sample under (a) static and (b) continuous flow conditions of 1 mL/min using a sample concentration of 30 g/L (in CDCl_3) and 40 g/L (in CHCl_3) in figure (a) and (b), respectively. Flow cell FC9 (see Table 4.1, p. 70) was utilized. The data represents the resonances of the ethoxy group ($-\text{OCH}_2-$, $\delta = 4.0$ ppm) from the PEMA and aromatic protons (*o*-/*m*-/*p*-Ar C-H, $\delta = 6.80$ – 7.1 ppm) from the PS components. The 1-Pulse-spoil pulse sequence was utilized. A 2nd order polynomial was fitted to the different data sets to illustrate the effect of continuous-flow measurements compared to static conditions.

relative decrease. It was decided that a recycle delay time of 0.75 s would be used, and not much higher values as it is more beneficial for an on-flow run to use shorter recycle delays when performing SEC-NMR measurements, as more transients can be accumulated. The intensities of the PS aromatic protons (especially the *m*-/*p*-Ar C-H) decrease more severely with decreasing recycle delay times, where the PEMA only shows small effects as a result of the much shorter relaxation times. A variety of studies have been published concerning optimization of LC-NMR parameters.^[126,216,217,235–238] For example, the *m*-/*p*-Ar C-H protons ($\delta = 7.1$ ppm) are reduced in intensity from 80% at a recycle delay time of 0.75 s to 62% at 0.25 s, and the ethoxy ($-\text{OCH}_2-$, $\delta = 4.0$ ppm) from 100% at 0.75 s to 97% at 0.25 s, measured at a flow rate of 1 mL/min. Consequently, using incorrect pulse angles or recycle delay times will adversely affect the chemical compositional determination as a function of molar mass. However, using too short pulse lengths will result in low NMR sensitivity and long recycle delay times will cause poor chromatographic resolution. Therefore, the 90° pulse angle was used in conjunction with a recycle delay time of 0.75 s at a flow rate of 1 mL/min to ensure sufficient NMR sensitivity and chromatographic resolution. **Figure 4.47** depicts a comparison of the ^1H -NMR spectroscopy measurements of the PS-*b*-PEMA (50:50 *mol%*) sample at 400 and 62 MHz at static- and 62 MHz under continuous-flow-conditions.

An overlay of the three NMR spectra is illustrated in Figure 4.47, where the top two spectra (black and blue lines) represent the bulk NMR analysis at static conditions for the measurements conducted at 400 and 62 MHz (256 scans per spectrum, 34 g/L sample concentration, CDCl_3). The bottom spectrum (red line) depicts the on-flow measurement at the peak maximum of the PS-*b*-PEMA elution, where 4 scans per spectrum have been taken for the sample in CHCl_3 . Although the amount of scans are far less for the on-flow measurement with reduced S/N , upon comparison, it is clear that the basic information,

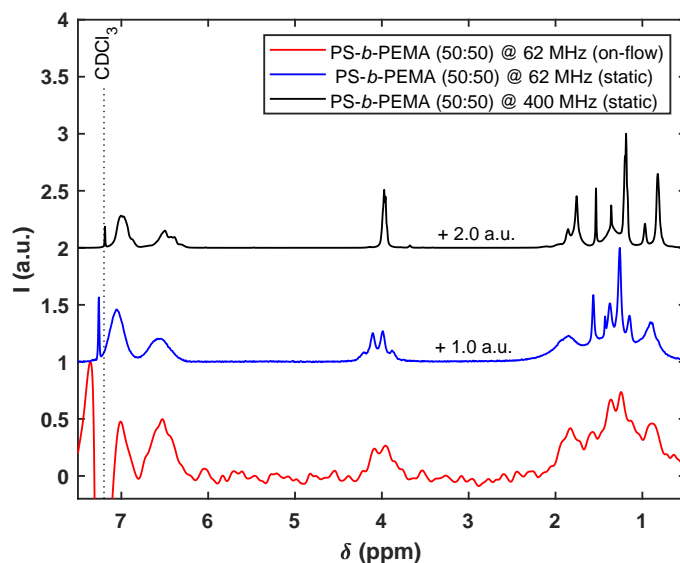


Figure 4.47: Comparison of the ^1H -NMR spectra (stacking by 1.0 a.u.) of the PS-*b*-PEMA (50:50 *mol%* – see Table 4.15) sample measured at 400 and 62 MHz under static conditions, including a continuous-flow measurement at 62 MHz. The high- and low-field static measurements were performed in CDCl_3 , with a sample concentration of 34 g/L measured in standard 5 mm NMR tubes. The NMR parameters are the same as described in the caption of Figure 4.42 (p. 132) with the number of scans per spectrum being 128 and 40 for the high- and low-field measurements, respectively. The on-flow measurement consists of 4 scans per spectrum (2 s) in CHCl_3 using the 1-Pulse-spoil pulse sequence, taken at the peak maximum, as determined by SEC.

related to major resonant frequencies, are retained. Considering the ethoxy group, the S/N -values of 56 (on-flow, $n_s = 4$), 152 ($\delta = 3.95$ ppm, low-field, static, $n_s = 40$) and 3452 ($\delta = 3.95$ ppm, static, high-field, $n_s = 128$) were obtained. This can be ascribed (mostly) to low sample concentration and lack of spectra summation over many scans, without loss in resolution from the chromatographic separation. Furthermore, the absolute resolution in terms of FWHM in Hz were similar for broader peaks; the ethoxy group had FWHM values of 19.4 Hz (on-flow), 18.6 Hz (static), and 16 Hz (high-field), however, in the case of very narrow peaks like for example a methoxy group (in PMMA) the peak is generally broadened by > 50 – 100% . The latter is mainly due to the much higher chemical shift resolution obtainable in high-field NMR spectroscopy. **Figures 4.48–4.50** represent the results of the SEC-NMR analysis of the PS-*b*-PEMA (95:5 *mol%*) sample and the chemical compositional changes as a function of molar mass distribution for the PS-*b*-PEMA (70:30 and 50:50 *mol%*) samples. All the measurements were performed using the 1-Pulse-spoil pulse sequence (see Section 4.4.5, p. 99) and flow cell, FC9 (see Table 4.1, p. 70). Furthermore, the peak statistics for the three PS-*b*-PEMA block copolymers are reported in **Table 4.16** for the solvent (CHCl_3 , $\delta = 7.26$ ppm), ortho-aromatic ($\delta = 6.54$ ppm) protons for the PS component, and the ethoxy ($\delta = 3.97$ ppm) protons from the PEMA component.

As seen from Figure 4.48, it was not possible to detect the ethoxy group ($\delta = 4$ ppm, position indicated by an arrow on the figure) with a high amount of certainty under flow-conditions. This gives an indication that the technique is limited (intrinsically) to

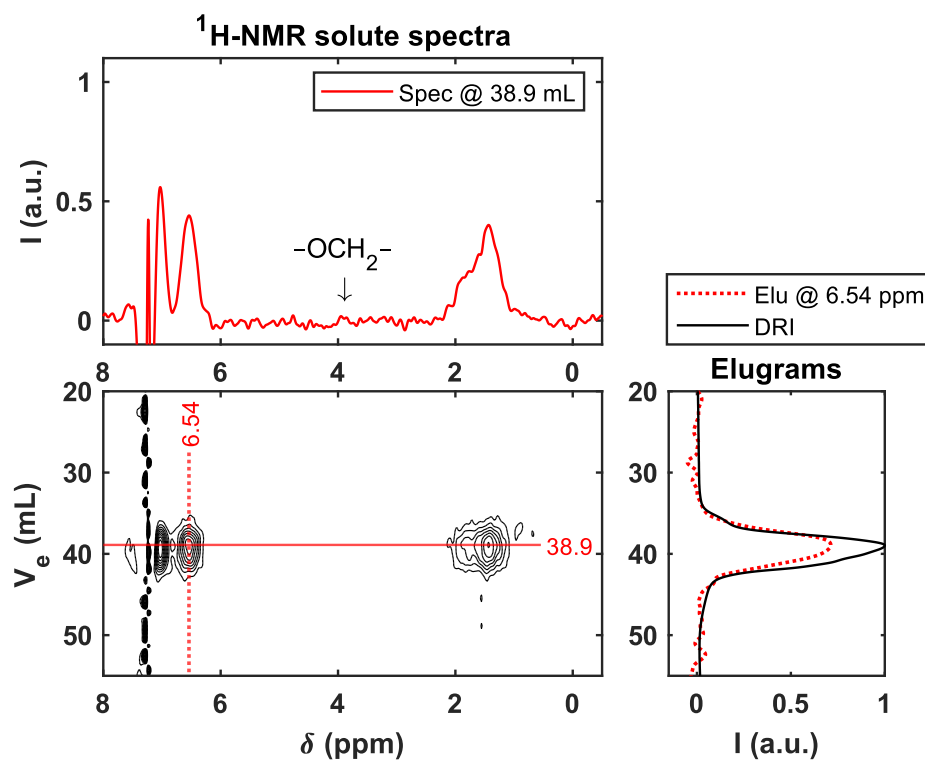


Figure 4.48: SEC-NMR analysis of the PS-*b*-PEMA (95:5 mol%, $M_w = 144\,400$ g/mol, $D = 1.08$) block copolymer in CHCl_3 at 1 mL/min with a total injected mass of 2 mg. The corresponding 1D extracted data, i.e. elugrams (right) and ^1H -NMR spectrum (top), from the 2D contour map (1–10 steps, 0.02 intensity increments) of the SEC-NMR data in the region of interest are presented. The top part of the figure represents the ^1H -NMR spectrum for the group of signals that can be identified at 38.9 mL, with an arrow inset indicating the position of the ethoxy group. The right part of the figure represents the corresponding elugram cut for the PS ortho-aromatic ($\delta = 6.54$ ppm) peak overlaid with the DRI trace, and no detectable PEMA ethoxy group ($-\text{OCH}_2-$, $\delta = 3.97$ ppm), as this is below the limit of detection.

Table 4.16: The analyte statistics reported by the TMDE software for the PS-*b*-PEMA (see Table 4.15) block copolymer in CHCl_3 at 1 mL/min with a total injected mass of 2 mg measured with SEC-NMR in CHCl_3 . The S/N values cannot be compared directly with the number of equivalent ^1H atoms as the values are based on the maximum peak height and not the integral.

Sample	Analyte peak	V_e (mL)	δ (ppm)	S/N (processed)	FWHM on-flow (Hz)
PEMA5	CHCl_3	continuous	7.26	114	4.51
	<i>o</i> -Ar C-H (PS)	38.9	6.54	95.4	20.1
	$-\text{OCH}_2-$ (PEMA)	38.9	3.97	–	–
PEMA30	CHCl_3	continuous	7.26	298	4.40
	<i>o</i> -Ar C-H (PS)	39.3	6.54	43.8	22.3
	$-\text{OCH}_2-$ (PEMA)	39.3	3.97	55.5	16.1
PEMA50	CHCl_3	continuous	7.26	305	4.40
	<i>o</i> -Ar C-H (PS)	38.4	6.54	76.4	15.1
	$-\text{OCH}_2-$ (PEMA)	38.4	3.97	42.0	17.0

block copolymers with block ratios that has to be > 5 mol% in order to allow for successful detection. Furthermore, no chemical composition information was determined for this sample, as it was intended to display the limit of the technique, with respect to the limit of

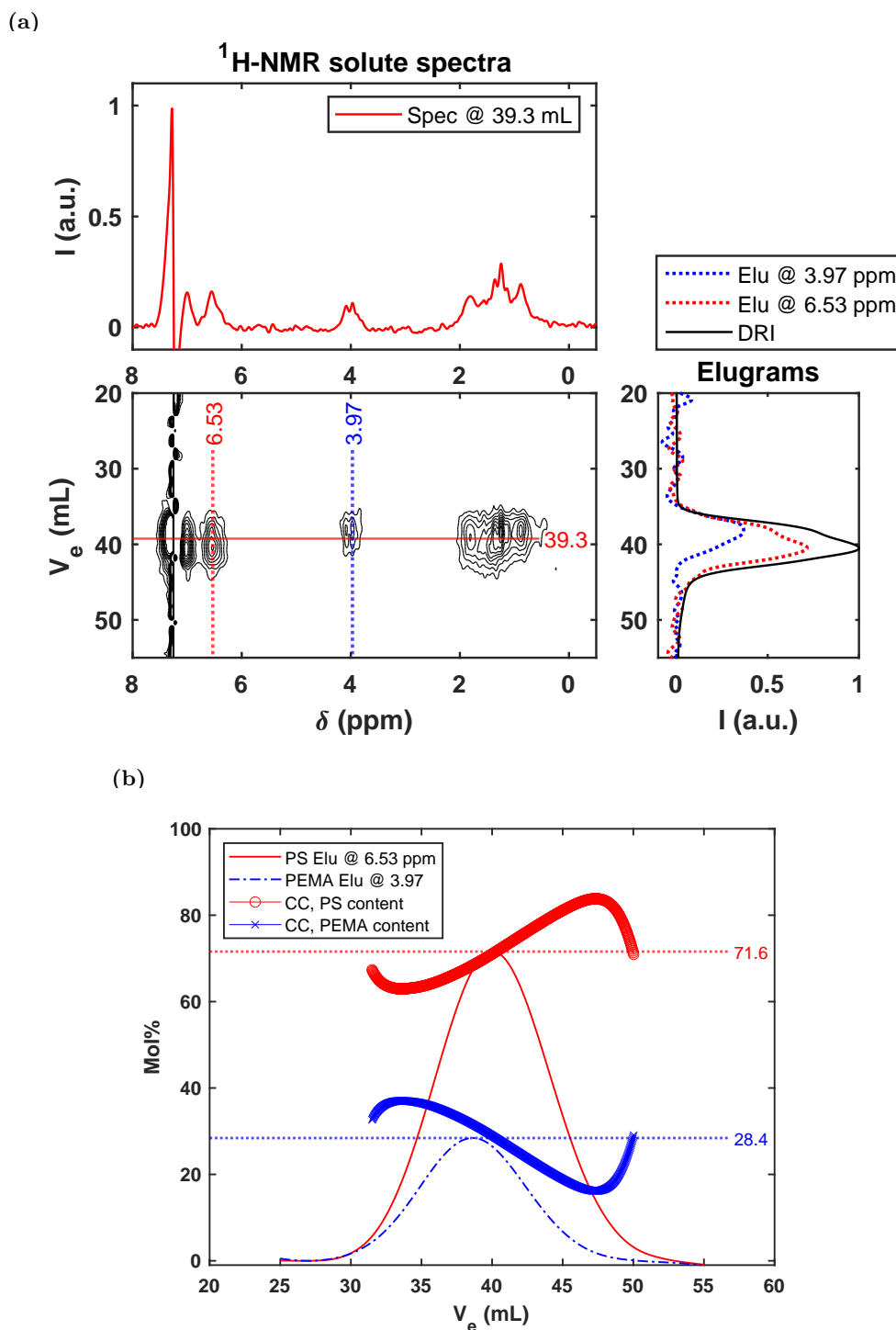


Figure 4.49: SEC-NMR analysis of a PS-*b*-PEMA (70:30 mol%, $M_n = 112\,700$ g/mol, $D = 1.36$) block copolymer in CHCl_3 at 1 mL/min with a total injected mass of 2 mg. In figure (a), the corresponding 1D extracted data, i.e. elugrams (right) and $^1\text{H-NMR}$ spectrum (top), from the 2D contour map (1–10 steps, 0.02 intensity increments) of the SEC-NMR data in the region of interest are presented. The top part of figure (a) represents the $^1\text{H-NMR}$ spectrum for the group of signals that can be identified at 39.3 mL. The right part of figure (a) represents the corresponding elugram cuts for the PS ortho-aromatic ($\delta = 6.53$ ppm) peak and the PEMA ethoxy group ($-\text{OCH}_2-$, $\delta = 3.97$ ppm), overlaid with the DRI trace. Figure (b) represents the chemical composition of the block copolymer as a function of elution volume, determined from NMR elugrams of the *o*-aromatic protons ($\delta = 6.53$ ppm) of the PS component and the ethoxy group ($-\text{OCH}_2-$, $\delta = 3.97$ ppm) of the PEMA component.

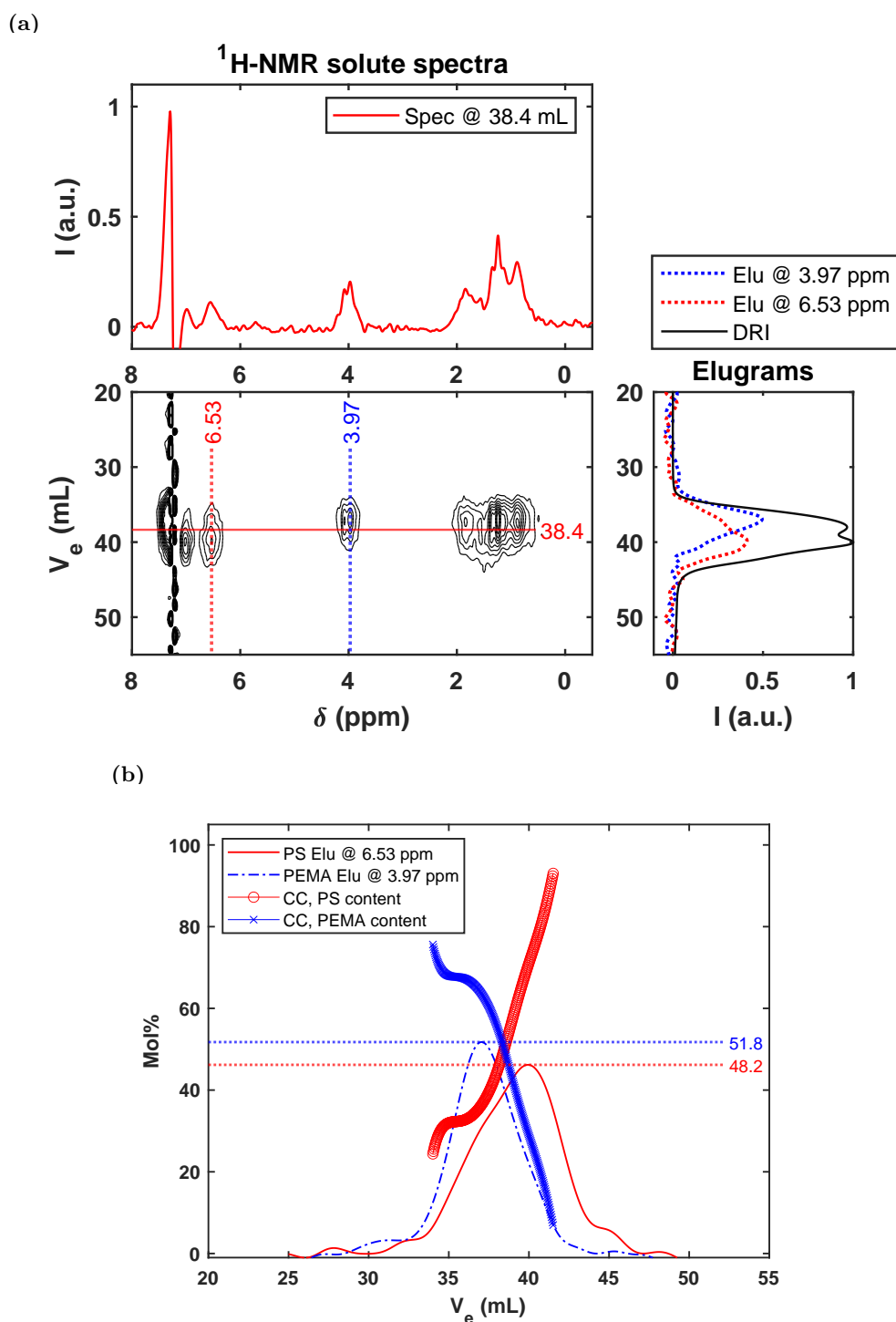


Figure 4.50: SEC-NMR analysis of a PS-*b*-PEMA (50:50 mol%, $M_n = 112\,700$ g/mol, $D = 1.36$) block copolymer in CHCl_3 at 1 mL/min with a total injected mass of 2 mg. In figure (a), the corresponding 1D extracted data, i.e. elugrams (right) and $^1\text{H-NMR}$ spectrum (top), from the 2D contour map (1–10 steps, 0.02 intensity increments) of the SEC-NMR data in the region of interest are presented. The top part of figure (a) represents the $^1\text{H-NMR}$ spectrum for the group of signals that can be identified at 38.4 mL. The right part of figure (a) represents the corresponding elugram cuts for the PS ortho-aromatic ($\delta = 6.53$ ppm) peak and the PEMA ethoxy group ($-\text{OCH}_2-$, $\delta = 3.97$ ppm), overlaid with the DRI trace. Figure (b) represents the chemical composition of the block copolymer as a function of elution volume, with the representative NMR elugrams of the *o*-aromatic protons ($\delta = 6.53$ ppm) of the PS component and the ethoxy group ($-\text{OCH}_2-$, $\delta = 3.97$ ppm) of the PEMA component.

detection. The limit of detection (LOD) and limit of quantification (LOQ) will be presented in the forthcoming Section 4.6.4. For the PS-*b*-PEMA (70:30 and 50:50 *mol%*) samples, presented in Figures 4.49 and 4.50, the PEMA block ratios were of sufficient quantity to allow for the successful determination of the chemical compositional changes as a function of the elution volume (or molar mass). It is evident from the aforementioned figures that these samples show shoulders in the chromatograms. In the case of both the PS-*b*-PEMA (70:30 and 50:50 *mol%*) samples, the PEMA component elutes monomodally, whereas the PS component has a bimodality to it. Furthermore, the M_p values of the PEMA components are higher than that of the PS. Additionally, the PS components increase with decreasing molar mass, while the PEMA components show an inverse trend. The fluctuating *mol%* for both the PS-*b*-PEMA (70:30 and 50:50 *mol%*) samples also indicates that the samples are heterogeneous in nature. There is also an observable shift of the PS and PEMA elugram cuts, with the PEMA component having a higher molar mass fraction than that of the PS component. Consequently, the molar content of the PS fraction increases with decreasing molar mass (this is an inverse trend as observed for the PS-*b*-PMMA sample illustrated in Figure 4.43, p. 134). The respective *mol%* plots, which provide the chemical composition as a function of elution volume, can be used to back-calculate the M_n , M_w and M_p values. The heterogeneity with respect to the PS and PEMA components can possibly be ascribed to these samples containing a significant amount of PS homopolymer precursor material, with the PS homopolymer having a smaller molar mass than the copolymer, resulting in the observed bimodality of the PS component. The chemical compositional changes can also be used to determine the average chemical composition, presented in Table 4.17. These determined values are in a relative good agreement with the bulk determined data by high field (400 MHz) $^1\text{H-NMR}$ spectroscopy (under static conditions).

Table 4.17: Chemical composition determination via high field (400 MHz) $^1\text{H-NMR}$ spectroscopy and SEC-NMR (62 MHz) measurements of the three PS-*b*-PEMA samples.

Sample	M_w (g/mol)	\bar{D}	$^1\text{H-NMR}$ @ 400 MHz	SEC-NMR @ 62 MHz
			S/EMA (<i>mol%</i>)	S/EMA (<i>mol%</i>)
PEMA5	144 400	1.08	95.2/4.8	–
PEMA30	112 700	1.36	70.9/29.1	71.6/28.4
PEMA50	146 100	1.34	52.6/47.4	51.8/48.2

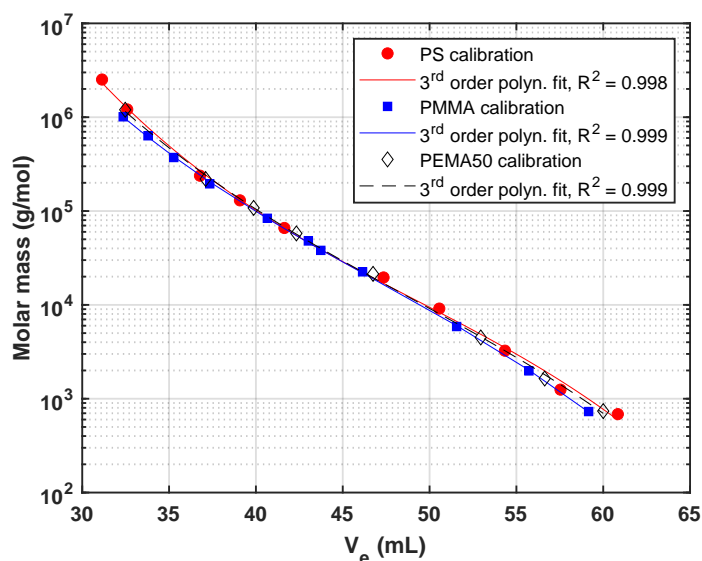
In addition to determining the chemical composition (CC) of the respective species via SEC-NMR, the molar mass distribution can be determined from the determined CC for all of the respective samples. The M_n and M_w can be determined by using the following equations:^{[33, p. 281][195]}

$$M_n = \frac{\sum_{i=1}^n I_i}{\sum_{i=1}^n \frac{I_i}{M_i}}, \quad (4.6.3)$$

and

$$M_w = \frac{\sum_{i=1}^n I_i M_i}{\sum_{i=1}^n I_i}, \quad (4.6.4)$$

where $I_i (= N_i M_i)$ is the NMR intensity, with N_i and M_i being the number of molecules and molar mass of the i^{th} volume component of each monomeric species in the SEC dimension, respectively. These back-calculations are based on the individual calibration curves of the PS and PMMA homopolymers – see **Figure 4.51**.



Fit: $y = ax^3 + bx^2 + cx + d$			
Variable	PS	PMMA	PEMA50
a	-1.01e-4	-8.28e-5	-7.81e-5
b	0.0148	0.0117	0.0114
c	-0.825	-0.648	-0.657
d	20.7	17.6	18.0

Figure 4.51: SEC-NMR calibration curves of the molar mass as a function of the elution volume for PS and PMMA in CHCl_3 . The calibrations were constructed on a semi-preparative linear M column (see Table 4.3, p. 76) with injected masses corresponding to the guidelines provided in Table 4.4 (p. 78). Both the PS and PMMA calibration data points were fitted with a 3rd order polynomial fit ($y = ax^3 + bx^2 + cx + d$). Furthermore, FC9 (see Table 4.1, p. 70) was utilized for the construction of the respective calibration curves. See **Appendix A.7, Table A.2** (p. 280) for the details related to calibration standard sets (including their lot numbers) used. The PEMA50 calibration curve is reconstructed via Equation 4.6.5 – see text for details.

Unfortunately, it was not possible to exactly match the concentration used for the on-flow measurements with the sample concentrations used for the construction of the calibration curve. Consequently, the relative error with respect to molar mass extrapolation would theoretically be slightly higher. Furthermore, the PEMA component would be affected slightly more as a PMMA, and not PEMA, calibration was utilized. Nevertheless, it still

illustrates the fundamental idea. By employing the equations given in Equation 4.6.3 and 4.6.4, the molar masses, M_n and M_w , can be calculated. The results as determined by SEC-NMR and triple-SEC analysis are presented in **Table 4.18**

Table 4.18: Molar mass comparison between SEC-NMR and triple-SEC for the PS-*b*-PEMA sample series (see Table 4.15, p. 136).

Sample	PS calibration			PMMA calibration		
	M_n (g/mol)	M_w (g/mol)	\mathcal{D}	M_n (g/mol)	M_w (g/mol)	\mathcal{D}
PEMA5 (triple-SEC)	134 200	144 400	1.08	130 400	146 400	1.12
PEMA5 (SEC-NMR)	97 800	143 700	1.47	94 600	130 600	1.38
PEMA30 (triple-SEC)	83 000	112 700	1.36	71 200	87 100	1.22
PEMA30 (SEC-NMR)	78 200	118 200	1.51	76 100	110 900	1.46
PEMA50 (triple-SEC)	106 700	146 100	1.34	94 600	168 140	1.78
PEMA50 (SEC-NMR)	101 400	167 700	1.65	97 300	152 600	1.57

As seen in Table 4.18, the molar masses are comparable for SEC-NMR and triple-SEC measurements. It should be noted that the SEC-NMR determined molar masses provide slightly higher dispersity values, which can be ascribed to the use of higher injection volumes, a relatively large NMR flow cell, the use of a PMMA calibration instead of PEMA, and the use of a linear M opposed to the analytical SEC column, which has better separation efficiency. As seen from the PS and PMMA calibration curves for the SEC-NMR calibration, the PS calibration seem to overestimate the molar masses at the higher and lower molar mass ranges, whereas the PMMA calibration seem to underestimate it. An alternative approach to determine copolymers is to implement a combination of both calibrations, in conjunction with the chemical composition information used as weighting factor. The aforementioned is possible by employing the following equation:^[195]

$$\log(M_{copolymer}) = \chi_1^{mol} \log(M_1) + \chi_2^{mol} \log(M_2), \quad (4.6.5)$$

where χ_1^{mol} and χ_2^{mol} are the molar content of the respective co-monomers, with M_1 and M_2 being the molar masses as determined from the homopolymer calibrations (see Figure 4.51). In addition, according to Kilz et al.^[239] **Equation 4.6.5** allows for the calibration of the individual molar masses of the respective blocks of a copolymer, by interpolation between the calibration lines of the homopolymers. The calibration of the copolymer molar mass for the PEMA50 sample is illustrated in Figure 4.51, to show the comparison to the individual PS and PMMA calibration curves. The latter assists in calculating the correct molar masses for the respective block copolymers from the SEC-NMR data. The molar mass corrected data with the aid of the chemical composition determination is presented in **Table 4.19**.

The results presented in Table 4.19 indicates that a more accurate molar mass determination is possible for copolymers when using the chemical compositional corrected molar mass calibration for the respective samples. There is still a certain degree of error associated to the results due the to use of a PMMA homopolymer calibration instead of a PEMA

Table 4.19: Chemical composition-corrected molar masses for triple-SEC and SEC-NMR on the PS-*b*-PEMA sample series (see Table 4.15, p.136).

Sample	M_n (g/mol)	M_w (g/mol)	\bar{D}
PEMA30 (triple-SEC) ^a	119 300	142 400	1.19
PEMA30 (SEC-NMR)	104 700	152 600	1.46
PEMA50 (triple-SEC)	133 600	167 000	1.25
PEMA50 (SEC-NMR)	102 800	167 100	1.63

^a The detector responses used for correction can be found in **Appendix A.7, Table A.3** (p. 281).

calibration. These results are promising as SEC-NMR does not require any calibration related to the chemical composition, making the experimental approach more simple. It should be noted that for the current SEC-NMR technique, block copolymer analysis is typically limited to species where the block ratio of both blocks are ≤ 5 mol%. Therefore, it is recommended, when using the current set-up, to preferably analyse block copolymers where the individual block ratios are in excess of 5% in order to obtain quantifiable results. The results for the characterization of the physical blend and block copolymers clearly show that the hyphenation of NMR at 62 MHz to SEC is a valuable technique to analyse homo- and co-polymers. The determination of the molar mass distribution of copolymers can also be determined reliably using SEC-NMR. A more in-depth characterization was conducted on a series of PS-*b*-PEMA block copolymers with various block ratios. By performing more accurate molar mass calibration using PS and PMMA calibration standards, information on the molar mass distribution and chemical composition could be determined within a single SEC-NMR measurement. By taking into account the relaxation rates of the resonances of interest, more accurate and reliable chemical composition information could be determined. Furthermore, the determined CCs of each block copolymer allows for the determination of the corrected molar mass distribution. The results are comparable to the data determined by triple-SEC. The use of SEC-NMR has the benefit of the simultaneous detection of each respective monomeric species of a block copolymer without prior calibration. Obtaining more complex information such as the microstructure of the co-monomers, is more complex at lower NMR field strengths and is possible at higher field strengths (> 300 MHz) as illustrated in the work of Hiller et al.^[186,189] One point to consider when performing SEC-NMR characterization, is the challenge with respect to the solvent signal, which in the simplest case can be circumvented by employing solvents that do not overlap with analyte resonant frequencies of interest.

4.6.4 Sensitivity Limits

It has been shown that the S/N ratio is an important parameter for successfully utilizing SEC-NMR as a tool, especially when employing low-to-medium field strength NMR spectrometers, i.e. 20–80 MHz. There is a variety of influencing parameters by which the sensitivity of an NMR experiment can be affected – see Ernst et al.^[67, pp. 148–157] Emphasis should be placed on Figure 4.15 (p. 89), as there is always a compromise between sensitivity, selectivity and solvent suppression for a specific problem at hand. To address the usability

of SEC-NMR when performing quantitative analysis, the limit of detection (LOD) and limit of quantification (LOQ) of the SEC-NMR set-up was investigated. Definitions related to the LOD and LOQ have been provided in Section 2.4.2 (p. 50). The LOD and LOQ for the on-line hyphenation of NMR to SEC has already been presented by Höpfner et al.,^[14] however, at the time of the measurements, flow cell, FC3 (see Table 4.1, p. 70), was employed to construct the LOD and LOQ plot. Flow cell FC3 is not an optimized flow cell as it consisted of the flush cut geometry (see Figure 4.3, p. 67). Therefore, the LOD and LOQ was remeasured with the aid of the same sample and concentration series utilized in the construction of the first LOD and LOQ graph, but employing flow cell FC9 (see Table 4.1). A PS calibration standard ($M_n = 30\,300$ g/mol, $D = 1.03$) comprising a series of seven different dilute PS solutions with injected masses of $m = 0.02, 0.03, 0.06, 0.1, 0.25, 0.5,$ and 1 mg and an injection volume of $500\ \mu\text{L}$ for each was used for the investigation. Polystyrene was initially chosen for the investigation, since it is a more challenging sample due to the aromatic proton resonances ($\delta = 6.8\text{--}7.1$ ppm) being so close to CHCl_3 solvent resonance of $\delta = 7.24$ ppm. However, with the re-measurement of the data, the analysis was conducted in THF to determine the effect of solvent subtraction on the aliphatic protons ($\delta = 1.45$ ppm). The LOD and LOQ values were previously found to be 0.10 and 0.36 mg for the aliphatic ($\delta = 1.45$ ppm) and *m*-/*p*-aromatic ($\delta = 7.05$ ppm) protons. The results using FC9 are presented in **Figure 4.52**

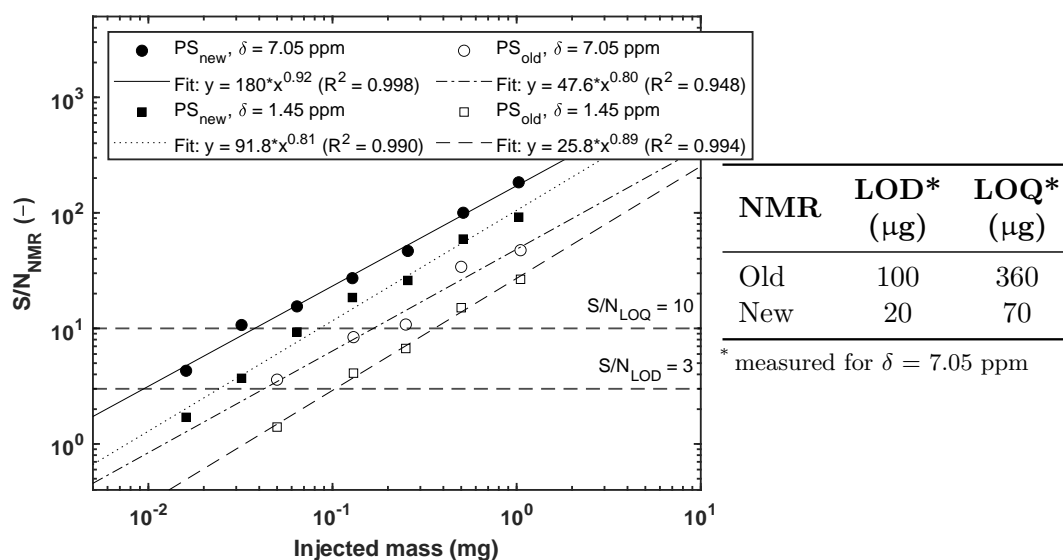


Figure 4.52: The S/N as a function of the injected mass of a PS ($M_n = 30\,300$ g/mol, $D = 1.03$) calibration standard via SEC-NMR analysis. A comparison between data already published^[14] (using FC3 – see Table 4.1, p. 70), denoted in the legend as 'old', and a continuation of the SEC-NMR system optimization (using FC9 – see Table 4.1) is presented. The S/N values for the aliphatic ($\delta = 1.45$ ppm) and *m*-/*p*-aromatic ($\delta = 7.05$ ppm) protons were recorded. The two horizontal dashed lines represent the LOD ($S/N = 3$) and LOQ ($S/N = 10$) limits. These limits for the respective data sets were determined by the intercept of the power law fits employed. The peak maxima were used for the S/N calculations. Furthermore, for the published data^[14] (old) the measurements were performed in CHCl_3 , and the latest data (new) was measured in THF.

As shown in Figure 4.52, the NMR response is in agreement with that of the expected linear relation of the S/N as a function of the injected PS mass fraction. As described by Höpfner et al.,^[14] the data is fitted with a power law function $S/N = A \times m^C$. The C-term should theoretically be 1, indicating a perfect linear response, with the A-term representing the detector response associated to a specific signal (or analyte). Following re-measurement of the PS calibration standard, the C-terms for the aliphatic- and aromatic-protons were $C = 0.81$ and $C = 0.92$, respectively. The determination of the LOD and LOQ values for the on-line SEC-NMR measurements are performed by taking the intercept of the power law fit at a $S/N = 3$ and $S/N = 10$ for the LOD and LOQ values, respectively (see Section 2.4.2, p. 50). With the optimized SEC-NMR set-up the LOD and LOQ values for the PS have been found to be $S/N_{\text{LOD}} = 0.02$ mg and $S/N_{\text{LOQ}} = 0.07$ mg, respectively, for the aliphatic protons ($\delta = 1.45$ ppm), compared to the previous $S/N_{\text{LOD}} = 0.10$ mg and $S/N_{\text{LOQ}} = 0.36$ mg. The optimized SEC-NMR set-up amounted to a factor of 5 improvement in the LOD and LOQ values, using a PS calibration sample. Additionally, by comparing these results to the aromatic protons ($\delta = 7.05$ ppm), the LOD and LOQ values are higher due to the narrow peak. However, the LOD and LOQ values are preferred in terms of the aliphatic protons as all the other signals (peak maxima) in the PS sample would be either of the similar height or larger, thus providing a good relative LOD and LOQ for the sample, and serving as a lower estimate for other narrow dispersity (D) samples. Taking a look at the fit of the (new) aliphatic protons, it has, to a lesser degree, a correlation to the data ($R^2 = 0.987$) and the C-term deviates more from 1 than in the case of the fit to the aromatic protons. This can be ascribed to the influence of the close proximity of the THF solvent resonances, which distorts the baseline after solvent subtraction, however, the basic linear regression is obtained. The opposite is observed for the previously reported (old) data, since CHCl_3 was used as solvent.^[14] This validates the observation that quantification of the analyte resonances close to the solvent peak is possible, but with a reduced accuracy. It is imperative that these LOD and LOQ values are only used as a guide, since it is highly dependent on the experimental conditions being employed, i.e. pulse sequence, flow cell, flow rate, SEC column, sample concentration etc., including the peak shape of the analyte being investigated, for example the methoxy ($\delta = 3.6$ ppm) peak of PMMA would have a very different result than that of the aromatic protons in PS.

The progressive increase with respect to the obtainable S/N ratio is summarized in **Table 4.20**, looking at the overall effect on a methoxy group ($-\text{OCH}_3$, $\delta = 3.6$ ppm) of a PMMA calibration standard ($M_n = 28\,700$ g/mol, $D = 1.08$) as each parameter was optimized during the course of the work. The overall gain in S/N during method development amounted to an increase in S/N with a factor of 363. The importance of these overall improvements is that it enables SEC-NMR measurements to be performed below the overloading limit of the SEC column, which is imperative as it allows for retaining chromatographic integrity. This opens a variety of possibilities where SEC-NMR, with the NMR spectrometer having a carrier frequency of 62 MHz, can be employed as standard characterization technique within universities or as a quality control measure in industry.

Table 4.20: Summary of the optimization parameters for SEC-NMR hyphenation. The improvement in S/N values was established by looking at the methoxy group ($-\text{OCH}_3$, $\delta = 3.6$ ppm) of a PMMA calibration standard ($M_n = 28\,700$ g/mol, $D = 1.08$). Adapted from Botha et al.^[15] with permission from the Royal Society of Chemistry.

Optimization parameter	Choice and/or recommendation	Increase in S/N (-)
Flow cell: Geometry & V_{total}	FC9 (see Table 4.1), < 500 μL	2.10*
SEC: Injected mass	Close to overloading limit ^a	2.00*
SEC: Flow rate	1 mL/min	2.30*
SEC: Column	Semi-preparative (see Table 4.3)	1.50*
NMR: Acquisition length	0.5 ^b s & 1 ^c s	1.10*
NMR: Receiver gain	As high as possible ^d	1.40*
Data processing: Phasing	x/-x only	1.03
Data processing: Drift correction	2 nd order polynomial	1.20
Data processing: Filter SEC dim.	Tukey window function	1.20
Data processing: Filter NMR dim.	Gaussian convolution	2.00
Data processing: 2D de-noising	Data processing combination	16.0*
Overall increase in S/N		357

^a This is highly sample dependent.

^b For the 1-Pulse-spoil pulse sequence – see Section 4.4.5 (p. 99).

^c For the IvR-spoil pulse sequence – see Section 4.4.5 (p. 99).

^d To a receiver gain setting just before ADC overflow.

* Values used to obtain the overall increase in S/N .

4.6.5 Industrial Polymer Application

The following section is dedicated to a small portion of work performed on industrial samples in co-operation with the rubber industry, in the context of the AiF-iGF 19925N project. This was also a measure to establish how the developed technique performs on samples with higher dispersity indexes, as well as non-calibration standard material, i.e. having synthetic routes which are not as well-controlled as anionic polymerization such as solution polymerization etc. The samples of focus were two commercial styrene-butadiene rubbers (SBR), referred to as SBR-A and SBR-B. Styrene-butadiene rubber is one of the most widely used copolymers in the world with an estimated 8.14 million metric tons produced world-wide in 2018,^[4] and accounts for about 50% of car tyres being produced from various types/grades of SBR.^[4] Styrene-butadiene rubbers are roughly classified into three types of co-polymers according to the sequence distribution of the monomer units. Depending on the synthetic procedure employed, they are classified as (1) random co-polymers, styrene-butadiene (SB) or (2) block co-polymers, styrene-butadiene-styrene (SBS) or (3) partially blocked systems are obtained.^[5, p. 190] For the characterization of the mechanical and physical properties, the significance of the sequence distribution and chemical composition in SBRs has been classified as the dominating factors. SBRs and SBR-butadiene rubber (BR) blends are of major importance in the automotive industry for the production of tyres. Depending on the molar mass and chemical composition of the SBR and BR, as well as the SBR to BR ratio, the performance of the materials can vary significantly. Therefore, it is always of importance to the suppliers to obtain information on

the molar mass and S/B ratio of the SBR, molar mass of the BR, SBR/BR ratio, and exact microstructure of the butadiene units in SBR and BR (*cis*- vs. *trans*-, 1,2- vs. 1,4-units). Typically, SBRs are cross-linked in order to obtain their final mechanical properties. While there are a variety of techniques to separate and characterize the processing additives and oils in cross-linked rubbers, there is no efficient technique to separate the polymer itself. If the rubber is cross-linked, and therefore, insoluble, liquid chromatographic type separation is impossible.

The developed 2D SEC-NMR technique was employed, to establish if there was (1) bimodality with respect to the molar mass (MM) of the samples, and (2) if so, are there other chemistries involved, i.e. is the sample only distributed with respect to MM or MM and chemical composition. The main chemistries involved in the samples, and $^1\text{H-NMR}$ spectra, measured at 62 MHz, in CDCl_3 and $\text{THF-}d_8$ at ambient temperature are illustrated in **Figure 4.53**, with the relevant chemical shifts used for identification, listed next to the figure.

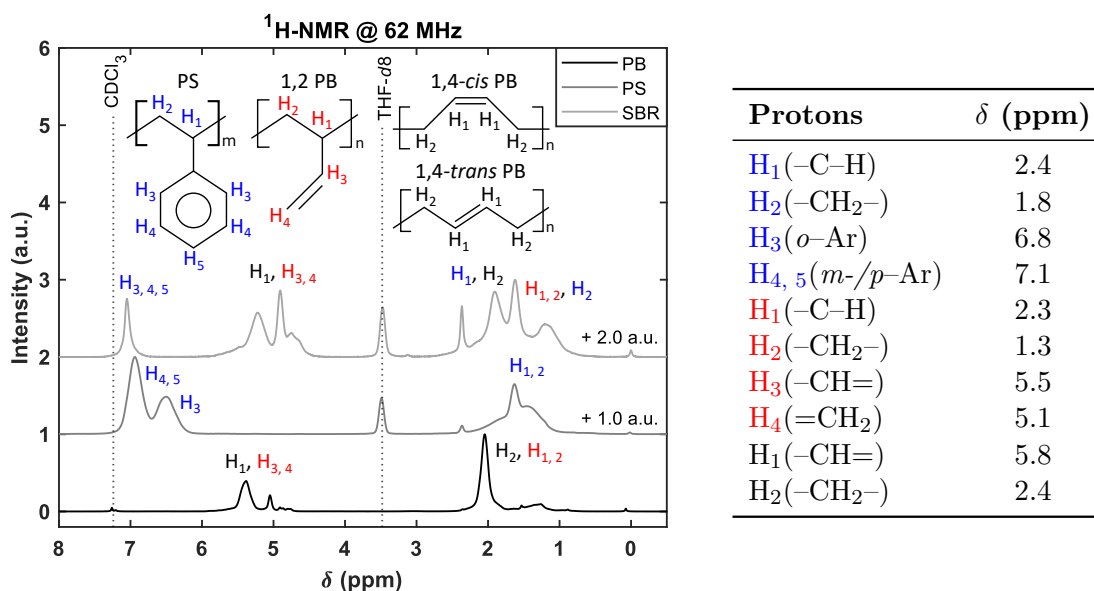


Figure 4.53: Static $^1\text{H-NMR}$ spectra (stacking of 1 a.u.) of the PS ($M_n = 50\,000$ g/mol, $D = 1.03$, $c = 31$ g/L), PB ($M_n = 26\,200$ g/mol, $D = 1.11$, $c = 21.5$ g/L) homopolymers and an SBR-A ($M_n = 286\,000$ g/mol, $D = 1.9$, $c = 28$ g/L) at 62 MHz in CDCl_3 used as reference for the SEC-NMR measurements. The samples were analyzed in standard 5 mm (outer diameter) NMR tubes. The NMR parameters were as follows; FID acquisition time of 6.5 s, with a total repetition time of 15 s, and 128 scans per spectrum. The PB sample was analyzed in CDCl_3 and the PS and SBR in $\text{THF-}d_8$.

The proton resonances are labelled on the respective 1D-NMR spectra, based on the assignment provided in the inset table of Figure 4.53. The SBR-A sample (top light grey line) seems to comprise a mixture of *cis*- and *trans*-butadiene isomers, including the 1,2-configuration ($\delta = 4.5\text{--}6.0$ ppm), however, it seems like the 1,2-configuration (vinyl) is dominating within the sample. In these random co-polymers, monomer sequences play an important role as their effect is pronounced, since there are no long sequences of either

styrene or butadiene co-monomers. This, however, is known to give rise to peak broadening. As seen for the PB sample (bottom black line), from the 1D spectrum, it is dominated by the 1,4-configuration (see the chemical structure inset in Figure 4.53), however, it is not possible to say with certainty whether 1,4-*cis*- or 1,4-*trans*-butadiene is dominating, as this would require a stronger field strength to improve the spectral resolution. In **Table 4.21** an overview of information extracted from the 1D-NMR Spectra for the two SBR samples is provided.

Table 4.21: Chemical composition determination of the SBR samples as determined from high field (400 MHz) NMR spectroscopy. In addition, the molar mass and dispersity indexes, determined by SEC-NMR measurements, is provided.

Sample	M_n (g/mol)	D	Relative integral ratios (S/1,2-B/1,4-B) ^a	mol% PS	mol% 1,2-PB	mol% 1,4-PB (<i>cis</i> & <i>trans</i>)
SBR-A	211 900	2.07	1/3.4/1.2	9.20	27.4	63.4
SBR-B	215 100	1.90	1/1.7/1.5	13.8	53.3	32.9

^a S: styrene, B: butadiene.

Since most industrial laboratories typically use THF as solvent for polymer characterization when performing SEC, the SEC-NMR measurements of the two SBR samples were initially carried out in THF. In the case of using THF as mobile phase in polymer characterization, it is typically accompanied with overlap between the strong solvent band and the analytes' resonances of interest. The latter is due to THF having two relatively broad multiplet resonances, with the one peak maximum located at a chemical shift of $\delta = 1.84$ ppm, overlapping with polymeric aliphatic protons, and the second at $\delta = 3.6$ ppm, which in some cases overlap with certain functional group resonances, such as esters and/or ethers. In the case of the SBR characterization, the aliphatic protons of the PS and PB components have resonances between $\delta = 1.0$ – 2.5 ppm, making quantification in this range challenging. Fortunately, the aromatic protons ($\delta = 6.4$ – 7.2 ppm) of the PS and vinylic protons ($\delta = 4.8$ – 5.8 ppm) of the PB are not affected and could potentially be used. Consequently, the two SBR samples, SBR-A and SBR-B, were analysed with the aid of the developed SEC-NMR technique, using THF as mobile phase, at a flow rate of 1 mL/min with a total injected sample mass of 2 mg. In addition, a special purpose SEC column, i.e. the SDV-High column (see Table 4.3, p. 76), was used (for some but not all industrial samples) due to its large molar mass separation range. The inversion recovery pulse sequence, IvR-spoil (see Section 4.4.5, p. 99), was used for solvent suppression due to the use of THF as mobile phase and has been illustrated in Figure 4.26 (p. 107) to perform better on THF than the 1-Pulse-spoil pulse sequence. The corresponding results are presented in **Figure 4.54**.

As seen in Figure 4.54, parts of the sample were detectable, i.e. the vinylic protons around a chemical shift of $\delta = 4$ ppm and some aliphatic protons (around $\delta = 1$ ppm). Unfortunately, not much information is extractable from these measurements due to two major reasons: (1) the inversion recovery pulse sequence is a factor of 2 slower than the 1-Pulse-spoil pulse sequence, therefore spectral accumulation is restricted, thus reducing the obtainable S/N ;

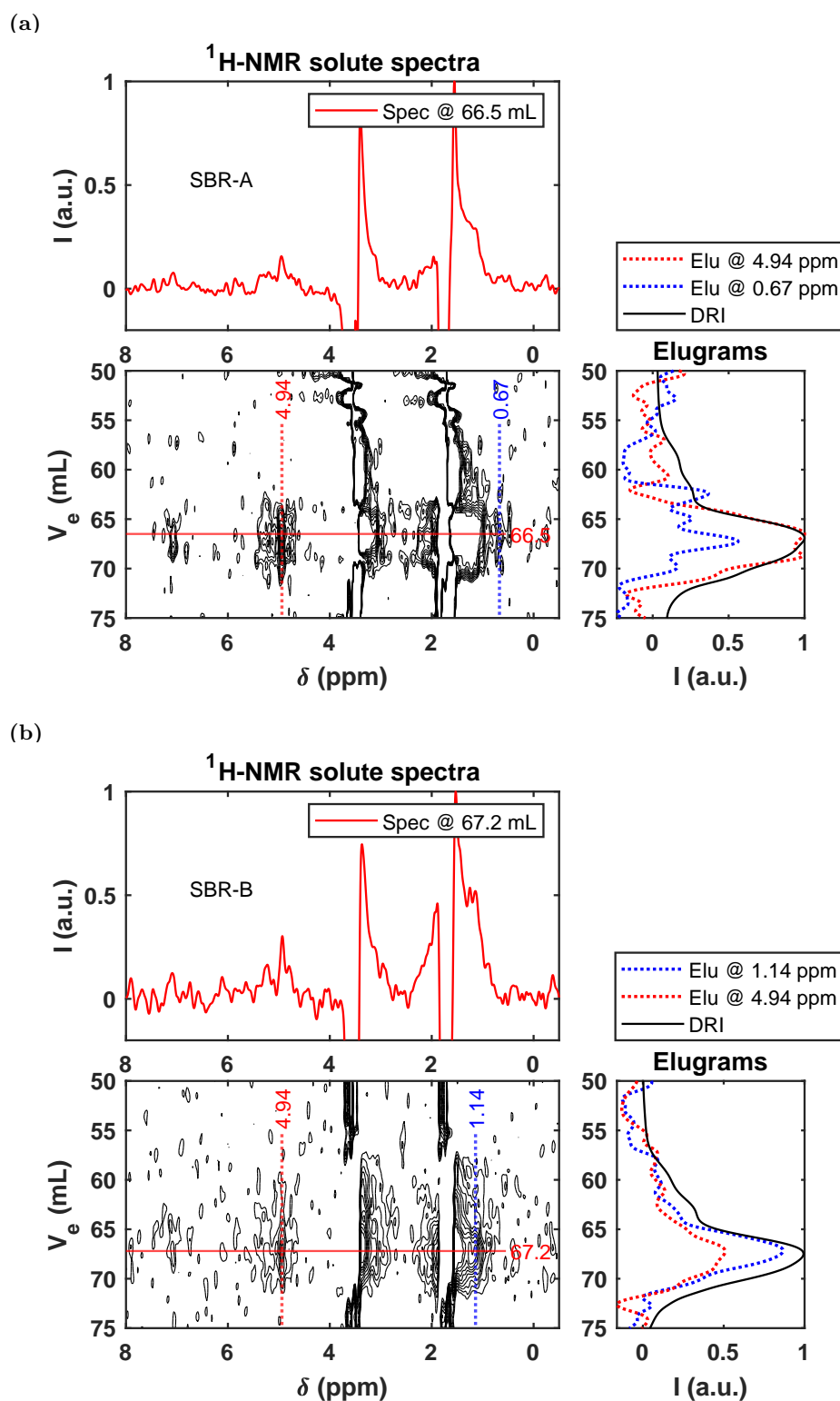


Figure 4.54: SEC-NMR analysis of (a) SBR-A ($M_n = 211\,900$ g/mol, $D = 2.07$, $c = 4$ g/L) and (b) SBR-B ($M_n = 215\,100$ g/mol, $D = 1.90$, $c = 4$ g/L) measured in THF at 1 mL/min with a total injected mass of 2 mg. The corresponding 1D extracted data for both samples, i.e. elugrams (right) and ¹H-NMR spectrum (top), from the 2D contour map (1–10 steps, 0.02 intensity increments) of the SEC-NMR data in the region of interest are presented. The IvR-spoil pulse sequence (see Section 4.4.5, p. 99) was utilized, with a total of 1500 recorded FIDs, a receiver gain setting of 43 dB and repetition time of 1 s, with 4 scans per spectrum. The SDV-High SEC column (see Table 4.3) was used for chromatographic separation.

(2) the FWHM values of the DRI trace of SBR-A and SBR-B are $\text{FWHM} = 6.44 \text{ mL}$ and $\text{FWHM} = 5.46 \text{ mL}$, respectively, which, due to the broadness, reduces the concentration per unit time slice. Due to this, an alternative approach was investigated. Fortunately, SBR is soluble in chloroform, and since sensitivity is a challenge due to the peak broadness and spectral accumulation, the 1-Pulse-spoil pulse sequence was applied to the same SBR samples with the same injected mass and flow rate (2 mg, 1 mL/min) as was employed for the measurements in THF, however, the SDV-High column was replaced by the Linear M column. The reason for the column change was to obtain better chromatographic resolution, due to the reduced pore size distribution and separation range (see Table 4.3, p. 76). The corresponding results are presented in **Figure 4.55**.

Due to the change in solvent from THF to CHCl_3 and the use of a different column, the results in Figure 4.54 differs in position of the elution volume of the SBRs and only slightly in the resonant frequencies due to the change in coil swelling of the polymers compared to Figure 4.55. As seen from Figure 4.55 there is a major improvement in S/N in all the respective plots, resulting in all the resonance groups of interest, i.e. aromatic ($\delta = 6.0\text{--}7.2 \text{ ppm}$) and vinylic ($\delta = 5.0\text{--}5.8 \text{ ppm}$) protons, being visible. In Figure 4.55 the corresponding 2D contour plots, including the respective 1D NMR spectra and SEC elugram plots, of the SEC-NMR measurements (in chloroform) is presented. As evident from Figure 4.55 (a) and (b) there are two distinctive molar mass fractions present in the samples, one higher and one lower molar mass, which was not resolved in the SEC-NMR measurement in THF (see Figure 4.54) due to the different SEC column employed. In both the SBR-A and SBR-B samples the higher molar mass fractions, i.e. $V_e = 41.6$ and 41.4 mL , respectively, are associated to the SBR component of the samples, as the aromatic ($\delta = 6.0\text{--}7.2 \text{ ppm}$), vinylic ($\delta = 5.0\text{--}5.8 \text{ ppm}$) and aliphatic ($\delta = 0.5\text{--}2.2 \text{ ppm}$) proton resonances are clearly visible. The aromatic protons have a slightly distorted peak shape, which is mostly due to the solvent subtraction. The lower molar mass components, i.e. $V_e = 62.1$ and 62.4 mL for SBR-A and -B, respectively, are interesting as there are only aliphatic protons visible. Considering that the lower molar mass fractions in both SBR samples have a molar mass of $\text{MM} < 1000 \text{ g/mol}$ and comprises only of hydrocarbons, it could potentially be identified as a processing agent, e.g. low molar mass plasticizer. An overview of the peak statistics for the measurements in THF and CHCl_3 as obtained by the TMDE software is provided in **Table 4.22**.

As seen from the data presented in Table 4.22, the extracted molar mass for the SBR measured in THF and CHCl_3 (using a PS calibration in the respective solvents) are comparable, i.e. $\text{SBR-A}_{\text{THF}}$, $M_n = 211\,900 \text{ g/mol}$, $\text{SBR-A}_{\text{CHCl}_3}$, $M_n = 226\,400 \text{ g/mol}$, $\text{SBR-B}_{\text{THF}}$, $M_n = 215\,100 \text{ g/mol}$, and $\text{SBR-B}_{\text{CHCl}_3}$, $M_n = 224\,900 \text{ g/mol}$, with the molar masses extracted in chloroform being slightly higher than in THF. A major observable difference is when the amount of NMR peaks and corresponding S/N values are compared for the THF and CHCl_3 data. It was only possible to extract two resonant frequencies for the SEC-NMR measurement in THF, i.e. the vinylic ($\delta = 4.94 \text{ ppm}$) and aliphatic ($\delta = 0.6\text{--}1.2 \text{ ppm}$) protons, whereas for the measurements conducted in CHCl_3 using the faster 1-Pulse-spoil pulse sequence, five different resonance frequencies for the main SBR

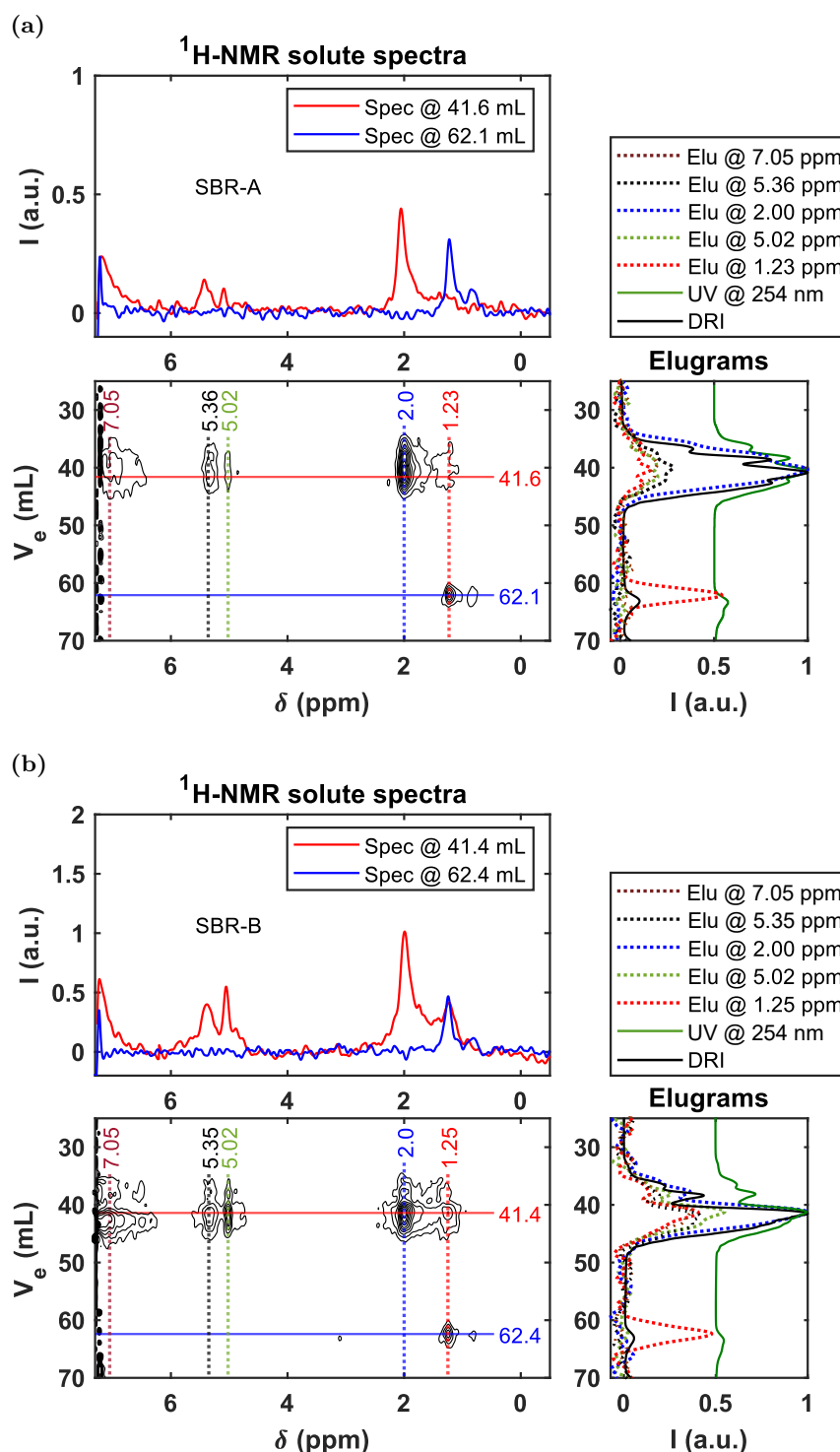


Figure 4.55: SEC-NMR analysis of (a) SBR-A ($M_n = 211\,900$ g/mol, $\mathcal{D} = 2.07$, $c = 4$ g/L) and (b) SBR-B ($M_n = 215\,100$ g/mol, $\mathcal{D} = 1.90$, $c = 4$ g/L) measured in CHCl_3 at 1 mL/min with a total injected mass of 2 mg. The corresponding 1D extracted data for both samples, i.e. elugrams (right) and $^1\text{H-NMR}$ spectrum (top), from the 2D contour map (1–10 steps, 0.02 intensity increments) of the SEC-NMR data in the region of interest, are presented. The 1-Pulse-spoil pulse sequence (see Section 4.4.5, p. 99) was utilized, with a total of 2600 recorded FIDs, a receiver gain setting of 43 dB and repetition time of 0.5 s, with 4 scans per spectrum. A Linear M SEC column (see Table 4.3, p. 76) was used for chromatographic separation.

peaks could be extracted. These include the aromatic ($\delta = 7.0$ ppm) protons from the PS component, the vinylic ($\delta = 5.36$ ppm) protons from the (H_1) 1,4-PB and (H_3) 1,2-PB

Table 4.22: An overview of the peak statistics pertaining to the chemical shift, S/N , FWHM, and molar mass information as obtained by SEC-NMR measurements on the SBR samples in THF and CHCl_3 .

SEC-NMR in THF																																																													
Sample	δ (ppm)	S/N_{NMR} ($-$) ^a	Fraction position, V_e (mL)	FWHM _{SEC} (mL)	M_n (g/mol)	\bar{D}																																																							
SBR-A	4.94	5.2	66.5	6.44	211 900	2.07																																																							
	0.67	3.4					SBR-B	4.94	8.4	67.2	5.46	215 100	1.90	1.14	13	SEC-NMR in CHCl_3							SBR-A	7.05	–	41.6	6.48	226 400	1.82	5.36	32.1	5.02	25.4	2.00	114	1.23	21.6	SBR-B	1.23	66.0	62.2	2.28	900	1.65	7.05	–	41.4	4.52	224 900	1.65	5.35	40.5	5.02	56.8	2.00	103	1.25	41.9		1.25	53.4
SBR-B	4.94	8.4	67.2	5.46	215 100	1.90																																																							
	1.14	13					SEC-NMR in CHCl_3							SBR-A	7.05	–	41.6	6.48	226 400	1.82	5.36	32.1		5.02	25.4					2.00	114	1.23	21.6	SBR-B	1.23	66.0	62.2		2.28	900	1.65	7.05	–	41.4	4.52	224 900					1.65	5.35	40.5	5.02	56.8	2.00	103	1.25	41.9		1.25
SEC-NMR in CHCl_3																																																													
SBR-A	7.05	–	41.6	6.48	226 400	1.82																																																							
	5.36	32.1																																																											
	5.02	25.4																																																											
	2.00	114																																																											
	1.23	21.6					SBR-B	1.23	66.0	62.2	2.28	900	1.65	7.05	–	41.4	4.52	224 900	1.65	5.35	40.5	5.02	56.8	2.00	103	1.25	41.9		1.25	53.4	62.4	2.65	950	1.60																											
SBR-B	1.23	66.0	62.2	2.28	900	1.65																																																							
	7.05	–	41.4	4.52	224 900	1.65																																																							
	5.35	40.5																																																											
	5.02	56.8																																																											
	2.00	103																																																											
1.25	41.9						1.25	53.4	62.4	2.65	950	1.60																																																	
	1.25	53.4	62.4	2.65	950	1.60																																																							

^a S/N data not provided for the aromatic PS peak of SBR-A and -B in CHCl_3 , due to distortions in the peak as a result of solvent subtraction.

(see Figure 4.53 for assignment) components, and the major aliphatic ($\delta = 1.0$ – 2.5 ppm) protons. In addition, from the second lower molar mass fraction, a single resonant frequency could be extracted in the aliphatic region at $\delta = 1.2$ ppm. The S/N improved for the vinylic protons by a factor of 5 for both SBR samples and for the aliphatic protons around a factor (on average) of 4. From a qualitative perspective, the SEC-NMR measurements of the SBR samples indicate that SBR-A seem to have a higher 1,4-PB than 1,2-PB content, whereas SBR-B have a higher 1,2-PB than a 1,4-PB content, which is in agreement with the observed data from the high-field NMR measurement. Naturally, more in-depth characterization needs to be performed to verify this statement, but at a first approximation the results fit the expectation. The SEC-NMR measurements performed in CHCl_3 using the 1-Pulse-spoil pulse sequence, indicated the presence of two distinctive different molar mass species/groups within the samples at ca. $V_e = 41$ and 62 mL, respectively, and that these species are different in chemical composition. The high molar mass fraction, i.e. $V_e = 41$ mL, being attributed to the SBR component and the lower molar mass fraction, i.e. $V_e = 62$ mL to a hydrocarbon species, resembling something like a low molar mass plasticizer or processing agent. The qualitative characterization of the SBRs

illustrates that the developed SEC-NMR technique is powerful for qualitative component analysis/identification, and is a complementary technique to its counterpart 1D techniques.

4.7 Standard Operating Procedure (SOP): SEC-MR-NMR

The next section is dedicated to providing a summary, in the form of a standard operating procedure (SOP), on how to approach an unknown sample subjected to SEC-MR-NMR analysis. The itemized procedure is as follows:

- Perform a solubility check on the analyte. The less resonant frequencies the solvent has the better, i.e. reducing NMR spectrum distortions.
- After solvent establishment, perform static ^1H -NMR measurements, preferably on both high field and benchtop NMR spectrometers, in deuterated solvents, to obtain a clear picture on all the visible resonances within the sample. Typical concentrations to be used vary in the range of 10–30 g/L. This will also provide an indication as to how the chosen solvent affects the analyte's region of interest with respect to resonance overlap.
- Based on the solvent selection, choose an appropriate pulse sequence, either the 1-Pulse-spoil or IvR-spoil (see Figure 4.23, p. 100).
- Refer to **Table 4.23** for an overview of the experimental parameter guideline to achieve successful SEC-MR-NMR measurements.
- It is important to note that the guidelines provided in Table 4.23 are only recommendations for the specific set-up, and should only serve as a generalized guide, as some of the parameters are highly sample dependent.

Table 4.23: Standard operating procedure for SEC-MR-NMR measurements of an unknown sample, using either the 1-Pulse-spoil or IvR-spoil pulse sequences in CHCl_3 and THF, respectively. Recommendations related to flow cell selection, SEC- and NMR-parameters, and data processing using the TMDE software are provided.

Parameter	Pulse Sequence	
	1-Pulse-spoil(CHCl_3 , degassed)	IvR-spoil(THF, degassed)
SEC Dimension		
Flow cell	FC9	FC9
SEC column	Semi-prep.	Semi-prep.
Flow rate (mL/min)	1	1
Sample conc. (g/L)	1–6	1–6
Injection volume (μL)	500	500
Measurement time (min)	85	85
NMR Dimension		
Pulse length (μs)	12–14	12–14
Number of scans	4	4
Total FIDs	2600	1300
FID points	2048 (2k)	2048 (2k)
Acquisition time (ms)	410	410
Acquisition delay (μs)	100	100
Repetition time (μs)	500	1000
Receiver gain, RxG (dB)	$35 < \text{RxG} < 49$	$35 < \text{RxG} < 52$
Spoil amplitude (a.u.)	5000	5000
Spoil time (ms)	20	20
Data Processing		
Zero-filling factor	2–8	2–8
Apodization function	Gaussian	Gaussian
Bandwidth NMR dim. (s)	0.1	0.1
Noise NMR dim. (ppm)	-20 to -10	-20 to -10
Solvent Peak max. (ppm)	7.25	3.58
Phasing method ^a	3 (0 th & 1 st)	7 (interactive)
Filter SEC dim.	Tukey ($\alpha = 0.55$)	Tukey ($\alpha = 0.55$)
Bandwidth SEC dim. (s)	32	32
Noise SEC dim. (min)	10–20	10–20
Solvent ref. subtraction (min)	5–10	5–10
Polynomial order baseline corr.	1–3	1–3

^a see Table 4.9 (118).

Chapter 5

EC-QCL Instrument Evaluation

This chapter is subdivided into four sections, similar to Chapter 4 (p. 62), having a method development theme in which the prototype EC-QCL will be evaluated as potential chemically sensitive detector for SEC. Each section consists of an introductory part followed by the corresponding results and discussion, and finally the concluding remarks. The EC-QCL instrument evaluation sections consist of the following; an overview of the instrumental set-up, numerical data treatment, sensitivity limits, and the EC-QCL as potential LC detector.

5.1 Introduction

The use of infrared (IR) spectroscopy is of great importance to the field of analytical chemistry as all organic compounds absorb in the mid-IR region ($\lambda = 2.5\text{--}25\ \mu\text{m}$ or $\tilde{\nu} = 4000\text{--}400\ \text{cm}^{-1}$) of the electromagnetic spectrum, as seen in Figure 2.8 (p. 21). One key advantage of mid-IR absorption bands is that they are typically well resolved and can be utilized for the identification of defined vibrational transitions of specific organic functional groups. This enables mid-IR spectra to provide qualitative information, with high precision, on an analyte of interest. In the case of hyphenating liquid chromatography (LC) to IR detection, the absorption of the IR radiation by the mobile-phase, i.e. solvent, generally results in very strong spectral interferences. As described in Chapter 3 (p. 56), in order to address the need for obtaining correlated information, such as molar mass distribution and chemical composition, topology, or functionality of a variety of different hyphenated techniques has been developed utilizing combinations of SEC with molecular spectroscopy, i.e. NMR,^[187,189,240] MS,^[174] and IR.^[7,177,241,242] In the context of SEC-IR hyphenation, the off-line^[241] and on-line hyphenated^[7,177,242] techniques are well-established, even for specialized set-ups such as high-temperature SEC.^[242] Furthermore, within this working group a newly developed method based on Fourier-transform (FT) IR spectrometer and numerical solvent suppression optimization has been developed by Beskers et al.^[7,177] The developed SEC-IR techniques performs well for the determination of the chemical composition (CC) as a function of molar mass distribution, however, as with the developed

SEC-NMR technique, they are limited with respect to their sensitivity, making end-group analyses nearly impossible at low sample concentrations. The developments in quantum cascade laser (QCL) technology in the mid-IR region are one of the most exciting advances in the context of spectroscopy, as it opens new possibilities not previously feasible with standard FT-IR spectrometers. According to the Lambert-Beer law,^[61, p. 142]

$$A = \log \frac{I_0}{I} = \epsilon \cdot l \cdot c, \quad (5.1.1)$$

with I_0 and I being the incident and transmitted light, ϵ is the molar attenuation coefficient (or absorptivity), l the optical path length, and c the concentration of the attenuating species. The absorbance (A) increases linearly with the path length of the light through the sample. Since QCLs (see Section 2.3, p. 43) have a much higher spectral power density, i.e. 10^4 more photons per wavenumber,¹ than black body radiation sources such as globars, i.e. thermal light sources like silicon carbide (SiC, $P \approx 10 \mu\text{W}$ per wavenumber), it enables the use of samples with longer optical path lengths, i.e. thickness, to be analysed without total absorption by the solvent.^[135] Consequently, the use of QCL detection in the liquid phase, where the optical path length vary significantly, and especially in the field of liquid chromatography, is of major interest due to the potentially high obtainable sensitivity of QCL detection, and the accompanying chemical information. This enables the possibility for function-group-specific chromatograms to be obtained. As with the SEC-IR development within this working group, developments related to the first prototype QCL spectrometer from Bruker Optik GmbH (Ettlingen, Germany) has been used as on-line chemical sensitive detector for SEC, reported by Morlock et al.^[8] Based on the findings, Morlock et al.^[8] showed that the obtainable limit of detection (LOD) measured on the prototype QCL was a factor of 4 better compared to a Bruker Vertex 70 FT-IR spectrometer, even though the FT-IR instrument consisted of liquid nitrogen cooled mercury-cadmium-telluride (MCT) detection opposed to the less sensitive lithium tantalate (LiTaO_3) detectors on the prototype QCL spectrometer. This highlighted the use of QCL detectors as complementary detector to standard FT-IR instruments. Since QCL sources typically cover limited wavenumber ranges, e.g. 200 cm^{-1} , but at much higher sensitivities, FT-IR instruments provide information on the entire mid-IR range, but at reduced sensitivities. Due to the restriction imposed by the prototype QCL spectrometer with respect to the LiTaO_3 detectors, and the potential of the QCL as LC detector, the development of an entirely new external cavity (EC) QCL spectrometer was undertaken with first results published by Kübel et al.^[16] The forthcoming sections will elaborate on some of the developmental procedures undertaken to enable the use of the EC-QCL as LC detector, and simultaneously enhancing the S/N of the detector by post data acquisition software development.

¹The strongest laser in the world is the confinement beam at the National Ignition Facility. It is a UV laser used in the Fusion Research Laboratory and has an energy output of 500 TW per pulse. Due to its intensity, the laser is only 'fired' on earth for a 15 nanosecond interval. In that 15 nanoseconds it has an energy output equivalent to 250 mL of petroleum.

5.2 EC-QCL Instrumental Set-up

The next section is dedicated to providing a descriptive overview of the design specifications of the prototype EC-QCL spectrometer. It entails the step-by-step description of the key components related to the instrument, as well illustrating typical tuning ranges of the different sources contained within. Technical details related to individual sources are also provided.

5.2.1 Introduction

The EC-QCL spectrometer, presented in **Figure 5.1**, was hyphenated to an Agilent 1260 Infinity SEC system (Waldbron, Germany – see **Appendix A.5**, Figures A.3 and A.4, p. 274), using a linear M semi-preparative SEC column (see Table 4.3) for chromatographic separation. The system was exclusively operated in butylated hydroxytoluene (BHT) stabilized THF, at a volumetric flow rate of 1 mL/min. The SEC system, unlike the system for the SEC-NMR hyphenation, consisted of an auto-sampling unit, where an injection volume of 500 μ L was typically employed.

The EC-QCL spectrometer, as designed by Dr. J. Kübel, enables the housing of up to two QCL laser boxes (marked EC-QCL Box 1 and 2 on Figure 5.1) with a total of up to eight EC-QCL laser sources (or chips), i.e. four per box, allowing for user flexibility and the potential for future expansion. Within the design, all of the available laser sources can be utilized, even for a single experiment, by means of an automated beam switch (marked as 1 on Figure 5.1) that allows for the differentiation between the available sources. The speciality of the spectrometer includes: (1) the IR light sources being based on EC-QCL technology, allowing for both pulse-mode and continuous-wave operation; (2) custom designed flow cell and replaceable sample compartment, allowing for various sample interfaces; and (3) the use of two liquid nitrogen cooled mercury-cadmium-telluride (MCT) detectors. The use of two detectors, also referred to as balanced detection, is advantageous, as it allows for the compensations of any laser intensity fluctuations. Furthermore, the detectors consist of pre-amplifiers that enables individual detector adjustment for optimum detection. Following the beam switch, the laser beam intensity can be attenuated by two neutral density IR filter wheels (marked as 2 on Figure 5.1), comprising the following filter attenuators: open (no attenuation), 50%, 75%, 90%, 97%, and 99% attenuation. The first filter (in the main beam path) serves as an initial protection for the two MCT detectors to prevent detector overload and damage when exposed for extended periods of time, to adjust the main beam intensity, and the second filter wheel is placed just before the reference detector (marked as 4 on Figure 5.1). When performing measurements in pulsed-mode operation, the pulse-trains created by the laser provides the required modulation for the detectors, however in continuous-wave (CW) operation (not used in this work) a chopper (marked as 3 on Figure 5.1) is required to modulate the laser beam. A zinc selenide (ZnSe) beam splitter, with a 90:10 splitting ratio, is employed for the partial beam reflection, i.e. 10%, directly into the reference detector. The main part of the laser beam. i.e. remaining

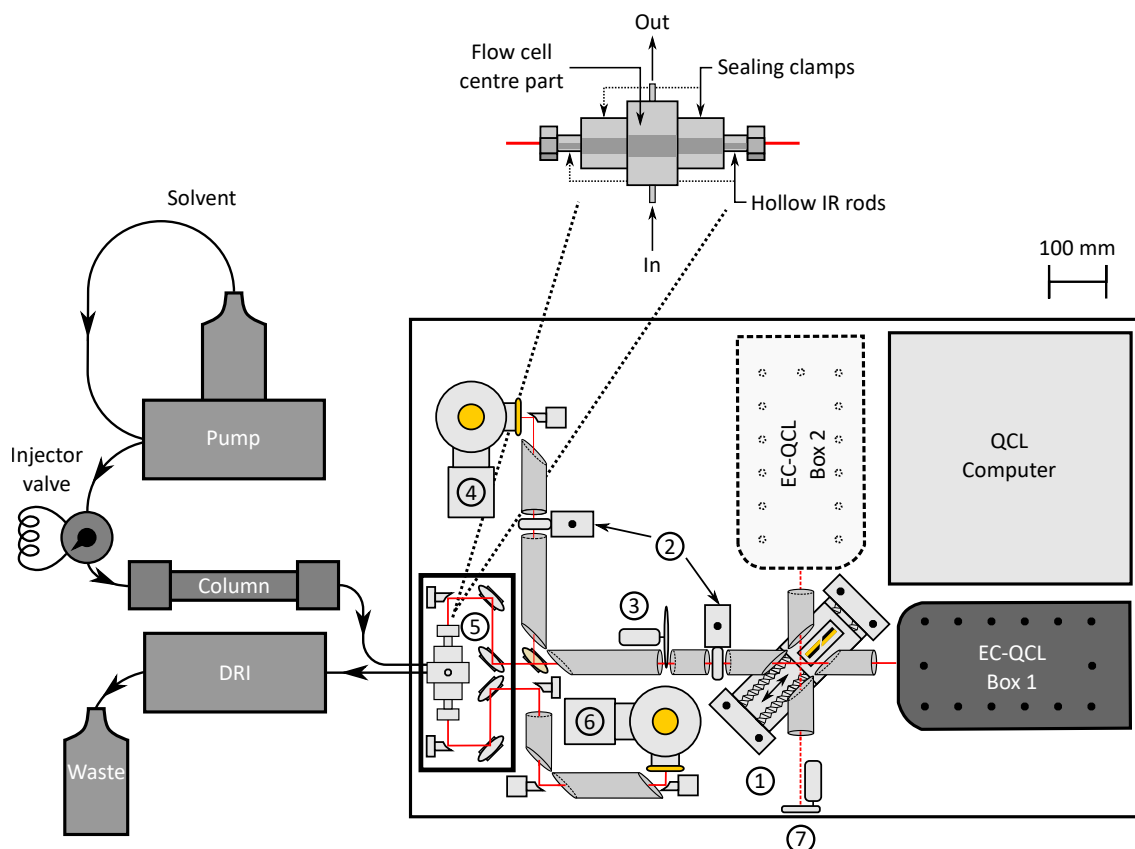


Figure 5.1: The SEC-EC-QCL set-up, with a more in-depth view on the interior of the spectrometer. The key components, marked with numbers, include: (1) beam switch, (2) filter wheel, (3) chopper, (4) MCT reference detector, (5) sample chamber and flow cell, (6) MCT sample detector, and (7) beam outlet for spectrometer adaptations. The set-up resembles a general SEC set-up, with the EC-QCL spectrometer just as an 'add-on' detector. All parts are connected with 0.25 mm i.d. polytetrafluoroethylene (PTFE) tubing – see Appendix A.5, Figure A.3 (p. 274) for a photograph of the set-up. Adapted with permission.^[16] Copyright 2019, Wiley-VCH GmbH.

90%, is guided through the custom built flow cell (marked as 5 on Figure 5.1), and used for SEC hyphenation with off-axial parabolic mirrors to the sample detector (marked as 6 on Figure 5.1) for acquisition. The custom built flow cell, also designed by Dr. J. Kübel, is an adjustable transmission-style flow cell, which allows the IR path to be adjusted to lengths of 2–10 mm, with a minimum flow cell volume of 320 μL and IR path length of 4.1 mm. As with the SEC-NMR set-up, after chromatographic separation, the analyte and mobile-phase flow from the bottom to top of the flow cell against gravity to avoid air pocket formation in the cell that might cause beam scattering. The reader is referred to Kübel et al.^[16] for a detailed description of the flow cell. In addition a photo (including an expansion drawing) of the flow cell is presented in Figure A.5 (p. 276). The laser material is tempered to 19 °C.

5.2.2 Pulse-mode Operation, Tuning Range, and Specifications

The EC-QCL as detector for LC, was evaluated by exclusively using pulsed-mode operation, with photon pulse-trains, as illustrated in **Figure 5.2** at a frequency of 100 kHz and a

pulse length of 540 ns, thus a duty cycle of 5.4% (out of a maximum system duty cycle of 10%).

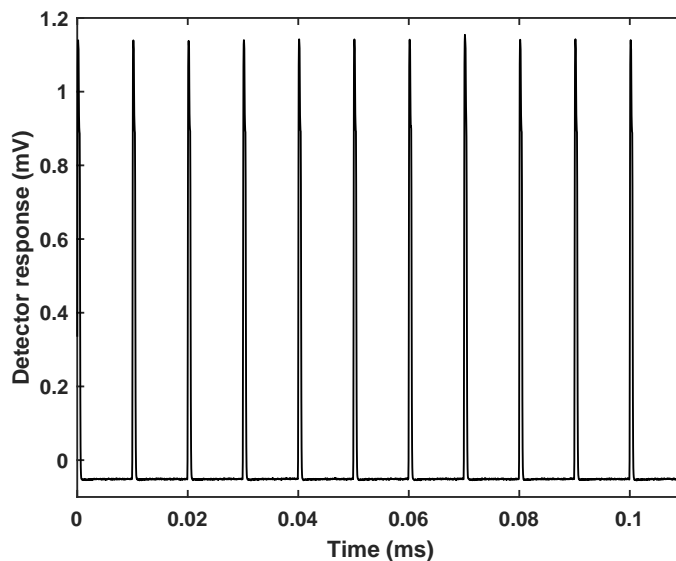


Figure 5.2: A pulse-train (showing 10 pulses) on the EC-QCL spectrometer using laser source QCL-1 (see Table 5.1) at full power $I = 1000$ mA, at a wavenumber of $\tilde{\nu} = 1900$ cm^{-1} . A pulse width of 540 ns was employed. The attenuation settings were as follows: main filter: 50%, and reference filter: 50%.

The evaluation of the pulse-trains in Figure 5.2 on the QCL-1 source indicated that there were a relative standard deviation (RSD) of the areas under the consecutive pulses (measured on 100 pulses) of $\text{RSD} = 2.66\%$, indicating system stability. The continuous-wave operation was not tested, since there were severe problems with communication between the QCL computer and the laser chips, which was ascribed to a 'bug' in the Labview software and will possibly be addressed and detailed in future work. For signal digitization, a 16-bit $(20 \text{ MS/s})^2$ ADC was integrated into the set-up. The laser beam is mostly guided through PVC tubing, and flushed with nitrogen gas, to minimize any atmospheric interference from sources such as residual H_2O and carbon dioxide. The operation of the entire spectrometer is performed on a designated custom written Labview program. The current set-up consists of three collinear tunable EC-QCL sources (Daylight Solutions, San Diego, CA, USA), which are able to operate in both pulsed-mode and continuous-wave operation. The tuning ranges of the respective EC-QCL sources are presented in **Figure 5.3** and system specifications related to pulsed-mode operation in **Table 5.1**.

Figure 5.3 shows the available tuning ranges of the EC-QCL sources currently in operation, for both pulsed-mode and continuous-wave operation relative to a transmission spectrum (full mid-IR range, $400\text{--}4000$ cm^{-1}) of a PS standard acquired on an FT-IR spectrometer. The EC-QCL sources can be tuned over a range of 200 cm^{-1} on average, as detailed in Table 5.1. The intensity of the laser signal depends on the wave number. The intensity profile approximates a Gaussian distribution with respect to its intensity as a function of

²The sampling rate is given in mega samples per second, which also circumvents confusion and distinguishes the signal frequency, i.e. bandwidth, which is typically given in Hz, kHz or MHz.

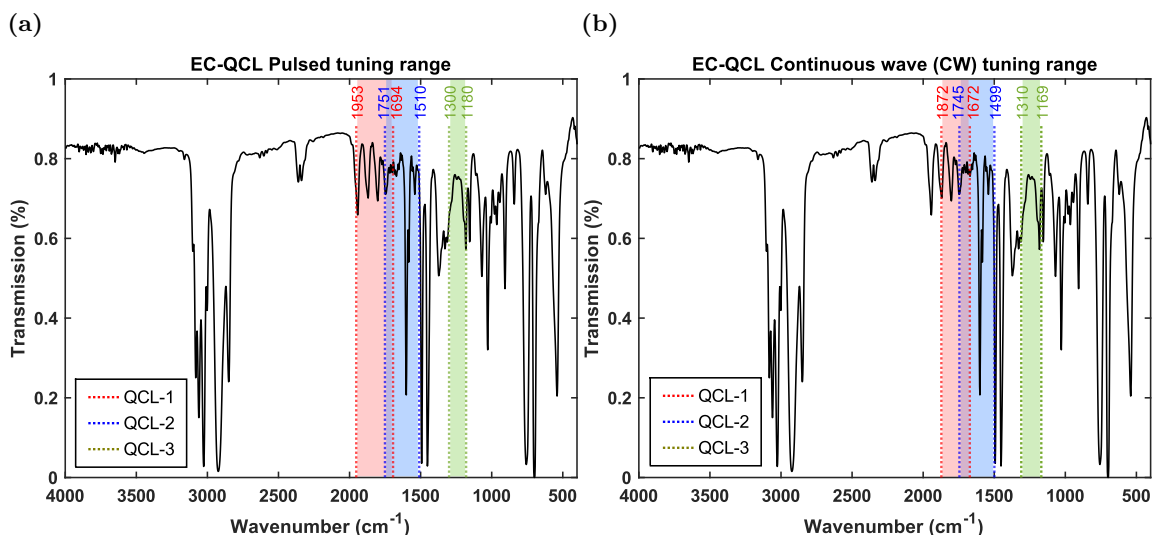


Figure 5.3: The available tuning range for the different QCL sources in (a) pulsed-mode (PM), and (b) continuous-wave (CW) operation, indicated on a transmission spectrum of a polystyrene thin film standard measured with an FT-IR spectrometer. In figure (a), the specified ranges for the QCL sources are as follows: QCL-1_{PM}: $\tilde{\nu} = 1953\text{--}1694\text{ cm}^{-1}$ (wavelength: $\lambda = 5.12\text{--}5.90\text{ }\mu\text{m}$), QCL-2_{PM}: $\tilde{\nu} = 1751\text{--}1510\text{ cm}^{-1}$ (wavelength: $\lambda = 5.71\text{--}6.62\text{ }\mu\text{m}$), and QCL-3_{PM}: $\tilde{\nu} = 1300\text{--}1180\text{ cm}^{-1}$ (wavelength: $\lambda = 7.69\text{--}8.47\text{ }\mu\text{m}$). In figure (b), the available ranges for the QCL sources are as follows: QCL-1_{CW}: $\tilde{\nu} = 1872\text{--}1672\text{ cm}^{-1}$ (wavelength: $\lambda = 5.34\text{--}5.98\text{ }\mu\text{m}$), QCL-2_{CW}: $\tilde{\nu} = 1745\text{--}1499\text{ cm}^{-1}$ (wavelength: $\lambda = 5.73\text{--}6.67\text{ }\mu\text{m}$), and QCL-3_{CW}: $\tilde{\nu} = 1310\text{--}1169\text{ cm}^{-1}$ (wavelength: $\lambda = 7.63\text{--}8.55\text{ }\mu\text{m}$).

wavenumber. The maximum reachable power of the three sources in pulsed-mode is listed in Table 5.1 at the respective wavenumbers. Having a high power throughput instrument is advantageous, as this allows for the use of larger flow cell volumes, i.e. path lengths, to be used and, consequently, resulting in higher obtainable sensitivities. A typical pulse response curve measured on QCL-1 and the principle of duty cycle is depicted in **Figure 5.4**.

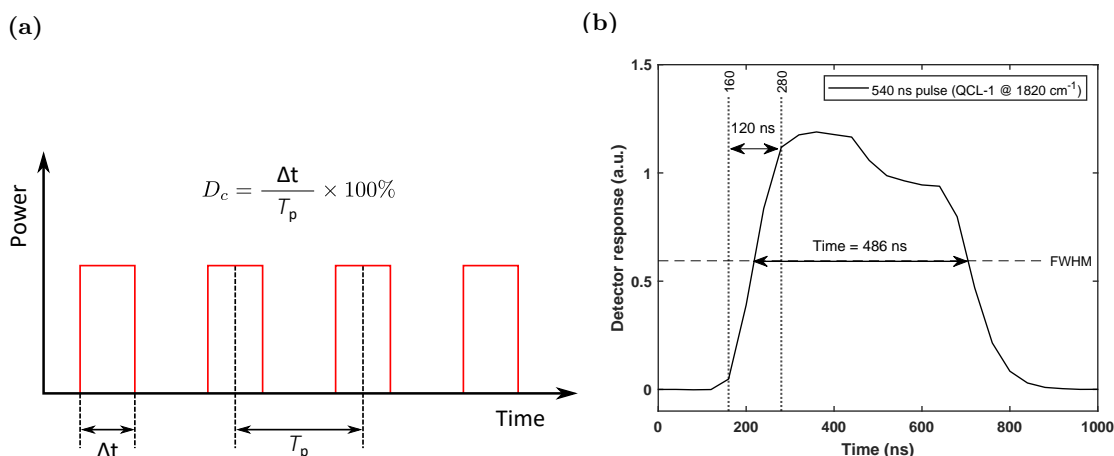


Figure 5.4: The pulse shape obtained from a 540 ns pulse length using the QCL-1 source at full power ($I = 1000\text{ mA}$) at $\tilde{\nu} = 1820\text{ cm}^{-1}$. Figure (a) illustrates the determination of the duty cycle, D_c , where Δt is the pulse duration in nano-seconds and T_p the period duration. Figure (b) is the detector response of the pulse shape at a 540 ns pulse length recorded using the Labview software (and integrated 16 bit ADC) as 'replacement' oscilloscope. The response curve was measured with a $V = 320\text{ }\mu\text{L}$ THF layer in the ZnSe flow cell between the source and the sample detector. A response time of ca. 120 ns is obtained.

Table 5.1: Summary of the pulsed-mode operations specification for the EC-QCL spectrometer from Daylight Solutions.

Pulsed-mode operation	
System parameter	Specification
Max. tuning speed (cm^{-1}/s)	3 000
Tuning range (cm^{-1})	QCL-1: 1953–1694 ($\Delta\tilde{\nu} = 259$) QCL-2: 1751–1510 ($\Delta\tilde{\nu} = 241$) QCL-3: 1300–1180 ($\Delta\tilde{\nu} = 120$)
Wavelength accuracy (cm^{-1})	< 1
Tuning modes	Step & measure
Max. peak power (mW)	QCL-1: 350 (1820 cm^{-1}) QCL-2: 230 (1660 cm^{-1}) QCL-3: 175 (1230 cm^{-1})
Current range (mA)	QCL-1: 1000 QCL-2: 750 QCL-3: 525
Pulse-to-pulse energy stability (StDev)	< 3%
Pulse repetition range	100 Hz – 1 MHz
Pulse width range (ns)	40–500 (20 ns steps)
Max. duty cycle (%)	10
Line width (cm^{-1})	< 1

In Figure 5.4 (b) the response curve of QCL-1 ($I = 1000 \text{ mA}$) at $\tilde{\nu} = 1820 \text{ cm}^{-1}$ was measured with a $320 \mu\text{L}$ THF layer between the laser source and the sample detector, using a ZnSe flow cell (see Figure 5.1) to avoid detector saturation. A linear response time of ca. 120 ns is obtained on the sample detector using QCL-1 at $\tilde{\nu} = 1820 \text{ cm}^{-1}$.

5.3 Selective Optimization of Measurement Parameters

The following section will provide details related to the optimization of selective parameters, allowing for initial testing of the EC-QCL spectrometer. These include: (1) column selection for the hyphenation of the EC-QCL spectrometer to SEC, (2) reduction of noise by means of pulse averaging, and (3) understanding timing issues related to the prototype instrument.

5.3.1 Introduction

The system flexibility of the EC-QCL set-up is what makes it a unique instrument, however, this leads to an optimization paradox, as there are too many parameter variations to explore to provide a single 'how to' recipe. Consequently, within the presented work, only a select few parameters have been addressed for optimization to allow for initial testing of the EC-QCL spectrometer as potential chemical sensitive detector for SEC. These parameters are described hereinafter.

5.3.2 Column Selection

An analytical (300×8 mm i.d.) and semi-preparative (300×20 mm i.d.) column were tested and compared by analysing a PMMA ($M_n = 50\,000$ g/mol, $D = 1.03$, $c = 5$ g/L) calibration standard to evaluate which type of column, i.e. analytical or semi-preparative (see Table 4.3, p. 76 for details), would be best suited to the custom designed flow cell. This is of importance as it also has a direct correlation to the obtainable chromatographic resolution. The corresponding results are illustrated in **Figure 5.5**.

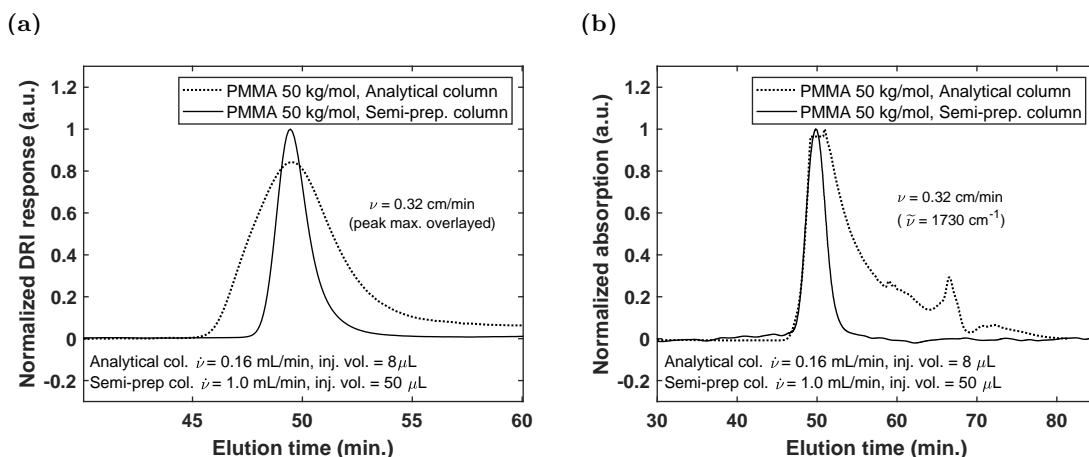


Figure 5.5: Effect of the column-to-flow-cell mismatch on the (a) DRI- and (b) QCL-signal. The sample was a PMMA ($M_n = 50\,000$ g/mol, $D = 1.03$, $c = 5$ g/L) calibration standard and injection volumes was 8 and 50 μL for the analytical and semi-preparative column, respectively. The flow cell volume was ca. 320 μL . The measurement in (b) had the following parameters: QCL source: QCL-1, wavenumber: $\tilde{\nu} = 1730$ cm^{-1} , current: $I = 1000$ mA, pulsewidth: $pw = 540$ ns, signal gain: $SG = 6.4$, reference gain: $RG = 5.0$, filter (main): $fm = \text{open}$ (no attenuation), and reference filter: $fr = 75\%$ attenuation.

As the minimum volume reachable for the specific flow cell was approximately 320 μL , it is clearly visible from Figure 5.5, that there is a column-to-flow-cell mismatch with respect to the injection band volumes, for both the DRI and QCL traces. To allow for comparison, the columns were employed with a linear flow velocity of $\nu = 0.32$ cm/min. Considering the peak-heights and -widths (FWHM) of the two columns, it is evident that the semi-preparative column is better suited. This can be ascribed to the analyte band of the analytical column (injection volume = 8 μL) being a factor of 40 less than that of the flow cell and a factor of 6.4 for the semi-preparative column (injection volume = 50 μL). The injection bands of 8 and 50 μL were chosen to have a direct comparison, as the semi-preparative column has a factor of 6.25 larger volume than the analytical column. Naturally, when the smaller analyte band, used for the analytical column, passes through the larger flow cell, band broadening occurs. This effect occurs on a volume- and not time-scale, resulting in peaks with the same elution time (see Equation 2.1.6, p. 8) but more severe band broadening. The SEC statistics were quantified by looking at the number of theoretical plates (N), asymmetric factor (A_s), and tailing factor (T_f). These values were calculated from the DRI traces (see Section 2.1.6, p. 14). The peak statistics for the DRI and QCL traces are listed in **Table 5.2**

As seen in Table 5.2, the number of theoretical plates for the semi-preparative column is

Table 5.2: Peak statistics for the DRI and QCL traces using either an analytical or semi-preparative column. The EC-QCL source QCL-1 (see Table 5.1) was used at a single wavenumber of $\tilde{\nu} = 1730 \text{ cm}^{-1}$ and current of $I = 1000 \text{ mA}$.

DRI				
Column	FWHM (min)	N	A_s^a	T_f^b
Analytical	6.33	339	1.99	1.94
Semi-prep.	3.17	1328	1.71	1.50
QCL-1				
Column	Wavenumber (cm^{-1})	FWHM	Noise (a.u.)	S/N (-)
Analytical	1730	5.8	0.00021	457
Semi-prep.	1730	2.7	0.00014	520

^a $A_s > 1$ = peak tailing and $A_s < 1$ = peak fronting.

^b Tailing factor $T_f = (a + b)/2a$, where a and b are the distances in min. (or mL) of the peak edge relative to the midpoint of the peak at $1/20^{\text{th}}$ of the peak height.

a factor of ca. 4 higher than the analytical column due to the factor of 2 lower FWHM, and, in addition, has a reduction of 15% and 26% in the asymmetric and tailing factor, respectively. The presented peak statistics are only valid for this specific column-to-flow-cell combination under these specific condition with the sample in question. The improved injection band match of the semi-preparative column to the QCL flow cell has a 13% improvement in S/N relative to the analytical column. Due to the current design of the QCL flow cell, the semi-preparative column, which can handle larger injection volumes, was chosen as the column of choice for the evaluation of the EC-QCL as potential LC detector. These results further indicate that in order to use an analytical column, the flow cell needs to be re-designed which accompanies smaller injection bands, and would not result in too severe in- and out-flow effects. A potential workaround to the re-design of the flow cell could be to make Teflon inserts, which would allow for a desired volume at a fixed flow cell length (this was not executed during the course of the presented results). The optical path length of ca. 4.1 mm (volume = 320 μL) for the flow cell was used for all the measurements, with no additional optimization performed. The reason for this is that at larger optical path lengths the design of the flow cell amounted to severe in- and out-flow effects, accompanied with leakage.

5.3.3 Pulse Averaging

Pulse averaging was investigated to establish whether the S/N of the system can be enhanced. Since balanced detection is utilized, both the reference and sample detectors were investigated. The characterization of the pulse-to-pulse noise of the detectors is presented in **Figure 5.6**. The measurements were performed under static conditions, including the flow cell, filled with THF using the laser source QCL-1 at $\tilde{\nu} = 1900 \text{ cm}^{-1}$ at full power ($I = 1000 \text{ mA}$).

In Figure 5.6, (a) and (b), the averaged response and relative standard deviation of the noise, respectively, for the reference detector are shown, with (c) and (d) corresponding

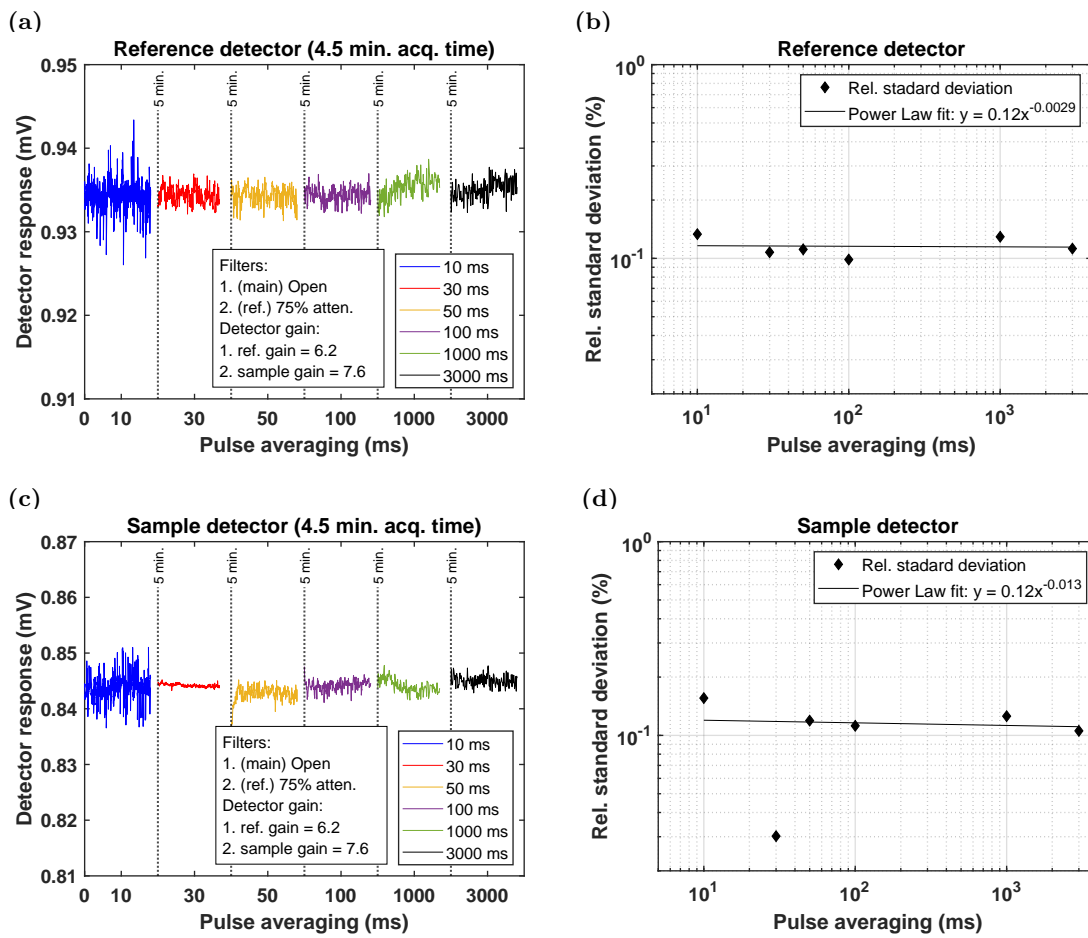


Figure 5.6: Characterization of the pulse-to-pulse noise of the reference and sample detectors, using an optical pathlength of 4.1 mm (320 μL) THF layer, with the QCL-1 source at full power $I = 1000$ mA using a wavenumber of $\tilde{\nu} = 1900$ cm^{-1} . Figures (a) and (b) represent a 4.5 min acquisition time at the respective pulse averages, showcasing the detector response and relative standard deviation of the noise for the reference detector, respectively. Figures (c) and (d) illustrate the aforementioned for the sample detector. The detector acquisition parameters are listed as inset in the respective figures.

to the sample detector. The results were cut and stacked next to each other with a five minute stacking interval. A total of six different pulse averaging times were tested, which included: 10, 30, 50, 100, 1000, and 3000 ms. It is theoretically expected that the noise would decrease with increasing averaging times, of course at the cost of resolution due to a reduction of the data points. Figure 5.6 only represents 4.5 min of acquisition time to illustrate the trend. In Figure 5.6 (a), by visually inspecting the noise, there is a reduction in the noise when using pulse averaging times of > 10 ms, after which it seems to remain constant for the rest of the pulse averaging times.

By closer inspection of the relative standard deviation, Figure 5.6 (b), there is a slight decrease in the noise up to 100 ms pulse averaging, after which it stays constant. This was an unexpected trend as, theoretically, the noise should steadily decrease by using larger pulse averaging times. The same trend was found for the sample detector in Figure 5.6 (c), however, the only difference being that, visually, it is clear that using a 30 ms averaging

on the sample detector reduced the noise significantly. Using a 50 ms pulse averaging resulted in an increase in the noise again, after which it then steadily decreased going to larger pulse averaging times, as expected. The 'outlier' of the 30 ms pulse averaging on the sample detector is an unexpected trend as there would be no physical reason for the jump to be so severe, other than a communication problem between the computer, laser, and detectors of the EC-QCL spectrometer.

5.3.4 Timing Irregularities

The aforementioned was merely a hypothesis, and an investigation related to this was launched to determine if the origin of the communication problem could be understood. The fundamental understanding of the data acquisition cycle of the EC-QCL is schematically illustrated in **Figure 5.7**.

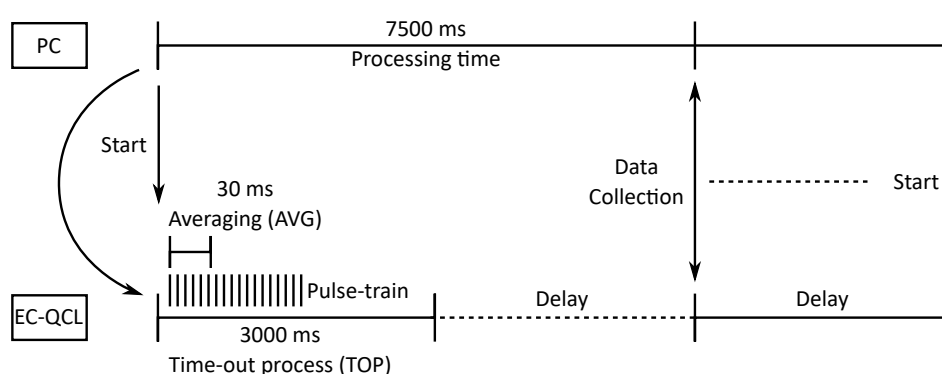


Figure 5.7: Illustration of the data acquisition cycle of the EC-QCL process. The processing cycle represents the pulse averaging time, time-out process time, delay period, processing time and data collection, as conceptually understood about the communication between the QCL computer and the EC-QCL instrument components. PC: personal computer.

In Figure 5.7 the processing cycle, as conceptually understood, is presented with the key timing processes related to data acquisition. After initializing the data acquisition procedure from the Labview software, the pulse-trains are averaged over the desired averaging time period, followed by a time-out process which involves a certain collection period, e.g. 3000 ms, of the averaged data packages. Once these packages have been collected, there is a delay period related to the signal digitization by the ADC, followed by the collection and storage of the data. Using a 30 ms pulse averaging and 3000 ms time-out process combination, amounts to a total read and collect period of 7500 ms. After this the processing cycle continues. It was found that the respective procedures within the data processing cycle resulted in irregular data spacing due to timing problems. The timing problem is not fully understood, nor was any plausible explanation or solution provided by the original software developers of the prototype EC-QCL instrument. The irregular data spacing is presented in **Figure 5.8** measured on QCL-1 at a wavenumber of $\tilde{\nu} = 1900 \text{ cm}^{-1}$. The same spacing problem is observed irrespective of the EC-QCL source employed. As clearly seen from Figure 5.8, the data point spacing is not regular, with all of the different averaging times resulting in two to three different timing ranges, which is a direct result of an internal (communication) timing problem. To show a clear comparison only

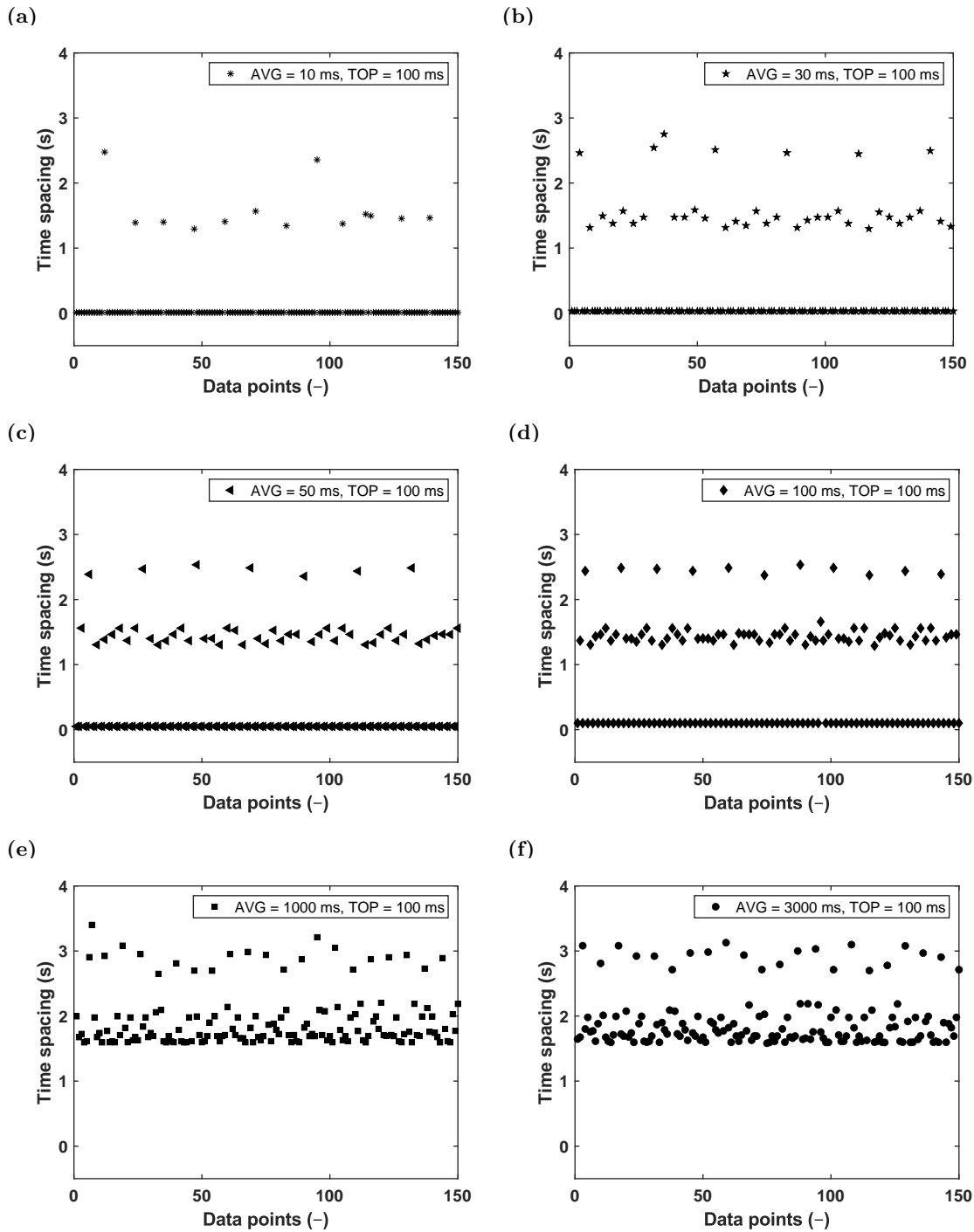


Figure 5.8: Irregular time spacing of the data points collected on the EC-QCL instrument using QCL-1 at $\tilde{\nu} = 1900 \text{ cm}^{-1}$. All of the measurements consisted of a fixed time-out processing (TOP) time of 100 ms. The pulse averaging are presented in the figure as (a) 10 ms, (b) 30 ms, (c) 50 ms, (d) 100 ms, (e) 1000 ms, and (f) 3000 ms.

150 data points have been used for illustration. It seems that when employing a fixed time-out processing (TOP) time of 100 ms and by changing the averaging times from (a) 10 ms, (b) 30 ms, (c) 50 ms, (d) 100 ms, (e) 1000 ms, and (e) 3000 ms, the timing problem worsens. This could potentially be ascribed to the reduction of the TOP, resulting in irregularities, however, this is merely a hypothesis. In Figure 5.8 (e) and (f) the averaging time was purpose fully set to a factor of 10 and 30 longer times, respectively, than the

TOP of 100 ms to determine if this really has an effect. The result indicates that this clearly plays a role, since the pulse averaging of 1000 and 3000 ms only have two timing ranges and not three like the rest, with the majority of the data points being close to zero on the time spacing axis. Considering the top (i.e. time spacing of 2.5 s) and mid-point (i.e. time spacing of 1.5 s) timing ranges for Figure 5.8 (a), the timing irregularities for both the top and mid-point ranges occur a factor of 3, 4, and 6 times more often for the pulse averaging times of 30, 50, and 100 ms, respectively, compared to the 10 ms pulse averaging. In the case of the 1000 and 3000 ms pulse averaging, this occurs a factor of 12 times more for the TOP timing ranges, and 8–12 times for the mid-point ranges, which is due to the TOP being much shorter. Furthermore, by keeping the pulse averaging the same and increasing the TOP time was investigated. A 30 ms pulse averaging was used in conjunction with an increasing TOP of 100, 1000, and 3000 ms. The results are depicted in **Figure 5.9**. It is expected that by increasing the TOP time to values much larger than the pulse averaging time should not have any effect on the data spacing, due to sufficient time for data acquisition and transfer to occur.

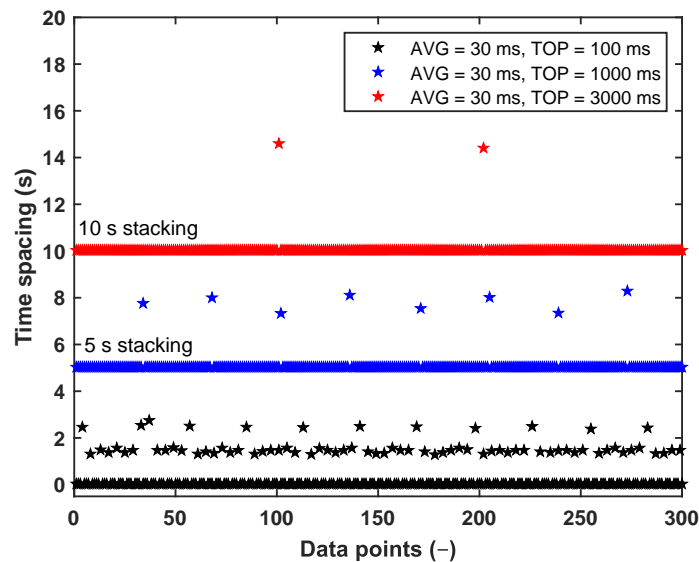


Figure 5.9: Effect of time-out processing (TOP) time on the data spacing irregularities on the EC-QCL instrument. The pulse averaging was kept constant at 30 ms, with the time-out processing time varying from 100–3000 ms. The data sets have been stacked by a five second interval for comparison purposes.

The results are not following the expected trend of having similar data spacing intervals as a function of the TOP, as seen from Figure 5.9. When going to larger TOP times, three main parameters change, (1) there is a reduction in the amount of time spacing ranging, i.e. two for the TOP times of 1000 and 3000 ms, opposed to the 100 ms; (2) the frequency of the timing error is also reduced; and (3) the time spacing between the different time ranges increases. The frequency of the time spacing errors is reduced from every four data points at a 100 ms TOP time, to every 34th data point at a TOP = 1000 ms, and every 101th data point at a TOP = 3000 ms. Furthermore, looking at the spacing between the different time ranges, at a TOP = 100 ms there is a time spacing error difference between the three time

spacing ranges with an average time difference of $\Delta t = 1.28$ s. This then increases to an average time difference at a TOP = 1000 and 3000 ms of $\Delta t = 2.4$ and 4.5 s, respectively. This further confirmed the hypothesis of a system communication problem, which resulted in timing irregularities. The true source of the communication problem was not found, nevertheless, a guideline for error reduction was found by selecting an appropriate pulse averaging and TOP time combination. Although not a perfect solution, it enabled the performance of preliminary testing on the EC-QCL, and assisted in understanding how to perform post data acquisition treatment, which will be detailed in the forthcoming section. From the results obtained in this section, the use of a semi-preparative SEC column is recommended, due to the larger EC-QCL flow cell volume ($V = 320 \mu\text{L}$), which allows for a better volume match to the semi-preparative column. In addition, the use of a pulse averaging time of 30 ms for both the reference and sample detectors were chosen, due to improved noise reduction for the sample detector. This is due to the use of balanced detection, which comprises the division of the sample- by reference-signal. To avoid artefacts due to the timing problem both the detectors used a 30 ms pulse averaging, even though the reference detector showed the best performance at a pulse averaging time of 100 ms. Finally, a time-out processing time of 1000 ms was chosen in combination with the 30 ms pulse averaging, due to the reduced frequency of timing irregularities. In principle it would make sense to use even longer TOP times, however, since the goal is to perform SEC-EC-QCL measurements, and there is only a limited window ($t < 20$ s at $\dot{v} = 1$ mL/min) to detect the analyte species, longer times were not chosen.

5.4 Numerical Data Treatment

This section is dedicated to the development of an in-house written post data acquisition processing software, referred to as Quantum Cascade Laser (QCL) analysis, that enables data processing of the SEC-EC-QCL data. This section provides the highlights of the purpose of the software package, including the various data processing procedures followed throughout the developmental process.

5.4.1 Introduction

As described in Section 4.5 (p. 109), there is a physical limit to what can be altered or changed during the method development phase with respect to the hardware. This is where post data acquisition processing plays an important role to further enhance the overall performance of a characterization technique. The SEC-EC-QCL hyphenation was also part of the project Q1 of the SFB 1176, where one of the objectives was to develop designated software for data processing. As explained in Figure 4.27 (p. 110), a global software structure was developed that enabled the use of various different functions for a certain task. As was the case for the software package developed for the SEC-EC-QCL instrument. The goal is to improve the S/N of the analytes' EC-QCL signal, even though

the EC-QCL is much more sensitive than the MR-NMR, as this could assist in the potential detection of end-groups on polymeric chains. Consequently, a great deal of time was invested in developing appropriate signal processing that would enable optimum system performance for SEC-EC-QCL hyphenation. The data processing software is colloquially referred to as *Quantum Cascade Laser (QCL) analysis*. Similarly to the TMDE software package developed for the SEC-NMR hyphenation, to avoid users having problems with the raw MATLAB script and allow for comparison between users, a graphical user interface (GUI) was developed, with the assistance of Ms. A. Bucka. A stand-alone application was not developed yet, as the EC-QCL instrument still requires some internal software alteration from the companies that was part of the development of the system before the post data acquisition software can be finalized. The GUI for the QCL analysis software is presented in **Figure 5.10**. This allows for a more user-friendly interface, which comes with a step-by-step user documentation (see Appendix A.2, p. 252).

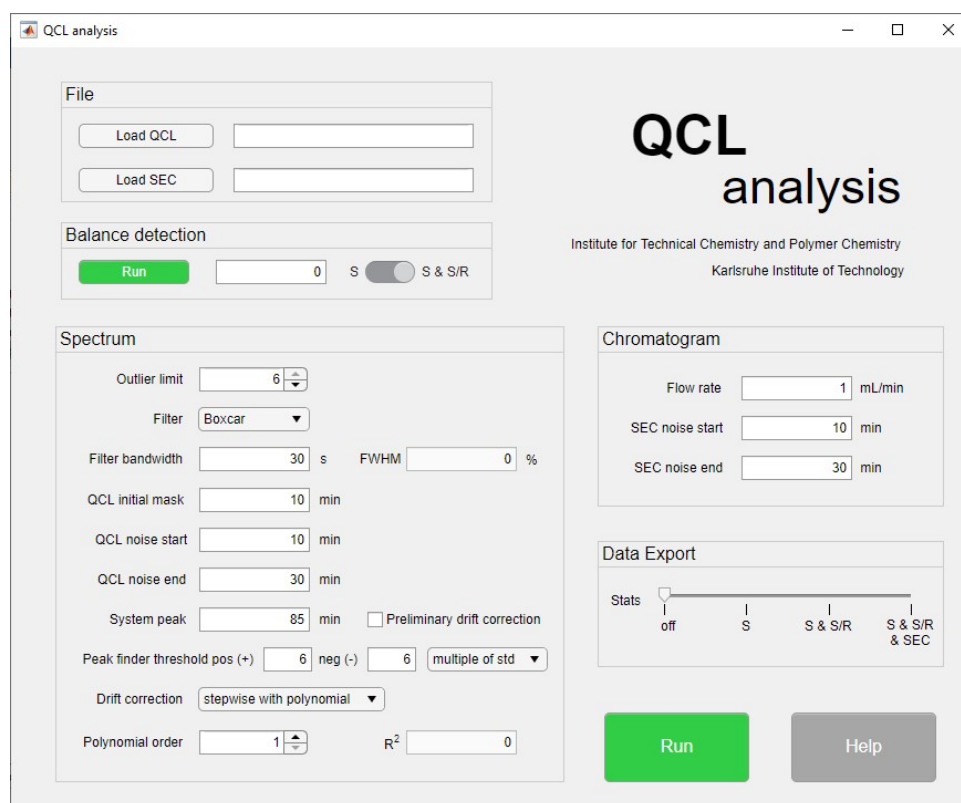


Figure 5.10: The QCL graphical user interface (GUI) for the signal processing of SEC and QCL data. All of the post data acquisition processing is performed within this panel. See the user documentation in Appendix A.2 (p. 252) of the QCL GUI and its various components.

The basic operating principle of the QCL analysis software is briefly explained hereinafter. The EC-QCL data is recorded at a single (selected) frequency over time and stored as a dBASE Structure List Object File (.str format), which is in principle a text file, and only exported after an SEC-EC-QCL measurement was completed. The data is not evaluated immediately due to timing interferences with data points, which worsens when the user performs any computational action such as exporting data, or using the keyboard of the QCL computer when data acquisition is in progress. Subsequently, the QCL software

allows for the evaluation of the stored data in both the SEC and QCL dimensions. The evaluation steps include the following order of events: (1) sample and reference detector correlation; (2) outlier exclusion due to timing irregularities; (3) performing baseline correction and smoothing (de-noising) of the data; (4) conversion of data to absorption; and finally (5) report, store, and visually represent the peak statistics for each of the peaks found. The correlation coefficients for the sample and reference detectors are measured to determine how well they match based on the Pearson correlation coefficients determined from a peak-free area, i.e. typically between 10–30 min. This also provides a measure of whether or not balanced detector correction, i.e. sample/reference detector response should be used or not. Due to the timing problems found, as shown in Section 5.3 (p. 164), applying any form of filter such as a boxcar or Gaussian window function to the data resorted in the formation of artefacts due to irregular data spacing.^[243] A solution, or rather temporary workaround to this problem, was to include a data outlier exclusion function. This involves the removal of data points which are not within a certain threshold of the standard deviation of the raw QCL data. For example, when using the pulse averaging time of 30 ms with a TOP of 1000 ms and setting the outlier threshold in the QCL analysis software to six times the standard deviation of the noise floor, all the data points which are not part of the main data set will be removed from any calculations and corrected for data point fluctuations. Looking at the data in Figure 5.9 (p. 170, the blue data set), every 34th data point will be excluded, and an interpolation would be performed between the consecutive data points. This is not a perfect solution as there would always be a certain degree of error involved related to the missing/removed data points, nevertheless, in order to perform initial testing of the instrument this was a necessary step. For baseline correction and smoothing, automatic peak finding is integrated into the processing for the identification of the location, i.e. elution time, and width of the absorption peaks. This is further used to mask the peak-containing area and exclude the SEC system peak prior to fitting the smoothing function, e.g. 2nd order polynomial, to the data set. The fitted polynomial function then gets subtracted from the data set to perform baseline correction. The corresponding regression coefficients are calculated for the fit function, in order to test if the fit is acceptable or not. It was found that when initially switching on an EC-QCL source and starting a measurement, the first 10 min of recorded data showed the largest amount of laser fluctuations. Similar to the SEC-NMR measurements, the first 10 minutes is excluded (masked) from any further processing in the software. To have more control over the effect of smoothing, which included the boxcar or Gaussian window functions (see Table 4.33, p. 119), the FWHM of the smoothed peaks relative to the raw data are calculated and reported as a percentage in the GUI panel. An acceptable FWHM increase of up to 10% is allowed, as this is within the measurement error of SEC and would not result in a severe reduction in chromatographic resolution. A default window size of 30 s is used in the QCL analysis software, as it was found that for narrowly distributed polymeric species, over-smoothing starts to occur above this point. The subsequent S/N ratios are determined from the maximum peak height of interest (S) to the standard deviation (σ) of the noise ($\sigma = N$) in a signal free region of the QCL spectrum (typically between 10–30

min), after the sequential corrections have been performed in steps (1)–(4).

5.4.2 Baseline Correction and De-noising

Illustrating how data processing is performed on SEC-EC-QCL measurements using the QCL analysis software, a PMMA ($M_w = 49\,400$ g/mol, $D = 1.03$, $c = 5$ g/L) calibration standard was employed, due to the strong carbonyl stretching vibration having its maximum at $\tilde{\nu} = 1730$ cm⁻¹.^[175, pp. 27–29] The aforementioned is beneficial as this is within the tuning range of QCL-1 (see Table 5.1, p. 164), which is the source that allows for the highest energy input of $I = 1000$ mA. The PMMA sample was characterized in THF at a volumetric flow rate of 1 mL/min and injected mass of 80 µg using a linear M semi-preparative SEC column (see Table 4.3, p. 76). As an example the recorded raw data at $\tilde{\nu} = 1730$ cm⁻¹, corresponding to the highest measured S/N , are shown in **Figure 5.11**.

As seen in Figure 5.11 (a), by employing the balanced detector correction, i.e. sample/reference detector response, signal fluctuations are minimized resulting in a more linear response, which makes drift correction an easier (mathematical) task. This correction is especially visible when comparing the elution time of 10–40 min of the top and bottom part of Figure 5.11 (a). The success of the balanced correction in this particular example is also attributed to the high correlation between the reference and sample detector, which had a Pearson correlation coefficient³ of 0.9443. If this value is far off from unity, balanced correction would have an adverse effect on reducing laser fluctuations. The data was smoothed with a 30 s Gaussian window function, and had an increase in the FWHM of 10.1% relative to the raw data. For baseline correction a step-wise 2nd order polynomial, with a regression of $R^2 = 0.9975$, was employed. In **Figure 5.12** an overview of smoothing and baseline fit combinations are provided on the sample at hand to illustrate their effect on S/N .

As shown in Figure 5.12, when using a filter band width of 1, 10, 30, and 60 s, the Gaussian window function outperforms the boxcar with respect to the enhancement in S/N , as expected. Due to the strength of the Gaussian window function, over-smoothing occurs much faster than in the case of the boxcar window function. With this in mind, caution should be exercised when employing a stronger smoothing function. Subsequently, the use of the pre-defined limit of an FWHM increase of 10% (FWHM = 148.5 s) assists in making a better judgement. In Appendix A.7, Table A.4 (p. 281), a full numerical overview on the use of the filter and polynomial fit order combinations is provided. It was found that for the specific sample under investigation, a 30 s Gaussian window function (FWHM = 148.7 s, 10.1%) and a 2nd order polynomial baseline correction amounted to the best enhancement in S/N (= 102). When comparing the highest obtainable S/N (= 77.8) for the best combination of the boxcar filter (band width = 60 s, fit = 2nd order polynomial, FWHM = 147.2 s, 9.0%) to the raw data S/N (= 23.1), the S/N increases with a factor of 3.4, and for the best Gaussian combination by a factor of 4.4 at $\tilde{\nu} = 1730$ cm⁻¹. An illustration of the effect of smoothing on the EC-QCL signal is presented in **Figure 5.13**

³In statistics the Pearson correlation coefficient (r) describes the linear correlation between two variables x and y , having values ranging between -1 and +1. A positive linear correlation has an $r = 1$, total negative linear correlation $r = -1$, and $r = 0$ having no linear correlation.

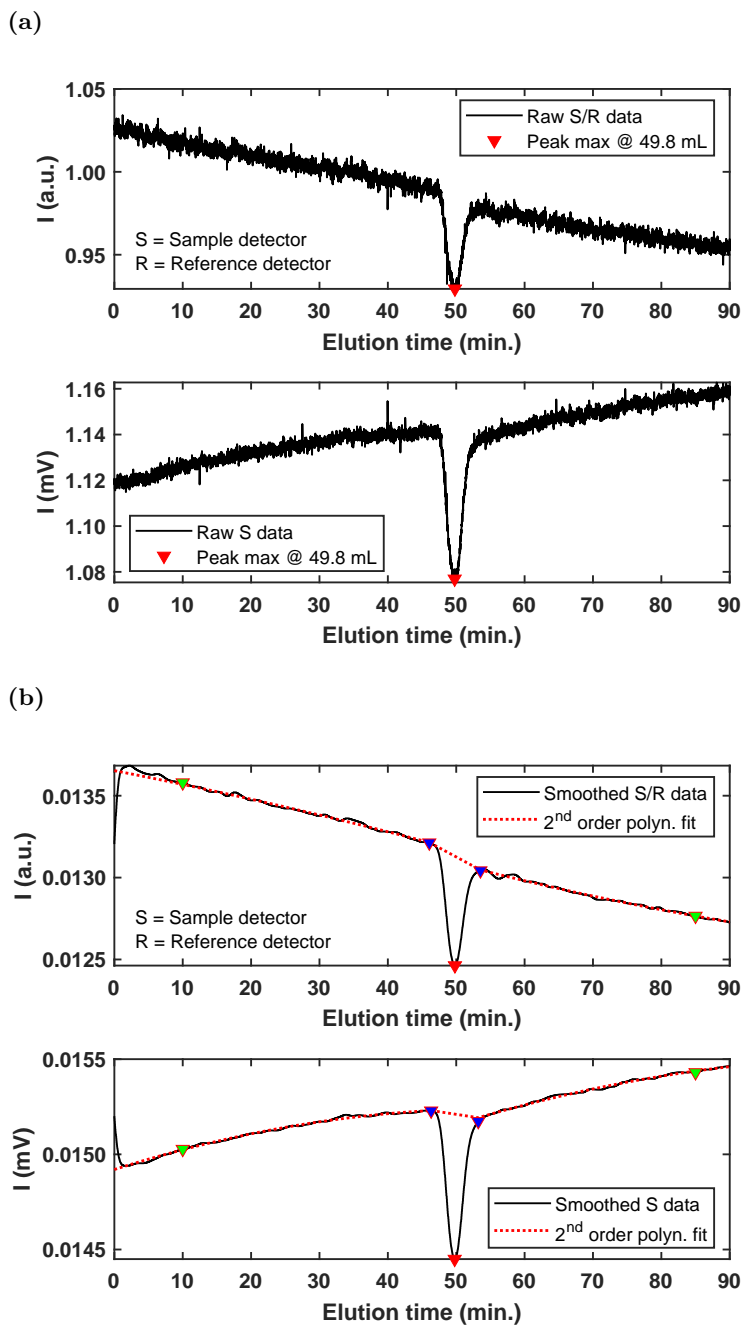


Figure 5.11: Baseline correction and de-noising of an SEC-EC-QCL measurement of PMMA ($M_w = 49\,400$ g/mol, $D = 1.03$, $c = 5$ g/L) calibration standard using the QCL analysis software. The measurement was performed at a flow rate of 1 mL/min in THF with an injected mass of 80 μ g at a single wavenumber of $\tilde{\nu} = 1730$ cm^{-1} . In figure (a) the raw data is illustrated with the peak maximum marked with a red triangle. The top part of figure (a) represents the balanced detector response and bottom part only the sample detector. Figure (b) illustrates the smoothed data with a Gaussian window function comprising of a 30 s window size, after which the data is fitted with a step-wise 2nd order polynomial function for baseline correction. The top part and bottom part of (b) represents the balanced and sample detector responses, respectively.

As shown in this section, numerical data treatment is a beneficial part to the optimization of the SEC-EC-QCL characterization. It enables the processing of data, which has hardware related challenges, such as the timing irregularities, and allows for a simple and effective way of further enhancing the S/N of an already powerful technique. In the example illustrated,

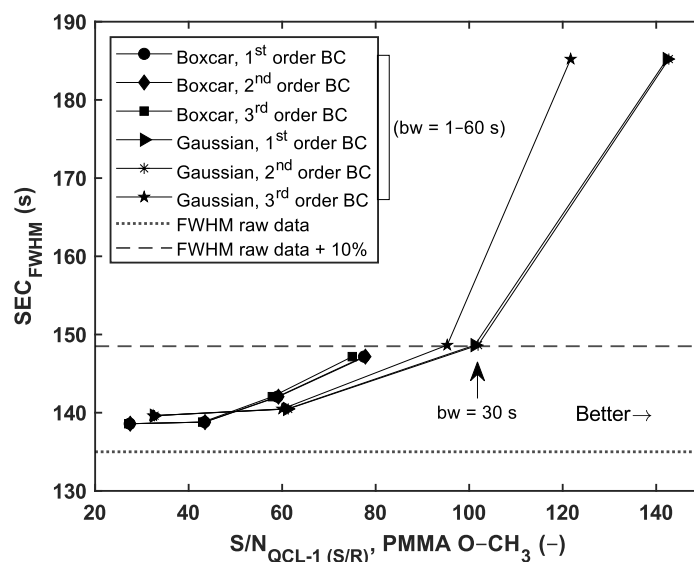


Figure 5.12: Effect of different smoothing and baseline fit combinations in SEC-EC-QCL on the S/N and FWHM determined on the carbonyl group ($C=O$, $\tilde{\nu} = 1730 \text{ cm}^{-1}$) of a PMMA calibration standard ($M_w = 49\,400 \text{ g/mol}$, $D = 1.03$, $c = 5 \text{ g/L}$). The measurements were performed in pulsed-mode using QCL-1 – see Table 5.1 (p. 164). A flow rate of 1 mL/min with a total injected mass of $80 \mu\text{g}$ of analyte was used. See Appendix A.7, Table A.4 (p. 281) for details. The S/N values were calculated from the sample divided by the reference detector response (S/R), i.e. balanced detection.

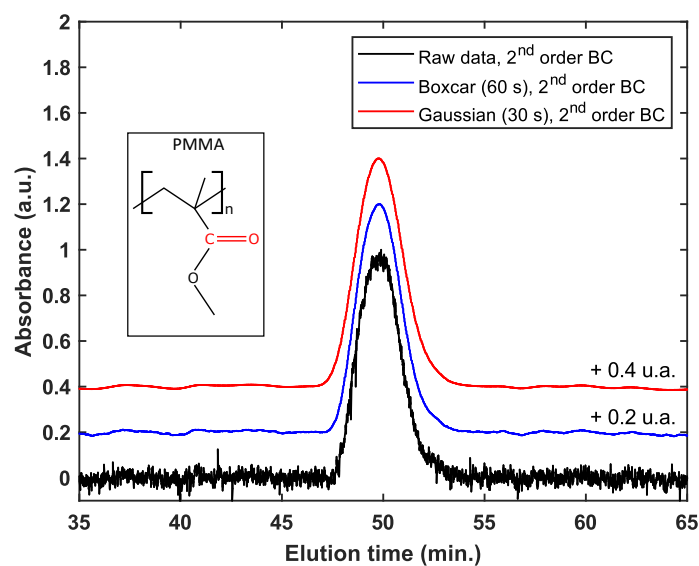


Figure 5.13: Smoothing comparison of a boxcar (60 s) and Gaussian (30 s) window function relative to the raw EC-QCL data measured at $\tilde{\nu} = 1730 \text{ cm}^{-1}$. The boxcar window function consisted of a 60 s bandwidth in combination with a 2nd order polynomial baseline correction (BC). The Gaussian window consisted of a 30 s bandwidth in combination with a 2nd order polynomial BC. The measurement was performed in THF at $\dot{\nu} = 1 \text{ mL/min}$.

post data acquisition allowed for a S/N enhancement of a factor of 4. This could be further improved by the addition of more advanced window functions, as in the case of the SEC-NMR software TMDE, and with the fine tuning of hardware related challenges like improvements in flow cell design and communication efficiency. The processing of

data, with respect to filter and fit combinations, is subject to the experimental conditions employed, such as the sample, solvent, flow rate, and pulsed-mode vs. scan-mode operation, to name a few.

5.5 Sensitivity Limits

This section explores the sensitivity limits with respect to the limit of detection (LOD) and -quantification (LOQ). The results will be compared to that of a standard FT-IR spectrometer, including the first prototype QCL presented by Morlock et al.^[8] to put the sensitivity of the new EC-QCL instruments in perspective.

5.5.1 Introduction

In the development of newly hyphenated techniques, such as SEC-EC-QCL, where the EC-QCL acts as a chemical sensitive detector, the limits, or at the very least approximations of the detection limits, such as the limit of detection and quantification (see Section 2.4.2, p. 50), is key in gauging the end-use or application of the technique. The limits will be explored for the SEC-EC-QCL in its current conditions, and it is expected that an improved result over the presented result will be obtained on the set-up once all the hardware related challenges have been finalized. The LOD and LOQ determination was chosen as it is presumably the most effective way of quantifying the sensitivity of the instrument.

5.5.2 LOD and LOQ Determination

The LOD and LOQ for the on-line hyphenated SEC-EC-QCL technique was measured on a PMMA calibration standard ($M_w = 49\,400$ g/mol, $D = 1.03$, $c = 5$ g/L) at $\tilde{\nu} = 1730$ cm⁻¹ due to the strong absorbance of the carbonyl group (C=O) at this wavenumber. A 2 mL stock solution of the sample was placed within the auto-sampling unit of the SEC system, where a series of six different injection volumes, i.e. 500, 50, 16, 5, 1.5, and 1 μ L, was introduced into the SEC-EC-QCL set-up. This amounted to a total injected mass of the PMMA sample of 2500, 250, 80, 25, 7.5, and 5 μ g. Although the volume changes, the injected mass is the crucial part, as it would result in the same principle of making a concentration series comprising of seven individual sample concentrations but using the same injection volume. The advantage of injecting smaller volumes is that there is fundamentally only one major source of error, which is the auto-sampler, as opposed to seven individually prepared samples, which would result in more scattering of the data points. The measurements were performed in THF as mobile phase at a volumetric flow rate of 1 mL/min. The corresponding results are presented in **Figure 5.14**.

As seen in Figure 5.14, the result for the SEC-EC-QCL measurements show the expected linear trend between the S/N (of the carbonyl group) and injected mass of the PMMA sample. The absolute system noise is not dependent on the injected mass of PMMA, as the noise was taken in a region of the elugram where only THF elutes. As seen from the

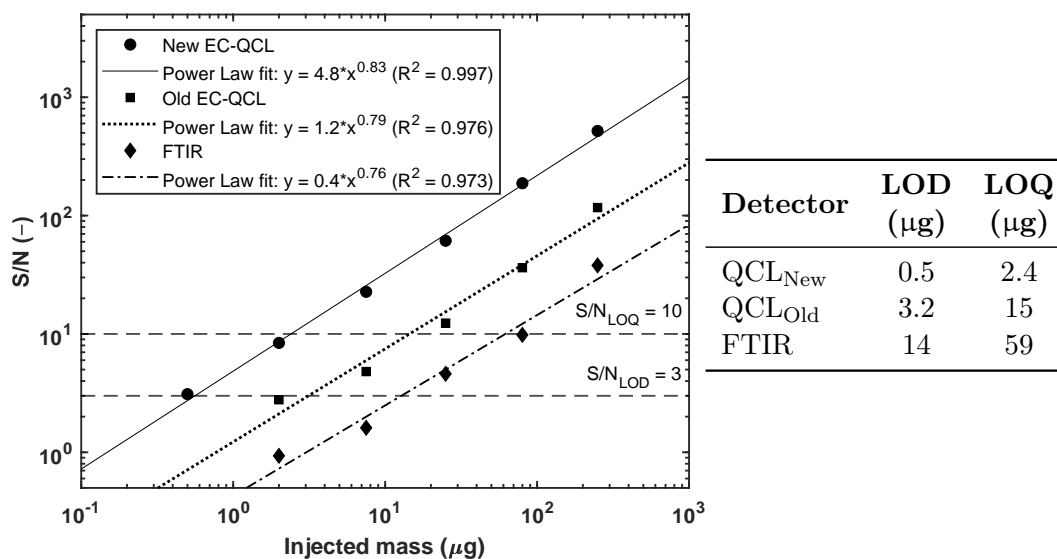


Figure 5.14: The S/N measured on the carbonyl group ($C=O$, $\tilde{\nu} = 1730 \text{ cm}^{-1}$) as a function of the injected mass of a PMMA calibration standard ($M_w = 49\,400 \text{ g/mol}$, $D = 1.03$, $c = 5 \text{ g/L}$) via SEC-EC-QCL. The LOD and LOQ determination on the SEC-EC-QCL set-up is compared to the FTIR and EC-QCL measured by Morlock et al.^[8] The two horizontal dashed lines represent the LOD ($S/N = 3$) and LOQ ($S/N = 10$) limits. These limits for the respective data sets were determined by the intercept of the power law fits employed. The measurements were performed in THF at a flow rate of 1 mL/min. Data for the SEC-FTIR and -QCL are reproduced with permission.^[8] Copyright 2018, Wiley-VCH. See Figure 4.52 (p. 147) for comparison to SEC-NMR.

respective data sets, the new EC-QCL spectrometer have a significantly higher sensitivity than the FTIR and (old) EC-QCL. For the LOD values, the new EC-QCL is a factor of 6.4 and 28 lower than the previous EC-QCL and FTIR, respectively. Similar improvements in S/N enhancement compared to an FTIR spectrometer have been published by Lendl et al.,^[196] with improvements in S/N of a factor of 50 when using a QCL detector in lieu of an FTIR spectrometer. The reader is also referred to Childs et al.^[244] for an overview of the sensitivity advantage of QCLs over FTIR spectrometers. The larger jump compared to the previous EC-QCL spectrometer is mostly ascribed to the use of liquid nitrogen cooled MCT detectors on the new EC-QCL compared to the previous less sensitive LiTaO₃ detectors. The LOD for the new EC-QCL of ca. 0.5 μg, clearly shows its potential as chemical sensitive detector for SEC, compared to FTIR or (not presented here) MR-NMR. The enhancement in sensitivity might allow for end-group analyses, as this type of information is of particular importance in fields of surface modifications, which requires the characterization of low quantity organic functional groups present in the material. The disadvantage of using SEC-EC-QCL, compared to bulk techniques such as SEC-FTIR or -NMR, is the limited wavelength (at much higher sensitivities) typically available for these instruments. Nevertheless, these hyphenated techniques and their true power as characterization source are best exploited when used as a complementary technique to each other, or ultimately in a single line-up.

5.6 EC-QCL as Potential SEC detector

The forthcoming section describes the application possibilities of the new SEC-EC-QCL technique. It will provide an overview of the potential of the developed technique with a focus on the characterization of a physical blend of two homopolymers and a homopolymer with specific functionality.

5.6.1 Introduction

The evaluation phase of the newly developed SEC-EC-QCL technique is to establish how well the EC-QCL will perform as a chemically sensitive detector for SEC. The aim is that the EC-QCL acts as a universal chemical sensitive detector, which is applicable on-line, and allows for the identification and quantification of compounds as a function of the different eluates and/or molar mass (see Figure 3.1, p. 57). Similar to the SEC-NMR hyphenation, the ultimate goal is that the technique can be employed with any polymer-solvent combination, in conjunction with size exclusion chromatography that would enable the determination of the standard SEC parameters, such as M_w , M_n and D , including the detection of the chemical composition of the eluting species. The main advantage of hyphenating EC-QCL to SEC, is the major improvement in sensitivity, which makes method development, with respect to chromatography, easier as it performs at its optimum when lower concentrations are used. During the course of the presented work, including this section, a semi-preparative column (see Table 4.3, p. 76) was employed for optimization purposes. However, in future developments this can be replaced by smaller analytical SEC columns, and even smaller interaction based columns, i.e. C18 non-polar columns, used for reversed-phase liquid adsorption chromatography (RP-LAC) due to the unique sensitivity. An investigation of a PS/PMMA physical blend and acetylated PS sample will be presented and characterized qualitatively using the SEC-EC-QCL hyphenated technique.

5.6.2 Homopolymers and Blends

To illustrate how SEC-EC-QCL can differentiate between two overlapping homopolymers, a PS ($M_w = 21\,200$ g/mol, $D = 1.02$, $c = 4.3$ g/L) and PMMA ($M_w = 49\,400$ g/mol, $D = 1.03$, $c = 1.4$ g/L) calibration standard were physically blended (4:1 wt%) and investigated. The lower weight percentage of the PMMA and molar mass difference of a factor of 2 between the PS and PMMA (non-baseline separated species) were purposefully chosen to test the SEC-EC-QCL technique under more challenging sample conditions. As described in Section 5.2 (p. 160), the three different QCL laser sources available have a limited wavelength range. Subsequently, the individual full mid-IR FTIR spectra were acquired for the PS, PMMA, and THF using the attenuated total reflectance (ATR) accessory of the FTIR spectrometer, as this would provide a clear indication as to where the least amount of spectral interference from the solvent would occur. The latter assists in selecting the appropriate EC-QCL source, and provides hints on which wavenumbers would be of

interest for analyte characterization. The FTIR comparison of the PS, PMMA, and THF is presented as a stacked spectrum in **Figure 5.15**.

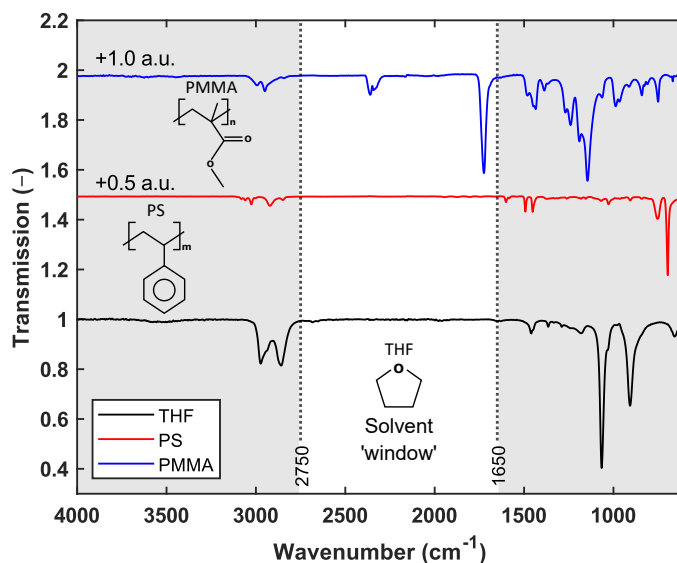


Figure 5.15: Stacked FTIR spectra of PS ($M_w = 21\,200$ g/mol, $D = 1.02$, solid), PMMA ($M_w = 49\,400$ g/mol, $D = 1.03$, solid), and THF acquired on a Bruker v70 FTIR spectrometer using an ATR attachment for the measurements. The grey regions from $\tilde{\nu} = 4000\text{--}2750$ and $1650\text{--}600$ cm^{-1} indicate where solvent-analyte interference occurs. The white region from $\tilde{\nu} = 2750\text{--}1650$ cm^{-1} represents the solvent 'window', ideal for analyte characterization.

In Figure 5.15 it becomes clear that the available region where minimal solvent interference occurs is only in a small portion of the identification/functional group region ($\tilde{\nu} \leq 1500$ cm^{-1})^[175, p. 16] of the mid-IR region at a wavenumber range of $\tilde{\nu} = 2750\text{--}1650$ cm^{-1} . It should be noted that the QCL analysis software removes the solvent, but as with any solvent subtraction, it is not a perfect process. Therefore, to reduce the solvent influence as much as possible, a range was selected where practically no interference occurs. Considering Figure 5.3 (p. 163), only two EC-QCL sources are applicable to the aforementioned range, QCL-1 and QCL-2. However, QCL-1 was chosen due to its higher current range compared to QCL-2 (see Table 5.1, p. 164), amounting in higher reachable sensitivities. Since PMMA has the isolated and strong absorbing carbonyl stretch vibration (C=O) at a wavenumber of $\tilde{\nu} = 1730$ cm^{-1} , which falls within the solvent 'window' and QCL-1 range, it was chosen for identification. Consequently, for the SEC-EC-QCL measurement the EC-QCL source QCL-1 at $\tilde{\nu} = 1730$ cm^{-1} at full power $I = 1000$ mA, was used for the EC-QCL detection. Furthermore, the analysis was performed on a semi-preparative SEC column at a flow rate of 1 mL/min with an injected volume of 10 μL (PS = 43 μg and PMMA = 14 μg injected mass) and a DRI detector at the end of the SEC-EC-QCL set-up. The results for the SEC-EC-QCL characterization of the PS/PMMA blend is presented in **Figure 5.16**. The data in Figure 5.16 was processed by using a 15 s Gaussian window function in combination with a 2nd order polynomial baseline correction as it provided the best S/N without significantly broadening the peak FWHM. The S/N for the carbonyl stretching vibration was $S/N = 37.7$, with an increase in FWHM of 7.5% relative to the raw data. Furthermore, it was possible to successfully distinguish the PS ($V_e = 52.1$ mL) and PMMA

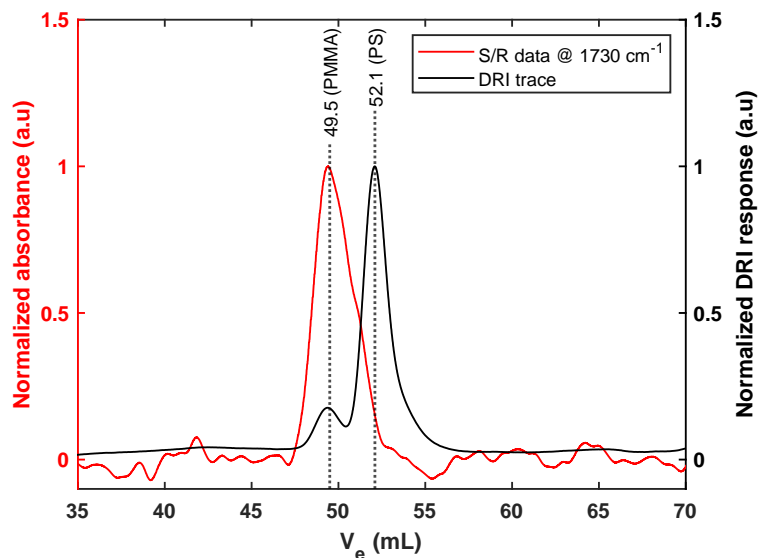


Figure 5.16: SEC-EC-QCL analysis of a PS/PMMA physical blend ($M_w = 21\ 200/49\ 400$ g/mol, $D = 1.02/1.03$, 4:1 wt%, $c = 5.7$ g/l) measured in THF at $\dot{v} = 1$ mL/min with a total injected mass of 43 and 14 μg for the PS and PMMA components, respectively. The EC-QCL source QCL-1 at a (single) wavenumber of $\tilde{\nu} = 1730\ \text{cm}^{-1}$ with a pulse width of 540 ns at full power ($I = 1000$ mA) was used. The S/R trace indicates that balanced detection was employed. The gain (G) setting on the sample (S) and reference (R) detectors were as follows; $SG = 6.4$ and $RG = 7.4$, with filter wheel settings of: main: 50% and reference: 50% attenuation.

($V_e = 49.5$ mL) fraction from each other using the EC-QCL as a chemically sensitive detector. The QCL trace overlays nicely with the DRI trace (adjusted for added dead volume of $V = 320\ \mu\text{L}$) confirming that the higher molar mass portion of the PS/PMMA blend belongs to the PMMA component. The results are impressive considering the flow cell is not optimal, as it has severe in- and out-flow effects, and that the detection is possible at injection volumes typically employed for interaction mode chromatography (also referred to as HPLC). This illustrates the potential of this technique as 'add-on' detector for chromatography at typical chromatographic concentrations and far below. One disadvantage is that a priori information of the sample, i.e. chemical composition, is required to choose the correct wavenumber for characterization. The use of the EC-QCL can be further exploited when used in scan mode opposed to single wavenumber mode, which allows for the continuous detection of the entire wavelength range. Unfortunately, during the course of this work, the scan mode on the EC-QCL spectrometer was not properly functioning due to instrumental communication challenges.

5.6.3 Functionalized Homopolymer

This section is dedicated to the characterization of a functionalized homopolymer, acetylated polystyrene (ac-PS). Polystyrene has a variety of properties, which makes it a favourable material in many fields. An example is syndiotactic polystyrene that has a very high melting point (270 $^{\circ}\text{C}$), low density, good chemical resistance, a rapid crystallization rate, and commendable mechanical properties, which makes it attractive in fields such as the

automotive and packaging industries. Like atactic polystyrene, it lacks certain properties such as impact resistance and low surface energies.^[245,246] Subsequently, the lack or absence of polar groups limits its end uses, like adhesion applications and the compatibility with other polar polymers. This has led to the interest in functionalizing PS to alter its chemistry for end-use applications. The modification of PS by adding polar groups is typically achieved via grafting onto the PS backbone. The sample under investigation was prepared via an acetylation reaction to prepare the acetylated polystyrene.^[245,246] The in-house synthesized ac-PS ($M_w = 70\,000$ g/mol, $D = 1.65$, $c = 2$ g/L) sample has an acetylation content of 15.8 mol%, determined by high field $^1\text{H-NMR}$ spectroscopy. The characterization of the acetylated (ac) PS was further confirmed by means of FTIR spectroscopy. The corresponding results, consisting of the stacked (0.25 a.u.) FTIR spectra of the pure PS and ac-PS are illustrated in **Figure 5.17**.

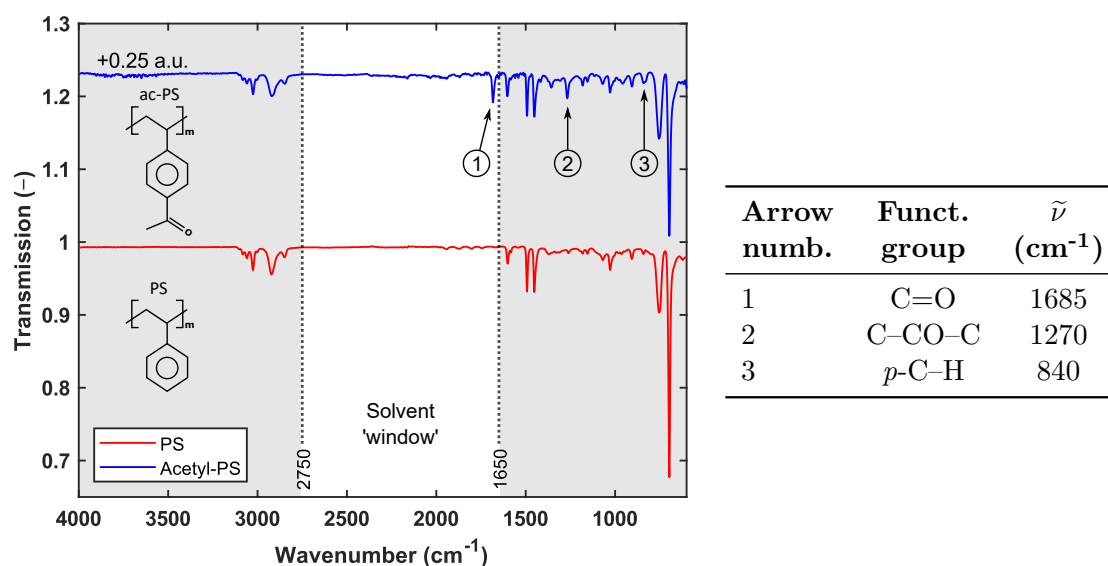


Figure 5.17: Stacked FTIR spectra of PS ($M_w = 21\,200$ g/mol, $D = 1.02$) and acetylated PS ($M_w = 49\,400$ g/mol, $D = 1.03$) acquired on a Bruker v70 FTIR spectrometer using an ATR attachment for the measurements. The grey regions from $\tilde{\nu} = 4000\text{--}2750$ and $1650\text{--}600$ cm⁻¹ indicate where solvent-analyte interference occurs in THF. The white region from $\tilde{\nu} = 2750\text{--}1650$ cm⁻¹ represents the solvent 'window', ideal for analyte characterization.

Similar to Figure 5.15 (p. 180), in Figure 5.17 the grey zones represent the regions where solvent interference from THF occurs. The most prominent IR bands for confirming the acetylation of the PS are observed at the wavenumbers $\tilde{\nu} = 1685$ and 1270 cm⁻¹, which are ascribed to the carbonyl (C=O) and aromatic ketone (C-CO-C) stretching and bending vibrations, respectively.^{[247–249][175, p. 59]} It is evident from Figure 5.17 that these vibrations are absent for the neat PS sample. In addition, further proof that the PS has been acetylated is provided by observing the increased intensity of the IR band at $\tilde{\nu} = 840$ cm⁻¹, corresponding to the out-of-plane C-H vibrations of the *para* (*p*)-substituted benzene.^[247] This evidence suggests that the acetylation has occurred predominantly at the *p*-position. Fortunately, from the FTIR analysis of the ac-PS, the presence of the

carbonyl stretching vibration of the acetyl moiety can further be investigated by means of SEC-EC-QCL analysis. Due to the lower acetylation content, ie. 15.8 mol%, of the sample, the QCL-1 source was chosen due to its higher current range, and because it covers the spectral range of the acetyl group. For the SEC-EC-QCL analysis, a $c = 2$ g/L Ac-PS ($M_w = 70\,000$ g/mol, $D = 1.65$, ac = 15.8 mol%) diluted with a $c = 1$ g/L neat PS ($M_w = 265\,000$ g/mol, $D = 1.04$) sample was prepared in THF, with an injected volume of 500 μL into the linear M SEC column at a volumetric flow rate of 1 mL/min. The SEC-EC-QCL measurement is presented in **Figure 5.18**.

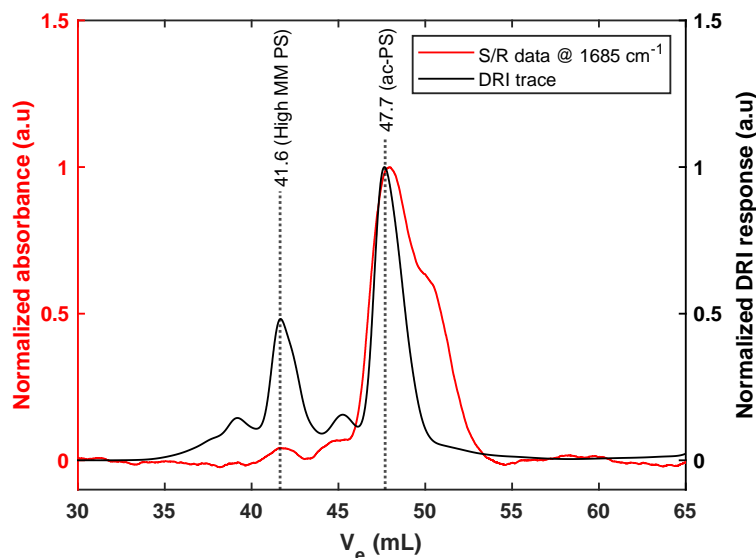


Figure 5.18: SEC-EC-QCL analysis of an ac-PS sample ($M_w = 70\,000$ g/mol, $D = 1.65$, ac = 15.8 mol%, $c = 2$ g/L) diluted with a pure PS ($M_w = 265\,000$ g/mol, $D = 1.04$, $c = 1$ g/L) sample, measured in THF at 1 mL/min with a total injected mass of 1 and 0.5 mg for the ac-PS and pure PS components, respectively. The EC-QCL source QCL-1 at a wavenumber of $\tilde{\nu} = 1685$ cm^{-1} with a pulse width of 540 ns at full power $I = 1000$ mA was employed. Balanced detection was employed. The gain setting on the sample (S) and reference (R) detectors were as follows: SG = 12.5 and RG = 18. The filter wheel settings were: main: 75% attenuation, and reference: open (no attenuation).

As evident from Figure 5.18, the presence of the carbonyl stretch ($\text{C}=\text{O}$, $\tilde{\nu} = 1685$ cm^{-1}) of the acetyl group was confirmed by means of SEC-EC-QCL analysis, as the EC-QCL trace overlays well with the DRI trace associated to the ac-PS fraction ($V_e = 47.7$ mL). Upon closer inspection of the DRI trace, the presence of two small peaks at the base of the main peaks at $V_e = 41.6$ and 47.7 mL are observed. These small peaks are ascribed to coupling by-products occurring during synthesis having a molar mass close to a factor of 2 higher than the main polymeric species. The data processing for the ac-PS sample included the use of a 60 s boxcar averaging in conjunction with a 2nd order polynomial baseline correction and provided the best S/N without significant peak broadening. Due to the peak shape, the Gaussian filter resulted in too severe band broadening and was therefore not used. The S/N for the carbonyl stretching vibration was $S/N = 177$, with an increase in FWHM of 8.7% relative to the raw data. Although the injected masses were not very low during this example, it does, however, provide insight on the end-use of the SEC-EC-QCL

set-up, as this is the first result on the current SEC-EC-QCL set-up, provided on the detection of functionalities on the backbone of an ac-PS sample. With some additional system optimization, the SEC-EC-QCL technique could be used for the routine detection of polymeric end-groups, whilst simultaneously measuring standard SEC parameters. This EC-QCL spectrometer is a unique instrument with respect to its sensitivity, having a factor of 28 improvement in LOD as opposed to an FTIR spectrometer. It is this sensitivity that opens the possibilities for measuring certain characteristic details of polymeric species that was previously not possible, opening a plethora of end-uses. As the results presented were an evaluation with respect to testing the EC-QCL as potential LC detector, the results indicate that the spectrometer would be of high value to the coupling of interaction-based chromatography, where much lower sample concentrations are employed. In conclusion, the examples illustrated within this work highlight the importance and potential commercial relevance of the development of new EC-QCL sources in the field of spectroscopy.

Chapter 6

Novel SEC method for S/N Enhancements

This chapter has a method development theme focussing on the proof of principle of a novel SEC approach referred to as sinusoidal SEC to enhance the obtainable S/N of a given analyte. The technique will be compared to standard single SEC injections. The approach of interlaced SEC will also be demonstrated, as this was the precursor technique for the development of sinusoidal SEC injections. This chapter is subdivided into three sections, namely: introduction, interlaced SEC injections, and the proof of principle for sinusoidal SEC. Each section consists of an introductory part, followed by the corresponding results and discussion and finally ending with the concluding remarks.

6.1 Introduction

One of the major challenges in separation science is to increase the sensitivity without further pre-concentration steps. Considering the different available modes of liquid chromatography (see Figure 2.1, p. 8), SEC often has a lower sensitivity, especially when hyphenated to detectors such as NMR.^[250] Consequently, it is typically desirable to perform method development with respect to enhancing the sensitivity of the detection. Size exclusion chromatography (SEC) is a widely used and well-known technique used for polymer characterization. Taking into consideration the subtleties of the separation mechanism and the frequently observed partial resolutions of components in these separations, many techniques for enhancing the method throughput have been applied. However, these are not always as practical as intended and generally trade-off resolution for speed.^[17-19,250,251] Shorter columns, high flow rates and reduced particle sizes of column material are examples of these approaches.^[17,52] In this work, a new technique will be demonstrated practically, where an unconventional ‘sinusoidal injection’ procedure is utilized to enhance the achievable sensitivity by an average factor of 70. Opposed to conventional single SEC injections where the chromatographic column is only partially utilized, the new proposed approach involves the continuous use of the column by applying an oscillatory solvent-analyte gradient,

based on a sinusoidal excitation function. A rudimentary theory was developed to show that the throughput improvements can be predicted to approximation by simple column characteristics. Experimental results for a series of unconventional ‘sinusoidal injections’ demonstrate the equivalency of the method to a conventional injections approach, the throughput increase, and pitfalls of the technique. The recorded sinusoidal detector traces are used to extract the analyte specific phase-angles with the aid of Fourier transformation. Similar to conventional SEC, where a molar mass relative to elution volume (or time) calibration is constructed to extract molar mass specific information, in sinusoidal SEC a phase-calibrated molar mass calibration is constructed for this purpose. The differences between single, interlaced, and sinusoidal SEC injections are depicted in **Figure 6.1**.

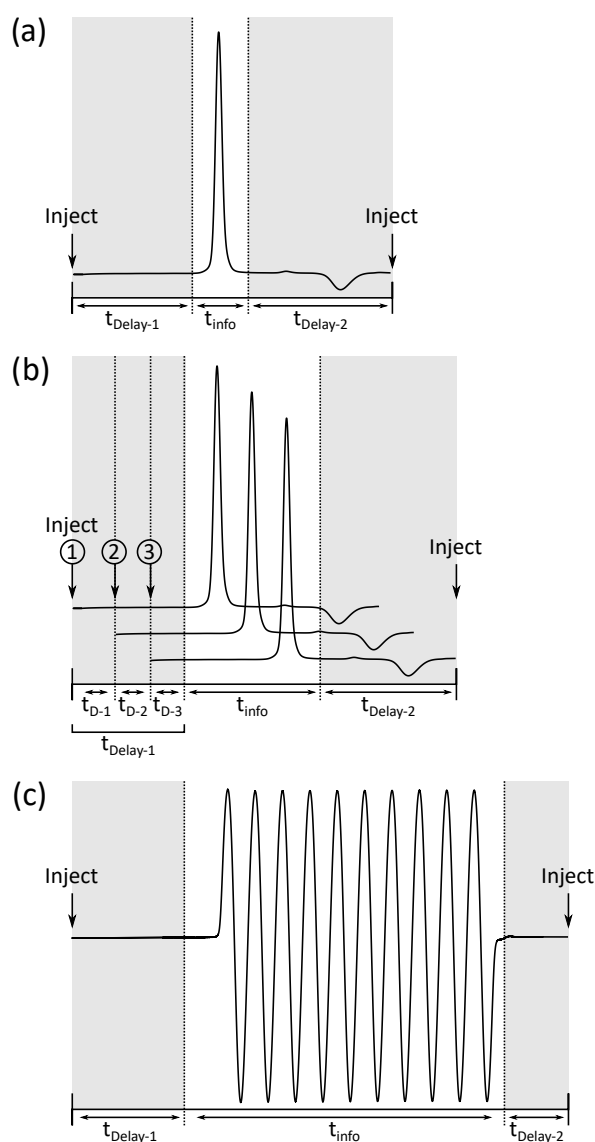


Figure 6.1: Comparison between (a) single, (b) interlaced, and (c) sinusoidal SEC injections for *S/N* enhancement. The elution phases in (a) correspond to the initial delay time, $t_{\text{Delay-1}}$, after sample injection, followed by analyte elution, i.e. information time, t_{info} , and then finally by a holding period, $t_{\text{Delay-2}}$, which involves waiting for system peak, salts etc., and stabilization of the pressure prior to the next injection for analysis. In (b), shorter delay times, $t_{\text{D-1}}$, $t_{\text{D-2}}$, and $t_{\text{D-3}}$, exist within $t_{\text{Delay-1}}$, corresponding to the delay times required to achieve interlacing.

As the major focus of this thesis was on the method development of SEC-MR-NMR hyphenation, the end-goal of the development of the novel SEC method for S/N enhancement is to utilize it in conjunction with SEC-MR-NMR, due to the lower sensitivity of NMR as a detector in general. This is especially true when using a benchtop NMR spectrometer with carrier frequencies $F < 60$ MHz ($B_0 < 1.45$ T), which has detection limits in the microgram range.^[14,88] Consequently, the sinusoidal SEC injection method could potentially be used to increase the sensitivity of SEC-NMR measurements.

The forthcoming sections will elaborate on the newly developed technique, sinusoidal SEC, with a comparison to obtainable S/N compared to single SEC injections. The idea of the sinusoidal SEC concept evolved from the interlaced SEC injection principle, which will briefly be described.

6.2 Interlaced SEC Injections

As the demand for higher throughput systems increase, the efficiency with respect to shorter measurement times becomes of importance. One solution to the problem is to simply expand the existing SEC equipment to allow for multiple conventional measurements simultaneously; however, this is not a cost-efficient solution. One crucial constraint for increasing system efficiency, is that the results obtained on the optimized system should be comparable to that of the conventional technique. As previously mentioned, much focus has been placed on optimizing SEC, with respect to miniaturization for faster and more efficient SEC, as described by Striegel.^[17] This has shown a great improvement in increasing the separation throughput and reducing measurement times up to as much as 90%.^[252] The major disadvantage is that 'the price paid' for speed is a reduction in the quality of the separation. A straightforward approach to increase the throughput in SEC by as much as a factor of 2, achievable via interlaced SEC without severely compromising the separation efficiency, has been illustrated as an effective alternative by Farnan et al.^[19] This improved throughput is described best by **Figure 6.2**.

Viewing Figure 6.1 (a) and (b) and Figure 6.2 together, the total measurement time in SEC can be subdivided into three main sections. The first includes a delay, $t_{\text{Delay-1}}$, just after the initial sample injection. The second section is attributed to the information time, t_{info} , where the analyte elutes. Finally, the third section is the hold time, $t_{\text{Delay-2}}$, which is a waiting period associated to the elution of stabilizers, salt, the system peak, and the re-equilibration of the system back pressure. After this delay, a second injection can commence. The total measurement time for conventional SEC can be described by the following:^[250]

$$t_{\text{total (conventional SEC)}} = n \cdot (t_{\text{Delay-1}} + t_{\text{info}} + t_{\text{Delay-2}}), \quad (6.2.1)$$

where n is the number of injections. As seen from **Equation 6.2.1**, to increase the throughput of SEC, the $t_{\text{Delay-1}}$ time must be reduced as much as possible. This is where interlaced SEC comes into play; the methodology behind the idea has been explained in detail by Farnan et al.^[19] and Kahle et al.^[251] The interlaced SEC principle works as

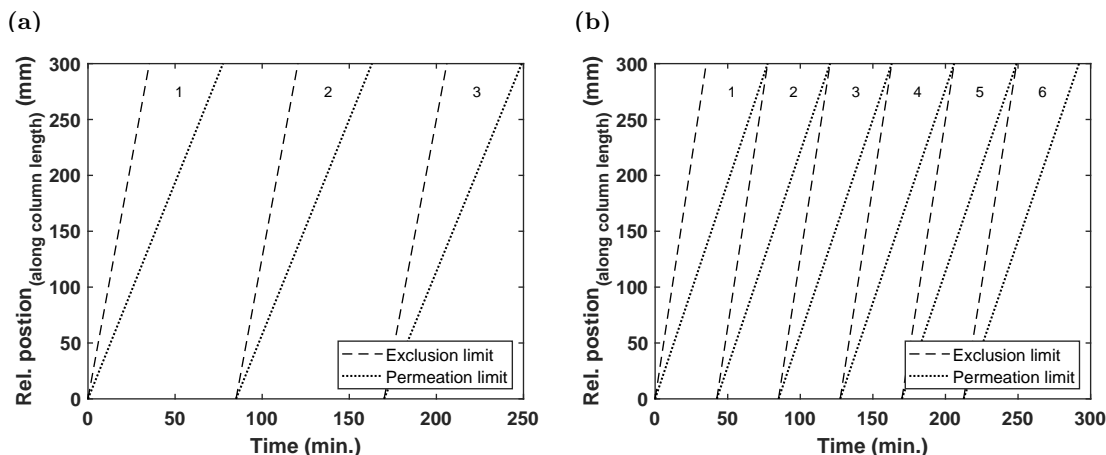


Figure 6.2: The increased separation throughput in SEC when going from (a) conventional single injection SEC to (b) interlaced SEC. The illustration is based on the total volume ($V_e = 85$ mL) of the linear M semi-preparative column when hyphenated to the MR-NMR set-up. The dashed and dotted lines represent the propagation of analytes associated with the total exclusion and total permeation limits, respectively. In (a) one column volume ($V_e = 85$ mL) is used per sample, whereas in (b) a second sample is injected into the SEC column prior to elution of the first injection.^[19]

follows: it involves the injections of a subsequent sample prior to the elution/completion of the first injected sample. By doing this, $t_{\text{Delay-1}}$ (see Figure 6.1 (a) and (b)) is reduced. As seen from Figure 6.1 (b), the subsequent information begins shortly after that of the first injection and so on. In the illustration in Figure 6.1, it is clear that more information related to the analyte can be extracted in the same timespan than for a single injection. There is, however, a restriction in interlaced SEC in that the amount of injections needs to be timed well in order to avoid co-elution of the system peak of the first injection and that of an analyte peak corresponding to a subsequent injection. Furthermore, the amount of injections that can be included into a single column volume is dependent on the sample, i.e. molar mass distribution and dispersity index, as it is important to have baseline separation between eluting analytes in order to retain chromatographic integrity and extract the relevant SEC parameters, i.e. M_n , M_w , and D . The total time required for an interlaced SEC measurement is thus^[250]

$$t_{\text{total (interlaced SEC)}} = t_{\text{Delay-1}} + n \cdot (t_{\text{info.}} + t_{\text{Delay-2}}). \quad (6.2.2)$$

Although interlaced SEC was initially developed to increase the system throughput, i.e. more samples measured in a shorter time, it can also be used to enhance the S/N of a system. To illustrate the effectiveness of interlaced SEC injections for S/N enhancement, the principle was applied to SEC-NMR, where a PMMA calibration standard ($M_w = 199$ kg/mol, $D = 1.02$, $c = 4$ g/L) was analysed. The idea behind using this specific molar mass was that three injections could be included into one column volume, as was pre-determined by conventional SEC. The measurements were performed in CHCl_3 , using the 1-Pulse-spoil pulse sequence (see Figure 4.23, p. 100) on a linear M semi-preparative SEC column (300×20 mm i.d.) with a flow rate of 1 mL/min. The delay intervals used for the subsequent injections were 10 min. The results for the interlaced SEC-NMR are depicted

in **Figure 6.3**.

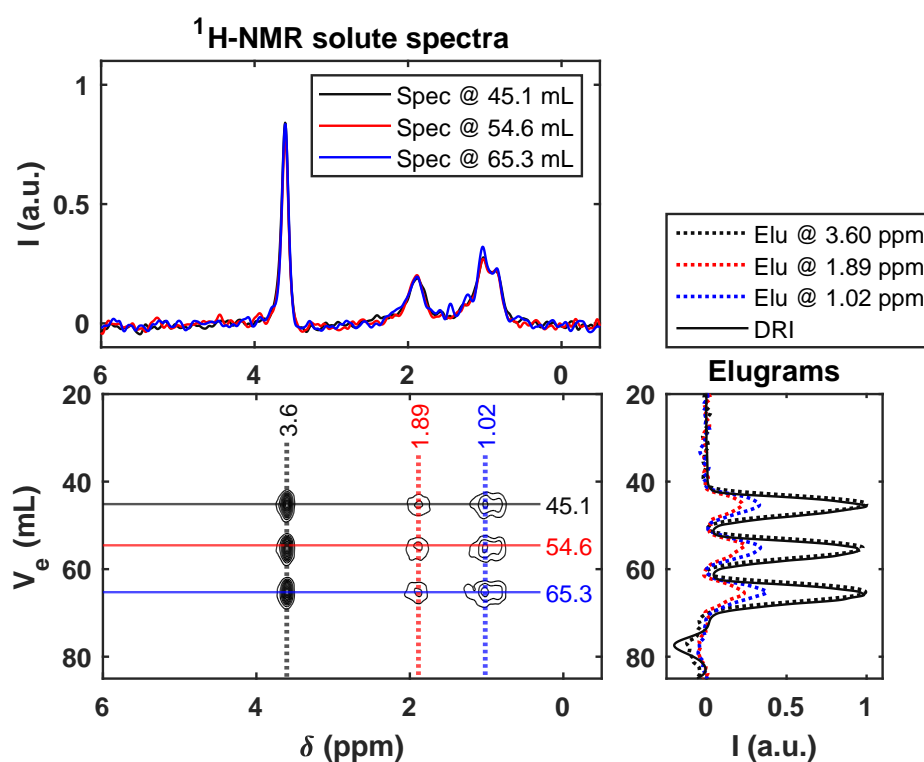


Figure 6.3: The interlaced SEC-NMR measurement performed on a PMMA calibration standard ($M_w = 199$ kg/mol, $D = 1.02$, $c = 4$ g/L) in CHCl_3 at a flow rate of 1 mL/min with an injection volume of 500 μL . A linear M semi-preparative SEC column and the 1-Pulse-spoil pulse sequence were utilized. To achieve interlacing, a 10 min delay period was used for each subsequent injection.

As seen in Figure 6.3, interlacing was achieved without having analyte band overlap while still retaining the chromatographic integrity. The total exclusion and permeation limits were estimated for the given SEC column with the aid of a calibration curve and were found to be 30 and 72 mL, respectively. This means that of the 85 min required for the execution of a single column volume, only 43 min are actually used for separation. Based on this information, a timeline with a priori information on the elution time of a given sample, can be choreographed to achieve successful interlaced SEC injections. In practice the injections are performed at pre-defined time intervals, as is the case for the PMMA sample, where an injection was manually performed every 10 min. In cases where interlacing is performed on standard SEC set-ups, a process referred to as detection gating is used,^[19] which limits the acquisition time of the experiment. Considering Figure 6.1 (b), the data acquisition is only turned on after the initial delay time, $t_{\text{Delay-1}}$, for the duration of the analyte elution period, t_{info} , then switched off again, with a relay continuation of this process for every interlaced SEC injection. Although continuous detection is possible, it is of little value in a standard SEC set-up. However, in the case of interlaced SEC-NMR, continuous data acquisition is required to perform the necessary post data acquisition processing, as described in Section 4.5 (p. 109). The results obtained in Figure 6.3 were further processed to quantify the effectiveness of the interlaced SEC-NMR measurement of the PMMA sample and are presented in **Figure 6.5**.

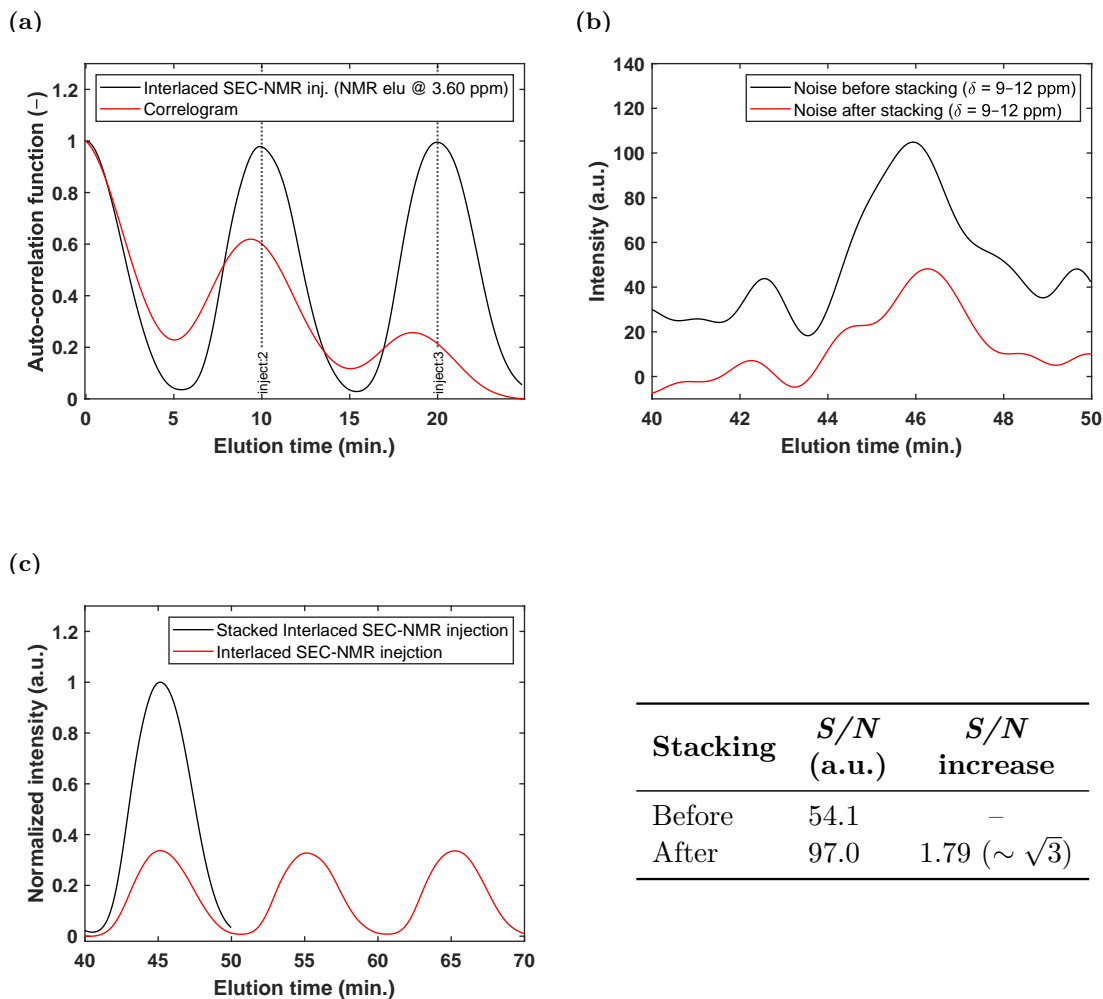


Figure 6.5: Quantification of the effectiveness of interlaced SEC-NMR measurements on a PMMA ($M_w = 199$ kg/mol, $D = 1.02$, $c = 4$ g/L) calibration standard. In (a) the auto-correlation function correlogram of the interlaced injections is depicted. Figure (b) displays the noise before and after stacking, and (c) shows the enhancement in signal intensity when the interlaced injections are cut and stacked onto each other.

In Figure 6.5 (a) the correlogram is presented, which was determined by an auto-correlation function, mathematically described by^[70, pp. 12–13]

$$p(t) = \int_{-\infty}^{\infty} f^*(\tau) \cdot f(t + \tau) dt, \quad (6.2.3)$$

where $*$ is the complex conjugate of the function. It describes the correlation between a certain value of a function, which differs by a time interval, τ . The magnitude of $p(t)$ depends on the degree of coherence of the system. As seen in Figure 6.5 (a), at the start there exists a strong coherence of the system, but as the time lags increase, the coherence of the system also decreases. This reduction is as a result of random noise within the 2D SEC-NMR system, however, it is indicative that at injection three, the total system coherence has decreased with about 80% relative to the first injection. To increase the S/N of the interlaced injections, numerically the simplest solution is to cut the respective injection peaks and stack them. The S/N , theoretically, should increase with $S/N \sim \sqrt{n}$,

where n is the number of stacked spectra. As seen from Figure 6.5 (b) and (c) the noise is not behaving in an unexpected manner, i.e. increasing or decreasing too severely when stacked, and the signal of the stacked injections increased by a factor of 3, which is trivial. Considering the S/N values provided in the inset table in Figure 6.5, the S/N after stacking has increased by a factor of 1.79, which is very close to the theoretical increase in S/N of 1.73 ($= \sqrt{3}$). From this it is evident that interlaced SEC-NMR injection follows an expected and predictable trend, which makes it a valuable alternative for S/N enhancement without a too severe compromise to the chromatographic integrity. Furthermore, it also illustrated that interlaced SEC works well with NMR hyphenation, and opened the possibility for the novel sinusoidal SEC approach to be attempted.

6.3 Proof of Principle: Novel Sinusoidal SEC Injections

The interlaced SEC technique illustrated that it had the potential to be used in combination with NMR spectroscopy. The successful peak detection, when simply injecting one sample after the other, led to the exploration of a potentially more efficient approach for enhancing the S/N and eliminating waiting periods. This involves the continuous 'injection' of an analyte by means of an oscillating concentration profile within the SEC column using a sinusoidal excitation gradient (see Figure 6.1 (c), p. 186). In conventional and/or interlaced SEC injections, there is a system peak due to the introduction of a pressure flux as a result of the injection, which causes a hold time, $t_{\text{Delay-2}}$ (see Figure 6.1) and restriction of the frequency of injection. The novel sinusoidal SEC bypasses the pressure flux as there is no 'physical' sample injection. An approach similar to gradient liquid adsorption chromatography (LAC) is employed, where a solvent gradient table is constructed and fed into a quaternary pump via software dictating the solvent ratio at any given time. Instead of having, for example, two pure solvents with varying solvent ratios, one of the solvent reservoirs is pure solvent whereas the other contains solvent plus analyte. Subsequently, by varying the ratio of the pure solvent to analyte reservoirs, a mock analyte injection is performed, however, without the undesirable pressure fluxes, eliminating waiting periods. Due to sinusoidal excitation characteristic, phase-angle information can be extracted and evaluated by means of Fourier transformation. The latter also allows for the construction of a phase-calibrated molar mass calibration curve allowing the determination of the molar mass related information. A schematic depiction of the set-up for sinusoidal SEC(-NMR) is presented in **Figure 6.6**.

To allow for the successful acquisition of the sinusoidal SEC measurements, several severe hardware adaptations to the standard SEC-NMR set-up had to be made (see Figure 4.1, p. 64). These alterations, presented in Figure 6.6, comprised the following: (1) dual UV detection, with the two detectors labelled as UVD-1 and UVD-2; (2) a bypass of the manual injector and DRI detector; (3) the inclusion of a mock 'injector' trigger (see Figure A.6, p. 277) that allows for the start of the solvent and solvent-analyte gradient, including data acquisition; finally (4) the use of an analytical linear M (300×8 mm i.d.) SEC column. These were the major alterations made to the SEC-NMR set-up. All the measurements for sinusoidal SEC were performed at a volumetric flow rate of 1 mL/min, unless otherwise

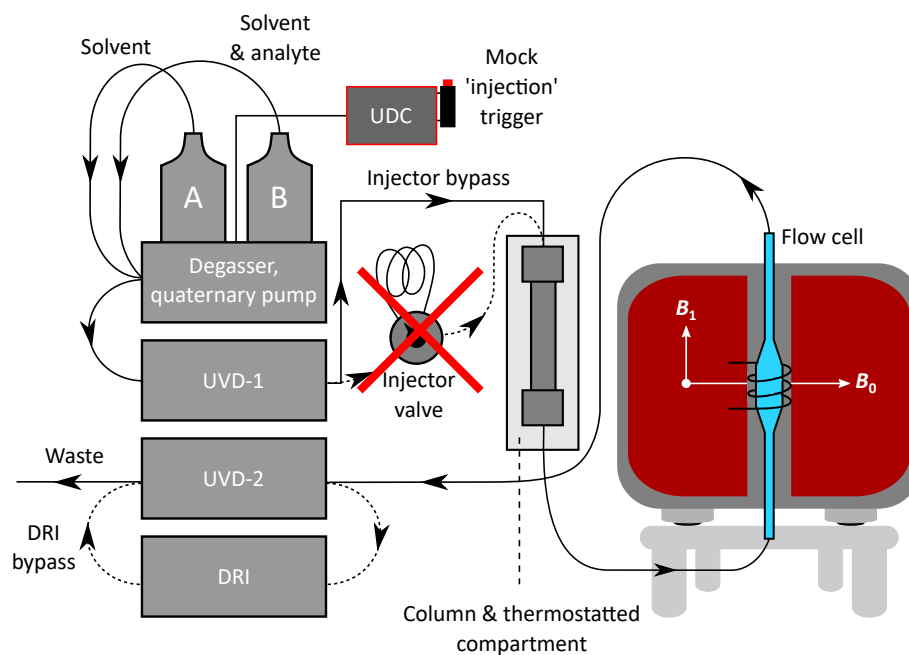


Figure 6.6: Depiction of the sinusoidal SEC-NMR set-up. The key differences compared to Figure 4.1 (p. 64) include the following: (1) dual UV detection is used, UVD-1 and UVD-2; (2) the DRI detector and manual injector are bypassed; (3) a mock 'injection' trigger system is used for the start of the solvent and solvent-analyte gradient, including the acquisition of the data; and (4) an analytical linear M SEC column is used (see Table 4.3, p. 76). A photo of the set-up is presented in Appendix A.5 (p. 273).

stated. A universal data centre (UDC) 810-box (PSS GmbH, Mainz, Germany) was used for signal acquisition of the two UV detectors. It consisted of a 24 n-bit ADC, used for signal digitization (1 Hz sampling rate).^[253] The dual UV detection was chosen for two reasons, (1) the good sensitivity of a standard UV detector,^[254] and (2) to monitor the in- and out-put sinusoidal signals, as UVD-1 was directly after the pump before the SEC column and UVD-2 directly after the SEC column. The DRI detector was bypassed since it is too sensitive to system fluctuations, i.e. pressure, contaminants etc. as opposed to the UV detectors, and would amount to unwanted noise (higher harmonics) when the signal is converted via Fourier transformation. To bypass the manual Rheodyne injector, another plan had to be devised, as the manual injector not only introduced the analyte into a standard SEC injection but also gave the signal to the SEC software to start data acquisition. Since a pressure flux as a result of physical injection wanted to be avoided, the mock 'injection' trigger was developed,¹ which simply creates a short circuit in the electronics when pressed, and provides a similar voltage spike as the manual injector. This starts the queued processes in the PSS WinGPC software, which includes the running of a solvent gradient table and data acquisition. The main advantage of the mock 'injector' trigger is that there is no major pressure flux involved as with physical injections. The replacement of the semi-preparative column with the analytical column was to reduce waiting times during the developmental phase, as the analytical column has a factor of 6.25 smaller volume than the semi-preparative column, consequently a factor of 6.25 faster.

¹This was developed with Dr. T. Beskers at PSS GmbH (Mainz).

Due to the novelty of the technique, and to reduce any induced uncertainties, the analytical column was calibrated via conventional SEC, with a PS calibration set, after which it was fitted with a third order polynomial, and the separation range with the most linear fit determined. This linear range was used as the period length for the construction of the sinusoidal excitation input signal. The corresponding results are presented in **Figure 6.7**

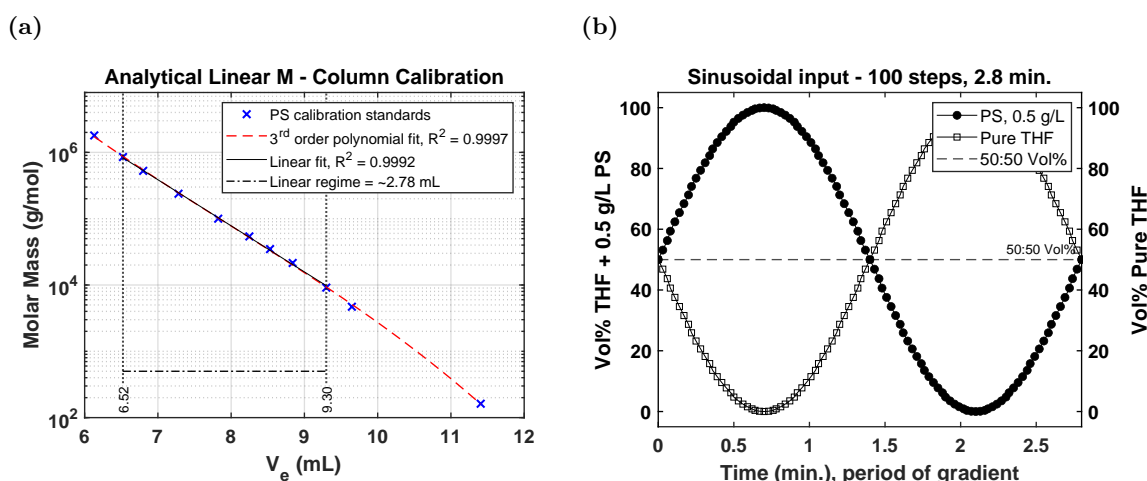


Figure 6.7: Illustration of (a) the linear regime of the analytical column established by means of a PS calibration set, and (b) a 2.8 min sinusoidal excitation corresponding to this linear range. The sinusoidal input excitation represents the change in the pure solvent, THF, relative to 0.5 g/L stock solution of a PS calibration standard as constructed with a 100 step gradient table. The pure excitation is illustrated in (b).

The excitation signal represented in Figure 6.7 (b), constructed out of a 100 (maximum) step gradient table, is oscillated for a predefined amount of relay-steps, which then generates the sinusoidal SEC injection profile. To achieve this, two designated solvent reservoirs are required, as illustrated in Figure 6.6 (p. 192). In the development, pure THF and a stock solution of PS in THF, typically with a concentration of 0.5 g/L, was used. The solvent and stock solution ratios were varied, starting from a 50:50 vol%, in such a way that they had a 180° phase off-set, which ensured that the desired sinusoidal concentration profile of the analyte was achieved. A fully sinusoidal excitation gradient is defined as the excitation frequency, i.e. period length, which necessitated the need to determine the relevant period length. As the goal was to improve the S/N enhancement and make the entire system more efficient, shorter excitation frequencies were also tested, however, it was hypothesized that shorter excitation frequencies would result in more non-linearities, thus a less stable sine-signal. To test the hypothesis, the 2.8 min sinusoidal excitation period was compared to a 1 min period using a PS calibration standard ($M_w = 75\,500$ g/mol, $D = 1.02$, $c = 0.5$ g/L). The lower sample concentration was chosen to avoid column overloading effects (see Section 4.3.3, p. 79). Furthermore, to avoid errors in the phase angle determination, it is advised to work within the linear response range, with respect to concentration, of the detector, which has been determined to be between 0.2–0.65 g/L for PS. The corresponding stability results are presented in **Figure 6.8**.

As evident in Figure 6.8, the proposed hypothesis was in fact correct. The reduction in the sinusoidal excitation frequency resulted in a two-fold observable change in the signal, (1) the

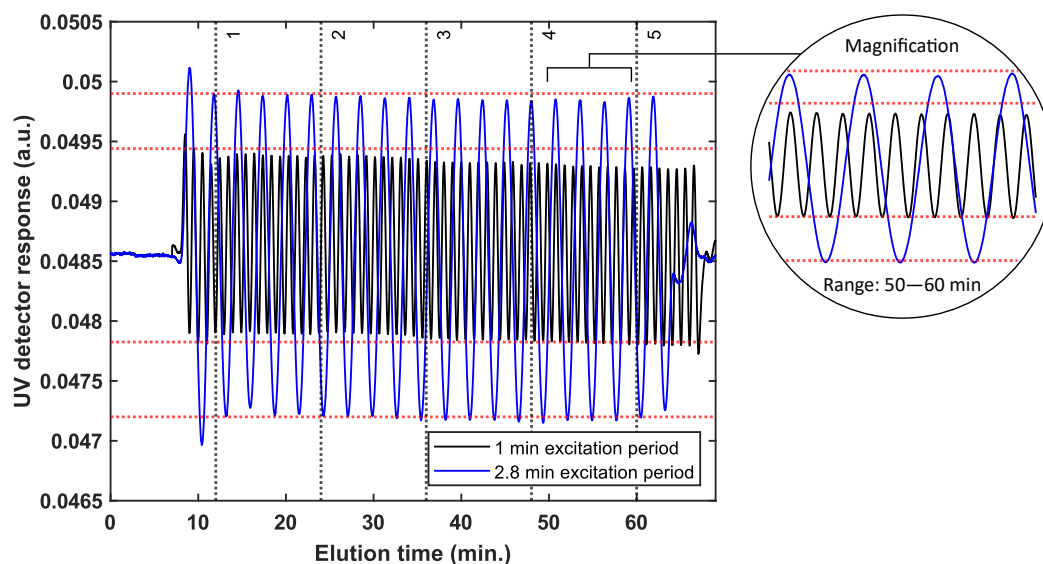


Figure 6.8: Stability evaluation of the sinusoidal SEC injections at 1 and 2.8 min excitation periods on a PS calibration standard ($M_w = 75\,500$ g/mol, $D = 1.02$, $c = 0.5$ g/L). The red horizontal dashed lines indicate the intensity change between the two excitation frequencies, and the vertical black lines numbered from 1 to 5 indicate the duration of a conventional SEC injection.

signal intensity reduced, resulting in an average S/N reduction of a factor of 1.5 compared to the longer excitation period, and (2) using the red dotted lines as eye guides, the system seem to drift more. It is not fully understood yet as to where these anomalies originate from, however, currently it is thought to be a product of the pump mixing uncertainties and column artefacts, i.e. intrinsic non-linearities. A more in-depth investigation is required, which was not conducted during the course of this work. Furthermore, this indicates that by using longer excitation periods the S/N should, theoretically, increase. Consequently, the increase in S/N with an increase in the excitation period comes down to a compromise between speed and sensitivity. The 2.8 min excitation period was, therefore, used as preferred sine period length. To have a better understanding of the forthcoming procedures, a brief description of some theoretical considerations related to this topic will be provided. The theoretical part related to the separation mechanism of conventional SEC has already been explained in Section 2.1.4 (p. 9). Since it is still important to be able to extract molar mass information from species analysed via sinusoidal SEC, the need for a calibration curve is required. As a conventional SEC calibration curve will not suffice, a new type of calibration curve is required. This was realized by using the respective phase-angles, ϕ , of the PS calibration standards, as opposed to the retention volume (or time), and can be determined as follows:²

²For consistency between this work and future work the equations and definitions used are the same as per M.Sc. thesis of Mr. M. Matz^[255] per supervision of the Author.

$$\Delta V_e = V_{e, \text{ standard}} - V_{e, \text{ reference}}$$

$$\text{and} \tag{6.3.1}$$

$$\Delta\phi = \frac{\Delta V_e}{\dot{v}} \cdot \frac{360^\circ}{T_p},$$

where V_e is the elution volume in mL, \dot{v} the volumetric flow rate, and T_p the experimental period duration in minutes. The $V_{e, \text{ standard}}$ is the elution volume of the PS standard, and $V_{e, \text{ reference}}$ is the reference elution volume. The latter was chosen as the highest V_e of the used PS calibration standards corresponding to the maximum of the linear regime of the SEC column, i.e. $M_p = 851 \text{ kg/mol}$, with a phase-angle set to $\phi = 0^\circ$. The experimental period duration, T_p , was set to 2.8 min for all experiments presented here, unless stated otherwise. It should further be noted that the determined phase angles are not absolute values like that of the elution volume, but rather relative values, and should be treated as such. The phase-calibrated molar mass calibration curve is presented in **Figure 6.9**.

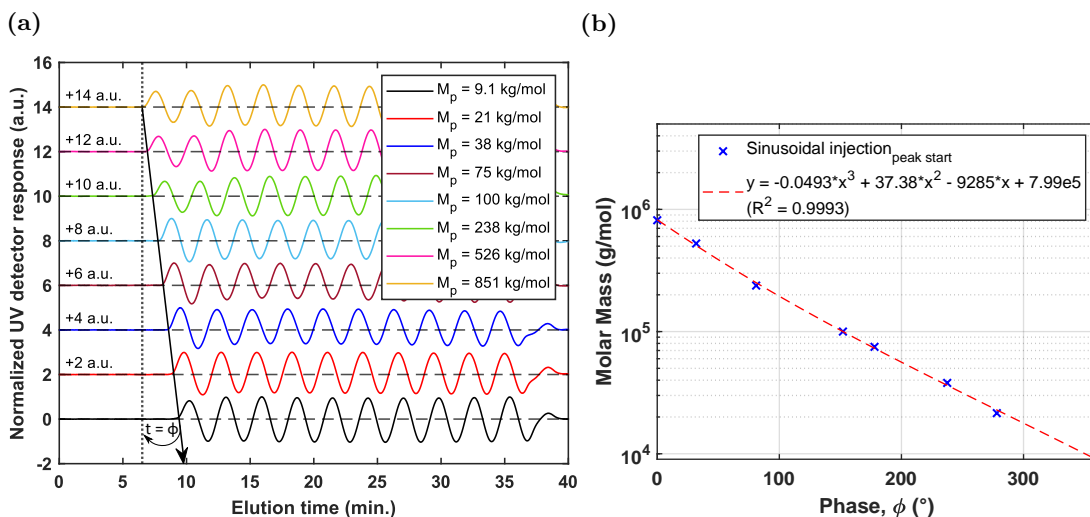


Figure 6.9: The phase-calibrated PS molar mass calibration of the sinusoidal SEC injections. The PS calibration standards were selected based on the established linear regime illustrated in Figure 6.7 (a), comprising eight standards. In (a) the lag times between the different PS calibration standards are illustrated, the lag time is used to convert time to angle, ϕ , using **Equation 6.3.1**. The corresponding phase calibration is illustrated in (b). All of the PS calibration stock solutions had a sample concentration of $\sim 0.5 \text{ g/L}$.

As the phase calibration is constructed on the 360° equivalence of a conventional retention time vs molar mass calibration, the accuracy of the molar mass extrapolation is dependent on analytes having a hydrodynamic volume falling within this duration of 360° . Subsequently, if an analyte elutes outside this range, i.e. before 0° or after 360° , the calculated molar mass would be incorrect, much like when an analyte elutes at the total exclusion- or permeation limit of a conventional SEC calibration. With the establishment of back-calculating the molar masses when performing sinusoidal SEC measurements, the next step was to analyse it with the NMR spectrometer, as it has been illustrated with the interlaced SEC injection approach to be a potential possibility. Furthermore, this was a test for the developed TMDE software, to determine if the post data acquisition processing would still be feasible when

an unorthodox approach is used for SEC. A PS calibration standard ($M_w = 8\,900$ g/mol, $D = 1.03$, $c = 0.5$ g/L) was measured on the SEC-NMR set-up in THF at 1 mL/min. Due to the low sample concentration, the 1-Pulse-spoil pulse sequence was used for solvent suppression. Although not as effective as the inversion recovery pulse sequence, it is a factor of 2 times faster, resulting in more acquired transients, thus increasing S/N . The auto-correlation of the data were calculated, similarly to the interlaced SEC approach to establish at which point system coherence is lost. The corresponding results are presented in **Figure 6.10**.

As seen in **Figure 6.10** (a), although not as noise-free, sinusoidal SEC-NMR works, and the TMDE software handles it well, as it finds all the relevant peaks and performs the required task as expected. For the 1D ^1H -NMR plot most of the spectra represented in the 2D plot were manually removed due to over-crowding and only three spectra at 12.3, 26.1, and 40.1 mL, corresponding to the first, middle, and last peaks were kept. Furthermore, upon closer inspection of the contour plot, the presence of the PS aromatic protons can be seen at a chemical shift of $\delta = 6.8\text{--}7.2$ ppm, starting from the very beginning of the data acquisition. This is expected as the system is first equalized with a 50:50 vol% of THF and analyte solution for 1–5 column volumes prior to the start of the gradient table, as presented in Figure 6.7 (b) (p. 193). The correlogram, as obtained by the auto-correlation function for the NMR elugram cut at $\delta = 7.13$ ppm, shown in Figure 6.10 (b), indicates that the total system coherence reduces by 50% after ca. 22.5 min (5 oscillations), after the initial onset of the sample elution, indicating sufficient system stability. To quantify the sensitivity, the signals obtained on the two UV detectors were converted to Fourier space. As the UV signals are time-discrete and correspond to at least one period of a periodic signal, it is possible to convert the data set to Fourier space via a discrete Fourier transformation (DFT). The DFT of the UV signals produces harmonics (sinusoidal components) and a 'constant' component, \hat{a}_0 , corresponding to the average input signal. This is referred to as DFT, where $\hat{a}_0 = (\hat{a}_0, \dots, \hat{a}_{K-1}) \in \mathbb{C}^K$ from a . The coefficients for \hat{a} obtained by the DFT, correspond to the amplitude of the decomposing components, \hat{a}_n also referred to as Fourier components. Typically, the compact mathematical notation of the polar coordinate system is used to determine frequency components, i.e. phase position by means of Euler's formula,^[256, pp. 92–125]

$$e^{i\phi} = \cos(\phi) + i \sin(\phi), \quad (6.3.2)$$

where the DFT is defined by the following:^[256, pp. 92–125]

$$\hat{a}_n = \sum_{j=0}^{K-1} e^{-2\pi i \frac{jn}{K}} \cdot a_j; \text{ for } n = 0, \dots, K-1. \quad (6.3.3)$$

Prior to converting the UV signals into Fourier space, the flat parts, i.e. initial and end non-sine parts of the signal, are removed so that only the sine part remains, to obtain the maximum S/N and to avoid sinc ($\sin(x)/x$) artefacts. Considering this, the UV traces were converted via DFT, and a sensitivity comparison between conventional SEC and sinusoidal SEC injections was performed. The corresponding results are presented in **Figure 6.11**

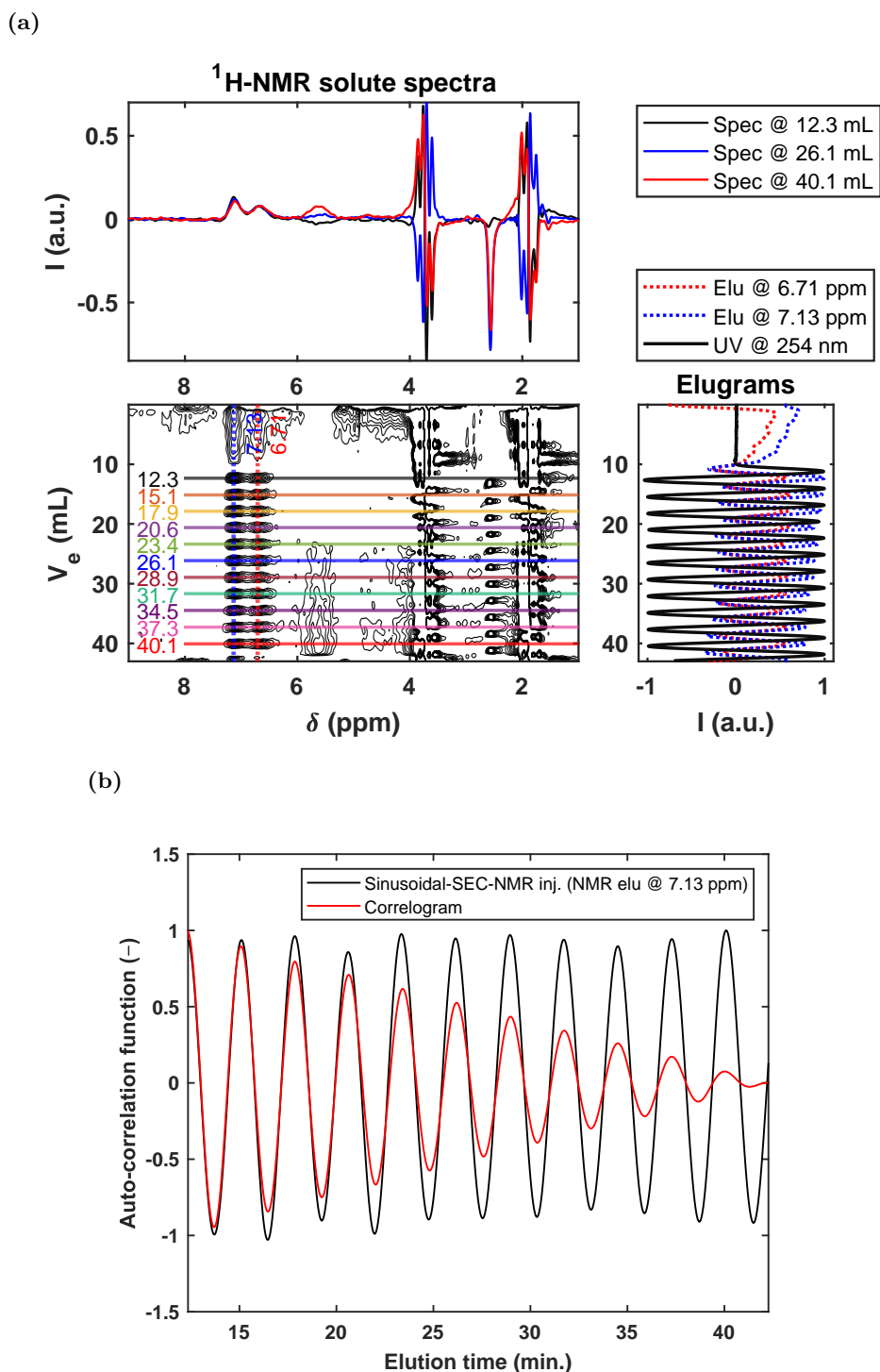


Figure 6.10: The (a) sinusoidal SEC-NMR measurement performed on a PS calibration standard ($M_w = 8\,900$ g/mol, $D = 1.03$, $c = 0.5$ g/L) and (b) corresponding auto-correlation function correlogram. A flow rate of 1 mL/min in THF on an analytical linear M SEC column was utilized. The 1-Pulse-spoil pulse sequence comprising 1300 FIDs was used for NMR data acquisition.

In Figure 6.11 (a), the determination of the S/N ratio from the DFT spectra is illustrated. The magnitude of the excitation frequency $M(\omega_0)$ was taken as signal intensity, and the noise was determined in a harmonic-free region, by taking the standard deviation of the signal in the frequency region of 0.4–0.5 Hz. The magnified inset depicts the higher harmonics for the two UV detectors. The origin or meaning of these higher harmonics is still

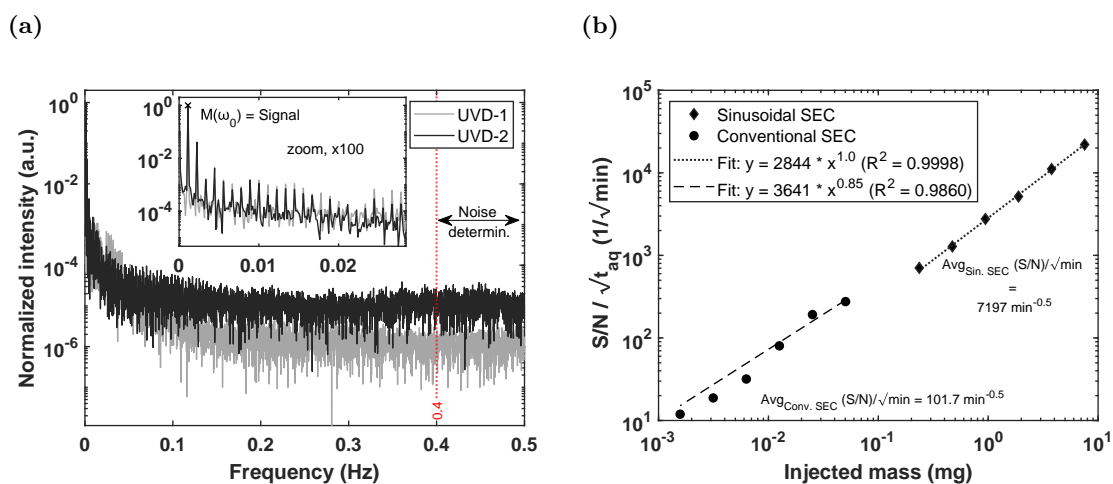


Figure 6.11: The (a) discrete Fourier spectrum of the converted UV traces and (b) S/N comparison between conventional and sinusoidal SEC injections, normalized to 13 min and 30 min, respectively. The inset in (a) depicts a magnified region illustrating the higher harmonics of the system, and the red dotted line shows the starting point for the noise determination. The measurements were performed on a PS calibration standard ($M_w = 96\,000$ g/mol, $D = 1.04$), with a concentration series range of 0.5–0.016 g/L in THF at 1 mL/min on an analytical linear M column. Measurements courtesy of Mr. M. Matz.

unclear and requires additional investigation. Furthermore, the magnitude for both the UV detectors decrease as a function of the frequency. The extent of the decrease is as a result of different detector settings used for the individual UV detectors, i.e. signal attenuation. In Figure 6.11 (b) a sensitivity comparison is made between that of conventional SEC and sinusoidal SEC injections. A concentration series comprising six different sample concentrations of a PS calibration standard ($M_w = 96\,000$ g/mol, $D = 1.04$) was analysed, i.e. 0.50, 0.25, 0.13, 0.063, 0.032, and 0.016 g/L, all prepared in THF at 1 mL/min for both techniques. For conventional SEC a 100 μL sample loop was utilized. The S/N values for conventional SEC were determined by taking the maximum signal height of the analyte and a peak-free region between 2–3 min. Furthermore, to have a better comparison, the S/N values were all normalized to the square root of the total acquisition time, $\sqrt{t_{aq}}$, per measurement. As seen from the comparison, the sinusoidal SEC produces better sensitivities, and was determined to be, on average, a factor of 70 better than conventional SEC measurements if enough sample is available. This increase is a result of two major differences, (1) the effective use of the column amounting to more injection averaging, which would be equivalent to injecting higher sample concentrations; and (2) the use of Fourier space for S/N determination, as the S/N increases with the square root of transients, $\sqrt{n} \sim \sqrt{t_{aq}}$.

Although the improvement in S/N is impressive in sinusoidal SEC the lack of integrity of the separation, unlike the interlaced SEC approach where it is well-preserved, could be the 'price paid' for sensitivity enhancement. An example of this is, in the case of a blend or a mixture, it would be a very challenging, if not impossible, task to extract the corresponding molar mass dependent phase-angles as a result of the superposed sinusoidal curves. It will also cause severe challenges in the Fourier space, due to an increase in noise and harmonics, which complicates interpretation. Nevertheless, if a single species were to

be analysed, that requires S/N enhancement when used in conjunction with, e.g. low field NMR spectroscopy, the use of sinusoidal SEC is a potential solution to this problem. In addition, the separation mechanism might be altered when using sinusoidal SEC, or have special cases as in conventional SEC. However, this was not investigated in the scope of this work and could improve the understanding of system anomalies when understood.

Chapter 7

Conclusion and Outlook

Conclusion

In this thesis, the major theme is method development, where the successful on-line hyphenation of a medium resolution (MR) benchtop ^1H -NMR spectrometer (62 MHz, ^1H) as chemically sensitive detector to size exclusion chromatography (SEC) is reported. Furthermore, the evaluation of a new unique EC-QCL as potential on-line chemical sensitive detector for SEC is presented. This enables the detection of molar mass dependent chemical composition correlations that were previously more challenging to determine. A proof of principle of a novel liquid chromatographic method utilizing sinusoidal excitation is established for S/N enhancement, illustrating its potential use with the benchtop NMR spectrometer.

The unique design of the Spinsolve 60 NMR spectrometer has the potential to be applied as a standard chemically sensitive SEC detector. The S/N obtained during the optimization is sufficient to allow for both qualitative and quantitative analysis of polymeric species, with the full spectra measured on-line at typical SEC concentrations after chromatographic separation ($c \ll 0.5$ g/L) using non-deuterated solvents, e.g. CHCl_3 and THF. The design and optimization of a custom-built flow cell reduces the in- and out-flow effects intrinsic to on-flow NMR measurements. This provides better compatibility with optimum chromatography conditions, and results in an improved S/N by a factor of 2.1. The S/N is further improved by a factor of 2–3 using shorter repetition times for pulse sequences and adjusting the receiver gain to match the intensity of the FIDs, corresponding to that of the solvent signals, using the full dynamic range of the ADC. Solvent suppression is mainly based on the exploitation of the T_1 difference between the degassed solvent and polymeric species, which results in suppression factors of 5 and 50 for the 1-Pulse-spoil and inversion recovery pulse sequences, respectively. A modified Tukey window function (SEC dimension) in combination with a Gaussian window function (NMR dimension) further improve S/N . These window functions also allow for the subtraction of any constant signal present, such as solvent, impurities, or residual water, for further numerical solvent suppression. This 2D-filtering increases the S/N by a factor of 16. The product of the overall improved optimization parameters amounts to a factor of 357 improvement in S/N , with a final S/N of the $-\text{OCH}_3$ ($\delta = 3.58$ ppm) equating to $S/N = 263$ on a semi-preparative SEC column

with a 1 mg injected mass.

The optimized setup, ^1H -NMR to SEC, was applied to a PS/PMMA blend and a PS-*b*-PMMA block copolymer. This technique is able to differentiate between the blend and the block copolymer, where there is a difference in hydrodynamic volume of the respective homopolymers, and it provides sufficient sensitivity and chemical shift resolution. The capabilities and limitations were exemplified on a PS-*b*-PEMA block copolymer series, where it was found that for the block copolymer analysis, ratios of > 5 mol% are required to enable quantification on the SEC-MR-NMR technique. Information on the MMD and CC of a bulk sample can be acquired after applicable molar mass calibration of the set-up in a single on-flow experiment (ca. 85 min) of a block copolymer. Furthermore, the technique was applied to industrial samples, where SBRs were the subject of investigation. The analysis of the SBRs illustrated that the developed SEC-NMR technique is powerful for qualitative component analysis/identification, and is a complementary technique to its counterpart 1D techniques. The method development was realized by employing model samples with low D and complexities, although the obtainable S/N values of the NMR signals depend on a wider variety of factors. The presented results show a substantial improvement over similar work done by Cudaj et al.^[10,187] on a 25 MHz prototype NMR spectrometer. Naturally, when hyphenating two (or more) techniques, there exist constraints and a trade-off between the speed and quality of the measurements. Improved results are typically obtained when using the hyphenated techniques as individual 1D experiments, such as performing SEC at optimal conditions and performing fraction collection, where the fractions can later be analysed by NMR experiments at optimal conditions. The major benefit of on-line hyphenation is its speed and ease of use, providing correlated information in real time. The development conducted within this Ph.D. thesis allows SEC-NMR to be used as a standard set-up for laboratories, like e.g. SEC-MALLS, allowing for a broad application range. The continuous technological advancement in the NMR field has opened a variety of new possibilities, making MR-NMR spectroscopy an attractive approach to use as a chemically sensitive detector in liquid chromatographic (LC) set-ups. One limitation is that for each technique a very specific skill-set and knowledge base is required. This requires interdisciplinary problem solving for suitable solutions. As evident from the ever-evolving complexity of polymeric species to meet certain application specifications, and the need to develop new advanced techniques for characterization, the future for on-line LC hyphenation to chemically sensitive spectroscopic techniques is promising.

The use of benchtop NMR as an on-line chemically sensitive detector in preparative chromatography, could constitute highly relevant applications for synthetic chemists. In terms of benchtop NMR hardware, $B_0 = 1.9\text{--}2.4$ T ($F = 80\text{--}100$ MHz) will most probably remain the maximum achievable field strength. However, with technological advancements, narrower line widths can be expected, which ultimately leads to higher S/N ratios. Recently (October 2020), within this working group, a proton optimized probehead Spinsolve 80 NMR spectrometer has been acquired, which has a further factor of 3 improvement in the S/N compared to the Spinsolve 60 used within this work. The corresponding detection limits measured on a PS calibration standard ($M_n = 30\,300$ g/mol, $D = 1.03$) are presented

in Figure 7.1.

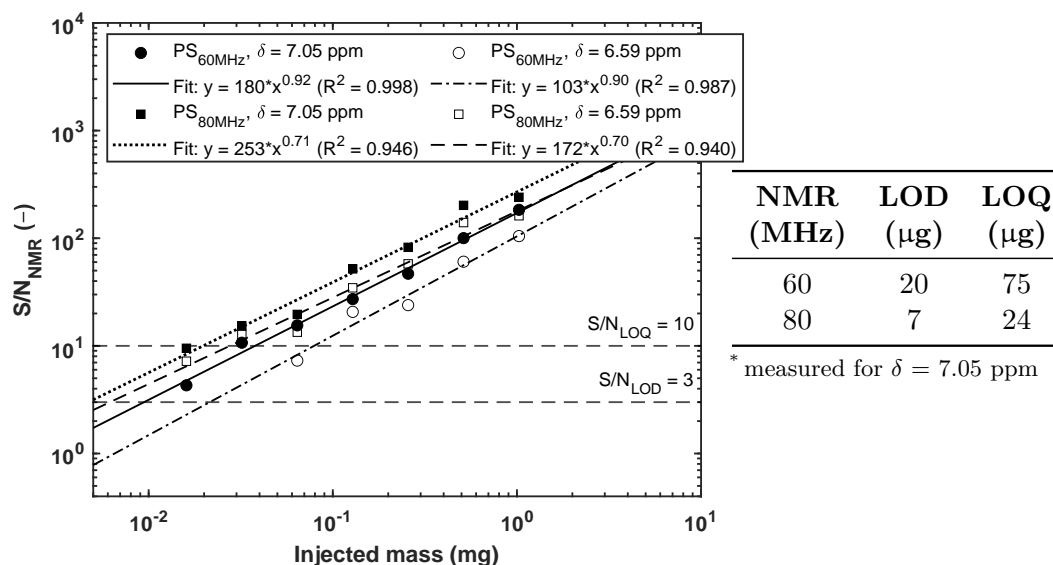


Figure 7.1: The S/N as a function of the injected mass of a PS ($M_n = 30\,300$ g/mol, $D = 1.03$) calibration standard via SEC-NMR analysis in THF at $\dot{v} = 1$ mL/min, comparing the 60 and 80 MHz NMR spectrometers. The two horizontal dashed lines represent the LOD ($S/N = 3$) and LOQ ($S/N = 10$) limits. These limits for the respective data sets were determined by the intercept of the power law fits employed. The peak maxima were used for the S/N calculations.

The work on the development of SEC-FTIR hyphenation within this working group also led to the exploration of the capabilities of an external cavity quantum cascade laser (EC-QCL) as potential detector for SEC. The dual detector set-up allows for the correction of laser fluctuations, which enables the numerical reduction of the total system noise. The obtainable sensitivity was determined and compared to a previous QCL and FT-IR spectrometer. The new prototype EC-QCL has an improvement in LOD over the previous QCL and FT-IR of a factor of 6.4 and 28, respectively. This amounted to the detection of an injected mass of $0.5\ \mu\text{g}$ for PMMA in THF, measuring the carbonyl stretch ($\text{C}=\text{O}$, $\tilde{\nu} = 1730\ \text{cm}^{-1}$). The severe reduction in the LOD confirms the relevance of this technique, as it can potentially be used for the on-line detection of species, which were previously not viable. The technique has also been applied to acetylated functionalized PS, with an acetylation content of $\sim 16\%$, where it was further diluted with homopolymer PS, and successfully characterized via SEC-EC-QCL. This emphasizes that the unique sensitivity of the EC-QCL detector will perform well in other modes of HPLC, such as LAC, where the injected masses are typically a decade lower than SEC.

The proof of concept of a novel LC method using sinusoidal injection for S/N enhancement without the need for the pre-concentration of analyte species was established. The uniqueness of the system, unlike other unorthodox methods for S/N enhancement like interlaced SEC, is that the SEC column is continuously loaded by an oscillating sinusoidal concentration gradient, allowing for unlimited measurement times. Due to the sinusoidal nature of the response signal, the data can be converted into its frequency components via

discrete Fourier transformation (DFT) and the corresponding phase-angles and S/N can be determined. Each polymeric species being introduced into the SEC has a unique phase-angle dependence based on its molar mass. This is used for the construction of phase-angle calibrated molar mass calibration curves for the back-calculation of SEC parameters of unknown analytes. The S/N could be enhanced as much as a factor of 70 compared to conventional SEC injections, when normalized to the measurement time. The latter is mostly due to the larger amount of analyte passing the UV detector. This shows great potential for the MR-NMR spectrometer, where sensitivity constraints always come into play. Initial Sinusoidal SEC-NMR runs were performed to illustrate that it is a plausible technique that can potentially enhance the S/N . Sinusoidal SEC is, however, limited when analysing mixtures, due to the analytes superposing onto each other, destroying the integrity of the separation. No unique phase-angles can therefore be extracted. However, when a single species is analysed and lacks sensitivity, sinusoidal SEC might be the solution to the problem.

Outlook

The improvement in sensitivity opens the possibility of employing benchtop NMR in combination with other modes of HPLC, such as LAC, which typically uses lower injected masses (generally a factor of 5 or more). The solvent suppression approach used for SEC-NMR, based on a T_1 -filter, will most likely not be as effective in, for example, LAC-NMR hyphenation. This is due to the characterization of lower molar mass components in LAC, making exploitation between the T_1 differences of the solvent and analyte less feasible. If no PFGs are available in the NMR spectrometer and a T_1 -filter approach is the route of choice, T_1 optimization by means of paramagnetic shift reagents is recommended. A benefit of LAC-NMR would be the use of solvent gradients, as chemical species could selectively be removed from the columns by changing the solvent gradient strength, and in doing so also minimize band broadening resulting in higher detector intensities. This would be advantageous for NMR detection, however, solvent subtraction would be more challenging. From a hardware perspective, one way to further enhance the S/N of the benchtop NMR spectrometers, would be the reduction of electronic noise (prior to pre-amplification) by cooling the probe with liquid nitrogen. This, however, will require extensive alteration to the assembly of the instrument. The 1-Pulse-spoil pulse sequence for SEC-NMR hyphenation used a 90° hard pulse. An investigation with respect to longer tipping angles, e.g. $\theta = 100\text{--}110^\circ$, which could potentially further reduce the solvent intensity, would be interesting. In theory, the longer tipping angle should not affect the rapid relaxation of the polymer signal, and decrease the solvent signal intensity, resulting in better suppression factors achieved for on-line measurements. One of the focal points of this work was to obtain the best possible S/N , from a solvent suppression perspective that typically resulted in working at non-quantitative NMR conditions, i.e. repetition times of $< 5 \times T_1$ of the analyte. An investigation of SEC-NMR hyphenation at quantitative NMR conditions would be highly beneficial, as this would shed light on the limitation of the technique. Flow cell development is crucial in retaining peak integrity, and avoiding back-mixing effects. As the

flow cells developed in this work were constructed of glass, and typically have irregularities in the glass walls due to the glass-blowing process, a different, more reproducible approach is recommended. One approach would be to precisely machine the sensitive volume of the flow cells from a material such as polyimide (Vespel[®]), as it is chemically resistant and has sufficient mechanical strength to allow for thin walls. To increase the residence time of the analyte within the sensitive region of the flow cell, a coil-like capillary could be placed within the sensitive region of the flow cell, however, this might be practically challenging to produce. Apart from performing SEC-NMR measurements, the knowledge generated thus far should be applied to reaction monitoring, as the sample concentrations are generally much higher and could severely benefit from the post data acquisition software TMDE. Application of SEC-NMR using 'green chemistry' mobile phases, such as water, would be interesting to investigate, as the demand for sustainability and environmental considerations are ever present. Finally, it is important to realize the main limitation of low field NMR, its limited resolution. Consequently, MR-NMR, in certain cases, should not be used as a stand-alone technique but rather as a complementary technique.

Acknowledgement

Although I wrote the entirety of this endeavour dutifully on my own accord, the work on which it is based upon, could not have been possible, as with many things in life, without the help and contribution of others. I would, therefore, like to take the opportunity to thank the following people, who played a pivotal role:

Firstly, I would like to express my sincere gratitude to my advisor and "Doktorvater" **Prof. Manfred Wilhelm** for taking a risk and providing me with the opportunity to do a very interesting Ph.D. in his group, for his continuous support of my Ph.D. study and related research, for his patience, motivation, and immense knowledge. I am also grateful for his enthusiasm related to my topic, which in many occasions sparked the research flame within me, and granted me the freedom to explore and express my individual creativity. In some cases he has changed my way of thinking, and for that, I will be forever grateful.

My utmost gratitude goes to my mentor **Dr. Johannes Höpfner**, for his input, contributions, support and encouragement throughout the initial course of my study. Our continuous exchange of ideas, and work ethic is something I will cherish – thanks for everything mate! You also facilitated my general understanding of NMR spectroscopy and programming. I would then also like to thank another member of our 'A-team' we had, **Ms. Britta Mayerhöfer**, for our continuous hypothesizing over the craziest ideas, and all the laughs, I for sure increased my level of wrinkles with you around. To **Ms. Aleksandra Bucka**, who worked as a Hiwi for me for the better part of two years, thank you for all your help related to programming. I could not have asked for a better Hiwi related to solving challenging problems with me, your work is dearly appreciated and highly valued.

To my close friend **Dr. Timo Beskers**, without you I would not have been in Germany, let alone do my Ph.D. Thank you for your ever levelheadedness, especially in the more stressful times. Thank you for always looking out for me and just the person you are, I could not have asked for a better friend and unofficial co-supervisor.

Thanks to **Dr. Christopher 'Kiki' Klein** and **Dr. Karl-Friedrich Ratzsch**, who took me in and showed me the ropes, and how to get to Vogelbräu in the most efficient way. I would also like to extend my gratitude for their extensive discussions on a variety of different subjects and help related to the more technical aspects of my study. Not only are

they both brilliant in their respective fields but they have also become very good friends of mine.

Prof. Burkhard Luy and **Mr. Sebastian Spann** for entertaining my questions related to NMR and taking the time for fruitful discussions. I would also like to express my gratitude for always finding an available spot and performing high field NMR-spectroscopy measurements for me.

My deepest appreciations goes to **Dr. Jürgen Kolz** (Magritek), who was always willing to assist with technical question and solutions. Also to **Prof. Thorsten Hofè** (PSS), who always supported us related to anything to do with SEC.

Beyond that my sincere thanks goes out to **Dr. Ingo Naue** and **Mr. Daniel Zimmermann**, who assisted me with technical drawings and getting started with CAD. **The workshop team** for their level of expertise who has built numerous things for my Ph.D. and who always accepted my highly advanced pencil drawings and broken German.

A special thank you goes without a doubt to **Ms. Sabine Weiland**, I guess I can speak on behalf of all the Ph.D.'s, to some extent you are like the beating heart of the AKW-group. Thanks for all your patience and assistance during this endeavor, you have made my life so much easier. **Dr. Nico Digenouts** thank you for your willingness to always help and the heated discussions on light scattering.

The entire **AKW-group** thank you for the discussions related to my work and always being willing to help out where necessary. I would like to thank each and everyone of you as all of you played a crucial role in my study. I will always cherish the coffee breaks, braai's (aka BBQs), parties and scientific trips. You all became like family to me and made Germany my new home away from home. You have also provided me with a whole new outlook on life due to the shear diversity of our group.

A special thanks to **Dr. Matthias Heck**, **Dr. Michael Pollard**, and **Dr. Karl-Friedrich Ratzsch** for proofreading the entirety of the thesis and providing valuable guidance and input.

My MZE desk-squad, **Noni**, **Markus**, and **Lorenz**, I would like to thank you for all the memorable times over the last year, and my sincere apologies for all the out-loud swearing and 'hitting' of my keyboard when programs, programming, and science, didn't go the way I wanted. I guess we have all been there, some just more frequently than others, haha.

My **Friends and Family** for perpetual, unconditional encouragement, support and interest, even though nine times out of ten they had honestly no clue what I was doing/talking about ;-). A special thank you goes out to my good friend **Shaun Forteath** for always helping this boertjie when he's are not writing Engels goodsly.

Finally, to my wife **Marilize**, without your support and unconditional love I would have never even attempted to pack up my life and move a half-a-world away from you to pursue my dream. You have seen me at my worst and best, thank you for all your patience (not to mention all the evenings spent on proof reading and corrections).

Nomenclature

Abbreviations

A	Absorption
Å	Angstrom ($1\text{Å} = 10^{-10}\text{ m}$)
ADC	Analogue-to-digital converter
APCI	Atmospheric pressure chemical ionization
AQ	Acquisition time
ATR	Attenuated Total Reflectance
B_0	Static magnetic field
B_1	Oscillating magnetic field
BHT	Butylated hydroxytoluene
CPMG	Carr-Purcell-Meiboom-Gill (pulse sequence)
CW	Continuous wave
CC	Chemical Composition
CCD	Chemical Composition Distribution
δ	Chemical shift (ppm)
ΔG	Change in Gibbs free energy
ΔH	Change in Enthalpy
ΔS	Change in Entropy
Δt	pulse duration
D	Dispersity Index ($=M_w/M_n$), also abbreviated as PDI
DFT	Discrete Fourier Transform
DRI	Differential refractive index (detector)
EC-QCL	External-cavity quantum cascade laser
ELSD	Evaporative Light Scattering Detector
ϵ	Molar attenuation coefficient
ESI	Electro-spray ionization
F	Frequency
FID	Free-induction decay
$F_{suppr.}$	Suppression factor of polymer signal
FT	Fourier transform
FT-IR	Fourier transform infra-red (spectroscopy)
FWHM	Full width at half maximum
G	Gibbs free energy
GC	Gas chromatography
GPC	Gel permeation chromatography
HPLC	High Performance Liquid Chromatography

I_0	Insident light
I	Transmitted light
i.d.....	Internal diameter
IR.....	Infrared
Laser.....	Light Amplification by Stimulated Emission of Radiation
LC.....	Liquid Chromatography
LAC.....	Liquid Adsorption Chromatography
LC-CC.....	Liquid Chromatography at Critical Conditions
MALDI-ToF.....	Matrix-assisted laser desorption/ionization time-of-flight
MALLS.....	Multi-angle laser light scattering
MCT.....	Mercury-cadmium-telluride
M_n	Number average molecular weight
MM.....	Molar mass
MMD.....	Molar mass distribution
MRI.....	Magnetic resonance imaging (spectroscopy)
MR-NMR.....	Medium-resolution nuclear magnetic resonance (spectroscopy)
MS.....	Mass spectrometry
M_w	Weight average molecular weight
o.d.....	Outer diamter (\varnothing)
PBCI.....	Particle beam chemical ionization
PEMA.....	Polyethyl methacrylate
PEO.....	Polyethyleneoxide
PFG.....	Pulsed field gradients
PMMA.....	Polymethyl methacrylate
ppm.....	parts per million
PS.....	Polystyrene
pts.....	points
PTFE.....	Polytetrafluoroethylene
RD.....	Recycle delay
Re.....	Reynolds number
RTD.....	Residence time distribution
RF.....	Radio frequency
RMS.....	Root Mean Square
RSD.....	relative standard deviation
RxG.....	Receiver gain
SBR.....	Styrene butadiene rubber
SDV.....	Styrene-divinylbenzene copolymer network (stationary phase)
SEC.....	Size-exclusion chromatography
S/N.....	Signal-to-noise ratio
T_1	Longitudinal relation time (spin-lattice relaxation)
T_2	Transverse relation time (spin-spin relaxation)
t_{ave}	Average residence time
T_c	Curie Temperature
$t_{Delay-1}$	Delay time
$t_{Delay-2}$	Hold time
THF.....	Tetrahydrofuran

t_{info}	Information time
TMDE	" <u>T</u> ime-resolved nuclear <u>M</u> agnetic Detection of <u>E</u> luates" and is the software package developed in this work
t_{min}	Minimum time
TMS	Tetramethylsilane
TOP	Time-out processing
T_p	Period duration
TSP	Thermospray ionization
$t_{total(conventionalSEC)}$..	Total measurement time for conventional SEC
UV	Ultra-violet
v_{ave}	Average velocity
V_e	Elution volume
Vis	Visible light
\dot{v}	Volumetric flow rate
v_{max}	Maximum velocity
WATERGATE	Water suppression by Gradient-Tailored Excitation (pulse sequence)
WEFT	Water elimination Fourier transform NMR spectroscopy
WET	Water suppression Enhanced through T_1 effects (pulse sequence)

Trigonometric Identities

The following trigonometric identities are provided to aid in expansion of trigonometric terms during calculations where the product operator formalism is utilized:

where	$\sin^2 A + \cos^2 A = 1$
	$\sin(A \pm B) = \sin A \cos B \pm \cos A \sin B$
	$\cos(A \pm B) = \cos A \cos B \pm \sin A \sin B$
	$\sin A \cos B = \frac{1}{2} [\sin(A + B) + \sin(A - B)]$
	$\cos A \sin B = \frac{1}{2} [\sin(A + B) - \sin(A - B)]$
	$\sin A \sin B = \frac{1}{2} [\cos(A - B) - \cos(A + B)]$
	$\cos A \cos B = \frac{1}{2} [\cos(A + B) + \cos(A - B)]$
	$\sin 2A = 2 \sin A \cos A$
	$\cos 2A = \cos^2 A - \sin^2 A$
	$\sin^2 A = \frac{1}{2} (1 - \cos 2A)$
	$\cos^2 A = \frac{1}{2} (1 + \cos 2A)$
	$\cos A = (e^{iA} + e^{-iA}) / 2$
	$\sin A = (e^{iA} - e^{-iA}) / 2i$
	$e^{iA} = \cos A + i \sin A$
	$e^{-iA} = \cos A - i \sin A$

List of Figures

2.1	The operational modes in HPLC.	8
2.2	Depiction of the SEC separation mechanism, including the calibration curve.	10
2.3	Statistical approach to molecular retention in a porous particle.	11
2.4	The SEC distribution with reference to the obtainable molar mass averages in SEC.	15
2.5	Band broadening principle in chromatography.	15
2.6	Band broadening parameters related to the Gaussian peak-shape function.	16
2.7	Depiction of the van Deemter curve.	18
2.8	Depiction of the electromagnetic spectrum.	21
2.9	The energy splitting diagram for nuclei with a spin quantum number of $I = \frac{1}{2}$	24
2.10	The principle of nuclear precession in an applied external magnetic field.	25
2.11	The principle of magnetization in the vector model.	29
2.12	A single pulse NMR experiment and the associated magnetization behaviour.	30
2.13	Benchtop NMR instrument comparison.	35
2.14	Depiction of the Halbach magnet array.	36
2.15	The S/N of permanent and superconducting magnets as a function of field strength and RF coils.	38
2.16	Detection principle in continuous-flow NMR spectroscopy.	39
2.17	Flow rate effect on ^1H -NMR spectral resolution.	41
2.18	The standard and U-type flow cell design for high field NMR spectroscopy.	42
2.19	QCL milestone timeline.	45
2.20	Depiction of the difference between inter-band and inter-subband lasers.	47
2.21	Basic principle behind the operation of a QCL.	48
2.22	Schematic depiction of the Littrow configuration used in EC-QCLs.	49
2.23	Illustration of a digital signal processing system.	54
2.24	Depiction of a continuous-time signal digitized to a discrete-time signal.	55
3.1	Depiction of the three important molecular characteristics	57
4.1	SEC-MR-NMR set-up.	64
4.2	Flow cell geometries for SEC-MR-NMR.	66
4.3	Depiction of various flow profiles.	67
4.4	Flow profile prediction by means of Reynolds number.	68
4.5	The residence time distribution (RTD) of five flow cells.	71

4.6	Flow cell performance based on an SEC-NMR application.	73
4.7	The "magic triangle" for the correct SEC column selection.	77
4.8	Illustration of column-to-flow-cell mismatch and how it affects the DRI and NMR signal.	79
4.9	The effect of column overloading on molar mass and \bar{D} estimations.	81
4.10	The effect of column overloading on the number of theoretical plates and peak shape.	82
4.11	The S/N as a function of the flow rate.	84
4.12	Effect of the flow cell position relative to the NMR coil.	85
4.13	Effect of the flow cell position in SEC-NMR measurement.	86
4.14	Effect of the flow rate on both the DRI and NMR detectors.	87
4.15	Depiction of the compromise between parameters when performing method development using a benchtop NMR spectrometer.	89
4.16	A conventional nutation experiment for calibration of the pulse width.	91
4.17	Effect of flow rate on the 90° pulse length at a reduced sample length.	92
4.18	Depiction of the reduction of the apparent longitudinal (T_1) relaxation times as a function of flow rate.	94
4.19	Depiction of sinc (wiggles) artefacts as a result of FID clipping.	95
4.20	The effect of the recycle delay on the FWHM and S/N of a PMMA sample.	96
4.21	Effect of the receiver gain settings on S/N and FWHM on CHCl_3	98
4.22	Effect of receiver gain settings on the S/N of PMMA on-flow.	99
4.23	Illustration of the 1-Pulse-spoil and IvR-spoil pulse sequences.	100
4.24	The effect of molar mass on the T_1 -values of a PMMA calibration standard series.	101
4.25	The measure of suppression efficiency of the 1-Pulse-spoil pulse sequence on the solvent and analyte resonances of PS and PMMA calibration standards.	103
4.26	Comparison of the 1-Pulse-spoil and inversion recovery pulse sequences applied to CHCl_3 and THF.	107
4.27	A generalized depiction of an interlinked software platform for post data acquisition processing.	110
4.28	Depiction of the TMDE graphical user interface (GUI) for the signal processing of SEC and NMR data.	111
4.29	The window functions used for apodization in the TMDE software.	114
4.30	Effect of apodization on PMMA calibration standard signal.	115
4.31	Optimum bandwidth on S/N and FWHM of a PMMA calibration standard using a Gaussian window function.	116
4.32	Evaluation of the apodization functions on the S/N ratio as a function of FWHM of a PMMA calibration standard.	117
4.33	Illustration of the different window functions used for smoothing in the SEC dimension.	119
4.34	Effect of the different SEC filters on the S/N and FWHM of a PMMA calibration standard.	121

4.35	Depiction of the region associated with reference subtraction.	123
4.36	Depiction of improved definition of the NMR peak shape for solvent subtraction.	123
4.37	The effect of solvent subtraction on solvent peak reduction.	124
4.38	Depiction of drift correction along the SEC dimension for the NMR spectrum.	126
4.39	SEC-NMR data set before and after data treatment using the TMDE software.	128
4.40	Static ^1H -NMR spectra of PS and PMMA homopolymers at 62 MHz.	130
4.41	Characterization of a physical blend using SEC-NMR.	131
4.42	High field and low field NMR spectra comparison of the PS- <i>b</i> -PMMA block copolymer.	132
4.43	SEC-NMR analysis of a PS- <i>b</i> -PMMA block copolymer.	134
4.44	Depiction of the multiple distributions obtainable within a block copolymer.	136
4.45	High field NMR spectra comparison of the PS- <i>b</i> -PEMA block copolymers.	137
4.46	The effect of the recycle delay (acquisition length) on the S/N of a PS- <i>b</i> -PEMA sample.	138
4.47	Comparison of high- and low-field NMR spectroscopy under static- and continuous-flow-conditions of a PS- <i>b</i> -PEMA sample.	139
4.48	SEC-NMR analysis of the PS- <i>b</i> -PEMA (95:5 <i>mol%</i>) block copolymer.	140
4.49	SEC-NMR analysis of a PS- <i>b</i> -PEMA (70:30 <i>mol%</i>) block copolymer.	141
4.50	SEC-NMR analysis of a PS- <i>b</i> -PEMA (50:50 <i>mol%</i>) block copolymer.	142
4.51	SEC-NMR calibration curves of the molar mass as a function of the elution volume for PS and PMMA.	144
4.52	The S/N as a function of the injected mass of a PS calibration standard via SEC-NMR analysis.	147
4.53	Static ^1H -NMR spectra of PS, PB and SBR-A at 62 MHz.	150
4.54	SEC-NMR analysis of two commercial SBR samples in THF.	152
4.55	SEC-NMR analysis of two commercial SBR samples in CHCl_3	154
5.1	SEC-EC-QCL set-up.	161
5.2	Depiction of a pulse-train on the EC-QCL spectrometer.	162
5.3	Illustration of the available tuning range of the different QCL sources.	163
5.4	Depiction of the pulse shape obtained from a 540 ns pulse length using the QCL-1 source at $\tilde{\nu} = 1820 \text{ cm}^{-1}$	163
5.5	Effect of column-to-flow-cell mismatch on the DRI and QCL signal.	165
5.6	Characterization of the pulse-to-pulse noise of the reference and sample detectors.	167
5.7	Illustration of the data acquisition cycle of the EC-QCL process.	168
5.8	Irregular time spacing of the data points collected on the EC-QCL instrument.	169
5.9	Effect of time-out processing (TOP) time on the data spacing irregularities on the EC-QCL instrument.	170
5.10	Depiction of the QCL graphical user interface (GUI) for the signal processing of SEC and QCL data.	172
5.11	Baseline correction and de-noising of an SEC-EC-QCL measurements of PMMA using the QCL analysis software.	175

5.12	Effect of different smoothing and baseline fit combinations in SEC-EC-QCL on the S/N and FWHM of a PMMA calibration standard.	176
5.13	Smoothing comparison relative to the raw EC-QCL data.	176
5.14	The LOD and LOQ determination on the SEC-EC-QCL set-up.	178
5.15	Stacked FTIR spectra of PS, PMMA, and THF.	180
5.16	SEC-EC-QCL analysis of a PS/PMMA physical blend in THF.	181
5.17	Stacked FTIR spectra of PS and acetylated-PS.	182
5.18	SEC-EC-QCL analysis of an acetylated-PS sample in THF.	183
6.1	Comparison of single, interlaced, and sinusoidal SEC injections.	186
6.2	Illustration of the increased separation throughput in SEC when performing interlaced SEC.	188
6.3	The interlaced SEC-NMR measurement performed on a PMMA calibration standard.	189
6.5	Quantification of the effectiveness of interlaced SEC-NMR measurements on a PMMA calibration standard.	190
6.6	Depiction of the sinusoidal SEC-NMR set-up.	192
6.7	Illustration of the linear regime of the analytical column and a sinusoidal excitation corresponding to it.	193
6.8	Stability evaluation of the sinusoidal SEC injections at 1 and 2.8 min excitation periods.	194
6.9	The phase calibrated PS molar mass calibration of the sinusoidal SEC injection.	195
6.10	The sinusoidal SEC-NMR measurement performed on a PS calibration standard and corresponding correlogram.	197
6.11	Discrete Fourier spectrum of the converted UV traces and S/N comparison between conventional and sinusoidal SEC injections.	198
7.1	The S/N as a function of the injected mass of a PS calibration standard via SEC-NMR analysis comparing the 60 and 80 MHz NMR spectrometers.	202
A.1	Photograph of the SEC-MR-NMR hyphenation.	273
A.2	Photograph of the flow cell box.	274
A.3	Photograph of the EC-QCL spectrometer.	274
A.4	SEC set-up used for hyphenation to the EC-QCL detector.	275
A.5	Photograph of the EC-QCL flow cell with an expansion drawing.	276
A.6	Photograph of the mock 'injection' trigger used for sinusoidal SEC.	277

List of Tables

1.1	Summary of polymer parameters, application properties, and characterization techniques.	3
2.1	Categorization of LC detectors according to their applicability.	19
2.2	Magnetic properties of selected nuclei with a spin quantum number of $I = \frac{1}{2}$	23
2.3	Description of Hamilton operators with respect to NMR interactions.	27
2.4	Summary of commercially available benchtop NMR spectrometers in 2020.	34
2.5	An overview of magnetic properties for a selection of permanent magnet materials.	37
4.1	An overview of the performance of custom built flow cells.	70
4.2	Quantification of flow cell effects on the chromatographic- and spectroscopic-dimensions for an SEC-NMR experiment.	73
4.3	Size exclusion chromatography column parameters.	76
4.4	Recommended sample concentration needed for molar mass and molar mass distribution.	78
4.5	Effect of flow rate on the ^1H -NMR signal via the benchmark experiment.	83
4.6	Evaluation of the suppression efficiency of the 1-Pulse-spoil pulse sequence.	104
4.7	Comparison of the solvent suppression efficiency of the 1-Pulse-spoil to inversion recovery pulse sequences applied to PS in chloroform.	108
4.8	Summary of the window functions used for apodization in the TMDE software.	113
4.9	Summary of the phase correction techniques implemented by TMDE software.	118
4.10	Summary of the effect of solvent subtraction on solvent peak reduction.	125
4.11	Summary of the effect on S/N of different order baseline corrections to an SEC-NMR measurement.	127
4.12	The analyte statistics reported by the TMDE software for a physical blend of 1:1 wt% PS/PMMA measured with SEC-NMR.	131
4.13	Ratios of the respective blocks of the PS- <i>b</i> -PMMA sample determined by high and low field NMR spectroscopy.	133
4.14	The analyte statistics reported by the TMDE software for the PS- <i>b</i> -PMMA block copolymer measured by SEC-NMR.	133
4.15	Ratios of the respective blocks of the PS- <i>b</i> -PEMA sample series determined by high field NMR spectroscopy.	136

4.16	The analyte statistics reported by the TMDE software of the PS- <i>b</i> -PEMA block copolymers measured by SEC-NMR.	140
4.17	Chemical composition determination via high field NMR spectroscopy and SEC-NMR measurements.	143
4.18	Comparison of molar mass of PS- <i>b</i> -PEMA determined by SEC-NMR and triple-SEC.	145
4.19	Chemical composition-corrected molar masses of PS- <i>b</i> -PEMA determined by triple-SEC and SEC-NMR.	146
4.20	Summary of the optimization parameters for SEC-NMR hyphenation.	149
4.21	Chemical composition of SBR determined by high field NMR spectroscopy.	151
4.22	Chemical shift, S/N , FWHM, and molar mass information obtained by SEC-NMR on SBRs in THF and CHCl_3	155
4.23	Standard operating procedure for SEC-MR-NMR measurements.	157
5.1	Summary of the pulsed-mode operation specification for the EC-QCL spectrometer.	164
5.2	Peak statistics for the DRI and QCL traces using either an analytical or semi-preparative column.	166
A.1	Longitudinal relaxation times (T_1) of PS- <i>b</i> -PEMA under static and continuous flow conditions.	280
A.2	Calibration standard sets used for the construction of the PS and PMMA calibration curves.	280
A.3	Response factors for the UV and DRI detectors used for chemical composition correction.	281
A.4	Overview of the effect of smoothing and fit combination in SEC-EC-QCL on S/N and FWHM of a PMMA calibration standard.	281

Bibliography

- [1] C. Guise-Richardson, *Technology and Culture* **2010**, *51*, 357–387.
- [2] H. Staudinger, *Reports of the German Chemical Society (A and B Series)* **1920**, *53*, 1073–1085.
- [3] ChemistryWorld, The birth of the polymer age, <https://rb.gy/fhnhcc>, Accessed November 5, 2020.
- [4] PlasticsEurope, Plastics - the Facts 2019, An analysis of European plastics production, demand and waste data, <https://rb.gy/dnawel>, Accessed November 5, 2020.
- [5] H. Pasch, B. Trathnigg, *Multidimensional HPLC of Polymers*, Springer, **2013**.
- [6] L. Wheeler, J. Willis, *Applied Spectroscopy* **1993**, *47*, 1128–1130.
- [7] T. F. Beskers, T. Hofe, M. Wilhelm, *Polymer Chemistry* **2015**, *6*, 128–142.
- [8] S. Morlock, J. M. Kübel, T. F. Beskers, B. Lendl, M. Wilhelm, *Macromolecular Rapid Communications* **2018**, *39*, 1700307.
- [9] W. Hiller, H. Pasch, T. Macko, M. Hofmann, J. Ganz, M. Spraul, U. Braumann, R. Streck, J. Mason, F. Van Damme, *Journal of Magnetic Resonance* **2006**, *183*, 290–302.
- [10] M. Cudaj, G. Guthausen, T. Hofe, M. Wilhelm, *Macromolecular Rapid Communications* **2011**, *32*, 665–670.
- [11] H. Raich, P. Blümmler, *Concepts in Magnetic Resonance Part B: Magnetic Resonance Engineering: An Educational Journal* **2004**, *23*, 16–25.
- [12] E. Danieli, J. Perlo, B. Blümich, F. Casanova, *Angewandte Chemie International Edition* **2010**, *49*, 4133–4135.
- [13] B. Blümich, *Trends in Analytical Chemistry* **2016**, *83*, 2–11.
- [14] J. Höpfner, K.-F. Ratzsch, C. Botha, M. Wilhelm, *Macromolecular Rapid Communications* **2018**, *39*, 1700766.
- [15] C. Botha, J. Höpfner, B. Mayerhöfer, M. Wilhelm, *Polymer Chemistry* **2019**, *10*, 2230–2246.

- [16] J. M. Kübel, C. Botha, A. Bucka, J. Höpfner, H. Zimmermann, M. Godejohann, M. Wilhelm, *Macromolecular Rapid Communications* **2019**, *40*, 1900228.
- [17] A. M. Striegel, *Analytical and Bioanalytical Chemistry* **2008**, *390*, 303–305.
- [18] A. F. Siegle, O. Trapp, *Journal of Chromatography A* **2016**, *1448*, 93–97.
- [19] D. Farnan, G. T. Moreno, J. Stults, A. Becker, G. Tremintin, M. van Gils, *Journal of Chromatography A* **2009**, *1216*, 8904–8909.
- [20] L. S. Ettre, A. Zlatkis, *75 Years of Chromatography: a Historical Dialogue*, Elsevier, **2011**.
- [21] K. James, N. Wire, J. D. Bradfield, S. Moore, *The Holy Bible*, World Publishing Company, **1979**.
- [22] L. Snyder, J. Kirkland, J. Dolan, *Introduction to Modern Liquid Chromatography*, Wiley, **2011**.
- [23] R. P. Scott, *Chrom-ed Book Series* **2003**, *1*.
- [24] G. Glöckner, *Gradient HPLC of Copolymers and Chromatographic Cross-Fractionation*, Springer Berlin Heidelberg, **2012**.
- [25] S. Entelis, V. Evreinov, A. Gorshkov in *Functionality and Molecular Weight Distribution of Telechelic Polymers*, Springer, **1986**, pp. 129–175.
- [26] J.-A. Raust, *Ph.D. Thesis: Development of multidimensional Chromatography for complex (METH) Acrylate-based Copolymers used in cosmetic Applications*, Technische Universität Darmstadt, **2008**.
- [27] P.-G. De Gennes, *Reports on Progress in Physics* **1969**, *32*, 187.
- [28] G. Lathe, C. Ruthven, *The Biochemical Journal* **1955**, *60*, xxxiv–xxxiv.
- [29] G. H. Lathe, C. R. J. Ruthven, *Biochemical Journal* **1956**, *62*, 665–674.
- [30] J. C. Moore, *Journal of Polymer Science Part A: General Papers* **1964**, *2*, 835–843.
- [31] D. Berek, *Progress in Polymer Science* **2000**, *25*, 873–908.
- [32] D. Berek, *Journal of Separation Science* **2010**, *33*, 315–335.
- [33] A. Striegel, W. W. Yau, J. J. Kirkland, D. D. Bly, *Modern Size-Exclusion Liquid Chromatography: Practice of Gel Permeation and Gel Filtration Chromatography*, John Wiley & Sons, **2009**.
- [34] E. Malawer, L. Senak, *Handbook of Size Exclusion Chromatography* **2003**, 1–24.
- [35] S. Podzimek, *Light scattering, Size Exclusion Chromatography and Asymmetric Flow Field Flow Fractionation: Powerful Tools for the Characterization of Polymers, Proteins and Nanoparticles*, John Wiley & Sons, **2011**.

- [36] Z. Grubisic, P. Rempp, H. Benoit, *Journal of Polymer Science Part B: Polymer Letters* **1967**, *5*, 753–759.
- [37] A. M. Striegel, *Journal of Chromatography A* **2001**, *932*, 21–31.
- [38] L. K. Kostanski, D. M. Keller, A. E. Hamielec, *Journal of Biochemical and Biophysical Methods* **2004**, *58*, 159–186.
- [39] S. Mori, H. G. Barth, *Size Exclusion Chromatography*, Springer Science & Business Media, **2013**.
- [40] C. Wu, *Handbook Of Size Exclusion Chromatography and Related Techniques: Revised And Expanded*, Taylor & Francis, **2003**.
- [41] J. Cazes, *Journal of Chemical Education* **1966**, *43*, A567.
- [42] J. Cazes, *Journal of Chemical Education* **1966**, *43*, A625.
- [43] M. Lechner, E. Nordmeier, K. Gehrke in *Makromolekulare Chemie*, Springer, **2010**, pp. 48–170.
- [44] I. Simon, *Journal of Applied Crystallography* **1971**, *4*, 317–318.
- [45] R. F. T. Stepto, *Polymer International* **2010**, *59*, 23–24.
- [46] P. E. Pierce, J. E. Armonas, *Journal of Polymer Science Part C: Polymer Symposia* **1968**, *21*, 23–29.
- [47] S. Mori, T. Suzuki, A. Wada, *Journal of Liquid Chromatography* **1983**, *6*, 61–75.
- [48] L. Tung, J. Runyon, *Journal of Applied Polymer Science* **1969**, *13*, 2397–2409.
- [49] G. Meira, M. Netopilík, M. Potschka, I. Schnöll-Bitai, J. Vega, *Macromolecular Symposia* **2007**, *258*, 186–197.
- [50] J. Van Deemter, F. Zuiderweg, A. v. Klinkenberg, *Chemical Engineering Science* **1956**, *5*, 271–289.
- [51] S.-T. Popovici, W. T. Kok, P. J. Schoenmakers, *Journal of Chromatography A* **2004**, *1060*, 237–252.
- [52] S. T. Popovici, P. J. Schoenmakers, *Journal of Chromatography A* **2005**, *1099*, 92–102.
- [53] B. Zhang, X. Li, B. Yan, *Analytical and Bioanalytical Chemistry* **2008**, *390*, 299–301.
- [54] B. Trathnigg, *Progress in Polymer Science* **1995**, *20*, 615–650.
- [55] L. Huber, S. A. George, *Diode Array Detection in HPLC*, M. Dekker, **1993**.
- [56] M. I. James, B. J. Hunt, *Polymer Characterization*, Blackie Academic & Professional, **1993**.
- [57] B. H. Zimm, *The Journal of Chemical Physics* **1945**, *13*, 141–145.

- [58] C. Jackson, H. G. Barth, *Handbook of Size Exclusion Chromatography and Related Techniques* **2003**, 91, 99.
- [59] D. Held, P. Kilz, *The Column* **2008**, 4, 14–17.
- [60] S. Grcev, P. Schoenmakers, P. Iedema, *Polymer* **2004**, 45, 39–48.
- [61] D. A. Skoog, F. J. Holler, S. R. Crouch, *Principles of Instrumental Analysis*, Cengage learning, **2017**.
- [62] T. A. van Beek, *Phytochemical Analysis* **2020**.
- [63] S. G. Levine, *Journal of Chemical Education* **2001**, 78, 133.
- [64] M. Karplus, *Journal of the American Chemical Society* **1963**, 85, 2870–2871.
- [65] J. Stonehouse, P. Adell, J. Keeler, A. Shaka, *Journal of the American Chemical Society* **1994**, 116, 6037–6038.
- [66] A. Abragam, *Principles of Nuclear Magnetism*, Oxford University Press, **1961**.
- [67] R. R. Ernst, G. Bodenhausen, A. Wokaun, *Principles of Nuclear Magnetic Resonance in One and Two Dimensions, Vol. 14*, Clarendon Press Oxford, **1987**.
- [68] A. Derome, *Modern NMR Techniques for Chemistry Research*, Pergamon Press, **1987**.
- [69] J. Cavanagh, W. Fairbrother, A. Palmer, N. Skelton, *Protein NMR Spectroscopy: Principles and Practice*, Elsevier Science, **1995**.
- [70] S. W. Homans, *A Dictionary of Concepts in NMR*, Clarendon Press Oxford, **1992**.
- [71] M. H. Levitt, *Spin Dynamics: Basics of Nuclear Magnetic Resonance*, John Wiley & Sons, **2013**.
- [72] A. Edmonds, *Angular Momentum in Quantum Mechanics*, Princeton University Press, **1996**.
- [73] P. Atkins, J. De Paula, J. Keeler, *Atkins' Physical Chemistry*, Oxford University Press, **2018**.
- [74] P. Zeeman, *The London Edinburgh and Dublin Philosophical Magazine and Journal of Science* **1897**, 43, 226–239.
- [75] F. Bloch, *Physical Review* **1946**, 70, 460.
- [76] K. Schmidt-Rohr, H. W. Spiess, *Multidimensional Solid-State NMR and Polymers*, Elsevier, **2012**.
- [77] M. Mehring, *Principles of High Resolution NMR in Solids*, Springer Science & Business Media, **2012**.
- [78] E. Hahn, D. Maxwell, *Physical Review* **1952**, 88, 1070.

- [79] T. D. Claridge, *High-Resolution NMR Techniques in Organic Chemistry*, Vol. 27, Elsevier, **2016**.
- [80] T. C. Farrar, E. Becker, *Introduction to Pulse and Fourier Transform NMR Methods*, Academic Press New York, **1971**.
- [81] J. W. Cooley, J. W. Tukey, *Mathematics of Computation* **1965**, *19*, 297–301.
- [82] O. Sørensen, G. Eich, M. H. Levitt, G. Bodenhausen, R. Ernst, *Progress in Nuclear Magnetic Resonance Spectroscopy* **1984**, *16*, 163–192.
- [83] D. P. Goldenberg, *Concepts in Magnetic Resonance Part A* **2010**, *36*, 49–83.
- [84] N. Niccolai, M. d. l. P. Leon de Miles, S. P. Hehir, W. A. Gibbons, *Journal of the American Chemical Society* **1978**, *100*, 6528–6529.
- [85] E. L. Hahn, *Physical Review* **1950**, *80*, 580.
- [86] H. Y. Carr, E. M. Purcell, *Physical Review* **1954**, *94*, 630.
- [87] S. Meiboom, D. Gill, *Review of Scientific Instruments* **1958**, *29*, 688–691.
- [88] P. Giraudeau, F.-X. Felpin, *Reaction Chemistry & Engineering* **2018**, *3*, 399–413.
- [89] Bruker, The Fourier Benchtop, <https://rb.gy/wi621z>, Accessed June 4, 2020.
- [90] Magritek, Spinsolve 43, <https://rebrand.ly/jm3sg>, Accessed June 4, 2020.
- [91] Magritek, Spinsolve 60, <https://rebrand.ly/nt9sy>, Accessed June 4, 2020.
- [92] Magritek, Spinsolve 80, <https://rb.gy/rfqin6>, Accessed June 4, 2020.
- [93] Nanalysis, NMReady-60PRO, <https://rb.gy/pchiuf>, Accessed June 4, 2020.
- [94] Nanalysis, 100PRO, <https://rb.gy/fmuw5h>, Accessed June 4, 2020.
- [95] Oxford, X-Pulse, <https://rb.gy/labgg2>, Accessed June 4, 2020.
- [96] ThermoFischer, picoSpin Series II, <https://rb.gy/138ea1>, Accessed June 4, 2020.
- [97] Magritek, Spinsolve Ultra, <https://rb.gy/9pzsi1>, Accessed June 4, 2020.
- [98] B. Blümich, *Modern Magnetic Resonance* **2016**, 1–33.
- [99] E. Danieli, J. Perlo, A. Duchateau, G. Verzipl, V. Litvinov, B. Blümich, F. Casanova, *ChemPhysChem* **2014**, *15*, 3060–3066.
- [100] B. Gouilleux, B. Charrier, E. Danieli, J.-N. Dumez, S. Akoka, F.-X. Felpin, M. Rodriguez-Zubiri, P. Giraudeau, *Analyst* **2015**, *140*, 7854–7858.
- [101] Magritek, Spinsolve, <https://rebrand.ly/0mkt8>, Accessed June 4, 2020.
- [102] A. F. Holleman, *Lehrbuch der anorganischen Chemie*, Walter de Gruyter GmbH & Co KG, **2019**.
- [103] ThyssenKrupp Magnettechnik, Magnetische Eigenschaften (AlNiCo), <https://rb.gy/nkzxd1>, Accessed June 4, 2020.

- [104] M. De Campos, F. Landgraf, N. Saito, S. Romero, A. Neiva, F. Missell, E. De Morais, S. Gama, E. Obrucheva, B. Jalnin, *Journal of Applied Physics* **1998**, *84*, 368–373.
- [105] P. Campbell, *Permanent Magnet Materials and Their Application*, Cambridge University Press, **1996**.
- [106] K. Albert, *On-line LC-NMR and Related Techniques*, John Wiley & Sons, **2003**.
- [107] K. Albert, *Journal of Chromatography A* **1995**, *703*, 123–147.
- [108] G. Suryan in Proceedings of the Indian Academy of Sciences-Section A, *Vol. 33*, Springer, **1951**, p. 107.
- [109] K. Singh, B. Blümich, *Trends in Analytical Chemistry* **2016**, *83*, 12–26.
- [110] F. Dalitz, M. Cudaj, M. Maiwald, G. Guthausen, *Progress in Nuclear Magnetic Resonance Spectroscopy* **2012**, *60*, 52–70.
- [111] V. Sans, L. Porwol, V. Dragone, L. Cronin, *Chemical Science* **2015**, *6*, 1258–1264.
- [112] M. V. Silva Elipe, R. R. Milburn, *Magnetic Resonance in Chemistry* **2016**, *54*, 437–443.
- [113] B. Gouilleux, B. Charrier, S. Akoka, F.-X. Felpin, M. Rodriguez-Zubiri, P. Giraudeau, *Trends in Analytical Chemistry* **2016**, *83*, 65–75.
- [114] T. Parker, E. Limer, A. Watson, M. Defernez, D. Williamson, E. K. Kemsley, *Trends in Analytical Chemistry* **2014**, *57*, 147–158.
- [115] N. Watanabe, E. Niki, *Proceedings of the Japan Academy Series B* **1978**, *54*, 194–199.
- [116] E. Bayer, K. Albert, M. Nieder, E. Grom, T. Keller, *Journal of Chromatography A* **1979**, *186*, 497–507.
- [117] J. F. Haw, T. Glass, D. Hausler, E. Motell, H. Dorn, *Analytical Chemistry* **1980**, *52*, 1135–1140.
- [118] E. Bayer, K. Albert, M. Nieder, E. Grom, G. Wolff, M. Rindlisbacher, *Analytical Chemistry* **1982**, *54*, 1747–1750.
- [119] J. Buddrus, H. Herzog, *Organic Magnetic Resonance* **1980**, *13*, 153–155.
- [120] J. Buddrus, H. Herzog, J. W. Cooper, *Journal of Magnetic Resonance (1969)* **1981**, *42*, 453–459.
- [121] J. F. Haw, T. Glass, H. Dorn, *Analytical Chemistry* **1981**, *53*, 2327–2332.
- [122] J. F. Haw, T. Glass, H. Dorn, *Analytical Chemistry* **1981**, *53*, 2332–2336.
- [123] J. F. Haw, T. Glass, H. Dorn, *Journal of Magnetic Resonance (1969)* **1982**, *49*, 22–31.
- [124] J. F. Haw, T. Glass, H. Dorn, *Analytical Chemistry* **1983**, *55*, 22–29.

- [125] J. Buddrus, H. Herzog, *Analytical Chemistry* **1983**, *55*, 1611–1614.
- [126] D. A. Laude Jr, R. W. Lee, C. L. Wilkins, *Journal of Magnetic Resonance (1969)* **1984**, *60*, 453–459.
- [127] H. Dorn, *Analytical Chemistry* **1984**, *56*, 747A–758A.
- [128] K. Albert, M. Nieder, E. Bayer, M. Spraul, *Journal of Chromatography A* **1985**, *346*, 17–24.
- [129] S. A. Korhammer, A. Bernreuther, *Fresenius' Journal of Analytical Chemistry* **1996**, *354*, 131–135.
- [130] J. C. Lindon, J. K. Nicholson, I. D. Wilson, *Progress in Nuclear Magnetic Resonance Spectroscopy* **1996**, *29*, 1–49.
- [131] U. G. Sidelmann, E. M. Lenz, M. Spraul, M. Hofmann, J. Troke, P. N. Sanderson, J. C. Lindon, I. D. Wilson, J. K. Nicholson, *Analytical Chemistry* **1996**, *68*, 106–110.
- [132] A. Hölzel, G. Schlotterbeck, K. Albert, E. Bayer, *Chromatographia* **1996**, *42*, 499–505.
- [133] G. Schlotterbeck, H. Pasch, K. Albert, *Polymer Bulletin* **1997**, *38*, 673–679.
- [134] R. Pecharroman-Gallego, *Lasers in Engineering (Old City Publishing)* **2013**, *24*.
- [135] A. Lambrecht, M. Pfeifer, W. Konz, J. Herbst, F. Axtmann, *Analyst* **2014**, *139*, 2070–2078.
- [136] R. Kazarinov, R. A. Suris, *Sov. Phys.-Semicond.* **1971**, *5*, 707–709.
- [137] L. Esaki, R. Tsu, *IBM Journal of Research and Development* **1970**, *14*, 61–65.
- [138] J. Faist, F. Capasso, D. L. Sivco, C. Sirtori, A. L. Hutchinson, A. Y. Cho, *Science* **1994**, *264*, 553–556.
- [139] J. Faist, *Quantum Cascade Lasers*, Oxford University Press, **2013**.
- [140] C. Gmachl, F. Capasso, D. L. Sivco, A. Y. Cho, *Reports on Progress in Physics* **2001**, *64*, 1533.
- [141] J. Devenson, R. Teissier, O. Cathabard, A. Baranov, *Applied Physics Letters* **2007**, *90*, 111118.
- [142] S. Kumar, Q. Qin, B. S. Williams, Q. Hu, Z. R. Wasilewski, X. Wu, H. C. Liu in Conference on Lasers and Electro-Optics, Optical Society of America, **2007**, CWP1.
- [143] D. Revin, J. Cockburn, M. Steer, R. Airey, M. Hopkinson, A. Krysa, L. Wilson, S. Menzel, *Applied Physics Letters* **2007**, *90*, 021108.
- [144] G. Scalari, S. Blaser, J. Faist, H. Beere, E. Linfield, D. Ritchie, G. Davies, *Physical Review Letters* **2004**, *93*, 237403.

- [145] M. Semsiv, M. Wienold, S. Dressler, W. Masselink, *Applied Physics Letters* **2007**, *90*, 051111.
- [146] M. J. Weida, D. Arnone, T. Day, *Laser Focus World* **2006**, *42*, S13.
- [147] J. Faist, F. Capasso, C. Sirtori, D. L. Sivco, J. N. Baillargeon, A. L. Hutchinson, S.-N. G. Chu, A. Y. Cho, *Journal of Crystal Growth* **1997**, *175*, 22–28.
- [148] S. Kumar, *IEEE Journal of Selected Topics in Quantum Electronics* **2010**, *17*, 38–47.
- [149] M. S. Vitiello, G. Scalari, B. Williams, P. De Natale, *Optics Express* **2015**, *23*, 5167–5182.
- [150] L. West, S. Eglash, *Applied Physics Letters* **1985**, *46*, 1156–1158.
- [151] A. Kojevnikov, *Historical Studies in the Physical and Biological Sciences* **1999**, *29*, 295–331.
- [152] J. Ohtsubo, *Semiconductor Lasers: Stability, Instability and Chaos, Vol. 111*, Springer, **2012**.
- [153] G. Luo, C. Peng, H. Le, S. Pei, W.-Y. Hwang, B. Ishaug, J. Um, J. N. Baillargeon, C.-H. Lin, *Applied Physics Letters* **2001**, *78*, 2834–2836.
- [154] M. G. Littman, H. J. Metcalf, *Applied Optics* **1978**, *17*, 2224–2227.
- [155] T. O’Haver, *A pragmatic introduction to signal processing*, University of Maryland at College Park, **1997**.
- [156] J. G. Proakis, D. G. Manolakis, *Digital Signal Processing, Fourth International Edition*, Upper Saddle River, New Jersey: Pearson Prentice Hall, **2007**.
- [157] V. Thomsen, D. Schatzlein, D. Mercurio, *Spectroscopy* **2003**, *18*, 112–114.
- [158] D. MacDougall, W. B. Crummett, et al., *Analytical Chemistry* **1980**, *52*, 2242–2249.
- [159] M. J. Macielag in *Antibiotic Discovery and Development*, Springer, **2012**, pp. 793–820.
- [160] H. Kovacs, D. Moskau, M. Spraul, *Progress in Nuclear Magnetic Resonance Spectroscopy* **2005**, *2*, 131–155.
- [161] A. Webb in *NMR Spectroscopy in Pharmaceutical Analysis*, Elsevier, **2008**, pp. 83–130.
- [162] V. Rizzo, V. Pincioli, *Journal of Pharmaceutical and Biomedical Analysis* **2005**, *38*, 851–857.
- [163] G. F. Pauli, T. Godecke, B. U. Jaki, D. C. Lankin, *Journal of Natural Products* **2012**, *75*, 834–851.
- [164] G. Pagès, A. Gerdova, D. Williamson, V. Gilard, R. Martino, M. Malet-Martino, *Analytical Chemistry* **2014**, *86*, 11897–11904.

- [165] P. Horowitz, H. Winfield, *The Art of Electronics 2nd Edition*, Cambridge University Press, **1989**.
- [166] J. H. Lee, Y. Okuno, S. Cavagnero, *Journal of Magnetic Resonance* **2014**, *241*, 18–31.
- [167] D. Flannery, *The Square Root of 2: A Dialogue Concerning a Number and a Sequence*, Springer Science & Business Media, **2006**.
- [168] D. Moskau, *Concepts in Magnetic Resonance: An Educational Journal* **2002**, *15*, 164–176.
- [169] Atta-ur-Rahman, *One and Two Dimensional NMR Spectroscopy*, Elsevier Science, **2014**.
- [170] M. Delsuc, J. Lallemand, *Journal of Magnetic Resonance (1969)* **1986**, *69*, 504–507.
- [171] T. Kitayama, K. Ute in *Modern Magnetic Resonance*, Springer, **2008**, pp. 399–405.
- [172] T. Provder, *Advances in Chemistry Series* **1995**, *247*.
- [173] S. Crotty, S. Gerişlioğlu, K. J. Endres, C. Wesdemiotis, U. S. Schubert, *Analytica Chimica Acta* **2016**, *932*, 1–21.
- [174] T. Gruendling, S. Weidner, J. Falkenhagen, C. Barner-Kowollik, *Polymer Chemistry* **2010**, *1*, 599–617.
- [175] D. L. Pavia, G. M. Lampman, G. S. Kriz, J. A. Vyvyan, *Introduction to Spectroscopy*, Cengage Learning, **2008**.
- [176] J. L. Dwyer, M. Zhou, *International Journal of Spectroscopy* **2011**, *2011*, 1–12.
- [177] T. F. Beskers, T. Hofe, M. Wilhelm, *Macromolecular Rapid Communications* **2012**, *33*, 1747–1752.
- [178] H. Pasch, *Polymer Chemistry* **2013**, *4*, 2628–2650.
- [179] A. P. Gies, *Mass Spectrometry in Polymer Chemistry* **2011**, 33–56.
- [180] M. Karas, F. Hillenkamp, *Analytical Chemistry* **1988**, *60*, 2299–2301.
- [181] K. Tanaka, H. Waki, Y. Ido, S. Akita, Y. Yoshida, T. Yoshida, T. Matsuo, *Rapid Communications in Mass Spectrometry* **1988**, *2*, 151–153.
- [182] S. M. Weidner, J. Falkenhagen, *Analytical Chemistry* **2011**, *83*, 9153–9158.
- [183] Agilent Technologies, LSD Limit-of-Detection by LC-MS, <https://rb.gy/e9xgj1>, Accessed July 9, 2020.
- [184] I. Krämer, H. Pasch, H. Händel, K. Albert, *Macromolecular Chemistry and Physics* **1999**, *200*, 1734–1744.
- [185] V. Exarchou, M. Krucker, T. A. van Beek, J. Vervoort, I. P. Gerathanassis, K. Albert, *Magnetic Resonance in Chemistry* **2005**, *43*, 681–687.

- [186] W. Hiller, H. Pasch, P. Sinha, T. Wagner, J. Thiel, M. Wagner, K. Müllen, *Macromolecules* **2010**, *43*, 4853–4863.
- [187] M. Cudaj, G. Guthausen, T. Hofe, M. Wilhelm, *Macromolecular Chemistry and Physics* **2012**, *213*, 1933–1943.
- [188] T. Kitayama, K. Hatada, *NMR Spectroscopy of Polymers*, Springer Science & Business Media, **2013**.
- [189] W. Hiller, P. Sinha, M. Hehn, H. Pasch, *Progress in Polymer Science* **2014**, *39*, 979–1016.
- [190] W. Hiller, P. Sinha, H. Pasch, *Macromolecular Chemistry and Physics* **2007**, *208*, 1965–1978.
- [191] W. Hiller, P. Sinha, H. Pasch, *Macromolecular Chemistry and Physics* **2009**, *210*, 605–613.
- [192] G. Montaudo, D. Garozzo, M. S. Montaudo, C. Puglisi, F. Samperi, *Macromolecules* **1995**, *28*, 7983–7989.
- [193] M. S. Montaudo, *Polymer* **2002**, *43*, 1587–1597.
- [194] K. Klimke, M. Parkinson, C. Piel, W. Kaminsky, H. W. Spiess, M. Wilhelm, *Macromolecular Chemistry and Physics* **2006**, *207*, 382–395.
- [195] W. Hiller, M. Hehn, T. Hofe, K. Oleschko, *Analytical Chemistry* **2010**, *82*, 8244–8250.
- [196] B. Lendl, J. Frank, R. Schindler, A. Müller, M. Beck, J. Faist, *Analytical Chemistry* **2000**, *72*, 1645–1648.
- [197] A. Edelmann, C. Ruzicka, J. Frank, B. Lendl, W. Schrenk, E. Gornik, G. Strasser, *Journal of Chromatography A* **2001**, *934*, 123–128.
- [198] C. R. Webster, G. J. Flesch, D. C. Scott, J. E. Swanson, R. D. May, W. S. Woodward, C. Gmachl, F. Capasso, D. L. Sivco, J. N. Baillargeon, et al., *Applied Optics* **2001**, *40*, 321–326.
- [199] L. Hvozdar, S. Gianordoli, G. Strasser, W. Schrenk, K. Unterrainer, E. Gornik, C. S. Murthy, M. Kraft, V. Pustogow, B. Mizaikoff, et al., *Applied Optics* **2000**, *39*, 6926–6930.
- [200] A. A. Kosterev, F. K. Tittel, C. Gmachl, F. Capasso, D. L. Sivco, J. N. Baillargeon, A. L. Hutchinson, A. Y. Cho, *Applied Optics* **2000**, *39*, 6866–6872.
- [201] B. Paldus, T. Spence, R. Zare, J. Oomens, F. Harren, D. Parker, C. Gmachl, F. Capasso, D. Sivco, J. Baillargeon, et al., *Optics Letters* **1999**, *24*, 178–180.
- [202] R. J. Ogg, R. Kingsley, J. S. Taylor, *Journal of Magnetic Resonance Series B* **1994**, *104*, 1–10.

- [203] D. I. Hoult, R. Richards, *Journal of Magnetic Resonance (1969)* **1976**, *24*, 71–85.
- [204] A. T. Corey, PhD thesis, Colorado State University. Libraries, **1949**.
- [205] D. Vuckovic in *Proteomic and Metabolomic Approaches to Biomarker Discovery*, Elsevier, **2020**, pp. 53–83.
- [206] PSS Polymer Standards Service GmbH, How to Expand The Lifetime of Columns, <https://rb.gy/2ycaof>, Accessed November 25, 2020.
- [207] D. Held, *The Column* **2013**, *9*, 9–12.
- [208] R. A. Shalliker, H. J. Catchpoole, G. R. Dennis, G. Guiochon, *Journal of Chromatography A* **2007**, *1142*, 48–55.
- [209] S. H. Smallcombe, S. L. Patt, P. A. Keifer, *Journal of Magnetic Resonance Series A* **1995**, *2*, 295–303.
- [210] H. Santos, D. L. Turner, A. V. Xavier, *Journal of Magnetic Resonance (1969)* **1983**, *55*, 463–467.
- [211] P. A. Keifer, *Concepts in Magnetic Resonance: an Educational Journal* **1999**, *11*, 165–180.
- [212] P. S. Wu, G. Otting, *Journal of Magnetic Resonance* **2005**, *176*, 115–119.
- [213] Bruker, Bruker: TopSpin, <https://rb.gy/kyotgw>, Accessed September 21, 2020.
- [214] H. Mo, J. Harwood, D. Raftery, *Magnetic Resonance in Chemistry* **2011**, *49*, 655–658.
- [215] A. M. Torres, W. S. Price, *Concepts in Magnetic Resonance Part A* **2016**, *45*, e21387.
- [216] J. L. Sudmeier, U. L. Günther, K. Albert, W. W. Bachovchin, *Journal of Magnetic Resonance Series A* **1996**, *118*, 145–156.
- [217] C. Fyfe, M. Cocivera, S. Damji, T. Hostetter, D. Sproat, J. O'brien, *Journal of Magnetic Resonance (1969)* **1976**, *23*, 377–384.
- [218] A. J. Oosthoek-de Vries, J. Bart, R. M. Tiggelaar, J. W. Janssen, P. J. M. van Bantum, H. J. Gardeniers, A. P. Kentgens, *Analytical Chemistry* **2017**, *89*, 2296–2303.
- [219] H. Mo, J. S. Harwood, D. Raftery, *Magnetic Resonance in Chemistry* **2010**, *48*, 235–238.
- [220] S. L. Patt, B. D. Sykes, *The Journal of Chemical Physics* **1972**, *56*, 3182–3184.
- [221] F. Benz, J. Feeney, G. K. Roberts, *Journal of Magnetic Resonance (1969)* **1972**, *8*, 114–121.
- [222] T. Inubushi, E. D. Becker, *Journal of Magnetic Resonance (1969)* **1983**, *51*, 128–133.

- [223] B. Mayerhöfer, *M.Sc. Thesis: Optimization of Medium-Resolution NMR-Spectroscopy under Flow Conditions*, Karlsruher Institut für Technologie, **2018**.
- [224] J. M. Wing, *40th Anniversary Blog of Social Issues in Computing* **2014**, 2014, 26.
- [225] A. Ebel, W. Dreher, D. Leibfritz, *Journal of Magnetic Resonance* **2006**, 182, 330–338.
- [226] H. De Brouwer, *Journal of Magnetic Resonance* **2009**, 201, 230–238.
- [227] P. Hore, *Journal of Magnetic Resonance (1969)* **1985**, 62, 561–567.
- [228] P. Blümner, MATLAB NMR Library, **2003**, https://www.ag-heil.physik.uni-mainz.de/Dateien/The_MATLAB_NMR_Library.pdf.
- [229] F. J. Harris, *Proceedings of the IEEE* **1978**, 66, 51–83.
- [230] S. Starosielec, D. Hägele, *Signal Processing* **2014**, 102, 240–246.
- [231] B. Gouilleux, B. Charrier, S. Akoka, P. Giraudeau, *Magnetic Resonance in Chemistry* **2017**, 55, 91–98.
- [232] P. J. Flory, *Journal of the American Chemical Society* **1940**, 62, 1561–1565.
- [233] S. Koltzenburg, M. Maskos, O. Nuyken, *Polymer Chemistry*, Springer, **2017**.
- [234] K. Matyjaszewski, A. H. Müller, *Controlled and Living Polymerizations: from Mechanisms to Applications*, John Wiley & Sons, **2009**.
- [235] D. A. Laude, R. W. Lee, C. L. Wilkins, *Analytical Chemistry* **1985**, 57, 1281–1286.
- [236] D. A. Laude, R. W. Lee, C. L. Wilkins, *Analytical Chemistry* **1985**, 57, 1286–1290.
- [237] L. Griffiths, *Analytical Chemistry* **1995**, 67, 4091–4095.
- [238] L. Griffiths, *Magnetic Resonance in Chemistry* **1997**, 35, 257–261.
- [239] P. Kilz, H. Pasch, *Encyclopedia of Analytical Chemistry: Applications Theory and Instrumentation* **2006**.
- [240] V. Röntzsch, M. Wilhelm, G. Guthausen, *Magnetic Resonance in Chemistry* **2016**, 54, 494–501.
- [241] S. Kok, C. Wold, T. Hankemeier, P. Schoenmakers, *Journal of Chromatography A* **2003**, 1017, 83–96.
- [242] P. J. DesLauriers, D. C. Rohlffing, E. T. Hsieh, *Polymer* **2002**, 43, 159–170.
- [243] M. Reschke, T. Kunz, T. Laepple, *Computers & Geosciences* **2019**, 123, 65–72.
- [244] D. T. Childs, R. A. Hogg, D. G. Revin, I. U. Rehman, J. W. Cockburn, S. J. Matcher, *Applied Spectroscopy Reviews* **2015**, 50, 822–839.
- [245] G. Sun, T. Chen, S. Worley, *Polymer* **1996**, 37, 3753–3756.

- [246] J. M. Nasrullah, S. Raja, K. Vijayakumaran, R. Dhamodharan, *Journal of Polymer Science Part A: Polymer Chemistry* **2000**, *38*, 453–461.
- [247] Y. Gao, H.-M. Li, *Polymer International* **2004**, *53*, 1436–1441.
- [248] A. N. Siyal, S. Q. Memon, M. Khuhawar, *Polish Journal of Chemical Technology* **2012**, *14*, 11–18.
- [249] W. Dong, X. Wang, Z. Jiang, B. Tian, Y. Liu, J. Yang, W. Zhou, *Polymers* **2019**, *11*, 1033.
- [250] P. Diederich, S. K. Hansen, S. A. Oelmeier, B. Stolzenberger, J. Hubbuch, *Journal of Chromatography A* **2011**, *1218*, 9010–9018.
- [251] J. Kahle, H. Wätzig, *European Journal of Pharmaceutics and Biopharmaceutics* **2018**, *126*, 101–103.
- [252] H. Pasch, P. Kilz, *Macromolecular Rapid Communications* **2003**, *24*, 104–108.
- [253] PSS Polymer Standards Service GmbH, UDC 810 Interface, <https://rb.gy/sxp5mu>, Accessed August 10, 2019.
- [254] Agilent Technologies, 10 x more sensitivity with the Agilent 1290/1260 Infinity Diode Array Detector compared to Agilent 1200 Series UV Detectors, <https://rb.gy/m8wrqc>, Accessed November 4, 2020.
- [255] M. Matz, *M.Sc. Thesis: Development and Optimisation of a Novel Liquid Chromatographic Method with Period Excitation*, Karlsruher Institut für Technologie, **2020**.
- [256] T. Butz, *Fourier Transformation for Pedestrians*, Springer, **2006**.

Appendices

A.1 TMDE GUI Documentation



Institute for Technical Chemistry and Polymer Chemistry
Polymeric Materials

TMDE GUI Documentation

May 2020

Carlo Botha
Aleksandra Bucka
Dr. Johannes Höpfner
Prof. Dr. Manfred Wilhelm

Table of Contents

1. Introduction	3
2. Requirements	4
3. Standalone app	5
4. GUI components	5
4.1 File panel	6
4.2 Data Processing Panel	6
4.2.1 Apodization panel.....	7
4.2.2 Phase correction panel	8
4.2.3 Filter the data panel	9
4.2.4 Solvent panel and Noise panel	10
4.2.5 Subtract reference spectra panel	10
4.2.6 Find peaks panel	11
4.2.7 Drift correction panel	11
4.2.8 Average of spectra panel	11
4.3 Visualization Panel	12
4.4 Data Export Panel	13
5. How does the GUI work?	15
6. Results	17

1. Introduction

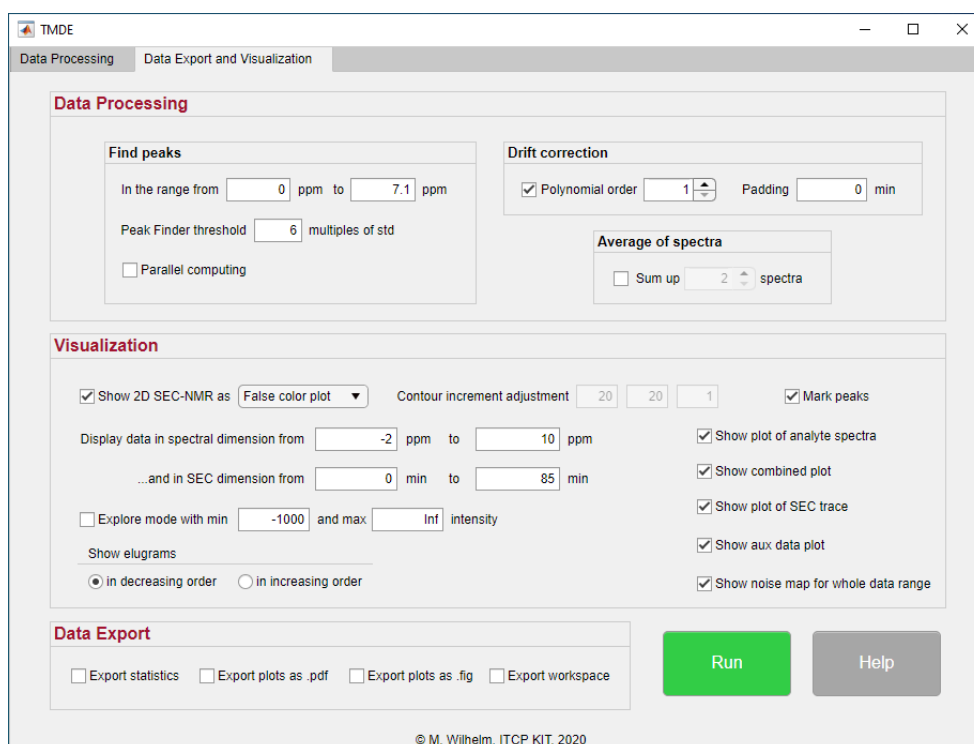
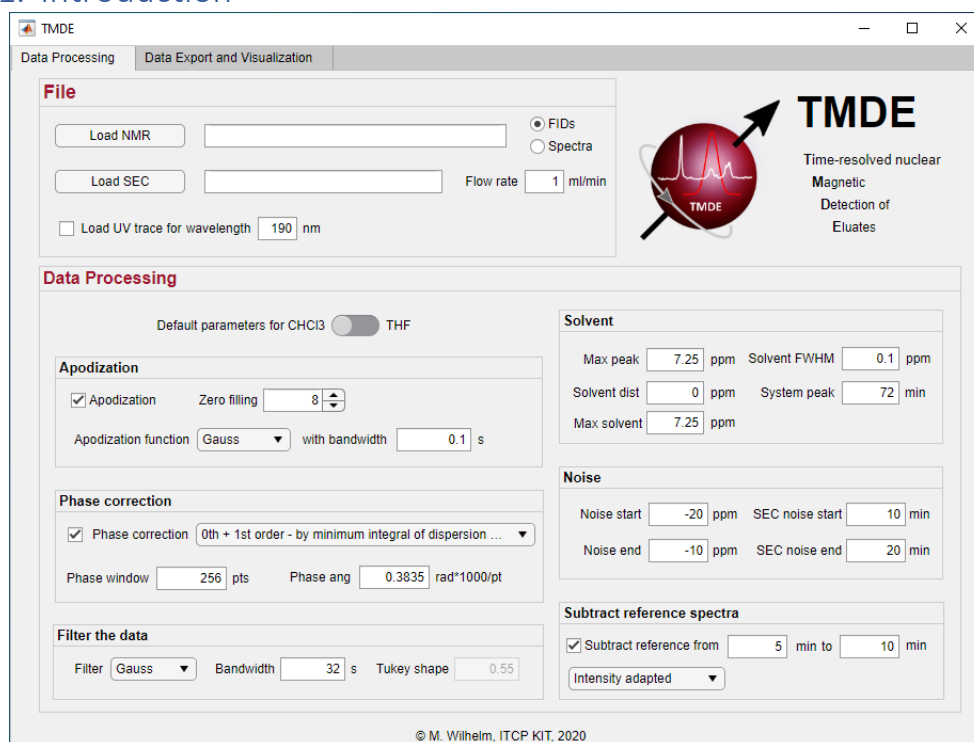


Figure 1: The graphical user interface (GUI), Time-resolved nuclear Magnetic Detection of Eluates (TMDE), illustrating the Data Processing tab.

This document provides information on how the Graphical User Interface (GUI – **Figure 1**), Time-resolved nuclear **M**agnetic **D**etection of **E**luates (TMDE) operates. It is designed for the simultaneous

analysis of nuclear magnetic resonance (NMR) spectroscopy and size exclusion chromatography (SEC) data.

The GUI consists of following steps:

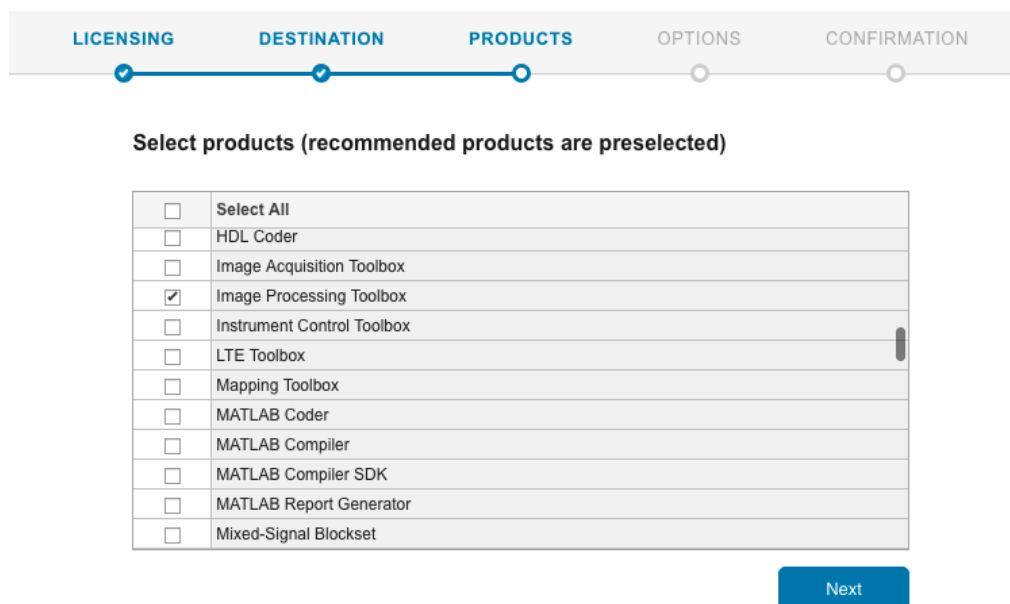
- Loading the NMR files (*.2d, *.dat, *.par)
- Loading the SEC file (*.txt)
- Input of parameters for data processing
- Selection of plots to be shown
- Export of statistics to Excel and saving plots to *.pdf and/or *.fig

The GUI enables the following tasks to be performed:

- Apodization and/or Zero filling
- Phase correction
- Smoothing
- Solvent suppression
- Peak detection
- Drift correction
- Averaging of spectra to reduce the amount of data
- Calculation of statistics

2. Requirements

In order to open and operate the GUI, select the file **NMRmaster.mlapp**. This file should be kept in the same folder as the file **NMRmaster_fun.m**, *functions* folder and the **NMR GUI documentation.pdf**. The GUI requires MATLAB r2018b or a later version and installation of the following toolboxes: Signal Processing, Image Processing and Statistics. Additionally, in order to perform fast computation, it is useful to install the Parallel Computing Toolbox. Microsoft Excel is required for data export. The required toolboxes can be selected during MATLAB installation (**Figure 2**).



<input type="checkbox"/>	Sensor Fusion and Tracking Toolbox
<input type="checkbox"/>	SerDes Toolbox
<input checked="" type="checkbox"/>	Signal Processing Toolbox
<input type="checkbox"/>	SimBiology
<input type="checkbox"/>	SimEvents
<input type="checkbox"/>	Simulink Test
<input type="checkbox"/>	Stateflow
<input checked="" type="checkbox"/>	Statistics and Machine Learning Toolbox
<input type="checkbox"/>	Symbolic Math Toolbox
<input type="checkbox"/>	System Composer

Figure 2: MATLAB toolboxes that are required for TMDE.

3. Standalone app

In order to convert the GUI to a standalone application, take following steps:

1. Open **Application Compiler** app by entering `applicationCompiler` in the MATLAB command window.
2. In the **MATLAB compiler** window, add the `NMRmaster.mlapp` as main file.
3. Decide whether to include the MATLAB Runtime installer in the generated application by selecting one of the two options in the **Packaging Options** section:
 - a. **Runtime downloaded from web** — Generates an installer that downloads the MATLAB Runtime and installs it along with the deployed MATLAB application.
 - b. **Runtime included in package** — Generates an installer that includes the MATLAB Runtime installer.
4. Add the GUI description and desktop icon image in the **Application Information**.
5. In the **Additional installer option** > **Files required for your application to run**, add (if not added already): `NMRmaster_fun.m`, `NMR GUI documentation.pdf` and all the files from the `functions` folder (browse to the `functions` folder and select all the files inside the folder by clicking CTRL-A).
6. To generate the packaged application, click **Package** in the top part of the Compiler. In the Save Project dialog box, specify the location to save the project.
7. When the process is completed, check the generated output.
8. The `for_redistribution` folder contains the executable, which can be shared with other users and used for installation of the standalone app.

To install the standalone application, a MATLAB license is not required. All the steps needed for compilation and installation of the standalone app are also explained here: <https://se.mathworks.com/help/compiler/create-and-install-a-standalone-application-from-matlab-code.html>.

Important: It is not possible to compile and run the app on different operating systems, i.e. a Windows compiled app can be only installed on Windows.

4. GUI components

The GUI consists of two tabs: a Data Processing tab and Data Export and Visualization tab (as shown in **Figure 1**). Each tab includes several panels with different functionalities, which will be described in detail. Holding the mouse over (mouse hover) various GUI elements also brings up a short description of that component.

4.1 File panel



Figure 3: File panel.

In the file panel (**Figure 3**), upload the NMR data which consists of three files:

- 2D NMR data file ***fiddata.2d*** for FIDs data or ***data.2d*** for spectral data,
- time points auxillary file, ***timelist.dat***,
- acquisition parameter auxillary file, ***acqu.par***.

In order to upload the data, click on the 'Load NMR' button and select the three files in the dialog box. Multiple selection is possible using the CTRL key and left mouse button. Data loading can take a moment which is indicated by the progress window. Choose between using FIDs or spectral data. The path to the chosen ****.2d*** file is later shown in the white box. Use mouse-hover over the box to see the entire path location, i.e. the exact path where the data is located on the given computer.

The SEC file with the ****.txt*** extension can be uploaded by clicking on the 'Load SEC' button. Enter the flow rate that is used to calculate the elution time for DRI data.

Both data sets (NMR and SEC) are necessary for the program to be executed. Optionally, the 'Load UV trace for wavelength...' box can also be selected to upload the UV trace from the SEC file and enables the corresponding wavelength to be inserted. The data will later be displayed in the generated plot.

Important: Make sure that the SEC file contains time data in the first column, DRI data in the second column and UV data in the third column.

4.2 Data Processing Panel

In this panel, two default parameter sets (**Figure 4**) for either CHCl₃ or THF can be selected, which upon selection will automatically fill in all the parameters in the various processing panels. Additionally, if another solvent has been used the new parameters can be inserted in each subpanel manually, which will overwrite the default parameters.



Figure 4: Switch between CHCl₃ and THF default parameters.

The **Apodization** (**Figure 5**) and **Filter the data** (**Figure 10**) panels work together for data processing. Applying certain combinations of the two filters affects the results.

4.2.1 Apodization panel



Figure 5: Apodization panel.

In the apodization panel (**Figure 5**), the box can be checked to enable apodization in the spectral dimension, by choosing one of the following functions in the dropdown menu:

- Gauss
- Lorentz-Gauss
- Lorentz
- Exponential
- Trafficante

and with the given filter bandwidth, given in seconds. The 'spinner (up-and-down arrows)' allows choosing of the zero-filling factor that defaults to eight. **Figure 6** gives a visual overview of how different bandwidths affect the data.

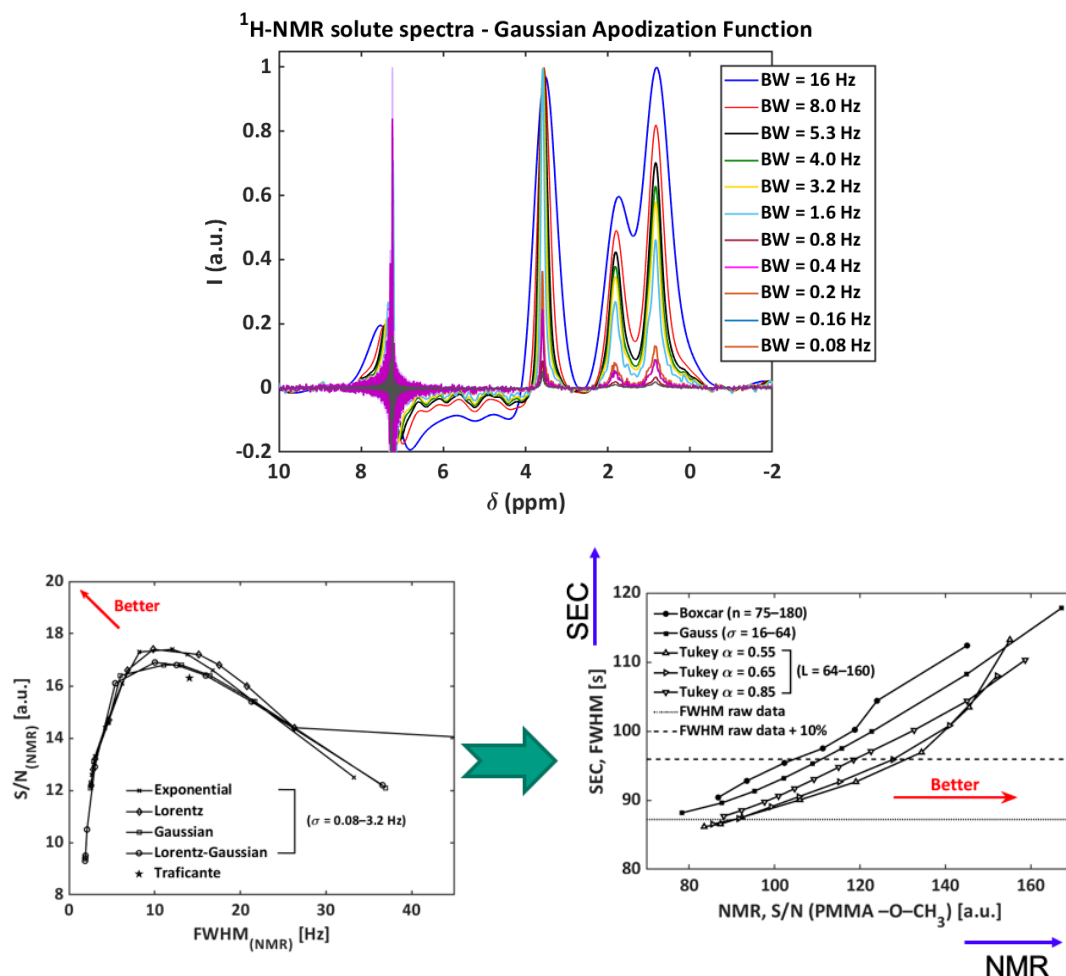


Figure 6: Effect of apodization bandwidth on S/N and line broadening for (top and bottom left) the NMR dimension. This filter is typically employed with an additional filter in the SEC dimension (4.2.3) for optimum results (bottom right). The sample comprised of a PMMA standard, with a molar mass of 30 000 g/mol and dispersity index, \mathcal{D} , of 1.03 using chloroform as solvent.

4.2.2 Phase correction panel



Figure 7: Phase correction panel.

In order to perform phase correction, choose one method between the seven methods defined in the drop-down menu. Enter the size of the window around the solvent/highest peak (in points) and the fixed value angle for the first order correction in the third method. This parameter is also used in the seventh method (Interactive phase correction tool, **Figure 8**) for the same dwell time and pivot point location.

The seventh method enables phase correction to be performed interactively (**Figure 8**). The tool is based on a script developed by Peter Blümler.

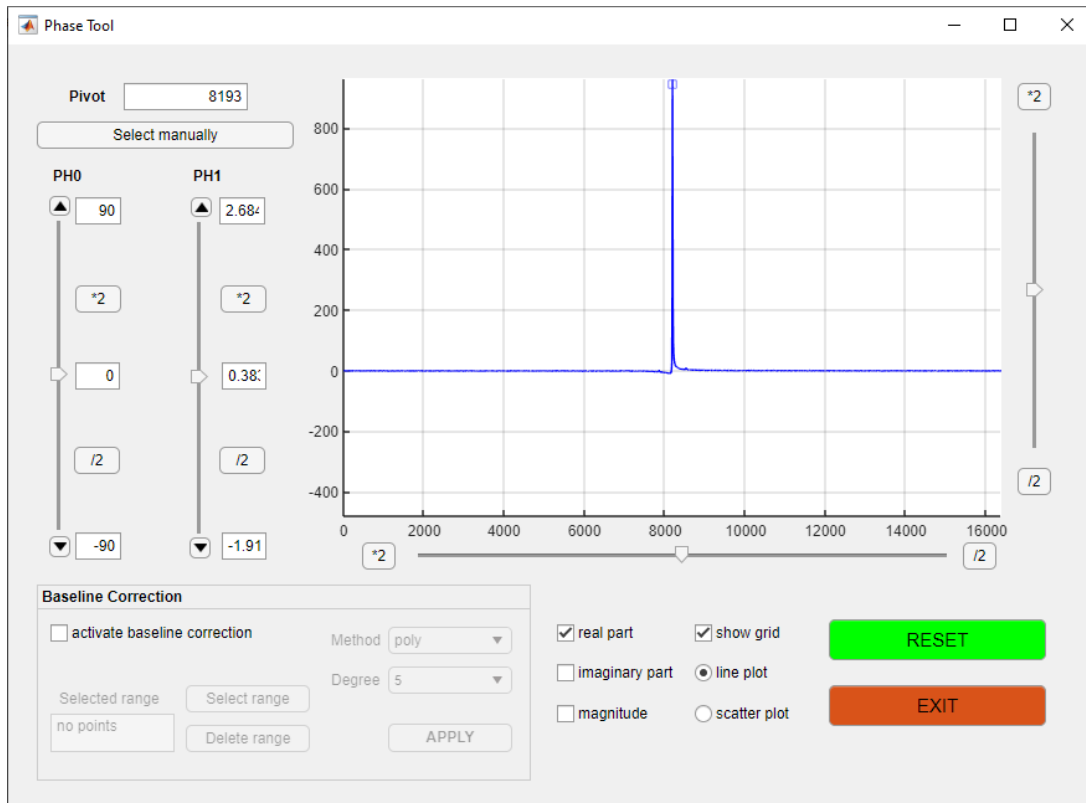


Figure 8: Phase correction tool.

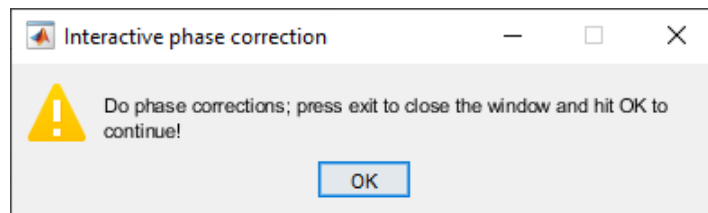


Figure 9: Short instruction to the phase correction tool.

Additional to the phase correction window (Figure 8), a short descriptive window appears on the screen (Figure 9). First, perform necessary phase corrections, then press the EXIT button in the phase correction tool window, and finally hit the OK button in the descriptive window (the descriptive window can be moved to the side while performing phase corrections).

The phase correction tool can also be turned off by unchecking the box.

4.2.3 Filter the data panel



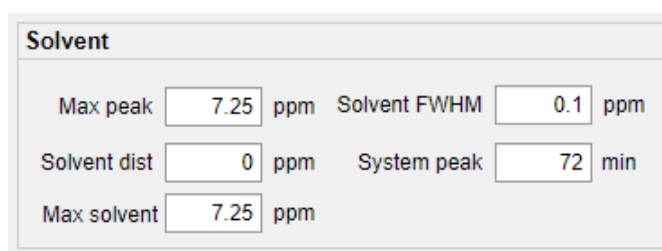
Figure 10: Filter the data panel

Data smoothing in the SEC dimension (**Figure 10**) can be performed with one of the following functions:

- Gauss
- Tukey (tapered cosine function)
- Boxcar
- No filter

Enter the filter bandwidth (or sliding window for boxcar) in seconds and in the case of the Tukey filter – the filter shape (this parameter becomes editable after selecting the Tukey filter). Smaller shape values approximate a rectangular shaped filter and larger ones a Gaussian filter. It is also possible to select the 'No filter' option from the drop-down menu.

4.2.4 Solvent panel and Noise panel



Solvent

Max peak ppm Solvent FWHM ppm

Solvent dist ppm System peak min

Max solvent ppm

Figure 11: Solvent panel.



Noise

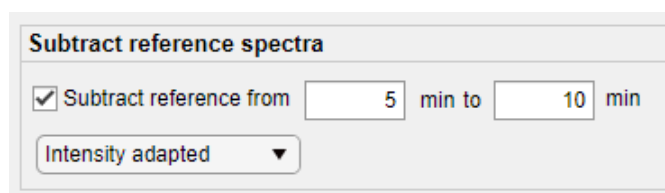
Noise start ppm SEC noise start min

Noise end ppm SEC noise end min

Figure 12: Noise panel.

The parameters in the solvent (**Figure 11**) and noise (**Figure 12**) panels are described in tooltips (a short description of each parameter by using mouse hover). The *Noise start* parameter should be smaller than the *Noise end* parameter and the *SEC noise start* parameter should be smaller than the *SEC noise end* parameter. The parameter's *Max peak* and *Max solvent* should only be different when the solvent peak is not the highest/strongest peak or in the case of a solvent that does not have a single resonance frequency, e.g. THF.

4.2.5 Subtract reference spectra panel



Subtract reference spectra

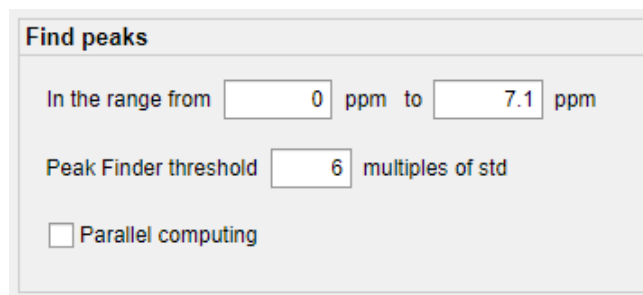
Subtract reference from min to min

▼

Figure 13: Subtract reference spectra panel.

In this panel (**Figure 13**), check the box in order to subtract reference spectra from the real data. The range for the reference spectrum should be defined in the editable fields, where the first value should be smaller than the second one. Using the drop-down menu, choose between either height adjusted subtraction (Intensity adapted) or direct subtraction (Fixed intensity) to be performed. For the first option, the reference spectrum is adjusted to the height of the peak maximum.

4.2.6 Find peaks panel



Find peaks

In the range from ppm to ppm

Peak Finder threshold multiples of std

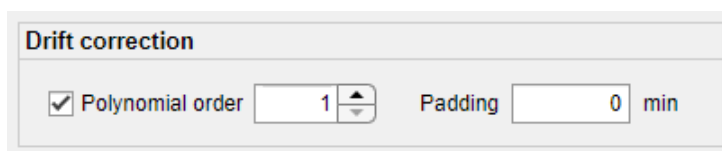
Parallel computing

Figure 14: Find peaks panel.

In order to detect peaks, specify the spectral range, where the peaks are expected to be found, as well as the peak height threshold in terms of multiples of the standard deviation. The standard deviation is calculated in the region defined by parameters in the Noise panel ([4.2.4](#)).

If *'Parallel computing'* is checked/turned on, the program connects to all the available cores of the computer, which allows faster computation, i.e. decreased data evaluation time. It is only possible if the MATLAB Parallel Computing Toolbox is installed. The initial start-up takes a short while. However, after activation it is activated for 30 minutes after which it will be automatically shut down.

4.2.7 Drift correction panel



Drift correction

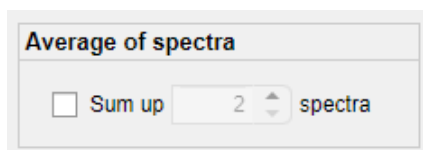
Polynomial order

Padding min

Figure 15: Drift correction panel.

This panel (**Figure 15**) enables drift correction to be performed on the data in the SEC dimension. The program fits a polynomial baseline with *'polynomial order'* to the peak-free area and subtracts it from the data. Linear fit (polynomial of the first order) is the default option and the third order polynomial is the highest possible one. Additionally, the range before and after each peak can be defined to ensure larger exclusion (*'Padding'*). By default, there is no padding (0 minutes).

4.2.8 Average of spectra panel



Average of spectra

Sum up spectra

Figure 16: Average of spectra panel.

By checking the 'Sum up' box (**Figure 16**) in this panel, the amount of data can be reduced. The program averages the number of spectra defined in the 'spinner'. This option has a similar effect to smoothing. It shows better signal-to-noise ratio, but reduced resolution. By default, the averaging is not used and the spinner is not editable.

4.3 Visualization Panel

Figure 17: Visualization panel.

The Visualization panel controls the following plots to be displayed:

- Plot of the 2D SEC-NMR data in form of a false colour plot or a contour plot (selected from the drop-down menu); the false colour plot can be displayed with marked peaks or not (check box); the contour plot needs additional adjustment (editable fields): the three parameters determine the number of levels at which the contours should be displayed, e.g.: the '*contour increment adjustment*' parameters 20, 20 and 1, is defined as levels with data intensity starting at (highest peak intensity/20) and ending at (highest peak intensity/1) in steps of (highest peak intensity/20).
- Plot of the analyte spectra (at the time slices corresponding to the peaks found)
- Combined plot of the analyte spectra, 2D SEC-NMR data and elugrams with the corresponding DRI- and UV-traces (if given)
- Plot of the SEC trace (DRI-trace)
- Plot of the auxiliary data; this one can be shown only if the phase correction, apodization, and solvent suppression were performed
- Noise map which shows the standard deviations calculated from equal regions of NMR data (the size of one region is 0.5 ppm x 2 min)

All plots (except for the noise map) are displayed in the range determined in the editable fields. The explore mode defines the intensity range to be displayed.

Additionally, there is an option to display the elugrams listed either from the highest to lowest or lowest to highest peak prominence.

4.4 Data Export Panel

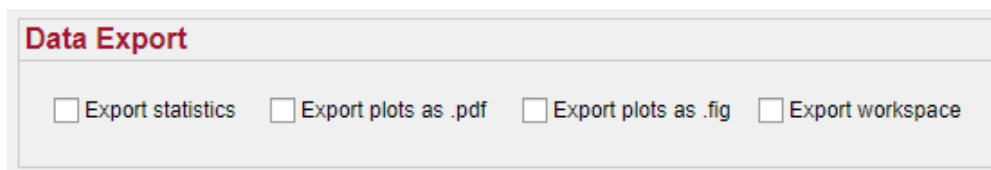


Figure 18: Data Export panel.

In the data export panel (**Figure 18**), there are several options to export data, i.e. to export statistics to Excel (as **stats_sec-nmr.xls**), write plots as ***.pdf** and/or MATLAB ***.fig** files and save the MATLAB workspace (as a **NMR_workspace.mat** file). Everything is saved in the same directory as the data uploaded in the File panel ([4.1](#)). The *.pdf plots are saved with a resolution of 300 dots per inch (dpi).

The exported Excel file consists of several tables (**Figure 19–Figure 20**).

TMDE Evaluation V2.0final													
Peak	ET	CS	SNR_SEC	noise_SEC	SNR_NMR	noise_NMR	int2D	FWHM_spec	FWTM_spec	FWHM_chrom	FWTM_chrom	FWHM_spec_PF	FWHM_chrom_PF
Peak 1	44,38	1,82	30,9	0,0006	71,1	0,0002	58	17	0	3,26	0	13,68	3,5
Peak 2	44,48	0,84	50,8	0,0006	122,5	0,0002	116	16,15	51,07	3,28	6,51	15,5	3,35
Peak 3	44,51	3,59	114,4	0,0006	264,1	0,0002	103	6,43	16,54	3,22	6,24	6,49	3,26

Figure 19: First table in the exported Excel file.

Solvent	ET	CS	SNR_SEC	noise_SEC	SNR_NMR	noise_NMR	int	FWHM_spec10	FWTM_spec10	Raw_Int10	RAW_SNR10	Base_width	Base_width_at_analyte
0	0	7,25	0	0	841,22	0	0	4,42	9,74	15	26901,5	0,354	0,477

Figure 20: Second table in the exported Excel file describing the solvent statistics.

FWHM	Val_max	Pos_max	A_F	T_F	broader_10	plate_count_col	plate_count_m
2,81	25111	44,63	1,53	1,32	32,8	4668	15561

Figure 21: Third table describing SEC statistics.

The first table (**Figure 19**) includes peak statistics:

- Elution time in minutes (ET)
- Chemical shift in ppm (CS)
- Signal-to-noise ratio in the SEC dimension (SNR_SEC)
- Noise in the SEC dimension (noise_SEC)
- Signal-to-noise ratio in the spectral dimension (SNR_NMR)
- Noise in the spectral dimension (noise_NMR)
- Integral under the 2D peak in s*ppm (int2D)
- Full width at half maximum in the spectral dimension (FWHM_spec) in Hz
- Full width at tenth maximum in the spectral dimension (FWTM_spec) in Hz
- Full width at half maximum in the chromatographic dimension in Hz (FWHM_chrom)
- Full width at tenth maximum in chromatographic dimension (FWTM_chrom) in minutes
- Full width at half maximum in the spectral dimension (FWHM_spec_Pf) in minutes
- Full width at half maximum in chromatographic dimension (FWTM_chrom_Pf) in minutes

The second table (**Figure 20**) includes solvent peak statistics:

- Chemical shift (CS) in ppm
- S/N in the spectral dimension (SNR_NMR)
- FWHM in the spectral dimension (FWHM_spec10) in Hz
- Full width at one tenth of the maximum peak height (FWTM_spec10) in Hz
- The unprocessed raw integral (Raw_Int10)
- The raw signal response (RAW_SNR10)
- Base width of the solvent (Base_width), in Hz
- Base width at the analyte height, in Hz

The third table (**Figure 21**) included SEC statistics, consisting of:

- Full width at half maximum (FWHM) in minutes
- Intensity value of the peak maximum (Val_max)
- Position of the peak maximum (Pos_max) in minutes
- Asymmetry factor (A_F)
- Tailing factor (T_F)
- 10 % broadening (broader_10) in seconds
- Theoretical plate number per column (plate_count_col)
- Theoretical plate number per meter (plate_count_m)

All the GUI parameters, that were set before running the program can be found in the table that extends down as columns starting at cell **A13** of the Excel file (not illustrated in the documentation). Additionally, the Excel file includes data from the *.par file that extends right as rows starting at cell **D13** (not illustrated in the documentation). Another important feature is that when certain parameters are being changed in the GUI, and then consequently followed by running the program, the statistics in the Excel file will never be over-written. Instead, a new sheet is created within the same Excel file, with a new date and time stamp on it. This also makes it easier to compare certain results when changing a specific parameter.

5. How does the GUI work?

Start the program by clicking on the *NMRmaster.mlapp* file. This file should be in the same directory with the *functions* folder and the *NMRmaster_fun.m* file as described in the section 2. Next, the GUI window with default parameters appears on the screen and the analysis can be started by uploading NMR, SEC and optionally UV data in the File panel (see 4.1).

The next step is to enter all necessary parameters in the panels described in the section 3. The pre-loaded default parameters can be used or switch between default parameters for CHCl₃ and THF. After doing so, the program can be started by clicking the RUN button in the Data Export and Visualization tab. The calculations begin and the GUI progress can be seen while executing different modules. In case of selection of the seventh method in the phase correction panel (Interactive phase correction), a small GUI appears on the screen as described in the subsection 4.2.2.

The execution of the module 'Finding peaks...' is followed by the appearance of the false color plot of 2D NMR data (it might take a few seconds). All peaks above the threshold are marked by white circles (Figure 22). At this step, decide which peaks were detected correctly and which to reject. There are two options to do that:

- 1.) Choose 'Yes, as area' in the dialog box. Then click and drag a rectangle that covers the peaks for rejection.
- 2.) Choose 'Yes, as point' in the dialog box. Then left click on the peak for rejection and press ENTER (Figure 23). It is important to keep the black lines on the active figure while pressing ENTER.

The peaks do not disappear immediately but are deleted from the data.

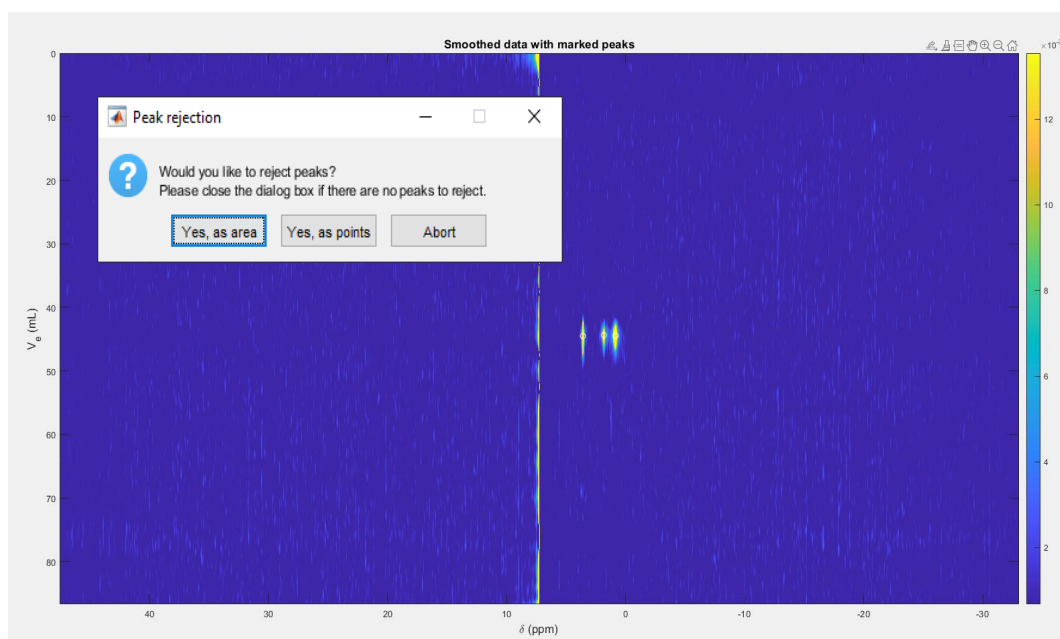


Figure 22: Peak rejection.

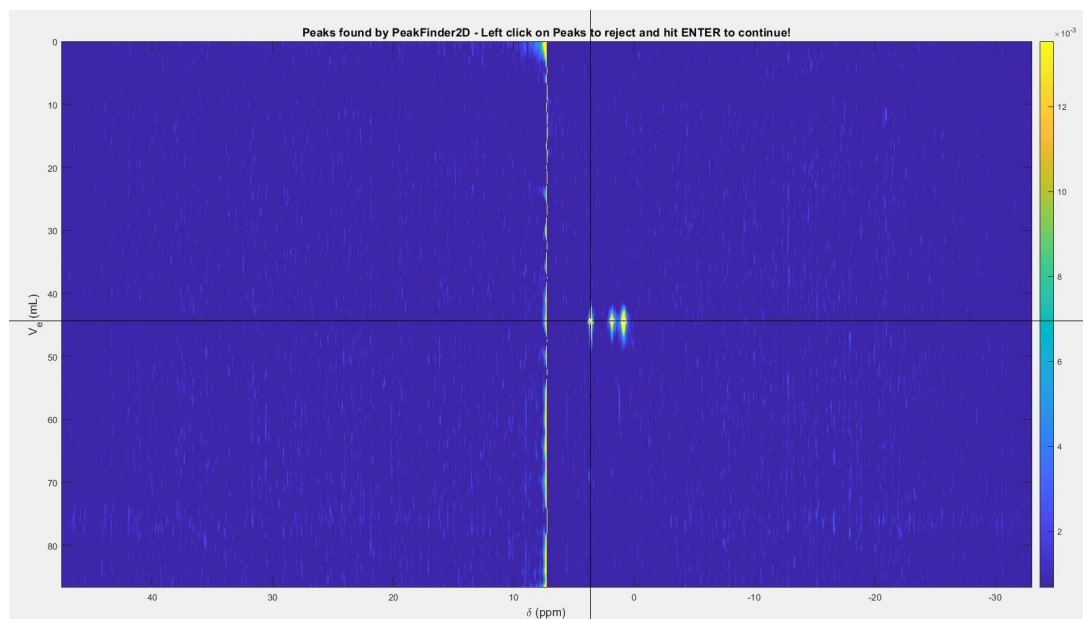


Figure 23: Point-like peak rejection.

Close the dialog box window (X) if there are no peaks to reject or the rejection process is finished. Alternatively, click on “Abort” which terminates the program execution. This step allows the adjustment of the threshold parameter and rerun the program. It is not possible to conduct further analysis if there are no peaks in the data, i.e. no peaks marked by white circle.

The TMDE software then executes further modules until the module ‘Generating output matrices...’ appears, which is followed by the appearance of the plots on screen determined in the Visualization panel (see 4.3). Please note that the plots on screen are stacked one behind the other. Additionally, the module “Saving plots...” is executed if selected in the Data Export panel (see 4.4). The end of the program is indicated by the message dialog box (**Figure 24**). Relevant warnings can appear during the execution of the GUI, which provides information about occurring problems or acts as navigation through the process.

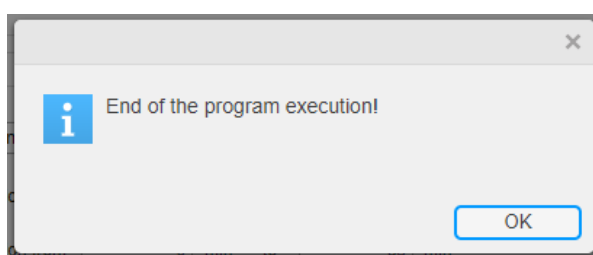


Figure 24: End of the GUI execution.

6. Results

The plots that appear on the screen at the end of the program execution are presented below as examples:

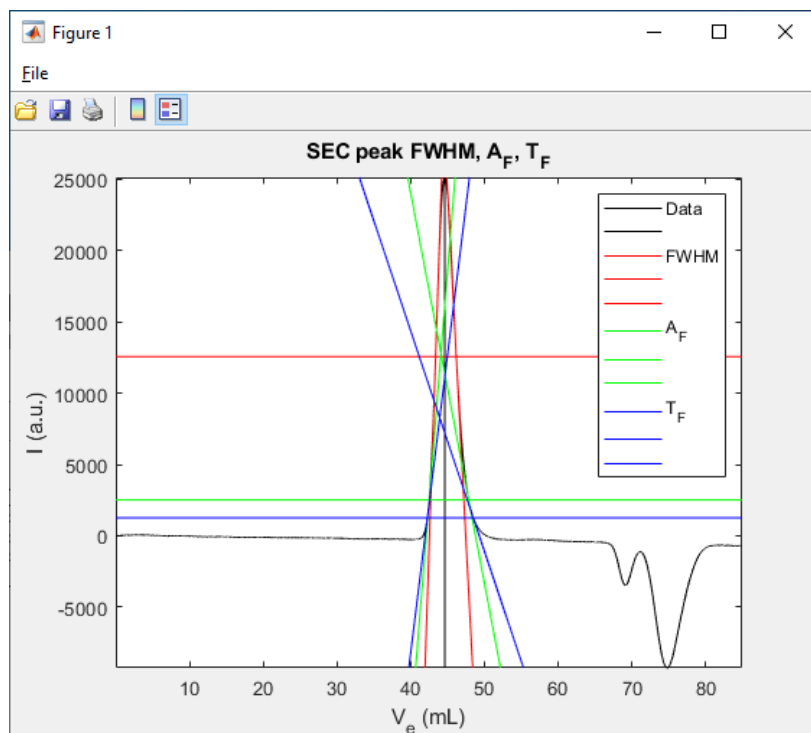


Figure 25: SEC trace with marked FWHM-, asymmetric (A_F)- and tailing factors (T_F).

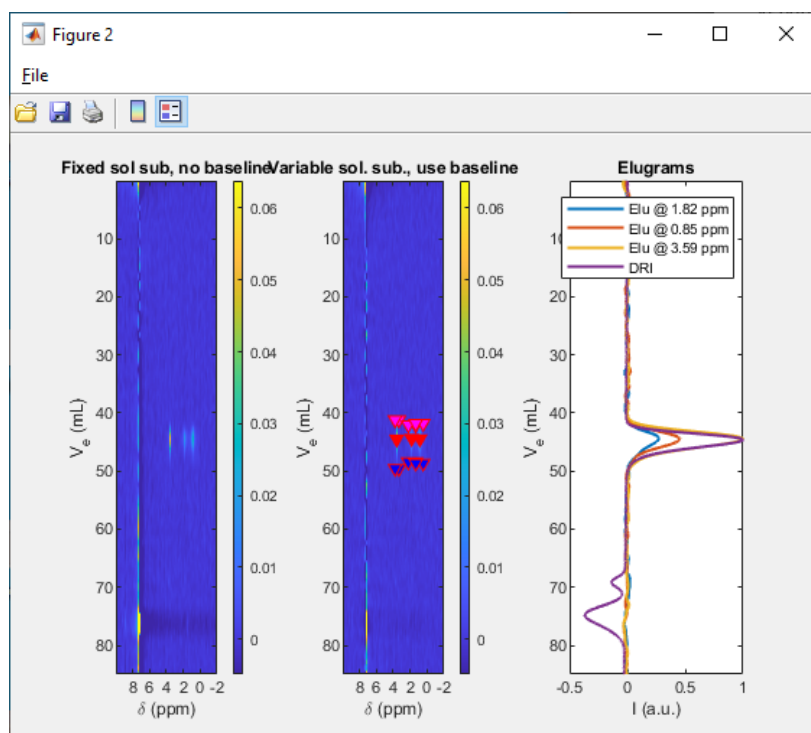


Figure 26: 2D data plot as false color plot with constant intensity signal subtracted (left) and adjusted intensity signal subtracted (middle). Right plot presents elugrams and DRI trace. If given, the elugrams plot includes additionally the UV trace.

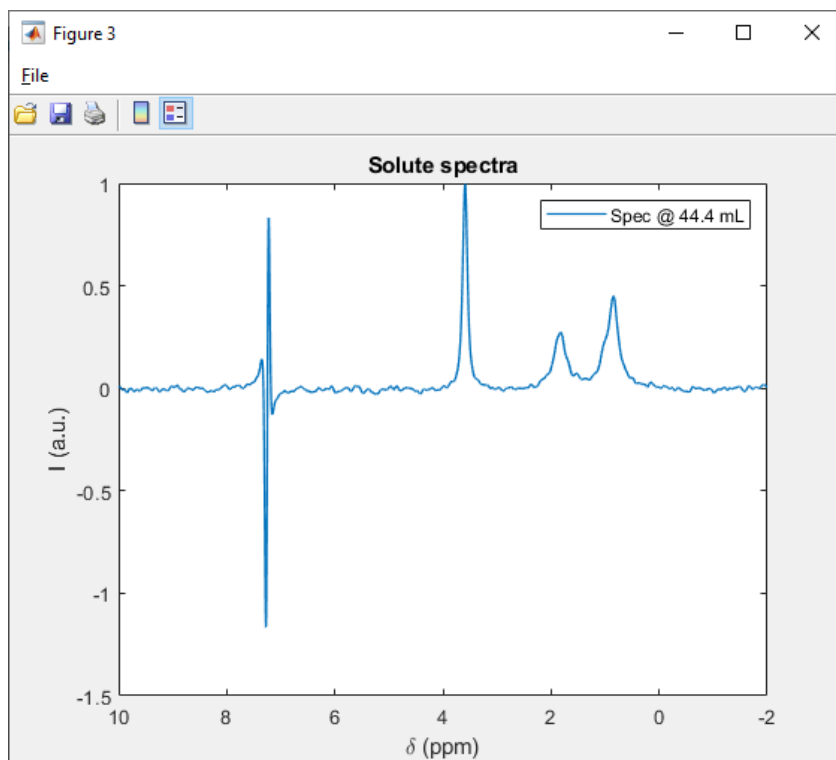


Figure 27: Plot of analyte spectrum with marked zoom-in and zoom-out options.

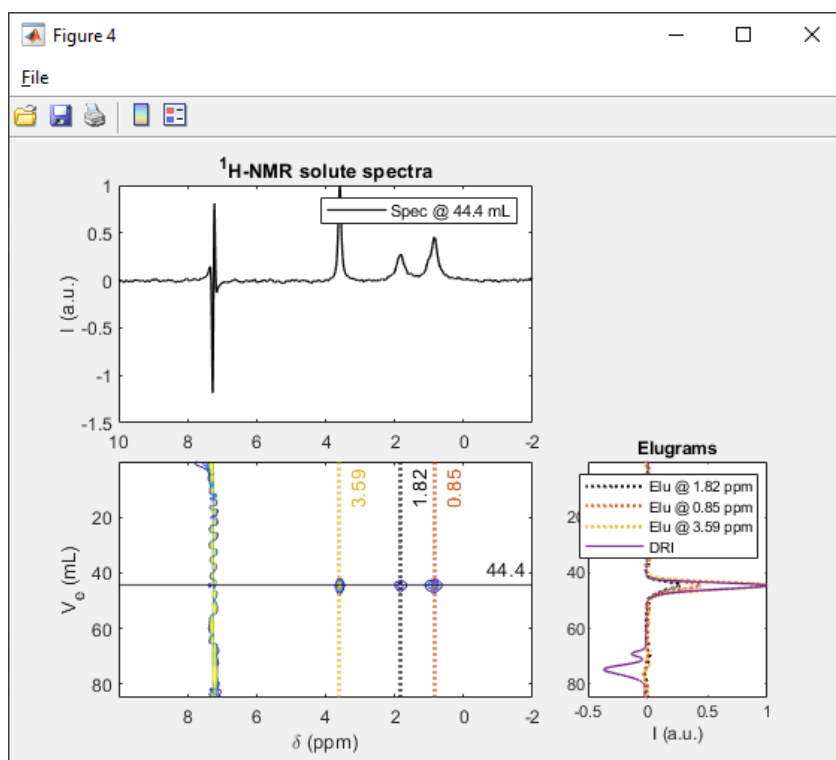


Figure 28: Combined plot of analyte spectra, 2D false color plot and elugrams with DRI trace. Spectra and elugrams are marked on the 2D plot by solid and dotted lines, respectively.

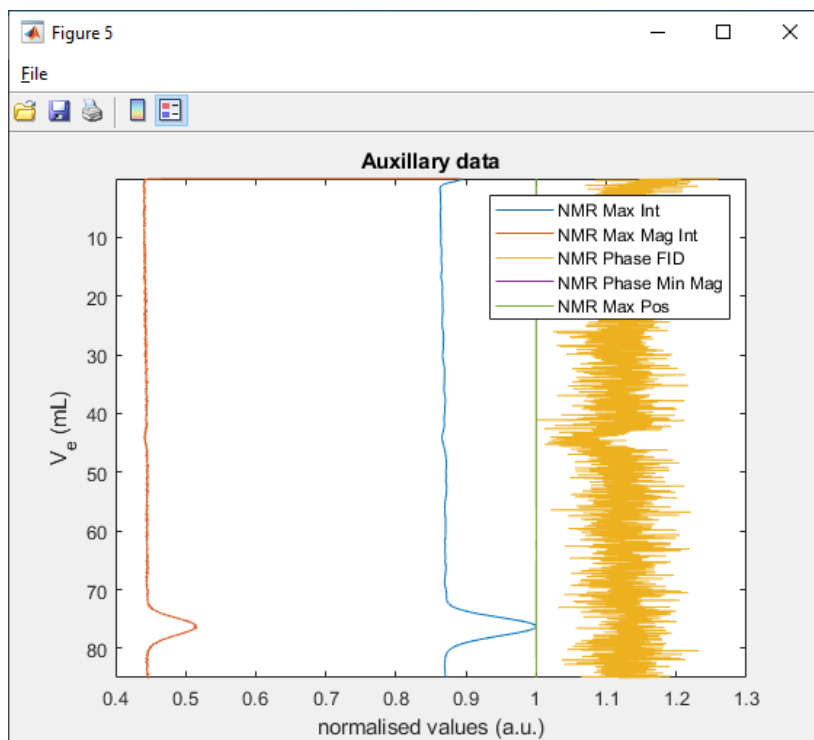


Figure 29: Auxillary data plot.

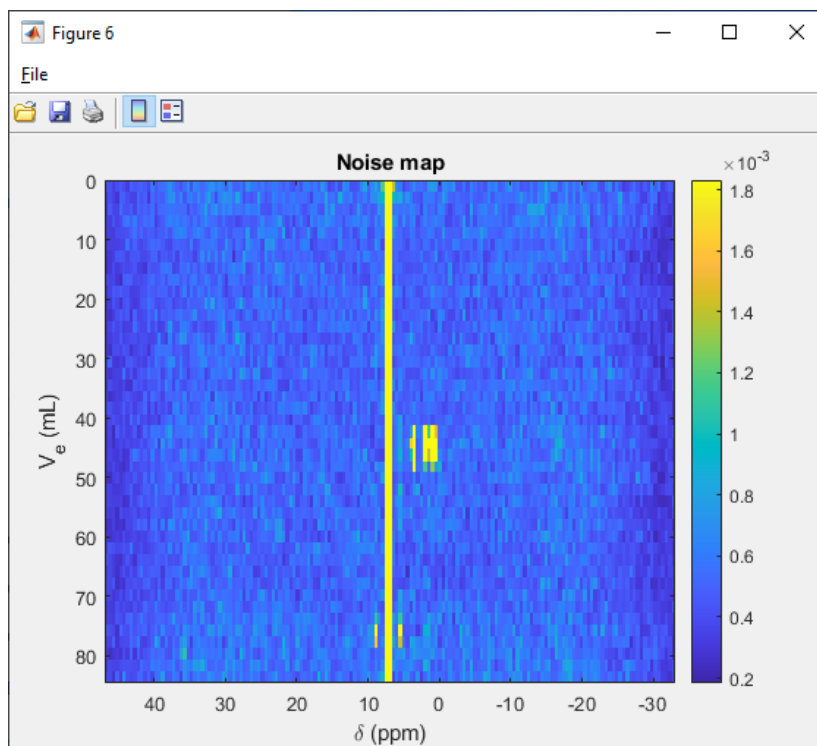


Figure 30: Noise map.

The number and content of figures can differ according to the chosen options in the Visualization panel (see 4.3). All numerical results can be found in the Excel file, as described in the subsection 4.4.

A.2 QCL GUI Documentation



Institute for Technical Chemistry and Polymer Chemistry
Polymeric Materials

QCL GUI Documentation

February 2019

Carlo Botha
Aleksandra Bucka
Dr. Johannes Höpfner
Dr. Jennifer Kübel
Prof. Dr. Manfred Wilhelm

Table of Contents

1. Introduction	3
2. Requirements	3
3. GUI components	4
3.1. File panel	4
3.2. Balance Detection Panel	5
3.3. Spectrum Panel	5
3.3.1. Outlier limit.....	6
3.3.2. Filter.....	6
3.3.3. Filter bandwidth	6
3.3.4. QCL initial mask and System peak	6
3.3.5. QCL noise start and QCL noise end.....	6
3.3.6. Peak finder threshold and preliminary drift correction	6
3.3.7. Drift Correction and Polynomial order	6
3.4. Chromatogram Panel	8
3.5. Data Export Panel	8
4. How does the GUI work?	10
5. Results	12
5.1 Full Width at Half Maximum (FWHM)	12
5.2 Coefficient of Determination (R^2)	12
5.3 Plots and statistics	13

1. Introduction

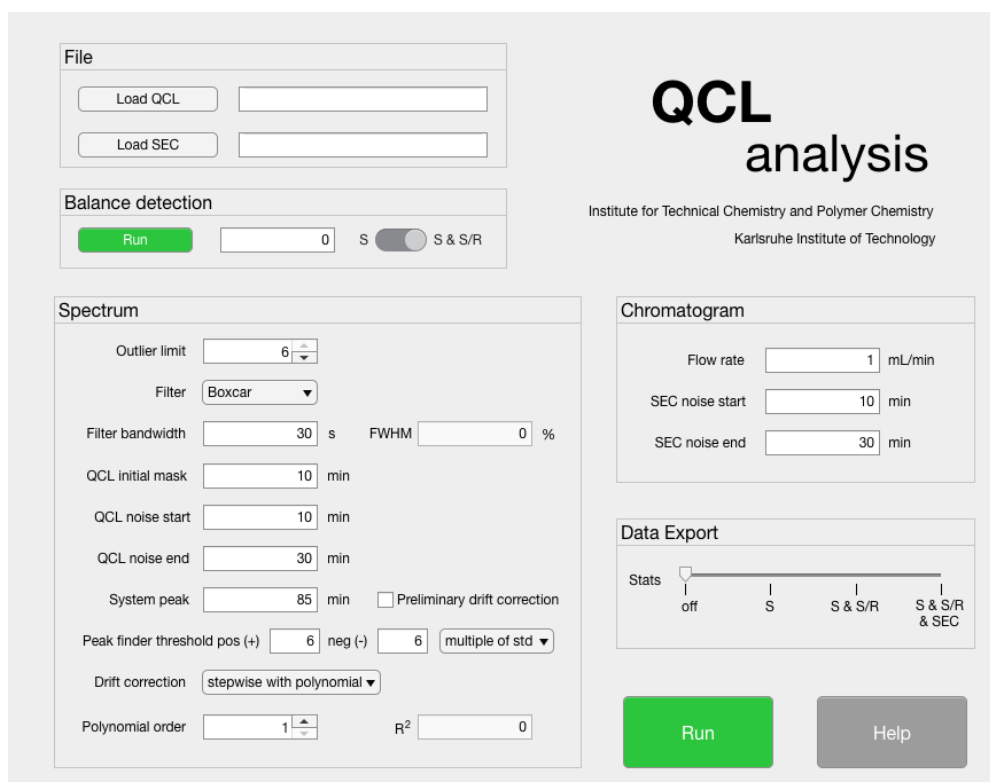


Figure 1: The QCL graphical user interface.

This document provides information on how the Graphical User Interface (GUI – **Figure 1**) operates. It is designed for the analysis of QCL and SEC data. The GUI consists of the following steps:

- Loading the QCL file
- Loading the SEC file
- Balance detection
- Input of parameters for analysis of QCL data (Spectrum panel)
- Input of parameters for analysis of SEC data (Chromatogram panel)
- Data export to Excel

The GUI enables smoothing of the data, automatic peak detection, drift correction, absorption calculation, estimation of statistics and export to a designated Excel file. The analysis can be performed on the QCL sample and sample/reference data. The statistics are also calculated for the raw SEC data (i.e. no data processing performed).

2. Requirements

In order to open and operate the GUI, select the file *QCLmaster.mlapp*. All additional requirements for the GUI are listed below:

- MATLAB r2018b (or newer versions)
- Signal Processing Toolbox

- *QCLmaster_fun.m*
- *corr_fun.m*
- *GUI documentation.pdf*
- *functions* folder with following functions:
 - *read_SEC.m*
 - *GAUSS1D.m*
 - *BoxcarAvg.m*
 - *PeakFinder_1D.m*
 - *GIN.m*
 - *TIMETOSPEC.m*
 - *ComputePeakStartEnd.m*
 - *CorrectDrift.m*
 - *CorrectDrift_step.m*
 - *Trans2Abs.m*
 - *NoiseMap_1D.m*
 - *ResidMap_1D.m*
 - *peak_FWHM.m*
 - *peakstats_SEC.m*
- Microsoft Excel for statistics export

The mlapp-file, m-files, pdf-file and the *functions* folder should be kept in the same folder directory.

3. GUI components

A short description of each component is provided by holding the mouse over (mouse hover) various GUI elements. In this section, a more detailed description on the GUI content can be found.

3.1. File panel



Figure 2: The file panel

In the *File panel* (**Figure 2**), QCL and SEC files can be uploaded for analysis. By clicking on the buttons (*Load QCL*, *Load SEC*), a dialog box opens, prompting to select the folder containing the data and selecting the required file. Both files should be in the same folder, the QCL file with a *.str extension and SEC file with *.txt extension. The chosen file paths appear in the fields next to the buttons. The mouse hover may be used to see the entire path. The program can only be executed, if **both** data sets have been loaded.

The QCL *.str file should consist of following columns:

- first column, containing the time data in seconds
- third column, containing the sample intensity data

- fourth column, containing the reference intensity data

The SEC *.txt file should contain time (elution volume values) and DRI data.

3.2. Balance Detection Panel



Figure 3: Balance detection panel.

In the *Balance detection* panel (**Figure 3**), the correlation between the QCL sample and reference data can be determined. The calculated Pearson correlation coefficient appears in the neighbouring box after clicking the *RUN* button. The coefficient is calculated from a peak-free area (e.g. 10–40 min). Values of the coefficient ranges from -1 to 1, where 1 implies strong correlation, -1 strong negative correlation and 0 means no correlation at all. Based on the result, choose between sample data (*S*) or sample and sample/reference data (*S & S/R*) to be used for further analysis. In case of low correlation (-0.5–0.5), it is recommended to choose the *S* option on the switch to perform analysis only on the sample data. The *Balance detection* panel can be used directly after loading the data in the *File* panel. Parameters from other panels are not necessary for the calculation of the coefficient. *S & S/R* is used by default.

3.3. Spectrum Panel

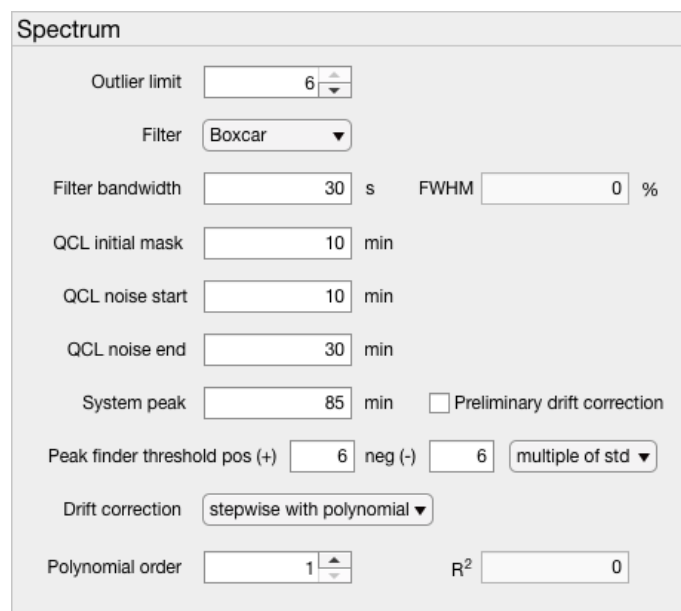


Figure 4: Spectrum panel.

In the spectrum panel (**Figure 4**), all the parameters necessary for QCL data analysis can be inserted. All the components of this panel are explained in detail in the forthcoming section.

3.3.1. Outlier limit

Using the up and down arrows (spinner), outliers can be excluded by choosing the threshold as a multiple of the standard deviation of the raw sample data. All data points that exceed this threshold are removed. The threshold ranges from 0 to 6, where 0 means no exclusion. 6 is the default value.

3.3.2. Filter

Using the drop-down menu, two different filter types appear. Data can also be analysed without smoothing by selecting the *No filter* option. The available filters are:

- Boxcar average
- Gauss filter

In case of uneven data spacing, artefacts can be possible, especially when using the Gauss filter. The Boxcar filter is set as the default filter.

3.3.3. Filter bandwidth

This option enables the control of the size of the sliding window for the boxcar filter or sigma value of the Gauss convolution function. The default size is 30 s. This value will affect the degree of data smoothing.

3.3.4. QCL initial mask and System peak

These parameters describe the range of data used for drift correction. *QCL initial mask* is also used as data start for peak detection. The default values are 10 and 85 min, respectively.

3.3.5. QCL noise start and QCL noise end

The noise range required for the determination of the peak detection threshold and the corresponding statistics exported to Excel is calculated as the standard deviation in the range between *QCL noise start* and *QCL noise end*. The default values are 10 and 30 min, respectively.

3.3.6. Peak finder threshold and preliminary drift correction

In order to detect peaks, a threshold of peak height should be determined. There are two options in the drop-down menu that allows to set the threshold:

- threshold as multiple of standard deviation (noise calculated in the range *QCL noise start* and *QCL noise end*, see above)
- threshold as a specific number

The thresholds should be chosen for positive (*pos +*) and negative (*neg -*) peaks. The default threshold is set to 6 times the standard deviation, for both positive and negative peaks.

By checking the box "preliminary drift correction", the program finds the initial baseline (by fitting a first order polynomial) and then performs peak finding. This option is useful in case of data with a low S/N ratio and a strong drift.

3.3.7. Drift Correction and Polynomial order

With this option, drift correction can be performed on the data. The function fits the polynomial baseline with the selected '*polynomial order*' to the peak free area and subtracts it from the data. Either one polynomial can be fit to the data with the option '*with polynomial*' (Figure 5) or multiple polynomials in a stepwise manner with the option '*stepwise with polynomial*' (Figure 6).

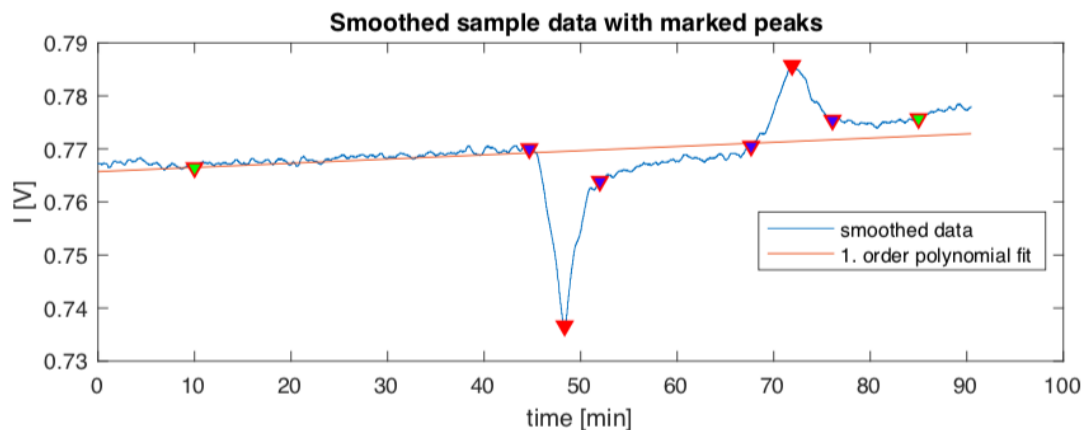


Figure 5: '*with polynomial*' option of drift correction.

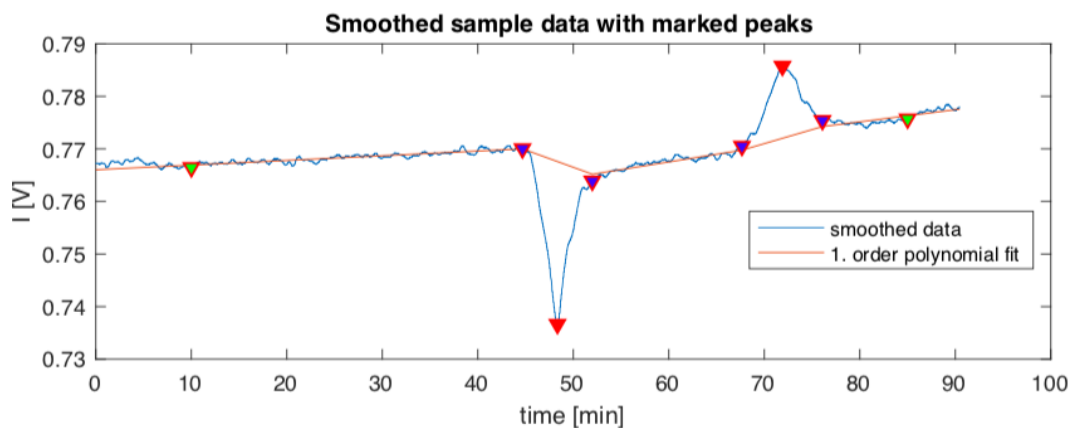


Figure 6: '*stepwise with polynomial*' option of drift correction.

As can be seen on the figures Figure 5 and Figure 6 the initial decay and the data after the system peak are not used for fitting (marked by the green triangles). The range used for drift correction can be controlled with the parameters: *QCL initial mask* and *System peak* (see below). For the data presented above, a better fitting is performed using the option '*stepwise with polynomial*'. This option should not be used for the data with close or overlapping peaks. The drift corrected data can be seen below (Figure 7 – the same data as on Figure 5 and Figure 6 after calculation of absorption).

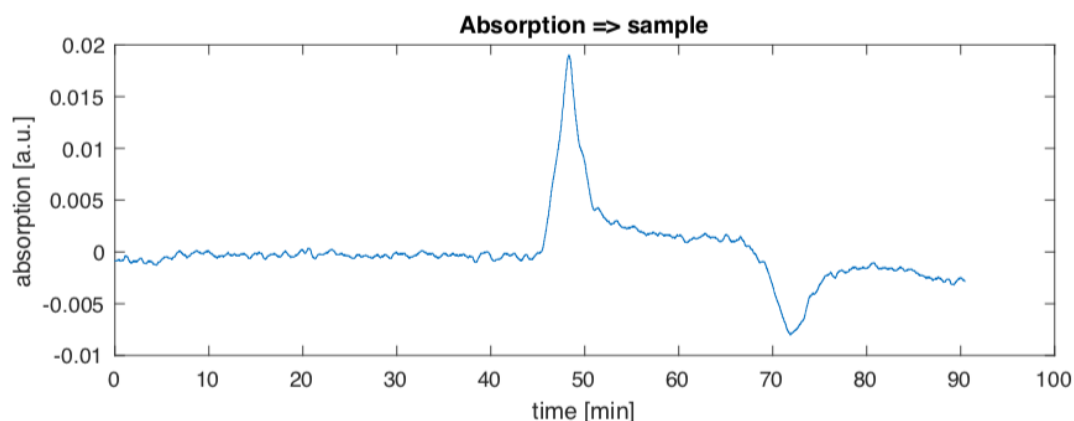


Figure 7: Drift corrected data.

The *no correction* option can also be selected from the drop-down menu, but further calculation of absorption can be imprecise as a result of that. The default option for drift correction is *stepwise with polynomial*. The polynomial orders possible for selection are; 1st, 2nd and 3rd. The default option is a 1st order polynomial.

The R^2 and *FWHM* parameters are evaluated by the program and are described in sections [5.1](#) and [5.2](#).

3.4. Chromatogram Panel

In the *chromatogram* panel (**Figure 1**), parameters such as: *flow rate* (by default 1 mL/min), *noise start* and *noise end* (by default 10 and 30 min, respectively), may be inserted, which are necessary for SEC data analysis. The parameters *SEC noise start* and *SEC noise end* determines the range for calculation of the standard deviation, which is necessary for statistics calculation.

3.5. Data Export Panel

The *Data Export Panel* (**Figure 1**), enables the export of measurement statistics to a designated Excel file, which are calculated by the program. There are three export options:

- export only QCL sample data statistics (*S*)
- export QCL sample and sample/reference data statistics (*S & S/R*)
- export sample, sample/reference and SEC data statistics (*S & S/R & SEC*)

Additionally, all the parameters used in the GUI are exported as well as absorption data, which are automatically calculated by the program.

S and S & S/R (Figure 8)

Statistics calculation for each detected peak consists of:

- elution time (in minutes)
- signal-to-noise (S/N) ratio
- noise
- FWHM of the smoothed data (in minutes)

- FWHM of the raw data (in minutes)

	Sample	
QCL	Peak_1	Peak_2
ET at peak max [min]	48,3	71,9
SN [—]	85	37,7
Noise [a.u.]	0,000365	0,000365
FWHM smoothed data	2,3	3,5
FWHM raw data [min]	2	2,9
	Sample_Reference	
QCL	Peak_1	Peak_2
ET at peak max [min]	48,3	71,8
SN [—]	61	26,2
Noise [a.u.]	0,00043	0,00043
FWHM smoothed data	2,3	3,6
FWHM raw data [min]	2	3,1

Figure 8: Example of the sample and sample/reference data statistics exported to Excel.

SEC data (Figure 9)

Statistics calculation for the highest peak consist of:

- elution time (in minutes)
- value of the peak
- asymmetry factor
- tailing factor
- FWHM of the smoothed data (in minutes)
- 10 % broadening (in seconds)
- noise
- signal-to-noise (S/N) ratio

SEC	Peak
ET at peak max [min]	49,4
Max value [a.u.]	3610,01
Asymmetry Factor [—]	1,75
Tailing Factor [—]	1,5
FWHM smoothed data	1,59
10% broadening [s]	18,62
Noise [a.u.]	6,17
SN [—]	585,8

Figure 9: Example of the SEC data statistics exported to Excel.

The value of 0 is assigned to the FWHM if the program was not able to calculate it correctly. The Excel file is saved in the same folder as the QCL and SEC data files with the name *stats_qcl.xls*. Each time data is being exported, a new worksheet is created with a new timestamp. It is not possible to choose S & S/R or S & S/R & SEC option from the slider if the S option in the *Balance detection* panel has been selected. No export is performed by default (*off*).

Important: For operating systems, other than Windows, three additional empty worksheets might be created in the Excel file. Please remove them manually in Excel. This will only happen once when the *stats_qcl.xls* file is created for the first time.

4. How does the GUI work?

Start the program by clicking on the *QCLmaster.mlapp* file. This file should be kept in the folder with the files described in section 2. Thus, the GUI window with default parameters (**Figure 1**) appears and the analysis can be started by uploading the QCL and SEC data in the *File panel* (see 3.1). The QCL data should consist of the sample and the reference data.

The correlation between the sample and the reference data can be checked in the *Balance panel* (see 3.2) and based on the result a decision can be made to perform analysis either only on the sample data or on both the sample and sample/reference data by switching between options (S or S & S/R). This step is not necessary for further analysis and the program works on the sample and sample/reference data by default.

In order to perform the analysis on the uploaded data, all the parameters needs to be inserted into the *Spectrum*, *Chromatogram* and *Data Export* panels (see 3.3, 3.4 and 3.5). The data analysis can be commenced by clicking on the main *Run* button. After doing so, a plot of smoothed data (or not smoothed data if the *No filter* option has been chosen) with peaks marked by red triangles appears on the screen (**Figure 10**). Depending on the selected peak finder threshold, the program can detect some high noise levels as peaks. Either close the figure window, adjust the threshold and rerun the program or reject unwanted peaks by clicking on the corresponding red triangles with the left mouse click and then pressing ENTER. The red triangles do not disappear immediately after clicking on them. Alternatively, only press ENTER if there is nothing to reject.

Further analysis cannot be conducted if there are no peaks in the data, i.e. no peaks that are marked with red triangles. The second plot with peaks to reject appears if the *S & S/R* option has been selected in the *Balance detection* panel. **Figure 10** presents the process of rejecting the point that was wrongly interpreted by the program as a peak.

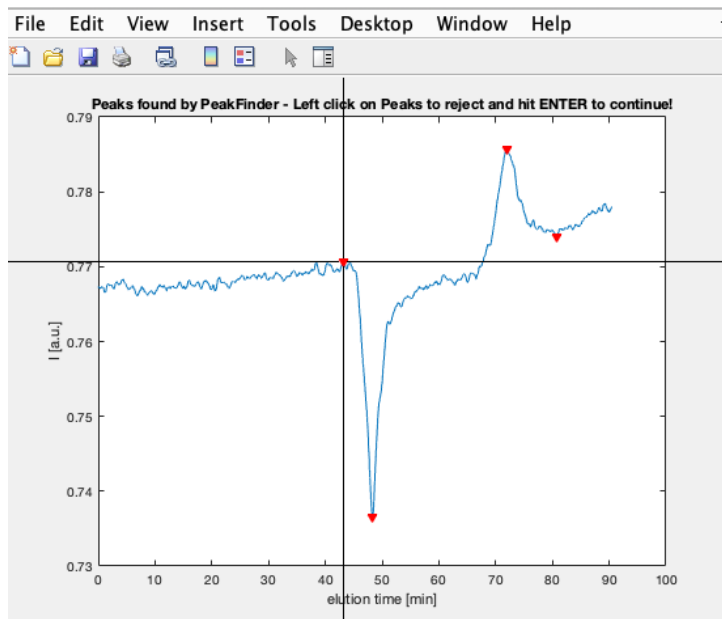


Figure 10: Plot with marked peaks to reject.

When the process of peak rejection is finalized, press ENTER. The peak rejection plot disappears followed by the appearance of the next plots on the screen. Each figure represents the peak with marked FWHM and the inner and outer tangents (**Figure 11**) that were used in order to estimate the FWHM (see [5.1](#)). The lower subplot represents a zoomed in view of the FWHM area of the peak, as can be seen on the bottom figure in **Figure 11**. At this step, verify if the FWHM for the raw data has been determined correctly by the program and select the proper option from the confirmation box that appears on the screen as well (**Figure 12**). Confirming the estimation by choosing 'Yes', further analysis can be performed and the plots with the results appear on the screen after a while (as described in section [5](#)). Otherwise, the execution of the program is stopped and parameters can be changed in the GUI in order to improve the estimation of the FWHM.

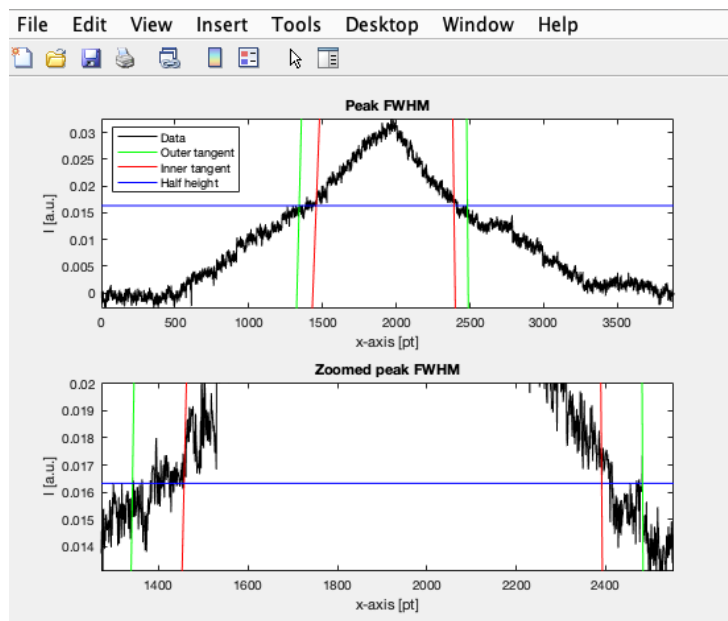


Figure 11: FWHM of the peak.

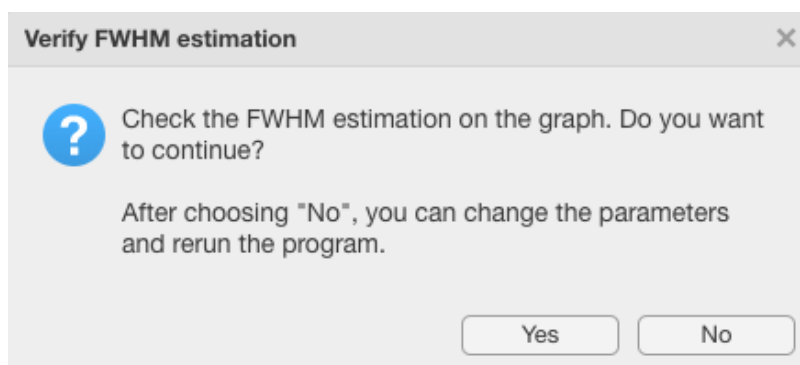


Figure 12: Confirmation box for FWHM verification.

Relevant warnings can appear during the execution of the GUI, which provides information related to occurring problems or acts as navigation through the process.

5. Results

After completing the process of FWHM verification, the following results can be expected:

5.1 Full Width at Half Maximum (FWHM)

The parameter in the *Spectrum* panel determines an increase of the highest peak FWHM of the smoothed sample data relative to the FWHM of raw sample data. The FWHM is calculated as a mean value of the inner and outer tangents, which are found for the peak. Results above 10% can imply that the *wrong filter* or *bandwidth* was used. The program is sometimes not able to calculate the FWHM correctly (e.g. in case of data with low S/N ratio) and it assigns the value of 0 to the FWHM of a such peak.

5.2 Coefficient of Determination (R^2)

The coefficient of determination (R^2) provides the measure of how well the selected polynomial fits the sample data. Results below 0.95 may indicate that the wrong *polynomial order* or *outlier limit* was selected.

5.3 Plots and statistics

The following figures appear on the screen as a representation of the results:

- plot of SEC data with marked FWHM, asymmetry factor and tailing factor
- plot of raw data with marked peaks (red triangles)
- plot of smoothed data with polynomial fit, marked peaks (red triangles), marked start and end of peaks (red-blue triangles) and marked start and end of useable data (red-green triangles, see 3.3.4); example in **Figure 6**
- plot of absorption
- noise map (see below)
- residuals map (see below)

Based on the chosen switch option in the *Balance detection* panel, figures can consist of either only one plot of sample data or of two subplots with sample and sample/reference data. The number and content of figures can differ according to the given parameters (e.g. no residuals map if no drift correction performed). Zoom-in and zoom-out options can be found in the top right corner of the plot as marked in **Figure 13** with the red ellipse. All plots are exported with corresponding names in PDF format to the same folder as the loaded QCL and SEC data files. The figures are overwritten if the GUI is ran with the same data more than once.

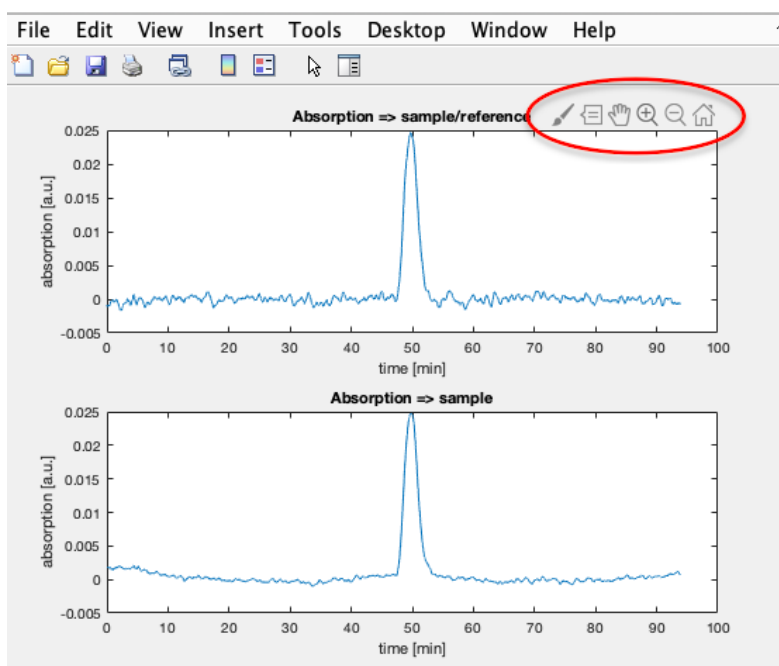


Figure 13: Zoom-in and zoom-out options of a plot.

The Noise map (Figure 14) shows standard deviations calculated from equal regions of QCL data. The size of one region is 1 minute.

The **Residuals map (Figure 15)** represents the deviations of data from the polynomial fit. The resolution matches the resolution of the noise map.

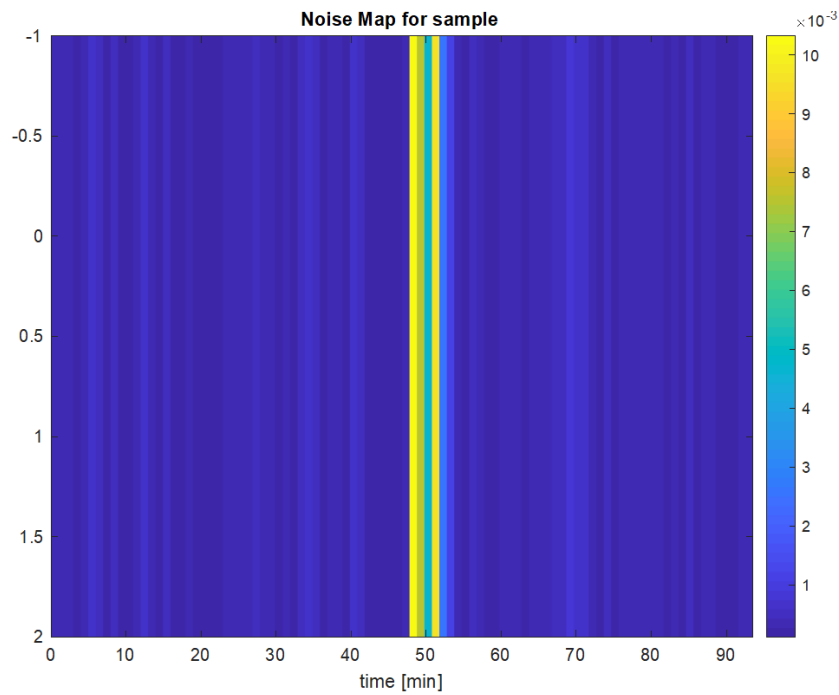


Figure 14: Noise map.

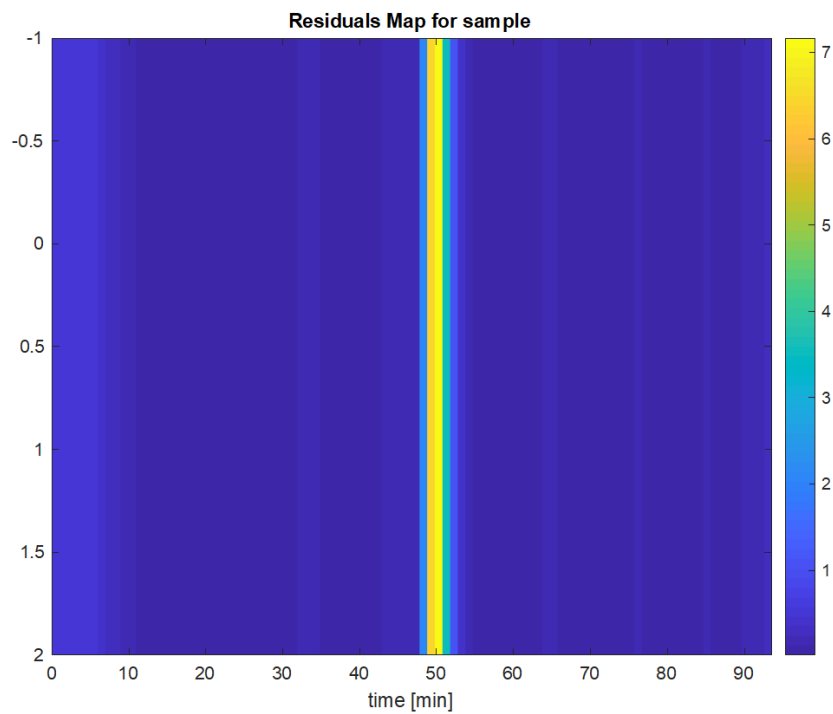


Figure 15: Residuals map.

All numerical results can be found in the Excel file, as described in the section [3.5](#).

A.4 Pulse Sequences

The two pulse sequences used within the scope of this work, including the optimized parameters utilized for protonated chloroform (CHCl_3) and tetrahydrofuran (THF), are provided. The respective pulse sequences were embedded within the Prospa language frame of the standard '1Pulse-H' sequence developed by Magritek GmbH (Aachen, Germany). The syntax arguments provided in brackets forms part of the Prospa programming language designating a desired parameter to be executed. The description following the # symbol, state the properties of the argument provided in brackets. A number of processing parameters were kept constant within this work which include; (1) the number of free induction decay (FID) points (2k, 2048), (2) the dwell time (200 μs , bandwidth = 5 kHz), (3) the acquisition length (100 μs), and (4) the number of transients per spectrum (4 scans/spectrum).

A.4.1 1HMonitor_1Pulse-spoil_V3_CB

The pulse sequence allows for the continuous recording of ^1H resonances, employing a simple one-pulse experiment and a spoil 'gradient'. The Spinsolve 60 spectrometer used within this work do not contain designated pulsed field gradients, consequently the spoil gradient is applied by means of the linear shim coils, i.e. x, y, and, z shim coils. The pulse sequence is adapted from '1HMonitor-1Pulse-spoil-JH-1' by Dr. J. Höpfner for continuous FID recording. The experimental order of the pulse sequence is as follows;

Delay1 – 90°-Pulse – Delay2 – Acquisition – Delay3 – Spoil Pulse – Delay4

Delay1	= 5 ms (finalizing lock scan)
90°-Pulse	= 12 μs
Delay2	= 100 μs
Acquisition	= 409.6 ms
Delay3	= 100 μs
Spoil pulse	= 20 ms (amplitude = 5000 a.u.)
Delay4	= variable delay, 65–70 ms
Total repetition time	= 500 ms

As per Prospa language;

```
procedure(pulse_program,dir,mode)
```

```
# Interface description (name, label, x, y, ctrl, vartype)
interface = ["nucleus", "Nucleus", "0", "0", "tb", "readonly_string",
"b1Freq1H", "B1 Frequency (MHz)", "0", "1", "tbw", "freq",
"repTime", "Repetition time (ms)", "0", "2", "tbw", "reptime",
"90Amplitude1H", "Pulse amplitude (dB)", "1", "0", "tb", "pulseamp",
"pulseLength1H", "Pulse length (us)", "1", "1", "tb", "pulselength",
"acqDelay", "Pulse acqu. delay (us)", "2", "0", "tb", "sdelay",
```

```

"spoilAmp", "Homospoil amplitude (a.u.)", "2", "1", "tbw", "float,[0,1e4]",
"spoilDur", "Homospoil duration (us)", "2", "2", "tbw", "sdelay",
"nrSpectra", "Number of spectra", "3", "1", "tb", "float,[1,1e5]",
"doplot", "Make plot/Print info", "3", "2", "cb", "no,yes"]

# Relationships to determine remaining variable values
relationships      = ["nDataPnts = nrPnts",
"a90               = 90Amplitude1H",
"d90               = pulseLength1H",
"d2                = acqDelay",
"n2                = xshim",
"n3                = yshim",
"n4                = zshim",
"n5                = xshim-(spoilAmp*xshim/(abs(xshim)+1))",
"n6                = yshim-(spoilAmp*yshim/(abs(yshim)+1))",
"n7                = zshim-(spoilAmp*zshim/(abs(zshim)+1))",
"d3                = spoilDur",
"totPnts           = nrPnts",
"totTime           = acqTime"]

# Define the tabs and their order
tabs               = ["Pulse_sequence", "Progress", "Acquisition", "Processing_Std",
"Display_Std", "File_Settings"]

# These parameters will be changed between experiments
variables          = [""]

# x and y spacing between controls
dim                = [190,26]

# Pulse sequence
initpp(dir)        # Reset internal parameter list
delay(5000)         # allow time to finish lock scan
pulse(mode,a90,p1,d90) # RF pulse
delay(d2)           # Pulse - acquire delay
acquire("overwrite",nDataPnts) # Acquire echo and wait
shim16(1,n5)        # x
shim16(2,n6)        # y
shim16(0,n7)        # z
delay(d3)           # homospoil delay
shim16(1,n2)        # x
shim16(2,n3)        # y

```

```

shim16(0,n4)          # z
delay(10000)         # settle delay
lst = endpp(mode)    # Return parameter list

# Phase cycle list
phaseList = [0,1,2,3;    # Pulse phase
0,1,2,3]               # Acquire phase

endproc(lst,tabs,interface,relationships,variables,dim,phaseList)

```

A.4.2 1HMonitor_IvR-spoil_V3_CB

The inversion recovery pulse sequence, like the aforementioned one-pulse experiment, allows for the continuous monitoring of ^1H resonance employing a fast inversion recovery experiment for solvent suppression. The pulse sequence is adapted from the 'Inversion Recovery' by Ms. B. Mayerhöfer, with the inclusion of the spoil pulse block implemented by Dr. J. Höpfner. The simplified experimental order of the pulse sequence is as follows;

**Delay1 – 180°-Composite Pulse – T_w – 90°-Pulse – Delay2 – Acquisition –
Delay3 – Spoil pulse**

Delay1	= 100 μs
180°-Pulse	= 24 μs
T_w	= 500 ms (under SEC conditions)
90°-Pulse	= 12 μs
Delay2	= 100 μs
Acquisition	= 409.6 ms
Delay3	= 100 μs
Spoil pulse	= 20 ms (amplitude = 5000 a.u.)
Correction slope	= 500 a.u./ms
Correction threshold	= 200 a.u.
Total repetition time	= 1 s

As per Prospa language;

```

procedure(pulse_program,dir,mode)

# Interface description (name, label, x, y, ctrl, vartype)
interface = ["nucleus","Nucleus","0","0","tb","readonly_string",
"b1Freq1H","B1 Frequency (MHz)","0","1","tbw","freq",
"repTime","Repetition time (ms)","0","2","tbw","reptime",
"90Amplitude1H","Pulse amplitude (dB)","1","0","tb","pulseamp",
"pulseLength1H","Pulse length (us)","1","1","tb","pulselength",

```

```
"acqDelay","Pulse acqu. delay (us)","2","0","tb","sdelay",
"pulseSpacing","waiting time (ms)","2","1","tb","sdelay",
"slope","slope for correction","3","1","tb","float",
"threshold","correction threshold","3","2","tb","float",
"spoilAmp","Homospoil amplitude (a.u.)","2","1","tbw","float,[0,1e4]",
"spoilDur","Homospoil duration (us)","2","2","tbw","sdelay",
"nrSpectra","Number of spectra","3","3","tb","float,[1,1e5]",
"doplot","Make plot/Print info","3","4","cb","no,yes"]
```

```
# Relationships to determine remaining variable values
```

```
relationships      = ["nDataPnts = nrPnts",
"a90Amp           = 90Amplitude1H",
"d90              = pulseLength1H",
"d180             = pulseLength1H*2",
"d2               = acqDelay",
"w1               = (pulseSpacing)*1000",
"m1               = slope",
"m2               = threshold",
"n2               = xshim",
"n3               = yshim",
"n4               = zshim",
"n5               = xshim-(spoilAmp*xshim/(abs(xshim)+1))",
"n6               = yshim-(spoilAmp*yshim/(abs(yshim)+1))",
"n7               = zshim-(spoilAmp*zshim/(abs(zshim)+1))",
"d3               = spoilDur",
"totPnts          = nrPnts",
"totTime          = acqTime"]
```

```
# Define the tabs and their order
```

```
tabs               = ["Pulse_sequence","Progress","Acquisition","Processing_Std",
"Display_Std","File_Settings"]
```

```
# These parameters will be changed between experiments
```

```
variables          = ["w1"]
```

```
# x and y spacing between controls
```

```
dim                = [170,26]
```

```
# Pulse sequence
```

```
initpp(dir)        # Reset internal parameter list
pulse(mode,a90Amp,p3,d90) # RF pulse
delay(d2)           # Ringdown delay
```

```

pulse(mode,a90Amp,p2,d90)      # RF pulse
delay(d2)                      # Ringdown delay
pulse(mode,a90Amp,p4,d90)      # RF pulse
delay(d2)                      # Ringdown delay
pulse(mode,a90Amp,p2,d180)     # Inversion RF pulse
delay(d2)                      # Ringdown delay
pulse(mode,a90Amp,p4,d90)      # RF pulse
delay(d2)                      # Ringdown delay
pulse(mode,a90Amp,p2,d90)      # RF pulse
delay(d2)                      # Ringdown delay
pulse(mode,a90Amp,p3,d90)      # RF pulse
wait(w1)                       # recovery duration
pulse(mode,a90Amp,p1,d90)      # Read pulse
delay(d2)                      # Pulse - acquire delay
acquire("overwrite",nDataPnts) # Acquire echo and wait
shim16(1,n5)                   # x
shim16(2,n6)                   # y
shim16(0,n7)                   # z
delay(d3)                      # homospoil delay
shim16(1,n2)                   # x
shim16(2,n3)                   # y
shim16(0,n4)                   # z
delay(10000)                   # settle delay

lst    = endpp(mode) # Return parameter list

# Phase cycle list
phaseList = [0,0,2,2,1,1,3,3;      # Pulse phase
0,2,0,2,0,2,0,2;                 # Inversion phase
1,3,1,3,1,3,1,3;                 # Composite phase
3,1,3,1,3,1,3,1;                 # Composite phase
0,0,2,2,1,1,3,3]                 # Acquire phase

# Phase cycle list composite pulse
phaseList = [0,2,0,2;              # Read pulse phase
0,0,2,2;                          # Inversion + composite phase
1,1,3,3;                          # Composite phase
3,3,1,1;                          # Composite phase
0,2,0,2]                          # Acquire phase

# Phase list simple 180deg pulse; full cycling
phaseList = [0,2,0,2,1,3,1,3;      # Read pulse phase

```

```

0,0,2,2,0,0,2,2;           # Inversion phase
0,2,0,2,1,3,1,3]         # Acquire phase

# Phase list simple 180deg pulse; no cycling
phaseList = [0;           # Read pulse phase
0;                       # Inversion phase
0]                        # Acquire phase

endproc(lst,tabs,interface,relationships,variables,dim,phaseList)

```

A.5 Hardware Photos



Figure A.1: Photograph of the SEC-MR-NMR set-up. This set-up is also modified in such a way to allow for the FT-SEC analysis. The labelled components in the figure are as follows; 1.) Quaternary pump and in-line degasser, 2.) 1st UV detector (1260 Infinity), 3.) 2nd UV detector (1260 Infinity II), 4.) DRI detector, 5.) Manual (Rheodyne) injector, 6.) UDC box and mock trigger (circle) for FT-SEC acquisition, 7.) Thermostatted column compartment, 8.) Spinsolve 60 NMR spectrometer (¹H optimized), and 9.) Controller interface for 3.) due to incompatible firmware version.



Figure A.2: Photograph of the flow cell box and with 15 flow cells inside. Included (the lid) is also a table with a full description of each flow cell, providing information such as flow cell volume, internal capillary diameter and geometry.

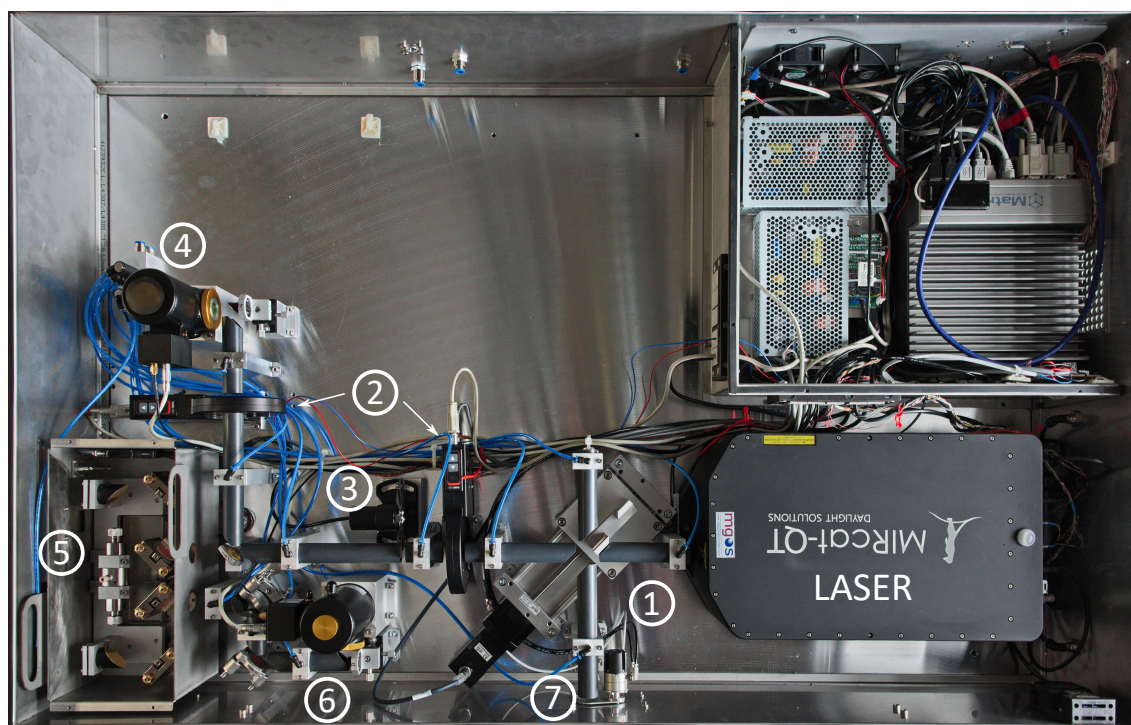


Figure A.3: Photograph of the EC-QCL spectrometer interior design with identification of the key components; (1) beam switch, (2) filter wheel, (3) chopper, (4) MCT reference detector, (5) sample chamber and flow cell, (6) MCT sample detector, and (7) beam outline for spectrometer adaptations.



Figure A.4: Photograph of the SEC set-up used for hyphenation to the EC-QCL detector. The identification of components labelled in the figure are as follows; (1) external solvent degasser, (2) isocratic pump, (3) auto-sampler, (4) linear M semi-preparative SEC column, and (5) DRI detector. The (red) arrow insets illustrates the analyte flow to the EC-QCL detector after chromatographic separation and then returning to the DRI detector.

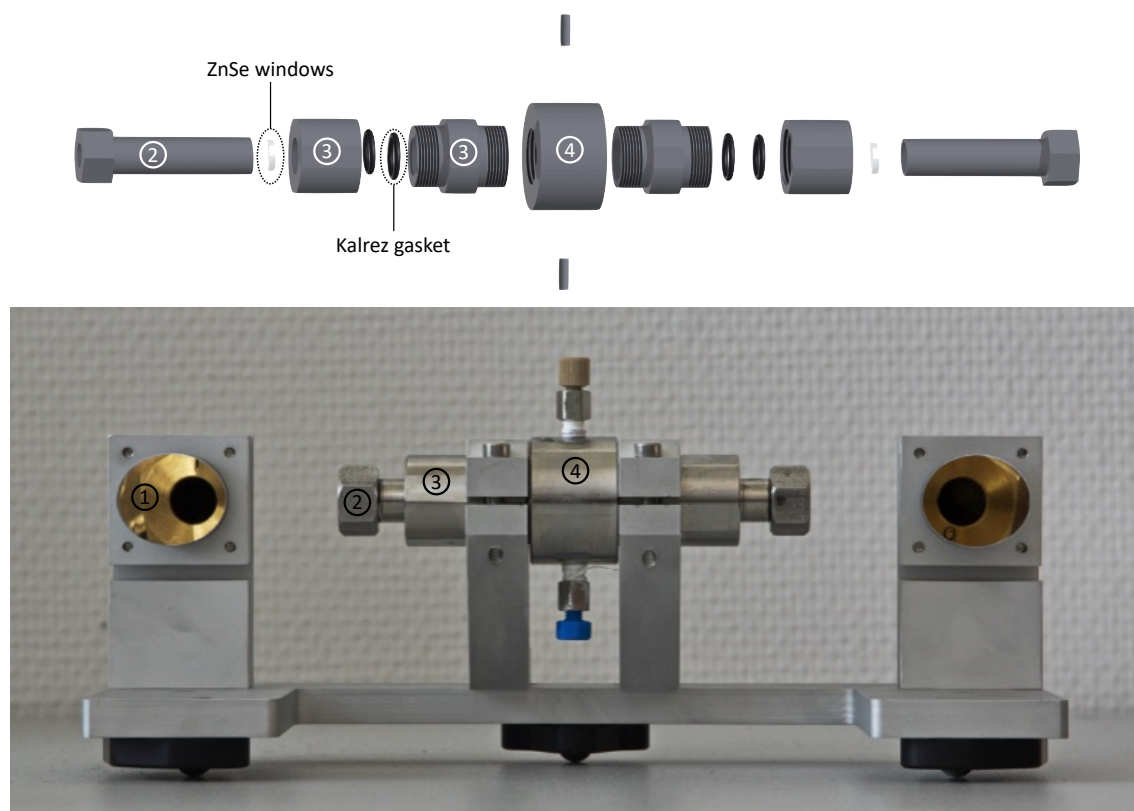


Figure A.5: Photograph of the EC-QCL flow cell with an expansion drawing (top) depicting more detail. The identification of the key components are as follows; (1) off-axial parabolic mirrors, (2) Hollow IR rod, (3) sealing clamps, and (4) flow cell centre piece.

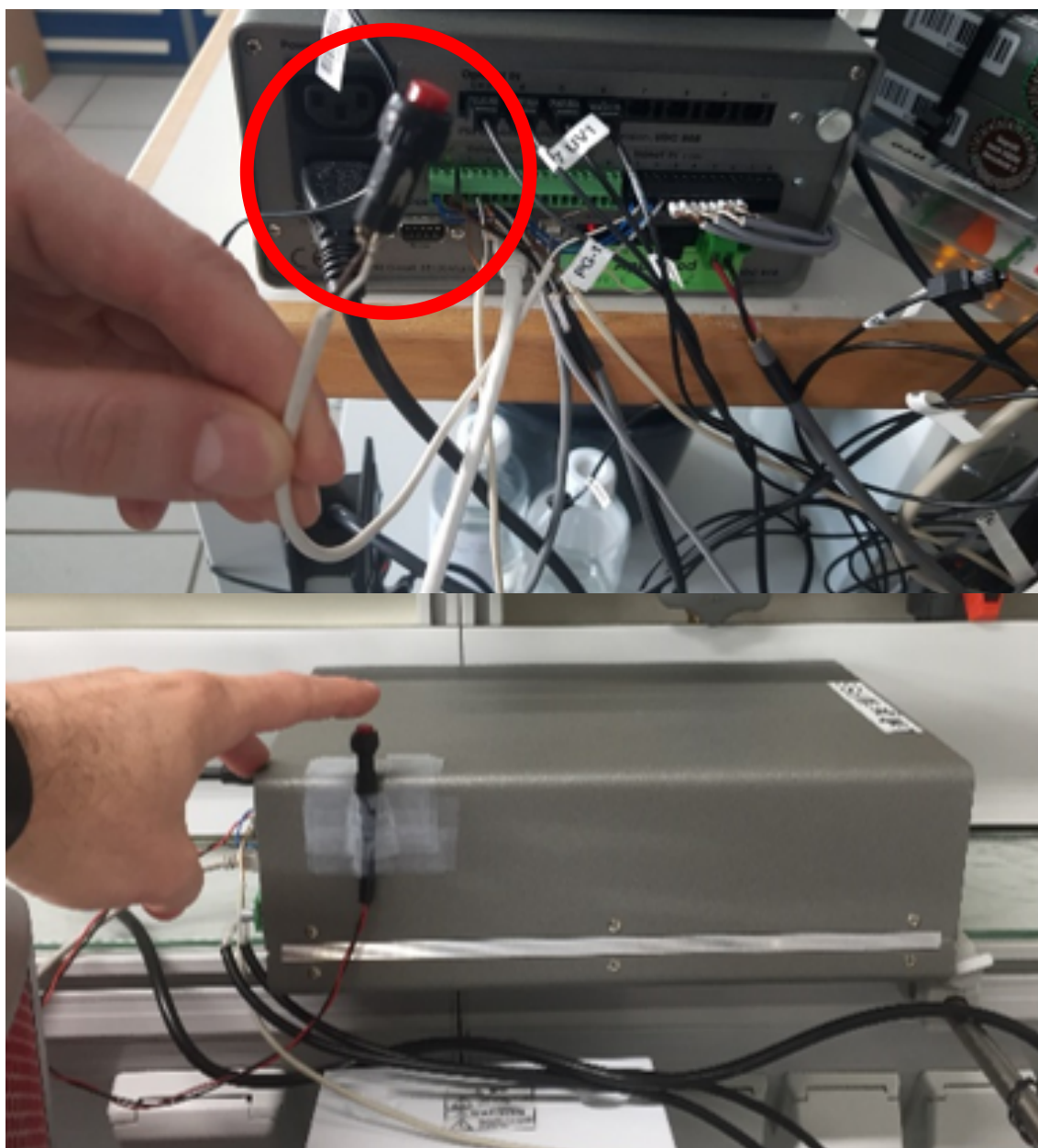


Figure A.6: Photograph of the mock 'injection' trigger used for sinusoidal SEC. The top part illustrates a close-up and bottom part as it looks currently on the UDC box of the SEC-NMR set-up.

A.6 Hardware Description

A.6.1 SEC System

An Agilent 1260 Infinity SECurity system (PSS GmbH, Mainz, Germany), comprising of an iso-cratic pump, in-line degasser was used for ca. 70% of the work presented within this work, but was later upgraded to an Agilent 1260 Infinity II quaternary pump with an integrated degasser unit as illustrated in Figure A.1. Furthermore, the system consisted of a manual injector (Rheodyne 7725i, 20, 100 and 500 μL sample loops with 6 ports), differential refractive index (DRI) detector, and two UV detectors (1260 Infinity and 1260 Infinity II, see Figure A.1, which was only included later for sinusoidal SEC

measurements). The chromatographic separation were performed with a PSS SDV linear M semi-preparative column (300 x 20 mm i.d., 10 μm particle size, mixed bed) and PSS SDV linear M analytical column (300 x 8 mm i.d., 5 μm particle size, mixed bed). Typical sample concentration for SEC-MR-NMR measurements was either 4 g/L or 1 g/L when using a semi-preparative or analytical column, respectively (unless stated otherwise). The injection volumes corresponded to the column employed, and were either 100 or 500 μL , for the analytical or semi-preparative columns, respectively (Injected mass = sample concentration x injection volume). The measurements were mostly performed in protonated CHCl_3 or THF as mobile phase with a volumetric flow rate of 1 mL/min, unless otherwise noted. The SEC components were mostly connected by either 0.25 mm i.d. polytetrafluoroethylene (PTFE) or steel tubing, except for a 0.17 mm i.d. steel tubing (length = 90 cm) from the pump head to the injector as this increased the back-pressure with ca. 3 bars assisting in pump stability. The tubing lengths were as short as possible to reduce excessive dead volume, with a total length of 405 cm ($V = 175 \mu\text{L}$) for SEC-NMR experiments and a length of 429 cm ($V = 187 \mu\text{L}$) for sinusoidal SEC experiments. The DRI data was acquired at a sampling frequency of 2 Hz and data acquisition was performed on PSS WinGPC software version 8.32, build 8844 (PSS GmbH, Mainz, Germany).

A.6.2 Benchtop NMR Spectroscopy System

The medium resolution Spinsolve 60 Ultra NMR spectrometer (carrier frequency: 62 MHz, ^1H (1.45 T), Magritek GmbH, Aachen, Germany) was used within this work. To enable the use of protonated solvents, the instrument is equipped with an external fluorine (^{19}F) lock system (see Chapter 2, Figure 2.16 p. 39) and allows for freely programmable pulse sequences. The spectrometer uses permanent magnets arranged in the Halbach array set-up (see Chapter 2, Figure 2.14 p. 36) with 15 dedicated shims (up to the 3rd order).^[99] To increase sensitivity it is equipped with a single channel ^1H probe head, with the B_0 magnetic field oriented perpendicular to the flow (xy-plane) with a solenoidal radio frequency (RF) coil.^[12] The single channel version of the Spinsolve 60 was used in this study due to the factor ~ 2 higher S/N compared to the dual channel spectrometer, as indicated by the manufacturer's specification sheets.^[91] A typical ^1H linewidth for CHCl_3 is 0.4–0.5 Hz (full width at half maximum, FWHM, at static conditions) and 12–14 Hz at 0.55% of the peak height.^[14,15] Static ^1H -NMR spectra were collected using standard 5 mm NMR tubes. Before every injection, the magnet was usually shimmed to a CHCl_3 or THF line width of 0.7 Hz or 0.9 Hz (FWHM, on-flow), respectively. Additionally, the B_1 frequency was set to the position of the (highest) solvent peak and the receiver phase was adjusted. These settings were then kept constant over the course of the chromatographic run. The pulse sequence consisted of a 90° read pulse (12 μs at full power, 0 dB pulse damping and 100 μs dead time), followed by free induction decay (FID) acquisition (2k points for 409 ms, 200 μs dwell time), and a crusher gradient (20 ms duration at a strength of 5000 a.u. corresponding to a strength of roughly 0.5 mT/m).^[14] The final delay is of variable length in the order of 70 ms to adjust the constant time for one cycle to 500 ms. Four scans with phase cycling of 90° pulses were averaged and the results stored as one

FID. Consequently, an 85 min sample run consists of 2600 FIDs, with 2k points each (1 FID every 2 s). The first dimension of the data being NMR spectral dimension and the second the SEC elution time. The pulse sequence works by exploiting the T_1 -relaxation difference between the polymer and solvent: the polymer relaxes ca. 5–7 times faster than the solvent, based on previous work.^[14,15] The Spinsolve 60 NMR spectrometer is only powered by a standard power cable (230 V) and connected to a desktop computer via a universal serial bus (USB) cable.

Software and Programming Interfaces

The Spinsolve instruments comes sock with two types of software interfaces. The standard Spinsolve software (version 1.13.5) is designed in such a way to enable non-expert to use a 'push-button' type interface to acquire 1D and more complex 2D NMR experiments, which include; ^1H (1D), ^{19}F (1D), COSY, TOCSY, J-resolved (^1H and ^{19}F), including T_1 (inversion-recovery pulse sequence) and T_2 (Carr-Purcell-Meiboom-Gill pulse sequence) measurements. In addition, the shimming is achieved with the aid of automatic shimming algorithms, including a standby-shim protocol. As the standard Spinsolve software is designed for non-expert use not all acquisition parameters are tunable, and also does not allow for freely programmable pulse sequences. In order to provide more user control over acquisition parameter Magritek has developed a second software interface, based on the Prospa programming language, referred to as SpinsolveExpert. It allows for full access to pulse sequence parameters, including pulse sequence programming capabilities, and to allow for full experimental-, process- and data-transfer-control. In addition, it has 1D and 2D processing and display facilities. The pulse sequences used within this work has been achieved by means of the SpinsolveExpert (version 1.26 - SPA810) software.

Magnet Shimming Protocol

Apart from the mechanical shimming performed by Magritek (prior to shipping) on the Halbach magnets to get the magnetic field as homogeneous as possible, additional fine tuned field corrections are required to obtain sub-Hertz resolution. The latter is achieved by finely tuning the electrical current of a set of electrical shim coils. The fine tuning is automatically achieve using a reference shimming standard comprising of $\text{D}_2\text{O}/\text{H}_2\text{O}$ (90/10 w/w%), with the aid of the shimming algorithms provided on the standard Spinsolve software. When performing SEC-NMR experiment, the shimming protocol involves a 'Powershim' (ca. 45 min) on the specific solvent in use, which correct for field inhomogeneities up to the 3rd order (x , y , z , z^2 , zx , zy , x^2-z^2 , xy , z^3 , z^2x , z^2y , $z(x^2-y^2)$, zxy , x^3 , y^3 according the respective Legendre polynomials). The shimming is carried out as an iterative process that ultimately results in a stable setting. After every SEC-NMR measurement within that given day, the 'Quickshim all' (ca. 10 min) protocol is executed to ensure a certain linewidth is maintain. For CHCl_3 ($\delta = 7.24$ ppm) at a volumetric flow rate of 1 mL/min using FC9 (see Chapter 4, Table 4.1 p. 70) a typical linewidth is <0.73 Hz (FWHM) and for THF ($\delta = 3.58$ ppm) a linewidth of <0.90 Hz (FWHM) is typically obtained using the aforementioned shimming protocol.

A.7 Materials Description

A list of the longitudinal relaxation times as a function of the flow conditions.

Table A.1: Longitudinal relaxation (T_1) times of a PS-*b*-PEMA sample at static- ($\dot{\nu} = 0$ mL/min) and continuous-flow ($\dot{\nu} = 1$ mL/min) conditions using chloroform as solvent.

Flow rate (mL/min)	T_1 (s)		
	$\delta_{m-/p-Ar} = 7.10$ ppm	$\delta_{o-Ar} = 6.65$ ppm	$\delta_{-OCH_2-} = 4.10$ ppm
0 ^a	0.408	0.243	0.321
0.2 ^b	0.402	0.241	0.317
0.4	0.397	0.239	0.314
0.6	0.391	0.237	0.311
0.8	0.386	0.235	0.307
1.0	0.381	0.233	0.304
1.2	0.376	0.231	0.301
1.4	0.372	0.229	0.298
1.6	0.367	0.228	0.295
1.8	0.362	0.226	0.292
2.0	0.358	0.224	0.289

^a Performed in CDCl₃.

^b Performed in CHCl₃.

Calibration standards used for the construction of the PS and PMMA calibration curves for SEC-NMR measurements.

Table A.2: Calibration standard sets used for the construction of the PS and PMMA calibration curves in chloroform using a semi-preparative linear M column (see Table 4.3, p. 76).

Calibration Standard Sets					
PS ^a			PMMA ^b		
M_p (g/mol)	M_w (g/mol)	M_n (g/mol)	M_p (g/mol)	M_w (g/mol)	M_n (g/mol)
685	690	630	800	831	730
1 250	1 250	1 120	2 200	2 180	1 980
3 250	3 250	3 100	6 370	6 270	5 880
9 130	8 900	8 650	23 500	23 200	22 500
19 600	19 100	18 100	41 400	40 300	38 100
66 000	62 500	59 300	50 000	49 400	48 000
130 000	125 000	120 000	88 500	86 700	83 700
238 000	239 000	233 000	201 000	199 000	195 000
526 000	524 000	502 000	392 000	380 000	372 000
1 210 000	1 170 000	1 070 000	675 000	655 000	634 000
2 520 000	2 460 000	2 300 000	1 190 000	1 100 000	1 010 000

^a PSS calibration standard lot number: pskitd-05.

^b PSS calibration standard lot number: mmkith-07.

Table A.3: Reference PS and PMMA calibration standards for determining the response factors of the UV and DRI detectors of the triple-SEC used for co-polymer characterization. (see Table 4.19, p. 146).

Response factor (mV/mg)		
Detector	PS ^a	PMMA ^b
UV ($\lambda = 254$ nm)	0.1854	4.53E-4
DRI ($\lambda = 660$ nm)	0.1978	9.01E-2

^a PS calibration standard ($M_p = 130$ kg/mol, $M_w = 125$ kg/mol, $D = 1.04$).

^b PMMA calibration standard ($M_p = 88.5$ kg/mol, $M_w = 86.7$ kg/mol, $D = 1.035$).

Table A.4: Overview of the effect of smoothing and fit combination in SEC-EC-QCL on S/N and FWHM of a PMMA calibration standard determined on the carbonyl group (C=O, $\tilde{\nu} = 1730$ cm⁻¹) of a PMMA calibration standard ($M_w = 49\,400$ g/mol, $D = 1.03$, $c = 5$ g/L). The measurements was performed in pulsed-mode using QCL-1. A flow rate of 1 mL/min with a total injected mass of 80 μ g of analyte was used. See Chapter 5, Figure 5.12 (p. 176)

Filter type	Filter width (s)	Polynomial fit order	R ²	Noise (a.u.)	S/N (a.u.)	FWHM (s)	FWHM increase (%)
No filter	N/A	1	0.961	2.53E-3	23.0	135	–
No filter	N/A	2	0.968	2.53E-3	23.1	135	–
No filter	N/A	3	0.973	2.53E-3	22.9	135	–
Boxcar	1	1	0.972	2.07E-3	27.4	138.6	2.66
Boxcar	1	2	0.978	2.07E-3	27.5	138.6	2.66
Boxcar	1	3	0.979	2.07E-3	27.2	138.6	2.66
Boxcar	10	1	0.984	1.28E-3	43.4	138.8	2.81
Boxcar	10	2	0.991	1.28E-3	43.5	138.8	2.81
Boxcar	10	3	0.991	1.29E-3	43.0	138.8	2.81
Boxcar	30	1	0.988	9.22E-4	59.0	142.1	5.22
Boxcar	30	2	0.995	9.22E-4	59.2	142.1	5.22
Boxcar	30	3	0.995	9.35E-4	57.9	142.1	5.22
Boxcar	60	1	0.990	6.85E-4	77.5	147.2	9.01
Boxcar	60	2	0.997	6.84E-4	77.8	147.2	9.01
Boxcar	60	3	0.997	7.04E-4	75.0	147.2	9.01
Gaussian	1	1	0.978	7.64E-7	32.6	139.6	3.42
Gaussian	1	2	0.985	7.64E-7	32.7	139.6	3.42
Gaussian	1	3	0.985	7.66E-7	32.4	139.6	3.42
Gaussian	10	1	0.988	3.95E-6	61.1	140.5	4.06
Gaussian	10	2	0.995	3.95E-6	61.3	140.5	4.06
Gaussian	10	3	0.996	4.01E-6	60.0	140.5	4.06
Gaussian	30	1	0.991	6.59E-6	101	148.7	10.1
Gaussian	30	2	0.998	6.57E-6	102	148.7	10.1
Gaussian	30	3	0.998	6.97E-6	95.3	148.7	10.1
Gaussian	60	1	0.993	7.52E-6	142	185.2	37.2
Gaussian	60	2	0.998	7.52E-6	143	185.2	37.2
Gaussian	60	3	0.999	8.76E-6	122	185.2	37.2

Publications & Conference Contributions

Publications & Conference Contributions

JOURNAL ARTICLES

- 2014 Botha, C.; Weber, W.; Pfukwa, H.; Pasch, H. (2014). *Controlled Radical Polymerization Using a Novel Symmetrical Selenium RAFT Agent*. *Macromolecular Chemistry and Physics*, 215(17), 1625-1632.
- 2018 Botha, C.; Kuntz, J. F.; Moire, C.; Farcet, C.; Pfukwa, H.; Pasch, H. (2018). *Molar mass analysis of hydrophobically modified hyaluronic acid by SEC-MALLS: facing the challenges of amphiphilic biomacromolecules*. *Macromolecular Chemistry and Physics*, 219(19), 1800233.
- 2018 Botha, C.; Viktor, Z.; Moire, C.; Farcet, C.; Brothier, F.; Pfukwa, H.; Pasch, H. (2018). *Separation of hydrophobically modified hyaluronic acid according to the degree of substitution by gradient elution high performance liquid chromatography*. *Analytical and bioanalytical chemistry*, 410(18), 4259-4273.
- 2018 Höpfner, J.; Ratzsch, K. F.; Botha, C.; Wilhelm, M. (2018). *Medium resolution ¹H-NMR at 62 MHz as a new chemically sensitive online detector for size-exclusion chromatography (SEC-NMR)*. *Macromolecular rapid communications*, 39(7), 1700766.
- 2018 Botha, C.; Höpfner, J.; Mayerhöfer, B.; Wilhelm, M. (2018). *Medium Resolution ¹H-NMR at 62 MHz as a chemical sensitive Online Detector for Size Exclusion Chromatography (SEC-NMR)*. 13th Fall Rubber Colloquium, 118, ISBN 9783981407631.
- 2019 Botha, C.; Höpfner, J.; Mayerhöfer, B.; Wilhelm, M. (2019). *On-line SEC-MR-NMR hyphenation: optimization of sensitivity and selectivity on a 62 MHz benchtop NMR spectrometer*. *Polymer Chemistry*, 10(18), 2230-2246.
- 2019 Kübel, J. M.; Botha, C.; Bucka, A.; Höpfner, J.; Zimmermann, H.; Godejohann, M.; Wilhelm, M. (2019). *A New Quantum Cascade IR-Laser Online Detector: Chemical-Sensitive Size-Exclusion Chromatography Measurement at Unprecedented Low Levels*. *Macromolecular rapid communications*, 40(18), 1900228.
- 2021 Höpfner, J.; Mayerhöfer, B.; Botha, C.; Bouillaud, D.; Farjon, J.; Giraudeau, P.; Wilhelm, M. (2021). *Solvent suppression techniques for coupling of size exclusion chromatography and ¹H-NMR using benchtop spectrometers at 43 and 62 MHz*. *Journal of Magnetic Resonance*, 323 (2021): 106889.
- 2021 Georgantopoulos, C. K.; Esfahani, M. K.; Botha, C.; Naue, I. F. C.; Dingenouts, N.; Causa, A.; Kádár, K.; Wilhelm, M. (2021). *Mechano-optical characterization of extrusion flow instabilities in styrene-butadiene rubbers: investigating the influence of molecular properties and die geometry*. *Macromolecular Materials and Engineering*, 306 (2): 2000801.
- 2021 Matz, M.; Botha, C.; Beskers, T.; Wilhelm, M. (2021). *Fourier Transformation Size Exclusion Chromatography*. In preparation.

CONFERENCE CONTRIBUTIONS

- 01/2015 SCM-7, Amsterdam, Netherlands – Botha, C.; Weber, W.; Pfukwa, H.; Pasch, H. (2014). *Controlled Radical Polymerization Using a Novel Symmetrical Selenium RAFT Agent*. – **Poster**
- 02/2018 Macromolecular Colloquium, Freiburg, Germany – Botha, C.; Höpfner, J.; Wilhelm, M. (2018). *Medium Resolution (MR) ¹H-NMR Spectroscopy as Chemical Selective Detector for on-line Size-Exclusion Chromatography (SEC-MR-NMR)*. – **Poster**
- 07/2018 EUROMAR18, Nantes, France – Botha, C.; Höpfner, J.; Mayerhöfer, B.; Wilhelm, M. (2018). *Medium Resolution ¹H-NMR at 62 MHz as a Chemically Sensitive Online Detector for the Chromatography of Polymers (SEC-NMR)*. – **Poster**
- 09/2018 GDCh, Karlsruhe, Germany – Botha, C.; Höpfner, J.; Mayerhöfer, B.; Wilhelm, M. (2018). *Medium Resolution ¹H-NMR at 62 MHz as a Chemically Sensitive Online Detector for the Chromatography of Polymers (SEC-NMR)*. – **Poster**

- 06/2019 EPF19, Crete, Greece – Botha, C.; Höpfner, J.; Kübel, J.; Wilhelm, M. (2019). *On-line Benchtop Correlation of Molar Mass Distribution and Chemical Composition via SEC-NMR and SEC-EC-QCL*. – **Poster**
- 06/2019 HPLC2019, Milan, Italy – Botha, C.; Höpfner, J.; Pollard, M.; Wilhelm, M. (2019). *Online SEC-MR-NMR – A Powerful Tool in Polymer Analysis, with a Direct Correlation between Molar Mass Distribution (MMD) and Chemical Composition (CC)*. – **Poster**
- 10/2020 PANIC, California, USA – Botha, C.; Pollard, M.; Wilhelm, M. (2020). *Medium Resolution ¹H-NMR at 62 MHz as a Chemically Sensitive Online Detector for the Chromatography of Polymers (SEC-NMR)*. – **Oral**

• Last updated: March 5, 2021 •